UNIVERSITY OF SOUTHAMPTON

GEOLOGY AND BASE-METAL MINERALIZATION ASSOCIATED WITH ARCHAEAN IRON-FORMATION IN THE POJUCA CORPO QUATRO DEPOSIT, CARAJÁS, BRAZIL

A thesis presented for the degree of
Doctor of Philosophy

By

Caroline Jane Winter

Department of Geology
University of Southampton
February 1994

UNIVERSITY OF SOUTHAMPTON

ABSTRACT

FACULTY OF SCIENCE

DEPARTMENT OF GEOLOGY

Doctor of Philosophy

GEOLOGY AND BASE-METAL MINERALIZATION ASSOCIATED WITH ARCHAEAN IRON-FORMATION IN THE POJUCA CORPO QUATRO DEPOSIT, CARAJÁS, BRAZIL

By Caroline J. Winter

The Pojuca Corpo Quatro deposit is host to 58Mt of Cu (at a grade of 0.9%) and 8.5Mt of Zn (1%), and is one of several base-metal (±Au) orebodies hosted within Archaean iron-formation on the northwestern edge of the Serra dos Carajás Belt, in the eastern Amazonian Craton of Pará State, Brazil. The near-vertical, SW-dipping strata, within which the Corpo Quatro (C4) deposit is hosted, is known as the Corpo Quatro Formation, and forms part of the regionally extensive Igarapé Pojuca Group, dated at 2759 Ma. A study of the Corpo Quatro Formation, which is composed of a sequence of interbedded volcanic and sedimentary strata, has revealed that the sequence was originally developed as a result of crustal thinning in an intra-continental rifting environment, in which intermittent volcanic activity was accompanied by the deposition of iron-formation and clastic sedimentary rocks. The volcanic activity is characterized by thick units of basaltic- to basaltic andesite affinity, which are comparable with those found in other lithological groups of the Carajás Belt (Igarapé Salobo Group and Grão Pará Group). Enveloped within the Corpo Quatro basalts, the sedimentary rocks display increased clastic input up sequence, from magnetite-rich iron-formation at the base to quartz-rich pelites at the top. The iron-formation (Rochas Bandadas) at the base of the sedimentary sequence displays mineralogical meso-banding typical of BIF, and grades upwards into silicate (amphibole)-rich iron-formation. This in turn grades into a quartz-rich unit (Rochas Fragmentos), which was formed as a result of mixing of clastic sediments derived from iron-formation and basaltic rock end members. This increase in detrital input is represented by significant enrichment in the relatively immobile elements Al, Ti, Zr, V and Cr, which were introduced via heavy minerals and clays.

The host rocks of the Corpo Quatro Formation underwent an episode of regional metamorphism which reached ~5-7kbar at upper greenschist to lower amphibolite facies (staurolite-andalusite zone), and was followed by Na-Ca-metasomatism which accompanied two closely timed stages of sulphide deposition generated by post-peak metamorphic fluids. The C4 base-metal mineralization occurs mostly in grunerite-rich iron-formation as stratiform and fracture-fill sulphides, and in sulphide-quartz veins which cross-cut the metamorphic sequence. The fluids responsible for mineralization have been identified as Na-Ca-dominant, with the metals probably transported as chloride complexes. The initial stage of mineralization (pyrrhotite-chalcopyrite±sphalerite) was deposited by Na-Ca-(K)-rich aqueous fluids of moderate salinity (4-34 wt.% NaCl eq.). It is believed that mineralization was lithologically controlled, and resulted from sulphidation of magnetite to produce pyrrhotite in the Rochas Bandadas and subsequent replacement of the pyrrhotite by the copper- and zinc-bearing sulphide minerals. Na-Ca-metasomatism of Fe-rich amphiboles in the Rochas Bandadas and albitization of the metabasalts resulted in further deposition of sulphide minerals at temperatures between 280 and 470°C. The second stage of ore mineralization was strongly related to the deposition of quartz-biotite veins, and was generated at slightly lower temperatures (280 to 420°C) by high salinity Na-Ca-K-Fe-rich fluids (15-41 wt.% NaCl eq.). Wallrock-fluid interaction caused retrograde alteration of garnet and hornblende to biotite in the Rochas Fragmentos, which resulted in the deposition of ore minerals (chalcopyrite, sphalerite, molybdenite, gold and nickel-bearing phases) at reaction sites, triggered by the increase in cation content of the high salinity fluids. Retrograde metamorphism continued after the deposition of base-metal mineralization at Pojuca C4, with the local development of chlorite-zone assemblages in narrow (up to 3m-wide) shear zones and the deposition of late calcite-bearing veins.

Acknowledgements

This study was initiated by Drs. R.Foster and S.Roberts and Prof.R.Nesbitt, and carried out as part of a collaborative link between the University of Southampton and the University of Campinas, Brazil. Financial support was generously provided by ISA Instruments (Paris) and Docegeo (Brazil).

The completion of this project, particularly the seemingly never-ending task of writing up, would not have been possible without the continuous support of friends, colleagues and supervisors Bob and Steve, who have helped me over the last three years in terms of advice and support, and enduring my doubts when the project seemed to be going nowhere. Thanks to the Docegeo staff at Belém, for enabling me to work at Pojuca, particularly to Ricardo, Denise, Reinaldo and Amaral, for their advice and company in Carajás and to whom I owe my somewhat limited knowledge of Portuguese. Thanks are also due to Roberto Xavier and Bernardino Figueiredo (Unicamp), for their support and organization skills, without whom fieldwork might have been impossible, and certainly less bearable.

The discussions and suggestions provided by Rex Taylor and Andy Barker, and the patience of Steve Roberts during hours of fluid inclusion and Raman work proved invaluable, and for the advice and assistance in geochemical matters, thanks to Ian Croudace. For sample preparation and technical expertise, thanks to Posy, Bob and John.

For work carried out outside Southampton, I would like to thank Jamie Wilkinson and Sarah Gleeson (Imperial) for giving up their time to get me some D-ICP results, and Andy Tindle (O.U.) for his patience and time running the microprobe.

I would also like to thank those who instilled my love (?) of geology - Laurie Doyle and Steve Flitton, and those who encouraged me, particularly in the field of mineral deposit studies - Drs. Tony Evans and Mike Whateley. Without you I would never have started this - Thanks guys!!

Continuous support and the necessary pint or three were invaluably provided by fellow post-grads, past and present. Special thanks are due to Stephen, for coping with my highs and lows throughout this project and providing inspiration when it wasn't there. Many thanks to Wink, Pam, Rich, John and Jason, for warding off insanity by providing a temporary escape from the interminable hours of writing up. Thanks also to Andrew, Melissa and Dougy, without whom the depression might have set in long ago, and to all fellow post-grads, particularly Helen, Chris Smart, Andy M., Chris F., Andy C., Giles, Lawrence, and Paul Hague, who have helped to make the years at Southampton happy ones. A special mention must also go to the extended family of the LMG 'Troggs' - you know who you are!

Special thanks must, finally, go to my family, who have supported me throughout my seemingly endless years of being a student. I promise it won't last much longer! To Mum, Dad, Sarah, Grandpa, Gally and Gumpa, who have always been there for me, to Granny (RIP), who never saw this work completed, and to Stephen, to whom my thanks are endless. This is for you all, with my love.

Contents

Chapter 6. Discussion

Chapter 1

Introduction to the Pojuca Corpo Quatro Deposit, Carajás, Brazil

1.1 *INTRODUCTION*

The Pojuca C4 deposit is a small copper-zinc orebody, hosting 58Mt of ore graded 0.99% Cu and 8.5Mt of ore running 1.0% Zn, in the Brazilian state of Pará, and is owned by Rio Doce Geologia e Mineração, a subdivision of the parastatal mining company Compahnia Vale do Rio Doce (CVRD). The deposit is in the district of Serra dos Carajás, which, in 1967, following the launch of a major Brazilian mineral exploration programme by the United States Steel Corporation, was identified as one of the worlds largest iron-ore fields (Machamer *et al.*, 1991). Following the discovery of iron in this previously unmapped, densely forested area of the Amazon Craton, many more metalliferous ore deposits were identified, including manganese, bauxite, copper, gold, nickel and tin (Machamer *et al.,op.cit*), making Serra dos Carajás one of the most important metallogenic discoveries in the world, easily comparable with the Hammersley Basin, Western Australia, and the Witwatersrand Basin, South Africa.

The Pojuca C4 deposit was discovered in 1977 by Amazônia Mineração SA (AMZA), following the initial detection of anomalies by a reconnaissance soil geochemistry survey, and two years of extensive stream sediment sampling and diamond drilling (Beisiegel and Ferias, 1978). The copper anomalies seen in the area, originally termed the MM1 prospect, became known as Corpos (bodies) 1, 2, 3 and 4, and at the end of 1982 development was concentrated around anomaly #4, or Corpo Quatro (Saueressig, 1988), with the construction of an exploration adit.

There has been little detailed research carried out on the nature and origin of the Corpo Quatro Cu-Zn mineralization, although the deposit has been described by Beisiegel and Ferias (1978) and by Saueressig (1988), both of whom suggested that the sulphide mineralization in this Archaean iron-formation is of 'typical' syngenetic exhalative type, an idea also supported by Hutchinson (1979) and Medeiros Neto (1987).

This thesis describes a systematic study of the Pojuca Corpo Quatro Formation and ore-body which was undertaken in order to characterise the host rocks and establish the nature and relative timing of mineralization in the area of the Corpo Quatro deposit.

1.2 *AIMS AND OBJECTIVES*

This study of the Pojuca Corpo Quatro Formation and copper-zinc deposit forms part of an on-going research programme focused on the regional geology of the Serra dos Carajás district, in an attempt to provide a better understanding of the stratigraphy, structure, deformation and mineralization in the area. The project forms part of an academic link set up between the Departments of Geology at the University of Southampton, U.K. and the University of Campinas (Unicamp), Brazil.

Prior to this work, knowledge on the Pojuca Corpo Quatro Cu-Zn deposit and the host Corpo Quatro Formation was limited. The local stratigraphy was summarized for internal company reports as

Figure 1.1 **Location map of Serra dos Carajás, Brazil.**

a result of the extensive drilling programme in the area, and the general characteristics of each lithologicalunit described. However, there remained the need for a detailed look at the Pojuca Corpo Quatro (C4) deposit, to fully characterize the petrology and geochemistry of the lithological units. Identification of the geochemical variation between lithological units have been made, and both regional and global comparisons with mineralogically and geochemically similar rocks have allowed the nature and probable environment of deposition of the primary sediments, and the degree of metamorphism to which these rocks have been subjected, to be established, thus adding to the present understanding of the geological history of the Carajás Belt.

The study also aims to determine the style of mineralization and the nature of the mineralizing fluids. The Corpo Quatro deposit has been previously interpreted as a syngenetic massive sulphide deposit (Hutchinson, 1979; Medeiros Neto, 1987), however an initial look at the textures and ore minerals, and the presence of sulphide bearing veins and sulphide-rich alteration zones suggests that this may not be true. A detailed study of the fluids associated with sulphide mineralization and alteration has allowed a new interpretation for the concentration of ore minerals to be made. As well as increasing the knowledge of processes active within the Carajás Belt, and therefore enabling a renewed look to be taken at other deposits in the area, this may also have some bearing on the discovery of future deposits within Serra dos Carajás.

1.3 *THESIS LAYOUT*

Following the brief introduction to the research programme in this chapter, Chapter 2 gives a broad summation of previous research on the geology of the Carajás Belt, describing the individual groups and formations in the Carajás region, as well as summarising the geological evolution of the region.

Chapter 3 focuses on the petrography of the Corpo Quatro Formation, discussing the mineralogy, metamorphism, and sulphide mineralization in each lithological unit. The geochemistry of the units comprising the Corpo Quatro Formation is detailed in Chapter 4, which includes a description and discussion of the geochemical variations between the individual units, as well as comparing the C4 Formation with other similar formations, both regionally and globally.

The study of the veins and associated fluids in the Corpo Quatro deposit is detailed in Chapter 5. Fluid inclusions have been examined using microthermometry, Raman spectroscopy and Decrepitation-linked mass spectrometry, enabling some conclusions to be reached about the mineralizing and other fluid events which have affected the Corpo Quatro Formation.

Discussions concerning individual sections of the thesis can be found at the ends of chapters 3, 4 and 5. Chapter 6 details some comparative information about other deposits in the Carajás region, as well as some aspects associated with similar deposits worldwide, providing an overall discussion which encompasses all aspects of the study, in order to provide an interpretation of the Corpo Quatro deposit in terms of its regional setting. Chapter 7 is a summary, listing the conclusions of this study. Analytical techniques and results, and a geological map of the G1-C4 adit, are presented in the Appendices.

1.4 *LOCATION OF THE FIELD AREA*

The Carajás Belt covers an area of 6000 km^2, and is located in the eastern part of the Amazon Basin (~50°W 6°S), some 550 km south of the city of Belém (*Fig. 1.1*). Serra dos Carajás is a mountainous region, which rises to 400 m above the surrounding plains. 100-200m high escarpments, composed of a ferruginous lateritic crust known as canga, rise from forested valleys to sparsely vegetated plateaus. Whereas the large Carajás iron ore deposits (N-1 to N-5, and S-1 to S-38) are situated on these plateaus, which form EW-trending ridges known as Serra Norte and Serra Sul, many of the copper and gold deposits, including the Pojuca C4 deposit, are found in the densely forested valleys.

The climate in the Amazon Basin is equatorial, and is dominated by the rainy season, when the total rainfall from November through to May can reach 1900mm. Daytime temperatures commonly rise to 45°C, and humidity is up to 100% in the valleys, while the plateaus enjoy a cooler, drier atmosphere. Chemical weathering is extreme, with the soil profile reaching depths of 60m.

The road system in Serra dos Carajás is poor, with laterite roads through the rain forest connecting the main mining and exploration camps. Transport by helicopter is necessary to reach most of the small drilling sites. The residential area sited on the N-5 clearing was built as an exploration and mining camp, and is close to the N-4 iron deposit. The new Carajás residential area, which lies some 10km from the Carajás airstrip, is known as Nucleo Urbano (*Fig. 1.2*). It is small (~1.7 km^2), with a population of about 7000, and lies about 140km (200km by road) to the southwest of Marabá, the nearest settlement.

Protection of the environment is important to CVRD, who govern all the mining activities in Serra dos Carajás, and environmental controls include careful monitoring of the social and ecological impact both in Serra dos Carajás and along the railway to Sao Luís, with extensive rehabilitation of mine sites, prohibiting unnecessary deforestation, the eradication of tropical disease, the creation of botanical and faunal nature reserves, and minimal disturbance to the Amazon Indian population.

The Pojuca Corpo Quatro deposit is situated in the northwest part of the Carajás Belt, about 40km northwest of the nearest town, Nucleo Urbano (about 40km, 1½ hours by 4-wheel drive-vehicle), and 25km southeast of the Salobo 3-A copper workings (*Fig. 1.2*). The deposit is situated in a valley which is drained by the Igarapé Pojuca stream. The camp and core-store lie in a clearing (*Fig. 1.3*), about 1½ km and 15 minutes by dirt track from the exploration adit (G1-C4). The Pojuca C4 deposit has never been worked as a mine, and the only rock exposure is found in G1-C4. However, some 14,000m of core has been drilled during exploration. Since 1984 there has been little activity on the Pojuca C4 deposit, as work has been concentrated on an extensive copper-gold anomaly which was identified in the east of the C4 area at the end of 1984. This anomaly has subsequently been termed Pojuca Leste.

Although both of these deposits, like Salobo Três Alfa Cu (Au) to the north west, are of too low a grade to consider mining in the present economic climate, the study of the style and method of mineral deposition is important in the regional understanding of the area.

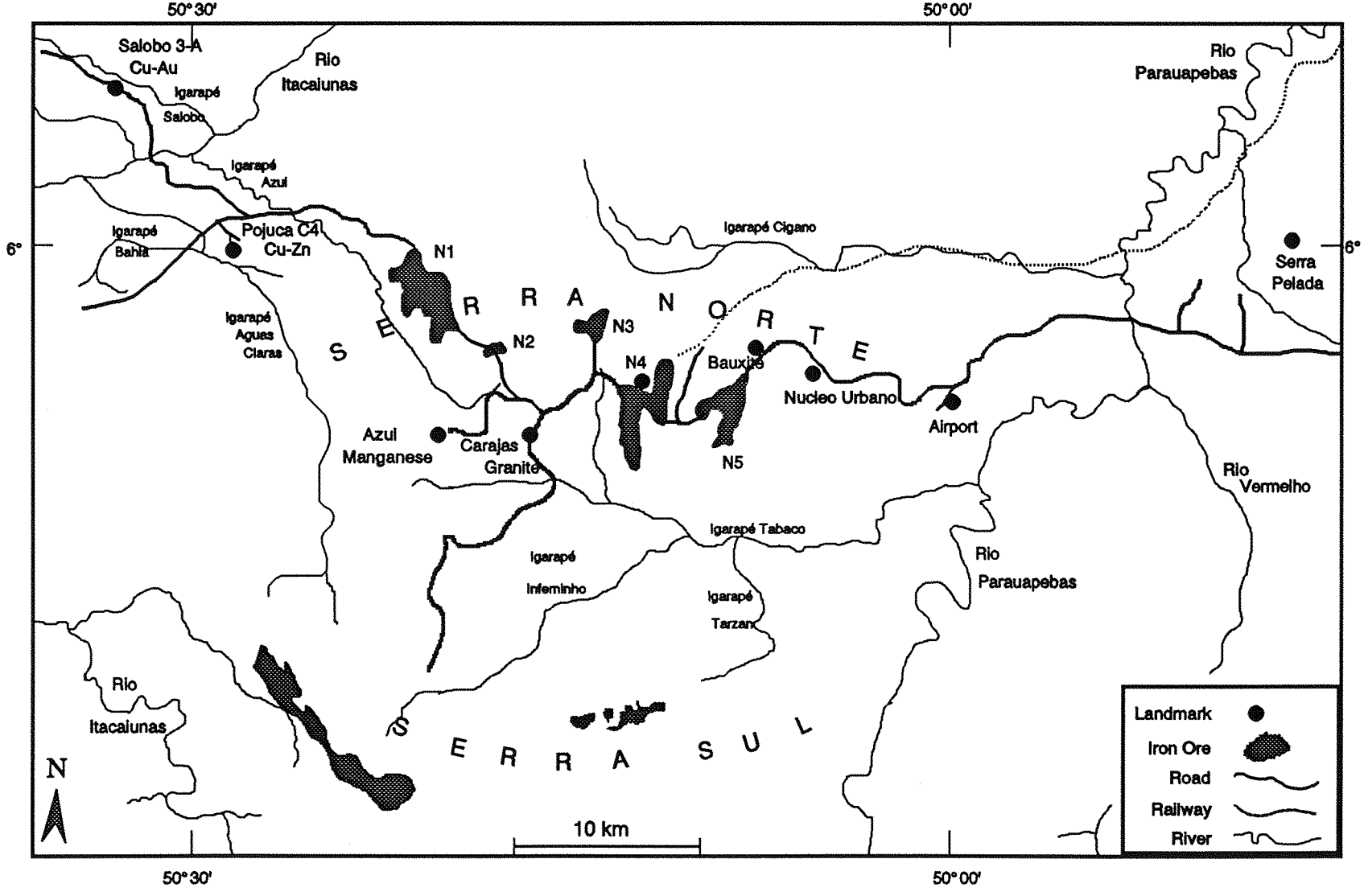

Figure 1.2 **Geographical map of the Serra dos Carajás Belt, showing locations of the main landmarks, camps, iron deposits and mines.**

Figure 1.3 **Pojuca Corpo Quatro and Serra dos Carajás**

A Steep sided valleys and high plateaus in the dense rainforest of Serra Norte, Carajás. Location of the main road can be seen cut into the valley side. Looking north west from N1.

B Location of N5 camp, Carajás, showing unforested ferruginous lateritic plateau (canga) rising above densely forested valleys

C Location and situation of the Pojuca camp and core shed, taken from above and looking south.

D Entrance to the G1-C4 adit at Pojuca

A

B

C

D

Chapter 2
Regional Geology of the Serra dos Carajás Belt

2.1 *INTRODUCTION*

The Pojuca Cu-Zn deposit lies at 50°30'W 6°S, in the area of SE Pará known as Serra dos Carajás (*Fig. 2.1*). The Serra dos Carajás mineral province is bound to the west by the Xingu River, the east by the Vermelho, Araguaia and Tocantins Rivers and the Araguaia fold belt, to the south by Serra dos Gradaus (*Fig. 2.1*), and the north by Serra do Bacajá, covering an area of ~10,000km^2. Serra dos Carajás forms a mountain belt reaching an elevation of 400-500m. Geologically, the area is not particularly well documented, and many discrepancies still exist between authors. This chapter summarizes the knowledge of the region.

Serra dos Carajás is situated within the Eastern Amazonian Archaean Craton, which is composed of granitoids, mafic and ultramafic complexes, granite-greenstone belts and volcano-sedimentary sequences (Docegeo, 1988), dated at between >2850 and 57Ma. (Machado *et al.*, 1991).

Pojuca lies in the north of the Serra dos Carajás region (*Fig. 2.1*), in a sigmoidal WNW-ESE-trending, faulted synclinorium referred to here-after as the Carajás Belt. The synclinorium is composed of metavolcanic and metasedimentary rocks overlying the granitic-gneiss basement of the Xingu Complex with an unknown degree of unconformity. The Carajás Belt is believed to represent an inverted rift basin of Upper Archaean age (Docegeo, 1988) and comprises rocks belonging to the Itacaiunas Supergroup (SIT) and Rio Fresco Group. These have been intruded by several anorogenic granites (Docegeo, op.cit.). The regional stratigraphy is summarized in *Figure 2.2.*

Age relationships and nomenclature of the main lithological units within the Carajás region, particularly those immediately overlying the Xingu Complex, are controversial, resulting from the lack of exposure, paucity of field relationships between lithological units, the extensive weathering of all units and the uncertainty of zircon-dates (U-Pb) in areas of polyphase metamorphism (Machado *et al.*, 1991).

Machado *et al.* (op.cit.) have taken the SIT to cover the period from c.2850 Ma (Xingu Complex) to 1800 Ma (Rio Fresco Group), while Araujo *et al.* (1988) divide the Carajás district into the Xingu Complex, the Grão Pará Group and the Rio Fresco Group, and do not define the SIT. This chapter is based on previous work carried out in the area, and as far as possible follows the terms defined by Docegeo (1988) and used in the construction of *Figure 2.2.* There is, however, still some dispute within this nomenclature, which will be discussed in section 2.3.

2.2 *THE XINGU COMPLEX*

This unit was defined by Silva *et al.*, (1974) and forms the basement to the Carajás Belt, surrounding it to the north and south (*Fig. 2.1*). In this area it is composed predominantly of tonalitic and granitic gneiss (Araujo *et al.*, 1988), migmatites, amphibolites and granodiorites (Docegeo, 1987), and mafic and ultramafic quartz-mica schists (Machado *et al.*, 1991). The general metamorphic grade is

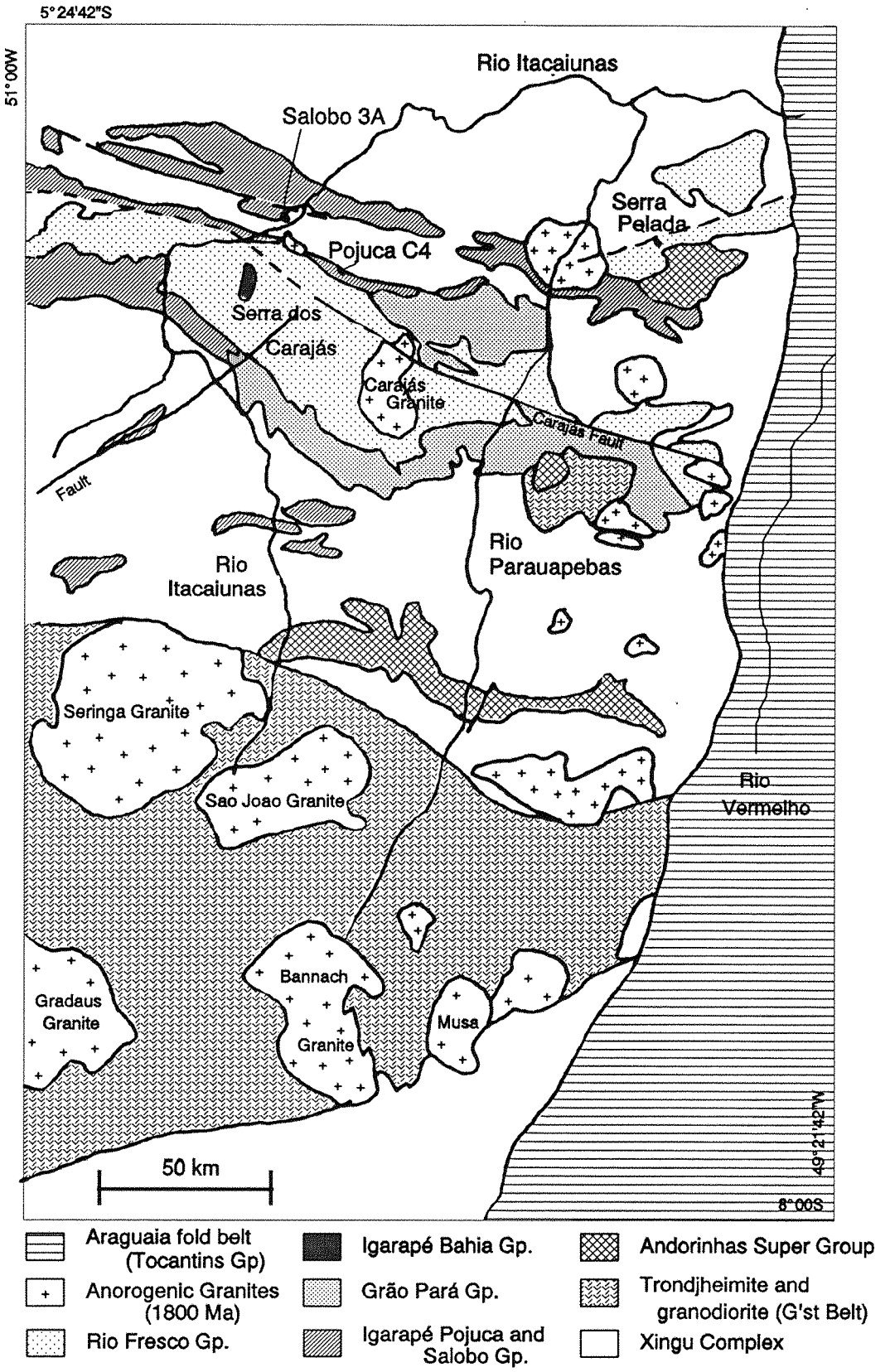

Figure 2.1 **Regional geology map of the Serra dos Carajás and Serra dos Gradaus mineral province (after Docegeo, 1988).**

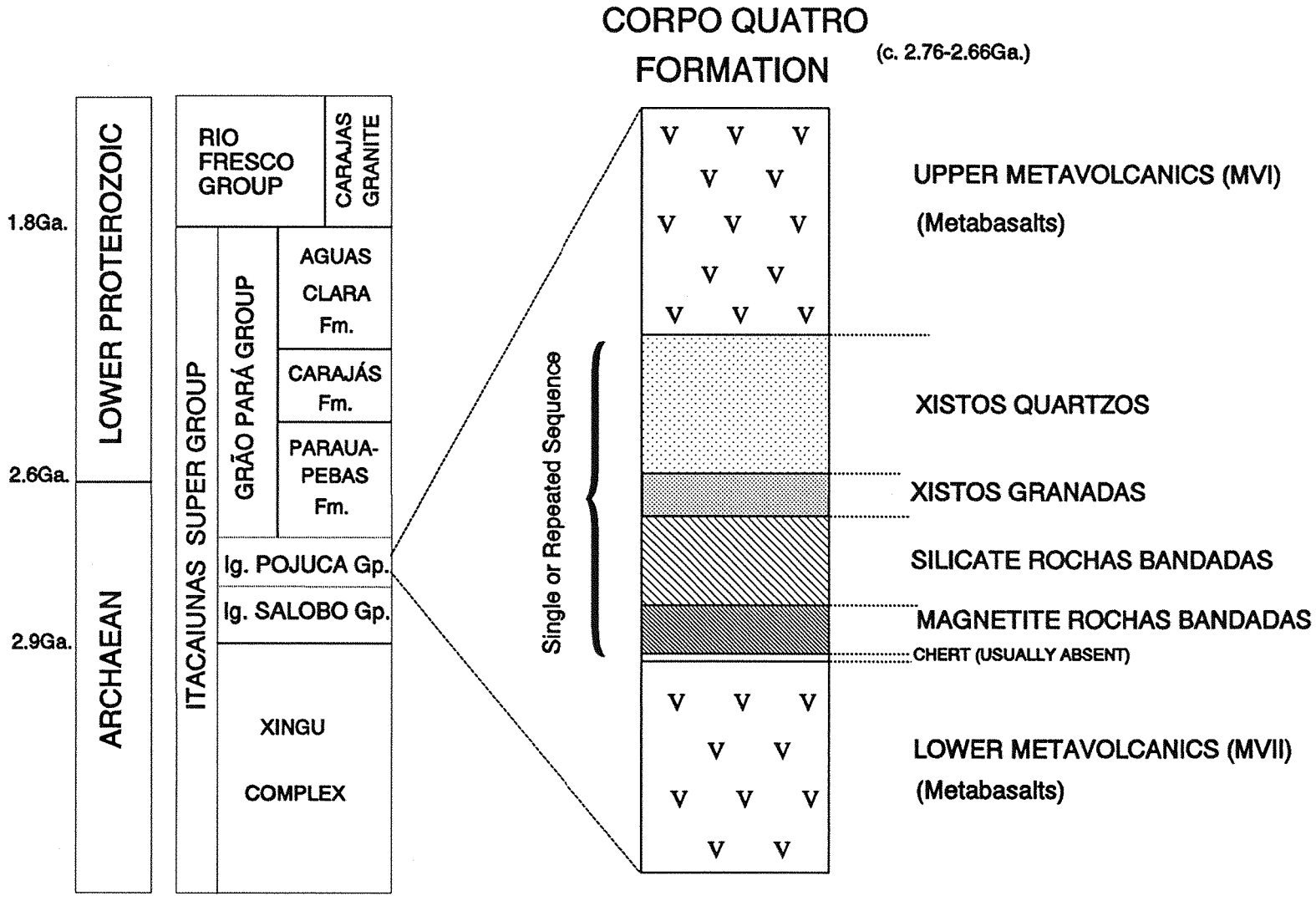

Figure 2.2 **Regional Stratigraphy of the Serra dos Carajás Belt, based on Docegeo (1988) and this study.**

amphibolite or granulite facies (Docegeo 1988). Early Rb-Sr dating gave ages between 1900 and 2250 Ma (Docegeo, *op.cit.*), although recent U-Pb methods (Machado *et al.*, 1991) have dated the migmatites within the Xingu Complex at 2859 Ma. The Xingu Complex has the geochemical characteristics of a typical Archaean granite-gneiss terrane (Machado *et al.*, 1991).

The Xingu Complex covers a wide area, and in addition to the Carajás Belt it encloses several smaller complexes composed of medium to high grade pyroxenites, gabbros and norites (Plaque Suite; Docegeo, 1987), and granitoids (of the Andorinhas Supergroup, Pium Complex; Araujo *et al.*, 1988). These characteristics led authors to believe that the Xingu Complex represents a metamorphically reworked granite-greenstone terrane, in which the Pium Complex was the greenstone belt and the Pláque and surrounding Xingu Complex were the granite-gneiss belts (Machado *et al.*, 1991). 2859±2 Ma is believed to be the date of migmatization, with retro-metamorphism at 2851±4 Ma (Machado *et al.*, op.cit.), prior to the deposition of the overlying Itacaiunas Supergroup and younger sediments.

2.3 *THE ITACAIUNAS SUPERGROUP*

The Itacaiunas Supergroup forms the base, ie. the northern and southern margins, of the Carajás synclinorium (*Fig. 2.1*), and is composed of a volcano-sedimentary sequence which underwent metamorphism during the late Archaean and early Proterozoic (Machado *et al.*, 1991). It includes the Grão Pará Group, a 4-6 km thick sequence comprising metavolcanic rocks and metasedimentary clastic and chemical rocks, as well as the associated Igarapé Salobo, Igarapé Pojuca, Igarapé Bahia and Buritirama Groups (*Fig. 2.2*)

There is some disagreement over age relationships between the Grão Pará, Igarapé Salobo and Igarapé Pojuca Groups. Their similarity and spatial relationships (*Fig. 2.1*) strongly suggest that the Igarapé Salobo and Pojuca Groups are lateral continuations of the main Grão Pará Group, either a 'condensed sequence' of the whole Group, or equivalent to the basal unit of the Grão Pará Group (Lindenmayer, 1990). Variation in metamorphic grade and dates of formation and/or metamorphism, however, indicate that the Igarapé Salobo and Pojuca Groups may in fact be older than the Grão Pará Group.

2.3.1 *The Igarapé Salobo Group*

Hirata *et al.* (1982) placed the Salobo sequence within a unit termed the Salobo-Pojuca Group, although recent work (Lindenmayer, 1990; Machado *et al.*, 1991) has established a number of significant differences between the two groups, and the Igarapé Salobo and Igarapé Pojuca Groups are now seen as individual sequences. On regional maps, however, the two are still grouped together.

The Igarapé Salobo Group lies to the NW of the N4 Iron Mine, on the NW edge of the Carajás Belt. It is thought to represent the oldest part of the Itacaiunas Supergroup, and its degree of unconformity on the underlying Xingu Complex is unknown. The type-section of this group is a subvertical, N70°W trending sequence, which is host to the Salobo Três Alfa (3A) Copper (Au-Mo-Ag) deposit, Brazil's largest copper deposit and believed by Docegeo (1982) to be of sedimentary exhalative

origin. The Igarapé Salobo Group can be divided into three separate formations: the lower Cascata Gneiss, hundreds of metres thick and composed of amphibolite and gneiss (metamorphosed sediments and volcanic rocks; Docegeo, 1988 and Lindenmayer, 1990); the Três Alfa Formation, which is 300m thick and host to the 3A copper deposit (Lindenmayer, 1990), and is composed of metamorphosed iron-formation, greywackes and quartzites, containing zircons dated at 2758±2 Ma.; and the upper Cinzento Formation, 200m of quartzites with intercalated andesitic gneiss, meta-arkoses and schists (Docegeo, 1988). The whole sequence underwent thermal metamorphism to c.750°C early in its history (Lindenmayer, 1990), followed by regional metamorphism to upper amphibolite grade. The Igarapé Salobo Group has been dated at 2851±4 Ma. (Machado *et al.*, 1991), the same age as the thermal event found in the Xingu Complex.

2.3.2 *The Igarapé Pojuca Group*

The Igarapé Pojuca Group occurs throughout the Carajás region (*Fig. 2.1*), but is most significant in the area of the C4 Cu-Zn (Mo) body on the north-west edge of the Carajás Belt. It is composed of three units; the lower, Bueno Formation, which is composed of metavolcanics and iron-formation; the upper, Gameleira Formation, predominantly composed of meta-arenites and siltstones; and the middle, Corpo Quatro Formation (Docegeo, 1987). The Corpo Quatro Formation is named after its type location, at the Pojuca Corpo Quatro Cu-Zn deposit, where it is composed of a sub-vertical metavolcano-sedimentary sequence similar to that seen at Salobo. It is the Corpo Quatro Formation which will be described in detail in this thesis. The Igarapé Pojuca Group has undergone less intense metamorphism than the Salobo Sequence, with no evidence of the early thermal metamorphic event. Like the Salobo deposit, Pojuca has until now been interpreted as a syngenetic exhalative massive sulphide deposit (Hutchinson, 1979). The Igarapé Pojuca Group is also host to a number of smaller copper and copper-zinc deposits, with associated molybdenum and gold (Corpos 1, 2 and 3 and Pojuca Leste).

2.3.3 *The Grão Pará Group*

The Grão Pará Group is the thickest of the Itacaiunas Supergroup subdivisions, and was defined in 1972 by CVRD/AMZA as a volcano-sedimentary sequence which underwent metamorphism to upper greenschist facies during the late Archaean and early Proterozoic (Machado *et al.*, 1991). It has been divided into three subgroups:

Aquas Claras Formation
Carajás Formation
Parauapebas Formation

Parauapebas Formation

The lowermost unit of the Grão Pará Group is sometimes referred to as the Lower Metavolcanic Sequence (Olszewski *et al.*, 1986), and is composed of a metavolcanic suite of basalts and basaltic andesites (Olszewski *et al.*, 1989) with 10 to 15% rhyolite (Olszewski *et al.*, 1986). There are occasional metasedimentary horizons within the sequence, predominantly iron-formations with minor clastic material.

The formation is 4 to 6km thick, and has been dated at 2759 Ma. (U/Pb) by Machado *et al.* (1991), Olszewski *et al.* (1989) and Hirata *et al.* (1987).

Field relations between the Pojuca and Salobo sequences and the rest of the Parauapebas are unclear, and recent zircon U-Pb dating (Machado *et al.*, 1991) has suggested that the Salobo underlies the Pojuca Formation, which in turn underlies the Parauapebas. This depends on whether dates are regarded as depositional or metamorphic, and the most recent work (Lindenmayer, 1990) suggests that they represent lateral variations of the same coeval event.

Carajás Formation

The Carajás Formation is the middle unit, and at present the most economically important unit within the Grão Pará Group. It is essentially a 300m-thick Itabirite (Machamer *et al.*, 1991), which is defined as a quartz-magnetite banded iron-formation, and has been subject to intense weathering to form a haematite deposit, one of the largest (17.9×10^9 t) and richest (>60% Fe) iron-ore deposits in the world (Machamer *et al.*, 1991).

The Carajás Formation and all younger units have undergone only low grade regional metamorphism, and still retain primary sedimentary structures and textures.

Aguas Claras Formation

This sequence forms the top of the Grão Pará Group, and is another volcano-sedimentary unit. It is not known in great detail due to its lack of economic potential. It is 1 to 3 km thick, and comprises basalts at the base and interbedded shales and sandstones towards the top (Olszewski *et al.*, 1986). The basal basalts are similar to those in the Parauapebas (including the Pojuca Formation) (Olszewski *et al.*, 1989 and this report), and have been found to be similar to both ancient and modern continental volcanics, completely atypical of normal Archaean greenstone volcanics, and unlike modern MORB, island arc and hotspot basalts. The top of the Aguas Claras Formation is composed of quartz-rich medium grained sediments which retain sedimentary structures such as ripple marks and cross bedding. Metamorphism has had little effect on this formation, and is of lower to mid-greenschist facies (Docegeo, 1988). The Aguas Claras is unconformably overlain by a massive sedimentary unit known as the Rio Fresco Group.

2.3.4 *The Igarapé Bahia Group*

This subvertical 1km thick volcano-sedimentary sequence has been divided into two formations. The first, the Grota do Vizinho Formation, is composed of basic volcanics, pyroclastics and clastic sediments (sericitized and chloritized pelites and greywackes), which have been dated at around 2750Ma (Ferreira Filho and Danni, 1986). This coarsens upwards, gradually, into the Sumidouro Formation, which is composed of quartz-rich sediments and interbedded basic volcanics (Docegeo, 1987). The sediments of the Grota do Vizinho Formation are host to a low grade (1%) copper deposit, as well as minor occurrences of Cu, Au, Ag and Mo which form as disseminations, fracture-fill and nodules of chalcopyrite and/or bornite. The Igarapé Bahia Group has undergone low grade (lower greenschist) metamorphism.

2.3.5 *The Buritirama Group*

This Group is found to the north of the Carajás Belt, within the Xingu Complex, and forms the uppermost unit of the Itacaiunas Supergroup. It is composed of clastic and chemical sediments (micaceous quartzite, banded quartzite and mica schists) and is host to a manganese deposit with estimated reserves of 17,730 Mt at 40.6 - 54.3 % MnO_2 (Andrade *et al.*, 1986).

2.4 *THE RIO FRESCO GROUP*

This is a massive sedimentary unit, reaching a thickness of 2km. It was deposited between 2000 and 1800Ma as a transgressive sequence in a basin extending from Serra Pelada in the north-east to Cumaru in the south of the Carajás region, and covers the whole of the central part of the Carajás Belt (*Fig. 2.1*). In the Carajás Belt the unconformable relationship between the Aguas Claras Formation and Rio Fresco Group is observed in a recent road cutting. The two Groups are otherwise essentially similar. Coarse grained sediments grade up into silts and chemical sediments (Docegeo, 1987), with graded and cross-bedding frequently seen in these relatively unmetamorphosed sediments (pers. observation). The Rio Fresco Group is intruded by anorogenic granites in the Carajás Belt, and it is believed by a number of authors (Ramos *et al.*, 1984; Wirth *et al.*, 1986) that the transgressive sequence was deposited after the Trans-Amazonian metamorphic event, which was responsible for gneissification within the region, and before anorogenic magmatism.

2.5 *GRANITIC MAGMATISM*

Several granitic intrusions are present in Serra dos Carajás (*Fig. 2.1*), providing evidence of Archaean and Proterozoic anorogenic magmatism (Machado *et al.*, 1991). The two small granitic bodies exposed in the Salobo Sequence near the 3A copper deposit have been dated at 2581 and 2551 Ma (Machado *et al.*, 1991), and they have no visible thermal effect on the nearby Pojuca Formation. Based on titanite and zircon U-Pb dating, their emplacement is thought to be related to the period of regional thrust faulting and metamorphism in the area, as described by Machado *et al.*, (1991), (shown schematically in *Figure 2.3*). There is evidence for the presence of a similar period of magmatism in the C4 area, in the form of granitic veins which cross-cut the Corpo Quatro Formation. The Carajás and the smaller Pojuca Granite, as well as several others outside the Carajás area, are Proterozoic and have been dated between 1883 and 1874±4 Ma. They are anorogenic, alkalic to syenitic granites, contain lode-type wolframite, cassiterite, molybdenite and chalcopyrite mineralization, and have had little thermal effect on the country rocks.

2.6 *REGIONAL HISTORY*

It is thought that during the late Archaean, the Carajás region underwent both thermal and regional metamorphism (Olszewski *et al.*, 1986). Thermal metamorphism affected the Salobo sequence, and occurred during the eruption of the Grão Pará Group volcanics into an opening continental basin. The Grão Pará Group has not been subject to thermal alteration. Following deposition of the Parauapebas

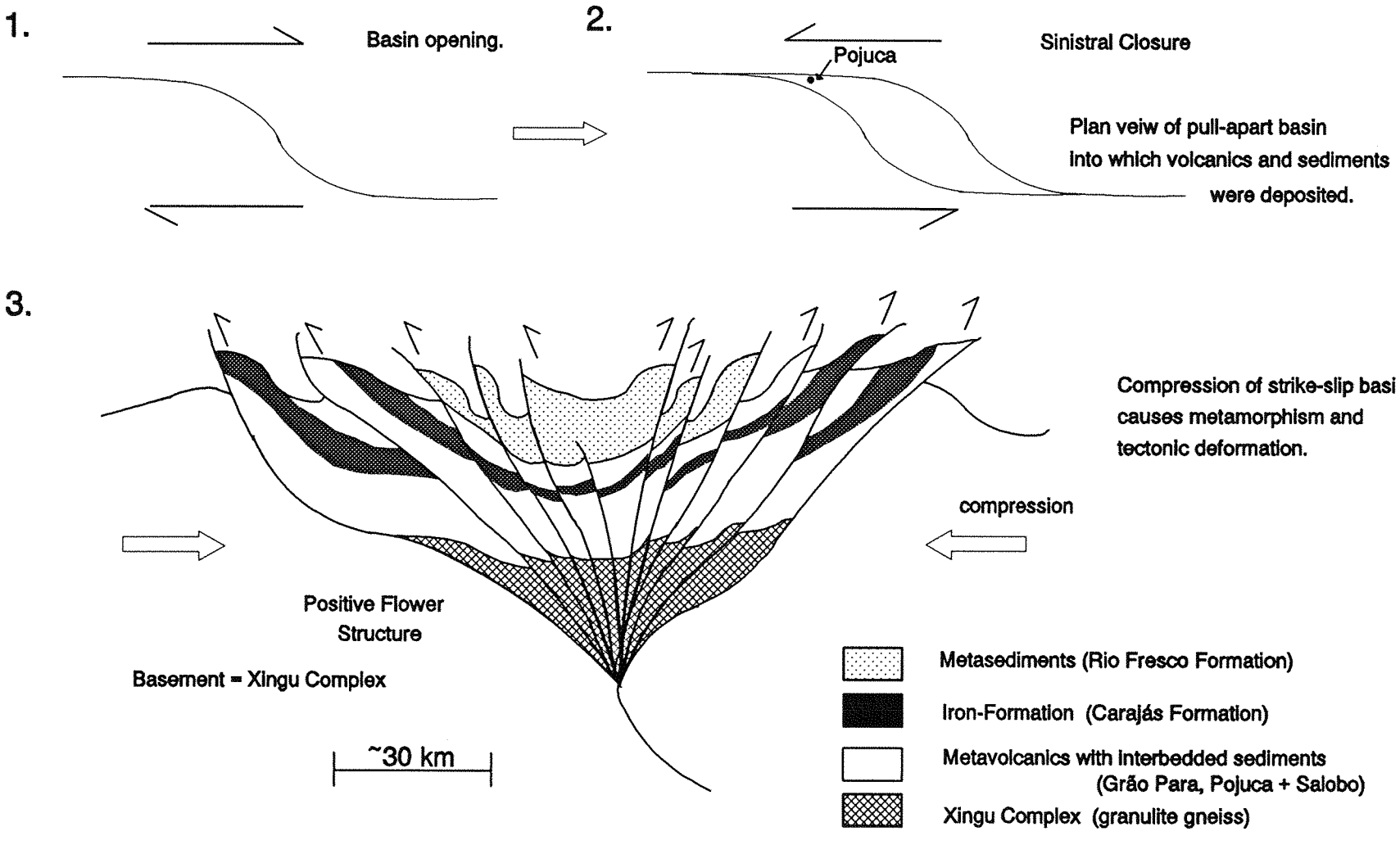

Figure 2.3 **Schematic structural history of the Serra dos Carajás Belt, from the basin opening to the development of a compressional flower structure (after Araujo *et al.*, 1988)**

volcanics and minor sedimentary units, and possibly the Carajás and Aguas Claras at about 2.5 Ga., it is thought that the area underwent compression, with related thrust faulting and metamorphism, and minor magmatism (seen at Salobo) between 2420 and 2320 Ma. (Zr dating by Machado *et al.*, 1991). This was probably the main metamorphic and tectonic event in the area, and was followed by anorogenic magmatism (c.1800Ma.). The structural history of the Igarapé Pojuca Group will be touched upon in Chapters 3 and 5, but more work must be carried out in this area.

Chapter 3
Petrography of the Corpo Quatro Formation

3.1 *INTRODUCTION*

The Pojuca Corpo Quatro (C4) deposit is a small body situated within the steep southwards dipping sequence known as the Corpo Quatro Formation. This is a sequence of metasediments, enclosed to the north and south by metamorphosed volcanic rocks (*Fig. 3.1*). The area around the Corpo Quatro deposit forms the type-section of the Corpo Quatro Formation, which is the middle part of the regionally extensive sequence known as the Igarapé Pojuca Group (*Fig. 2.2*). This Group was named after the Pojuca stream, which drains the area of the C4 deposit (Docegeo, 1987).

The C4 deposit predominantly hosts copper and zinc, with ore reserves of 58Mt averaging .9% Cu and 8.5Mt containing 1% Zn. Minor Ag, Mo, Cd and Au (up to 1ppm) are also present. Copper was first discovered in the area in 1975, by Amazônia Mineração SA (AMZA), using reconnaissance and detailed soil geochemistry. More detailed geochemical and geophysical surveying and ground mapping resulted in the identification of a copper-gold deposit (Pojuca Leste) and four copper-zinc bodies (Corpos 1, 2, 3 & 4) within the Igarapé Pojuca Group the C4 deposit, of which Corpo Quatro (C4) is the largest. A 218m-long, north-trending exploration adit (called G1-C4) was tunnelled through 82m of laterite soils into the C4 deposit at the 300m level, primarily for the purpose of ore reserve estimation. The following study is based on core-logging, adit mapping (*Appendix E*) and thin section studies of samples from the Corpo Quatro Formation.

Sulphide mineralization takes the form of chalcopyrite, pyrrhotite and sphalerite, with minor pyrite, marcasite and molybdenite, and is hosted within the metasediments of the Corpo Quatro Formation (*Table 3.1*). These sediments are up to 100m thick (*Fig. 3.2*) and consist of two major units: at the structural base is a banded, iron-rich rock termed the **Rochas Bandadas** (literally Banded Rocks), which is composed of alternating quartz and amphibole lamellae. This is overlain by quartz ± garnet-rich schists collectively termed the **Rochas Fragmentos** (literally Rocks with Fragments; Medeiros Neto and Villas, 1985) (*Fig. 3.3*). This Rochas Bandadas-Rochas Fragmentos association often forms a repeated sequence (*Fig. 3.2*), and has sharp, un-faulted contacts with the metavolcanic country rocks, which host only minor sulphide mineralization. The G1-C4 adit passes through all but the upper volcanic sequence of the Corpo Quatro Formation.

The metasedimentary-metavolcanic sequence seen in the Corpo Quatro Formation is found in the Igarapé Pojuca Group throughout the Carajás region, and similar sequences can be seen in both the Igarapé Salobo (Lindenmayer 1990; Hutchinson 1979) and Igarapé Bahia (Ferreira Filho and Danni, 1986) Groups.

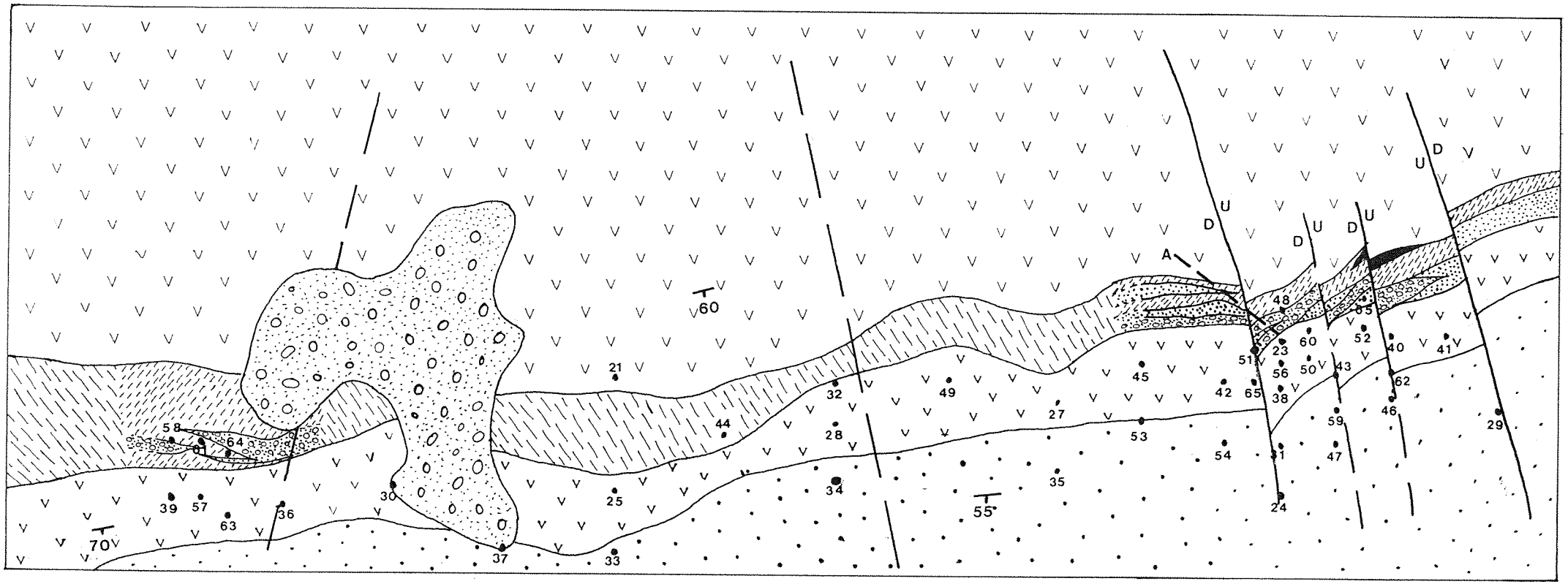

Figure 3.1 Geological Map of the Pojuca Corpo Quatro Area.

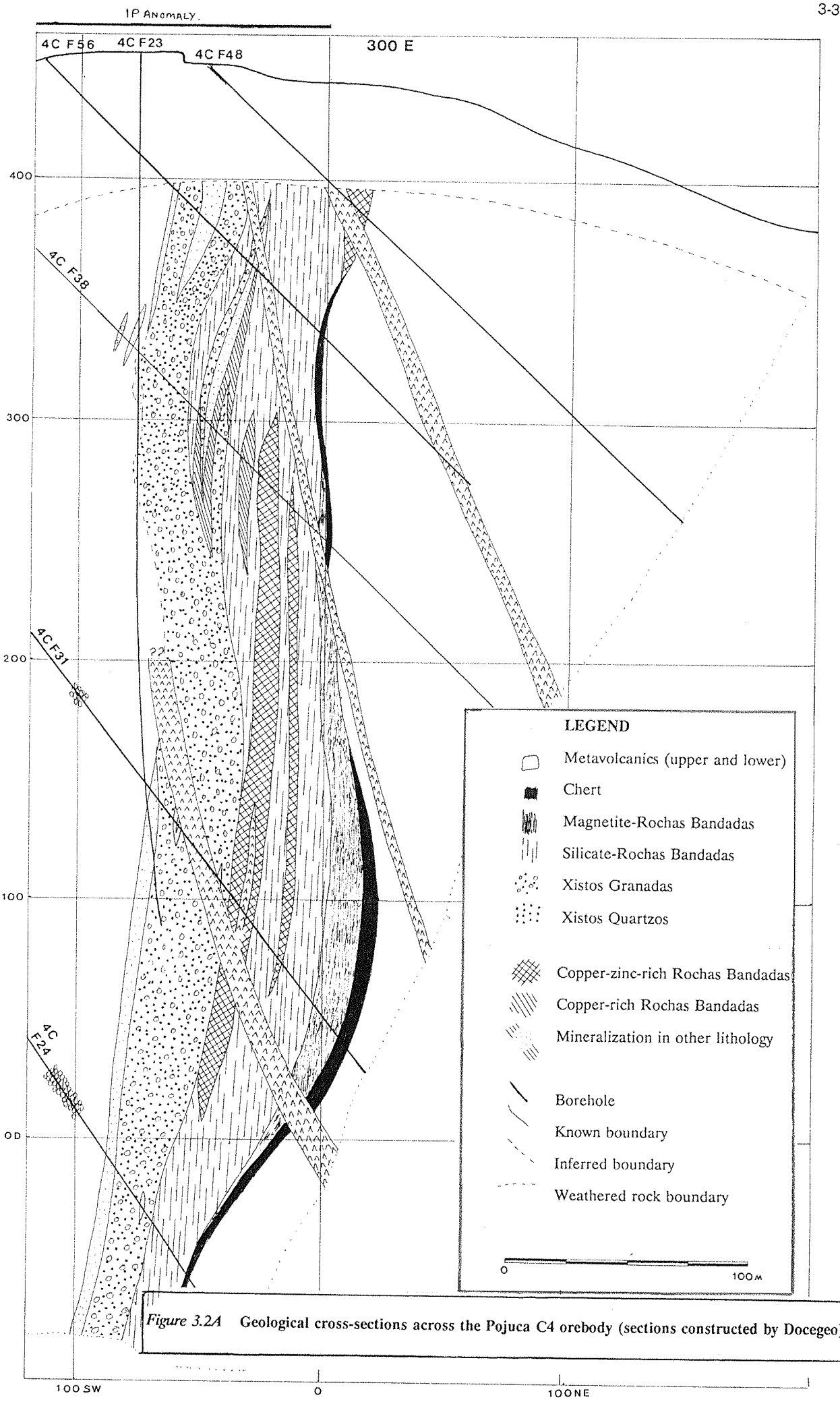

Figure 3.2A **Geological cross-sections across the Pojuca C4 orebody (sections constructed by Docegeo).**

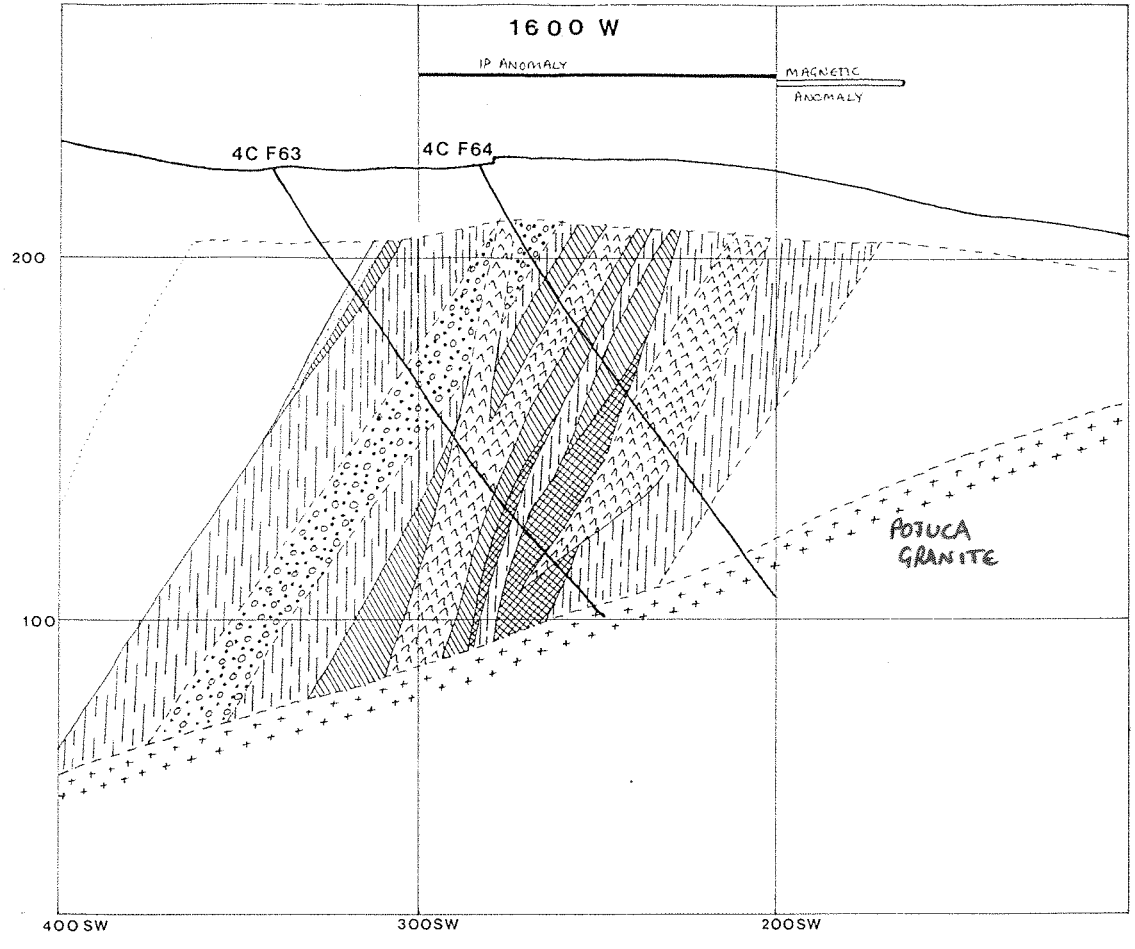

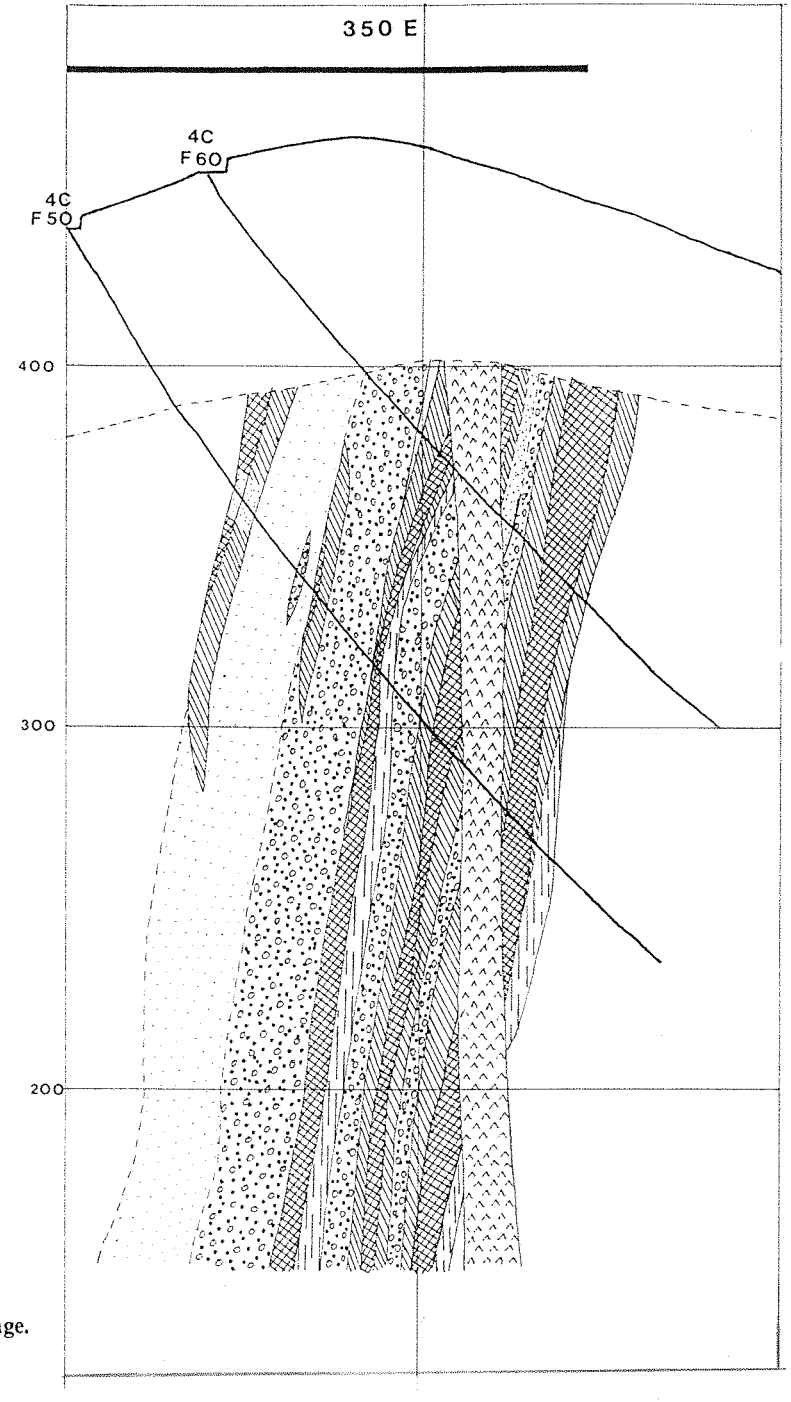

Figure 3.2B Geological cross-sections across the Pojuca C4 orebody (sections constructed by Docegeo). Legend as previous page.

Table 3.1. Metal concentrations in the principal lithologies of the Corpo Quatro Formation. Data, in ppm, from Medeiros (1987) and core logs (DOCEGEO).

	Silicate-Sulphide IF	BIF	Albite Zone	Metavolcanics
Copper (%)	Average 0.5 to 1, max. <5	<0.1	<1.0	<0.05
Zinc (%)	Average 0.2 to 0.7, max. <4	0.02	<0.01	<0.01
Mo (ppm)	40 to 80	10.0	0.1	0.1
Au (ppm)	<0.5	<0.05	Average 0.1, max. 0.56	<0.05
Ag (ppm)	2 to 4	<0.2	<0.2	<0.2
Cd (ppm)	20 to 80	3.0	3.0	3.0

3.2 *THE GEOLOGY OF THE CORPO QUATRO COUNTRY ROCKS*

The Corpo Quatro orebody is surrounded to the north and south by metabasalts (*Fig. 3.1*), comparable in age, origin and geochemistry to those of the Grão Pará Group (Chapter 4; Olszewski *et al.*, 1989; Machado *et al.*, 1991). The C4 metabasalts are of unknown thickness, probably greater than one kilometre, and are composed of massive units with no obvious fabric nor any evidence of flow or pillow structures. The volcanic rocks have been divided into two units, according to structural position relative to the C4 orebody, and named after the order in which they are reached in the drillcore. The first metavolcanic unit (**MVI**) is found to the south, and structurally below the metasediments, and the second (**MVII**) lies above, to the north of the C4 orebody. Mineralogy is uniform, with no apparent variation between the MVI and MVII, although in hand specimen the MVI has a finer grained appearance than the MVII. Throughout the MVI and MVII, millimetre to centimetre veinlets of quartz, calcite, feldspar or epidote (described in detail in Chapter 5), are frequently seen cross-cutting the host-rocks. The lower (MVII) basalts of G1-C4 also contain many narrow (10-50mm) north-dipping, NW-SE trending extensional faults, which contain veins of euhedral quartz.

In the Corpo Quatro Formation there is no apparent evidence of the extrusive nature of these basalts, although elsewhere, in the Grão Pará Group, brecciated flow tops indicate rapid surface cooling on eruption (Gibbs *et al.*, 1985).

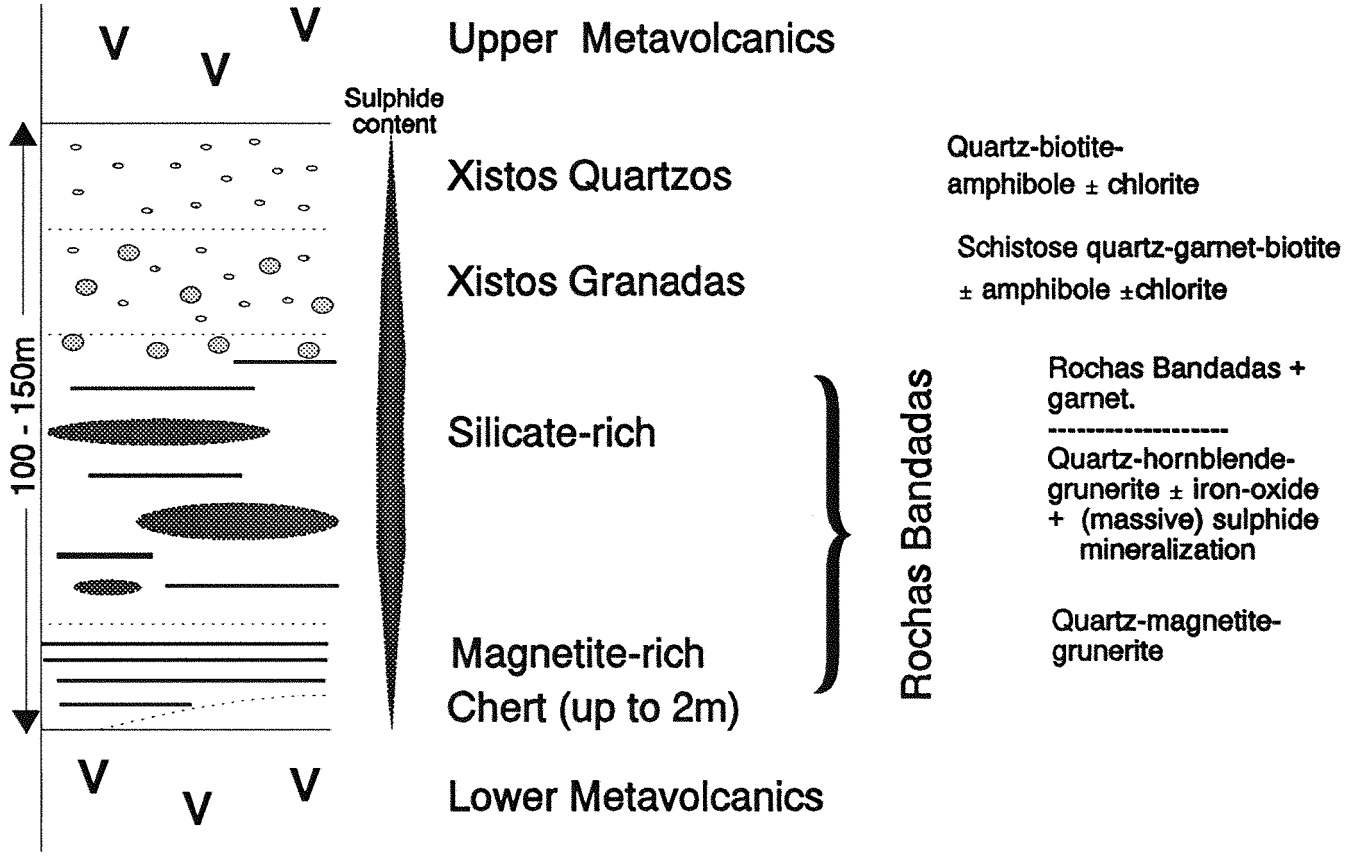

Figure 3.3 **Schematic stratigraphic section through the Corpo Quatro Formation at the Pojuca Corpo Quatro Cu-Zn deposit, based on drillcore and mapping in G1-C4.**

3.2.1 *Mineralogy of the C4 Metabasalts*

The metavolcanics of the Corpo Quatro Formation are fine to medium grained (up to 2mm) massive black-green rocks (*Fig. 3.4A*), which display no obvious internal fabric. Whereas the MVII are exposed in the G1-C4 adit, the MVI can only be observed in drillcore. The mineralogy of MVI and MVII is dominated by amphibole (up to 80 %) and plagioclase feldspar, with minor quartz, orthoclase feldspar and biotite (*Figs. 3.4B&C*). Amphibole and plagioclase crystals are anhedral as a result of alteration, particularly at grain boundaries, to biotite and/or sericite respectively.

Two different amphiboles are present in the C4 metabasalts: xenomorphic, green hornblende, displaying high (second to third order) birefringence, and a more euhedral, blue-green amphibole with first order birefringence, thought to belong to the actinolite family. This second amphibole appears to have developed as a result of the alteration of a pre-existing amphibole or pyroxene, of possible primary volcanic origin.

Amphibole and feldspar grain-size is generally less than 0.5mm, but locally increases to 2mm or more (see section 3.2.3 b). Amphiboles which are wholly enclosed by single feldspar crystals have been observed, as has the reverse, where feldspar laths are enclosed by individual hornblende crystals (*Fig. 3.4B*).

Matrix quartz is rarely present, occurring as equidimensional grains ranging in size from 0.03 to 0.3mm and exhibiting some evidence of strain in the form of undulose extinction (*Fig. 3.4C*). The equant shape and the absence of fluid inclusions in quartz grain cores suggest that the quartz has been recrystallized.

3.2.2 *Metamorphism of the C4 Basalts*

The main mineral assemblage in the Pojuca metavolcanics is green hornblende, oligoclase feldspar (An_{12-14}) and red-brown biotite, with minor chlorite. This assemblage is indicative of upper greenschist (Maruyama *et al.*, 1983) to amphibolite grade metamorphism (Turner, 1968). The only evidence of deformation of these rocks is found in drillcore, where narrow (<1 m) zones of schistose material displaying mineralogical segregation are found (*Fig. 3.4D*). Pyroxene, common in primary igneous and high amphibolite and granulite grade mafic rocks, is absent in the C4 basalts. Combined with the absence of garnet (the presence of which, however, can depend on chemical composition), this indicates that maximum metamorphic conditions were of low to medium amphibolite grade. The absence of haematite and the presence of magnetite and ilmenite also indicates that amphibolite rather than greenschist facies metamorphism has taken place (Miyashiro, 1978). This metamorphic grade is high when compared with the Grão Pará basalts to the south and east of Pojuca, which are composed of plagioclase feldspar, clinopyroxene and minor hornblende, displaying a relatively low grade, primary basaltic assemblage (Olszewski *et al.* 1989).

Figure 3.4 **Pojuca C4 metavolcanics**

A Pojuca C4 metavolcanic rock (MVII), composed of hornblende (dark) and plagioclase feldspar (white). Sample G66.

B Photomicrograph of the C4 MVII. Subhedral and anhedral hornblende (green) enclosing plagioclase laths (brown). Minor quartz and skeletal chalcopyrite. Sample G59. Plane-polarised light. Field of view 3.4mm.

C Photomicrograph of the C4 MVII, comprising plagioclase (brown), biotite (mottled) and quartz (white). Skeletal chalcopyrite imitates amphibole cleavage, and is later overgrown by hornblende. Sample G59. Cross-polarised light. Field of view 3.4mm.

D Photomicrograph of quartz-hornblende 'banding' in schistose MVI. Sample F8. Plane-polarised light. Field of view 6.8mm.

E Photomicrograph of hornblende-rich MVII, showing fine grained hornblende, polygonal quartz, and opaques, cross-cut by biotite veinlets. Plagioclase absent. Sample F5. Plane-polarised light. Field of view 3.4mm.

F Hand specimen showing the sharp contact between the unalbitized and albitized MVII, cross-cut by a chalcopyrite veinlet. Sample G45.

G Hand specimen from the G1-C4 Albite Zone. Rock comprises albite and minor opaques (ilmenite, grey-brown; chalcopyrite, not visible). Sample G54.

H Drill-core specimen showing clearly the association between albitization (white) and massive ilmenite (grey-brown) in the C4 metavolcanics.

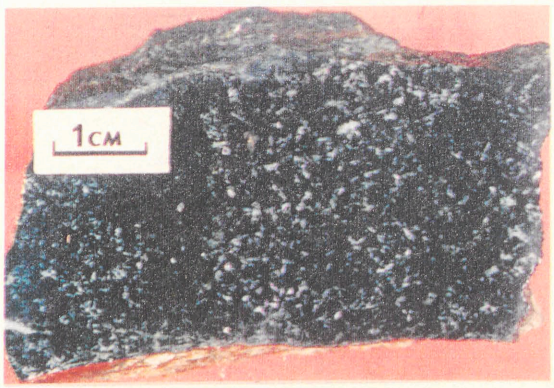

A

B

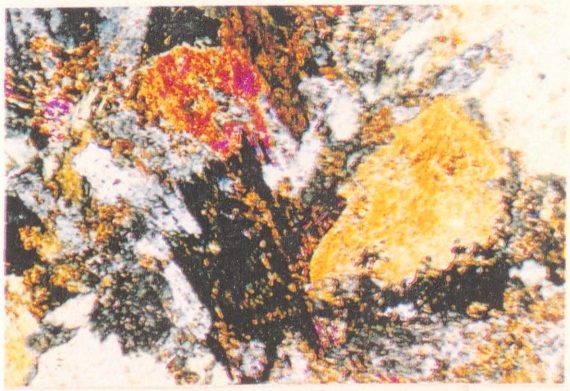

C

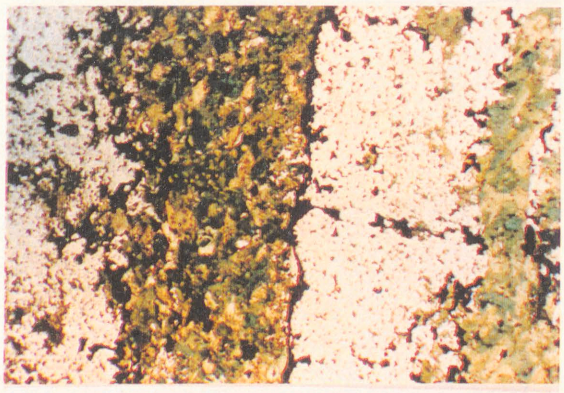

D

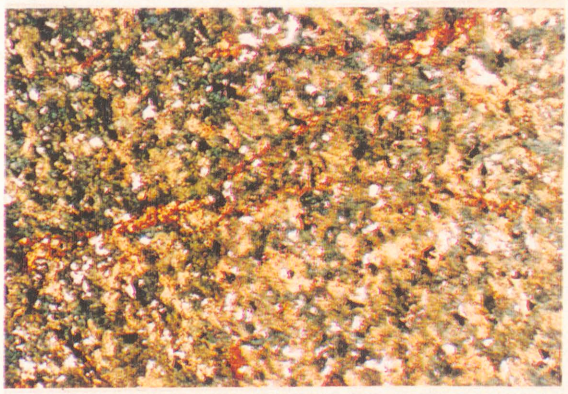

E

F

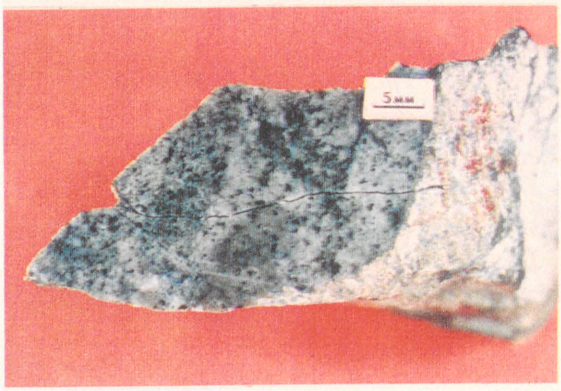

G

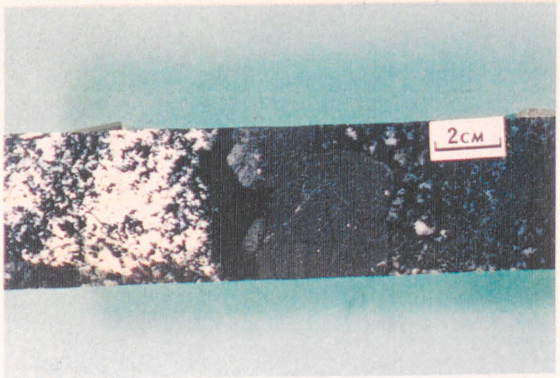

H

3.2.3 *Alteration of the C4 Metabasalts*

In addition to regional metamorphism, the C4 basalts have been subject to a number of other hydrothermal events, resulting in the development of alteration assemblages. These are discussed below.

Albitization

Albitization is present in both the upper and lower volcanics around the Corpo Quatro deposit. The alteration assemblage is composed almost entirely (approx.95%) of sericitized albite feldspar, and minor (up to 5%) epidote, ilmenite, chalcopyrite and chlorite (*Figs. 3.6A&B)*, which results in the rock taking on a bleached appearance. Approximately 10m to the south of the metasediments in G1-C4 is a 15m-wide unit of this predominantly pale grey to white rock, which is termed the **Albite Zone**, and is the largest area of albitization yet observed at Pojuca. The Albite Zone has sharp, discordant contacts with the green-black metabasites enveloping it (*Fig. 3.4F*), although it locally displays gradual contacts (over 5-10cm) with the wallrock. Albitization in the drillcore, in both MVI and MVII, is on a smaller scale, ranging from 1m to 10m across. Patches up to 2m across can be observed adjacent to plagioclase-filled fault zones in G1-C4 (*Fig. 3.5*), although the main Albite Zone in G1-C4 shows no direct relationship with any faulting. The Albite Zone, like the metabasalts, shows no internal fabric or foliation, but hosts narrow veins of coarse tourmaline crystals (up to 30mm-long) ± chalcopyrite and 20m to 30mm-wide quartz bands, which dip at 40° towards the SW (220°). The geochemistry of the Albite Zone is discussed in Chapter 4.

Cross-cutting the contact between the top of the Albite Zone and the metavolcanics in G1-C4, is a 1 to 1.5m wide zone of hornblendite, composed of irregularly distributed hornblende and ilmenite. Although ilmenite generally makes up only 10-30% of the assemblage, it locally constitutes up to 80% of the rock. The association between albitization and hornblende-ilmenite is also seen in the drillcore (*Fig. 3.4H*), but as the hornblendites do not contribute significantly to the geology of the Cu-Zn deposit they have not been studied in this project.

Potassic Metasomatism

Potassic alteration occurs throughout both the upper and lower metavolcanics. It is particularly apparent in thin section, where grain boundaries of amphibole and plagioclase feldspar have been altered to biotite and sericite respectively, creating an assemblage of anhedral silicate minerals from previously relatively euhedral metamorphic minerals, indicating that potassic hydrothermal alteration post-dated peak metamorphism.

Close to the zones of albitization in the drillcore, the grain size of both biotite and hornblende, and occasionally plagioclase (*Fig. 3.6C)*, increases from 0.5mm to 2mm or more. This is sometimes accompanied by quartz or plagioclase veinlets, and tourmalinization (*Fig. 3.6D)*, where euhedral, zoned tourmaline crystals nucleate around chalcopyrite. The euhedral nature of the tourmaline, which overprints the metamorphic mineral assemblage, indicates that tourmalinization is

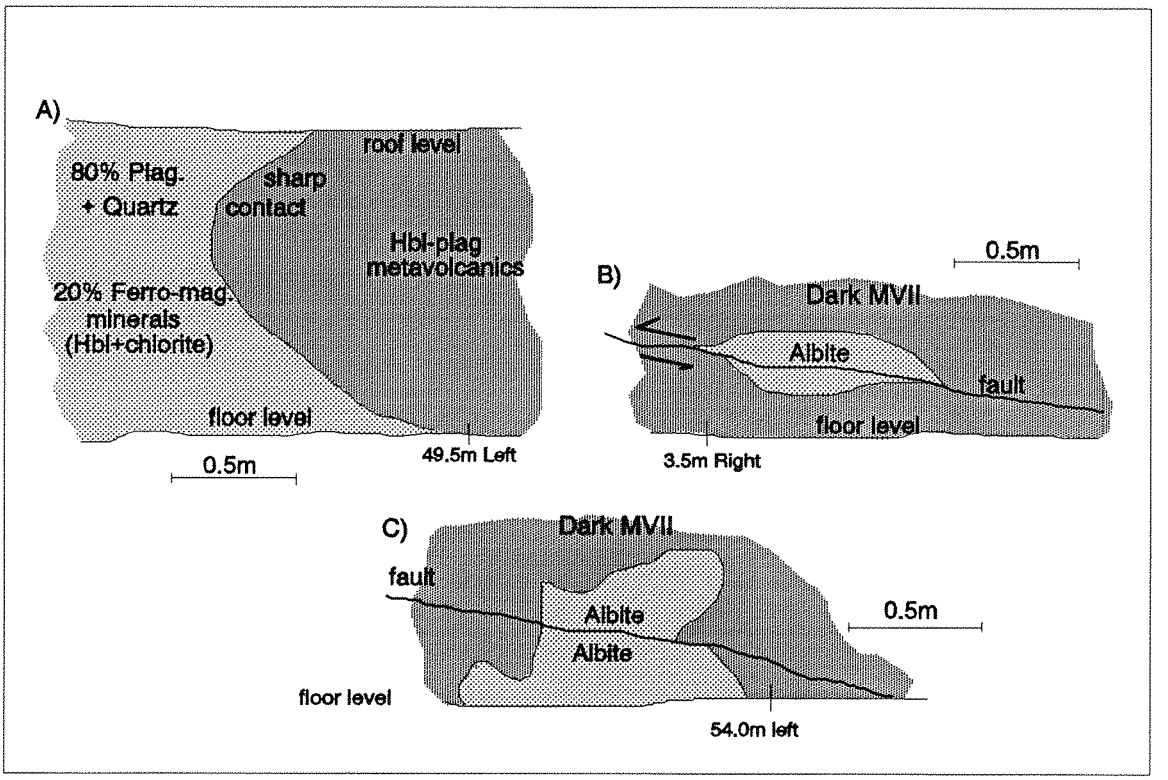

Figure 3.5 **Schematic sketches of the relationships between the G1-C4 Albite Zone and the host Corpo Quatro metavolcanics. Pale shading = Albitized basalt, dark shading = unalbitized basalt. A Contact between main zone of Albitization and host rock; B and C Albitization surrounding small faults in the metabasalts. Scale and location in G1-C4 shown.**

Figure 3.6 **Alteration in the Pojuca C4 metavolcanics**

A Photomicrograph from the G1-C4 Albite Zone, showing dominance of plagioclase (albite) over chlorite (green) and magnetite (opaque). Sample G60. Plane-polarised light. Field of view 6.8mm.

B Photomicrograph of plagioclase feldspar (grey, twinned), and sericite (high birefringence) with subordinate ilmenite and chalcopyrite (opaque) in the G1-C4 Albite Zone. Sample G61. Cross-polarised light. Field of view 3.4mm.

C Drill-cor specimen of C4 MVII which has undergone metasomatism and increase in grainsize, particularly of plagioclase feldspar (white). Sample F88.

D Photomicrograph of euhedral zoned tourmaline (green triangular and brown prismatic crystals, top and left) in a quartz-hornblende matrix in the C4 MVI. Sample F4. Plane-polarised light. Field of view 3.4mm.

E Drill-core showing 'dalmatianite' overprint on the C4 MVII. Cordierite = pale grey, anthophyllite = dark matrix.

F Photomicrograph of cordierite-anthophyllite alteration on MVI. Cordierite (white) surrounds biotite (brown) which appears to have nucleated around ilmenite grains. Sample B6. Cross-polarised light. Field of view 6.8mm.

G Photomicrograph of ilmenite (opaque) and rutile (translucent, brown) developed in the C4 Albite Zone. Sample F82. Plane-polarised light. Field of view 2.2mm.

H Photomicrograph as G, reflected light. Ilmenite grey, high reflectance in contrast with rutile.

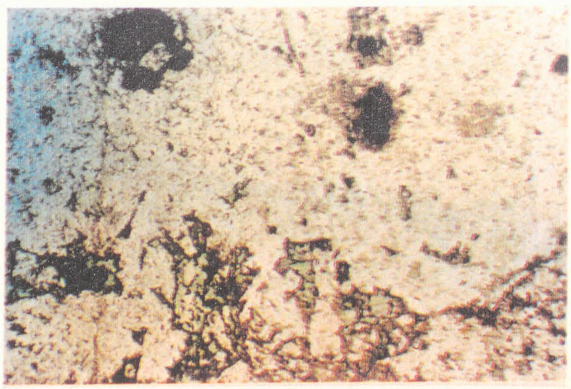

A

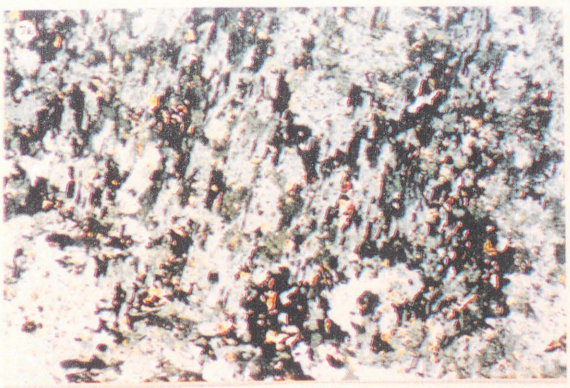

B

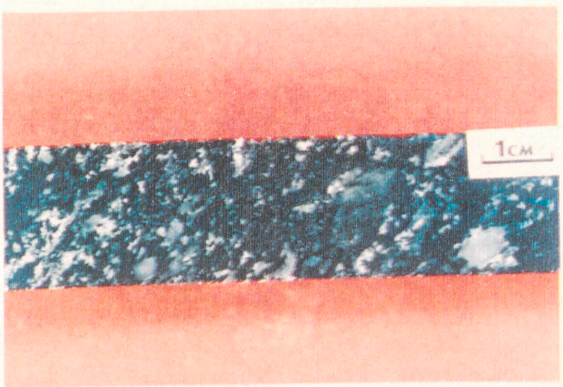

C

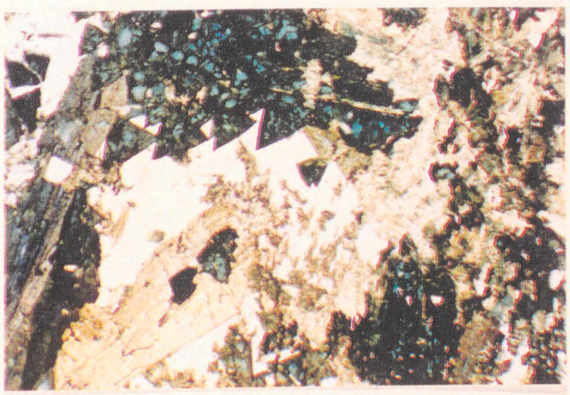

D

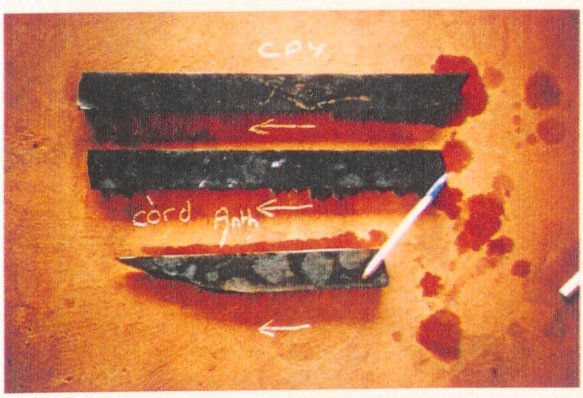

E

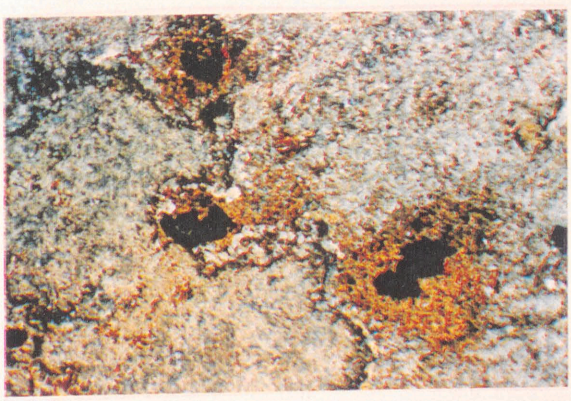

F

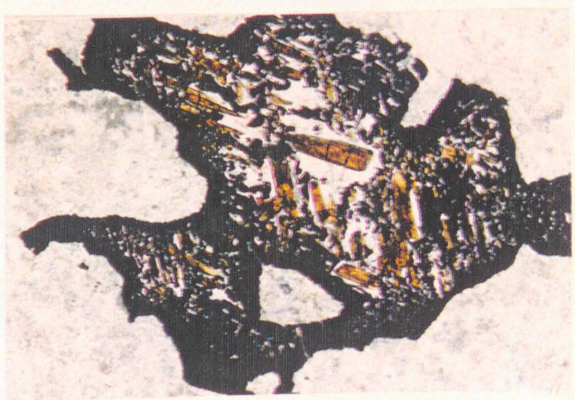

G

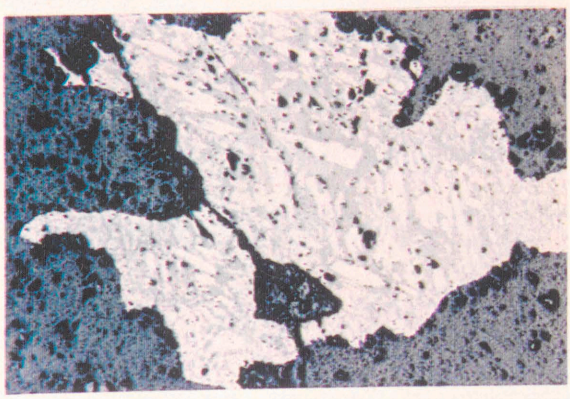

H

a late-stage event. Biotite 'spotting' is also evident in metabasalts at the margins of albitic alteration zones. The biotite crystals are 1-2mm across, and stand out against the green-grey of the groundmass.

Cordierite-Anthophyllite.

Cordierite-anthophyllite assemblages in the C4 metabasalts have been termed 'Dalmatianites' by Docegeo (Oliveira, *pers.com.*), due to their spotted appearance (*Fig. 3.6E)* and similarity to the dalmatianites described from the Manitouwadge area, Ontario, and the Rouyn-Noranda copper district, Quebec (Sangster and Scott, 1976). The spotted texture is created by large cordierite aggregates (up to 50mm across), which in plane-polarized light are coarse grained, pleochroic white-grey, with a hexagonal, sometimes spongy form, The cordierite is frequently altered to sericite (*Fig. 3.6F*), and is enclosed in a dark coloured anthophyllite-biotite matrix. Ilmenite forms individual rounded grains in the cordierite-anthophyllite assemblage, around which red-brown biotite has nucleated. In the Corpo Quatro Formation this assemblage occurs predominantly in the upper (MVI) metavolcanics, where it has been cross-cut by quartz-chalcopyrite veins.

Veining

Vein mineralogy in the G1-C4 metavolcanics is described in detail in Chapter 5, and shows an apparent zoning towards the overlying metasediments. This zoning has not been studied in the drillcore. Distal from the metasedimentary rocks, the veins are composed of barren quartz, whereas closer to the metasediments the veins are composed of chalcopyrite-bearing quartz, potassium feldspar, epidote and chalcopyrite. Calcite veins also become progressively more abundant up the sequence (*Fig. 3.7*). The chalcopyrite-bearing quartz and carbonate veins are commonly hosted within narrow (2-5mm) north-dipping, normal faults, whereas feldspar and epidote veins, which are also chalcopyrite-bearing, appear to be un-related to displacement (*Appendix E*). Cross-cutting carbonate veins suggest that there have been at least two phases of calcite precipitation.

Wallrock alteration caused by veining is limited to a microscopic (sub-millimetre) scale, with fine-grained green-black chlorite forming at the margins to carbonate veins, and biotite forming at the margins of quartz veins.

3.2.4 *Sulphide Mineralization in the C4 Metabasalts*

Chalcopyrite with accessory pyrrhotite make up <1% by volume of the Corpo Quatro metabasalts, occurring as subhedral to anhedral and skeletal disseminated grains, or in quartz or K-feldspar -epidote veins. Skeletal sulphides follow the characteristic 56/124° cleavage of pre-existing amphibole crystals, which have since been replaced by secondary hornblende and biotite (*Fig. 3.4A &B)*. Massive chalcopyrite mineralization is occasionally observed in the metavolcanics, for example drillcore F55 (219m) shows 20mm-wide massive chalcopyrite around a quartz-filled fracture. This chalcopyrite has been overprinted by euhedral, probably hydrothermal, dark green amphibole crystals.

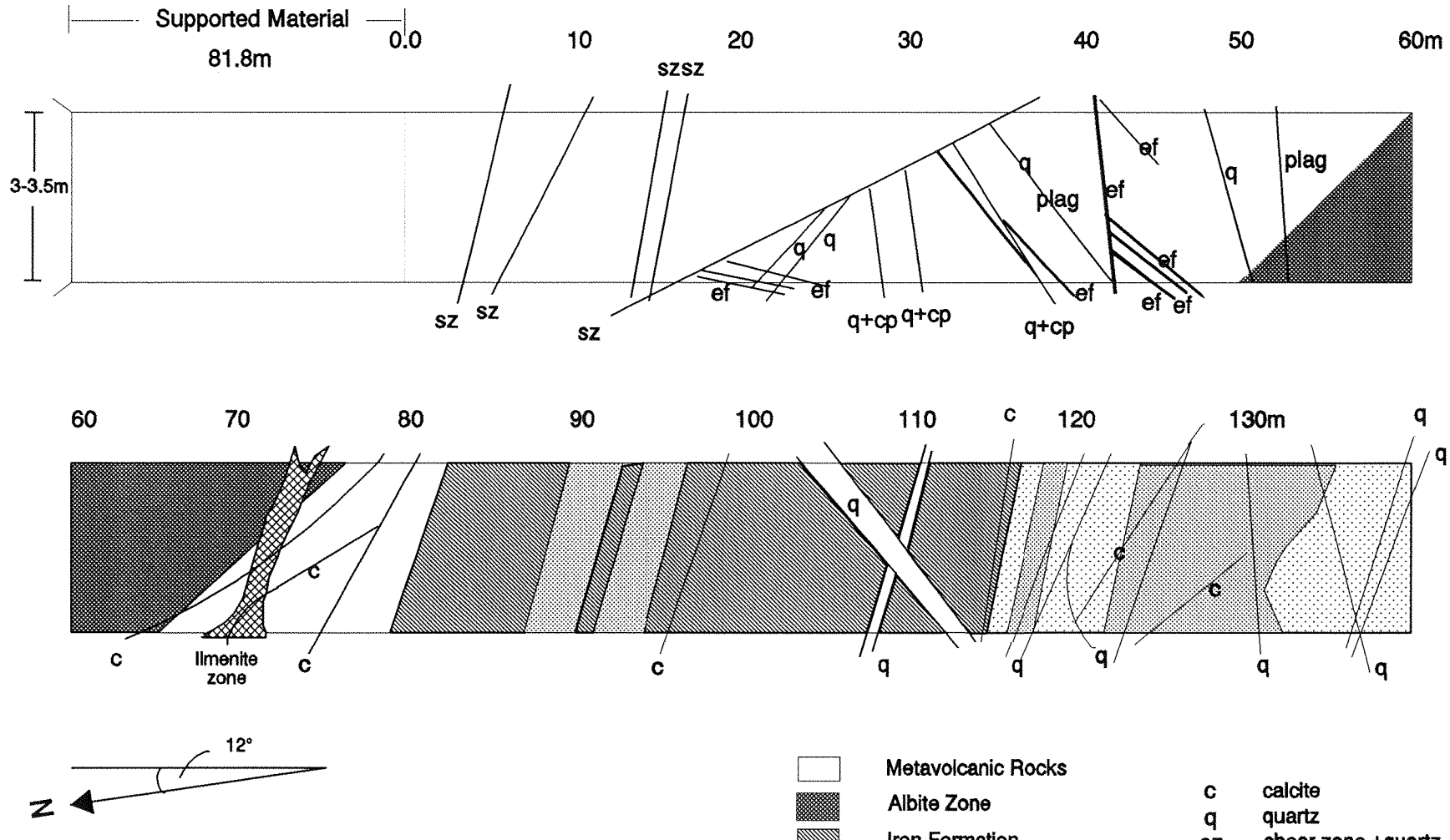

Figure 3.7 Schematic geological map of the G1-C4 Adit, Pojuca, showing the apparent zoning of the vein mineralogy from the metabasalts into the metasediments. (Mapped at waist height)

Sulphide mineralization is more common in the areas of albitization than in the unaltered metabasites; for example, the G1-C4 Albite Zone contains abundant chalcopyrite, which occurs as veinlets, as inclusions within and attached at the margins of ilmenite grains, and as massive, discrete aggregates, which can reach up to 1m across. Although gold is not visible, even in thin section, assay results from the Albite Zone give gold grades of up to 0.56ppm, averaging 0.3ppm, which is high compared with an average of <0.1ppm in the metasediments. Volumetrically, chalcopyrite constitutes up to 2% by volume of this lithology, and assay values (Docegeo, core logs) show that Cu grades of up to 1% are achieved.

3.2.5 *Oxide Mineralization in the C4 Metabasalts*

The oxide minerals magnetite (Fe_3O_4) and ilmenite ($FeTiO_3$) are a common feature of regionally metamorphosed mafic volcanics, not least in the C4 Formation, where it has already been mentioned that hornblendites contain abundant ilmenite (Section 3.2.3a). Coarse-grained ilmenite (1cm aggregates) is particularly common in the Albite Zone, where it commonly displays 111 twinning. The volume of ilmenite in the metavolcanic rock is noticeably increased in close proximity to tourmaline mineralization. This concentration in specific areas, implies that ilmenite is a result of the hydrothermal transport and deposition of titanium.

3.3 *THE PETROGRAPHY OF THE COPPER-ZINC HOST ROCKS*

Defined by Docegeo (1988) as the 'Rochas Bandadas' due to their banded texture, these rocks host most of the copper and zinc in the Corpo Quatro deposit. They are iron-rich metasediments, and lie structurally immediately above the MVII (*Fig. 3.2 and 3.3*). Copper and zinc are held in the form of chalcopyrite and sphalerite respectively, and grades commonly reach 4.5% Cu and 5% Zn towards the top of the sequence, while 9.7% Cu and 11% Zn are occasionally found over a 1-2m span. Mineralogical banding, which varies from crude to well defined (*Fig. 3.8D)*, dips at between 40 and 70° towards the SW (230°). The Rochas Bandadas show little evidence of deformation. Schistosity is rare, occasionally being developed in grunerite-rich horizons, and narrow, vein-hosting faults are less evident in the Rochas Bandadas than elsewhere in the Corpo Quatro Formation. Small-scale folding has been observed in drillcore, where it is particularly distinct in magnetite-rich horizons (*Fig. 3.11G*). It is not known whether this folding is of sedimentary or tectonic origin, but pyrrhotite is occasionally concentrated into the fold hinges, implying a post-diagenetic timing to this event.

The Rochas Bandadas have been divided into two types: a magnetite-rich unit, similar to a typical BIF, is found at the base of the metasediments, sometimes overlying up to 1m of massive chert. This is immediately overlain by a more amphibole-rich banded unit, termed the Silicate-Rochas Bandadas, in which most of the sulphide mineralization occurs.

3.3.1 *Magnetite-Rochas Bandadas*

The Magnetite-Rochas Bandadas (hereafter known as BIF) is a distinctive rock, composed of alternating grey-brown (magnetite and grunerite) and white (quartz) bands (*Fig. 3.8A*). Individual laminae range from 0.2 to 2cm wide (*Fig. 3.8B*) and the rock has an overall composition which is approximately 20% magnetite, 30% quartz and 50% grunerite. The presence of grunerite prevents this unit from being termed an 'itabirite' in the strict sense of the word. This term is normally confined to rocks consisting predominantly of quartz and magnetite ± haematite, which have been subject to low grade metamorphism (Dorr, 1973; Klein, 1978) similar to those occurring in the N4 deposit of the Carajás Formation (Machamer *et al*, 1991). The term 'oxide-iron-formation' is also avoided, as this is a facies name, implying a particular sedimentological assemblage, which, at this stage, is not known or relevant (Kimberley, 1989).

Grunerite occurs at the quartz-magnetite interface, and in thin section is pale green-yellow, fibrous, and shows weak alignment sub-parallel (about 10°) to the quartz-magnetite banding (*Fig. 3.8C*). This alignment may represent a weak schistosity. Repeated lamellar twinning typical of the grunerite-cummingtonite series is common, particularly in prismatic sections. Grunerite is also present as an intergrowth between quartz grains distal from magnetite bands, where it is much finer grained and takes a euhedral prismatic habit.

The quartz grains are equigranular and sub-polygonal with 120° dihedral angles. Individual grains vary greatly in diameter, from 0.1 to 1.5mm, averaging between 0.3 and 0.6mm across. There is no evidence of crystal alignment within individual quartz bands, and minor undulose extinction implies that most of the quartz is primary, having suffered grain boundary migration during metamorphism. The intergrowth of grunerite with quartz indicates that at least some of the quartz is a metamorphic product (see 3.3.2), probably of silicate-facies origin, which has undergone strain and partial grain boundary migration.

Interstitial angles of 120° are also common between magnetite grains, again indicating metamorphic annealing. Magnetite also occurs as individual anhedral equigranular grains throughout the BIF, as inclusions in quartz, and within grunerite bands.

3.3.2 *Silicate-Rochas Bandadas*

Those rocks occurring structurally above, to the south of the Corpo Quatro BIF are typically composed of 2 to 30mm-wide amphibole laminae (comprising amphiboles of both the grunerite and hornblende series) alternating with 5- to 20mm-thick quartz laminae (*Fig. 3.8D&E*) and narrow horizons of mixed sulphide (pyrrhotite, chalcopyrite and sphalerite) and iron-oxide (see section 3.3.3). SEM analyses have shown that ilmenite, rather than magnetite, forms the disseminated grains and narrow (1 to 2mm) bands of iron oxide throughout the Silicate-Rochas Bandadas (*Appendix C*). These will be described in section 3.3.4.

Amphiboles of the cummingtonite-grunerite series are volumetrically the most important mineral phase in this unit, where they take three forms: coarse, euhedral, twinned crystals; very fine prismatic

interlocking crystals; and coarse (0.5 to 4mm) fibrous or acicular twinned crystals (*Fig. 3.8F-I*). In plane-polarised light these amphiboles display colourless to pale-brown pleochroism, with third order birefringence in cross-polarised light, and frequently exhibit simple or repeated twinning in acicular and prismatic crystals. Microprobe analyses (EPMA; *Appendix C*) have shown that most of the Fe-Mg amphiboles are grunerite, with the formula unit Mg/Mg+Fe = 0.08, and an average of only 0.7 Wt.% $Na_2O + CaO + Al_2O_3$.

Amphiboles adjacent to sulphide-rich laminae show a coarsening and less acicular texture, than those in pure amphibole bands, with an absence of twinning (*Fig. 3.8G*). EPMA analyses have identified an increase in either aluminium or alkali content in these amphiboles, which fall in the anthophyllite field according to the International Mineralogical Association (IMA) amphibole classification (*Fig. 3.9; Appendix C*). The amphiboles in this study were classified using the *Amphibole FU's* software (kindly provided by Andy Tindle at the Open University), which is based on the IMA amphibole classification system.

Within millimetres of sulphide mineralization, grunerite and anthophyllite display alteration to a dark green to blue-green pleochroic member of the hornblende group (*Fig. 3.8F-I*). This alteration predominantly occurs along cleavage planes and grain boundaries, giving a 'christmas tree' texture. The alteration product has been identified by microprobe analyses as ferro-actinolitic or ferro-tschermakitic hornblende, with the average composition (Na,K) Ca_3 (Mg,Fe_8Al) $Si_{13}Al_3O_{44}$, and $(Na+K)<0.5$. For simplicity, these will be referred to as hornblende from here onwards in the text. The hornblende has second order birefringence in cross-polarised light, which is often masked by the deep green-blue body-colour. Where the body-colour is particularly dark, minute grains of unidentified opaque material are often seen enclosed within the amphibole (*Fig. 3.8I*).

The Silicate-Rochas Bandadas contain about 30% quartz, which is concentrated in horizons up to 20mm-wide and parallel to the amphibole and sulphide-oxide bands. Like that seen in the BIF, the quartz shows no crystal alignment, is polygonal to sub-polygonal, and often displays weak undulose extinction, indicating metamorphic annealing and post-metamorphic strain. Individual quartz grains are up to 0.1mm in diameter and host fine grained fibrous 'bow-tie'-texture amphiboles at grain boundaries, again, similar to those observed in the Magnetite-Rochas Bandadas.

Whereas metamorphic mica is rare in the Rochas Bandadas, biotite occurs in veinlets cross-cutting pyrrhotite and chalcopyrite, as well as in some of the sulphide-bearing quartz fractures (see Chapter 5). Occasionally amphiboles are also replaced by biotite along cleavage, although this is rare.

Ilmenite is the only oxide mineral found in the Silicate-Rochas Bandadas, and is primarily seen as individual laths in sulphide-bands or disseminated through quartz-bands. It is grey-brown in reflected light, is generally rectangular in form (*Fig. 3.11D*), and has higher relief than the sulphide minerals.

Figure 3.8 **The C4 Rochas Bandadas**

A Drill-core of typical magnetite-rich Rochas Bandadas, showing distinct mineralogical banding of quartz (pale) and magnetite-grunerite (dark).

B Hand specimen showing well defined mm to cm banding in Pojuca C4 'banded iron formation'. Quartz (pale brown), magnetite (grey-brown) and grunerite (dark grey). Sample F62.

C Photomicrograph of mineralogical segregation in the C4 Magnetite-Rochas Bandadas, comprising quartz, grunerite (brown) and magnetite (opaque). Sample B2. Plane-polarised light. Field of view 6.8mm.

D View of the Rochas Bandadas at 88m (Left) in the G1-C4 adit, showing distinct banding of quartz (yellowed) and amphibole-sulphides (dark). Width of view 1.5m.

E Drill-core specimens of sulphide-rich Rochas Bandadas, showing banded nature of quartz, amphiboles (dark, grunerite and hornblende) and chalcopyrite-pyrrhotite. Sample F63 (top) and F69 (bottom).

F Photomicrograph of fracture-sulphides (opaque, chalcopyrite-pyrrhotite) penetrating silicate cleavages (grunerite, colourless), showing hornblendization (green-brown to blue-green) of colourless amphiboles in close contact with sulphide minerals. Cleavages most obviously penetrated where sulphide fracture is deflected. Sample F40. Plane-polarised light. Field of view 4.4mm.

G Left: Photomicrograph of silicate banding in the Rochas Bandadas, showing fibrous twinned grunerite (top), coarser prismatic anthophyllite (clear, bottom) and alteration of amphiboles to ferro-actinolitic hornblende. Sample G37. Plane-polarised light. Field of view 2.2mm. Right: As left, cross-polarised light. Field of view 2.2mm.

H Photomicrograph of grunerite in the Rochas Bandadas which shows extensive alteration to green hornblende-amphibole in close spatial association with sulphide minerals (opaque). Note presence of minute opaques (probably oxide minerals) in green hornblende, which are absent in pale grunerite. Sample F39. Plane-polarised light. Field of view 4.4mm.

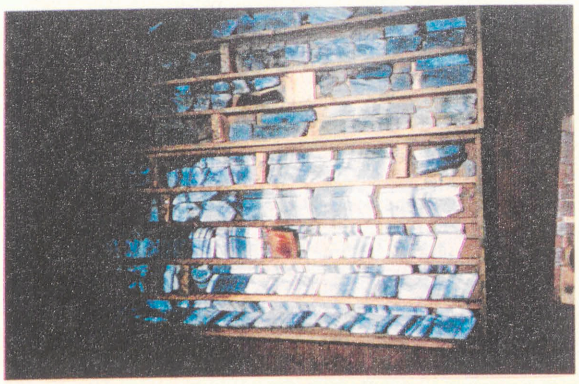

A

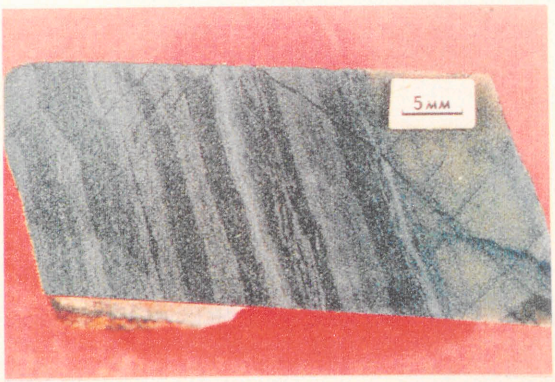

B

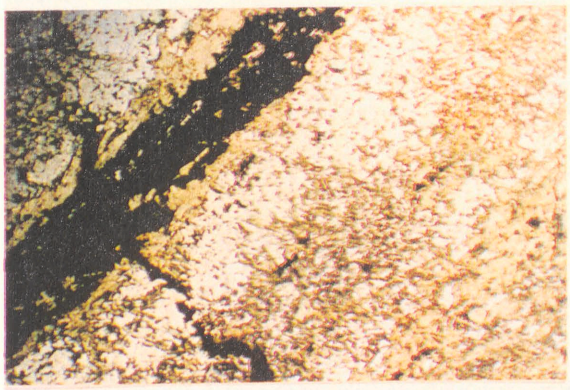

C

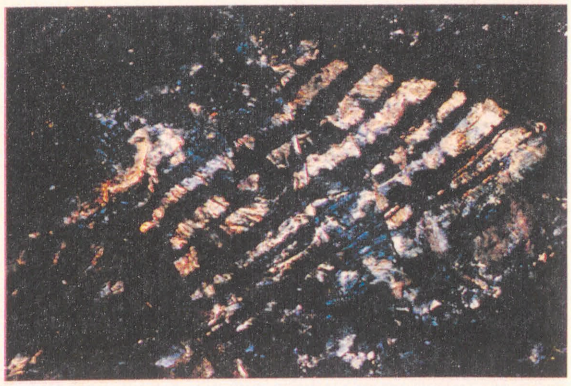

D

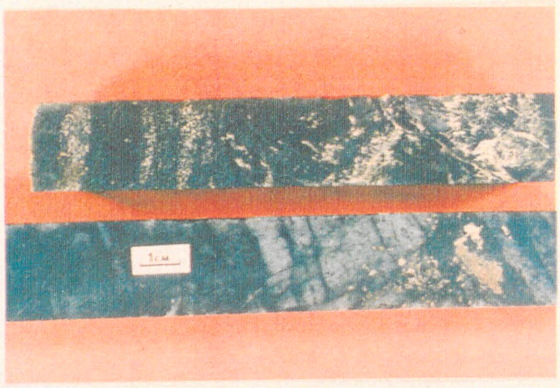

E

F

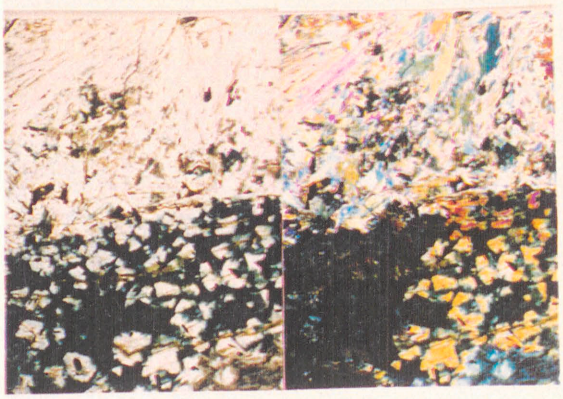

G

H

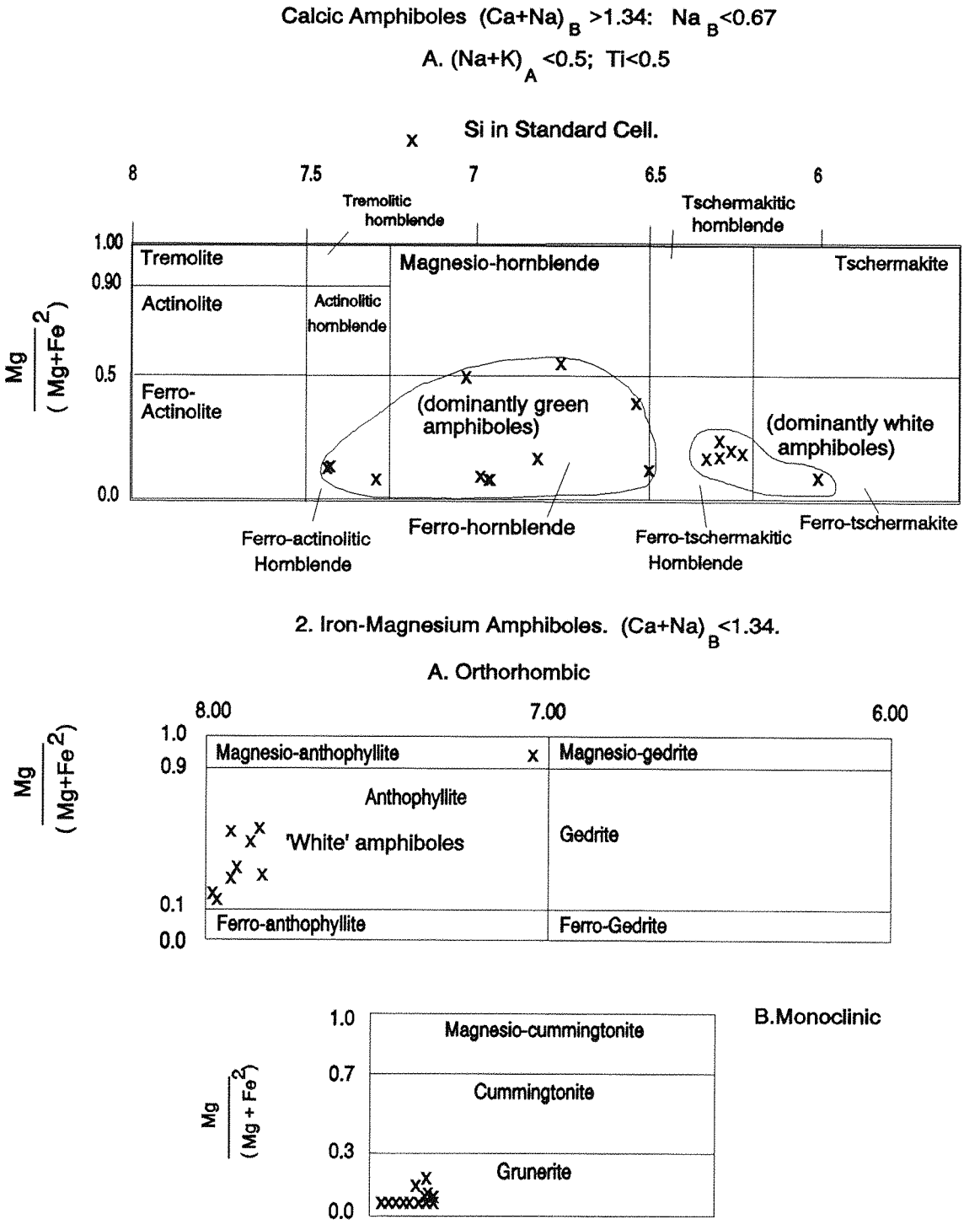

Figure 3.9 **Classification of amphiboles (after Leake, 1978), showing the calcic amphibole (Na+K<0.5) and Iron-magnesium amphibole groups. Also plotted are the positions of the amphiboles from the Corpo Quatro Rochas Bandadas, according to EPMA analyses (Appendix C)**

3.3.2 *Metamorphism of the C4 Rochas Bandadas*

In order to establish the precise metamorphic grade of an iron-formation, it is necessary to know at least the sedimentary facies to which the rocks belonged prior to metamorphism, if not the exact composition of the original rocks (Klein, 1973). Typical diagenetic minerals in iron-formation include carbonates (dolomite, ankerite, siderite and calcite) and hydrous iron silicates (minnesotaite, greenalite and stilpnomelane; Klein, *op.cit.*). None of these diagenetic phases are present in the C4 Rochas Bandadas, which are composed of the metamorphic assemblage of quartz and grunerite ± magnetite. Whilst the metamorphic and hydrothermal overprint of the Corpo Quatro Formation makes it almost impossible to discern the original composition, the amphiboles present in the Rochas Bandadas allow an estimate of metamorphic conditions to be made.

Magnetite-Rochas Bandadas

The C4 BIF has the relatively simple mineralogy of quartz, grunerite and magnetite, which, with the exception of the grunerite, appears similar to a metamorphosed oxide-facies iron-formation. Upon low grade metamorphism, a typical oxide-facies iron-formation undergoes the change from diagenetically altered silica (chert) and hydrous iron oxides to crystalline quartz and magnetite, which is the classic 'itabirite' assemblage defined by Dorr (1973), but this assemblage persists without the development of further silicate minerals through to high grade metamorphism (Klein, 1973).

Silicate-Rochas Bandadas

The Silicate-Rochas Bandadas contains no indicative metamorphic minerals, such as almandine, pyroxene or carbonates, and has more of a post-peak-metamorphic overprint than the BIF, in the form of hornblende and sulphide minerals. Grunerite, the most abundant metamorphic mineral in the sequence, can be the product of a number of reactions from different initial mineral assemblages:

Carbonate Facies:

$$7Ca(Fe,Mg)(CO_3)_2 + 8SiO_2 + H_2O \longrightarrow (Fe,Mg)_7Si_8O_{22}(OH)_2 + 7CaCO_3 + 7CO_2$$

(Ferrodolomite) (Grunerite) (*Equation 3.1*)

or:

$$7(Fe,Mg)CO_3 + 8Si0_2 + H_2O \longrightarrow (Fe,Mg)_7Si_8O_{22}(OH)_2 + 7CO_2$$

(Siderite) (Grunerite) (*Equation 3.2*)

Silicate Facies:

$$(Fe,Mg)_6Si_4O_{10}(OH)_8 + 4SiO_2 \longrightarrow 2(Fe,Mg)_3Si_4O_{10}(OH)_2 + 2H_2O$$

(Greenalite) (Minnesotaite)

and 7 Minnesotaite $\longrightarrow$ $3(Fe,Mg)_7Si_8O_{22}(OH)_2 + 4SiO_2 + 4H_2O$

(Grunerite) (*Equation 3.3*)

(Klein, 1983)

These reactions indicate that regional metamorphism to at least garnet grade has occurred (Klein, 1978), at a minimum temperature of 350 to 400°C. The amphibole microprobe data has been

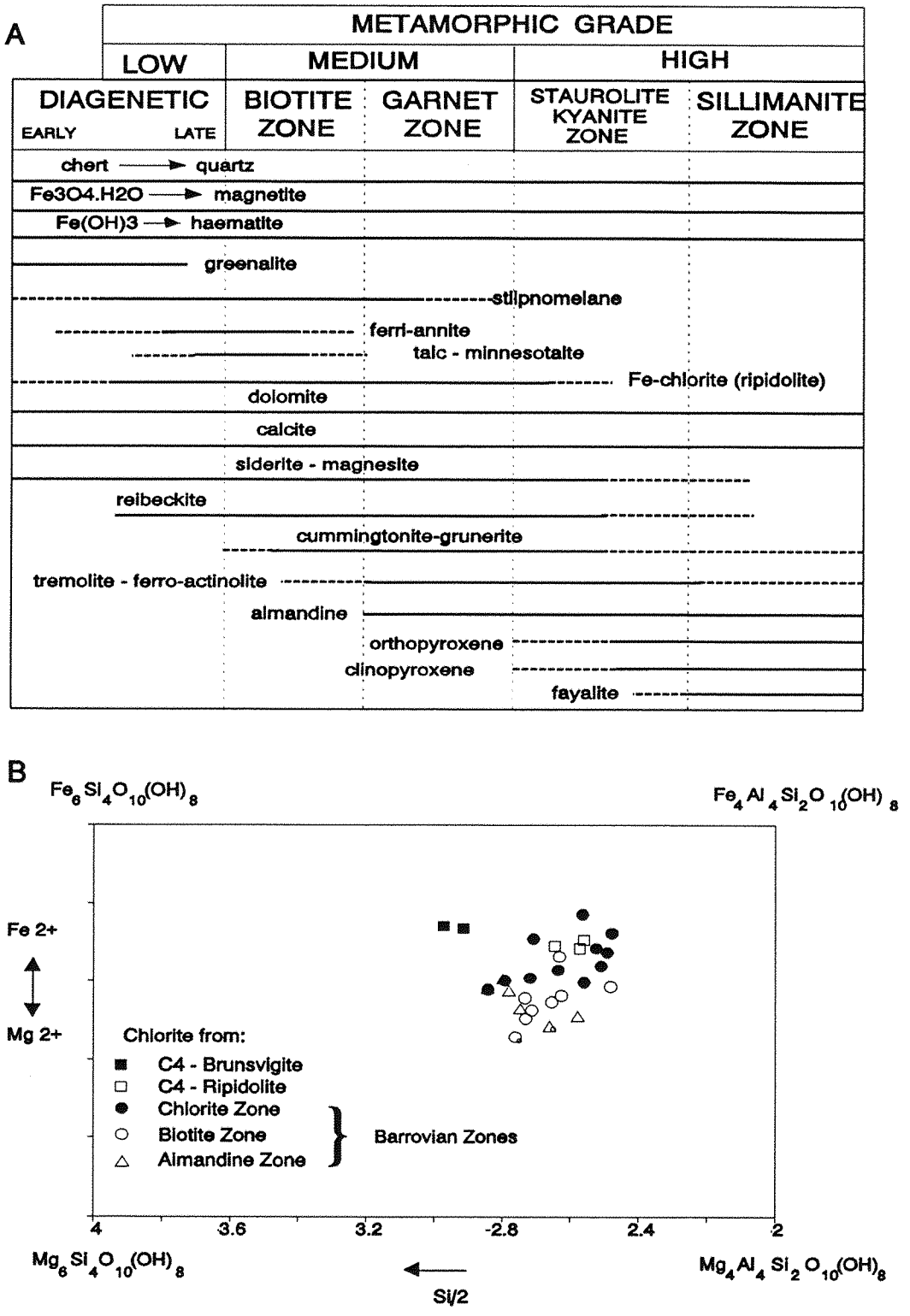

Figure 3.10 **A. Relative stabilities of minerals in iron formations (Klein, 1983); B Composition of metapelitic chlorites (Miyashiro, 1973), as a function of their metamorphic zone. C4 brunsvigite = replacement and ripidolite = metamorphic chlorite.**

put through several calcic-amphibole pressure calculation equations using the software which was used to identify the amphibole species (*Appendix C*). These equations work on aluminium content in amphiboles, usually reserved as an igneous geobarometer, and must therefore be treated with some caution. Tentative formational pressures of between 5 and 7kb for the colourless, metamorphic Ca-amphibole (anthophyllite) and 3-5kb for the blue-green amphibole (hornblende) can be established, indicating a drop in pressure prior to the post-peak-metamorphic formation of the green hornblende.

The coarsening of diagenetic quartz and magnetite grains has previously been used as an indicator of the metamorphic grade of iron-formations (James, 1955; Dorr, 1964), but to do this, it must be proved that the quartz is primary, formed as a result of the diagenesis of amorphous silica. The average diameter of quartz grains which have undergone greenschist facies metamorphism was found to be 0.01mm, rising to 0.5mm diameter in amphibolite facies iron-formation (Dorr, 1964). The grain-size of quartz in the C4 Rochas Bandadas, which varies between 0.3 and 0.6mm, is comparable to the amphibolite facies observations of Dorr (1964). Although this method of estimation is crude, it is supported by other mineralogical observations throughout the Corpo Quatro Formation, indicating that the Rochas Bandadas have been subjected to amphibolite-grade metamorphism.

The presence of abundant coexisting quartz and silicate minerals (particularly grunerite) and the lack of carbonate and oxide minerals in the Silicate-Rochas Bandadas suggest that the original sediment was likely to have been a silicate-quartz-oxide unit (equation 3), rather than a pure quartz-oxide facies or a carbonate-silicate facies iron-formation. The same can be said for the Magnetite-Rochas Bandadas. However, carbonate minerals are rare in parts of the carbonate-facies Michigan iron-formations which have suffered garnet-staurolite zone metamorphism, and are absent in those which have undergone sillimanite zone metamorphism (James, 1955). This indicates that unless diagenetic iron-formation is present for comparison, it is virtually impossible to identify the original facies to which an iron-formation belonged using mineral assemblage alone.

3.3.4 *Ore Mineralogy in the C4 Rochas Bandadas*

Magnetite-Rochas Bandadas

Chalcopyrite in the Magnetite-Rochas Bandadas (BIF) is rare, occurring as disseminated grains between quartz crystals, and along fractures cross-cutting the quartz bands. Pyrrhotite and chalcopyrite are occasionally seen replacing magnetite at the edge of magnetite horizons (*Fig. 3.11A*). Copper grades are low, zinc is virtually absent (*Table 3.1*), and gold assay values do not exceed 0.05ppm in the BIF (Medeiros, 1987; Docegeo, core logs).

Silicate-Rochas Bandadas

The main Cu-Zn ore in the C4 deposit is found in the silicate-rich iron-formation, where sulphide minerals consist of pyrrhotite, chalcopyrite and minor sphalerite with accessory pyrite, molybdenite and gold. Copper and zinc grades average 0.7 and 0.5% respectively, occasionally reaching 9.7%Cu and 11%Zn (F50, 176-178m). Sulphide minerals show a variety of textures, occurring in veins or fractures, in bands

parallel to the quartz-amphibole laminae, and as disseminated grains. These are described in the following pages. Gold grades appear to be at their highest (up to 0.5ppm) where magnetite and fibrous grunerite dominate the mineral assemblage, but the low assay grades (average <0.1ppm; *Table 3.1*) and the absence of visible gold preclude the study of the mineral from this project.

Banded Sulphides

The replacement of banded magnetite by sulphide minerals in the BIF is observed on a larger scale in the Silicate-Rochas Bandadas, where pyrrhotite, chalcopyrite and sphalerite coexist in 1mm to 15mm-wide sulphide bands parallel to the quartz-amphibole bands (*Fig. 3.11C&D)*. This gives the impression, in hand specimen, that the mineralization is primary syngenetic, and stratiform in nature (*Fig. 3.11B&G*). On closer study, however, these sulphides cross-cut metamorphic amphiboles and penetrate along the cleavage of grunerite and anthophyllite (*Fig. 3.8F & 3.12B)*. Around the sulphides, the colourless amphiboles commonly display alteration to the green coloured ferropargasite and ferro-actinolite described in section 3.3.2, indicative of post-metamorphic introduction of the sulphide minerals. In these sulphide replacement horizons, magnetite is rarely found. Relic ilmenite laths, however, are commonly enclosed within the sulphide minerals. It would appear, in these areas, that magnetite has been completely consumed by the formation of post-metamorphic sulphides.

Sphalerite is a relatively common component in the Banded Sulphides, where in polished thin section (transmitted, plane-polarized light) it appears as a bright red translucent mineral. It mainly occurs within fractures, cross-cutting and apparently replacing both pyrrhotite and chalcopyrite (*Fig. 3.12C)*, and occasionally encloses randomly orientated chalcopyrite blebs (*Fig. 3.11F*). Unlike chalcopyrite, which is generally found associated with pyrrhotite in these rocks, sphalerite may be unaccompanied by other sulphide minerals.

Pyrrhotite is known to readily replace magnetite in hydrothermally altered banded iron-formation (Gilligan, 1990). In the Pojuca deposit, however, both pyrrhotite and chalcopyrite are seen penetrating for several centimetres along individual laminae, and replacement is not limited to alteration haloes immediately around fracture mineralization as seen by Gilligan (*op.cit.*). The exact relationship between the two sulphide minerals in these bands is unclear, with pyrrhotite enclosing chalcopyrite and vice versa on a microscopic scale, while on hand specimen scale, chalcopyrite appears to envelop and replace pyrrhotite (*Fig. 3.11B)*.

Fracture Sulphides

Fractures, which are filled with sulphide minerals and which rarely exceed 3 to 4mm in width and 50mm in length, are common throughout the Rochas Bandadas, but are most frequent in the Silicate-Rochas Bandadas (*Fig. 3.11H & 3.12A*). Both sphalerite and pyrite are more common here than in the Banded Sulphides, although pyrrhotite and chalcopyrite remain the principal sulphides in this style of mineralization. Where Fracture Sulphides cross-cut anthophyllite or grunerite, these silicates show

Figure 3.11 **Mineralization in the Rochas Bandadas I.**

A Photomicrograph of magnetite band in Magnetite-Rochas Bandadas, which has been cross-cut by chalcopyrite (yellow) - pyrrhotite (white)-bearing vein. Shows partial replacement of magnetite (grey) by chalcopyrite. Sample G45. Reflected light. Field of view 4.4mm.

B Banded Sulphides. Massive chalcopyrite (yellow) in hornblende-rich specimen of Rochas Bandadas, showing apparent banding of the sulphide mineral horizon. Sample F42.

C Hand specimen of Banded Sulphides in the Rochas Bandadas, showing parallel banding of chalcopyrite (yellow) and pyrrhotite (brown), in hornblende (dark green-black), with acicular grunerite and quartz to the left of the mineralization. Sample G37.

D Photomicrograph of sulphide band in Figure 3.10 C. Chalcopyrite (yellow), pyrrhotite (pleochroic blue-white) and sphalerite (blue-grey) post-date residual ilmenite laths (grey-brown), which show replacement by chalcopyrite. Sample G37. Reflected light. Field of view 4.4mm.

E Photomicrograph of Banded Sulphides (chalcopyrite and pyrrhotite, opaque, and sphalerite, red) overprinting clear anthophyllite and green ferro-hornblende. Sulphides show further overprinting by anthophyllite needles. Sample F16. Plane-polarised light. Field of view 2.2mm.

F As Figure 3.10 E, reflected light. Sphalerite (blue-grey) shows randomly orientated blebs of chalcopyrite (yellow) as evidence of the replacement of chalcopyrite by sphalerite. Also pyrrhotite (pink-white). Overprinting of sulphides by silicate (anthophyllite) needles is striking. Sample F16. Plane-polarised light. Field of view 2.2mm.

G Drill-core specimen showing obvious folding of magnetite, and cross-cutting of magnetite by later pyrrhotite (brown-white) and chalcopyrite (pale yellow-white), which shows no evidence of having been folded or concentrated in fold hinges with the magnetite (grey-brown). Sample F91.

H Drill-core specimen showing discordant nature of the Fracture Sulphides (left) to the host Rochas Bandadas, which are banded parallel to the Banded Sulphides (right). Fracture Sulphides predominantly chalcopyrite, Banded Sulphides composed of both chalcopyrite and pyrrhotite. Sample F92.

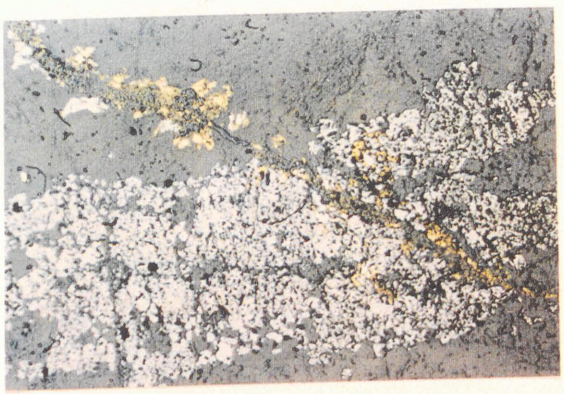

A

B

C

D

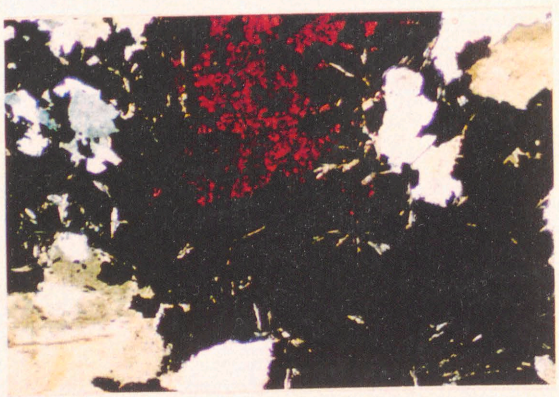

E

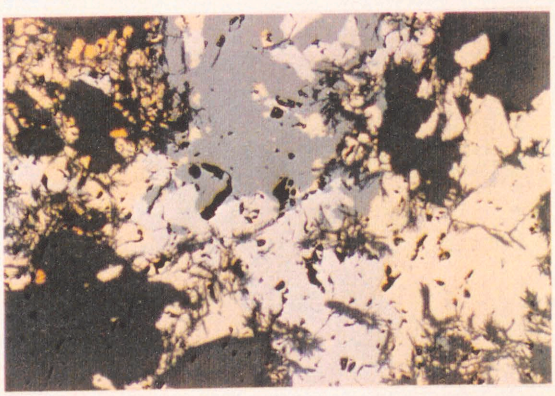

F

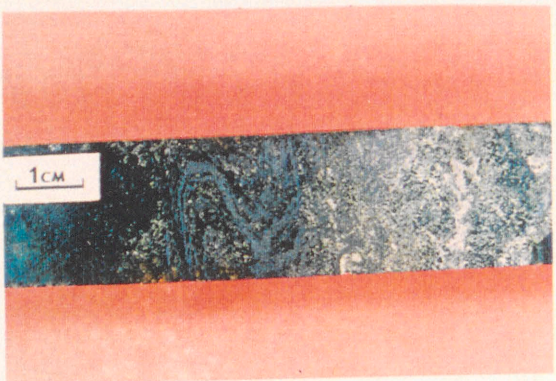

G

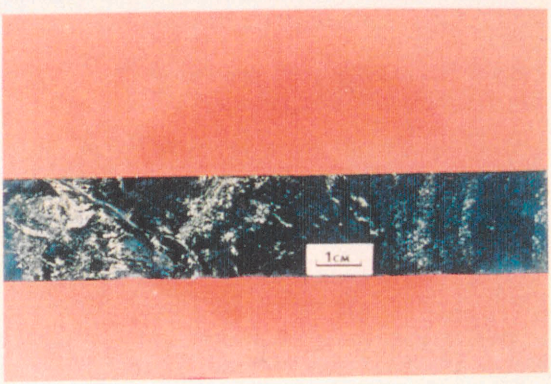

H

Figure 3.12 **Mineralization in the Rochas Bandadas II.**

A Hand specimen of massive fracture-style pyrrhotite (brown) and chalcopyrite (yellow) in banded hornblende-quartz Rochas Bandadas, showing distinct hornblendization around sulphide mineralization. Sample G101.

B Photomicrograph of fracture-hosted pyrrhotite and chalcopyrite, showing that chalcopyrite forms as a replacement of pyrrhotite along grain boundaries and cracks. Magnetite (centre right, grey, Mt) is a relict, and probably indicates massive replacement of magnetite by pyrrhotite. Sample F16. Reflected light. Field of view 2.2mm.

C Photomicrograph of fracture-hosted sphalerite (blue-grey), with associated pyrrhotite and chalcopyrite, in grunerite-rich Rochas Bandadas. Sample F16. Reflected light. Field of view 2.2mm.

D Photomicrograph of massive pyrrhotite in Fracture Sulphides. Euhedral pentlandite (Pn) at pyrrhotite grain boundaries and along cracks suggests replacement of pyrrhotite. Minor sphalerite and chalcopyrite, and magnetite (grey-brown, Mt) also present. Sample F16. Reflected light. Field of view 1.1mm.

E Photomicrograph of the brittle nature of early, deformed pyrite in Fracture Sulphides. Pyrite (fractured and euhedral) forms a nuclei for chalcopyrite. Sample G3. Reflected light. Field of view 0.55mm.

F Photomicrograph of replacement textures between pyrite (centre, yellow-white), chalcopyrite, and pyrrhotite. Pyrrhotite (pink-brown) intergrown with and altered to pyrite lamellae, with a texture believed to be of similar origin to 'Birds Eye Texture', and pyrite (central) shows replacement by chalcopyrite. Sample F70. Reflected light. Field of view 1.1mm.

G Photomicrograph of pyrrhotite being replaced by pentlandite (white) and chalcopyrite along cracks, which is in turn replaced by molybdenite (Mo). Sample F16. Reflected light. Field of view 0.55mm.

H As Figure 3.11 G. Reflected, cross-polarised light. Molybdenum has distinctive blue-white bireflectance, displaying twinning. Field of view 0.55mm.

I Drill-core specimen of disseminated-style ore in Rochas Bandadas, displaying pyrrhotite (brown), chalcopyrite (high reflectance, pale yellow) and minor sphalerite (grey) in hornblende-rich host (dark). Sample F16.

J Drill-core specimen of quartz-vein hosted chalcopyrite (tarnished), with apophyses vein hosting quartz and chalcopyrite, and associated disseminated chalcopyrite in host Rochas Bandadas. Sample F75.

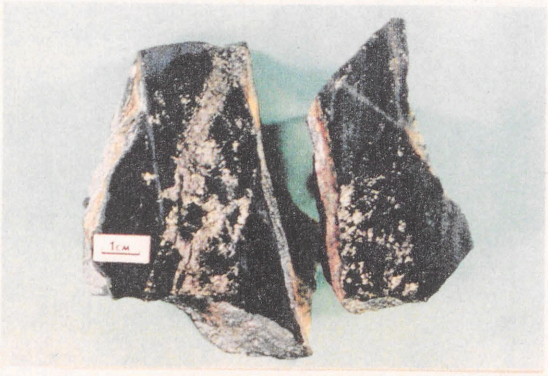

A

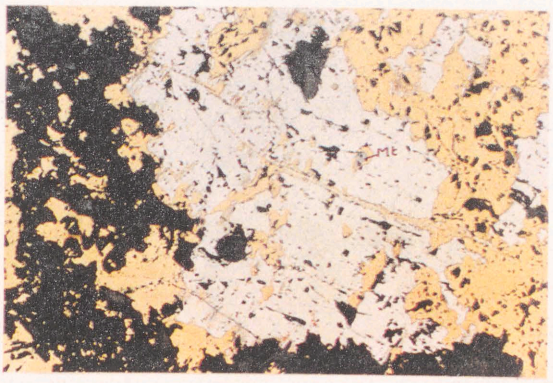

B

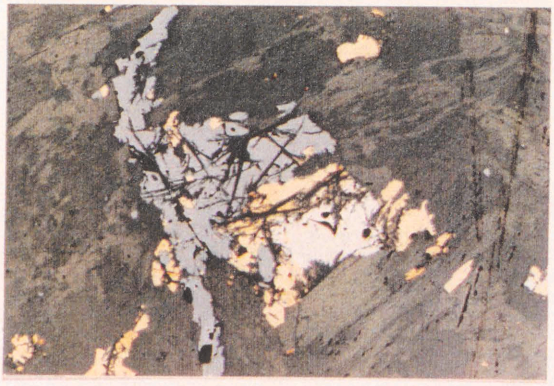

C

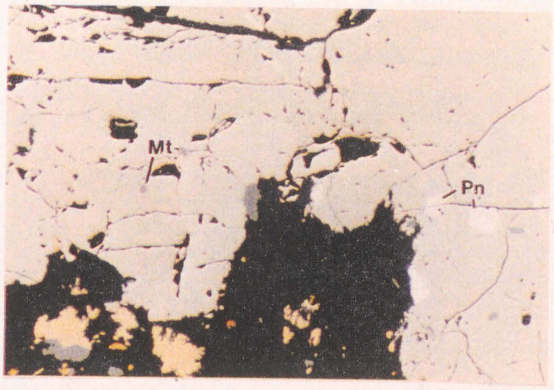

D

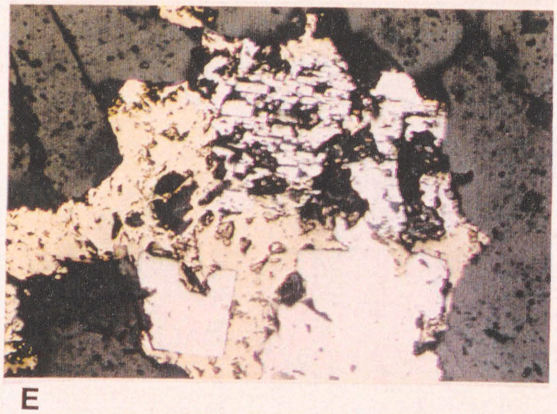

E

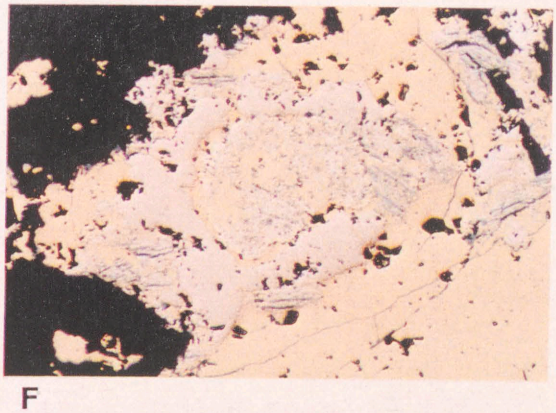

F

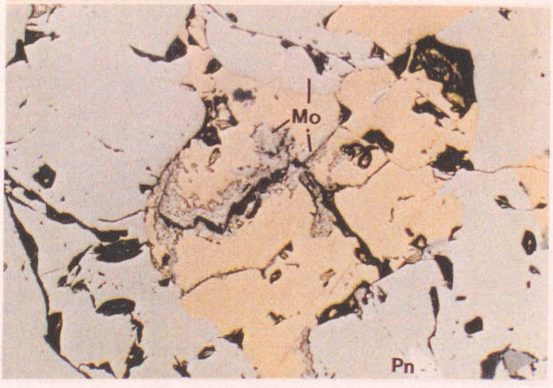

G

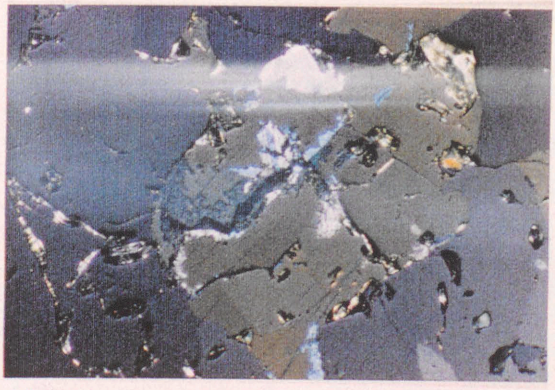

H

I

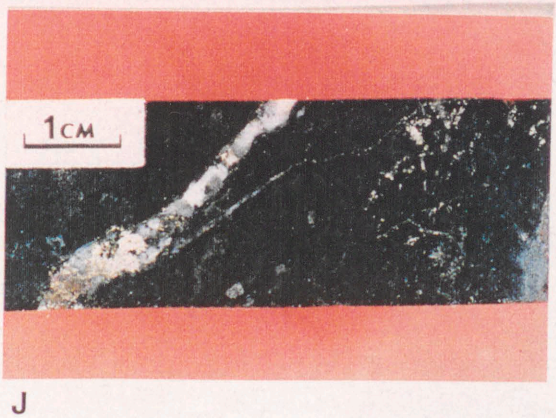

J

alteration to green hornblende-series amphiboles, as observed in association with the Banded Sulphides (*Appendix C*). Where the sulphide-fractures are discordant to silicates, sulphide minerals penetrate the cleavage of the colourless amphiboles (*Fig. 3.11B*).

Chalcopyrite and pyrrhotite coexist in the fracture-style of mineralization, where the sulphide grains are anhedral. Sphalerite replaces both chalcopyrite and sphalerite at inter-grain boundaries and along micro-fractures through the earlier sulphides.

Euhedral pentlandite crystals occasionally penetrate fracture-hosted pyrrhotite from grain edges and cracks (*Fig. 3.12D)*. This relationship has only been seen in the Fracture Sulphides, where pyrrhotite forms more massive bodies than in the Banded Sulphides. Pentlandite is commonly produced in pyrrhotite as an exsolution product, which results in crystallographically orientated pentlandite, or, in the case of stress-induced exsolution, flame-like forms. As the pentlandite observed in the Corpo Quatro sulphides forms euhedral crystals rather than either of the exsolution-induced textures, it has been interpreted as a replacement feature of pyrrhotite, implying hydrothermal introduction of nickel into the system.

Pyrite occurs in two forms in the fracture-sulphides: early pyrite, which shows brittle deformation in the form of cubic fracturing (*Fig. 3.12E*), has been overgrown and infilled by both pyrrhotite and undeformed pyrite. Pyrite also shows fine intergrowth lamellae at the margins of pyrrhotite grains, which is believed to be produced by a similar mechanism to bird's eye texture (*Fig. 3.12F*). There are two explanations for the presence of this pyrite; i) the early pyrite formed as a product of metamorphism, and has undergone post-metamorphic strain prior to further sulphide deposition. This is relatively common in iron-formation (Klein, 1978), or ii) pyrite was present as a diagenetic phase in the original sediment, and underwent brittle deformation during metamorphism. It is the later, undeformed pyrite which often displays a fine intergrown texture with pyrrhotite. It is therefore interpreted that the brittly deformed pyrite is a diagenetic product, while the undeformed pyrite is a product of prograde metamorphism. During metamorphism, increased temperature and sulphur activity is known to result in the decomposition of and the loss of sulphur from pyrite, resulting in the formation of intergrowths and apparent replacement of pyrite by pyrrhotite (Craig and Vokes, 1993; *Fig. 3.13*). This is thought to be the case at Pojuca Corpo Quatro, and therefore at least some of the pyrrhotite is a product of metamorphism.

Anhedral molybdenite, like sphalerite, replaces both pyrrhotite and chalcopyrite along cracks and grain boundaries. This relationship is not observed between sphalerite and molybdenite, and the two minerals are therefore interpreted as being synchronous and later in the paragenetic sequence than pyrrhotite and chalcopyrite.

Although free gold occurs within the Rochas Bandadas, only one grain has been seen, using the scanning electron microscope. This euhedral cubic crystal is 30μm across, and hosted by sphalerite which occurs in crack in chalcopyrite.

Disseminated Sulphides

Pyrrhotite and chalcopyrite are the most abundant disseminated sulphide minerals in the Rochas Bandadas (*Fig. 3.12I*). They form rounded to sub-rounded grains at inter-granular boundaries in the quartz

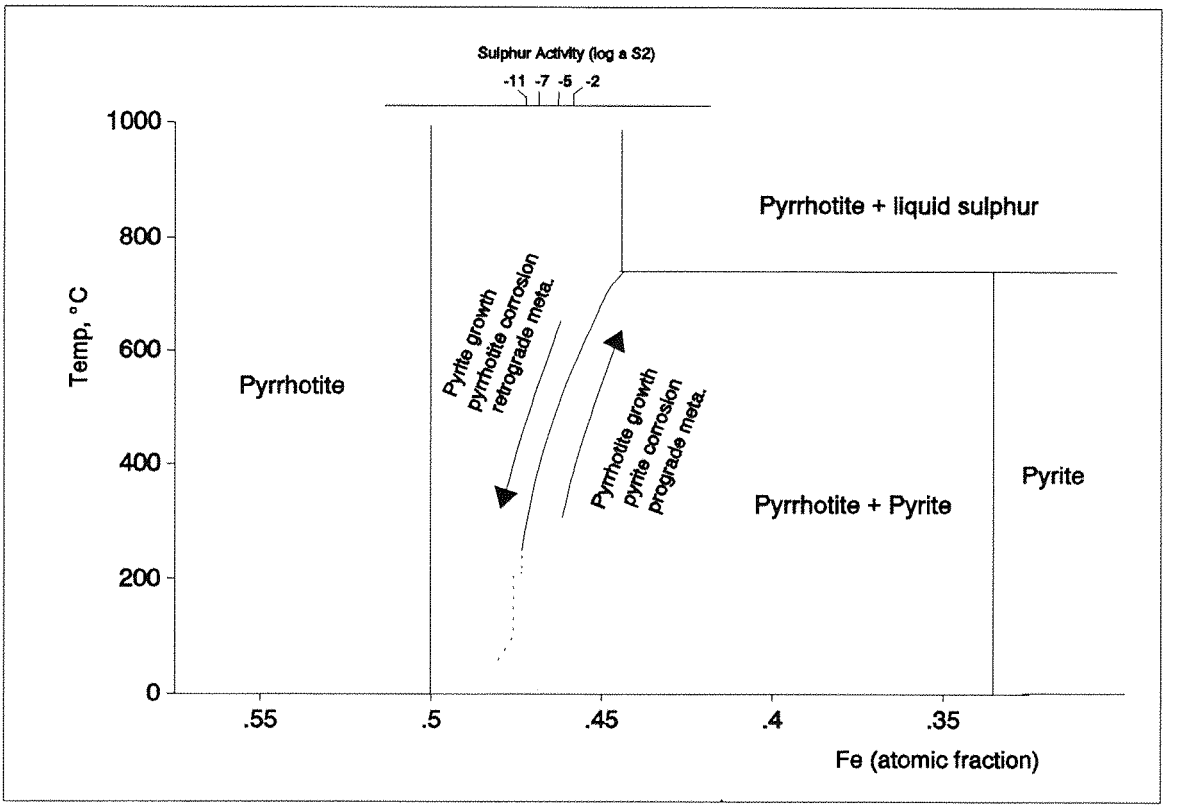

Figure 3.13 **Highly schematic diagram of the Fe-S system depicting prograde and retrograde metamorphism, and the consequential decomposition as sulphur is lost by pyrite and incorporated into pyrrhotite on prograde, and vice-versa on retrograde metamorphism (after Craig and Vokes, 1992).**

bands, and along cleavage and at mutual grain boundaries of grunerite and anthophyllite crystals within the amphibole bands of the Rochas Bandadas. Elongate grains of disseminated chalcopyrite and pyrrhotite are also found in micro-fractures cross-cutting and along cleavage planes of the amphibole crystals.

With the exception of brittly deformed pyrite and the presence of pyrrhotite in fold hinges, none of the Rochas Bandadas-hosted sulphide minerals show any evidence of having undergone prograde metamorphism. Typically, metamorphosed sulphide minerals show signs of ductile remobilization, nucleation around competent minerals such as pyrite, durchbewegung textures, pressure-induced twinning and the development of triple junctions at grain boundaries (Nold, 1983; Nebel *et al.*, 1991)). None of these textures have been observed in the Pojuca Corpo Quatro deposit.

All of the mineralization styles within the host rock show, in places, overprinting by acicular silicate minerals (*Fig. 3.11E*). These have been identified by electron probe micro-analysis as anthophyllite, which is a relatively common retrograde metamorphic product (Baker *et al.*, 1992). This phenomenon is quite common in sulphide deposits from metamorphic terranes (Cook and Halls, 1991), and brackets the timing of mineralization to before the end of the regional retrograde metamorphism in the area.

Vein Mineralization

Massive chalcopyrite and pyrrhotite, and occasional sphalerite and pyrite, are found in quartz and quartz-biotite veins throughout the metasediments, but particularly in the Rochas Bandadas (*Fig. 3.12J*). These sulphide-bearing veins average 10-30mm in width, although quartz-filled dilational jogs faults (such as that found at 102m in G1-C4) result in vein widths of up to 0.6m being reached. These veins are described in more detail in Chapter 5.

Increased volumes of sulphide minerals are commonly found in the host Rochas Bandadas in close proximity to wide, fault-hosted, quartz-chalcopyrite veins. This is particularly noticeable in G1-C4, where the sulphide content increases from ~20 to up to ~40% of the total rock volume within 1-2m of the fault zones. On a smaller scale, centimetre-wide quartz veins cross-cutting the mineralogical banding host apophyses which tend towards 'band-parallel', and chalcopyrite-pyrrhotite mineralization continues from the quartz vein into the amphibole-banding (*Fig. 3.12J & 5.6*) often resulting in the 'banded mineralization' described previously in this section.

3.4 *THE PETROGRAPHY OF THE ROCHAS FRAGMENTOS*

The Corpo Quatro Formation 'Rochas Fragmentos' are so-called because they contain elongate aggregates of quartz, which are sub-rounded to angular in shape and have a fragmental, clast-like appearance (*Fig. 3.14A*). These quartz 'fragments' are almost identical to those found in Jaspilite Breccias which overlie the Carajás Formation BIF in the large N4E iron-ore deposit (Hoppe *et al.*, 1987), and are thought be of sedimentary origin, representing intra-basinal clasts. The C4 Rochas Fragmentos have a gradational contact with the underlying Rochas Bandadas (*Fig. 3.3*), and although sulphide minerals are

present, are rarely of ore grade.

The unit can be divided into two distinct types according to mineralogy and appearance: those in which large porphyroblastic garnet dominate over quartz (the Xistos Granadas) and those in which garnet is absent (Xistos Quartzos). Schistosity is present, but is non-uniform, and the name 'Xistos' is a field term, not implying uniform schistosity throughout the unit. Normal faults, trending NW-SE and hosting quartz veins similar to those seen in the MVII in G1-C4, are common in the Rochas Fragmentos.

The main differences between the Rochas Bandadas and Rochas Fragmentos are:

i) the general absence of continuous mineralogical banding

ii) the absence of iron oxide minerals

iii) the decrease in total sulphide content

iv) the presence of schistosity developed in biotite- and chlorite-bearing areas

v) the presence of garnets and quartz aggregates.

The gradational contact between the Rochas Bandadas and Rochas Fragmentos is commonly represented by a rock which displays features of both the surrounding units, i.e. a garnet-biotite-chlorite-rich banded rock.

3.4.1 *Xistos Granadas*

These rocks take their name (literally, **Garnet-schist**) from the abundant pink almandine garnet which dominates the unit (*Fig. 3.14A*). The Xistos Granadas lie immediately to the south of, and structurally above, the Rochas Bandadas, and as such have been used as a marker horizon in the exploration for copper and zinc (Saueressig *pers.com.* 1990). They show a varying degree of mineral lamination and schistosity, and are composed of quartz, almandine and biotite, ± chlorite, grunerite, gahnite and graphite, accompanied by the sulphide minerals pyrrhotite sphalerite, chalcopyrite and pyrite, and occasionally unidentified minerals containing Co-Ni-As (*Appendix C*).

Almandine garnet porphyroblasts (formula Fe_5 (Ca,Mg,Mn) Al_4 Si_6O_{24}; *Appendix C* EPMA), form the most distinctive component in the unit, and these vary from completely anhedral to euhedral (*Figs. 3.14A-C*).

Elongate quartz clasts lie sub-parallel to the local mineralogical banding. They are sub-rounded quartz aggregates up to 50mm long and 15mm wide, composed of 0.08 to 0.3mm diameter polygonal re-crystallized quartz grains. These 'fragments' occur in a matrix of fine grained quartz (0.04-0.1mm) and biotite ± graphite ± chlorite, and contain disseminated chalcopyrite grains. (*Fig. 3.14A*).

The gradational zone between the Xistos Granadas and the Rochas Bandadas sometimes displays intense schistosity (*Fig. 3.14H*), and is composed of continuous alternating 5 to 15mm-wide bands of quartz±grunerite and garnet-chlorite (*Fig. 3.14G*). This schistose texture, also present elsewhere in the Xistos Granadas, is formed by the parallel alignment of chlorite and biotite between quartz grains at a low angle to the mineralogical banding.

Figure 3.14 **The C4 Xistos Granadas**

A Hand specimen of a typical non-schistose quartz-garnet Xistos Granadas, displaying subhedral to anhedral almandine in a quartz-biotite-graphite matrix (dark). Note early quartz-clasts (top). Sample G11.

B Photomicrograph of euhedral garnet (almandine) in a matrix of 'wrapped' quartz and graphite. Garnet displays 4-fold symmetry depicted by quartz and graphite inclusions. Sample F19. Plane-polarised light. Field of view 3.4mm.

C Photomicrograph of early-metamorphic garnet, showing the wrap-around texture created in the quartz-graphite-biotite matrix. Note polygonization of matrix quartz. Sample F19. Cross-polarised light. Field of view 6.8mm.

D Photomicrograph of almandine garnet showing overprinting by euhedral prismatic grunerite (pale green) and sulphide minerals. Sample B1. Plane-polarised light. Field of view 3.4mm.

E Typical microscopic view of Xistos Granadas, displaying relationship between sulphide minerals and silicates, with alteration of grunerite (colourless to pale green) to biotite (brown). Anhedral garnet (blocky, bottom right) is overprinted by grunerite. Sample F19. Plane-polarised light. Field of view 3.4mm.

F Drill-core specimen of typical schistose Xistos Granadas, displaying anhedral almandine in a schistose matrix of biotite and quartz (dark), chalcopyrite (metallic) and gahnite (dark green). Sample B4.

G Hand specimen from the schistose G1-C4 transition between Xistos Granadas and Rochas Bandadas, displaying horizons of amphibole (dark), quartz and garnet, and minor sulphide mineralization. Sample G5.

H Photomicrograph of chlorite-rich Xistos Granadas with an intense schistose fabric established by the presence of chlorite. Garnet has formed as a replacement of phyllo-silicates, and post-dates the schistose fabric. Sample G5. Plane-polarised light. Field of view 3.4mm.

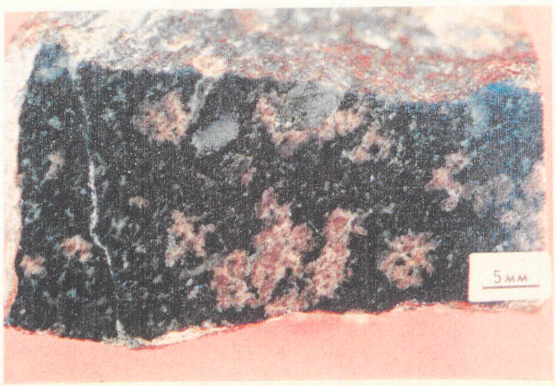

A

B

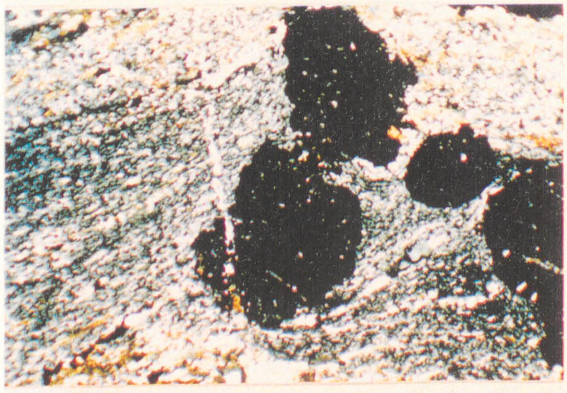

C

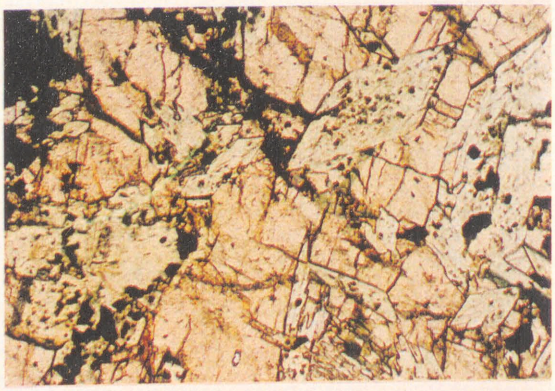

D

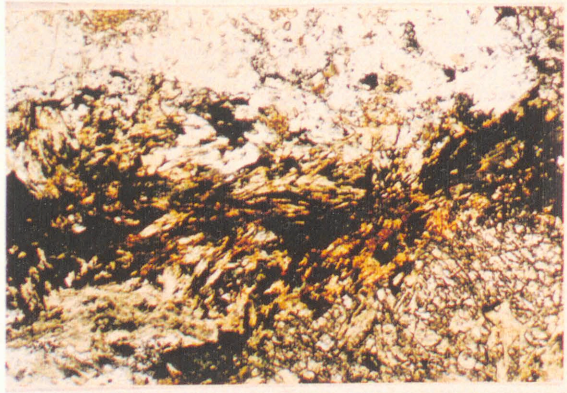

E

F

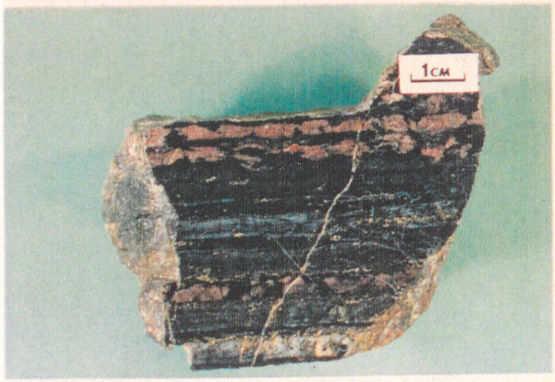

G

H

The majority of the almandine in the Xistos Granadas is subhedral to euhedral, and displays internal trails of graphite and/or quartz inclusions (*Fig. 3.15*). It has been overprinted by quartz and grunerite, and rotational textures have been developed in the outlying matrix (*Fig. 3.14B*). The almandine has also undergone extensive replacement by chlorite. Pressure shadows observed around some of the almandine crystals contain quartz which is coarser grained than that in the matrix (up to 0.2mm) as well as occasional sphalerite. These textures indicate that the garnet was formed relatively early in the metamorphic history of the rock, and has been overprinted by later deformational episodes and mineral assemblages. Deformation of this early garnet in the Xistos Granadas is brittle, with biotite commonly filling fractures in crystals (*Fig. 3.19B*) as well as forming a matrix mineral constituting about 15% of the rock (*Fig. 3.14E*).

There is also evidence for the local development of late-stage garnet at the expense of the phyllosilicates in the schistose zones of the Xistos Granadas, where almandine garnet is observed to overprint the schistosity of the chlorite-quartz assemblage (*Fig. 3.14H*). This late garnet is anhedral, and often forms garnet 'horizons', completely consuming chlorite during its development. It is also sometimes observed to overprint crenulations in the schistosity, giving the impression of an internal fabric, although it is obviously a later growth-phase than the chlorite in the schists.

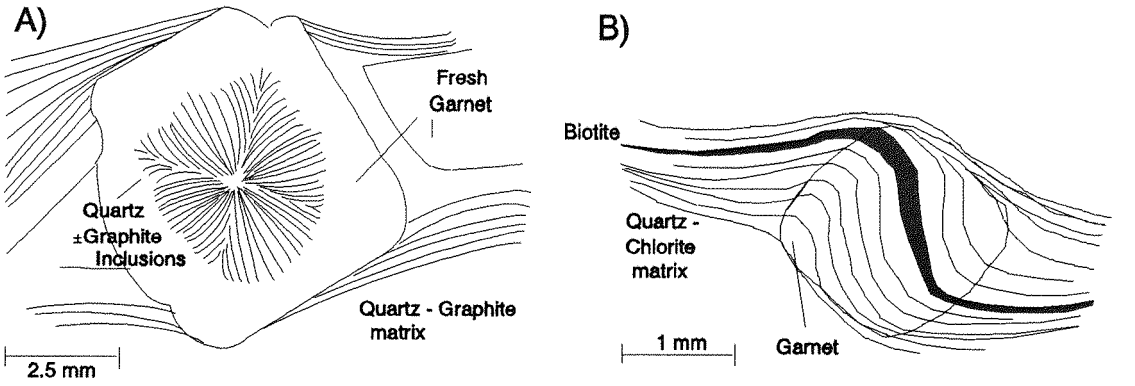

Figure 3.15 **Garnet textures observed in the Corpo Quatro Xistos Granadas. A Four-fold symmetry developed by inclusions of quartz and/or graphite in garnet core; B garnet overprinting the schistose fabric developed by biotite, chlorite and quartz.**

Grunerite and anthophyllite are not ubiquitous, but may constitute up to 60% of the Xistos Granadas. Hornblende is absent. Along cleavage planes and grain boundaries, grunerite is often observed to take on a brown coloration (*Fig. 3.14E*), similar to the way in which hornblende replaces grunerite in the Rochas Bandadas. This is where grunerite is beginning to be altered to biotite, and EPMA analyses indicate that it contains only ~2% K_2O (*Appendix C2*).

The zinc-rich spinel gahnite is a common mineral in the upper metasediments of the Pojuca C4 Formation, although its distribution is uneven and concentrated in sphalerite-rich areas. The gahnite is green in transmitted light, and shows anisotropy typical of the spinel family. The crystals are subhedral to rounded and 2 to 4mm in diameter. Some contain trails of graphite inclusions similar to the quartz inclusion trails seen in the early garnet, giving them a green-black colouring (*Fig. 3.14F*). Gahnite in the Xistos Granadas commonly shows partial alteration to chlorite at grain edges, particularly at its contact with sphalerite.

3.4.2 *Xistos Quartzos*

The C4 Xistos Quartzos either occur between the garnet-rich metasediments and the overlying metavolcanics, or interbedded with the Xistos Granadas, and are upwards of 20m thick (*Fig 3.2*). They can be divided into two types depending on their composition, but are both dominated by the absence of garnet and the presence of quartz fragments. The first type are composed of quartz-chlorite ± biotite, and generally have a schistose fabric, whereas the second type has a mineral assemblage of quartz-hornblende, and rarely displays schistosity. Both contain subordinate cummingtonite-anthophyllite, gahnite, almandine and sulphide minerals (*Fig. 3.16A-H*). Graphite is generally absent. It is not known whether the presence of chlorite is a cause or a result of the development of the schistose texture. The Xistos Quartzos take their name from the abundant quartz fragments, which, like those in the Xistos Granadas, are discordant with the local schistosity, and contain disseminated chalcopyrite and pyrrhotite at intergranular quartz boundaries. In the Xistos Quartzos, the quartz clasts are angular and commonly composed of the metamorphic assemblage of equigranular quartz and grunerite, similar to the quartz bands in the Rochas Bandadas.

Fresh garnet constitutes a maximum of only 1% of the Xistos Quartzos, where it occurs in chlorite-rich areas as an apparently late-stage mineral, overprinting the schistose fabric as observed in the Xistos Granadas. Altered garnet, which has been partially replaced by green and brown biotite along micro-fractures, and biotite pseudomorphs after garnet, are common throughout the Xistos Quartzos (*Fig. 3.16G*).

Gahnite forms green-black masses in areas of the Xistos Quartzos rich in altered garnet assemblages. Both gahnite and pseudomorphs after garnet show rotation textures in the surrounding matrix (*Fig. 3.16G*) and have been overprinted by subhedral amphiboles.

Figure 3.16 **The C4 Xistos Quartzos**

A Typical core samples of hornblende-rich Xistos Quartzos, showing clearly the quartz clasts in a dark matrix. Clasts occasionally show chalcopyrite-rich rims. Sample F76 (top) and F89 (bottom).

B Photomicrograph of quartz-hornblende Xistos Quartzos, showing the polygonal nature of the quartz making up the clast (left), in a matrix of quartz, hornblende (green) and biotite (brown). Sample F89. Plane-polarised light. Field of view 2.2mm

C Photomicrograph showing the development of a schistose fabric in a typical quartz-hornblende-chalcopyrite-pyrrhotite-rich Xistos Quartzos. Sample F70. Plane-polarised light. Field of view 2.2mm.

D Hand specimen of a typical chlorite-rich schistose Xistos Quartzos, showing large parallel quartz clasts and minor almandine (pink). Sample G12.

E Photomicrograph showing the relationship between silicates in the Xistos Quartzos. Grunerite (colourless to pale brown) is cross-cut and replaced by Zr-rich biotite along cleavage planes. Sample F58. Plane-polarised light. Field of view 3.4mm.

F Photomicrograph of typical chlorite-rich Xistos Quartzos. Chlorite (blue, xpl), biotite (brown, masked by body colour) and minor grunerite (white ppl, high birefringence xpl) give the rock its schistosity. Sample G43. Plane-polarised light (left), cross-polarised light (right). Total Field of view 3.4mm.

G Photomicrograph showing gahnite (dark green) altered to chlorite (pale green) and biotite pseudomorph after garnet, in schistose Xistos Quartzos with quartz-chlorite-grunerite matrix. Sample F39. Plane-polarised light. Field of view 6.8mm.

H Photomicrograph of late garnet (opaque) overprinting quartz-grunerite fabric in Xistos Quartzos. Central garnet is rich in quartz inclusions, while outer garnet is formed by the replacement of a dominantly phyllo-silicate assemblage and contains only minor inclusions of quartz. Sample F58. Cross-polarised light. Field of view 4.4mm.

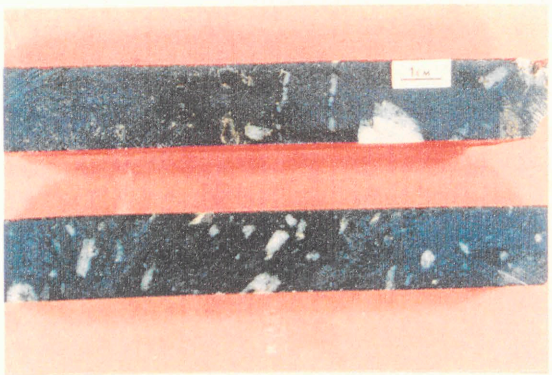

A

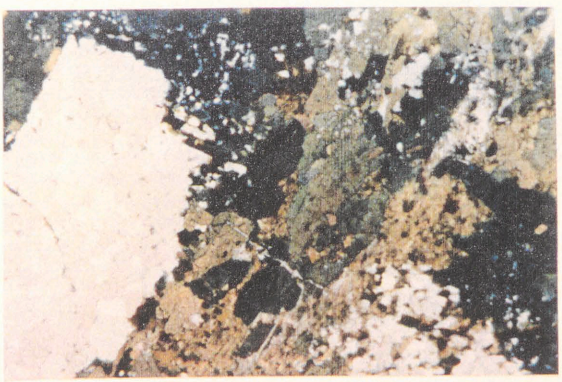

B

C

D

E

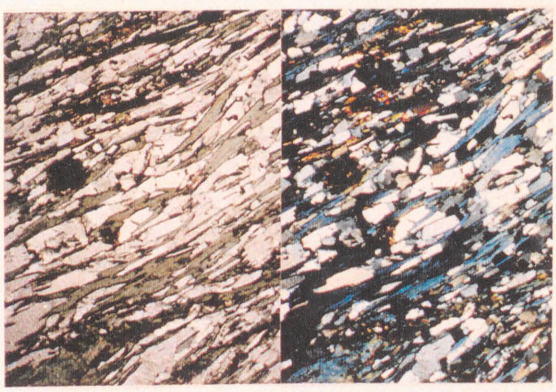

F

G

H

3.4.3 *Metamorphism and Alteration of the Rochas Fragmentos.*

The metamorphic mineral assemblage of quartz, biotite, garnet and amphibole ± graphite, which is present throughout the Rochas Fragmentos, is indicative of garnet grade metamorphism, corresponding with the medium grade, lower amphibolite facies metamorphism seen in the Rochas Bandadas. The grain size in the quartz fragments, consistently 0.1 to 0.6mm, also indicates amphibolite facies metamorphism (James, 1955). The matrix quartz is finer grained than the clast quartz, and does not appear to be indicative of the metamorphic grade according to the James (1955) classification, and is thought to represent quartz which has formed as a product of metamorphic reactions, rather than having been recrystallized during the metamorphism of pre-existing silica.

The overprinting of early garnet by euhedral grunerite, and the internal graphite-quartz inclusion symmetry and wrapping of the quartz-graphite-amphibole-biotite matrix implies that this garnet was dominantly of pre-kinematic development, having formed early during regional metamorphism, and has been overprinted by later metamorphic minerals. The early almandine in the Xistos Granadas is often at least partially altered to chlorite, which is a common retrograde reaction (Barker and Bennett, 1992).

The presence of late anhedral almandine overprinting the schistose fabric created by phyllosilicates during regional metamorphism, is indicative of a localized late hydrothermal event. Almandine is known to form as a result of increased temperature (Hsu, 1968), in association with thermal as well as regional metamorphism, and therefore implies the presence of a late, thermal event in the Corpo Quatro Formation. This may relate to the introduction of the Pojuca Granite (see section 3.5).

Chlorite is present as an alteration product of grunerite, garnet and gahnite, where it is identified as brunsvigite by electron probe analysis (*Appendix C*). Chlorite also forms the schistose texture of the Xistos Quartzos, where it is in equilibrium with quartz, and is identified as repidolite using EPMA. On the basis of silica content and $Fe^{2+}/Fe^{2+}+Mg^{2+}$ = 0.66, the repidolite is indicative of retrograde, chlorite zone metamorphism. The brunsvigite, however, does not fall within the metamorphic chlorite field on the silica-Fe diagram (*Fig. 3.10*). This may, therefore, be the result of hydrothermal overprint.

The presence of gahnite in metapelites has been attributed to the desulphurization of zinc-bearing minerals in the presence of quartz during metamorphism (Frost, 1973), and this is the first evidence at Pojuca that sphalerite may have been present at least during, if not prior to, the main metamorphic event. Sphalerite in garnet pressure shadows is also indicative of this, although in the Rochas Fragmentos, as in the Rochas Bandadas, sphalerite shows no sign of metamorphic alteration (see section 3.4.5).

Graphite as a metamorphic indicator.

Graphite may develop in a number of metamorphic environments, as a result of the high grade metamorphism of amorphous carbon in metamorphosed pelites (Klein, 1973), or of the addition of CO_2 to iron-oxide ($2FeO + CO_2 = Fe_2O_3 + C$; Thompson, 1972). The absence of haematite in the Corpo Quatro Formation suggests that the metamorphism of amorphous carbon in the original sediment was probably the cause of graphite in the Pojuca deposit.

Carbonaceous material, including graphite, undergoes a modification and ordering of crystal

structure on metamorphism, and it is possible to quantify this change in terms of chlorite, biotite-garnet, staurolite-andalusite-kyanite, and sillimanite-granulite metamorphic zones by laser Raman spectroscopy (Pasteris and Wopenka, 1991). Graphite produces a Raman scatter with characteristic peaks at ~1355 cm^{-1} ('D' or disordered peak), ~1582 cm^{-1} ('O', or ordered peak) and 2735 cm^{-1} ('S', second order peak), with subordinate peaks at ~3248 and 2450 cm^{-1} in well ordered, or highly crystalline forms of graphite. Raman peaks are typically measured using peak intensity and the peak width at half peak height, and it has been found that by applying a combination of two or more of these dimensions, the grade of metamorphism suffered by the graphite can be established. Laser Raman spectroscopy has been undertaken on several graphite grains in quartz from polished thin sections of graphite-bearing Xistos Granadas, producing consistent results. An example of two spectra are given in *Figure 3.17* and *Table 3.2*.

Table 3.2 **Peak positions, intensities and ratios of Raman O, D and S peaks for graphite in Xistos Granadas from the Pojuca C4 Formation.**

	Graphite Sample 1	Graphite Sample 2
Peak position O	1581	1581
Peak position D	1356	1358.9
Peak position S	2725.7	2729.3
Half peak width O	18	18
Half peak width D	54	56.4
Peak intensity O	30.8	24.97
Peak intensity D	4.46	3.58
Peak intensity S	20.29	14.4
Intensity D/O	0.145	0.143
Intensity S/O	0.65	0.58

The most informative metamorphic indicator using the Raman technique has been found to be the combination of the O peak width and the D/O intensity ratio (Wopenka and Pasteris, 1993), both of which show that the graphite in the Xistos Granadas have undergone medium grade metamorphism (*Fig. 3.18A&B*). The presence of the small 3245 peak in the Raman spectra from the Pojuca samples suggests that this graphite is relatively well ordered, and the half-width for the O peak (18 cm^{-1}) corresponds with the 16±2 cm^{-1} half width for the sillimanite zone rather than the 22±2 cm^{-1} for the staurolite zone (Wopenka and Pasteris, 1993). The presence of the D peak, however, rules out true sillimanite grade metamorphism, and its half-peak width (*Fig. 3.18C)* is suggestive of garnet to staurolite grade. While garnet zone graphite displays a symmetrical S peak, the asymmetry of the S peak in the C4 graphite again

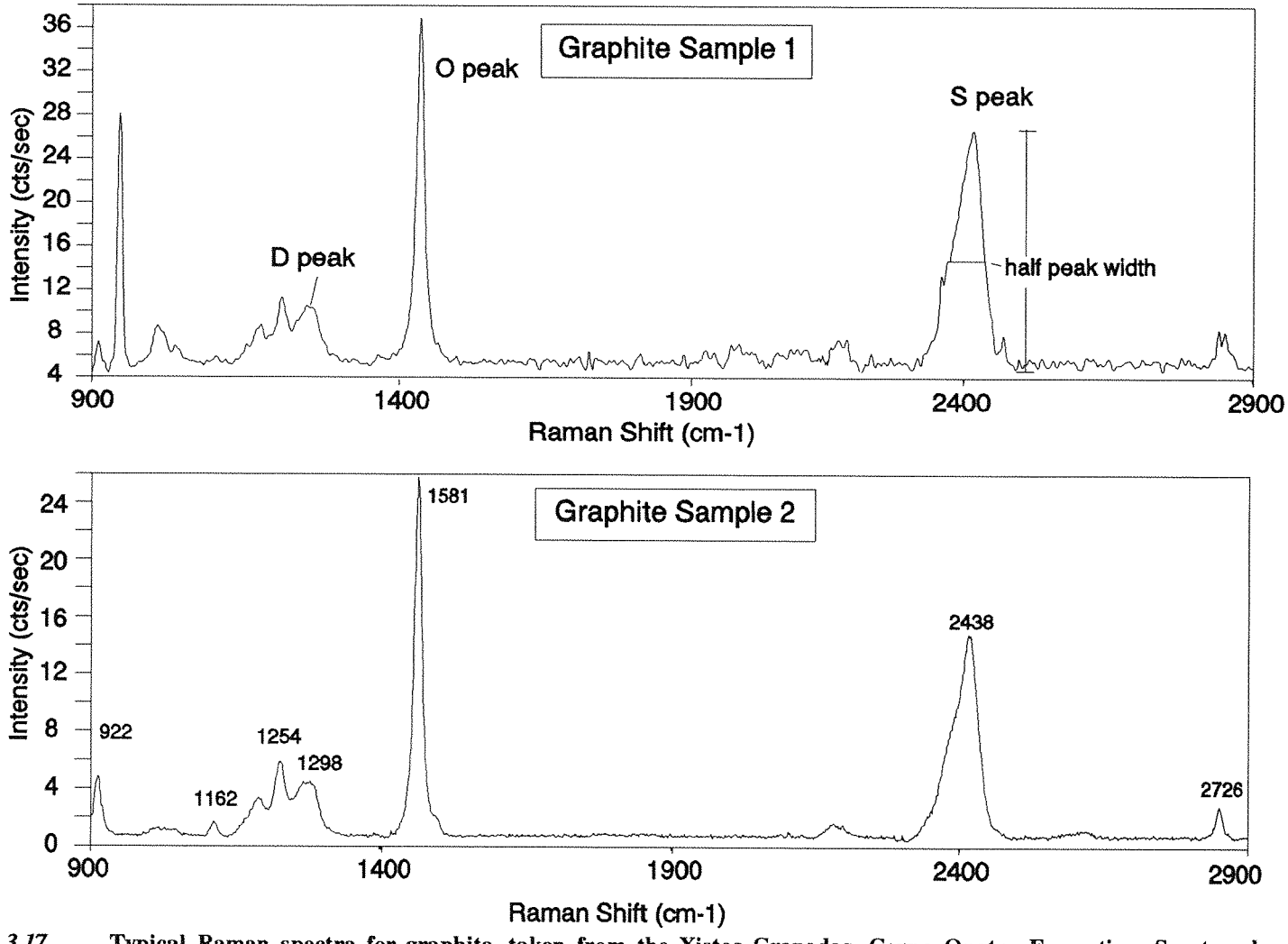

Figure 3.17 **Typical Raman spectra for graphite, taken from the Xistos Granadas, Corpo Quatro Formation. Spectra show the positions of the dominant graphite peaks (D,O and S) and the position at which half-width measurements are taken.**

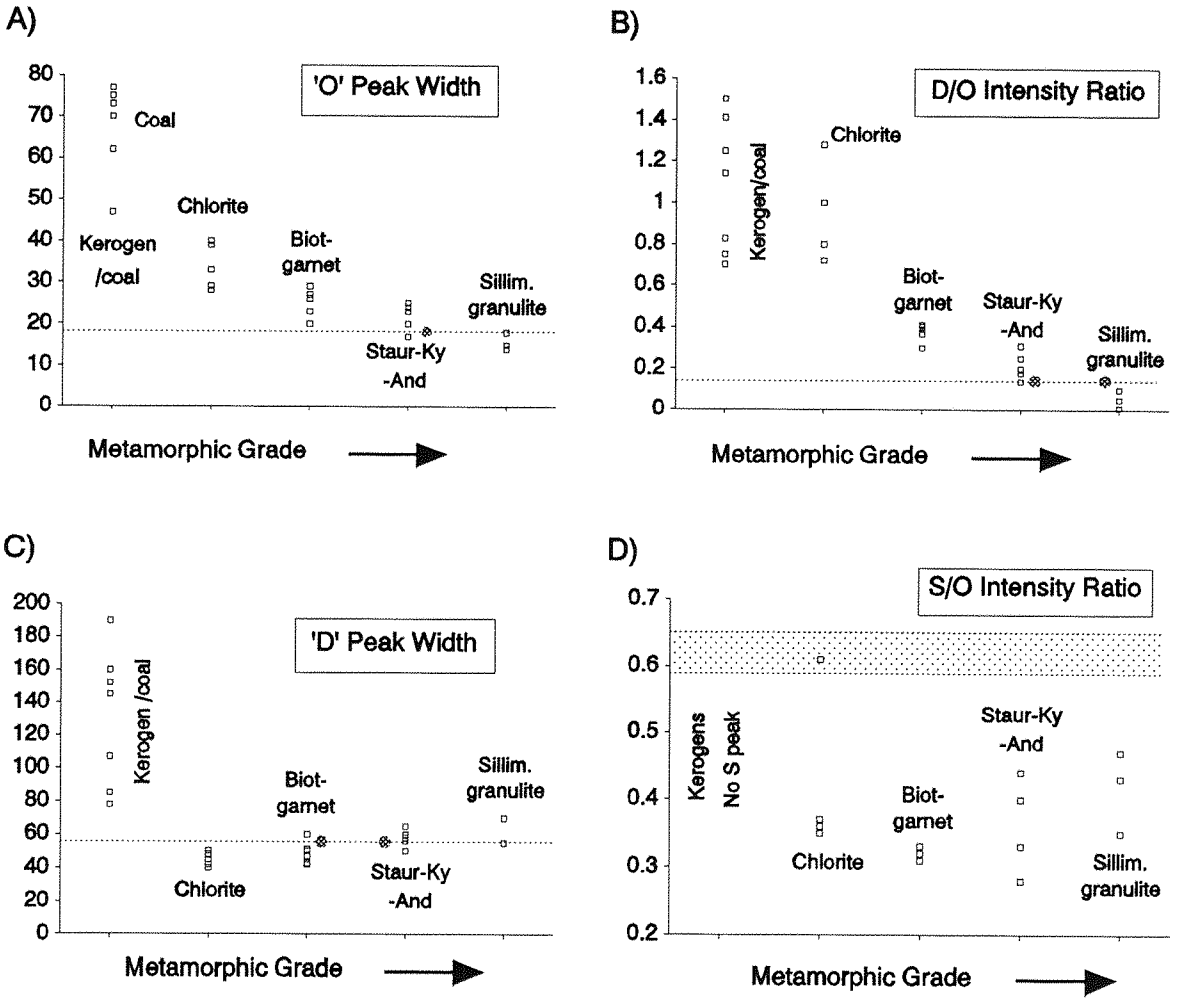

Figure 3.18 **Graphite Raman spectra as a metamorphic indicator: A Half peak widths of 'O' peak; B Half peak widths of 'D' peak; C Intensity ratios of D:O peaks; D Intensity ratios of S:O peaks, against increasing metamorphic grade. Open squares = data from Wopenka and Pasteris (1993); filled circles, dotted lines and infilled box = data from the Corpo Quatro metapelitic graphite**

gives confirmation that the Pojuca samples have undergone metamorphism to the staurolite zone. The S/O ratio has been found to show no correlation with metamorphic grade (Wopenka and Pasteris, *op.cit.*), which explains why the S/O peak intensity ratios of the C4 samples in *Figure 3.18D* do not correspond with medium to high grade metamorphism.

The variable mineral assemblage throughout the Rochas Fragmentos strongly suggests that the primary sedimentary unit was of variable composition. The difference in the development of schistosity throughout the Rochas Fragmentos, with the higher silica content and the pervasive alteration of minerals such as almandine and gahnite to chlorite and biotite in the zones of intense schistosity, imply that the unit has become increasingly differentiated since metamorphism. This schistosity is mainly developed in the Xistos Quartzos and in the Rochas Bandadas-Xistos Granadas gradational zone, where early garnets show alteration to biotite and there is localized development of late garnet, formed at the expense of phyllo-silicates such as chlorite. These units show evidence for major shear deformation. The presence of the late garnet in the schistose zones may indicate the local introduction of heat and hydrothermal activity. It would appear that regional strain was preferentially partitioned into these rocks rather than the metavolcanics or Rochas Bandadas, which may have been more susceptible to brittle rather than ductile deformation, as indicated by the abundance of faults and veins in these units.

3.4.4 *Sulphide Mineralization in the C4 Rochas Fragmentos.*

The total sulphide content of the Rochas Fragmentos is lower than that of the Rochas Bandadas, as shown in the cross sections of *Figure 3.2*. The distribution of sulphide minerals is non-uniform, and banded sulphides are rare, occurring only in the gradational area of the Xistos Granadas, where mineralogical banding is also present. Mineralization in the Xistos Quartzos is less common than in the garnet-rich unit, with pyrite and minor chalcopyrite and sphalerite occurring only in fractures less than 1mm wide.

Although pyrite and sphalerite are both more abundant here than in the Rochas Bandadas, this cannot be considered as sulphide zoning, a common feature of massive sulphide deposits (Huston and Large, 1989), as the Rochas Bandadas-Rochas Fragmentos sequence is often a repeated one, throughout which the variation of sulphide content is apparent. This is discussed in more detail in Chapter 6.

The predominant style of mineralization in the Rochas Fragmentos is in fractures and disseminated grains, as described in section 3.3.3. Sphalerite hosts apparently crystallographically orientated chalcopyrite blebs, and cross-cuts metamorphic grunerite crystals which have developed the local schistosity (*Fig. 3.19C*). Pyrite, too, is occasionally observed in fractures cross-cutting the schistosity, but has been deformed and elongated parallel to the schistose fabric and therefore predates the development of the schistosity. Pyrite has also undergone brittle deformation in places, and forms apparent nucleation sites around which pyrrhotite and chalcopyrite develop (*Fig. 3.19F*). Pyrrhotite and chalcopyrite occur as disseminated grains in both the quartz matrix and the clasts (*Fig. 3.14A*), and pyrrhotite contains randomly distributed inclusions of chalcopyrite. These textures, particularly the

Figure 3.19 **Mineralization in the C4 Rochas Fragmentos**

A Drill core specimen of Xistos Granadas, showing the pervasive nature of late chalcopyrite surrounding earlier euhedral garnet, in a matrix of biotite-quartz-graphite. Sample F64.

B Photomicrograph of post-metamorphic sulphide development (chalcopyrite, opaque) around euhedral almandine. Garnet (high relief) displays brittle fractures filled by biotite (yellow-brown) and marginal alteration to chlorite. Sample G35. Plane-polarised light. Field of view 4.4mm.

C Photomicrograph of sphalerite (red and brown, translucent) showing caries texture with quartz (colourless, centre). Sample B6. Plane-polarised light. Field of view 0.55mm.

D Sphalerite (red) overprinting euhedral grunerite (colourless). Brown mineral is biotite. Sample B6. Plane-polarised light. Field of view 2.2mm.

E Photomicrograph of schistose chlorite-quartz-rich Xistos Quartzos hosting a cross-cutting pyrite vein, which displays orthogonal offshoots following the local fabric. Sample G43. Reflected light. Field of view 2.2mm.

F Photomicrograph showing the presence of synchronous pyrite and silicate minerals in a chlorite-rich Xistos Quartzos, and the nucleation of pyrrhotite onto pyrite. Minor chalcopyrite also present. Sample G43. Reflected light. Field of view 0.55mm.

G Photomicrograph of unidentified white sulphide mineral, composition in Wt %: Fe 14.8, Co 30.6, As 44.3, Ni 10.3 (SEM analysis). Mineral shows blue-white to pink-white reflectance pleochroism. Chalcopyrite, also present, shows overprinting by chlorite. Sample G3. Reflected Plane-polarised light. Field of view 1.1mm.

A

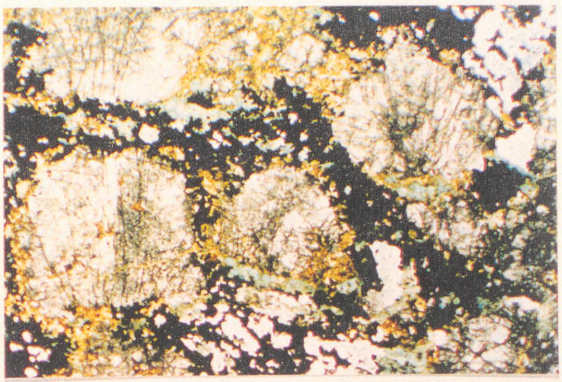

B

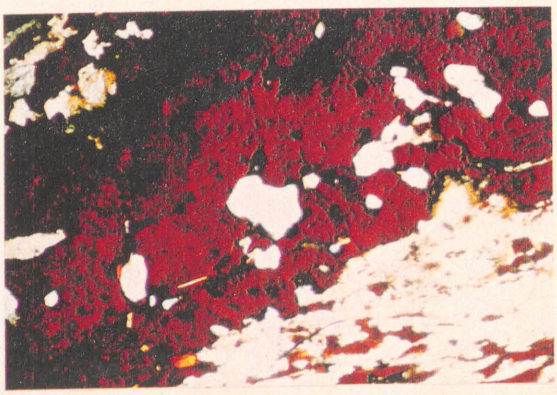

C

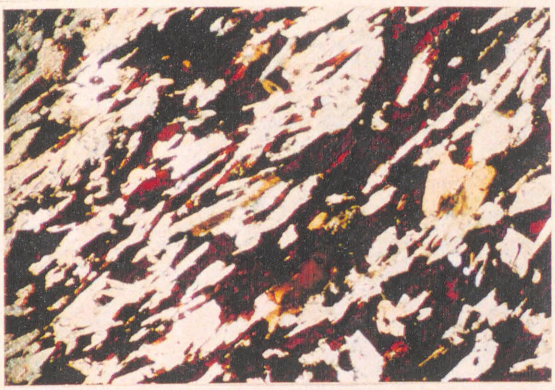

D

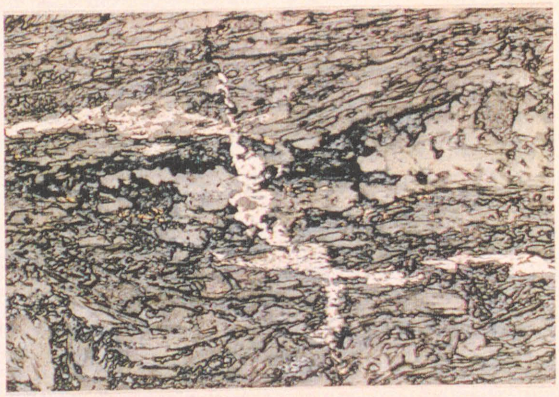

E

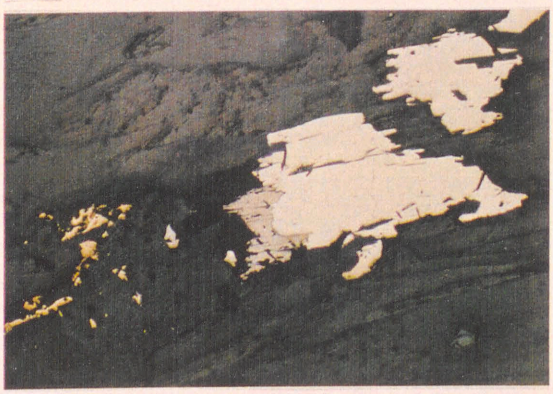

F

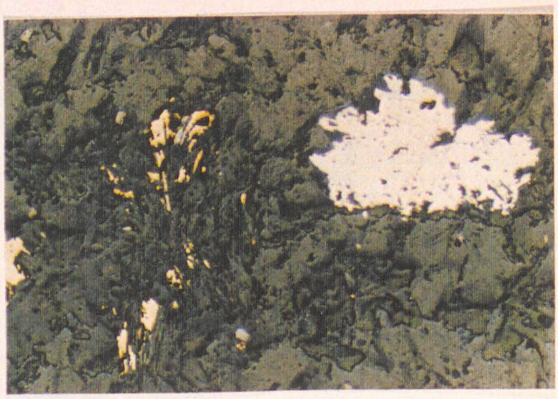

G

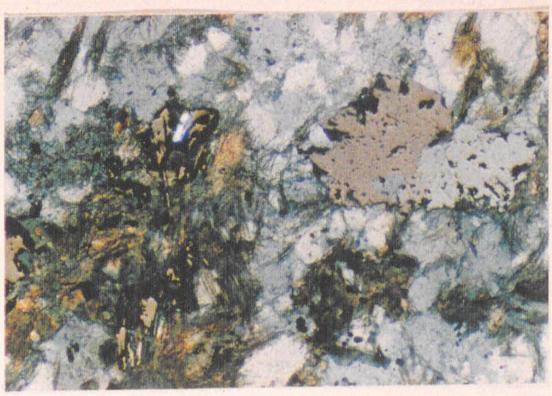

H

nucleation of sulphides around pyrite, are more comparable with those seen in metamorphosed sulphide deposits than the textures seen in the Rochas Bandadas.

Microscopic inclusions of blue-white, weakly pleochroic, unidentified nickel-arsenides have been observed within pyrite grains in the schistose Xistos Quartzos. Unidentified nickel-arsenides (formulas $(Co,Fe)SAs_2$ and $(Ni,Fe)_2Co_2As_{2-3}$; *Appendix C*) have also been observed in the chlorite-rich schistose zones of the Xistos Quartzos, where they are rarely in contact with other sulphide minerals. They form anhedral bodies up to 0.3mm across, are blue-white and strongly pleochroic, with blue-grey to mauve bireflectance (*Fig. 3.19G&H*). These minerals appear to be conformable with the hydrothermal introduction of nickel, where, in the Rochas Bandadas, this is manifested in the form of pentlandite in pyrrhotite.

The sulphides in contact with silicate minerals in the Rochas Fragmentos show the same cleavage-penetration texture seen in the Rochas Bandadas. Here, however, they penetrate biotite and chlorite cleavage as well as that of grunerite. In these rocks, biotite and chlorite are a common replacement feature of grunerite, forming as a result of the hydrothermal alteration of the amphiboles (*Fig. 3.14E*), suggesting either that the sulphides are replacing biotite, or that they replace grunerite which is subsequently altered to biotite. Biotite veinlets also cross-cut sulphide minerals throughout the sequence, indicating that the sulphide minerals were formed post-amphibole but pre-biotite-chlorite growth.

It has been considered that the disseminated pyrrhotite found in quartz may have formed as the result of pyrite or magnetite metamorphism in the presence of graphite, although no pseudomorphs or relict grains of these minerals have been found. Pyrite, typical of low metamorphic grades, alters to pyrrhotite on increased temperature:

$$3FeS_2 + Fe_3O_4 + 2C = 6FeS + 2CO_2$$ (Thompson, 1972).

The presence of pyrrhotite in metapelites has been considered as a metamorphic isograd (Thompson, *op.cit.*) but the uneven distribution of this mineral in the Pojuca Corpo Quatro sequence suggests that it is of post metamorphic origin. Pyrite, however, is often seen in close association with garnet, forming brittly deformed cubes which are replaced and enclosed by both pyrrhotite and chalcopyrite, indicating that at least some pyrite is early maybe of either syn-metamorphic or diagenetic origin.

Unlike pyrrhotite and pyrite, chalcopyrite and sphalerite are not known to occur as products of metamorphism, and as they have not been metamorphosed they are thought to be the result of late stage hydrothermal activity. The orientated blebs of chalcopyrite in sphalerite are unlike the random blebs in Rochas Bandadas-hosted sphalerite, and are indicative of either synchronous growth of the two or unmixing of copper-rich sphalerite on cooling. The association of intense schistosity with nickel-arsenides is indicative that these unidentified minerals were introduced during periods of intense deformation, which was responsible for the shearing seen in the thick (2 to 4m-wide) rock units.

3.5 THE POJUCA GRANITE

In the western part of the Corpo Quatro prospect, the boreholes intersect a granitoid body known

as the Pojuca Granite. This is a coarse-grained, white or pink-white rock, composed of a hypidiomorphic mass of feldspar (20% orthoclase, 20% plagioclase, and variable amounts of microcline, perthite and antiperthite) and quartz, zircon-rich biotite and accessory apatite. The granite has been observed to host minor amounts of molybdenite and chalcopyrite.

The composition of this rock, based particularly on the equal proportions of plagioclase and orthoclase feldspars, results in its classification as an adamellite. The stock has been dated using U-Pb from the zircon fraction, defining an upper age limit of 1874±2Ma (Machado *et al.*, 1991). No geochemical analyses have been carried out on this intrusion.

The Pojuca Granite has had no visible thermal effect on the Corpo Quatro metasediments into which it was intruded, even though the presence of perthite textures and microcline are both indicative of predominantly slow cooling (Hatch *et al.*, 1972). There is no direct evidence for the presence of veins related to this granite, although this may be a function of the lack of exposure. The intrusion is therefore believed to have been a relatively dry granite, which is supported by the existence of perthitic feldspars. No post-emplacement deformational features have been observed in the Pojuca Granite.

The relationship between the Pojuca Granite and the pink, K-feldspar-rich granitic veins, which cross-cut the Corpo Quatro Formation (described in Chapter 5), is unknown, but it is believed that they are unrelated. This is discussed further in Chapter 6.

3.6 *DISCUSSION*

The sub-vertical Corpo Quatro Formation, which hosts the small Pojuca Corpo Quatro deposit and forms part of the Igarapé Pojuca Group, is composed of metabasites of extrusive origin, sandwiching the C4 metasediments which comprise metamorphosed iron-formation (Rochas Bandadas) and mixed chemical-clastic sediments (Xistos Granadas and Xistos Quartzos). The Xistos Granadas are similar in texture to conglomerates observed overlying iron-formation in the Starra deposit of the Mt Isa district, Australia (Davidson *et al.*, 1989) and in the N4E deposit of the Carajás Formation. The contact between the sedimentary Xistos Granadas and Rochas Fragmentos units is gradational, over 0.5 to 1m, and is seen as sedimentary rather than tectonic. The contact between the two units in the G1-C4 adit forms an intensely schistose, faulted zone. This is similar to the schistose areas found throughout the Corpo Quatro Formation, and is believed to represent a sheared gradational boundary. The boundary is composed of a mixture of the textures and minerals seen in the Rochas Bandadas and Xistos Granadas. The boundaries between the upper and lower volcanics and the sedimentary units are sharp rather than gradational, and show no evidence of faulting where they are observed in G1-C4 and in the drillcore. Together with the brecciated flow tops seen elsewhere in the Carajás region and the regional nature of inter-bedded volcanic and sedimentary units throughout the Carajás Belt (Lindenmayer, 1990; Medeiros Neto and Villas, 1985), this suggests that the extrusive volcanics of the Corpo Quatro Formation are conformable with the interbedded metasediments. It also implies that the metasedimentary units represent repeated sedimentary cycles, not structurally controlled imbricate slices.

The mineral assemblages throughout the sequence are indicative of lower amphibolite grade

metamorphism, with hornblende, plagioclase feldspar and biotite making up the metabasites and grunerite, quartz, garnet and biotite forming the bulk of the metasedimentary mineral assemblage. P-T conditions can be estimated from these mineral assemblages, combined with the formation pressure estimate given by Fe-amphiboles in the Rochas Bandadas and the presence of oligoclase feldspar and minor chlorite in the metabasites at Pojuca. The estimated maximum P-T conditions are shown on *Figure 3.20*, and are between 5 and 7 Kbar and 500° and 580°C (Maruyama *et al.*, 1983).

The interpretation of the cordierite-anthophyllite assemblage, which occurs predominantly in the MVI metabasites, above the sulphide-bearing strata, depends on the way-up of the strata. Cordierite-anthophyllite metabasites are common below syngenetic massive sulphide deposits, where they form as the result of a metamorphic overprint of hydrothermal alteration (Franklin *et al.*, 1981). Had the Corpo Quatro Formation been overturned, the presence of the localized cordierite (which is heavily altered to biotite) and anthophyllite in the MVI may provide evidence that sulphide mineralization in the sequence is of exhalative massive sulphide origin, with the cordierite-anthophyllite representing the metamorphosed feeder zone below syngenetic sulphide mineralization. There is, however, no definitive evidence for the inversion of the sequence, particularly if the quartz clasts in the Rochas Fragmentos are considered to have been derived from the Corpo Quatro Rochas Bandadas, or an equivalent, iron-formation. The very nature of the sulphide mineralization is indicative of post-metamorphic introduction rather than massive sulphide deposition, as discussed further in Chapter 6. The cordierite-anthophyllite assemblage has therefore been interpreted as the result of the metasomatic introduction or redistribution of magnesium within the system during metamorphic activity, rather than a syn-sedimentary process.

The Rochas Bandadas mineral assemblage (quartz-amphibole ± magnetite) is unusual in terms of comparable Archaean iron-formations, which typically contain orthopyroxene and carbonate minerals when metamorphosed to medium or high grade (Gilligan, 1990; Klein, 1978). The mineral assemblage seen in the Corpo Quatro Formation is similar to that observed in the Igarapé Salobo Group Iron-Formation (Lindenmayer, 1990) and it may be appropriate, at this stage, to define a new class of iron-formation: the Pojuca-Salobo Type, which is composed of alternating horizons of quartz and grunerite ± magnetite and hornblende, but in which pyroxene and carbonate, traditionally used in metamorphic grade determination, are absent.

Gross (1980, 1988) defined Canadian iron-formation in terms of broad tectonic setting, into the Algoma-type and Lake Superior-type iron-formations. These both contain oxide, silicate, carbonate and sulphide facies iron-formation, but have different geochemical signatures and associated lithologies, the Algoma-type consistently found in association with greywackes and volcanic rocks, deposited close to volcanic centres, and the Lake Superior-type deposited in near-shore environments and associated with dolomites, quartzites and black shales. No broad-scale geochemical classifications may be made, as the chemical comparisons between the two types of iron-formations vary depending on the facies. In terms of lithological associations, the Pojuca Corpo Quatro iron-formations are most comparable with Algoma type iron-formation. Other aspects of comparison will be discussed in Chapters 4 and 6. The predominant silicate in the Corpo Quatro Formation iron-formations is grunerite, which, as shown in section 3.3.2, may

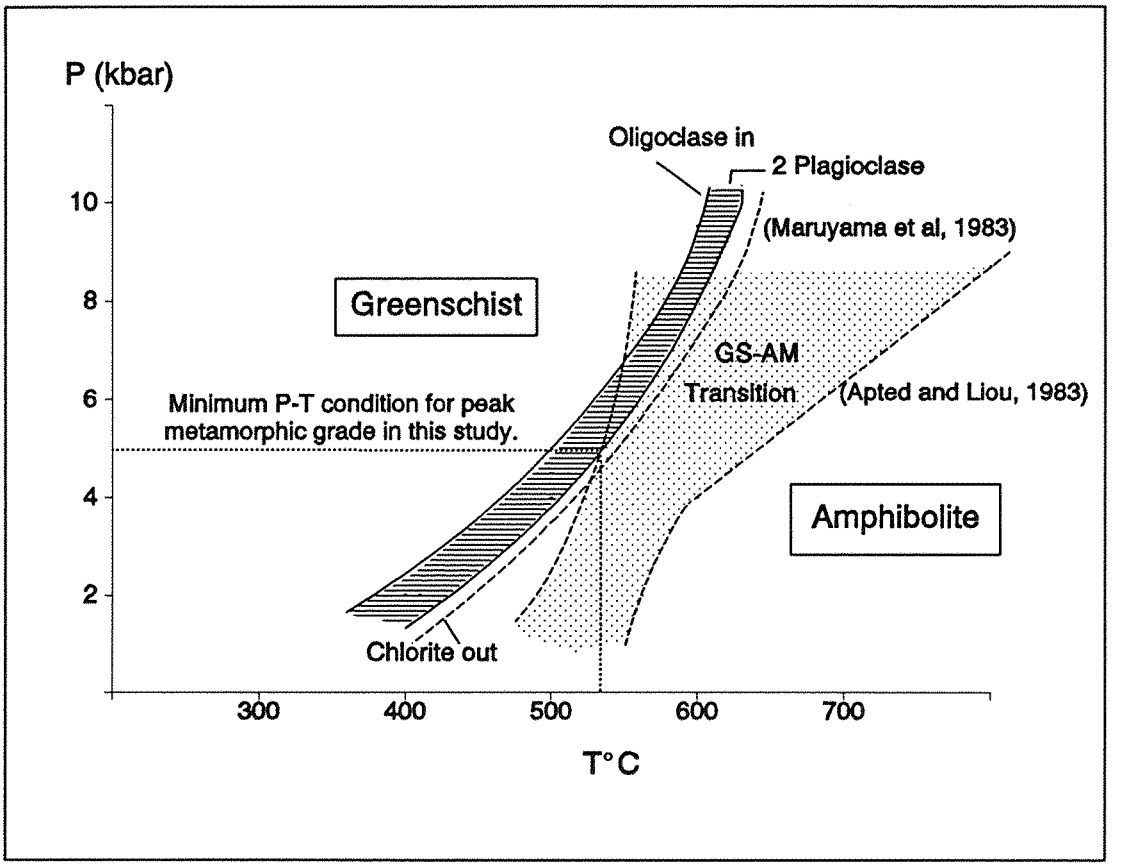

Figure 3.20 **Phase relations of the greenschist (GS) - amphibolite (AM) transition in metabasites, showing the estimated conditions of metamorphism in the Corpo Quatro Formation. Transition zone positioned according to Apted and Lion (1983) and GS-AM boundary according to Maruyama *et al.* (1983). (After Maruyama *et al.*, 1983)**

be formed by a number of different metamorphic reactions. It is therefore not possible to determine the iron-formation facies to which the Rochas Bandadas belonged prior to metamorphism.

The change in metamorphic assemblage from the Xistos Granadas (quartz-biotite-garnet±graphite±grunerite) to the Xistos Quartzos (quartz-hornblende ± chlorite ± biotite ± garnet) is suggestive of a change in lithology during deposition, rather than a change purely during hydrothermal alteration. There has, however, been a strong post-metamorphic hydrothermal overprint in these rocks, which resulted in the alteration of garnet and gahnite to biotite and chlorite in the Xistos Quartzos, and in the development of schistosity in patches throughout the Rochas Fragmentos. No schistosity has been developed within the Rochas Bandadas, although in these rocks grunerite is sometimes observed to take on a schistose texture. The general lack of mineral alignment indicates that the mineralogical banding in the Rochas Bandadas is primary rather than tectonic. The formation of the schistose fabric may either be a function of the abundance of minerals with the ability to display schistosity (chlorite and biotite) in the Rochas Fragmentos, as is believed to be the case in the similar metasediments of the Igarapé Salobo Group (Lindenmayer, 1990), or may have been caused by a later shearing event. The irregular distribution of this feature and its presence in the metavolcanics and in some of the granitic veins (see Chapter 5), means that the latter explanation is favoured, with the development of wide (3-4m) shear zones, which were probably formed during retrograde metamorphism. However, the ability of the rock to assume the schistose fabric appears to have been enhanced by the mineralogy.

Ripidolite is the dominant chlorite in the shear zones. This mineral has been shown to be the retrograde chlorite in the Corpo Quatro Formation, indicating that the replacement of pre-existing mineral assemblages in the shear zones was the result of retrogression. This also provides a time constraint on the formation of the shear zones, which must have occurred during or immediately prior to chlorite retrograde metamorphism.

Post-metamorphic potassic alteration of amphiboles (grunerite in the sedimentary rocks and hornblende in the volcanic sequence) to biotite is evident throughout the sequence, particularly in the schistose Rochas Fragmentos, and the decomposition of both brown and green biotite to chlorite is common, especially in the Xistos Quartzos.

In close proximity to both banded and fracture style mineralization, colourless iron-magnesium amphiboles (grunerite and anthophyllite) are observed to be altered to green calcic amphiboles (ferro-actinolitic and ferro-tschermakitic hornblende) in and around these fractures. This alteration appears to be a result of Ca-rich hydrothermal fluids reacting with the pre-existing metamorphic amphiboles, while the formation of minute iron sulphide inclusions, probably pyrrhotite, within the hornblende (*Fig. 3.8I*) consumed any excess iron in the system. The intimate relationship between sulphide mineralization and hornblendization (*Fig. 3.8*; see section 3.3.3) suggests that the two effects were synchronous, resulting from the same fluids. Not all sulphides, however, display this affiliation with hornblende, and vice-versa. Thus it may also be possible that the Ca-rich fluids were introduced during a later hydrothermal event, and utilized the weaknesses, particularly the veins, created in the host rock by the earlier mineralizing fluids.

Sulphide mineralization in the metasedimentary rocks at Pojuca has an apparently lithological

control, with sphalerite and pyrite and minor nickel-arsenides predominating in the upper, clastic sediments, whereas chalcopyrite and pyrrhotite, and an erratic sphalerite distribution, are present in the Rochas Bandadas.

Copper and zinc mineralization occurs as chalcopyrite and sphalerite in two forms; banded and fracture-fill sulphides, both of which occur in the absence of additional quartz. The majority of this sulphide mineralization occurs within the Rochas Bandadas. The Banded Sulphides appear, at first, to represent sedimentary ore deposition. Chalcopyrite, pyrrhotite and minor pyrite, but rarely sphalerite, are also commonly found within quartz veins in the Rochas Bandadas, whereas the extensional quartz-bearing faults commonly found in the metabasites and the Rochas Fragmentos are mainly barren. Sulphide-bearing quartz-carbonate veins in drillcore have been observed to host offshoots, or apophyses, which eventually become sulphide-only veins within and parallel to amphibole horizons in the C4 Formation metasediments. This, combined with the notable increase in sulphide content in close proximity to the massive reverse-fault hosted quartz-veins in G1-C4, suggests that both banded and fracture-type mineralization in the host-rocks are intricately related to vein emplacement. This is described in more detail in Chapter 5.

Pyrite and pyrrhotite are known to form in response to the metamorphism of pelitic and carbon-bearing schists (Klein, 1973) although magnetite, commonly preserved during this reaction, is rarely seen in this situation at Pojuca. Pyrrhotite is also known to form from pyrite at elevated temperatures, when sulphur is removed from pyrite to form pyrrhotite (*Fig. 3.13*). This pyrrhotite may revert back to pyrite under retrograde conditions. If pyrite had been present in the original sedimentary pile, however, more abundant primary pyrite grains should be expected within the pyrrhotite of the Corpo Quatro Formation.

The presence of chalcopyrite blebs in sphalerite is evidence that the sphalerite has not undergone metamorphism, as chalcopyrite tends to coalesce or form crystallographically controlled exsolution textures as a result of increased temperature and/or pressure (Craig and Vaughan, 1981). The chalcopyrite may, therefore, be the result of either replacement of sphalerite along anhedral grain boundaries, or of pre-existing chalcopyrite grains being overgrown by sphalerite. The occurrence of sphalerite cross-cutting chalcopyrite is also suggestive of sphalerite post-dating chalcopyrite.

Ilmenite and magnetite may coexist as separate grains or as exsolution pairs in sediments metamorphosed to garnet-staurolite and sillimanite zones (Rumble, 1976). It is also known that ilmenite may form by the introduction of titanium into magnetite at high temperatures. Slow, post-metamorphic cooling gives rise to unmixing, during which ilmenite laths develop within the magnetite (Edwards, 1965). In the C4 Rochas Bandadas, the two minerals do not coexist, and it is suggested that ilmenite laths formed on exsolution during metamorphism, and are now present as apparently residual grains where magnetite has been wholly replaced by sulphide minerals.

The sulphide minerals which occur in the Rochas Bandadas do not show any of the metamorphic or deformational evidence such as annealing, satellite grains or overgrowth which are common in metamorphosed exhalative MSDs (which are described at length by Sangster and Scott (1976), Davidson *et al.* (1989), Large *et al.* (1988) and others). The penetrative nature, particularly of chalcopyrite, into the

amphiboles, indicates that the replacement of amphiboles occurred during post-metamorphic, hydrothermal activity. Sulphide mineralization, therefore, occurred, or was at least remobilized, after amphibole growth and hence after peak metamorphism, implying that the banded-style of sulphide minerals are post-peak metamorphic.

A paragenetic sequence can be developed using textural relationships between sulphide minerals in the Corpo Quatro Formation. Brittly deformed pyrite in the Rochas Fragmentos is surrounded by undeformed pyrite and pyrrhotite, whereas in the Rochas Bandadas pyrrhotite and chalcopyrite replace magnetite and enclose ilmenite laths. This indicates that pyrite was present in the iron-formation at an early, pre-metamorphic stage, and that pyrrhotite and chalcopyrite are a late, post-metamorphic replacement feature. Pyrrhotite surrounding deformed pyrite, however, is common in metamorphosed sulphide bodies, where pyrite has been altered to pyrrhotite, and indicates that at least some of the pyrrhotite in the Corpo Quatro Formation may be a product of metamorphism. Chalcopyrite has an ambiguous relationship with pyrrhotite, although in most cases it appears to surround and replace the latter along cracks and grain boundaries. Sphalerite occurs in fractures cross-cutting all other sulphide minerals, and the replacement of chalcopyrite by sphalerite is evident in the form of chalcopyrite 'spots' in sphalerite. Molybdenum, pentlandite, Co-Ni-arsenides and gold, although not studied extensively due to their scarcity in the deposit, also appear to occur in fractures cross-cutting the other sulphide minerals, and are therefore believed to be the result of late stage mineralization, resulting from the hydrothermal introduction of Co, Ni and Mo. This hydrothermal event was related to post-peak-metamorphic fluids, which may have been associated with granitic activity in the area. This will be discussed in more detail in Chapter 6. The following paragenetic sequence has been proposed for the mineralization in the Corpo Quatro Formation:

Table 3.3 **Summary diagram of the proposed paragenetic sequence of base-metal sulphides and associated minerals in the Corpo Quatro Formation.**

Geological Event	Mineralization
Diagenesis	Pyrite
Peak Regional Metamorphism	(Pyrrhotite)
Main Mineralization	Pyrrhotite & Chalcopyrite
	Sphalerite
Secondary Mineralization	Sphalerite, minor chalcopyrite
	Molybdenite/Pentlandite/ Gold/Ni-arsenides

Chapter 4
Geochemistry of the Corpo Quatro Formation

4.1 *INTRODUCTION*

The geochemistry of the Corpo Quatro Formation has been studied using whole-rock X-ray fluorescence (XRF) analysis of trace and major elements in un-weathered samples from each lithological unit. Local hydrothermal overprint has been identified in the Corpo Quatro metavolcanics by geochemically comparing these rocks with volcanics from the Grão Pará and Igarapé Salobo Groups, which were studied by Gibbs *et al.* (1985) and Olszewski *et al.* (1989), and Lindenmayer (1990) respectively. No regional comparisons are available for the Corpo Quatro sediments. The geochemistry the Corpo Quatro (C4) Formation has been compared with similar Archaean metasedimentary and metavolcanic rocks from around the world, in order to ascertain the pre-metamorphic rock types in the area, and subsequently to identify their environment of deposition. A study has also been made of the chemical variation between the individual units of the C4 Formation, and between the mineralized and barren rock, to better understand the hydrothermal events which have occurred in the area.

4.2 *GEOCHEMICAL CHARACTERISTICS OF THE BARREN CORPO QUATRO FORMATION*

Barren, or hydrothermally unaltered, unweathered samples were chosen from each of the lithological units within the Corpo Quatro Formation on the basis of their appearance in hand specimen. Barren metavolcanic samples were chosen for their fresh, unalbitized, unmetasomatized appearance. The hydrothermally altered samples will be considered in section 4.3.1.

Physically, the only method of differentiating between regionally metamorphosed sediments and those which have undergone subsequent hydrothermal alteration is the presence of sulphide minerals. Those samples containing no visible mineralization are, in this study, considered barren.

Locations of samples from the G1-C4 adit are shown in *Figure 4.1*, and samples from boreholes are listed in *Appendix A*.

4.2.1 *The Corpo Quatro Metavolcanics*

As shown in Chapter 3, the Corpo Quatro metavolcanics have undergone considerable alteration, both during metamorphism and by post-metamorphic hydrothermal activity. Consequently, the geochemical signatures of these rocks today may not provide a reliable indication of their original tectonic setting. They have been analyzed in this study in an attempt to classify the volcanics in terms of geochemistry, to identify the hydrothermal overprint, and to compare the least altered C4 samples with similar volcanic rocks in the Carajás region.

Thirteen unweathered samples of fine to medium grained volcanic rock from the Corpo Quatro Formation were analyzed. Ten of these samples show no outward evidence of post-metamorphic alteration, and of these, six come from the G1-C4 adit, where they were taken at 5m intervals towards

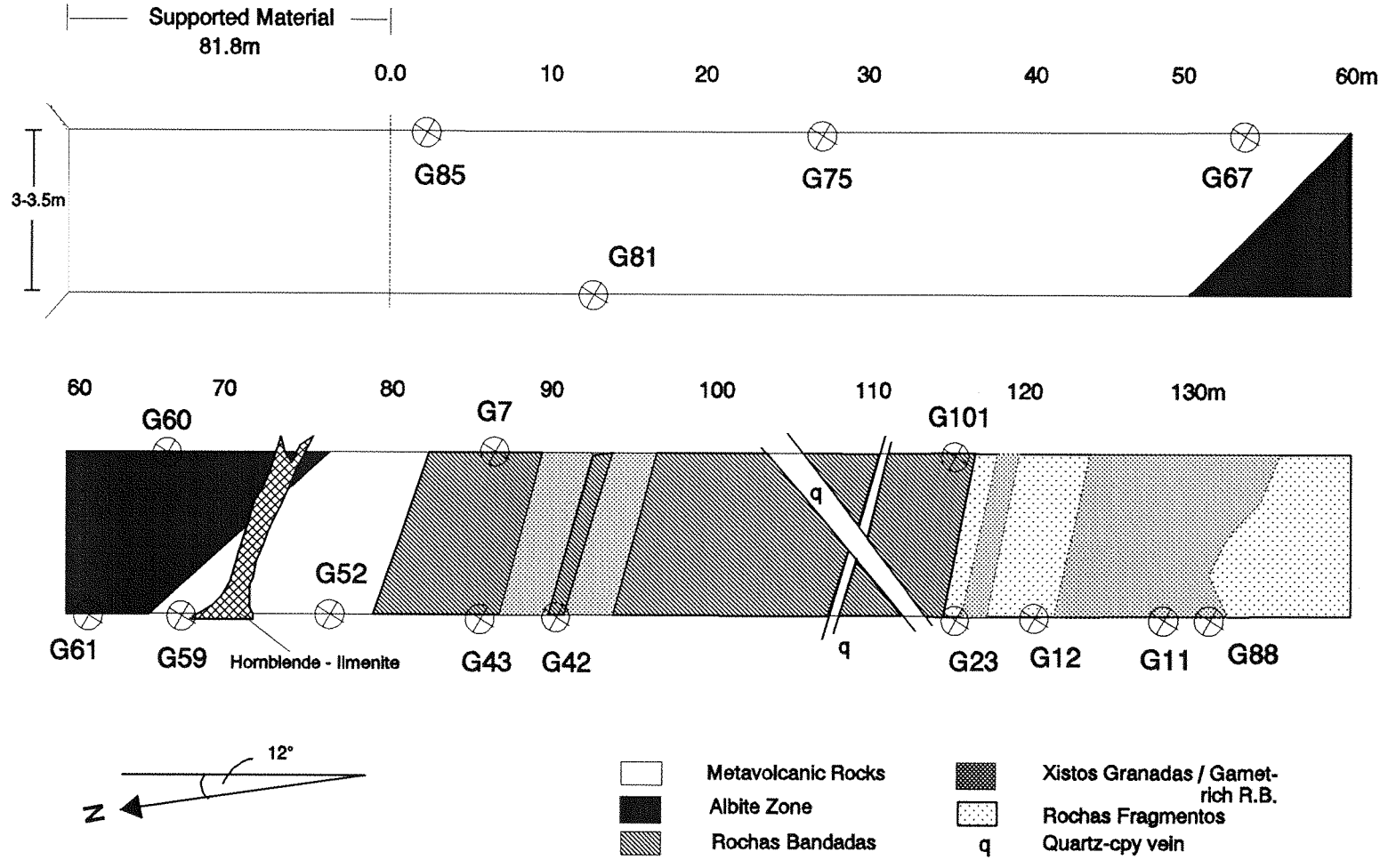

Figure 4.1 Schematic geological plan of the G1-C4 Adit, Pojuca, showing sample locations of adit samples (Pre-fixed 'G') used for geochemical analyses

the Albite Zone, and four from drillcore. Two samples from the Albite Zone and one sample of cordierite-anthophyllite rock were also analyzed, in order to show the geochemical changes developed in the demonstrably hydrothermally altered metavolcanics. These will be considered in section 4.3.1. Major and trace element concentrations are presented in *Appendix B2*, and mean element concentrations and ranges of the six least altered samples are given in *Table 4.1.*

Table 4.1 **Geochemistry of the Corpo Quatro Formation Metavolcanics (Mean and range of XRF data from the six least altered samples, F49, F50, F53, G59, G81, G85). Raw data in Appendix B2.**

Major Elements (%)			Trace Elements (ppm)		
	Mean	Range		Mean	Range
SiO_2	51.79	48.1-54.45	MnO	1658	1309-2060
TiO_2	0.69	0.6-0.75	TiO_2	7102	6153-7581
Al_2O_3	15.00	14.1-15.37	Rb	101	45-166
Fe_2O_3	16.40	14.45-19.9	Sr	77	55-103
MnO	0.17	0.13-0.21	Y	23	15-28
MgO	5.13	4.79-5.39	Zr	91	76-103
CaO	5.40	5.04-6.19	Nb	7	6-8
Na_2O	3.13	2.79-3.41	Th	2	2-3
K_2O	1.93	1.1-2.77	U	1	1-3
P_2O_5	0.08	0.07-0.09	Pb	3	1-4
			Zn	60	52-66
			Ni	56	50-67
Trace Elements (ppm)			Ga	16	14-18
Ba	426	287-533	Cr	180	137-207
La	11	7-16	V	217	203-239
Ce	25	17-35	Cu	23	14-31

A comparison between the Corpo Quatro and the Grão Pará Group Volcanics.

Before discussing the geochemical petrogenesis of the basalts, it is important to discern the metamorphic and hydrothermal overprint. The volcanics in the Grão Pará Group (GPG) are considered approximately coeval with the Igarapé Pojuca Group (IPG) volcanics (Medieros Neto and Villas, 1985), and therefore with the Corpo Quatro Formation. The Grão Pará Group metavolcanics show medium

grade metamorphism, to a maximum of upper greenschist facies, displaying primary clinopyroxene and fresh plagioclase, with blue-green amphibole developed only in the areas of most intense metamorphism (Gibbs, *et al.*, 1985), and show no evidence of having been exposed to extensive post-metamorphic hydrothermal activity compared with the lower amphibolite facies Corpo Quatro volcanics. The geochemistry of the two sets of metabasites can therefore be compared in order to establish the major post-metamorphic geochemical changes which have taken place in the Corpo Quatro Formation. The C4 samples least influenced by alteration relative to the GPG volcanics can then be compared with well constrained Archaean metavolcanics to provide information on their probable tectonic setting, while the more altered samples can be compared with each other in terms of local element remobilization (see section 4.3.1).

The lower Grão Pará Group metavolcanics of the Parauapebas Formation have been studied in detail by Gibbs *et al.* (1985) and Olszewski *et al.* (1989), and have been classified as basalts, basaltic-trachyandesites and rhyolites (*Fig. 4.2*). In terms of the silica-alkali content, the majority of the C4 samples plot in the basalt to basaltic andesite field (*Fig. 4.2*), similar to those of the Grão Pará Group. In order to use the IUGS igneous classification system, it must be assumed that there has been little mobility of the elements Si, K and Na. However, these elements are mobile, and K and Na are particularly likely to have been remobilized during hydrothermal activity. The IUGS scheme must therefore be used with some caution.

As the Grão Pará Group and the Corpo Quatro Formation metavolcanics apparently plot in the same region of the IUGS diagram (*Fig. 4.2*), a direct comparison can be made between the two groups to identify the geochemical overprint and the least altered samples in the Corpo Quatro Formation metavolcanics. To do this, the Corpo Quatro data has been normalized to the data obtained by Gibbs *et al.* (1985) for the GPG metavolcanics. Trace element data for the GPG basalts is limited to seven elements which can be compared with the Corpo Quatro data of this study. Further analyses are being carried out at present in a continuation of the Carajás project (Oliveira *et al.*, in prep).

The mean of two typical basaltic andesite samples from the Parauapebas Formation (Lower Grão Pará Group; *Table 4.2*) has been used to normalize each individual element in the Corpo Quatro basalts. These data are presented in *Figures 4.3A-F*. Relative to basalts from the Grão Pará Group, the least altered C4 samples are G85 and G81 (which are furthest from the G1-C4 Albite Zone), G59, F53, F50, and F49, and that there is little geochemical variation between each borehole sample (*Fig. 4.3A&B*). Sample F33, the cordierite-anthophyllite-rich sample, is shown in these plots for comparison.

Using these six least altered samples to compare the two sets of basalts, the C4 metavolcanics display a general enrichment in Fe, K and Rb, and a depletion in Ti, Ca and Sr. Other major and trace element concentrations in the MVII are similar to those in the GPG volcanics. The samples from adit G1-C4 (prefixed by'G') were taken at regular distances away from the Albite Zone, and are highly variable in both the major and trace elements, displaying large variations in the mobile elements (Na, K, Sr, Ba and Rb) relative to the basalts of the Grão Pará Group (*Fig. 4.3C&D*). The immobile elements Ni and Ce show little variation in these adit samples. The geochemical effects of the Albite Zone on the C4

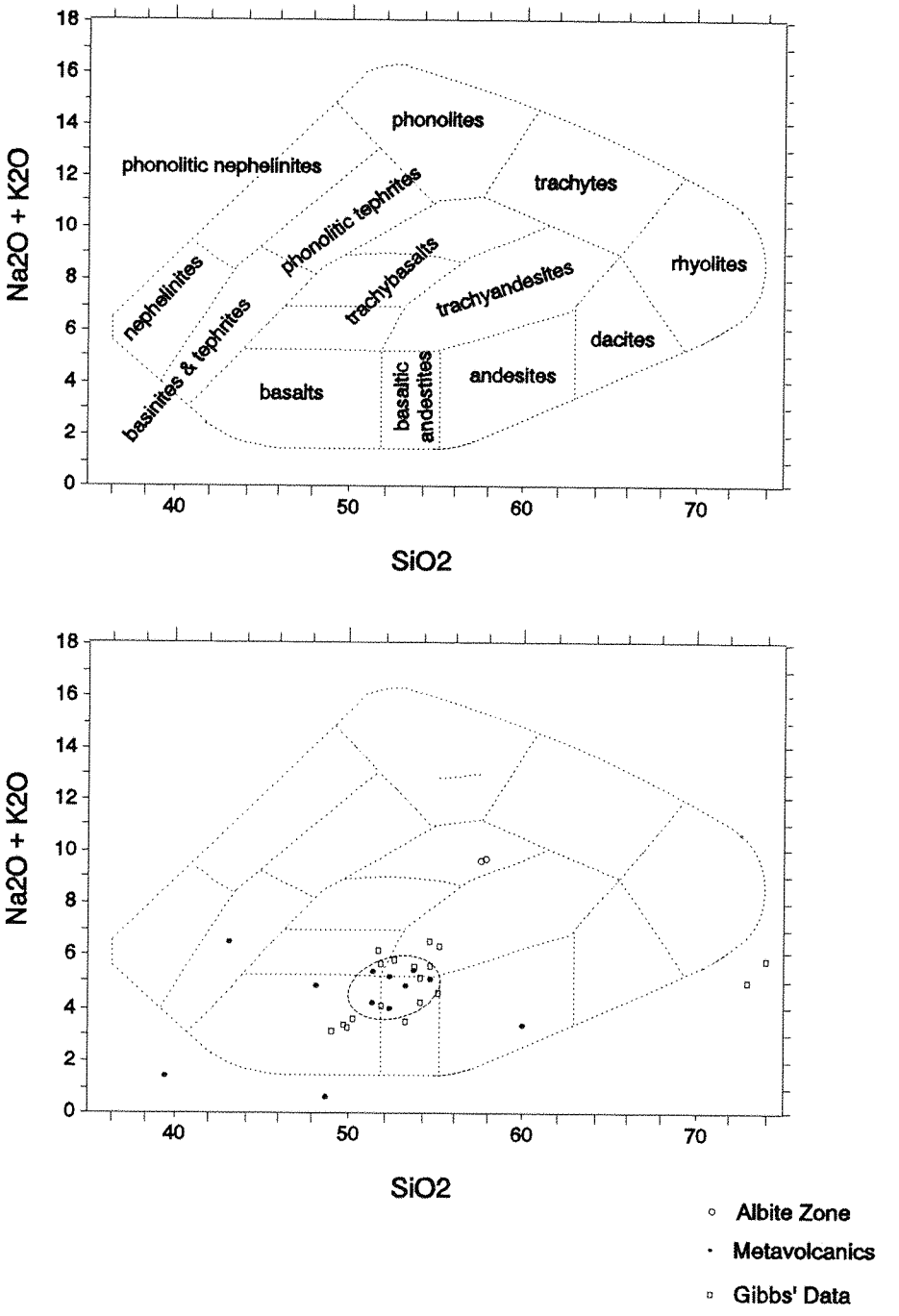

Figure 4.2 **IUGS classification diagram of igneous rocks: Data plotted for the Corpo Quatro Volcanics (○ and ●) and the Grão Pará Group Volcanics (□). (GPG Data from Gibbs *et al.*, 1985)**

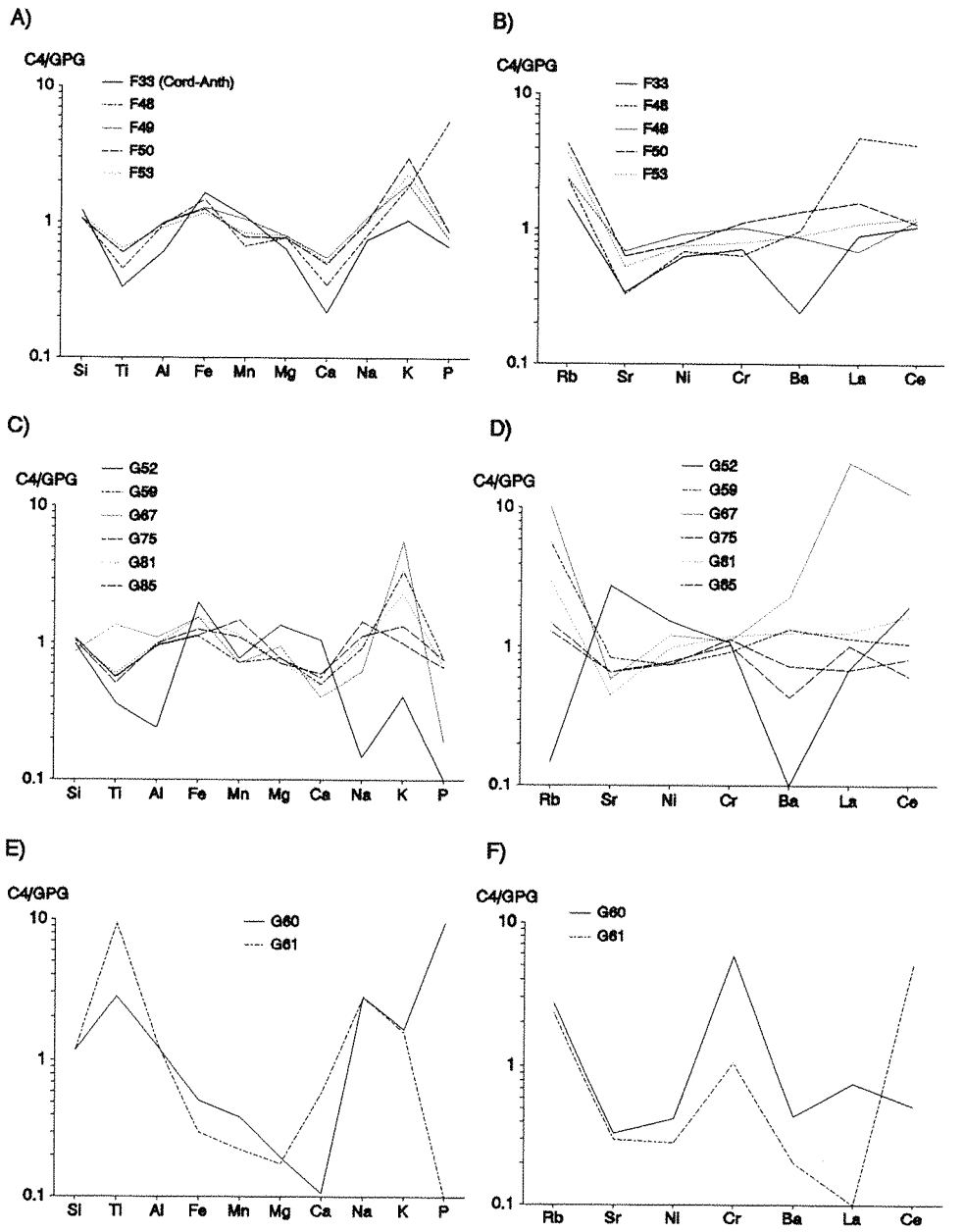

Figure 4.3 **Corpo Quatro Metabasites normalized to the Grão Pará Group basalts (Gibbs *et al.*, 1985). A and B Borehole samples; C and D G1-C4 samples; E and F Samples from the G1-C4 Albite Zone. Sample locations given in *Appendix A2*)**

metabasites is described in section 4.3.1.

Table 4.2 **Major and trace element data for the Grão Pará Group metabasites (Gibbs *et al.*, 1985). The mean of two typical samples has been used to normalize the C4 metabasalt data.**

%	GB-87	GB-82/B	MEAN	ppm	GB-87	GB-82/B	MEAN
SiO2	53.36	53.82	53.59	Rb	43	79	61
TiO2	0.84	0.76	0.8	Sr	146	130	138
Al2O3	15.09	14.47	14.78	Th	4	4	4
Fe2O3	12.17	11.1	11.64	U	1	1	1
MnO	0.22	0.52	0.37	Ni	82	63	73
MgO	5.45	6.58	6.02	Cr	70	141	106
CaO	8.78	7.14	7.96	Ba	1847	1847	1847
Na2O	2.48	2.91	2.70	La	15	13	14
K2O	1.17	2.3	1.74	Ce	30	26	28
P2O5	0.08	0.07	0.08				

Gibbs *et al.* (1985) observed felsic as well as mafic volcanics within the Grão Pará Group (*Fig. 4.2*), indicating this to be a bimodal sequence. There is no evidence for acidic volcanic activity within the Igarapé Pojuca Group, although the similarity in age and lithology of metavolcanics throughout the region (Olszewski *et al.*, 1989) indicates that all the volcanic rocks in the Carajás area are of similar origin. Bimodal volcanic sequences lack the andesitic material typical of subduction-related and greenstone belt volcanism, and are indicative of island-arc or continental style eruptions (Snyder *et al.*, 1990). They are atypical of Archaean greenstone belt magmatism but are more common in the <2.5 Ga Proterozoic belts (Hall and Hughes, 1990) with which the Carajás region has tentatively been compared (Olszewski *et al.*, 1986).

The Corpo Quatro Metavolcanics in a Worldwide Perspective

Although the MVII can be plotted on the IUGS classification diagram using silica and total alkali content, resulting in a basaltic to basaltic andesite interpretation, the other major elements in the MVII may not indicate the same field. In order to compare 'expected' concentrations of metal oxides with those predicted for different igneous standards, metal oxide contours have been fitted to the IUGS diagram (Cox *et al.*, 1979). The contrast between predicted and actual values of these oxides gives a broad idea as to the post-depositional modification of the rocks. *Figure 4.4A_E* shows the positions of the least altered C4 volcanics in terms of silica-alkali content, and the different metal oxide contents of these rocks. From

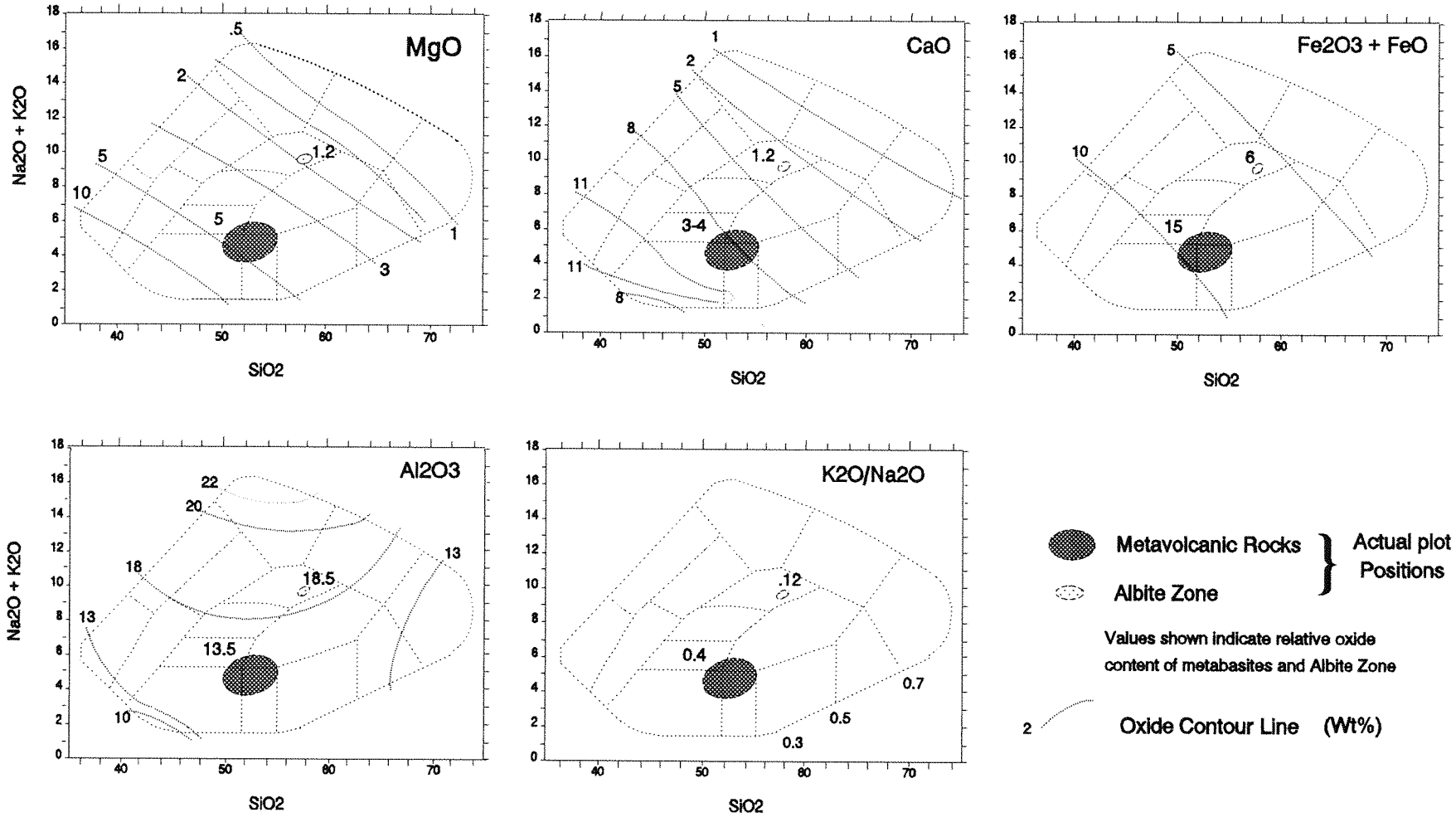

Figure 4.4 Oxide contours plotted on the IUGS Classification system for igneous rocks, showing the positions of the C4 metabasalts and the Albite Zone samples according to Alkali + silica (as Fig. 4.2) and the concentration of different oxides (Wt.%). after Cox et al., 1979.

these plots, it is clear that the C4 basalts show a depletion in Ca, an enrichment in Fe, and a high K:Na according to their silica-alkali content when compared with typical modern basalts.

The relative concentration of many trace elements in the earth's crust has changed since the Archaean, with most trace elements showing present day enrichment, although Co, Cr and Ni have been depleted (Condie, 1985). Together with the metamorphic and hydrothermal remobilization of many of the trace elements, this means that geochemical studies of Archaean rocks undertaken in order to determine their tectonic setting must be treated with some caution.

Multi-element plots of trace elements ratioed to N-MORB are generally used as an indication of tectonic origin of metabasites. *Figure 4.5* displays an enrichment in the LREEs (La & Ce), Ba, K and Rb relative to MORB. Ba, K and Rb are mobile elements, and therefore not valuable as tectonic indicators. REE, Ti, Y, Nb, Zr and Th, however, are generally considered to be relatively immobile, and have been found to be reliable indicators of original magmatic composition and tectonic environment (Wirth *et al.*, 1990; Condie, 1985). Thus the LREE enrichment in *Figure 4.5* is indicative of assimilation of continental crust during eruption of the magma (Cattell and Taylor, 1990). This supports the findings of Olszewski *et al.* (1989), who interpreted the volcanic rocks from the Carajás region as being of continental rift setting. The ratios of the immobile elements are also found to be characteristic of basalts of different ages (Condie, 1985.), and *Table 4.3* shows that the MVII are fairly typical of Archaean basalts in terms of these elements.

Table 4.3 **Element Ratios for Basalts of Different Ages, and for the Corpo Quatro Formation Metavolcanics (after Condie, 1985).**

Age (Ma)	>2.5	2.5 - 1.2	<1.2	IPG Volcanics
Al_2O_3/TiO_2	16-17	6-17	6-20	22
CaO/TiO_2	10-11	4-10	4-15	7.8
Ti/Zr	50-100	30-150	15-150	78.5
Ti/Y	200-300	100-500	100-500	316
Zr/Y	2-5	2-8	2-10	4.0
Zr/Nb	15-25	15-30	10-30	13
Ti/V	10-30	10-50	10-100	32.7
K/Rb	250-500	250-900	250-1000	193
Ba/Sr	0.5-0.8	0.2-1.0	0.1-1.0	3.2

Table 4.3 also uses Ba, Ca and Sr to classify basalts. These elements are relatively mobile under hydrothermal conditions, and it has been shown (*Fig. 4.3* and section 4.2.2) that these elements show significant modification in the C4 basalts since their deposition.

The concentration of immobile elements (Ni, Ce, Cr, Zr) in the C4 metavolcanics is similar to both the Grão Pará Group basalts and the Salobo Amphibolites (*Table 4.3*). Relative to other Archaean basalts of comparable age, however, the immobile elements in metavolcanic rocks from the Carajás region show considerable depletion in Cr and Ni, and enrichment in Ce, La and Nb (*Table 4.4*). Although a variation in these elements in more recent basalts is considered indicative of different magma sources (the depletion of Cr and Ni in the C4 basalts would indicate more affinity to present day island arc tholeiites than to MORB, as argued by Dardenne *et al.*, 1988), Gill (1979) illustrates that the concentration of these elements in Archaean tholeiites is very variable.

Using the immobile element data to plot the IPG metavolcanics on major and trace element discrimination diagrams (*Fig. 4.5*) demonstrates that the C4 basalts fall predominantly in the 'within-plate' tholeiite and volcanic-arc basalt fields, which is a characteristic of most Archaean basalts (Gill, 1979). It has been suggested that the Y/Nb value of a basaltic rock gives an indication as to its nature (Pearce and Cann, 1973). This lies between 2 and 6 for the C4 basalts (*Appendix B*), again suggesting that these are of tholeiitic, 'within-plate' nature, comparable with typical modern continental and ocean floor basalts (Pearce and Cann, 1973; Taylor and McLennan, 1985).

Table 4.4 **Average trace element concentrations in Archaean basalts (no. of samples in brackets): AT = typical Archaean tholeiitic basalt (Condie, 1985); Kamb. = Kambalda tholeiitic basalt, (Arndt and Jenner, 1986), data in brackets is for average greenstone belt basalts, 2.5-3 Ga., (Condie, 1990); IPG = Igarapé Pojuca Group, this study; GPG = Grão Pará Group (Gibbs *et al.*, 1985); ISG = Igarapé Salobo Group (Lindenmayer, 1990); na.= not analyzed.**

(%)	SiO_2	TiO_2	Al_2O_3	Fe_2O_3	MnO	MgO	CaO	Na_2O	K_2O	P_2O_5
AT	52.0	.92	15.0	10.8	.19	8.0	10.0	2.6	.34	.13
Kamb.	50.6	.81	15.6	11.3	.18	5.9	11.2	3.6	.6	(.12)
GPG	49.3	1.18	15.5	12.8	.18	6.7	10.3	3.0	.8	.11
ISG	49.3	1.82	12.8	17.7	.33	4.8	7.6	2.8	1.3	.22
IPG	51.8	.69	15.0	16.4	.17	5.1	5.4	3.1	1.9	.08

(ppm)	TiO_2	Rb	Sr	Y	Zr	Nb	Ni	Cr	V	Ba	La	Ce
AT	9200	11	157	27	90	5	135	350	249	130	5	na
Kamb.	8100	(9)	188	21	51	1	177	375	295	(204)	3	7
GPG	11750	30	121	na	na	na	68	117	na	394	10	21
ISG	18200	58	109	36	158	9	52	103	275	386	26	56
IPG	7102	100	77	23	91	7	56	180	217	426	11	25

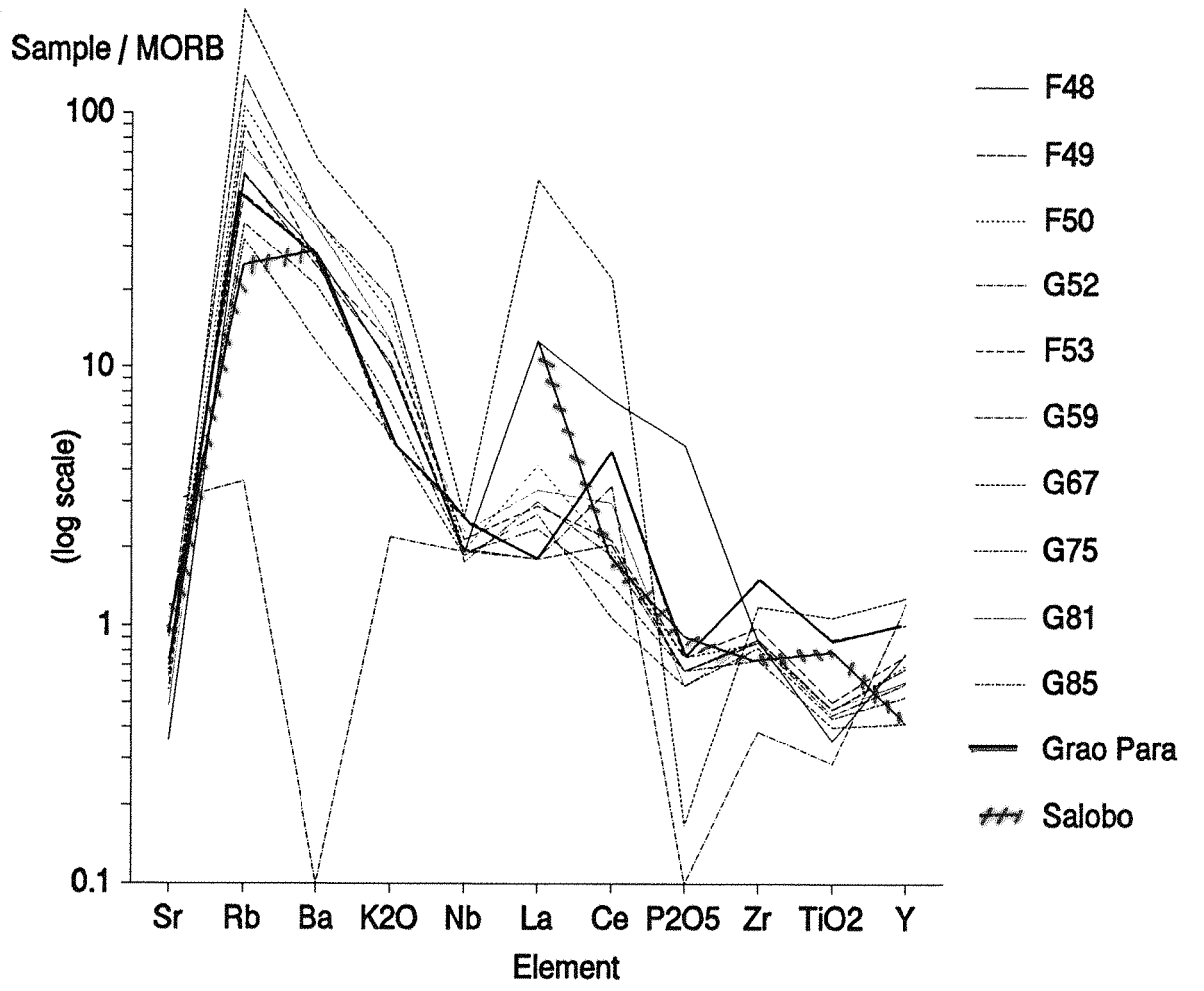

Figure 4.5 **Multi-element plot of the Carajás Basalts; Corpo Quatro Formation (this study); Igarapé Salobo Group (Lindenmayer, 1990) and Grão Pará Group (Gibbs *et al.*, 1985).**

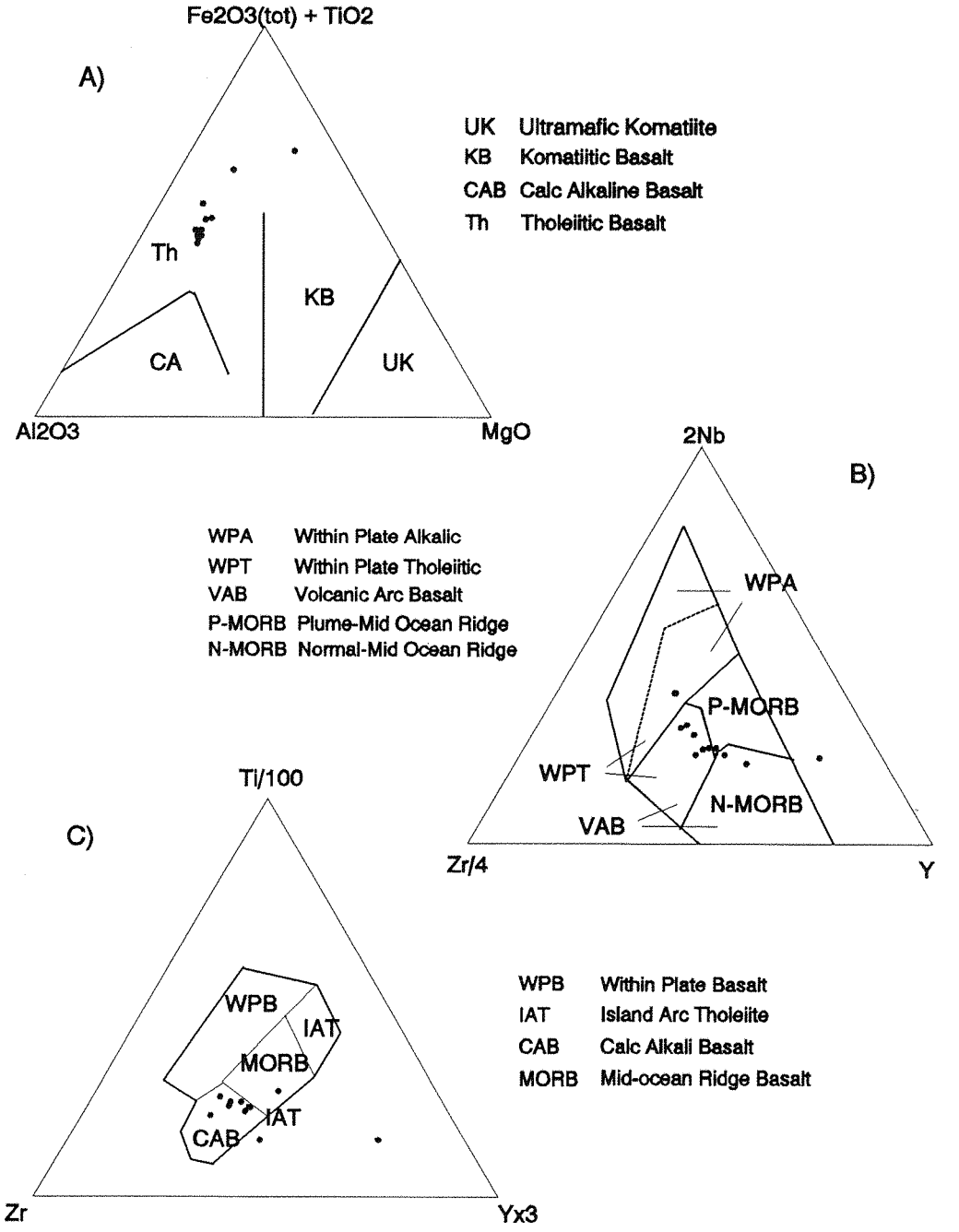

Figure 4.6 **Tectonomagmatic discrimination diagrams of the Corpo Quatro basalts relative to modern day basalts: A Fe+Ti-Al-Mg plot (after Jensen, 1976); B Nb-Zr-Y plot (after Meschede, 1986); C Ti-Zr-Y plot (after Pearce and Cann, 1973)**

In terms of mobile elements, metavolcanics from the Carajás region are generally enriched in K, Fe, Ba and Rb relative to typical Archaean tholeiites. Compared with typical Archaean basalts and with other metabasalts of the Carajás district, the C4 metabasalts display a further enrichment in Rb and K, and depletion in Ca, Ti and Sr (*Table 4.4*). The lack of clinopyroxene in the Corpo Quatro basalts would not account for this depletion, and these are the elements, therefore, which show post-metamorphic hydrothermal mobilization in the C4 metabasites.

4.2.2 *The Nature and Origin of the Corpo Quatro Metasediments*

Analyses of the Corpo Quatro metasediments were carried out using X-ray fluorescence spectroscopy (XRF) of both barren and mineralized samples of the Rochas Bandadas, Xistos Granadas and Xistos Quartzos units described in Chapter 3.

Barren samples are defined here as those samples appearing to contain no sulphides. In order to study the barren sediments of the Corpo Quatro Formation, analytical data were obtained for four samples of Rochas Bandadas, six of Xistos Granadas, and two Xistos Quartzos. The mean geochemical data for both barren and mineralized rock is given in *Table 4.5*. Obtaining representative analyses of heterogeneous rocks such as the Rochas Bandadas is difficult, but the use of large (0.5 to 1kg) samples, which include all representative mineral assemblages, gives a good representation of the rock as a whole.

Archaean metasediments have been examined by a number of workers, and generally been found to occur as either volcaniclastic and chemical sediments, interbedded with volcanic rocks in the lower part of greenstone belts, or as a series of thick, clastic deposits overlying greenstone belt volcanics. Late Archaean sedimentary sequences and their geochemistry are discussed at length by Taylor and McLennan (1985), who classify them as typically comprising volcaniclastic or terrigenous clastic sediments, iron-formation and deep-water, thick, shale-greywacke sequences. Much work has been carried out on Archaean iron-formations, classifying them according to mineralogy and environment of deposition (Kimberley, 1989). The main classification is that of Gross (1980, 1988), who subdivided the Canadian Archaean iron-formations on the basis of their environment of deposition and geochemistry. The C4 metasediments will be considered in terms of comparable Archaean sediments in the next section.

Chapter 3 concludes that the Corpo Quatro sediments comprise a basal chemical unit (the Rochas Bandadas), and contain an increasing degree of clastic input up the sequence towards the Xistos Quartzos at the top. The geochemistry of the individual Corpo Quatro units has been compared with that of similar Archaean metasediments in order to classify the sedimentary protoliths, and internal comparisons have been made to establish chemical variation within the Corpo Quatro Formation.

Table 4.5 **Mean XRF geochemical data for the Corpo Quatro Formation metasedimentary rocks: Barren Samples (Rochas Bandadas excludes sample F95). Complete data set in Appendix B2.**

	Rochas Bandadas		Xistos Granadas		Xistos Quartzos	
(%)	Mean	Range	Mean	Range	Mean	Range
SiO_2	57.1	53.8-62	56.54	38-77.5	56.30	55.9-56.7
TiO_2	0.08	.03-.12	0.33	.16-.55	0.57	.53-.6
Al_2O_3	0.95	.3-1.6	10.93	6.7-16	12.2	12-12.3
Fe_2O_3	38.03	30.4-45.5	25.53	12.5-38	19.1	18-20
MnO	0.303	.18-.5	0.57	.21-1.8	0.14	.12-.15
MgO	2.39	1.5-3.9	3.33	1.5-5.1	3.78	3.1-4.3
CaO	1.98	.4-4.6	2.39	.8-6.4	4.94	2-8
Na_2O	0.0	0.0	0.16	0-0.47	1.08	.6-1.5
K_2O	0.16	.06-.3	1.28	.1-3.4	2.81	1.6-4
P_2O_5	0.08	0-.16	0.06	.04-.07	0.07	.6-.8
SO_3	0.01	0-.01	0.03	0-.11	0.03	0-.06
CuO	0.13	.06-.3	0.08	0-.2	0.1	.01-.23
(ppm)						
Rb	12	0-30	46	55-194	26	18-35
Sr	<D.L.	<D.L.	8	0-28	3	0-5
Y	9	5-16	34	10-101	30	10-50
Zr	17	7-27	132	81-196	88	71-104
Nb	3	0-8	8	5-10	7	6-7
Th	<D.L.	<D.L.	7	0-12	4	0-8
U	<D.L.	<D.L.	<D.L.	<D.L.	<D.L.	<D.L.
Pb	<D.L.	<D.L.	<D.L.	<D.L.	<D.L.	<D.L.
Zn	900	229-605	481	121-762	204	119-290
Ni	34	8-66	16	0-28	34	20-49
Ga	4	0-5	9	0-14	13	12-14
Cu	1240	623-3626	1084	93-2054	1190	125-2254
Cr	<D.L.	<D.L.	112	0-219	199	180-218
V	13	0-24	102	17-197	160	152-169
Ba	17	0-50	213	29-459	393	138-646
La	9	0-28	47	0-158	23	0-40
Ce	14	0-42	70	0-243	36	0-73
As	<D.L.	<D.L.	7	0-34	<D.L.	<D.L.
Mo	4	0-7	60	0-266	13	0-26
Sn	<D.L.	<D.L.	<D.L.	<D.L.	14	0-27
Bi	<D.L.	<D.L.	<D.L.	<D.L.	<D.L.	<D.L.
Sb	<D.L.	<D.L.	<D.L.	<D.L.	<D.L.	<D.L.

Table 4.5 (cont..) **Mean XRF geochemical data for the Corpo Quatro Formation metasedimentary rocks: Mineralized Samples. Complete data set in Appendix B2.**

(%)	Rochas Bandadas		Xistos Granadas		Xistos Quartzos	
	Mean	Range	Mean	Range	Mean	Range
SiO_2	50.81	40.3-59.8	61.17	40.3-75.4	56.60	43.9-69.3
TiO_2	0.17	0.08-0.32	0.30	0.1-0.6	0.42	0.2-0.54
Al_2O_3	4.45	2.33-8.49	7.46	1.0-13.6	11.22	9.1-12.5
Fe_2O_3	33.73	22.57-42.42	25.45	16.1-37.1	24.82	19.2-28.7
MnO	0.34	0.25-0.56	0.27	0.1-0.4	0.14	0.1-0.22
MgO	2.55	1.2-3.9	3.76	0.7-6.2	4.42	2.35-6.27
CaO	5.32	3.14-7.68	1.24	0.2-2.3	3.24	0.2-8.02
Na_2O	0.18	0.0-0.48	0.01	0.0-0.05	0.27	0.0-0.8
K_2O	0.48	0.2-1.1	1.31	0.2-3.1	0.93	0.3-2.0
P_2O_5	0.12	0.03-0.3	0.07	0.02-0.1	0.07	0.6-0.7
SO_3	0.66	0.06-1.74	0.12	0.0-0.34	0.08	0-0.19
CuO	1.38	0.01-2.48	1.60	0.01-5.94	0.13	0-0.4
(ppm)						
Rb	38	8-150	82	24-149	87	4-100
Sr	7	1-18	6	1-21	17	1-35
Y	14	11-21	17	4-26	18	10-25
Zr	51	25-79	79	17-110	93	94-104
Nb	6	4-7	7	4-8	7	7-8
Th	2	0-4	5	0-11	3	3-5
U	1	0-3	1	0-4	2	1-3
Pb	3	3-5	4	2-7	4	3-4
Zn	1283	161-2967	1086	218-2508	149	96-162
Ni	61	50-83	83	16-117	32	2-39
Ga	7	2-16	10	4-15	11	3-14
Cu	10972	120-22900	16409	108-44534	1319	35-4589
Cr	6	0-25	48	0-187	102	0-232
V	70	11-263	65	11-194	97	27-174
Ba	54	24-102	180	59-367	95	25-244
La	19	11-37	36	7-120	42	0-15
Ce	35	24-48	53	0-177	63	4-25
MnO	3539	2462-5397	2449	850-3539	1603	797-2169
TiO_2	1712	727-3348	3235	819-5744	3531	1696-5802
As	<D.L.	<D.L.	22	0-130	1	0-4
Mo	13	2-42	13	3-40	3	2-5
Sn	12	0-20	9	1-27	13	0-30
Bi	<D.L.	<D.L.	<D.L.	<D.L.	<D.L.	<D.L.
Sb	<D.L.	<D.L.	<D.L.	<D.L.	<D.L.	<D.L.

Geochemical Characteristics of the Corpo Quatro Metasediments

The Corpo Quatro metasediments have been compared with similar Archaean metasediments by using the geochemistry of the barren samples, which are considered to have undergone the least post-metamorphic modification and therefore provide the best insight into the original lithogeochemistry. The geochemistry within the individual units is roughly consistent (*Fig. 4.7*), and mean element compositions are presented in *Table 4.5*.

A true iron formation contains in excess of 15% Fe (24% Fe_2O_3; Kimberley, 1989). The Corpo Quatro Rochas Bandadas contains, on average, 38% Fe_2O_3, and the Xistos Granadas 25.5% Fe_2O_3, making it geochemically correct to classify these two units as iron formation. The Xistos Quartzos contains an average of only 19% Fe_2O_3, but is rich in aluminium compared with the other units and can therefore be classified as an iron-rich pelite (Taylor and McLennan, 1985). Geochemically, as well as petrographically therefore, the three major units in the Pojuca Corpo Quatro metasediments represent markedly different conditions of sedimentation.

By making a direct comparison between the Corpo Quatro Formation sediments and other similar Archaean sediments, it is possible to identify the sedimentological precursors. The mean element data for each unit (*Table 4.5*) have been compared with the data published on similar lithological sequences by Taylor and McLennan (1985) and Turnock and Trueman (1990) (*Table 4.6*) and Gross (1980, 1988) (*Table 4.7*).

Taylor and McLennan (1985) geochemically characterized typical Archaean greywackes, mudstones and greenstone-belt sedimentary sequences. The Rochas Bandadas and Xistos Granadas contain high iron contents, and cannot be compared with the clastic sediments of Taylor and McLennan (*op.cit*). The Xistos Quartzos, which are relatively iron poor, have been compared with typical Archaean metasediments and are found to display similar chemical characteristics to shales, particularly to the Kalgoorlie Shale Member. On the basis of its REE pattern this has been interpreted as a volcaniclastic shale deposit (Taylor and McLennan, *op. cit*). The affinity of the Xistos Quartzos to a pelitic sediment is supported by a comparison made between the Corpo Quatro sediments and those of the Bird Lake area, Manitoba (Turnock and Trueman, 1990), where the Xistos Quartzos is almost identical in major element geochemistry to the Bird Lake Ferruginous Pelite. REE patterns are generally used as the most reliable indicator of sedimentary provenance, but are unfortunately not yet available for the rocks of the Corpo Quatro Formation.

Classified as iron-formations, the Rochas Bandadas and Xistos Granadas can also be compared with the sedimentary ironstones and their related metasediments in the Bird Lake area, which are reported to show mineral assemblages similar to those in the Corpo Quatro Formation; i.e. garnet and biotite plus either cummingtonite-hornblende or grunerite-actinolite. It is clear from the two sets of data (*Table 4.6*) that the Rochas Bandadas shows similarities with grunerite-rich BIF from the Bird Lake sequence, and that the Xistos Granadas, but for a slightly high K_2O content, is virtually identical to the Bird Lake area Garnet Ironstone.

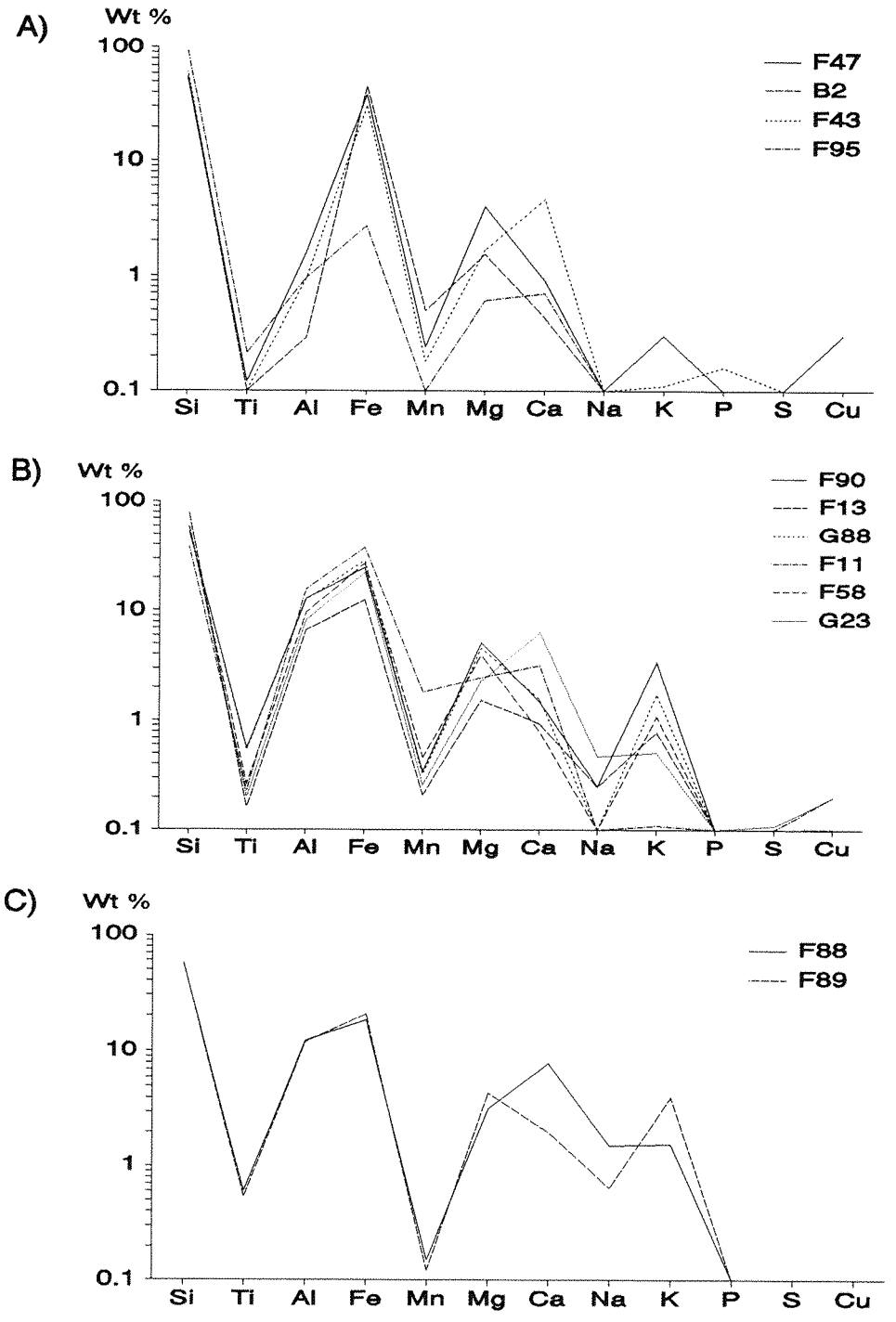

Figure 4.7 **Element contents (Wt.%) of the barren Corpo Quatro Formation sediments (log scale): A Rochas Bandadas; B Xistos Granadas; C Xistos Quartzos.**

Table 4.6 **Mean Element Data for the Barren C4 Metasediments (this study), the Bird Lake, Manitoba Iron-rich Archaean Sediments (Turnock and Trueman, 1990) and the Kalgoorlie Shale Member, Yilgarn Block (Taylor and McLennan, 1985)**

	Corpo Quatro Formation			Bird Lake Area, Manitoba			Kalgoorlie
(%)	Rochas Bandadas	Xistos Granadas	Xistos Quartzos	Grunerite Layer	Garnet Ironstone	Ferruginous Pelite	Shale Member
SiO_2	57.1	58.54	56.31	51.5	26.62	58.86	64.16
TiO_2	.08	.33	.57	.02	.22	.52	.47
Al_2O_3	.95	10.93	12.19	3.82	9.85	12.31	13.1
Fe_2O_3	38.03	25.54	19.09	35.48(Tot)	27.84(Tot)	16.5(Tot)	17.03(FeO)
MnO	.303	.57	.14	1.99	1.54	.45	.02
MgO	2.39	3.34	3.78	3.54	2.8	3.33	1.45
CaO	1.98	2.4	4.94	3.17	1.75	5.49	.59
Na_2O	0	.16	1.08	.02	.01	.58	.52
K_2O	.16	1.28	2.81	.04	.34	.78	2.57
P_2O_5	.08	.06	.07	.02	.02	.14	.08
(ppm)							
Zr	21	83	58	3	94	152	147
Ba	15	152	382	87	99	31	540
Co	5	60	36	1	1	27	96
Cu	749	567	1159	12	101	133	400
Ni	23	9	34	7	13	89	56
Rb	12	59	26	2	22	19	61
V	.2	2.7	4.5	-	6	56	65
Zn	75	312	204	21	84	108	-

Gross (1980, 1988) classified Canadian iron-formations into Algoma and Lake Superior-type, based their on environment of deposition, geochemical composition and associated rock types. The Algoma-type iron-formation is characterized by its association with greywackes and volcanic rocks, and the Superior-type by black shales, dolomites and quartzites. The chemical characteristics of both of the Pojuca iron-formations (Rochas Bandadas and Xistos Granadas) have been compared with those of the Canadian iron formations (*Table 4.7*). A number of elements (Ca, Fe_{Tot}, Mg) in the C4 Formation were found to be most analogous to the Algoma-type iron-formation, and consideration of the related sedimentary and volcanic rocks in the C4 Formation places the Corpo Quatro iron-formations in the Algoma-type classification (Gross and McLeod, 1980) based on their proximity to the C4 metabasites. The majority of both major and trace element concentrations in the C4 Rochas Bandadas and Xistos Granadas, however, are more similar to the Lake Superior class of iron-formation (*Table 4.7*). This supports the ideas of Kimberley (1989) who pointed out that as all iron-formations are different, broad-scale classification according to known 'types' inevitably results in confusion caused by trying to 'fit' a unit

to a known type. The C4 Rochas Bandadas and Xistos Granadas, therefore, have not been classified in this manner and it is seen as sufficient simply to refer to them as iron-formations.

Table 4.7 **Mean Element Content of Algoma and Lake Superior Type Iron-formations from the Canadian Archaean Iron-formations (after Gross, 1988)**

	Oxide		Silicate		Carbonate		Sulphide
	Algoma	Superior	Algoma	Superior	Algoma	Superior	Algoma
SiO_2	47.8	47.7	64.2	58.8	44.5	36.9	40.9
TiO_2	.075	.017	.191	.16	.31	.034	.262
Al_2O_3	2.66	1.28	2.53	2.18	6.68	1.31	6.65
Fe_2O_3	44.2	44.3	21.9	27.6	17.8	30.5	29.6
MnO	.11	.51	.22	.4	.17	.74	.23
MgO	1.58	1.24	3.57	2.85	6.18	4.46	2.3
CaO	1.67	1.61	4.95	2.26	4.67	4.93	2.46
Na_2O	.33	.11	.23	.19	1.24	.14	.86
K_2O	.72	.15	.25	.56	.89	.14	.95
P_2O_5	.22	.06	.08	.1	.15	.14	.11
(ppm)							
Ba	210	170	130	150	240	40	150
Co	38	30	40	30	30	30	80
Cr	78	110	140	100	390	80	160
Cu	50	10	20	40	80	10	630
Ni	80	30	340	50	220	40	130
Sr	70	30	90	20	210	30	100
V	60	30	110	100	170	60	90
Y	20	40	20	40	40	60	30
Zn	60	30	50	40	90	100	.3%
Zr	40	60	60	170	80	70	120

Comparative methods of geochemical analysis within the Corpo Quatro Metasediments

In order to establish variation between the different sedimentary units of the Pojuca Corpo Quatro Formation, a chemical comparison has been carried out from unit to unit. By comparing those rocks which

have undergone least alteration (i.e. metamorphosed, barren samples) chemical changes which are predominantly the result of sedimentological variation should be identified.

The 'constant sum' method of data collection, used as standard practice in geochemical analyses, results in inherent problems during the statistical evaluation of data, an aspect discussed recently by a number of authors (Grant, 1986; Rollinson, 1992). This is caused by 'mathematical closure', and can be illustrated as follows:

If a rock contains *absolute* values of oxides, given below in column **a**, and a known amount of two oxides is changed (column **b**, 10g SiO_2 added, 4g K_2O removed), the weight percentages of the total will change.

	a		**b**	
	True weight	Weight %	True weight	Weight %
SiO_2	50g	43.5	60g	49.6
Al_2O_3	20g	17.4	20g	16.5
Fe_2O_3	30g	26.2	30g	24.8
CaO	10g	8.7	10g	8.3
K_2O	5g	4.2	1g	0.8
Total	115g		121g	

This has caused an *artificial* decrease in the weight percentages of both Al_2O_3 and Fe_2O_3, and will result in a misleading interpretation of the data.

In an attempt to overcome the dilution effects caused by abnormally high SiO_2 in some samples, several methods of data comparison have been used, although as it will be shown each of these methods has its drawbacks, and a method which can overcome all of these problems is required.

Normalization to SiO_2 Extreme diversity in the quartz content of different samples and lithological units results in SiO_2 being the most variable oxide in the geochemical analyses. This variation reflects primary quartz content (clasts, quartz laminae etc) rather than either SiO_2 in other silicate minerals, which are seen to remain constant in the thin section, or hydrothermal quartz. SiO_2 has been used to normalize the data to a 'constant quartz' value for each individual sample, and other elements can then be compared directly, identifying real and apparent variations in oxide content.

In order to keep all the data equivalent to an iron-formation analysis, sample F47, which is chemically and lithologically closest to the 'average' barren Rochas Bandadas, was used as the standard. All barren Rochas Bandadas were normalized to 55.59% SiO_2 (the value of silica in the standard), and the remaining oxides then re-calculated according to 55.59% SiO_2, using the following equation:

$$\frac{n_{(x)}}{i_{(s)}} = \frac{\frac{i_{(x)}}{(100-SiO_{2(x)})} * (100-SiO_{2(s)})}{i_{(s)}} \qquad \text{(Equation 4.1)}$$

Where **i =** **Wt.% of oxide to be recalculated**
s = **Standard sample for unit (F47 for barren rocks, F47, F89 or G88 for mineralized rocks)**
x = **Sample to be recalculated**
n = **New value of oxide**

Example: To calculate the ratio of 'normalized' Fe_2O_3 in sample G88 (Xistos Granadas) to that of sample F47 (Standard Rochas Bandadas) (See Appendix B2 for data)

$$Fe_2O_{3_{(G88)}} = \frac{28.72}{(100-52.76)} * (100-55.59)$$

$$\frac{Fe_2O_{3_{(G88)}}}{Fe_2O_{3_{(F47)}}} = \frac{26.99}{38.07} = 0.71$$

Most elements in the Rochas Bandadas samples (with the exception of F95, which contains only quartz and hornblende, with a total of 95% SiO_2) show clustering, with an equal spread around the 1:1 sample:F47 oxide ratio (*Fig. 4.8A*). Sample F47 is therefore considered valid as an 'average' or standard Rochas Bandadas, by which to normalize all the metasediments in the Corpo Quatro Formation. Equation 4.1 has been used to calculate these new values, so comparisons can be made between the major element concentrations in each unit.

The variation in TiO_2, Al_2O_3, CaO and P_2O_5 between samples in the Rochas Bandadas (*Fig. 4.8A*) can be explained by looking at the relative concentrations of these elements in the Rochas Fragmentos. All of these elements are enriched in the Rochas Fragmentos relative to the Rochas Bandadas, and the variation in the Rochas Bandadas therefore represents different amounts of contamination by detrital clastic material in the chemical sediments. The P_2O_5 variation, which is up to 12 times as high in sample F43 as F47, is a result of the very low values in the standard sample (F47=0.01% P_2O_5). This is an inherent problem with this method of comparison, as no sample is 'average' in all the elements.

The quartz-normalized diagrams were constructed to show variation between the standard Rochas Bandadas and the Rochas Fragmentos. Both the Xistos Granadas and Xistos Quartzos display up to a five fold enrichment in TiO_2 and CaO, and an eight to ten-fold increase in Al_2O_3 and P_2O_5 relative to the Rochas Bandadas (*Fig. 4.8*), although as already pointed out, the increase in P_2O_5 is artificially high

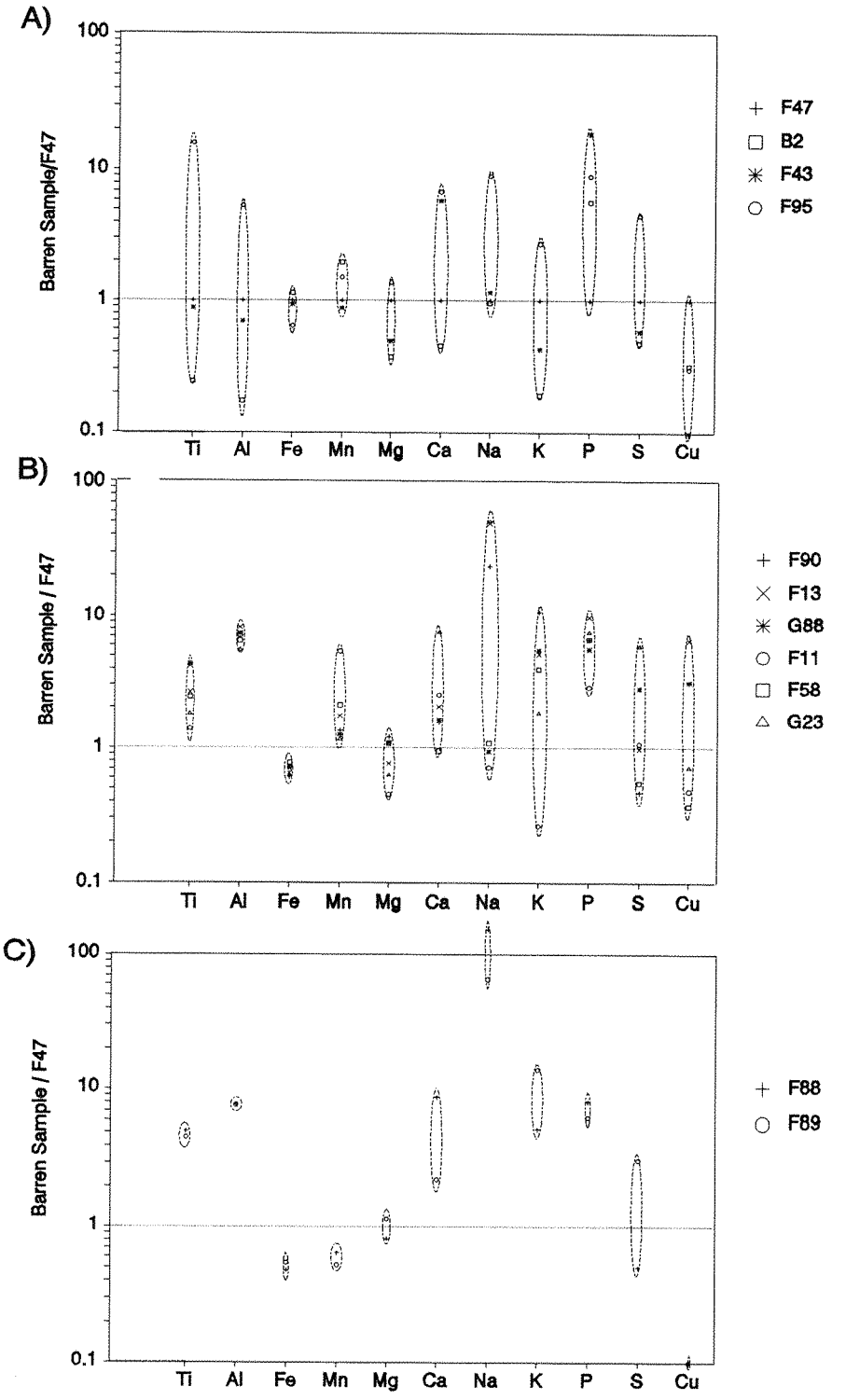

Figure 4.8 **Barren samples from the Corpo Quatro Formation sediments, normalized using the 'silica method' to Rochas Bandadas sample F47 (see text for explanation). A value of 0.1 has been used instead of 0.0 to normalize Na_2O and Cu. A Rochas Bandadas; B Xistos Granadas; C Xistos Quartzos.**

because of the low phosphorus content of the standard. The enrichment of Ti, Ca, P and Al is the same in both sets of data, indicating little change in these elements from the Xistos Granadas to the Xistos Quartzos. K_2O and Na_2O, however, show little increase from the Rochas Bandadas into the Xistos Granadas (*Fig. 4.8B*), but display between ten- and one hundred-fold enrichment in the Xistos Quartzos. The increase in K_2O can be explained by a mineralogical change, from biotite-poor Rochas Bandadas to biotite-bearing Xistos Granadas, into biotite-rich Xistos Quartzos. The sodium increase, however, is not so easily explained. As expected, sodium increases from the quartz-grunerite-dominated Rochas Bandadas to the Rochas Fragmentos, but in a mineral assemblage containing quartz, biotite, hornblende and chlorite there is no apparent reason for the dramatic increase seen between the Xistos Granadas and the Xistos Quartzos.

A slight depletion in Fe_2O_3 is noted in the Rochas Fragmentos relative to the Rochas Bandadas, and MnO is also lower in the Xistos Quartzos. This is probably explained by the depletion of grunerite and hornblende in these rocks. However, the Xistos Granadas are enriched in manganese relative to the Rochas Bandadas, and this can be interpreted by the abundance of Mn-bearing almandine garnet in this unit (*Appendix C2*).

The Isocon Diagram: It is possible to express the geochemical changes between fresh and hydrothermally altered rock graphically on an isocon diagram (Grant, 1986). This method employs the theory behind Gresens' (1967) equation of volume change, and plots unaltered against altered rocks from the same lithology. It is proposed that the straight line, or isocon, plotted through the origin and the majority of the elements represents the geochemical constant (Grant, 1986). All elements lying on this isocon were therefore unaffected by the hydrothermal alteration in question. The gradient of the isocon is equal to the volume change imposed on the rock during alteration. This method has been employed for the C4 metasediments, not only to examine changes between mineralized and barren samples from the same unit (section 4.3.2), but to study chemical variations between the individual units. In this case, volume change is irrelevant, and the isocon drawn to identify increase or decrease in element abundance is a line of constant mass, i.e. 1:1. Although extreme element variation in individual samples is appreciated, the mean bulk composition of each data set (*Table 4.5*) has been used to plot parent (C_O) against daughter (C_A) lithologies, thereby reducing the effects of sample heterogeneity, which becomes a problem if individual samples are plotted.

Rock-type comparisons have been carried out using *Figures 4.9A&B*, which plot the rock-types against one-another. This method compares trace as well as major elements, which on this, unlike the SiO_2 method, are easily plotted on the same diagram. The use of a log scale was found to disguise small variation in elements (10-20%), and a linear scale has therefore been employed. For clarity, some of the values have been adjusted by factors of ten. Many elements lie close to the isocon, and due to sample and analytical error, those data points within a 5% error margin of the isocon (within the dotted lines) are regarded unreliable in signifying chemical change.

The heavy 'detrital' elements Ti, Zr, V, Y, Nb and Cr show an increase from the basal Rochas Bandadas to the Xistos Granadas (*Fig. 4.9A*), but of the 'immobiles', only Cr, V and Ti display

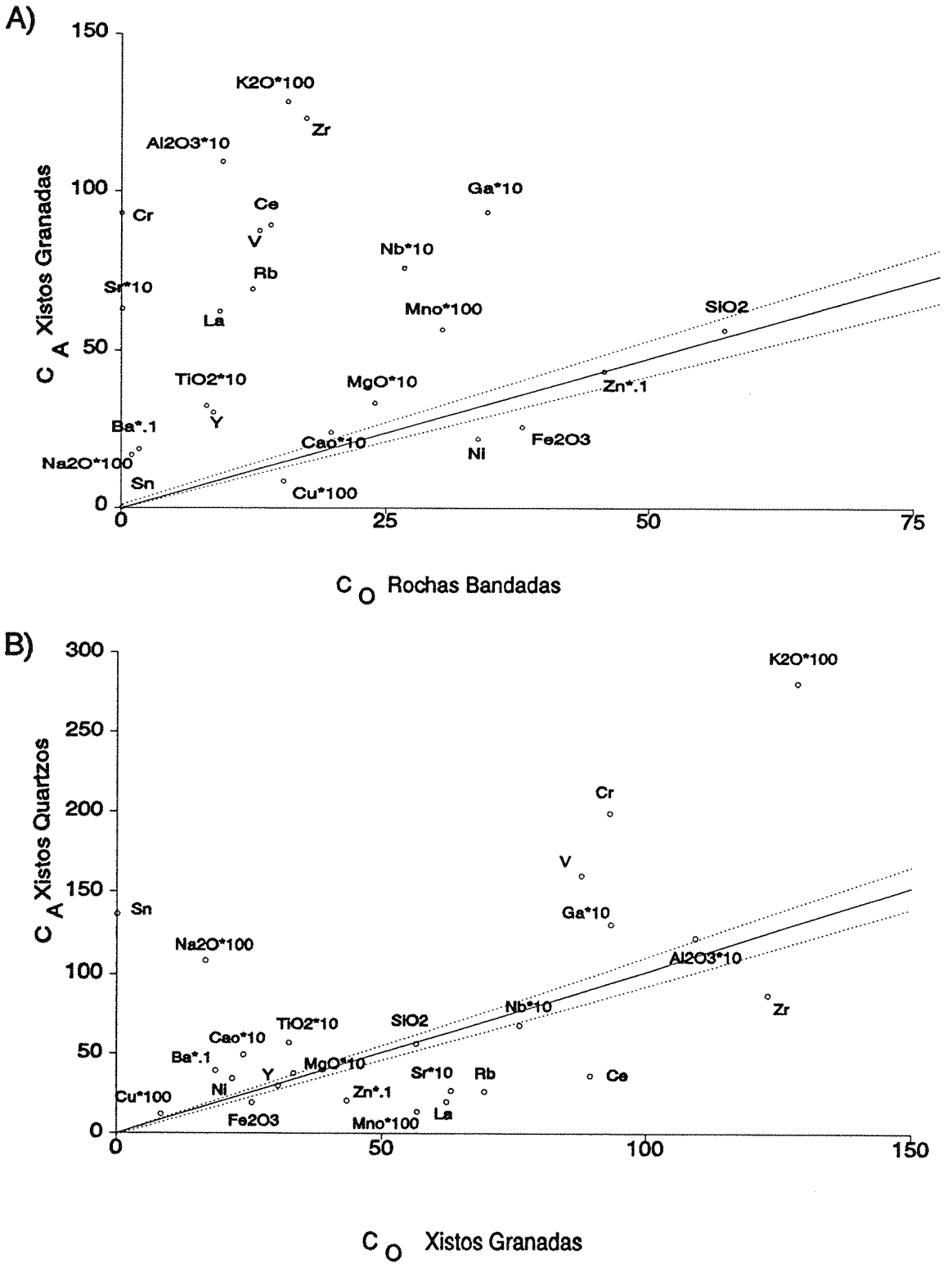

Figure 4.9 **Isocon plots showing chemical variation between A Rochas Bandadas and Xistos Granadas, and B Xistos Granadas and Xistos Quartzos. Oxides = Wt%, trace elements = ppm. A scaling factor of ten is used for clarity.**

a further enrichment into the Xistos Quartzos. The mobile elements Ga, K, Na, Rb, La and Ba also increase in concentration upwards throughout the sequence according to *Figure 4.9*. No variation in the mean silica content is observed up the sequence, but there is a slight decrease in iron from the Rochas Bandadas to the Xistos Granadas. From the increase in heavy elements it is apparent from the isocon plots that detrital sedimentation was of increasing importance up the sequence. The zirconium decrease from the Xistos Granadas into the Xistos Quartzos, however, does not correspond with the increases in the other detrital elements and is unexplained.

Normalization to Zr: Whilst detrital zircon is mobile during secondary erosion processes, Zr is considered to be a relatively immobile element under hydrothermal conditions, lying on the 'immobile' isocons with Y and V in *Figure 4.10*. Zr, therefore, has been used as another method of normalizing the major and trace elements in the C4 metasediments. Zr has been used as the lithological characteristics of the Corpo Quatro Formation suggest it to be less mobile than Ti in the hydrothermal system.

By assuming that Zr represents the amount of clastic detrital component present in a rock, and normalizing element data to Zr, it is possible to establish whether enrichment in other heavy elements, such as Al, Nb and Ti, is due to increased sedimentary activity, or to different hydrothermal processes. A constant Zr ratio throughout the sequence would mean that an element possessed the same depositional and mobilization characteristics as Zr, and therefore that its presence was solely due to detrital sedimentation. Only the elements regarded to be of interest during hydrothermal alteration or clastic deposition have been considered in this section.

With the Zr normalization method, the least altered samples from each unit was used to identify trends in element concentration from the Rochas Bandadas to the Xistos Quartzos (*Appendix B, Fig. 4.10*). These samples were chosen on the basis of the lowest Rb/Sr ratio, combined with the lowest copper and potassium content, and are; F43 (Rochas Bandadas; Zr = 18ppm), F11 (Xistos Granadas; Zr = 88ppm) and F88 (Xistos Quartzos; Zr = 72ppm). Each sample element was divided by its corresponding zirconium value. The elements of interest in this study are those which may reveal information about depositional variation. The results have been displayed graphically in *Figure 4.10*.

Although none of the elements show a perfectly constant ratio with Zr throughout the lithological units, Fe, Ti, Al, Mg, Na and V are roughly constant, with all except Fe and Mg displaying a slight increase towards the Xistos Quartzos. By considering an enrichment in Zr to represent an increase in detrital material, the presence of these elements is also interpreted as being of predominantly sedimentary origin.

From the Rochas Bandadas into the Xistos Granadas, depletion relative to Zr is displayed by all elements except Al, Cr, Mn, V and Y. Of these, Al, Mn and Y remain constant into the Xistos Quartzos. The ferro-magnesian elements Fe, Mg and Ni, as well as Ca, Sr, Zn, La and Ce, all show depletion into the Xistos Granadas, and with the exception of Fe they all display an increase into the Xistos Quartzos. Although it appears that these elements are less likely than the traditional immobile elements to have been carried in detrital minerals, they are comparatively mobile, and their relative depletion may be due to later hydrothermal leaching.

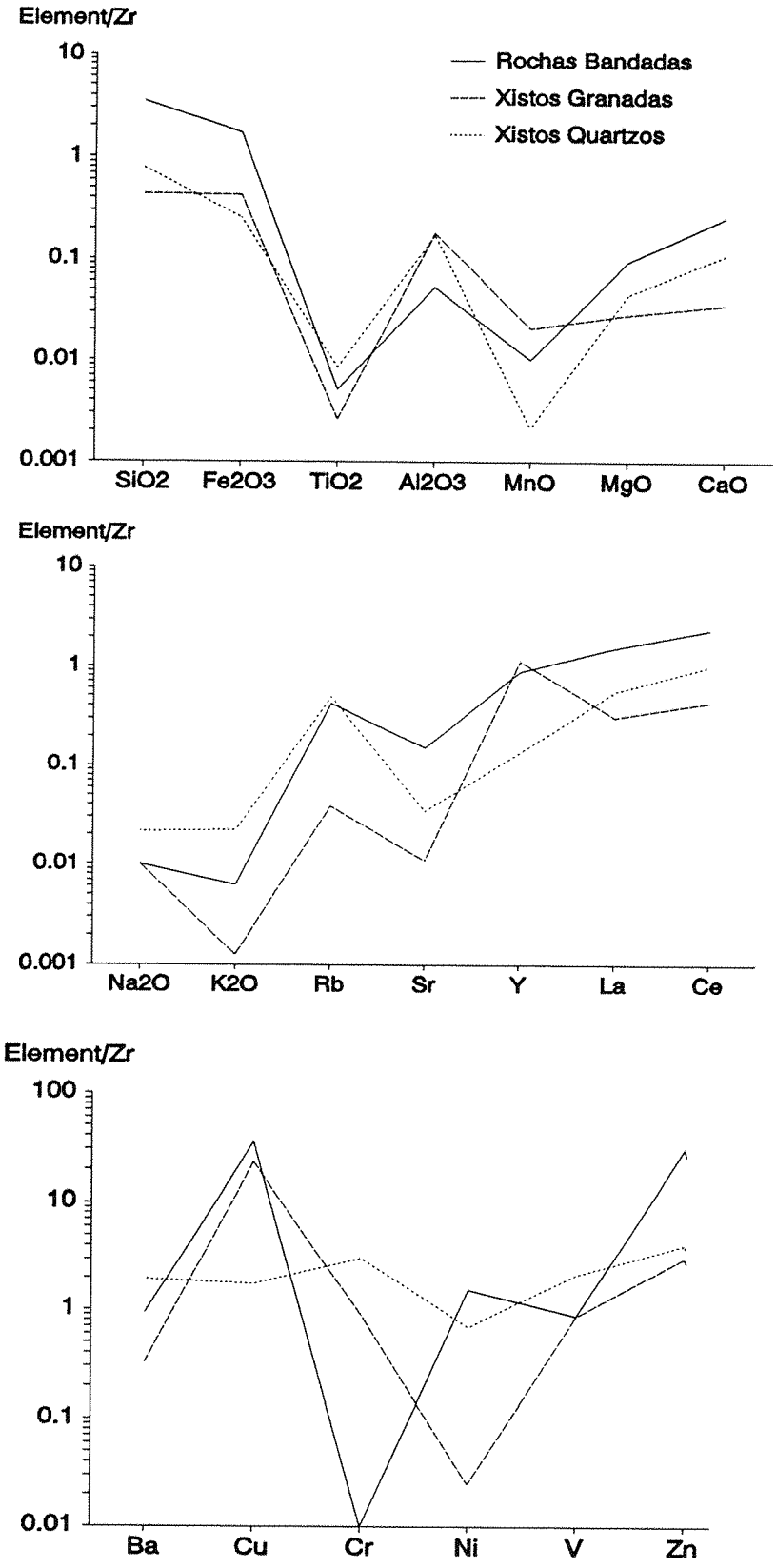

Figure 4.10 **The Corpo Quatro Formation sedimentary rocks normalized to Zr, using the 'standard' samples F43 (Rochas Bandadas), F11 (Xistos Granadas) and F88 (Xistos Quartzos).**

Enrichment is also shown by Na, K, Rb, Ba and Ni from the Xistos Granadas to the Xistos Quartzos. This implies that these elements have a second source other than clastic debris, and probably represents an increased clay component relative to detrital Zr-rich material in the original Xistos Quartzos. The massive enrichment in Al and Cr in the upper sediments may be also be explained in this manner, although it must also be considered that all these elements are relatively mobile, and may have been enriched in the Rochas Fragmentos as a result of later hydrothermal activity.

Inherent problems with this method of data comparison are similar to those encountered previously, particularly as the value of a sample relative to Zr will be entirely dependent on whether the mean analytical value or a standard sample is used for comparison. However, it does provide a clear representation of those elements which display a constant ratio to Zr, and, providing this element is relatively immobile in the hydrothermal environment, the sedimentary components can be identified.

Although there are some minor variations between each of the comparative methods used, all three methods show an increase in the major elements Ti, Al, Na, Ca and Mn, and a decrease in Fe, Cu and Mg from the structural base to the Xistos Granadas. The Zr and isocon methods of normalization, which incorporate trace as well as major element data, show additional increases in Cr, V and Y, and depletion in Zn, Rb and Ga. The chemical changes from the Xistos Granadas into the Xistos Quartzos are also similar using the different methods, with enrichment in Ca, K, Rb, Ba, La and Ce and minor Ti, and depletion in Cu, Mn and Y.

The enrichment in heavy detrital elements (Al, Ti, V and Y in particular) and depletion in ferro-magnesian elements upwards through the sequence appears to indicate that the depositional environment was increasingly dominated by clastic rather than chemical deposition. Although Ca, Na and K enrichment from the Rochas Bandadas to the Xistos Granadas are accounted for by the mineralogical change from ferro-magnesian amphiboles to phyllosilicates, those changes from the Xistos Granadas to the Xistos Quartzos are difficult to account for. However, the accompanying increase in Ba and Rb means that the potassium (and maybe also the sodium and calcium), represents the increase in biotite content seen in thin section in the host rock, which may therefore be of metamorphic rather than sedimentary input.

Although Nb is typically a 'heavy' element, held in detrital minerals, it is more common from felsic rather than mafic terrains. Its depletion up the sedimentary sequence may, as previously suggested in this chapter, indicate that these sediments were formed by the clastic deposition of material eroded from a mafic protolith.

Table 4.5 (*& Fig. 4.11A*) shows that a positive correlation exists between aluminium and potassium in the Rochas Bandadas and the Xistos Granadas, with a roughly constant K:Al ratio (K/Al = 4 to 9). Al/Na and K/Na ratios are consistently high in the barren sediments (16 - 50 and 1 - 13 respectively). *Figure 4.11B*, plotted using raw data (LOI corrected) shows that there is a correlation between Fe and Cu in the C4 metasediments, indicating that they may be of the same hydrothermal provenance, or that copper may have been concentrated in iron-rich areas, as a result of the replacement of iron-sulphides and oxides by chalcopyrite.

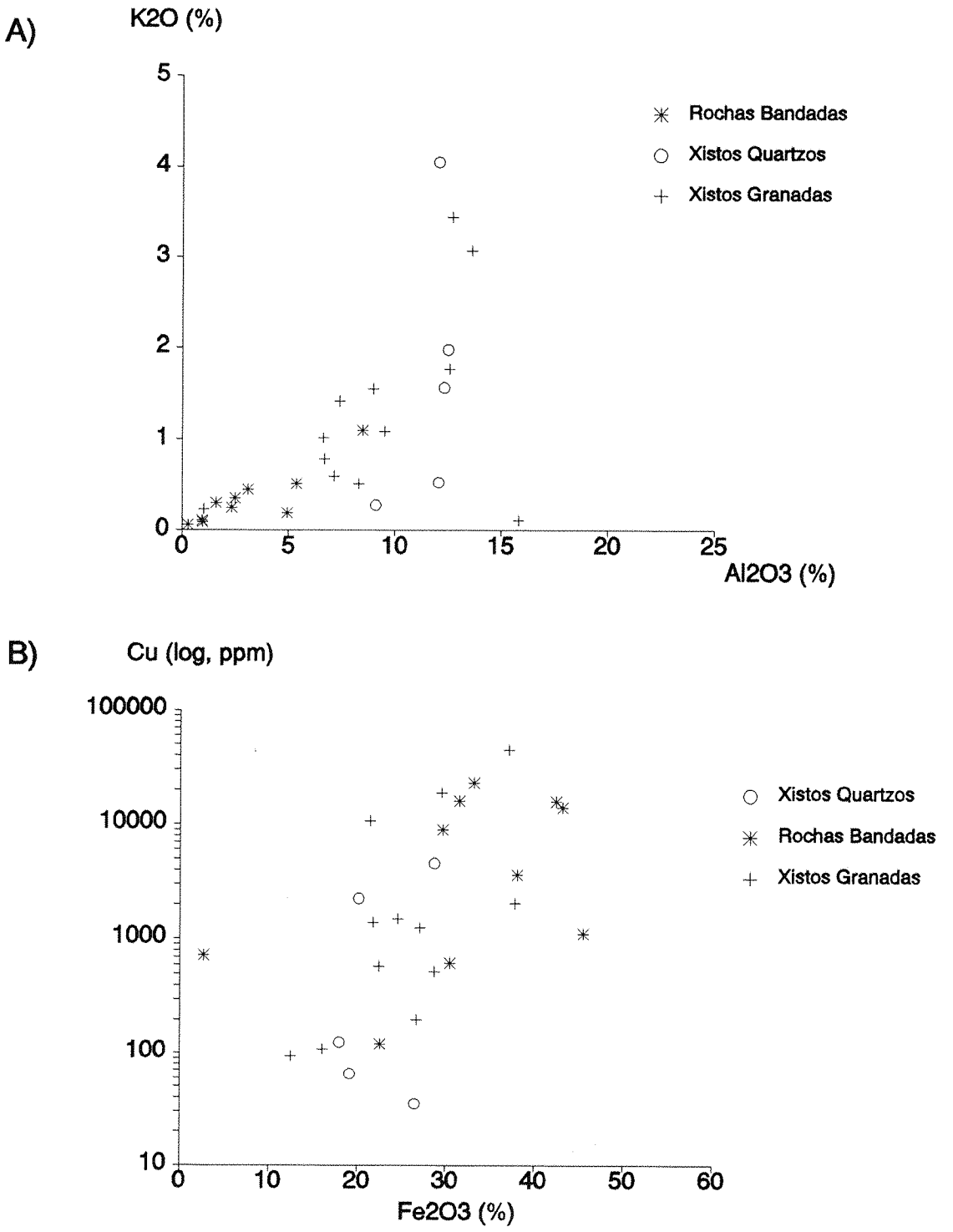

Figure 4.11 **A Al_2O_3 plotted against K_2O; B Log-normal plot of $Fe_2O_{3(TOT)}$ vs. Cu for the Corpo Quatro Formation metasediments. See text for explanations.**

4.3 *GEOCHEMICAL ALTERATION IN THE CORPO QUATRO FORMATION*

Post-metamorphic alteration of the Corpo Quatro Formation is demonstrated in a number of styles. Those considered in this section are principally associated with mineralization. Other forms of post-metamorphic alteration, such as the development of areas of intense schistosity described in Chapter 3, are not considered here.

4.3.1 *Hydrothermal Overprint on the Corpo Quatro Metabasites*

Three samples of visibly hydrothermally altered volcanic rocks have been analyzed. Two of these (G60 and G61) are from the G1-C4 Albite Zone, and one (F33) is from an area of cordierite-anthophyllite-rich dalmatianite in the upper C4 volcanics. The effect of albitization has also been considered in this section, in the form of a traverse of the G1-C4 volcanic samples, which passes through the Albite Zone.

The Effects of Albitization on the C4 Metabasites

The G1-C4 Albite Zone, described in detail in Chapter 3, is the largest exposure of this type of alteration in the Corpo Quatro Formation. Geochemically, it is very different to the metabasalt host-rocks found throughout the I.P.G. (*Fig. 4.3*), plotting as a trachybasalt on the IUGS classification diagram (*Fig. 4.2*). By plotting some oxide 'contours' on the silica-alkali diagram (*Fig. 4.3*; Cox *et al.*, 1979), it can be seen that the Albite Zone is depleted in Mg, K and Ca, and enriched in Na compared with a typical trachybasalt, and is therefore not representative of fresh igneous rock, confirming field observations made in Chapter 3 that the Albite Zone is a product of hydrothermal alteration, or albitization.

The chemical variation produced by the Albite Zone can be visualized using the traverse plots along the adit G1-C4 (*Fig. 4.12A&B*), which plot major and trace element concentrations across the Albite Zone. These show that in terms of major element geochemistry the Albite Zone displays a relative depletion in Mg, Fe, P and Ca, and a marked increase in Al and Na. These changes are also obvious from *Figure 4.4*, and reflect the mineral assemblage which is dominated by albite (Chapter 3, section 3.1.3). The increase in the relatively immobile element aluminium may therefore be an apparent rather than real effect, caused by the leaching of ferro-magnesian minerals from this unit. Trace element variations reveal a marked reduction in Y, Ni, Cr and Zn, and an enrichment in Cu in the Albite Zone relative to the metabasites. The high field strength elements (Nb and Zr) show variation throughout the adit samples, and have no obvious enrichment or depletion in the Albite Zone, again indicating the hydrothermal nature of the lithological variation. No gradational chemical alteration (either enrichment or depletion) is observed in the basalts around to the Albite Zone, but sample G67, which comes from immediately below the Albite Zone (*Fig. 4.1*), displays a marked enrichment in many of the elements (K, Zn, Ni, Y, Rb, Ga, Ba, Ce and La) when compared with the underlying metabasalts and the Albite Zone. These elements display depletion in the Albite Zone itself, and the enrichment may therefore be explained by their leaching from the Albite Zone, and re-deposition in the footwall (and, in the case of Rb, Ba and K, in the hanging wall) of the Albite Zone.

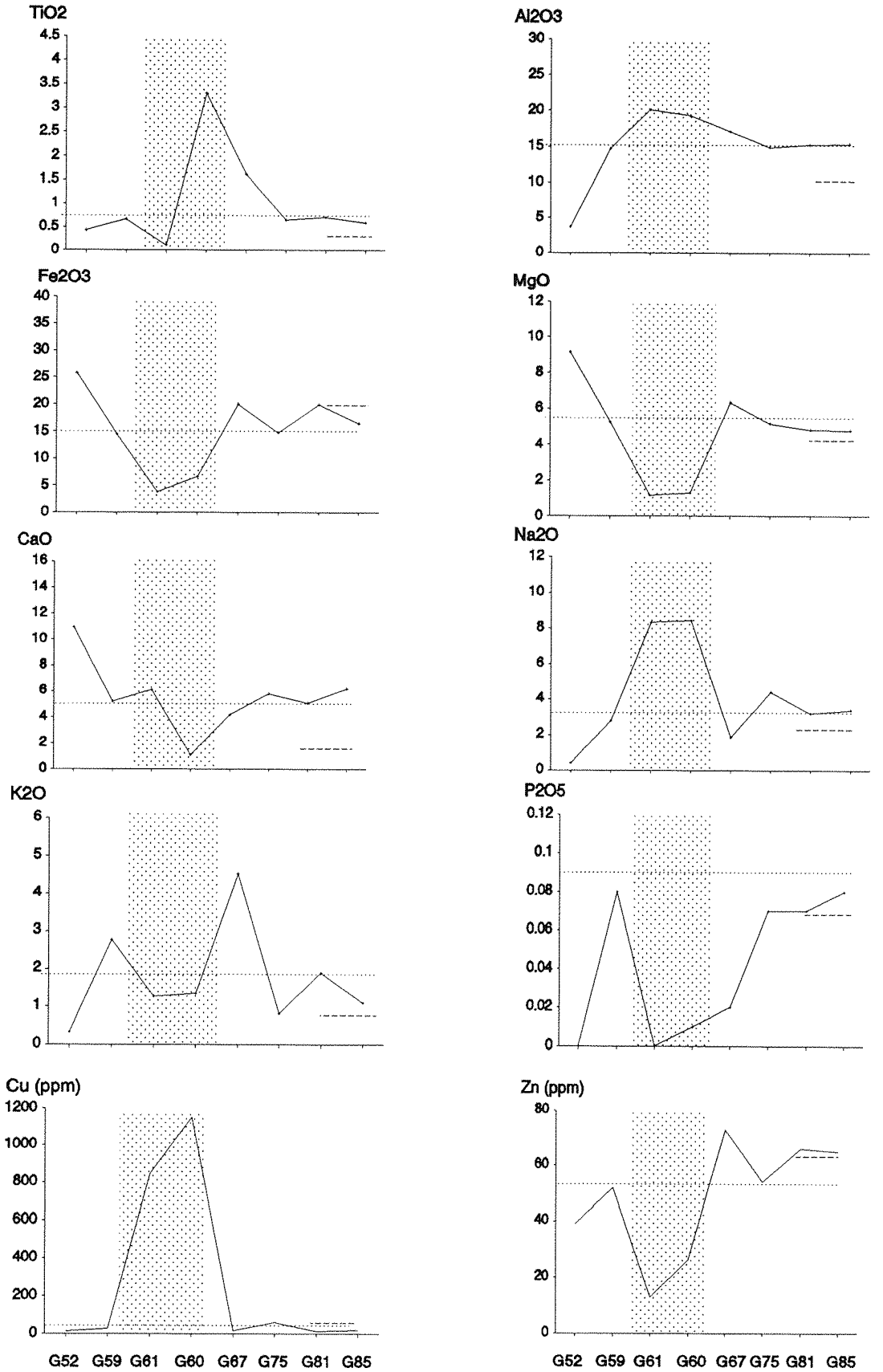

Figure 4.12a **Traverse plots of major elements across the G1-C4 Albite Zone. Shaded area = Albite Zone, dotted lines = mean data from borehole samples (Samples F48, F49, F50 and F53) dashed lines = Cordierite-anthophyllite (F33) data.**

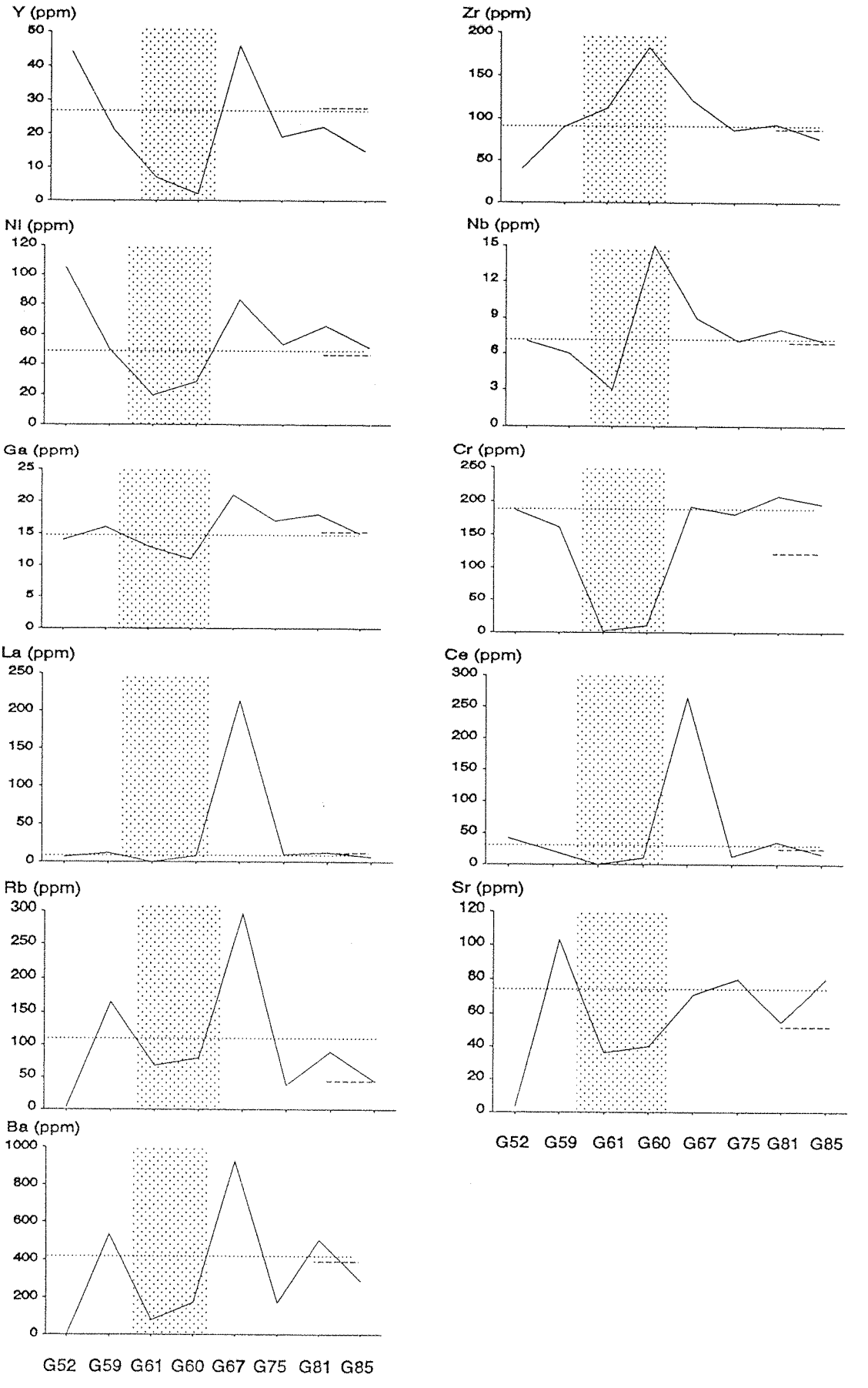

Figure 4.12b Traverse plots of trace elements across the G1-C4 Albite Zone. Details as Figure 4.12a.

The profiles of K, Rb and Ba (*Fig. 4.12*) are identical, indicating that these elements have the same hydrothermal history. However, these three elements appear to have been remobilized within the system rather than introduced into it, as they do not display enrichment in the Albite Zone. The plots represent changes in the amount of amphibole to biotite alteration seen in thin section in the metavolcanics, as Rb and Ba substitute for potassium in biotite. It would therefore appear that biotite alteration is most prolific as a wallrock alteration product of albitization, as observed in Chapter 3. The Cu and Na_2O profiles are also similar, and in this case they both display massive enrichment in the Albite Zone, indicating that they were introduced together during a hydrothermal event. The background (unalbitized) metavolcanic rock, however, is depleted in copper relative to most Archaean tholeiites and N-MORB (mean=23ppm compared to 66ppm and 74ppm respectively; Condie, 1985). Zinc does not show the same profile, displaying depletion in the Albite Zone. This may suggest one of two things: either the zinc was removed from the Albite Zone during its formation, and was subsequently redeposited as sphalerite in the sedimentary strata, or zinc was introduced during an entirely separate stage to the copper in the C4 deposit. The former is most likely, explaining the Zn depletion seen in the Albite Zone when compared with the surrounding metabasalts. However, evidence in the sulphide mineral textures (Chapter 3) has already suggested that the latter may be true.

Nature of the Dalmatianite in the IPG Metavolcanics:

The 'dalmatianite' assemblage (described as in Chapter 3, section 3.2.3), shows extensive alteration of cordierite to sericite ($KAl_3Si_3O_{12}(OH)_2$), so that the Al enrichment normally expected with cordierite ($(Mg,Fe)_2Al_4Si_5O_{18}.nH_2O$) is absent (*Fig. 4.12*). The only elements to be enriched in these rocks are Cu and particularly Fe and Zn. This seems to indicate that the cordierite-anthophyllite rock, itself an alteration assemblage, has been overprinted by a further hydrothermal event resulting in sericitization and enrichment in Fe and Zn. It is therefore apparent, again, that copper and zinc may not have been introduced into the C4 deposit at the same time. It is not possible to ascertain the origin of the cordierite-anthophyllite assemblage from this study.

4.3.2 *The geochemical effects of mineralization on the Corpo Quatro Metasediments*

In order to establish any geochemical modifications undergone by the C4 metasediments during the process of mineralization, the sulphide-rich samples from the C4 deposit have been compared with their barren counterparts using the isocon and SiO_2 methods of data analysis described in section 4.2.2. These methods have been used, despite their shortcomings, in the absence of a more suitable method of comparison. The comparison of barren and mineralized samples means that only the effects brought on by mineralization should be identified in this study.

For the purpose of this study, mineralized samples are defined as containing significant visible sulphides (>0.5% by volume) in hand specimen. Geochemical data was obtained for six mineralized samples of Rochas Bandadas, six of Xistos Granadas and three of Xistos Quartzos. Due to the high copper content in some of the samples, Cu was analyzed as a major element to enable totals close to

100% to be reached. It was not possible to acquire comparable samples distal to the orebody, and therefore some of the apparently barren samples contain high copper and zinc values.

A brief study of the raw data (*Table 4.5*) indicates immediately that of all three lithologies, the Rochas Bandadas show the most geochemical alteration in mineralized samples. This is due to the abundance of sulphide minerals in the unit when compared with the Xistos Granadas and Xistos Quartzos. The substantial enrichment in Al, Ca and Cu, and minor increases in Na and K on mineralization observed in *Table 4.5* in the Rochas Bandadas must, at this stage, be regarded with some caution due to mathematical closure described in section 4.2.2 as a result of summation to 100%.

Normalization to SiO_2: Although mineralization occurs in quartz veins in the Corpo Quatro Formation, it has been shown in Chapter 3 that most of the sulphide enrichment occurs as banded or fracture-fill sulphides within metamorphosed quartz and amphibole horizons, and there is little apparent increase in quartz accompanying mineralization. *Table 4.5* also indicates that there appears to have been no major enrichment in SiO_2 on mineralization. Therefore, the main variation in silica in a sample is due to primary sedimentary difference or to silicification at some time other than during mineralization. The samples used for geochemical analyses did not contain any quartz veins, and therefore it is believed that a sulphide enrichment does not presuppose a silica increase. As such, it is considered that SiO_2 can be used to normalize each sulphide-rich sample, reducing the effects of mathematical closure caused by the summation of compositional data to 100%, and taking into account the silica variation in each sample. The ratio of parent (barren) to daughter (mineralized) composition enables the identification of elemental losses and gains in the major elements.

Equation *4.1* was applied to each sulphide-bearing sample, using the 'standard' representative barren sample for each unit (sample F43, F11 and F88). These samples were chosen on the basis of their Rb/Sr ratio, K_2O and Cu contents, as these are believed to be the best indicators of hydrothermal alteration. F43 was chosen as the standard Rochas Bandadas, as it contains lower levels of Zn and Cu than F47, which was used as the standard when comparing barren rock types. The results are plotted graphically in *Figure 4.13A-C.*

Relative to the parent rock, the mineralized Rochas Bandadas show significant enrichment in Al_2O_3, Na_2O, MnO and K_2O (*Fig. 4.13A*), as well as in Cu and SO_3, implying that these major elements were introduced during the main phase of copper mineralization. SO_3 data must be treated with some caution as some sulphur may be lost during sample preparation (see *Appendix B*). A study of the Xistos Granadas and Xistos Quartzos plots (*Fig. 4.13*) shows that apart from copper and sulphur, none of the elements enriched during mineralization of the Rochas Bandadas show a corresponding increase in the Rochas Fragmentos.

The Isocon Diagram: This method of comparison was designed for use with parent and daughter pairs of the same lithology (Grant, 1986), and has been employed as a second method by which to compare barren and mineralized data sets from each of the three C4 metasedimentary units. The use of average geochemical compositions overcomes most of the problems incurred by sample error and

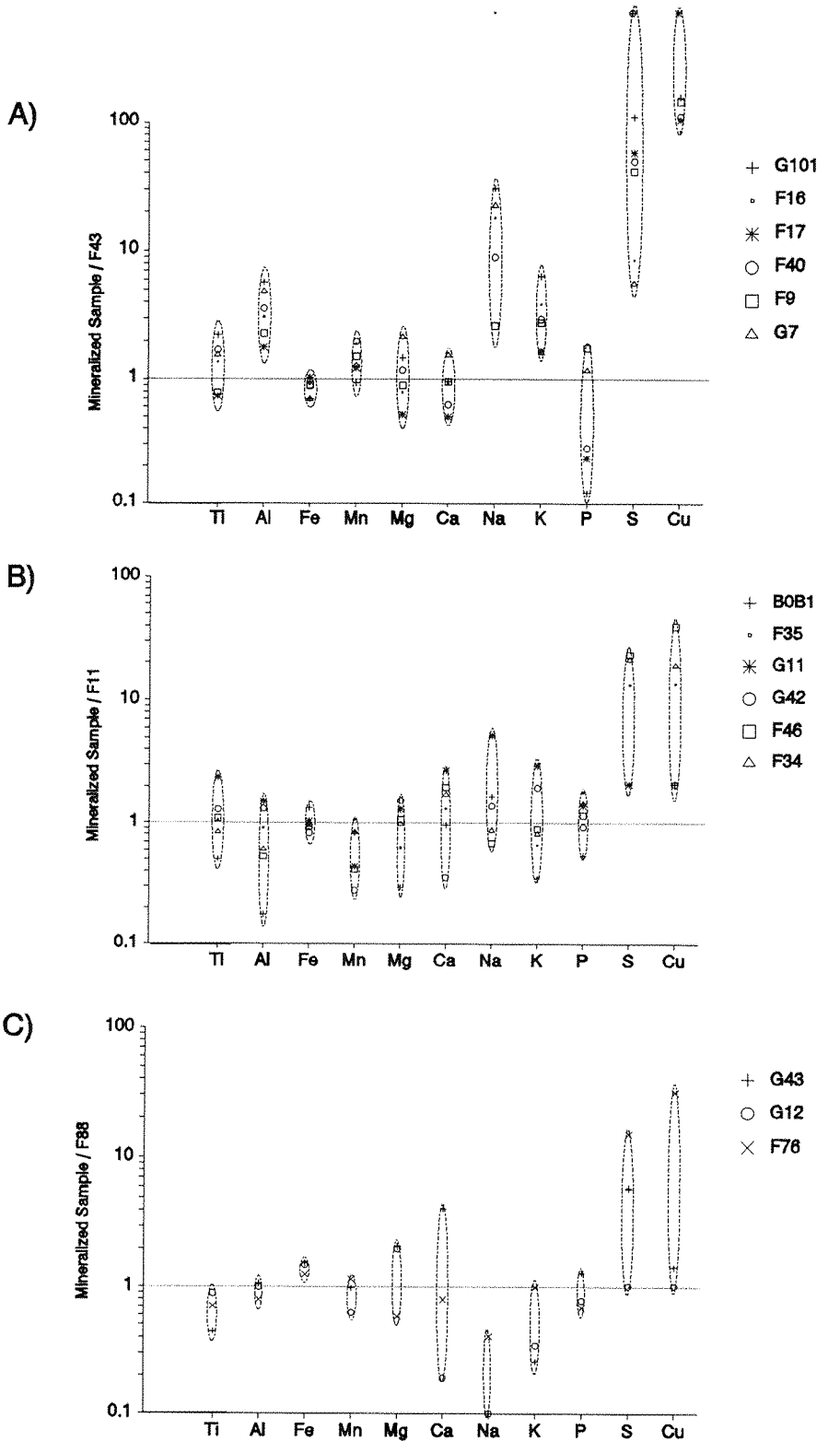

Figure 4.13 **Mineralized samples from the Corpo Quatro Formation sediments, normalized to 'standard' barren samples using the 'silica method'. A Rochas Bandadas, normalized to F43; B Xistos Granadas normalized to F11; Xistos Quartzos normalized to F88. A value of 0.1 has been used instead of 0.0 to normalize Na_2O and Cu.**

anomalous values, although by taking the mean of the data, extreme values may still result in misleading plots (see Zn and V, discussed later). Geochemical data below the determination level (3xLowest Limit of Detection, LLD, see *Appendix B1*) have been ignored.

Aluminium is usually chosen as a constant in the Grant isocon plots. However, it has been shown in the previous section, and in Chapter 3 where Al in amphiboles increases in close proximity to sulphide mineralization, that Al may have been mobile in these sediments during the mineralization stage. The 'constant', or isocon, must therefore be drawn through the immobile elements. Zr, Y, Ti and Nb are generally considered the best elements for this, although it has been shown by Giere (1990) that Ti and Zr may be highly mobile under certain geological conditions. There is some evidence for the transportation of Ti (in ilmenite concentrations) in the Corpo Quatro Formation, although it generally lies on an isocon with the other immobiles, indicating that these were the least mobile during hydrothermal alteration. The 'line of best-fit', defined by Grant (1986) as the line along which elements have not undergone modification during alteration, could take a number of positions in each of the isocon plots (*Fig. 4.14*). The line passing through as many of the so-called 'immobiles' as possible (Nb, Y, V ±Ti, Zr) was chosen.

From the plots (*Fig. 4.14A-C*), it is apparent that the elements Ti, Ba, Cr, Nb, Ga, Y and Ce displayed little or no mobility during the hydrothermal activity associated with mineralization in the Corpo Quatro sediments. The apparent enrichment of the usually immobile element vanadium in the Rochas Bandadas can be explained by the use of mean values, where the anomalous V value of 263ppm in one Rochas Bandadas sample raises the mean of the other samples, which lie between 10 and 45ppm. However, the enrichment in Zr in both the Rochas Bandadas and the Xistos Quartzos relative to their barren counterparts indicates that this element has been hydrothermally transported during mineralization.

Elements showing significant enrichment during mineralization of the Rochas Bandadas are Al, Cu, Na, Ca, Rb, K, Sn and Sr, whilst Si displays depletion in the altered samples (*Fig. 4.14A*). Zn is not significantly enriched in the mineralization Rochas Bandadas, and this is caused by the averaging effect in which two copper-rich samples, classified as mineralized, contain only 200ppm Zn compared with 700-900ppm in other samples. This is partly a result of sample selection, as sphalerite is not clearly visible against the dark coloured hornblende in hand specimen, and partly because, as became apparent in section 4.3.1, zinc may have been introduced during a separate event to the copper, and as such zinc-rich samples were rarely chosen for analysis.

Whereas the spread of elements around the isocon is great for the Rochas Bandadas, the elements are more clustered around the Rochas Fragmentos isocons. This can be related to the lack of mineralogical change associated with mineralization in these rocks (Chapter 3). The positions of Cu and Zn on the Xistos Quartzos isocon plot indicate that visible sulphides do not account for the majority of the mineralization in this unit. The main indication of sulphide-associated geochemical modification can therefore be gained from the Rochas Bandadas and Xistos Granadas plots. A comparison between these shows that the main enrichment occurs in Cu, Sn, K and Rb on mineralization.

The isocon method was established to compare two samples of which one is the completely unaltered equivalent of the other. At Pojuca, metamorphosed and partially mineralized rocks are being

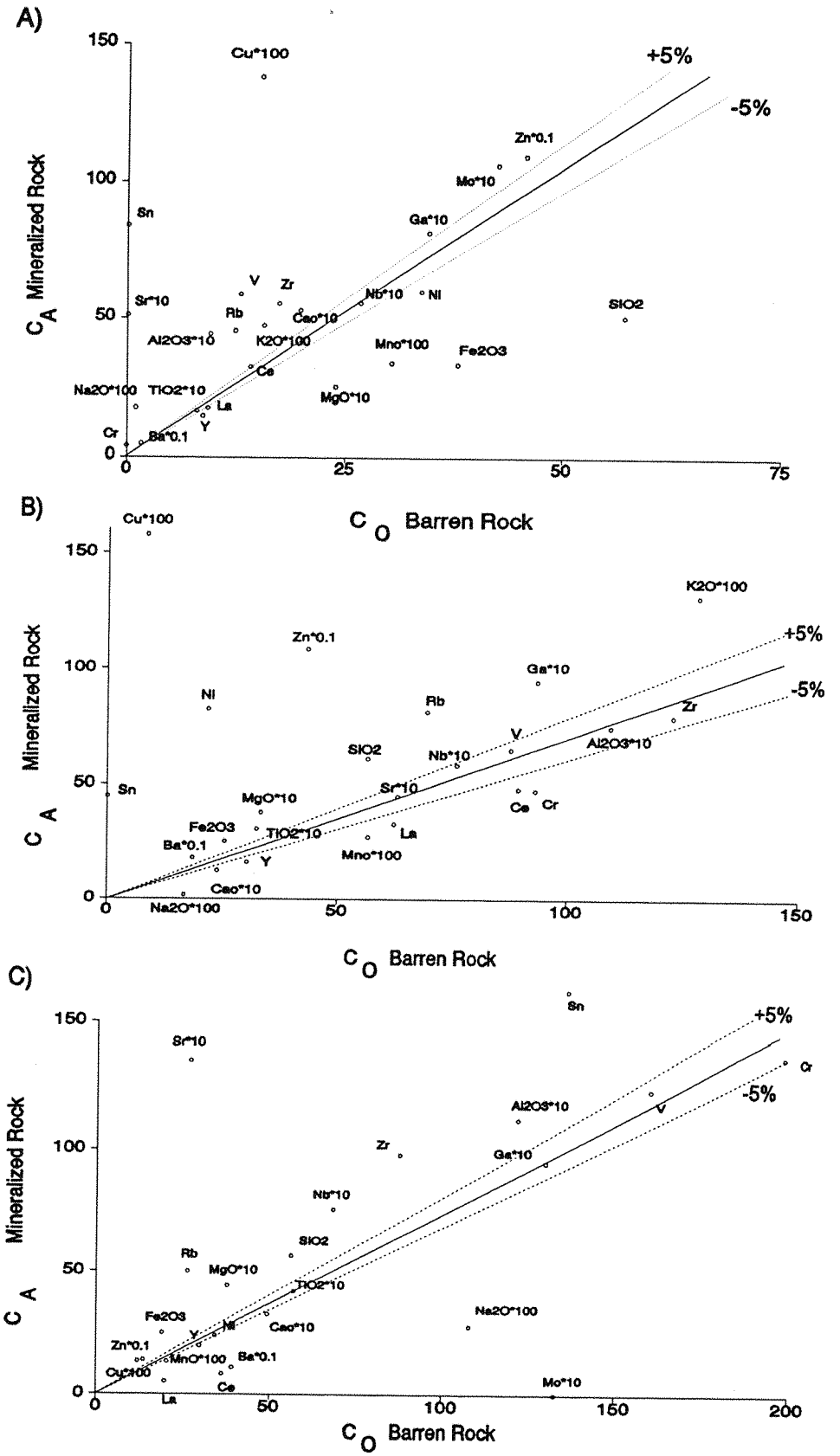

Figure 4.14 **Isocon plots showing chemical variation between barren (C_O) and mineralized (C_A) samples of the Corpo Quatro sediments. Plotted using mean data (see *Table 4.5*). A Rochas Bandadas; B Xistos Granadas; C Xistos Quartzos. Oxides = Wt%, trace elements = ppm. A scaling factor of ten is used for clarity.**

compared with sulphide-rich rocks, and the chemical changes are variable within different lithologies. Although care must be taken to combine this method with the silica normalization and mineralogical changes, the demonstration that certain elements did appear to be immobile during mineralization means that the method is still valid. The use of mean values has inherent problems when dealing with skewed distributions, as described in the text, but these problems are amplified when single samples are used.

By using and comparing the two methods (isocon and SiO_2 normalization) to establish chemical changes between barren and mineralized sediments of the Corpo Quatro Formation, it has become clear that on mineralization of the Rochas Bandadas there has been significant enrichment in the major elements Cu, Na, K and Al, and in the trace elements Rb, Sn, V and Sr. The alkali metals are not enriched, however, in the Rochas Fragmentos, which show an increase in the elements Fe, Mg, Si and Cu on mineralization. The increases in Cu and Fe can be directly related to the presence of chalcopyrite, and Fe, Mg and Si to the presence of Fe-Mg-amphiboles. The only notable depletion in the Rochas Bandadas is that of SiO_2, which may be an artificial effect caused by increase in sulphide volume in these rocks. This increase in ferro-magnesian silicates may be a cause, rather than a result of the copper enrichment, which would therefore appear to be preferentially deposited in amphibole-rich strata. This is consistent with the depletion seen in Na in the Rochas Fragmentos. Although there is no definitive textural evidence for this, sulphide minerals do appear to be more abundant in garnet-grunerite-biotite assemblages than in chlorite-rich, amphibole-poor assemblages. The dearth of chemical changes in the Rochas Fragmentos compared with those in the Rochas Bandadas may be explained by the lack of mineralogical change observed in the upper sediments in sulphide-rich areas. The best indication of geochemical alteration accompanying mineralization can therefore be gained from the Rochas Bandadas.

4.4 *DISCUSSION AND CONCLUSIONS*

Geochemical data sets are usually compared using the mean data set of XRF analyses. When making internal comparisons between individual units which show a wide variation in one or more elements, however, it is necessary to use a method which will overcome the inherent problems of mathematical closure. This was not necessary in comparing the geochemical data from the C4 metabasalts, but the C4 metasediments, which show great variation in silica, iron and aluminium, require more than a direct data comparison. The methods used in this study are not ideal, and there is a need for a more reliable method which has none of the shortcomings of the normalative techniques used. In the absence of such a system, geochemical comparisons of even the mean or standard sample data from the Corpo Quatro sediments introduces misleading results.

The internal comparisons made between the Corpo Quatro metabasalts and other Archaean basalts, and within the Corpo Quatro basalts have been carried out on standard XRF data. These comparisons may be made despite the metamorphic overprint and hydrothermal alteration of the Corpo Quatro metabasalts, in order to determine the source of the magma. Comparisons between typically immobile elements (especially Ni, Ce, Cr and Zr) have indicated that the volcanics of the Corpo Quatro

Formation are of tholeiitic, within-plate type, show depletion in Ca and Cu, have a high K/Na ratio, and are enriched in Fe_2O_3 relative to other Archaean tholeiites and present day MORB. The lack of significant variation between the immobile elements in the Grão Pará Group and the Corpo Quatro Formation metabasites suggests a similar origin for the two groups of volcanic rocks.

Comparing the Grão Pará Group with the Corpo Quatro basalts has demonstrated that there has been significant modification of the relatively mobile elements during local secondary hydrothermal activity, resulting in relative enrichment in Fe, Rb, Ba, La and Ce, and depletion in Ti, Ca, Sr and Mn.

Local lithological variation in the Corpo Quatro metabasites is dominated by albitic and potassic alteration, which has resulted in a wide variation in both Na and K in the altered samples. The Albite Zone displays pervasive sodic alteration accompanied by enrichment in Al, Na and Cu, and locally in Ti and Zr, and depletion in Fe, Mg, Cr, K, Rb and Ba. The profiles of these elements indicate the Albite Zone to be the product of a major hydrothermal event, during which Na and Cu enrichment resulted in albitization, accompanied by leaching of K, Ba and Rb from the host metabasites by the breakdown of ferro-magnesian minerals (biotite and hornblende).

Internal chemical comparisons between the Corpo Quatro Formation sediments have been made using 'normalizing' methods (silica-normalization, Zr-normalization, and the isocon plot). The main problem encountered in using these methods results from spurious element values. The choice of the 'standard' sample in each case is therefore important, as it represents the bulk composition of the individual unit, and any local heterogeneity may result in misleading data. This is not always overcome by the use of mean values, as discussed with respect to the isocon method earlier in this section, and there are disadvantages in both approaches.

The standard samples used were chosen on their degree of alteration; for the mineralized vs. barren comparisons, least and most altered samples were identified using a combination of the Rb:Sr ratio (low in unaltered rocks), K_2O and Cu content. For barren-rock comparisons, the sample closest to the mean data set of the respective unit was chosen as the standard.

The isocon plot allows every element to be plotted on a single graph. The use of individual samples was found to give a sample-prejudiced view of alteration; for example, a 'standard' barren sample may in fact contain more zinc than a mineralized sample, for the reasons explained earlier that sphalerite is not easy to see in hand specimen, and is not always accompanied by other sulphide minerals. If this sample is compared with a copper-rich, zinc-poor sample, there is an apparent depletion of zinc in mineralized relative to barren rock. The use of the mean value of a unit overcame this problem. The silica normalization method allows comparison of all major elements other than silica, which are likely to undergo changes between sedimentary units or during alteration. No major problems were encountered, although a particularly low value, such as $P_2O_5 = 0.1$, will result in any increase appearing to be massive. It is, however, not practical to plot trace elements in this manner. The zirconium normalization method assumes that Zr is immobile during hydrothermal alteration, and therefore represents sedimentological variation rather than post-depositional mobilization. However, Giere (1990) suggested that Zr may be mobile. The variation of Zr from the isocon, particularly in the Xistos Quartzos, means that this element may not be as immobile as was previously believed. It must also be considered that the mineralized

samples of Xistos Quartzos may happen to show more 'clastic' tendencies than the barren samples, although this is unlikely as it has already been pointed out that mineralization shows a stronger association with grunerite-rich, thus iron-formation-type strata.

Despite the shortcomings of these methods, and some minor discrepancies which can be attributed to the slight variation between mean and standard values, most of the elements analyzed display the same variation according to each method. It is therefore concluded that they can be used as a general guide as to the changes undergone during sediment deposition and mineralization in the Corpo Quatro Formation.

It has been established that the C4 metasedimentary rocks display a coherent increase in K, Al and Ti in barren rock through the sequence from Rochas Bandadas to Xistos Quartzos. This indicates a change from ferro-siliceous to more aluminous sediments, with a corresponding change from chemical to more clastic sedimentary conditions. This change has been observed by a number of other authors, in the Igarapé Salobo Group (Lindenmayer, 1990), where the iron-formation grades eventually into meta-greywackes, and in the Yilgarn Block Iron Formations of Western Australia, where iron-formation grades into Fe-rich shales (Gole, 1981). Unlike the Salobo metasediments, the Rochas Fragmentos contain more Fe, Ca and K, and less Si and Na than typical Archaean greywackes, displaying an average Al:Na ratio of 55, a K:Na ratio of >3, and Fe+Mg up to 40%. Typical Archaean greywackes are described as having high Fe+Mg totals (up to 10%) and low Al:Na (<6) and K:Na (0.4 and 1.0) ratios (Taylor and McLennan, 1985).

A source for clastic input to the Corpo Quatro Formation

It must be considered that the increased 'clastic' component observed from the base to the top of the Corpo Quatro metasediments may result from the input of either volcanic or clastic material. Although the alkali metals have undergone hydrothermal mobilization, a similar degree of alteration is seen throughout the units. By plotting the entire (barren) Pojuca C4 Formation on S-A-F and K-A-F ternary diagrams (*Fig. 4.15*), it can be shown that the Xistos Granadas and the Xistos Quartzos fall on a line between the Pojuca metabasites and the 'pure' Rochas Bandadas. This indicates the Rochas Fragmentos to be composed of a mixture of volcanic material and the underlying iron-formation. Although the very high iron content in the Rochas Fragmentos (up to 45%) may also be attributed to volcaniclastic input, *Figure 4.15* shows that it is more likely to represent continued chemical sedimentation in the sequence.

The earlier geochemical comparison made between the Corpo Quatro Formation and other Archaean metasedimentary rocks, using mean XRF values, has indicated that the Xistos Quartzos resemble the Kalgoorlie Shale Member, itself believed to have been derived from a mixture of mafic and felsic extrusives (*Table 4.6*; Sample KH38, Taylor and McLennan, 1985). This further exhibits the possibility that the C4 sediments are at least partially composed of volcani-clastic material. The volcanic material has been shown to be of similar geochemical composition to the C4 metabasites, but its source must in fact be an earlier, or synchronous distal volcanic episode, as the MVII underlie the Rochas Bandadas and the MVI overlie the Xistos Quartzos. As all the basaltic rocks of the Itacaiunas Supergroup

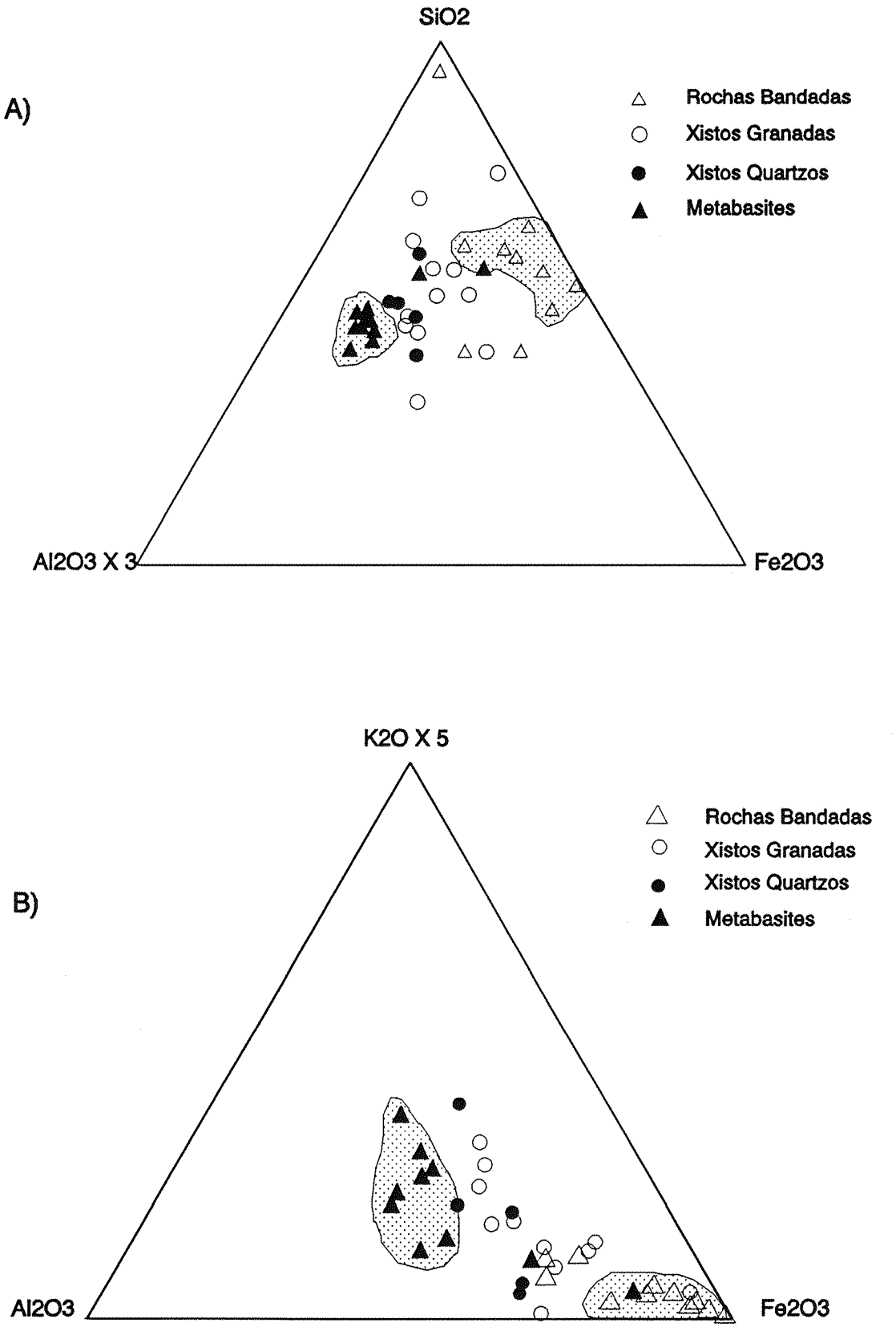

Figure 4.15 **Ternary plots of the individual lithological units in the Corpo Quatro Formation. A SiO_2-Al_2O_3-Fe2O3; B K_2O-Fe_2O_3-Al_2O_3. Plots clearly show that the Rochas Fragmentos lie between the metabasalts and the Rochas Bandadas. (After Lindenmayer, 1990)**

show similar geochemical signatures (Gibbs *et al.*, 1985; Meirelles and Dardenne, 1991; this study), the source of the volcanic material may either be one of the volcanic units of the Grão Pará Group, implying that the Igarapé Pojuca Group is coeval with the GPG, or the Igarapé Salobo Group volcanics, which are older than the Igarapé Pojuca Group.

Changes in mineral assemblage undergone on mineralization are not obvious in the Rochas Fragmentos, although the Rochas Bandadas display an increase in calcic amphiboles content (in the form of hornblendization of pre-existing amphiboles) in close proximity to the sulphide mineralization. This alteration is substantiated by significant enrichment in the elements Na and Al in the Rochas Bandadas, which also display enrichment in potassium and in the trace elements Rb, Sn, V, Sr, and Cu. The increase in the potassium, and its associated trace elements Rb and Sr is thought to indicate an increase in biotite content, although this is not confirmed by petrographic studies. The Rochas Fragmentos display increases Fe, Mg and Si associated with copper enrichment, and these elements are probably held in ferro-magnesian silicates.

A comparison between the changes undergone by the C4 metabasites relative to the Grão Pará Group volcanics, and by the mineralized C4 metasediments, indicates enrichment in both K and Rb in all but the Xistos Quartzos, and depletion in calcium in all but the mineralized Rochas Bandadas. This may indicate that calcium has been leached from other strata during fluid-rock interaction, and has subsequently been redeposited in the Rochas Bandadas, which is where the majority of sulphide minerals are located.

Chapter 5

Veining and Fluid Characteristics in the Corpo Quatro Formation

5.1 *INTRODUCTION AND RATIONALE*

Textural studies of sulphide mineralization in the Pojuca C4 ore body (Chapter 3) have indicated that the copper and zinc contents of this Archaean iron-formation may be directly related to quartz (± carbonate) veining, raising the possibility that the mineralization may be of epigenetic nature rather than being a 'typical' syngenetic sed-ex massive sulphide deposit, as has previously been suggested (Hutchinson, 1979; Saueressig, 1988).

In order to evaluate this hypothesis further, a systematic study of the quartz and calcite veins (both barren and sulphide-bearing) and associated fluid inclusions, and also of the fluid inclusions in the host metasedimentary units of the Corpo Quatro Formation has been undertaken. A study of the veins in Pojuca C4, particularly those in the G1-C4 adit, where relationships between different vein sets, faults, deformation and mineralization can be observed, allows a classification of fluid events to be made in terms of relative timing. A systematic study of the microthermometric properties of the fluid inclusions in these veins, as well as those in the host rock quartz which are in close association with the mineralization, combined with the fluid chemical analysis (D-ICP, laser Raman) and petrological observations of Chapter 3, the *P-V-T-X* properties of each fluid set can be established, therefore indicating properties and relative timing of the fluids contributing to ore genesis at Pojuca C4.

5.2 *NATURE OF VEINING IN THE POJUCA C4 DEPOSIT*

The Pojuca Corpo Quatro Formation has been subjected to several hydrothermal events, resulting in the generation of quartz, calcite, epidote and feldspar vein sets ranging from less than one millimetre to tens of centimetres wide. The majority of the quartz- and calcite-bearing veins occur in fault zones, while the tourmaline and feldspar-bearing veins show no apparent fault relationship. The following section describes vein occurrences and mineralogy, and includes structural data obtained from veins in the G1-C4 adit.

Quartz dominates the veins in the Corpo Quatro Formation, where it occurs in a number of different vein sets, as barren quartz, quartz-chalcopyrite ± biotite, and quartz-biotite assemblages, often with associated calcite. Plagioclase-K-feldspar-epidote veins are abundant in the metavolcanic country rocks, and calcite veining, which post-dated all other events, is present in all lithologies within the Corpo Quatro Formation.

5.2.1 *Quartz Veins:* Barren Quartz (Q1)

Sulphide-free quartz veins, which sometimes contain minor biotite, occur both within narrow (less than 5cm wide), and wider (up to 1m wide) normal faults throughout the Corpo Quatro Formation, which

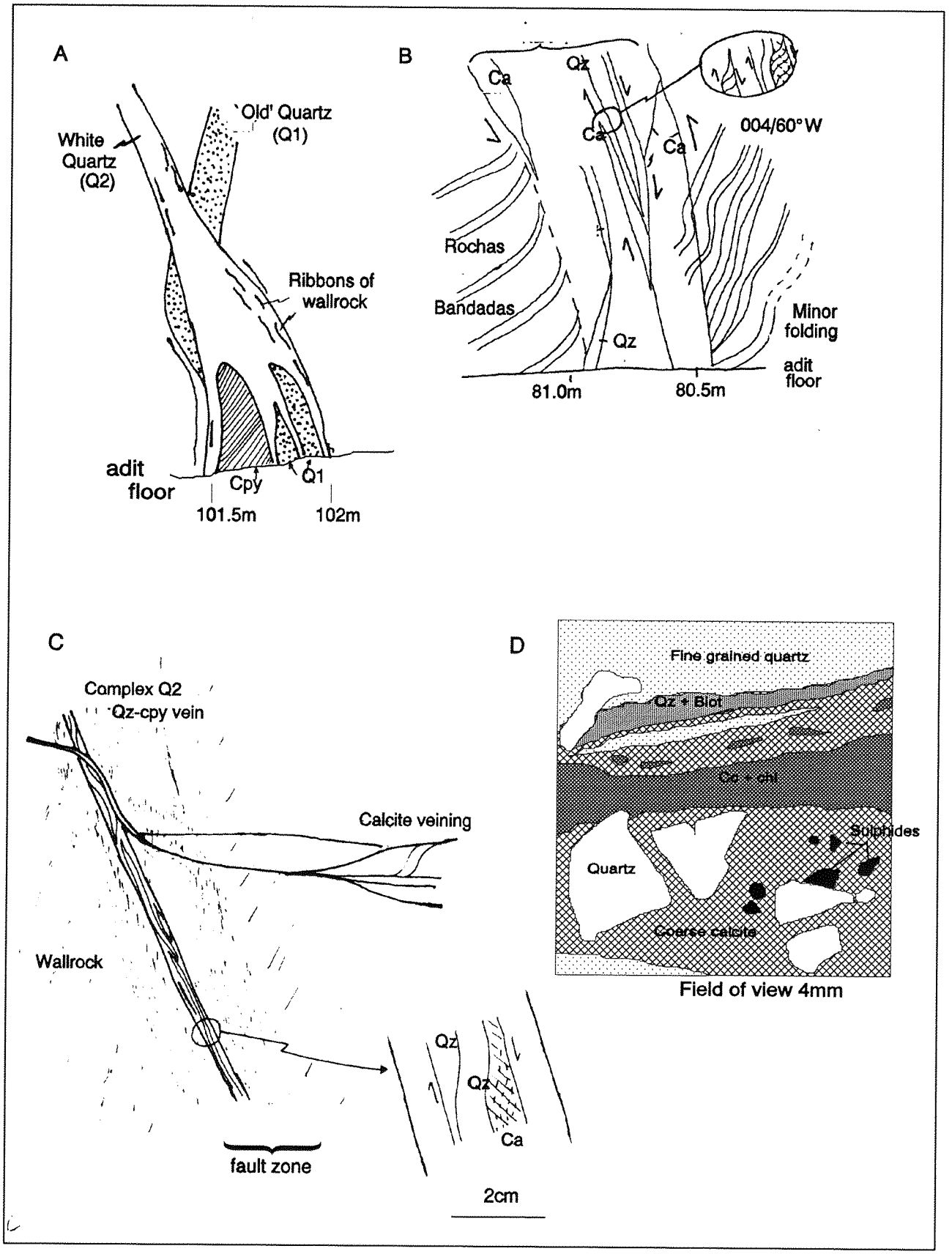

Figure 5.1 **Field relationships of quartz veining in the Corpo Quatro Deposit. A Cross-cutting relationships between Q1 and Q2 veins in G1-C4; B and C Q2 veins occupying normal faults, and showing overprinting by calcite (Q3) veining in G1-C4; D Schematic microscope view of a quartz vein which has been fragmented and overprinted by calcite (Sample G13, MVII)**

have been subsequently overprinted by chalcopyrite-bearing quartz (*Fig. 5.1*). The barren quartz is grey-white with a vitreous lustre, and in thin section shows 'cloudy' patches which are due to the presence of abundant small (<5μm) two-phase aqueous fluid inclusions which constitute approximately 10% of the quartz. In the clearer quartz, the same small inclusions occur in secondary trails which cross-cut the quartz grain boundaries.

Quartz-chalcopyrite-biotite (Q2):

Q2 veins are particularly common in the Rochas Bandadas and sometimes in the Xistos Granadas of G1-C4, and have been sub-divided into Q2-A, quartz chalcopyrite ± biotite, and Q2-B, which consist of quartz-biotite, with occasional sulphide minerals constituting up to 1% by volume. In addition to chalcopyrite, Q2 type veins occasionally contain minor sphalerite and pyrrhotite. Up to 20mm wide, the veins occasionally display dilational jogs up to 0.6m across (*Fig. 5.4A*), and are primarily located in inclined, NW- (occasionally SW-) trending normal fault zones (*Figs. 5.1 and 5.2*) up to 1m wide, sometimes cross-cutting and overprinting older barren veins of type Q1. Biotite cross-cuts the chalcopyrite in both Q2-A and Q2-B veins, with acicular biotite crystals, identified by electron-probe micro-analysis (EPMA) to be undergoing decomposition to chlorite, penetrating chalcopyrite grains.

In close proximity to the Q2 sulphide-bearing veins, the C4 metasediments are observed to be enriched, relative to other areas within the adit, in narrow quartz-sulphide-filled fractures (1-3mm) and banded and fracture-style chalcopyrite, sphalerite and pyrrhotite (*Fig. 5.3*), as described in Chapter 3. Although this relationship occurs in the G1-C4 adit on a scale of 1-2 m, it is also seen near Q2 veins in the drill core, where quartz-chalcopyrite veinlets form apophyses to quartz ± sulphide veins, and the surrounding metasediments are again rich in chalcopyrite and pyrrhotite with occasional sphalerite (*Fig. 5.4B*).

The Q2 veins are therefore believed to represent the fluid channels responsible for the main phase of copper and zinc mineralization in the Corpo Quatro Formation, which have subsequently been overprinted by biotite.

Barren quartz ± biotite ± calcite (Q3):

Quartz-biotite veins occur in narrow (<15cm), near-vertical, SE-NW trending fault zones (*Fig.5.2C*). The veins themselves are generally less than 1cm wide, widening in fault jogs to 10cm, and sometimes host minor chalcopyrite, sphalerite and pyrrhotite. There is little conclusive evidence for direction of movement across these faults, but some strike-slip is apparent from slickensides.

Q3 veins occasionally cross-cut the Q2 veins (above), but have subsequently been overprinted by a carbonate phase (*Fig. 5.1*), which either forms as a margin to the quartz in a syntaxial manner, or a matrix around broken up quartz fragments (*Fig. 5.1*). Calcite also forms mono-mineralic veins which are generally perpendicular offshoots of the calcite margins around quartz-bearing Q2 and Q3 veins. These are barren, up to 5mm wide, and occur in brittle fault zones similar to those hosting the Q2 and Q3 veins.

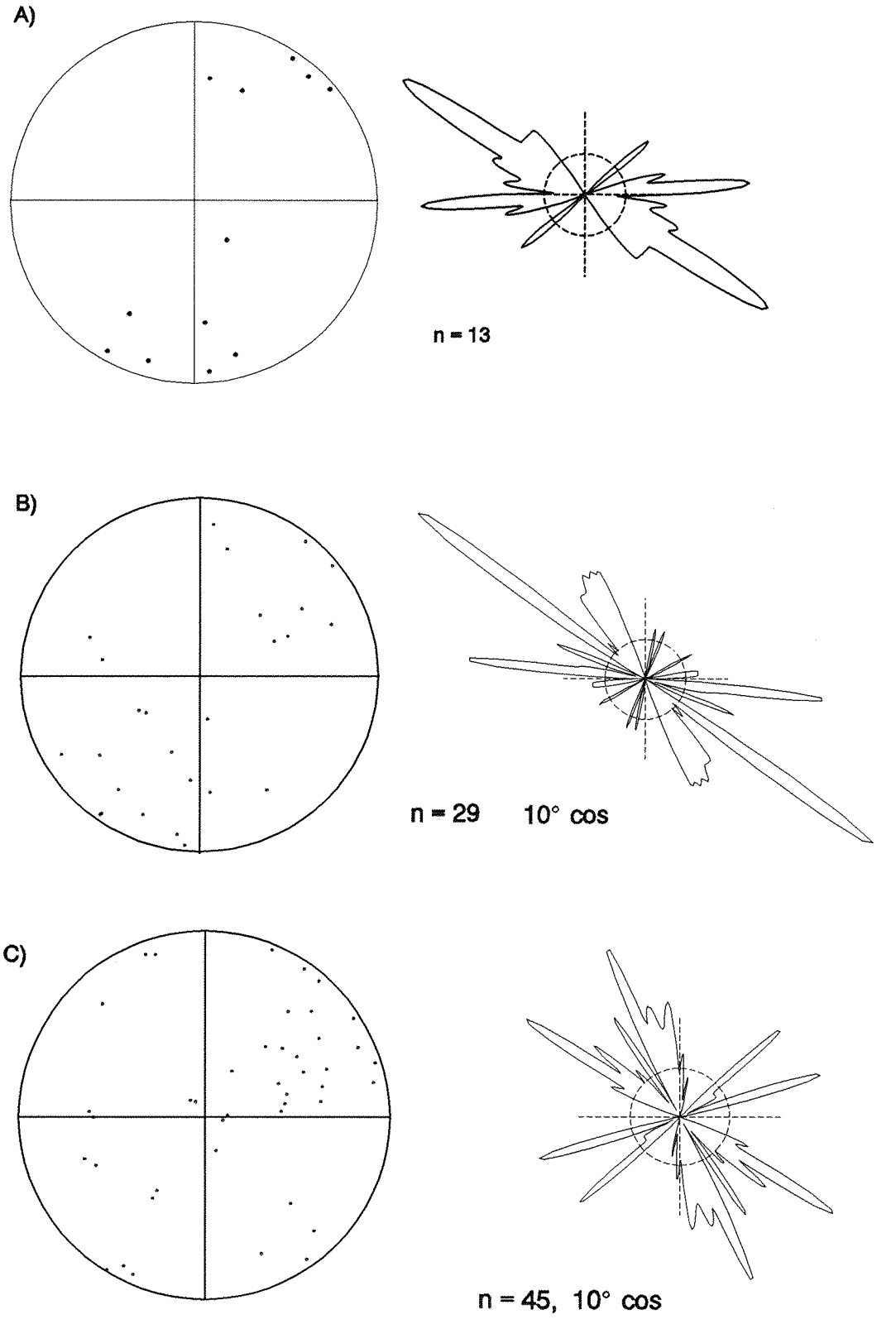

Figure 5.2 **Poles to veins from G1-C4 adit, projected onto a lower-hemisphere equal area net projection. A Q2 quartz-chalcopyrite-biotite veins; B Q3 Quartz-calcite veins; C Calcite veins.**

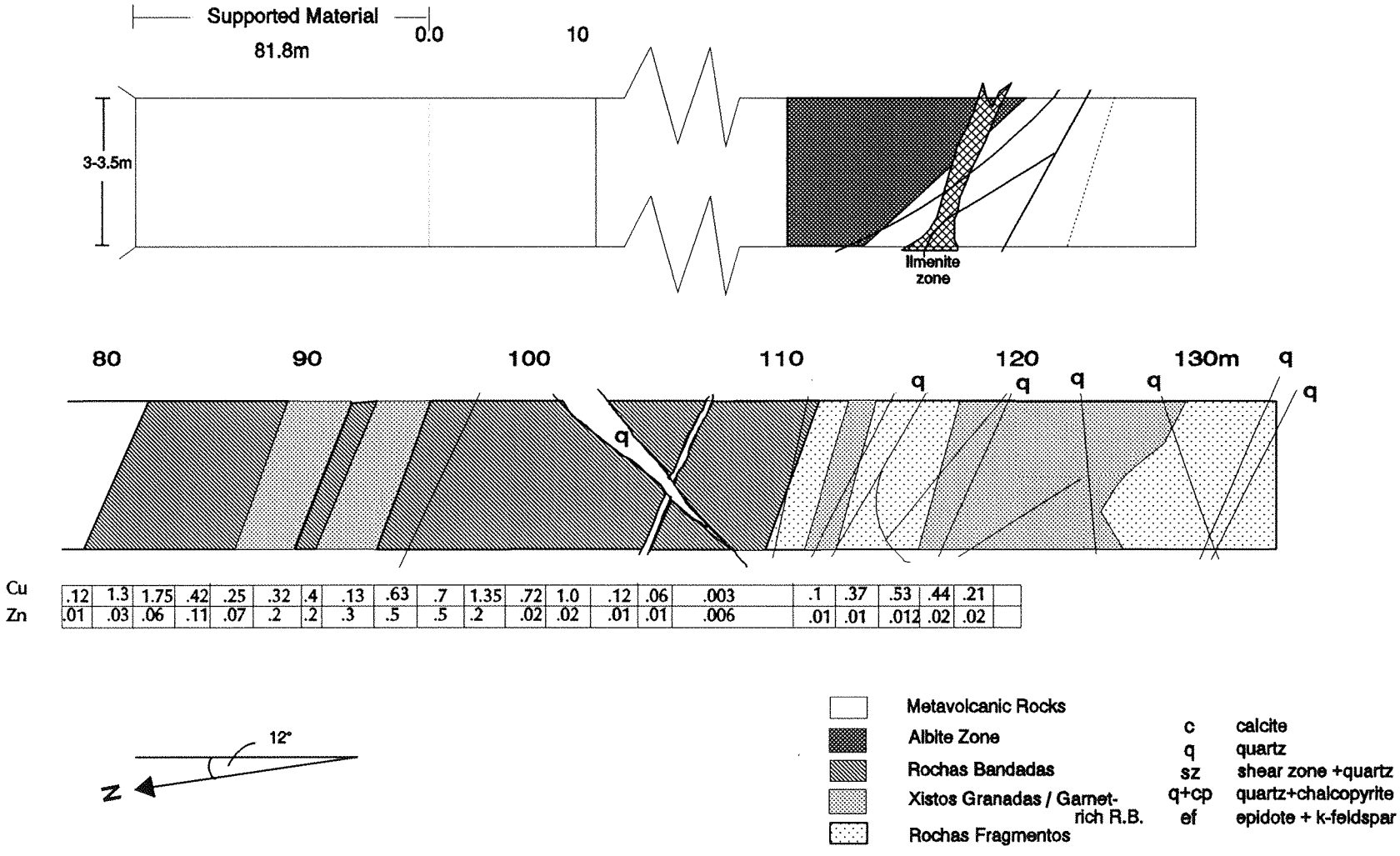

Figure 5.3 Schematic geological plan of the G1-C4 adit, Pojuca, showing copper and zinc grades from DOCEGEO assay records. Sampling carried out on front wall during adit construction.

The location and appearance of the calcite veins leads to the conclusion that the calcite veining post-dates all the quartz veining events in the Corpo Quatro deposit.

The orientation of the normal faults in which Q2 and Q3-type veins occur is almost identical (*Fig. 5.2*), and probably indicates that the veins formed during the same extensional event. Thus the sulphide-bearing quartz veins and barren quartz veins represent earlier and later components of the same fluid event. Calcite veins, which post-date Q2 and Q3 quartz, appear to have utilized the same fluid channels.

5.2.2 *Epidote-feldspar (EF) Veins*

Veins of epidote-feldspar (plagioclase and pink orthoclase) ± chalcopyrite occur in the metavolcanic rocks below the mineralized metasediments, and vary in width from 2 to 15mm, trending NW and SW. The feldspar is located at the margins of and orthogonal to the epidote (*Fig. 5.4E*), comparable to the structures developed in the calcite-quartz (Q3) veins, although unlike these structures the plagioclase appears to have slightly pre-dated the epidote, and therefore developed in an antitaxial manner. EF veins are particularly common at the margins of and close to areas of albitic alteration in the C4 metavolcanics, where they occasionally show albitization around their margins. Both epidote and K-feldspar are also found concentrated into veins in the albite zone.

5.2.3 *Tourmaline-chalcopyrite (TC) Veins*

Tourmaline ± chalcopyrite veins are observed predominantly within the large albite zones, particularly in the G1-C4 adit (*Fig. 5.4F*). They dip steeply to the west, trend NW or SW, and rarely exceed 5mm in width. Euhedral acicular tourmaline crystals (up to 15mm long) are intergrown with massive or disseminated chalcopyrite in a plagioclase matrix.

The TC veins found outside the large albite zones invariably show concentrated albitic alteration at their margins. This TC-albite relationship strongly implies that the fluids responsible for tourmalinization were also responsible for the albitization observed in the C4 Metavolcanic rocks.

The epidote-feldspar and tourmaline-chalcopyrite vein-types have similar structural orientations (*Fig. 5.5*), and no cross-cutting relationships have been observed between the two sets of veins, which may indicate that these vein sets were developed during the same phase of brittle deformation.

5.2.4 *Granitic Veins*

Veins of granitic material are abundant in drillcore from the western part of the Corpo Quatro prospect, and have also been observed in drillcore from the Pojuca C2 body. These veins are composed of quartz, orthoclase and plagioclase feldspar, with a small amount (2-3%) of biotite, having a similar mineral assemblage to the Pojuca Granite (described in Chapter 3 and also lying in the western part of the prospect). They do, however, contain a higher proportion of k-feldspar than the Pojuca Granite, and are coarser grained, giving them an almost pegmatitic, pink appearance (*Fig. 5.4G*). The margins of the veins, which appear to have formed in a syntaxial manner, are composed of concentrated plagioclase and

Figure 5.4 **Veining in the Corpo Quatro Formation**

A Type Q2-A quartz vein situated in a fault jog at 102m (left wall) in adit G1-C4. Vein displays massive chalcopyrite, and includes ribbons of wall rock (black), as well as older (type Q1) quartz (grey). As Figure 5.1A. Field notebook for scale.

B Drill core specimen of: (top) type Q2-A quartz vein with chalcopyrite, which has formed as an apophyses to the main Q2 quartz vein in the left of the photograph. Note chalcopyrite mineralization in the host rock to the right of the quartz-chalcopyrite vein. Sample F75; and (bottom) quartz-chalcopyrite veining found 1m above the Albite Zone in MVII. Note the chalcopyrite-bearing offshoots to the main vein. Sample F80.

C Photomicrograph of a Q2-A chalcopyrite-bearing vein, showing coarse quartz associated with chalcopyrite (opaque, bottom) and cross-cutting ribbons of fine grained quartz associated with the biotite (top right). Sample G20. Cross-polarised light. Field of view 2.2mm.

D Photomicrograph of Q2-B quartz (coarse) which has been overprinted by fine grained Q3 type quartz. Chip 35/A. Cross-polarised light (high birefringence of quartz due to thickness of fluid inclusion chip). Field of view 3.5mm.

E Orthoclase veining (pink) orthogonal to a near-vertical epidote vein, taken at 39m (right wall) in adit G1-C4. Evidence of the orthoclase pre-dating the epidote veining.

F Photograph taken at 64m (right wall) in G1-C4 adit, displaying albitization of the host-rock (grey-white), which is cross-cut by tourmaline veinlets (black) and contains massive chalcopyrite. (yellow, metallic).

G Photograph taken of drillcore C2-1 (C2 body) displaying both schistose and non-schistose granitic veins. The schistosity (bottom) has been post-dated by a quartz vein, which contains minor epidote and has a margin of calcite.

H Photograph of textures commonly displayed by the host rock enclosing granitic veins, with the development of a quartz-biotite-chalcopyrite stockwork. Photograph shows clearly the concentrated margin of quartz and plagioclase feldspar. Sample F12.

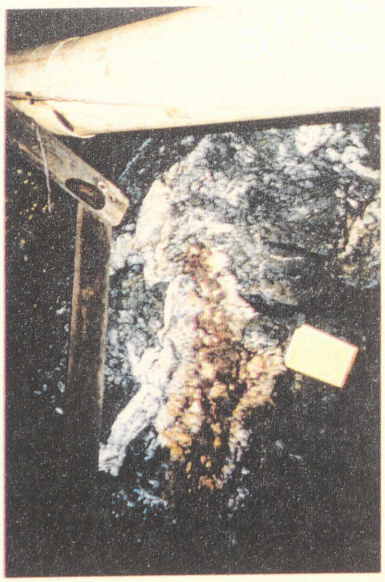

A

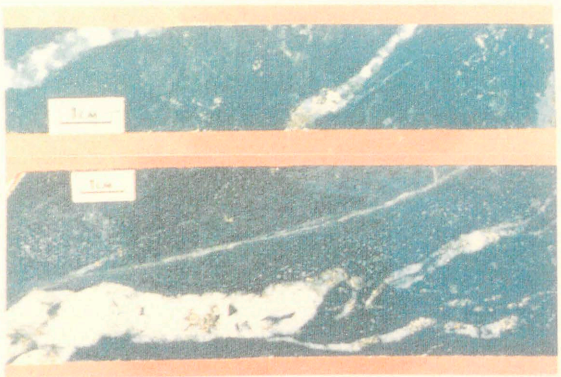

B

C

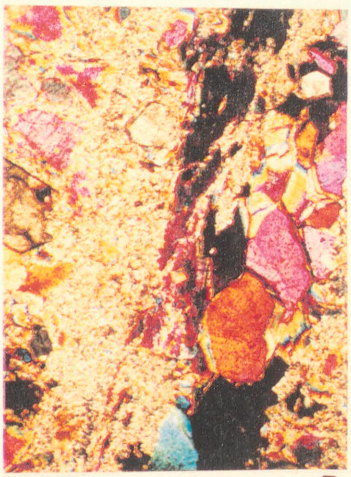

D

E

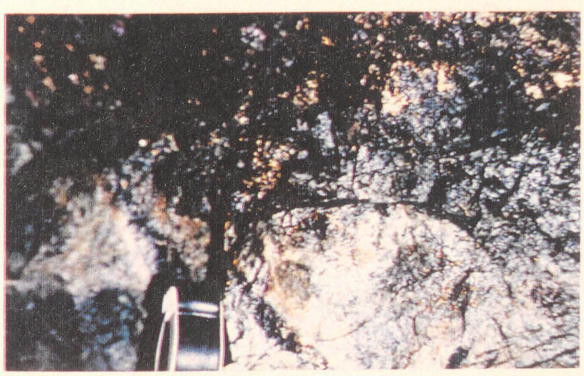

F

G

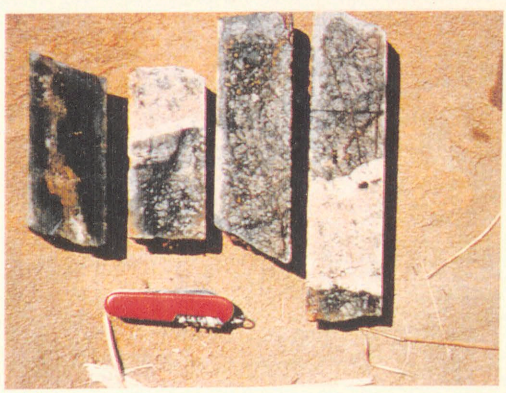

H

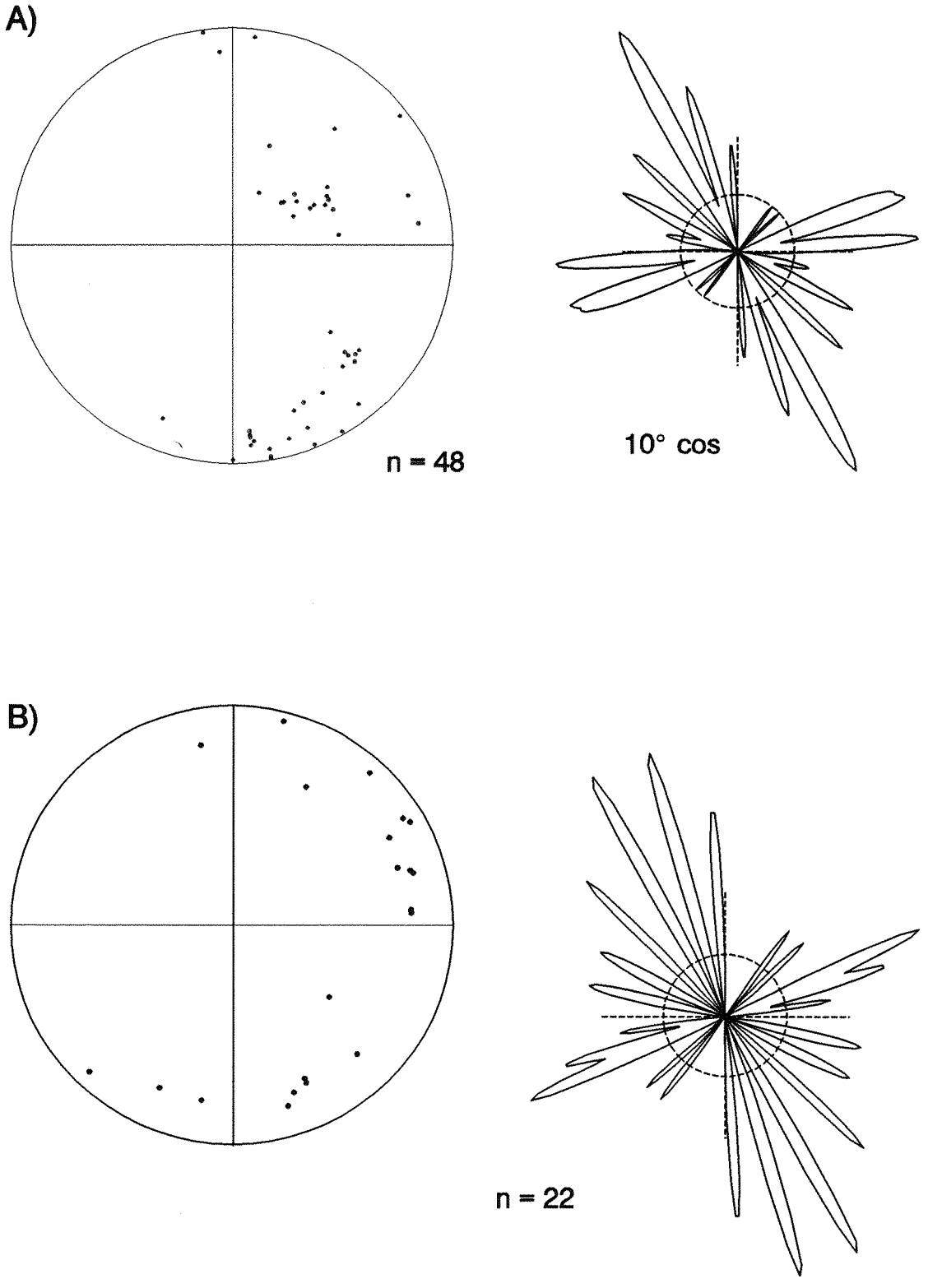

Figure 5.5 **Poles to veins from G1-C4 adit, projected onto a lower hemisphere equal area net projection. A Epidote-feldspar (orthoclase) veins; B Tourmaline-chalcopyrite veins (mainly from the Albite Zone).**

quartz. The veins are up to 40cm wide, and have mainly been found in biotite-rich Xistos Quartzos.

Host rock between these veins is commonly granitized, with a patchy orthoclase and quartz composition and a stockwork of quartz-biotite veinlets (*Fig. 5.4G*). The granitic material occasionally displays a schistose fabric (*Fig. 5.4H*).

Although the granitic veins themselves appear to contain no sulphide mineralization, the quartz-bearing offshoots, which cross-cut the schistose fabric of the host rock, are commonly rich in chalcopyrite. Some of the veins have been overprinted by a tectonic fabric similar to that observed in the Rochas Fragmentos, which is a local feature and post-dates minor regional schistosity developed in the host rocks.

Within the drillcore, both type Q3 (calcite) and barren epidote-feldspar veins are observed to cross-cut the granitic veins.

5.2.5 *Summary of the veining in the Pojuca Corpo Quatro Deposit*

All of the veining described at Pojuca post-dated regional metamorphism, with mineralogical banding (in the Rochas Bandadas) and mineral alignment (in the Rochas Fragmentos) being cross-cut by the apparently un-deformed, un-metamorphosed veins, in which quartz shows no evidence of metamorphism or of deformation, such as straining, polygonization or recrystallization (Spry, 1969). The alteration associated with the quartz and calcite veining (hornblende, and biotite and chlorite margins around the veins) overprints the metamorphic mineral assemblages seen in the host rock, although apart from albitization around the EF and TC veins, and granitization around some of the granitic veins, there is little evidence of wallrock alteration in contact with the veins themselves. In intensely schistose areas of the Rochas Fragmentos some of the earlier quartz veins (Q2) appear to have undergone deformation, in the form of shearing. This shearing is a very local effect, which has a similar effect on the quartz veins as it does on the granitic veins described above (*Fig. 5.4H*).

Based on rare cross-cutting relationships, a vein chronology can be established for the Corpo Quatro Formation. Grey barren quartz veins (Q1) are cross-cut by chalcopyrite-bearing Q2, which in turn are cut by Q3 calcite-quartz veins. In the C4 metavolcanic units, albitization in the eastern area of the C4 deposit appears to have been accompanied by chalcopyrite-bearing EF and tourmaline veining, whereas in the western half of the deposit chalcopyrite-bearing quartz is strongly related to granitic veins and the Pojuca Granite. Calcite veining cross-cuts (and therefore post-dates) all other vein generations, as well as the schistosity developed in the metasedimentary units of the Corpo Quatro Formation. However, although calcite veins post-date the granitic veins, they have not been seen cross-cutting the Pojuca Granite.

From these observations a summary diagram can be established (*Fig. 5.6*), and combined with orientation data plotted in *Figures 5.2* and *5.5*, the following table has been created:

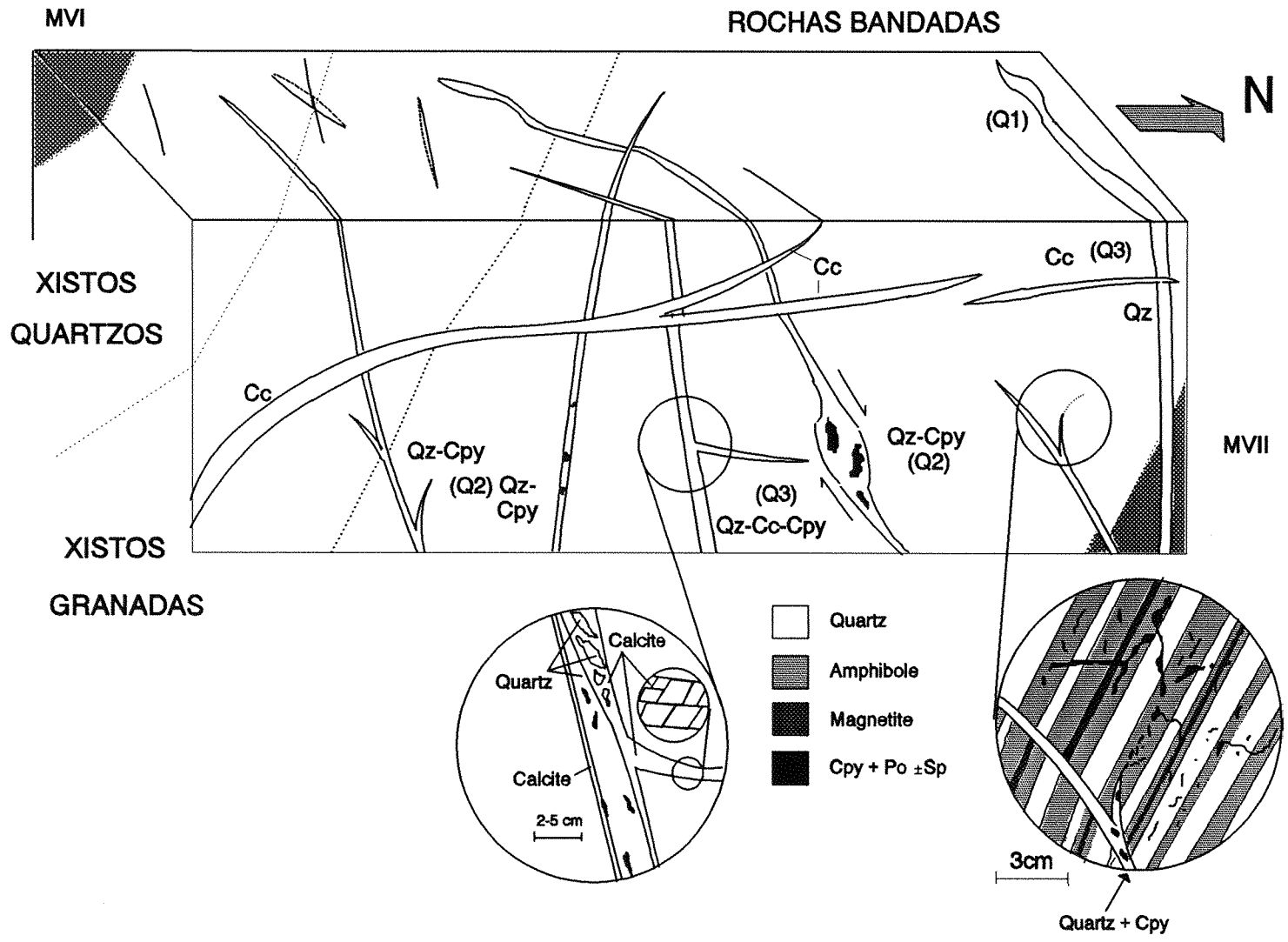

Figure 5.6 **Schematic block diagram summarizing the main types of veining and their relationship with the host rocks in the Corpo Quatro Formation at the Pojuca Corpo Quatro Cu-Zn deposit. Not to scale. Insets show calcite overprinting quartz in a Q2 sulphide-bearing vein, and occurrence of sulphide minerals in veins, and as apophyses forming sulphides with a 'banded' appearance.**

Table 5.1 Summary of the main fluid events observed in G1-C4 of the Corpo Quatro Deposit.

EVENT	Mineral Assembl.	Orientation	Dip	Host Rock Type	Physical Characteristics	Fluids Summary
Q1	Quartz ± biotite	SE-NW	20 - 50°	All lithologies	Width = variable, <20mm In normal faults Grey-white quartz often overprinted by Q2	Two phase aqueous inclusions Secondary <5μm
Q2-A	Quartz-cpy-(tourm / biotite) ± Sp ± Po Main Mineralization	SE-NW E-W	60 - 90° SW	Metasediments	Width = up to 15mm Occasional 'jogs' up to 1m wide Occur in normal and reverse faults	Two phase aqueous inclusions Secondary and pseudosecondary 5 - 20μm
	Albite Albite-epidote Tourm-cpy	SW-NE	70 - 90° (variable)	Metavolcanics (generally MVII)	Width = <3mm Discontinuous Tourmaline needles up to 15mm long	No fluid inclusions
Q2-B	Quartz-biotite ± cpy ± calcite	SSE-NNW SE-NW	40 - 90° NE	All lithologies	Width = <10mm Occur in faults <0.15m	Aqueous l-v, l-v-s and l-v-multi-solid inclusions in qz. <10μm
	Epidote-K.feldspar	NNW-SSE (SW-NE)	30 - 90° SW (or NW)	Metavolcanics	Width <20mm, ave.3-6mm Plagioclase at wallrock contact, epidote in centre.	No Fluid inclusions
Q3	Calcite	SE-NW	0 - 90° SW	All lithologies	Width = <10mm Discontinuous, often displaying arrays (bridging)	l-v primary in calcite, <20μm. (Most calcite too friable to make chips)

5.3 *FLUID INCLUSION STUDIES IN THE POJUCA C4 DEPOSIT*

Fluid inclusions are a potentially useful tool in the study of ore deposits, as they can provide the most representative view of the palaeofluid responsible for hydrothermal alteration and ore accumulation in a host rock (Roedder and Bodnar, 1980). In order to determine, as far as possible, the nature of the fluids at the time of mineral deposition, fluid inclusions from the veins and host rock quartz have been studied using microthermometry, Raman spectroscopy and D-ICP analyses, to gain qualitative and semi-quantitative data on the conditions (temperature, density and pressure) and nature (chemistry, salinity) of the mineralizing and subsequent fluids.

5.3.1 *Sample Selection*

Fluid inclusions are located throughout the Corpo Quatro Formation, primarily in gangue minerals, and most typically in quartz and calcite, as well as in quartz of the host rocks of the Corpo Quatro Formation. No fluid inclusions have been found in other minerals, such as sphalerite or almandine garnet, where they can be present (Shepherd *et al.*, 1985).

Due to their friable nature, calcite veins make poor fluid inclusion chips. Most of the calcite studied occurs between quartz crystals in quartz-calcite veins, as described in section 5.2. Inclusions in host-rock quartz were classified using the polished thin sections made for petrological study, and inclusion chips were prepared from inclusion-rich quartz which showed an intimate association with sulphide mineralization. Quartz and calcite chips from vein material (both barren and sulphide-bearing) were prepared without prior observation, as detailed petrological studies of the veining was deemed unnecessary and inclusion-host grain relationships can be observed in an inclusion chip. Quartz chips suitable for fluid inclusion studies were chosen on the basis of microscopic observation.

In total, fluid inclusion chips were prepared for study from 40 quartz samples (17 from host-rock, 23 quartz- and quartz-calcite veins), of which many proved unsuitable even for optical observation due to inclusions having leaked, being too small, or being contained in 'cloudy' quartz (described in section 5.2; Q1 veins), or 'dirty' quartz, which contains abundant mineraloid inclusions (hornblende, identified by laser Raman with peaks at 667 cm^{-1} and 1042 cm^{-1}, and in the 3630 cm^{-1} OH region) in which the fluid inclusions could not be seen. A number of chips from a total of 18 samples have been studied using microthermometric techniques.

5.3.2 *Nature and Occurrence of the fluid inclusions in the Pojuca C4 Formation*

Of the veins described in section 5.2, fluid inclusions were found only in quartz- and quartz-calcite bearing veins. They are also abundant in host-rock quartz, particularly in the metasedimentary units of the Corpo Quatro Formation.

Optical examination allows the classification of these inclusions into four main populations, based on phase relations at room temperature and the nature and mode of occurrence of the inclusions. These

populations, whose classification is irrespective of timing, are later sub-subdivided, where possible, according to microthermometric properties.

Type T1. (L_{aq}-V±S)

Type T1 are two-phase aqueous inclusions, which sometimes contain a cubic, isotropic daughter mineral identified as halite. These fluid inclusions vary in diameter from 2 to ~20μm, occasionally reaching 60 or 70μm, and have a degree of fill (F) from 0.85 to 0.9 (*Fig. 5.7A&B*). This type of inclusion occurs in both a primary and secondary style, in different types of quartz (see section 5.3.3). Primary type T1 inclusions exhibit regular, roughly negative crystal form (*Fig. 5.8B*), while secondary type T1 inclusions in quartz are more irregular in habit (*Fig. 5.8C-F*). Type T1 inclusions in calcite form regular negative crystal shapes (*Fig. 5.7B&C, Fig 5.8H*). Type T1 inclusions are occasionally observed to host trapped anhedral green mineraloids, which have been identified using laser Raman spectroscopy as hornblende, showing the characteristic 667 cm^{-1} and 1045 cm^{-1} peaks found by analysing a known hornblende from the C4 Rochas Bandadas (*Fig. 5.9*).

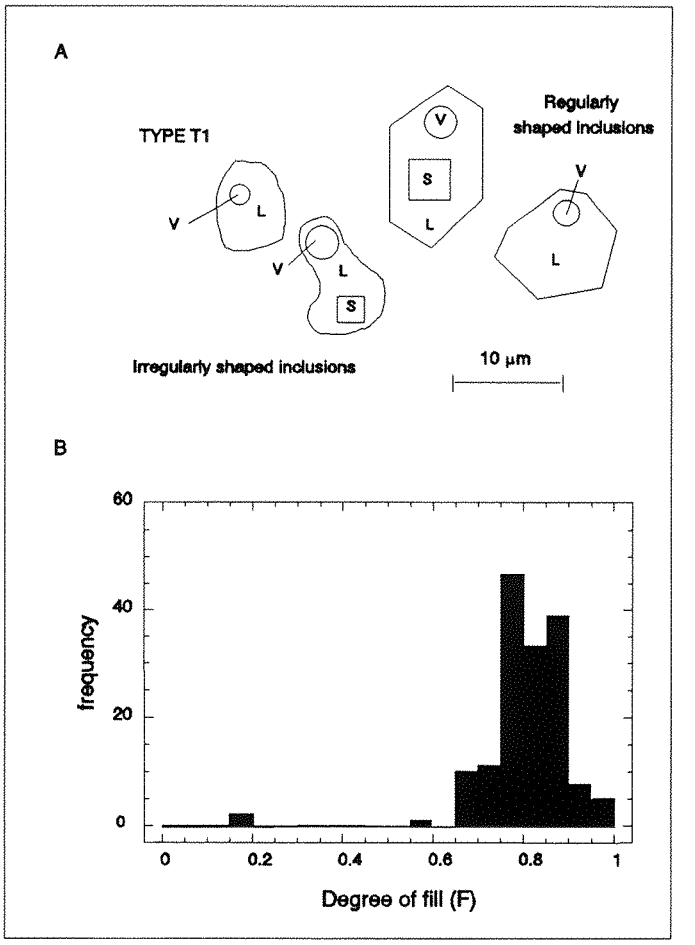

Figure 5.7a **Type T1 fluid inclusions from Q2 veins and host rock. A Typical fluid inclusions, L=liquid H_2O, V=vapour, S=daughter phase (Halite); B Histogram of degree of fill (F) in type T1 fluid inclusions.**

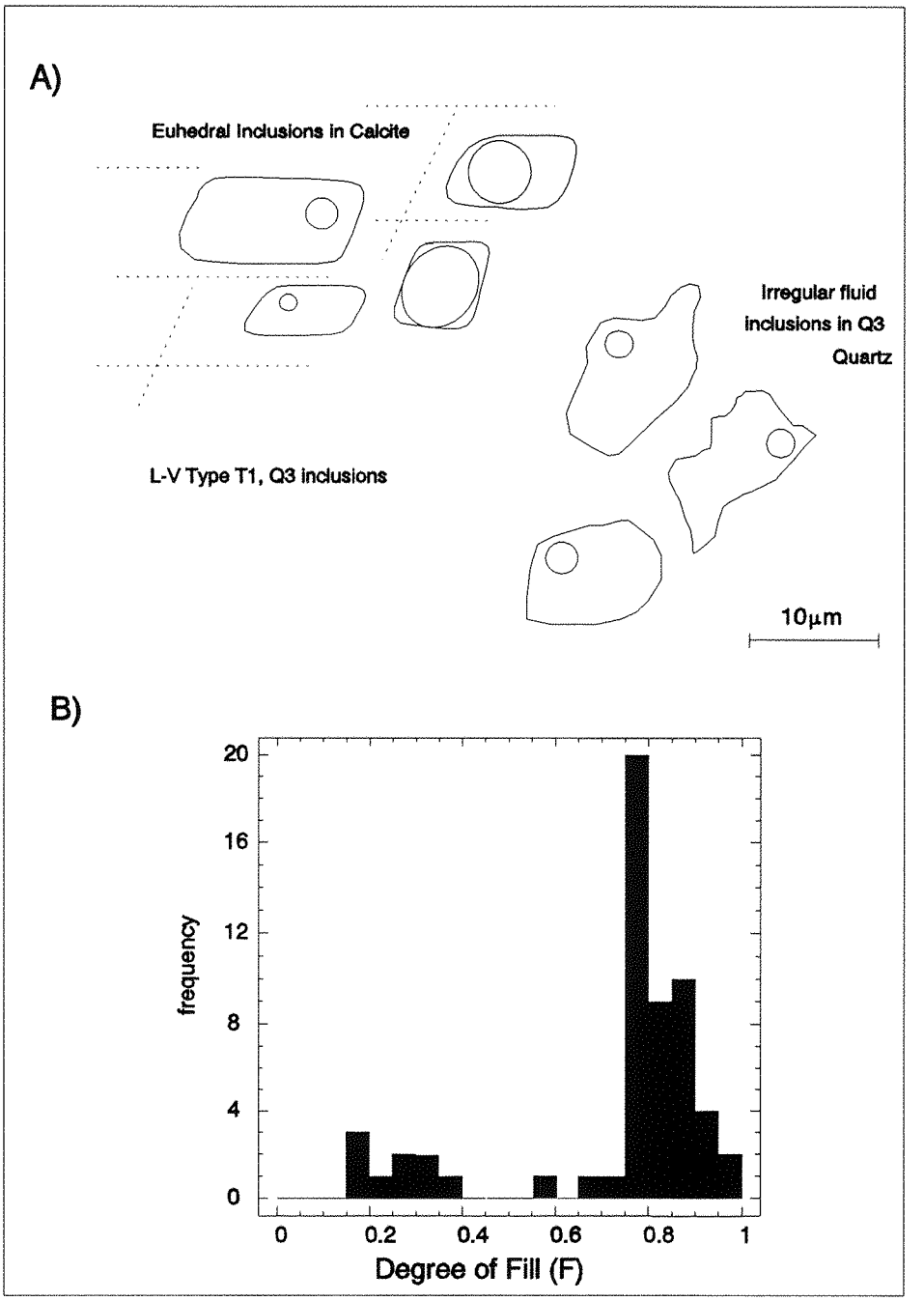

Figure 5.7b **Type T1 fluid inclusions from Q3 veins. A Typical inclusions in Q3 calcite and quartz; B Histogram of degree of fill (F) in type T1, Q3 fluid inclusions.**

Figure 5.8 **Type T1 Aqueous Inclusions**

A L-V-S and L-V trails of secondary T1 fluid inclusions cross-cutting Rochas Bandadas quartz. Chip 10/E. Plane-polarised light. Field of view 1.1mm.

B Typical primary regular-shaped type T1 L-V inclusions in Q2-A type chalcopyrite-bearing quartz vein. Chip 30. Field of view 220μm.

C Typical secondary type T1 inclusions in Rochas Bandadas quartz. Irregular shaped inclusions, of mixed L-V and L-V-S type forming a NW-SE trail across the 220μm field of view. Chip 10/E.

D Irregularly shaped primary L-V type T1 inclusions in vein quartz. Chip 23. Field of view 220μm.

E Irregularly shaped secondary L-V type T1 inclusions in Rochas Bandadas quartz. Chip 10/2. Field of view 220μm.

F Irregular L-V±S inclusions (T1) forming a secondary E-W trail across host quartz, with a NW-SE trail of L-V-S-S inclusions containing a birefringent daughter mineral (F, probably Fe-chloride), and halite (H). Sample G46. Field of view 220μm.

G Secondary trails of late T1 inclusions cross-cutting clear chalcopyrite-bearing vein quartz. Inclusions are therefore related to Q3-stage quartz. Chip 35/F. Field of view 1.1mm.

H Primary T1 L-V inclusions of variable fill, in Q3-type calcite vein host. Chip 25. Field of view 220μm.

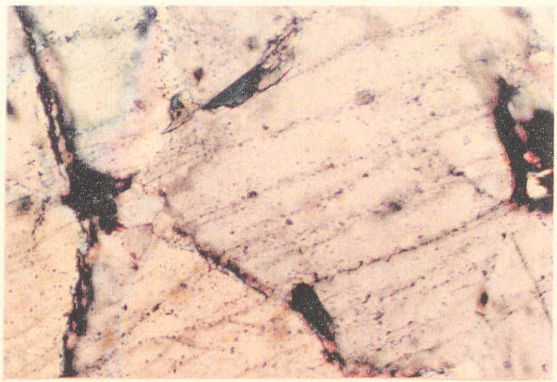

A

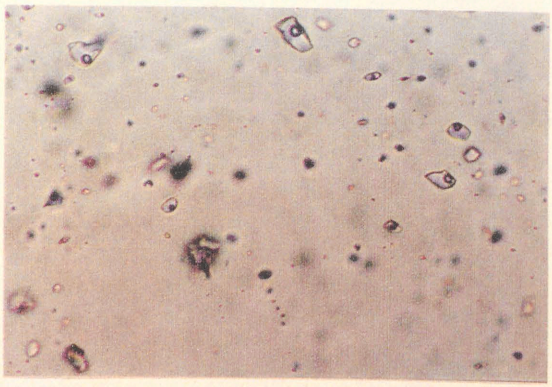

B

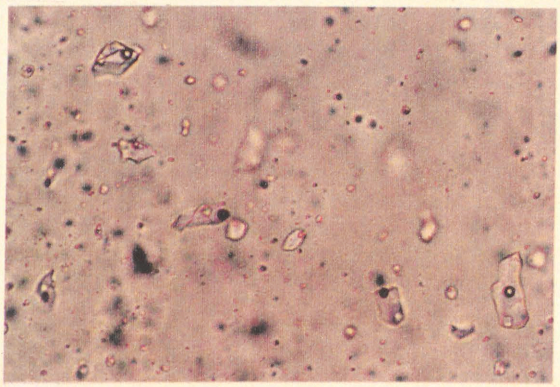

C

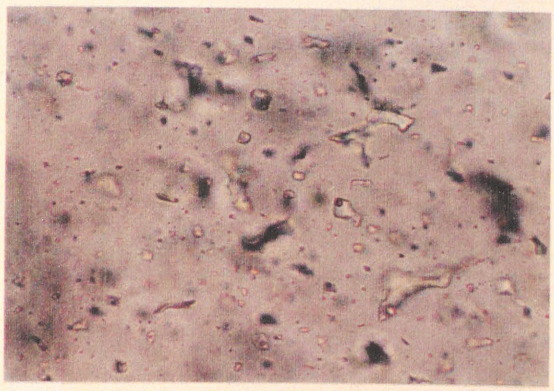

D

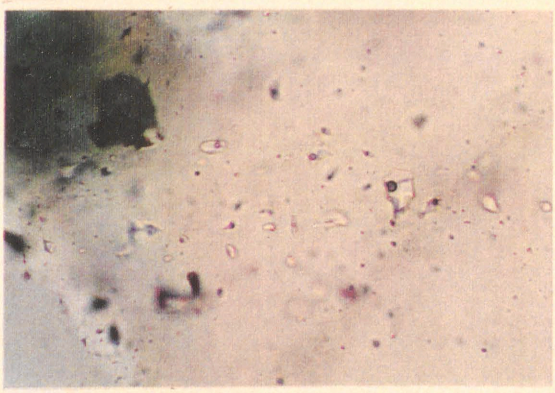

E

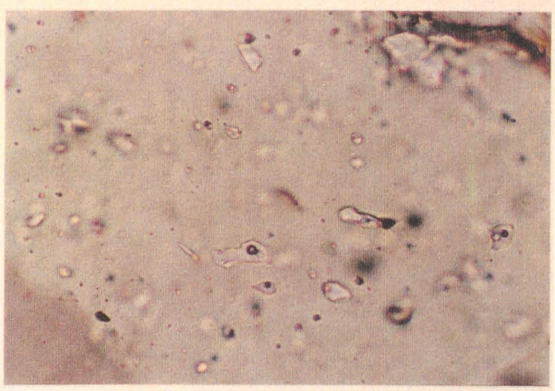

F

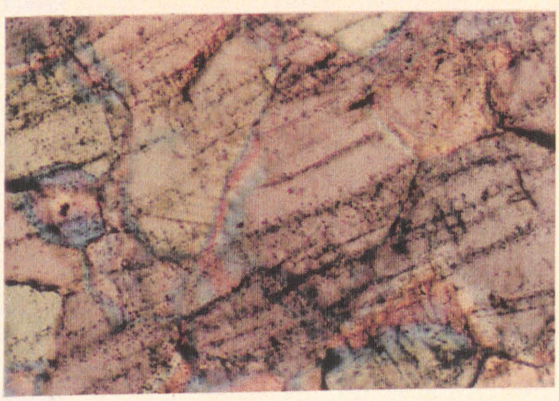

G

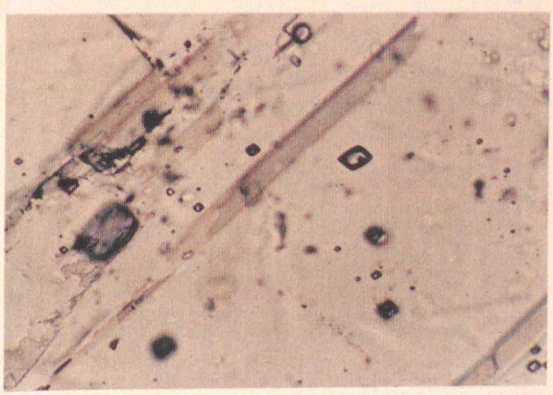

H

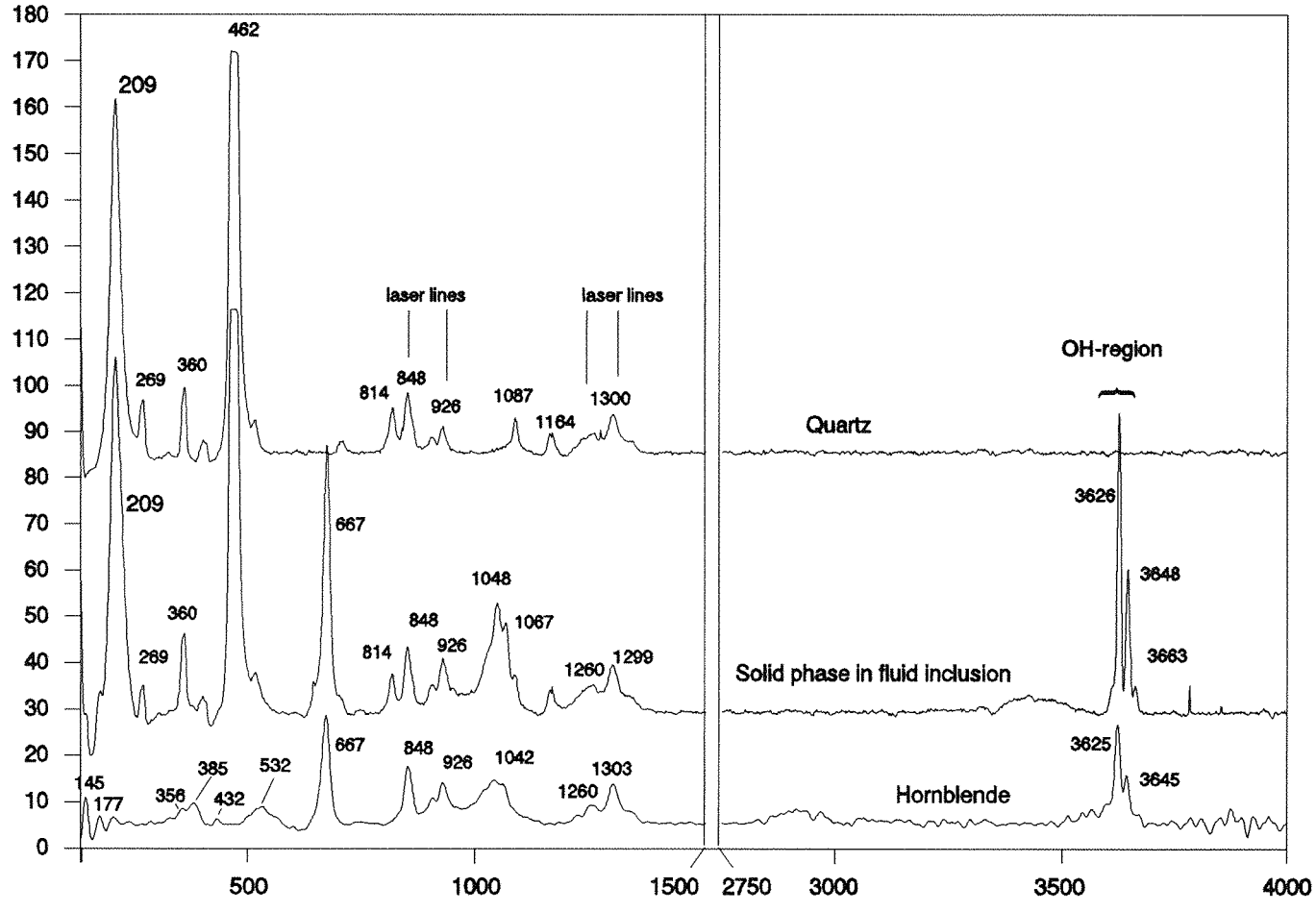

Figure 5.9 Raman spectra for quartz (top) and hornblende (bottom) crystals, and for the trapped phase in type T1 fluid inclusions (centre). The trapped phase shows a mixture of quartz and hornblende peaks, and is therefore hornblende. Laser lines, present in all spectra, are shown. OH-peaks are only developed in the hornblende. Additional 'peak' on the inclusion phase speactra is from water in the fluid inclusion.

Type T2. (L_{aq}-V-S±SS)

Type T2 inclusions are aqueous and highly saline, containing one or more daughter minerals (*Fig. 5.10* and *5.11A-D*). They range in size from 2μm to ~30μm, with F = ~0.85 (*Fig. 5.10*). The daughter minerals vary, although three types have been tentatively identified using SEM and optical properties: i) Halite (NaCl), a clear, roughly cubic, isotropic mineral; ii) Iron chloride, green birefringent and rectangular (*Fig. 5.11F&G*); and iii) Sylvite (KCl), forming small, clear, rounded crystals. SEM analyses of some of these small, rounded daughter minerals have shown that some are in fact a mixed, Na-K-chloride. Fe-chlorides (*Fig. 5.11H&J*) constitute between 20 and 30% of the inclusion volume, sylvite ~10%, and halite may form up to 60% of the total. The constant phase ratio of Fe- and K-chlorides throughout the inclusions indicates that the salts are true daughter minerals. The variability of the halite proportions suggests that this fluid may have been inhomogeneous at the time of trapping, although on heating, these minerals dissolve into the solution and are therefore true daughter minerals.

Type T3. (L_{aq}-L_{CO2}-V)

Type T3 are aqueo-carbonic inclusions, which at room temperature contain liquid H_2O and liquid CO_2 (*Fig. 5.12*), and tend to have more depth to them, with darker outlines to the vapour phase, than do the aqueous inclusions. Microthermometric and Raman analyses of these inclusions have revealed the presence of CH_4. On cooling these inclusions to between 10 and 20°C below room temperature, a vapour phase is formed. Type T3 inclusions have an irregular, rounded form, in which CO_2 constitutes between 50 and 100% of the inclusion volume (*Fig. 5.13A-C*). This variation in degree of fill is often seen within one population, indicating the possibility of fluid unmixing during trapping.

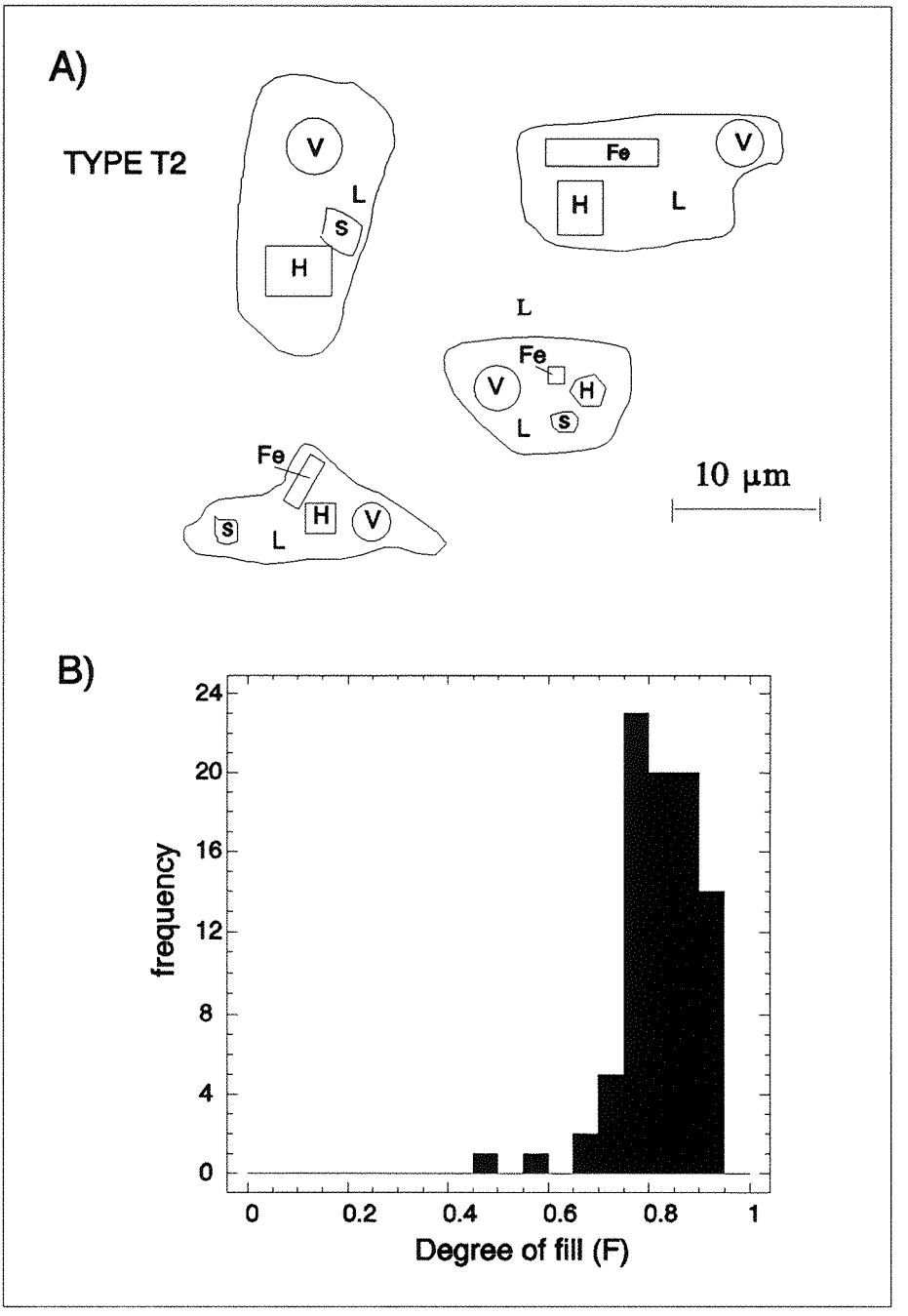

Figure 5.10 **Type T2 fluid inclusions from Q2-B veins and host rock. A Typical inclusions in quartz, H=halite, s=sylvite, Fe=iron chloride, V=vapour, L=liquid H_2O; B Histogram of degree of fill (F) in type T2 fluid inclusions.**

Figure 5.11 **Type T2 Fluid Inclusions**

A Type T2 aqueous inclusions in a granite-hosted quartz grain. Inclusions show irregular shapes, and appear to be primary. Daughter minerals are halite (H), Fe-chlorides (F), and perhaps sylvite (s). Field of view 220μm.

B Multisolid T2 inclusions containing daughter mineral: clear cube, halite; green cube, FeCl; small bright high relief mineral, sylvite. In Rochas Bandadas quartz. Field of view 22μm

C Typical examples of regularly shaped L-V-S±SS inclusions. H = halite, F = iron-chloride, s? = probably sylvite. Some of the inclusions contain only one daughter phase. Sample G46. Field of view 150μm.

D & E Irregular multi-solid T2 fluid inclusions. Plane-polarised light (D) and cross-polarised light (E). Daughter minerals identifiable using cross-polarized light, isotropic cube = halite, birefringent phases = iron and potassium chlorides. Chip 10/2. Field of view 110μm.

F & G Photomicrographs of birefringent daughter minerals (Fe- and K-chlorides) typically found in T2 inclusions. Chip 35/A. Field of view 220μm.

Scanning electron microscope images of daughter minerals in opened T2 fluid inclusions.
(Scale bar in the bottom centre of each image)

H Halite (NaCl) and mixed Fe-Na-chloride daughter minerals (Fe-Na-Cl = 27wt.%Fe, 18wt.%Na, 55wt.%Cl). Sample G100, Chip 35.

I Fe-chloride daughter with minor Na and Mg. (79wt.%Fe, 6wt.%Na, 5wt.%Mg, 10wt.%Cl). Chip 35.

J Halite (NaCl) and FeCl daughter minerals. Halite too dark to see. (Halite = 39wt.% Na, 14wt%Fe, 46wt.% Cl; Fe-chloride = 88wt.%Fe, 12wt.%Cl). Chip 35.

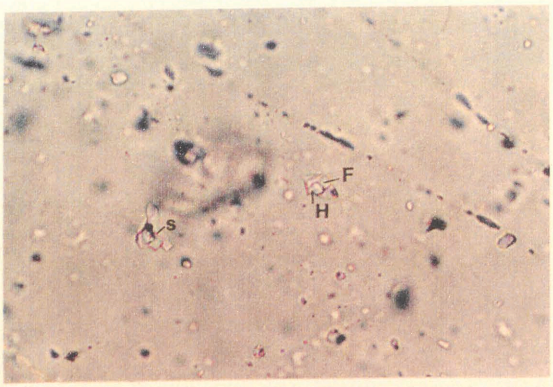
F
H
S

A

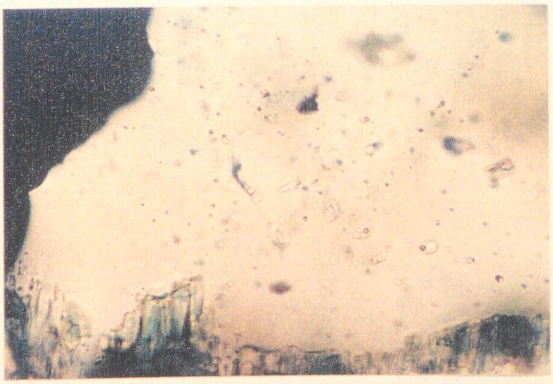

B


F
H
S?

C

D

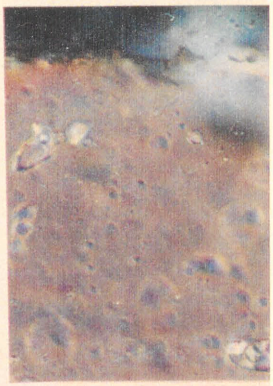

E

F

G


FeCl
NaCl
1µm
G100 20KV X16,000 38mm

H

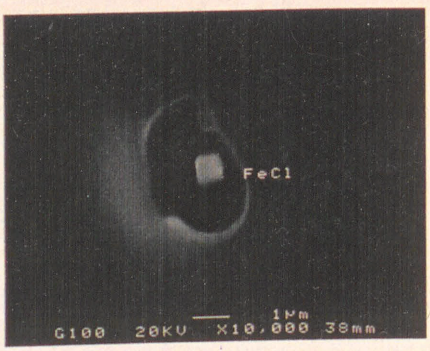
FeCl
1µm
G100 20KV X10,000 38mm

I

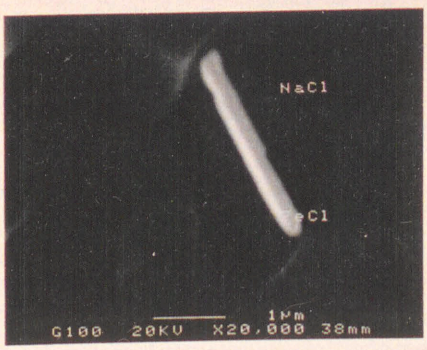
NaCl
FeCl
1µm
G100 20KV X20,000 38mm

J

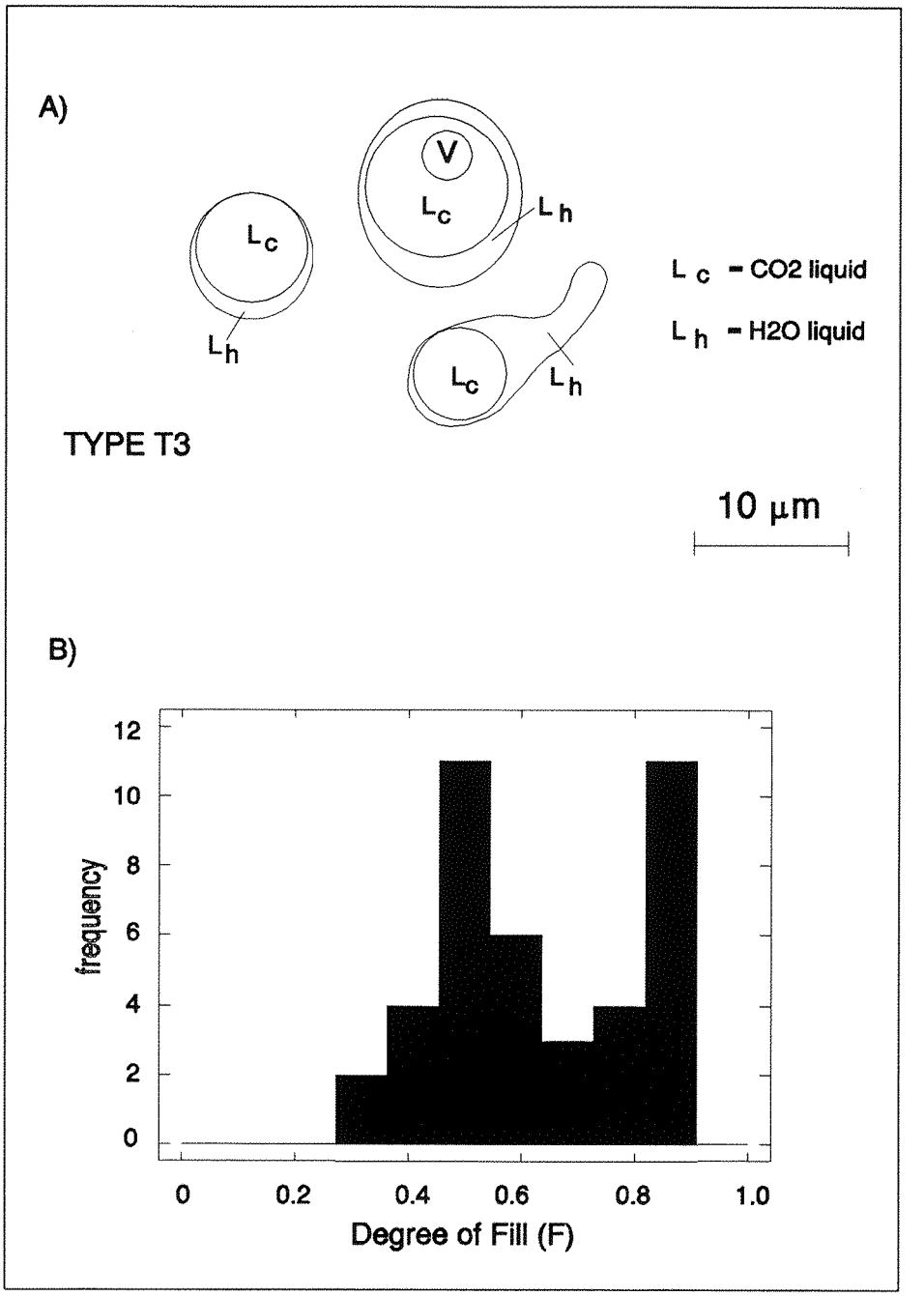

Figure 5.12 **Type T3 aqueo-carbonic fluid inclusions. A Typical inclusions in quartz, L_h=liquid H_2O, L_c=liquid CO_2; B Histogram of degree of fill (F) in type T3 fluid inclusions.**

Figure 5.13 **Types T3, T4 and T5 Inclusions**

A Photomicrograph of a typical trail of secondary T3 2-phase aqueo-carbonic inclusions at room temperature, showing H_2O and carbonic liquid. No vapour phase is present. Dark, CO_2-rich inclusions out of the plane of focus are seen to cross-cut the quartz grain boundary. Chip 10/E. Field of view 220μm.

B Carbonic T3 inclusions in coexistence with T1 L-V-S fluid inclusions. Chip 10/2. Field of view 0.55mm.

C T3 carbonic inclusions in the same field of view as both T1 (L-V) and T2 (L-V-S-S) aqueous inclusions. Chip 10/E. Field of view 220μm.

D Photomicrograph of the location of type T4 inclusions, taken in cross-polarised light. T4 inclusions occur in pink quartz which appears to overprint the white mineralizing quartz. T3 inclusions have been observed in the white quartz. Chip 35/A. Field of view 1.1mm.

E T4 aqueo-carbonic inclusion (centre) containing liquid H_2O and liquid and gas CO_2, with minute, unidentified, daughter minerals. T2 inclusions also present in field of view. Chip 35/A. Field of view 220μm.

F Large T4 inclusions (left, centre and right) containing multiple daughter minerals similar to those observed in T2 inclusions, as well as liquid and gas CO_2. Chip 35/A. Field of view 220μm.

G Typical T5 fluid inclusions of variable fill, occurring on a plane along a quartz grain boundary (white, centre) which is cross-cut by type T1 and T2 fluid inclusions. Chip 10/2. Cross-polarised light. Field of view 0.55mm.

H As Figure 5.13 G, showing a plane of T5 inclusions along a grain boundary. Evidence for leakage can be seen in some of the inclusions. Chip 10/2. Plane-polarised light. Field of view 220μm.

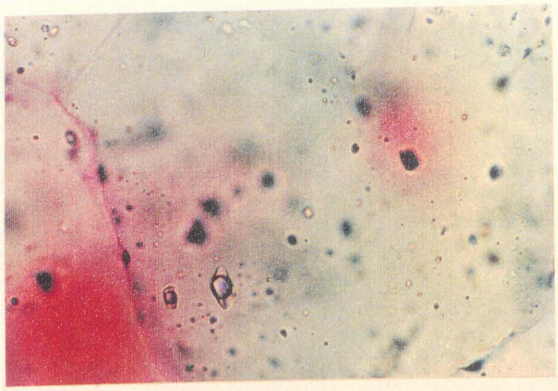

A

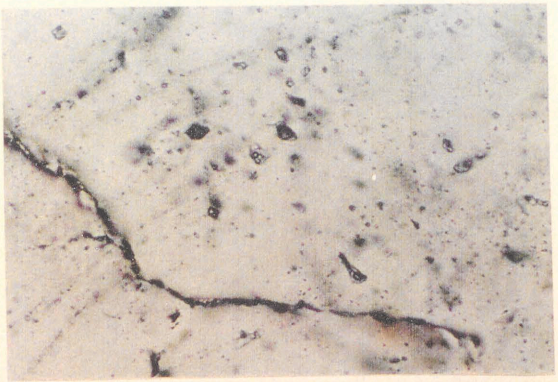

B

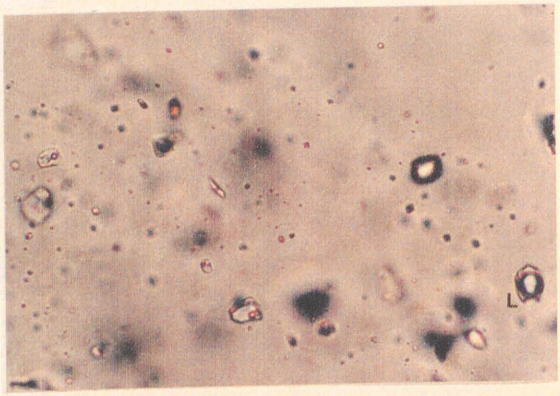

C

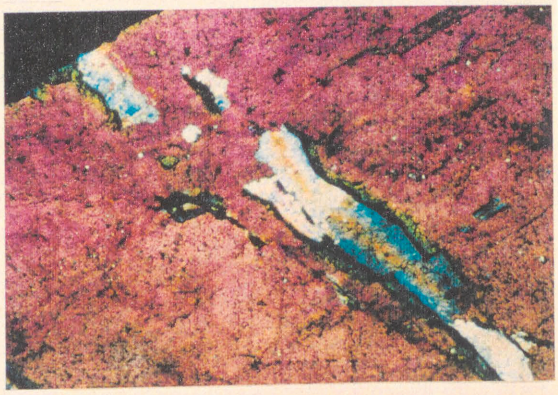

D

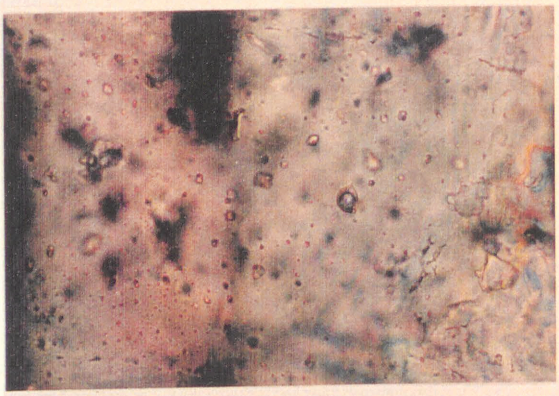

E

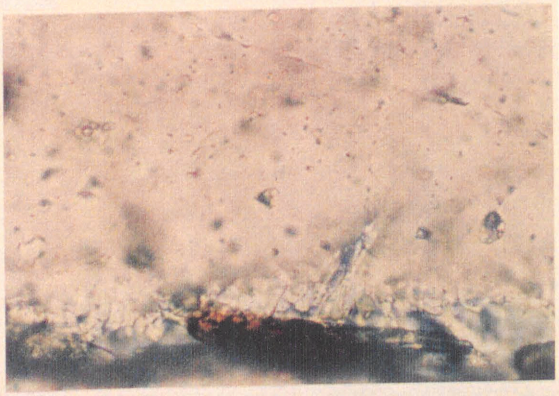

F

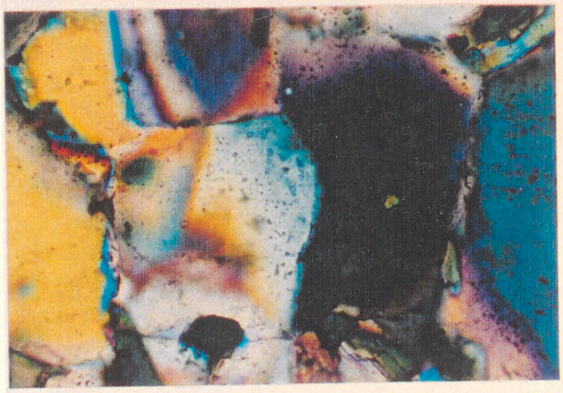

G

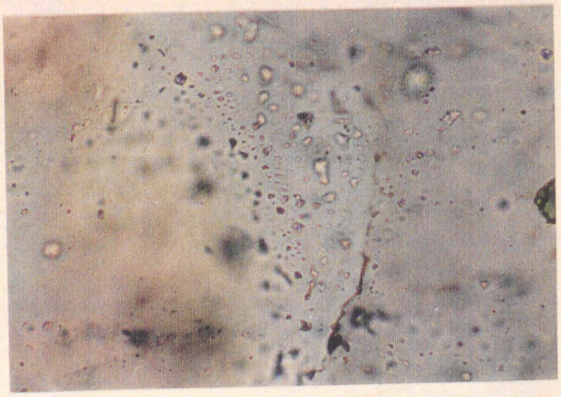

H

Type T4. (L_{aq}-L_{CO2}-V-SS±S)

Type T4 fluid inclusions have been observed in limited numbers in only one sample of quartz. They are three-phase aqueo-carbonic inclusions, similar to type T3 inclusions, although at room temperature a vapour phase is present, and they contain two or three daughter minerals. The size of inclusion ranges from 12 to 35μm, of which the gas phase (L+V) constitutes between 30 and 60%. Daughter minerals, which in total form only 10-15% of the volume, are unidentified, but include a clear, isotropic, sub-rounded, cubic phase and both yellow-white and green birefringent rounded and cubic phases (*Fig. 5.13E&F*). These are tentatively identified as Halite, Fe-chloride and $CaCO_3$, although this has not been analytically confirmed and no definable Raman Spectra has been produced by these daughter minerals. Type T4 inclusions have only been observed in type Q2-B quartz veins (*Fig. 5.13D*).

Type T5. (L-V)

A fifth type of inclusion has been observed at grain boundaries in quartz grains in the Rochas Bandadas (*Fig. 5.13G&H*). These inclusions are two-phase aqueous L+V inclusions, with irregular form and very uneven surfaces. It is thought that these represent primary inclusions which have migrated to grain boundaries during deformation, prior to the formation of types T1, T2 and T3. Their small size (<5μm) and 2-dimensional shape prevents observation of phase changes, and they therefore warranted no further study.

5.3.3 *Fluid Inclusion Characteristics of the C4 Formation Lithological Units*

Metavolcanic Rocks

Quartz grains are rare in the Corpo Quatro Formation Metavolcanics, and fluid inclusions are sparse. Most of the inclusions appear to be randomly distributed and often isolated, but the scarcity of adjoining quartz grains, and the subsequent absence of cross-cutting trails, makes it difficult to assess whether the inclusions are primary or secondary. There are two fluid inclusion populations, the most common being type T1, two-phase aqueous (L+V), which are up to 4μm in length with a 0.9 to 0.95 degree of fill (F). The second, type T2, are up to 6μm across, again with F= 0.95, but are highly saline with one or more daughter minerals (L+V+S±S).

Type T3 inclusions have been observed in some of the schistose metavolcanic samples. These are isolated, hexagonal, monophase and two-phase H_2O-CO_2 inclusions up to 4μm across.

Rochas Bandadas

The Rochas Bandadas contain numerous inclusion trails (*Fig. 5.8A*), as well as isolated inclusions. Type T1 and T2 inclusions are present in abundance, while T3 are less plentiful, and no relative age relationships are discernable between the different types. Type T3, CO_2-rich inclusions, are rounded or oval in shape, while types T1 and T2 have hexagonal to completely irregular shapes.

Rochas Bandadas quartz in close proximity to 'hornblendized' grunerite (see Chapter 3) and chalcopyrite-sphalerite mineralization is particularly rich in type T1 inclusions. These are saline and commonly host a cubic, clear-green daughter mineral which occupies up to 30% of the inclusion. Highly saline inclusions are also abundant close to pyrrhotite mineralization, although the daughter minerals present are green and rectangular. Such inclusions are thought to be of type T2, and their relationship with other sulphide mineralization is not clear.

Rochas Fragmentos

Fluid inclusions within the Xistos Granadas are rare, with a few trails of two-phase aqueous (type T1) inclusions, only some of which host daughter minerals. Most of the fluid inclusions are less than 3μm, although some reach 5μm.

Fluid inclusions within the chlorite-rich Xistos Quartzos are plentiful, and are of type T1, L-V aqueous. They range in size from 2 to 6μm and in shape from rounded to rectangular. They are secondary, lying on trails cross-cutting grain boundaries. Fluid inclusions in biotite-rich Xistos Quartzos are slightly larger than those in chlorite-rich areas, and type T2 inclusions with one or two daughter phases are far more common. The daughter minerals appear, again, to be iron chloride and sylvite, and these highly saline fluids were probably responsible for the potassic alteration of amphibole to biotite.

Fluid inclusions associated with sulphide veinlets are plentiful, although small (less than 10μm). They are of both L-V and L-V-S type, the L-V-S inclusions containing cubic, clear-green isotropic daughter minerals which are most likely halite.

Vein-Quartz hosted

Vein quartz from vein-types Q1, Q2 and Q3 all contain abundant fluid inclusions, which enable a tentative fluid chronology to be established. The early Q1 and Q2-A veins, however, are frequently overprinted by later quartz types, resulting in quartz taking on a variety of appearances in any single sample, so making an interpretation difficult.

The earliest quartz has a grey appearance, caused by the abundance of minute primary fluid inclusions described in section 5.2.1. This cloudy quartz is intergrown with clearer quartz grains, which contain larger, primary L-V±S inclusions.

Q2, biotite-bearing veins, also contain two types of quartz. The first is closely associated with sulphide grains, is clear, euhedral, and encloses both regular-shaped, primary inclusions and irregular-shaped pseudo-secondary type T1 inclusions which are up to 15μm-across. This is overprinted by misty inclusion-rich quartz-overgrowths in which primary trails of irregularly-shaped L-V inclusions up to 5μm occur.

Chalcopyrite-bearing quartz (Q2-A and Q2-B) contains abundant type T1 and T2, and occasional type T3 and T4 inclusions. Type T1 occur as both primary and secondary inclusions in vein quartz. Primary type T1s are found concentrated in Q2-A veins, in areas of sulphide mineralization, where they

are of regular, almost negative-crystal shape, and do not cross-cut grain boundaries. L-V±S inclusions which occur as secondary trails in earlier quartz are generally irregularly shaped, and cross-cut crystal faces. Type T1 inclusions are also found in later, barren quartz-biotite±chlorite (Q3) veins, as well as in calcite veins, in which they are predominantly primary. As these are indistinguishable in earlier quartz, the inclusions must be grouped together. Type T2, daughter mineral-rich inclusions tend to be secondary in Q1 and Q2-A veins, or primary in biotite-bearing (Q2-B) quartz where they are most abundant. Type T3 inclusions have only seldom been found in vein quartz. Chip #30 (sample G92, Q2-A) contains what appear to be type T3 and T4 inclusions in late quartz which cross-cuts the sulphide-bearing material.

Calcite veins also contain fluid inclusions, although the brittle nature of the calcite prevents the collection of suitable samples for fluid inclusion studies. The calcite studied occurs within quartz veins as described in section 5.2.1. Here the inclusions have a negative-crystal form, and type T1 appearance, in which daughter-phases are absent (*Fig. 5.7B&C*). These inclusions are interpreted as being late, post-dating all other fluids (see section 5.2.1). The inclusions are, however, of variable fill. For example, chip #25 contains type T1 inclusions of which 40% have F=.8, 5% F=.5 and 15% F=.9 to 1. the other 40% have been decrepitated during sample preparation and are believed to have been vapour-rich. It is therefore possible that these inclusions are representative of a boiling assemblage.

Table 5.2 **Summary of fluid inclusion types in the Pojuca Corpo Quatro Deposit**

	Type	Location	Size(μm)	Mean Fill	Comments
T1	L-V±S	Q1, Q2-A and host rock	2-20	.85-.9	May contain NaCl
T1 (calcite)	L-V	Q3 Qz and Cc		.15-1.0	
T2	L-V-S±SS	Q2-B, host rock	2-30	.65-.95	Na, K and Fe-Cl
T3	Aqueo-carbonic	Q2-A, host rock	5-30	.1-.7	
T4	" + Solids	Q2-B	12-35	.2-.6	Na and FeCl, $CaCO_3$
T5	Aqueous	Host rock	<5	variable	

5.4 *MICROTHERMOMETRY*

Microthermometric studies have been carried out on types T1, T2 and T3 inclusions from all types of quartz occurring in the Corpo Quatro Formation. Heating and freezing analyses were not performed on types T4 or T5 inclusions, due to limitations in size and optical characteristics; type T4 rarely exceed 12μm across, and are multi-solid inclusions in which liquid is hardly visible, and type T5 are flattened and shown to have undergone leakage during metamorphism, making analysis worthless. Fluid characteristics of the different inclusion types are similar throughout the quartz types, and will be treated in terms of types T1, T2 and T3 rather than in quartz types.

5.4.1 *Recognition of Microthermometric Phenomena*

Standard microthermometric techniques have been employed to study types T1, T2 and T3 inclusions, using the heating-freezing methods described by Roedder (1984) and Shepherd *et al.*, (1985). Up to four heating-freezing runs were carried out on each fluid inclusion in order to establish characteristics such as first melt temperature (T_{fm}), melting of the CO_2 solid (Tm_{CO2}), ice melting (Tm_{ice}) etc. Calibration, accuracy and precision of the instrumentation are described in Appendix D1. The accuracy of the measurements is, however, largely dependent on the ease with which the particular phase change is observed.

The phase changes which can be recognised in an aqueous fluid are: freezing, T_{fm}, T_{rm}, Tm_{Ice}, Tm_h and Th. The criteria used for the recognition of these phase changes in the fluid inclusions in this study are given below:

Freezing Upon supercooling, most fluid inclusions undergo instantaneous freezing somewhere between -60 and -130°C. On freezing an aqueous inclusion, one of two things may happen: either a clear solid is formed (*Fig. 5.14A*), whereupon the only visible evidence for freezing is a slight decrease in the size of the vapour bubble, or the inclusion may take on a brown or green coloured granular appearance (*Fig. 5.14B*).

First Melt/Eutectic Temperature (T_{fm}) 'First melt' occurs at the eutectic temperature for a given chemical system, and is the point at which liquid, ice and hydrates are all stable. For hydrates to form, free $H_2O(L)$ is required, and the reaction which forms these hydrates occurs at the eutectic.

T_{fm} is easiest to measure in those inclusions which remain clear on freezing. This phenomena, like all of the following measurements, is made on slow ($<2°min^{-1}$) heating rather than during a cooling sequence to avoid overshooting the true temperature due to metastability. As hydrates or individual ice crystals begin to form at the eutectic, the clear inclusions take on a granular appearance, which has been described by Shepherd *et al.* (1985) as a *'crazy-paving texture'*.

In inclusions which form a granular mass on freezing, first melt is more difficult to recognise and may occur over a period of ten degrees, but the temperatures are similar to those observed in the previous situation. Small amounts of water may become visible as dark rims form around ice particles, or a pale rim of green hydrohalite may form at the edge of an inclusion or a daughter mineral. Vapour bubbles may also become rounded, but in many cases this was not observed until much later in the heating routine. A crazy-paving texture may also be observed in this situation, as straight dark lines of water form within the solid. There is no apparent chemical control on the type of melt observed, as both may be seen in a single inclusion trail. The precision of these measurements is therefore not very good, and can only be recorded to ±5°C at best.

Figure 5.14 **Melting observations in fluid inclusions**

A & B Photomicrographs of the same field of view in a quartz inclusion chip, showing, on different focal planes, the presence of type T1 inclusions which have frozen to give a clear (A) and granular (B) appearance. Temperature -160°C. Field of view 130μm. Chip #3.

C - F Phase changes in a fluid inclusion which has been frozen using the 'sequential freezing' method. Field of view, C=85μm, D,E,F=110μm. Chip #10/E Inclusion #5 (larger of the two).

C Taken at -130°C. Hydrohalite (h), ice (I), vapour (V) and super-saturated liquid (L) are present.

D Taken at -72°C. Melting has begun, and a slight rounding of the hydrohalite and ice crystals can be seen.

E Taken at -42.7°C. Ice and hydrohalite are still present, but significantly reduced in size.

F Taken at 3.5°C. Ice and hydrohalite have both melted, and halite (H) has reformed in the liquid. Growth of halite is spontaneous following Tm_{HH} at -0.5°C.

G - K Phase changes in a fluid inclusion which has been supercooled, and becomes slightly granular on freezing. Field of view 130μm. Type T2 inclusion (L-V-SS, unidentified daughter minerals) in chip #3.

G Taken at -150°C. Note bubble squeeze on freezing.

H Taken at -82°C. Melting is difficult to observe, but the vapour bubble has become rounded, indicating that melting has started.

I Taken at -70°C. Ice and hydrate crystals are visible in melting mass. Ice is rounded, hydrates are darker and elongate.

J Taken at -48°C. Only ice remains, and is attached to vapour bubble.

K Taken at room temperature. Daughter minerals and vapour remain in the fluid.

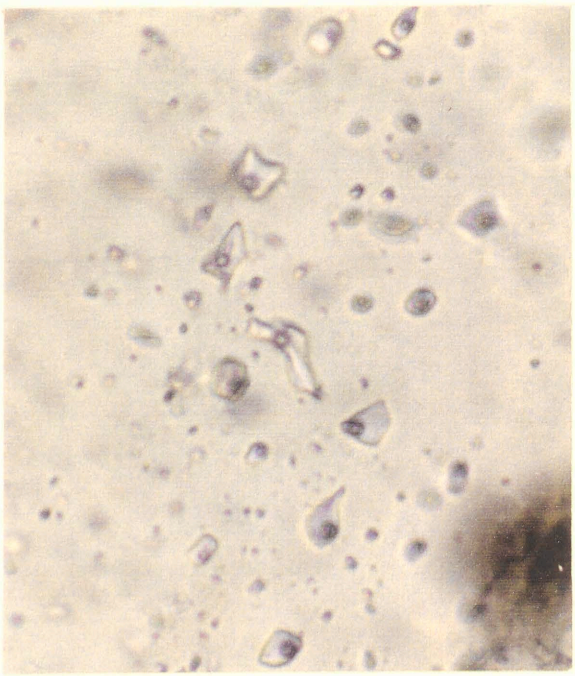

A

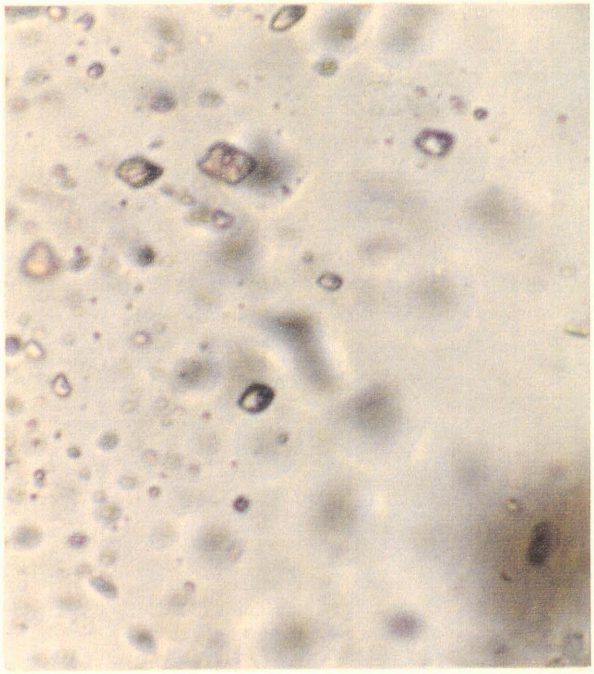

B

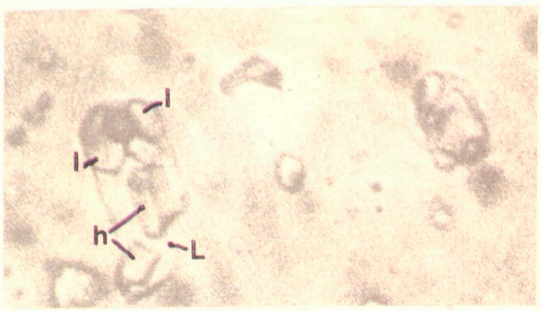

C

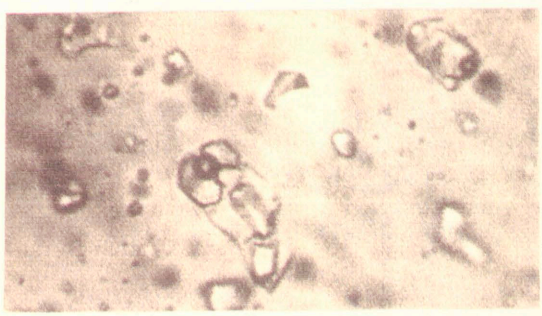

D

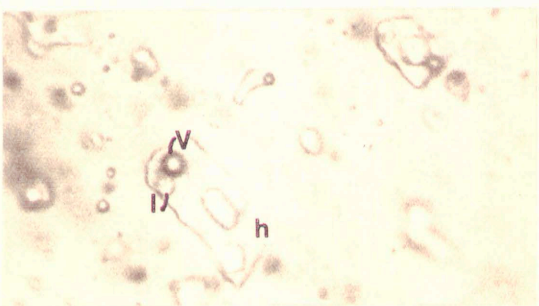

E

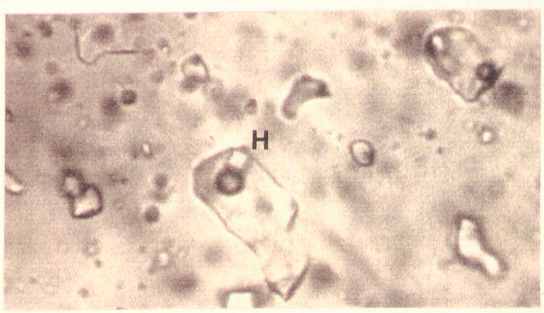

F

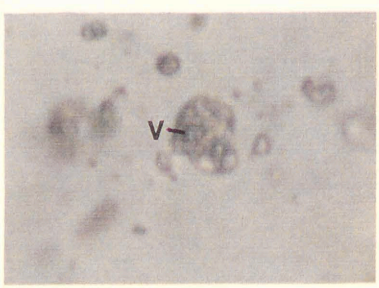

G

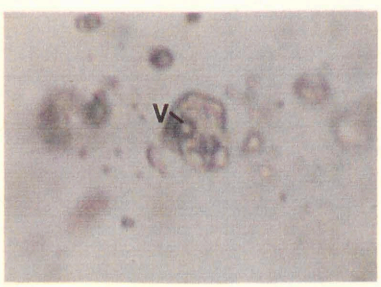

H

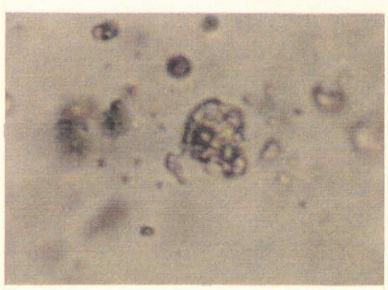

I

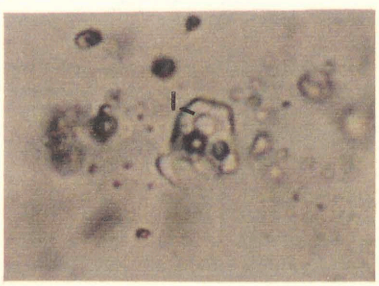

J

K

The sequential freezing method, described by Haynes (1985), gives a more accurate T_{fm} measurement, although it is more time-consuming. This method entails heating the inclusion from frozen until only one ice crystal remains, then refreezing and growing this crystal (*Fig. 5.14C&D*). Providing ice is the last phase to melt, and takes up less than 50 to 75% of the total inclusion space, hydrates can be seen forming a granular mass at the eutectic temperature on re-heating. If ice takes up too much of the inclusion, the hydrates cannot be seen in the dark rim at the fluid-quartz interface. If ice is not the last phase to melt, hydrates are already present in the inclusion and the distinctive granular pattern is not observed.

A comparison of the 'supercooled' versus the 'sequential freezing' methods of eutectic measurements gave very similar results, and therefore the supercooling method is preferred. However, the sequential freezing method was used several times in each chip-population to ensure an accurate temperature was obtained.

Accuracy in the measurement of T_{fm} depends on the way in which the inclusion froze. If the solid is clear, the granular effect can be spotted to within 1° of the initiation of melting. If, however, the inclusion freezes with a granular appearance, melting may not be observed until 5 to 10° above T_{fm}.

Rapid Melt Although melting is frequently observed at low temperatures (~-80°C), this initial melting is sometimes followed, after 5 to 10°, by the melt mixture turning back to ice, This is termed re-freezing, and can be a common phenomena. In this case, the 'first melt' is perceived as a metastable eutectic, as described by Davis *et al.* (1990). For this reason, '*rapid melt*' was measured where possible. 'Rapid melt' is a period of marked melting which occurs over an interval of 2-3°, during which ice or hydrate crystals become rounded in a more visible sea of liquid (*Fig. 5.14E&I*). The precision with which this phase change can be measured is therefore much higher than for the T_{fm} measurements. A phase of rapid melting in inclusions has also been observed by Heinrich *et al.* (1989; visible melt) and Davis *et al.* (1990), and it is taken to be more indicative than T_{fm} of the stable eutectic of the fluid system.

Hydrate Melt (Tm_{HH}, Tm_h) Hydrates form as the result of low temperature reactions between H_2O and either ionic species in the solution or daughter minerals present in a fluid inclusion. Most hydrates have a similar refractive index to the host quartz and are therefore not easily visible. They were found to form only on slow heating (~2°min^{-1}) from frozen or by holding the fluid inclusion chip at low temperatures (between -70 and -100°C) for several minutes.

Hydrates are relatively easily distinguished from ice by their tendency not to attach themselves to the vapour bubble, and by their darker colouring (*Fig. 5.14G&H*). They generally have a slightly higher RI, brightening on racking up, and a more platy appearance than ice (Shepherd *et al.* 1985).

Birefringence, typically employed to identify individual hydrates, could not be used as no polariser is present on the freezing stage microscope. Apart from the hydrohalite, which has a slightly green appearance, it is virtually impossible to distinguish between the different hydrates formed in an inclusion

(Davis *et al.*, 1990), and their presence, therefore does not aid chemical interpretation.

Ice Melting (Tm_{ice}) Ice is easily observed in both aqueous and aqueo-carbonic inclusions, as it forms rounded (sometimes hexagonal) plates in the fluid, once melting has progressed for ~10°. Ice is generally white when compared with hydrates and the fluid in the inclusions, and is easily distinguished by its low relief, becoming whiter when the objective is racked down. During melting, the ice is observed to cling to the vapour bubble. This is not seen in hydrates.

Hydrate and ice melting are relatively easily observed in a fluid inclusion of reasonable size (>~8μm), and the accuracy of the temperature at which they occur is subject mainly to that of the instrumentation. Measurements recorded at slow heating rates (<0.5°C) are believed to be accurate to within 2°.

Melting temperature of ice (freezing point depression) is representative of **salinity** (Wt% NaCl Equivalent) in a relatively simple system (H_2O-NaCl; Potter *et al.*, 1978) which can be calculated in a number of ways depending on the phases present in the inclusion: in a two phase inclusion, the calculation is based on Tm_{Ice}, using the equation of Potter *et al.* (1978):

$$-1.76958 * Tm_{Ice} - 0.042384 * Tm_{Ice}^2 - 0.00052778 * Tm_{Ice}^3 \qquad \textit{(Equation 5.1)}$$

This is based on the NaCl-H_2O system and therefore results in an under-estimation of the true salinity for and more complex compositions. The salinity of an aqueous inclusion containing one or more daughter minerals is based on the dissolution temperature of the last daughter mineral remaining. For l-v-s (halite) inclusions, this can be estimated using the solubility curve of Shepherd *et al.* (1985), but becomes difficult for inclusions with two or more daughters.

These methods can be applied in an ideal situation, although problems are encountered in Corpo Quatro types T1 and T2 inclusions, where Tm_{ice} is frequently lower than -26°C, and the weight % NaCl equivalent method cannot be applied. In these cases, salinity must be approximated from a ternary diagram and stated in Wt% Na + Wt% Ca (or other cation). This is also an estimate, as data is not available for the multi-component systems present in most ore deposit related fluids.

Liquid-Vapour Homogenization (Th_{L-V}) Temperature of homogenization on heating is easily observed, both in aqueous (L+V→L) and carbonic (CO_2(L+V) → CO_2(L) = Th_{CO2}, and H_2O(L) + CO_2(L) → H_2O(L) = Th_{TOT}) inclusions. Total homogenization was rare in the carbonic inclusions studied, as internal pressure exceeded external pressure of the chip at temperatures below that of homogenization and decrepitation occurred.

Dissolution of halite in an L-V-S inclusion is easily observed in most cases, although the other daughter minerals present rarely underwent complete dissolution prior to leakage or decrepitation of the inclusion. When this occurs, it may either imply that the mineral was trapped rather than a true daughter,

or that external pressures were great at the time of trapping.

Total Homogenization (Th_{tot}) Total homogenization is the final phase change to occur, when the fluid inclusion becomes entirely liquid or vapour, either by dissolution of the daughter mineral, or by liquid-vapour homogenization. In the Corpo Quatro fluid inclusions, all total homogenizations recorded were to the liquid phase.

As homogenization is recorded while heating at a rate of between 1 and 3° min^{-1}, this measurement is only accurate to within ~10°C. Because the range of temperatures observed in any one fluid inclusion population is large (>50° in a single sample), and a small change in Th_{tot} makes little difference in the final pressure and temperature calculations, this error is deemed acceptable.

In aqueo-carbonic inclusions, the phase changes Tm_{CO2}, Tm_{Clath} and Th_{CO2} are observed, in addition to T_{fm}, Tm_{ice} and Th_{TOT} as described for aqueous inclusions.

Melting of Solid Carbonic Phase (Tm_{CO2}) On cooling a carbonic fluid inclusion, the liquid CO_2 is observed to freeze suddenly at some temperature below -56.6°C, whereupon it forms a dark mass of solid CO_2 which also contains CO_2 vapour. In order to obtain an accurate CO_2 melting temperature, a heating rate of between 0.5 and 1°min^{-1} was used. By using faster rates the true melting temperature was overshot, and a slower rate caused the final melting point to be missed. As the same heating rate is used for the calibration standard as for the unknown samples, the accuracy of the measurements, once corrected, should be accurate to within 0.1°. To include any analytical deviation, however, an error of ±0.5°C will be used.

Clathrate Melting (Tm_{Clath}) Clathrates form as a low temperature (sub -28°C) reaction between water and liquid gases. They have an RI virtually identical to that of water, and are therefore rarely visible. Sequential heating-freezing of gas-rich fluid inclusions, often employed to aid identification of clathrate melting, because the clathrate compresses the CO_2 bubble (Brown and Lamb, 1989). The type T3 fluid inclusions in the Corpo Quatro deposit, however, rarely showed this 'bubble squeeze', and Tm_{Clath} was therefore only measured occasionally.

Whilst the accuracy of Tm_{CO2} is ± ~0.5°C, as it is an easily observed phenomena in most aqueo-carbonic inclusions, Tm_{Clath} is rarely visible, and clathrates have a tendency to be metastable, so their melting must be observed on a very slow heating rate in order to achieve accuracy to within 1°C. The **salinity** of three-phase (or more) carbonic inclusions can be established using the Tm_{Ice} method (*Equation 5.1*), which will result in an over-estimation if clathrates are present at the time of ice melting (Collins, 1979) or by using the alternative equation which utilizes Tm_{Clath} (Collins, *op.cit.*):

$$0.05286 * (10-Tm_{Clath}) * (Tm_{Clath} + 29.361) \quad \textit{(Equation 5.2)}$$

Clathrate melting temperature, however, is dependent on the gas species present, and is the presence of methane or nitrogen as well as CO_2 in a clathrate will raise its melting temperature, giving a false representation of salinity. It is therefore ideal to use both Tm_{ice} and Tm_{Clath} to estimate salinity in aqueo-carbonic inclusions.

5.4.2 *Analytical Results:*

Type T1 Inclusions: Q2-A veins and host-rock quartz.

Thermometric studies have been carried out on type T1 inclusions, using quartz from the Rochas Bandadas (chips 3, 10 and 11) and mineralized vein quartz (chips 26, 30, 31, 35, 36, 40 and 41). The behaviour of the type T1 inclusions is not significantly different throughout the quartz types, which will therefore be described and plotted together.

Type T1 inclusions freeze on supercooling to between -70 and -110°C, whereupon they take on either a clear or a granular appearance, followed by a *first melt* between -89 and -50°C. The T_{fm} histogram for type T1 inclusions is bimodal, and the two sub-classes, T1a and T1b, are based on T_{fm} being greater or less than -68°C, the natural break in the sample population. Type T1a are classified as those inclusions which have a eutectic below -68°C, and consist of inclusions found in both host-rock and vein quartz. Type T1b, with their T_{fm} above -68°C, are found predominantly within the host rock quartz (*Fig. 5.15*). The division, however, bears no relationship to the location of the inclusions in the sample chip, or their appearance either on supercooling or at room temperature, and the inclusions will therefore be described in terms of microthermometric properties rather than host-type.

Type T1a inclusions, upon slow heating, show signs of first melt between -89 and -68°C, with the mode at -79°C. Further heating results in *rapid melt* (see section 5.4.1) generally between -46 and -30°C (*Fig. 5.15A&B*), but sometimes in the region -62 to -52°C. Type T1b inclusions, which have a eutectic range from -66 and -50°C, with the mode at -61°C (*Fig. 5.15A*), rarely showed a rapid melting phase.

Following the eutectic melt in both T1a and b inclusions, ice and up to two different hydrates remain, forming rounded crystals in the liquid. One of these hydrates, which has a green tinge and high relief, has been observed to crystallize into a halite cube at Tm_{HH} in L-V-S inclusions, and is therefore hydrohalite ($NaCl.2H_2O$). The second hydrate is grey-white, and unidentifiable from microthermometry. Ice and hydrates in types T1a and T1b melt between -46 and 0°C (*Figs. 5.15C-E*), with hydrohalite from host-rock-quartz inclusions tending to melt in the lower part (-46 to -24°C) and hydrohalite from Q2-A veins in the upper part (-32 to -3°C) of this temperature range (*Fig. 5.15*). The Tm_{ice} range, from -50 to -2°C, forms a trimodal distribution (*Fig. 5.15C*), with the ice in T1a inclusions melting over the whole range of temperatures, with modal values at -27 and -12°C, while Tm_{ice} in T1b inclusions is concentrated in the

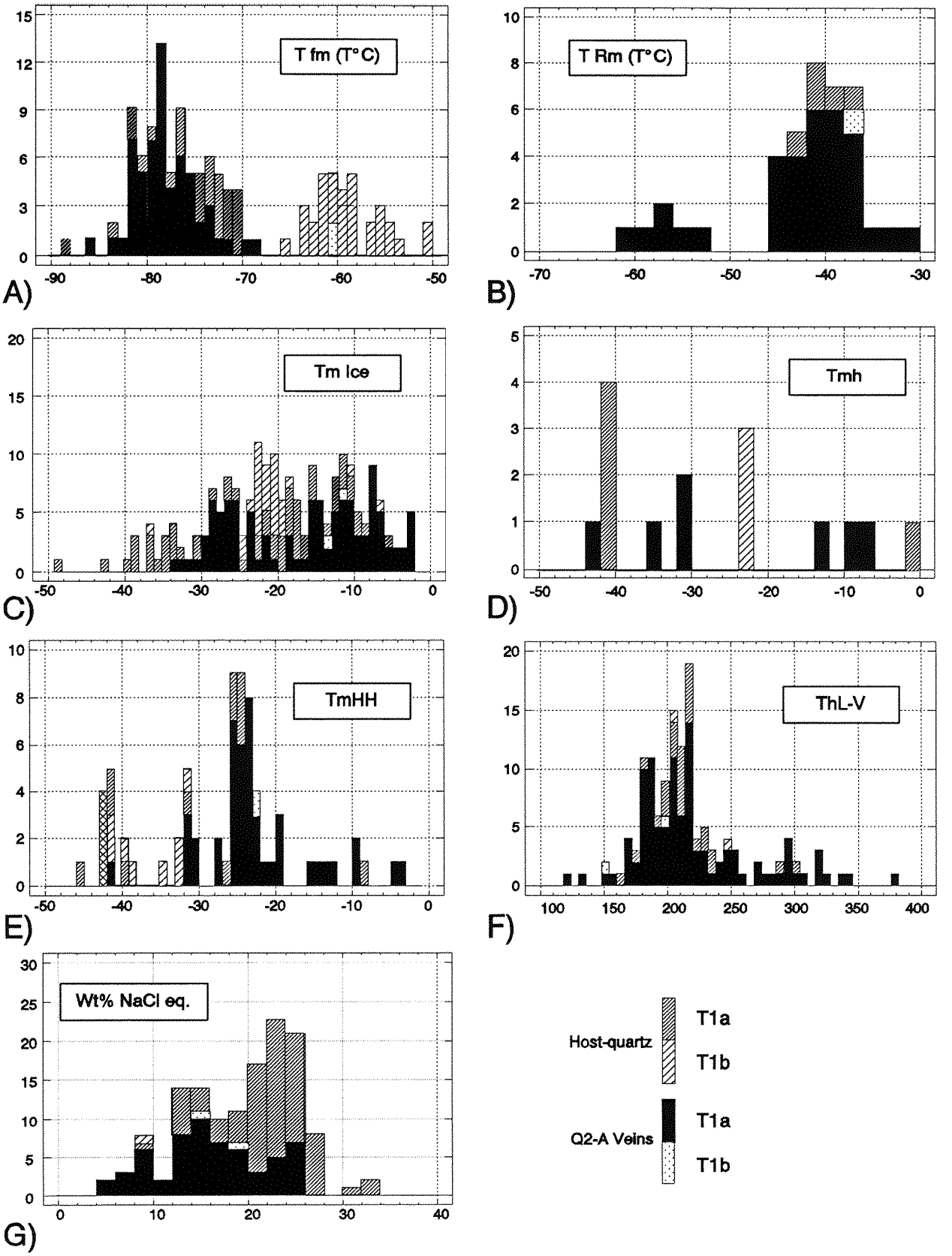

Figure 5.15 **Summary histograms for the Corpo Quatro type T1 fluid inclusions from Q2-A veins and Rochas Bandadas. Types T1a and T1b (detailed in text) differentiated.**

range -25 to -6°C, with the mode at -22°C.

In two-phase aqueous inclusions, the hydrate(s) melt before the ice, while in the three-phase (L-V-S) inclusions the hydrates melt after ice. Hydrohalite remains metastable in some cases up to +6°C (Roedder, 1971). The melting of ice and hydrates in undersaturated inclusions of the NaCl-H_2O system is well documented (Crawford, 1981; Roedder, 1984; Hall *et al.*, 1988; Davis *et al.*, 1990), for which it is stated that $NaCl.2H_2O$ will melt at around -20.8°C (the eutectic for this system; Potter *et al.*, 1978), and ice will melt at some higher temperature below -0.1°C, depending on salinity. Allowing for a slight depression in Tm_{Ice} or Tm_{HH} due to a metastable eutectic (Davis *et al.* 1990), the majority of the Tm_{HH} lie between -20 and -28°C (*Fig. 5.15C*), and that the corresponding ice melts between -20 and -2°C (*Fig. 5.15E*). However, it is also obvious that there are a significant number of Tm_{Ice} and Tm_{HH} values which lie below -30°C, and these cannot be explained by the simple NaCl-H_2O system. A possible explanation for this is presented in the next section.

Type T1 fluid inclusions show a wide range of homogenization temperatures, from 120 to 380°C, with the mode between 170 and 220°C. Th_{tot}, or the dissolution of daughter minerals, has rarely been observed.

Salinity calculations on the basis of Tm_{Ice} are only possible where $Tm_{Ice} \leq -20.8$ ($\pm \sim 2$)°C. The type T1 inclusions fitting this criteria have minimum salinities (see section 5.4.1) ranging from 4 to 34 Wt% NaCl eq. (*Fig. 5.15F*).

Type T1 inclusions: Q3 veins.

Type T1 inclusions identical in appearance to those in the Rochas Bandadas and Q2-A veins have been studied in the late quartz±calcite (Q3) veins using chips #25 (calcite) and #32 (quartz and calcite). These show similar freezing characteristics to the Type T1 inclusions studied in the previous section, and the histograms for this population are presented in *Figure 5.16*. The apparent tightly clustering of the eutectic melt, between -77 and -69°C, maybe a function of the sample number, with the modal value of -76°C, but is in the same region as the other inclusion types studied. A melting burst, between -44 and -37°C, has been observed in only three of the 39 Q3-vein inclusions on which low temperature measurements were carried out. Ice, hydrate and hydro-halite melting temperatures are varied, lying between 0 and -40°, with a modal value for Tm_{HH} between -24 and -27°C, and for Tm_{ice} at -11°C, again similar to those in the Q2-A and host rock quartz.

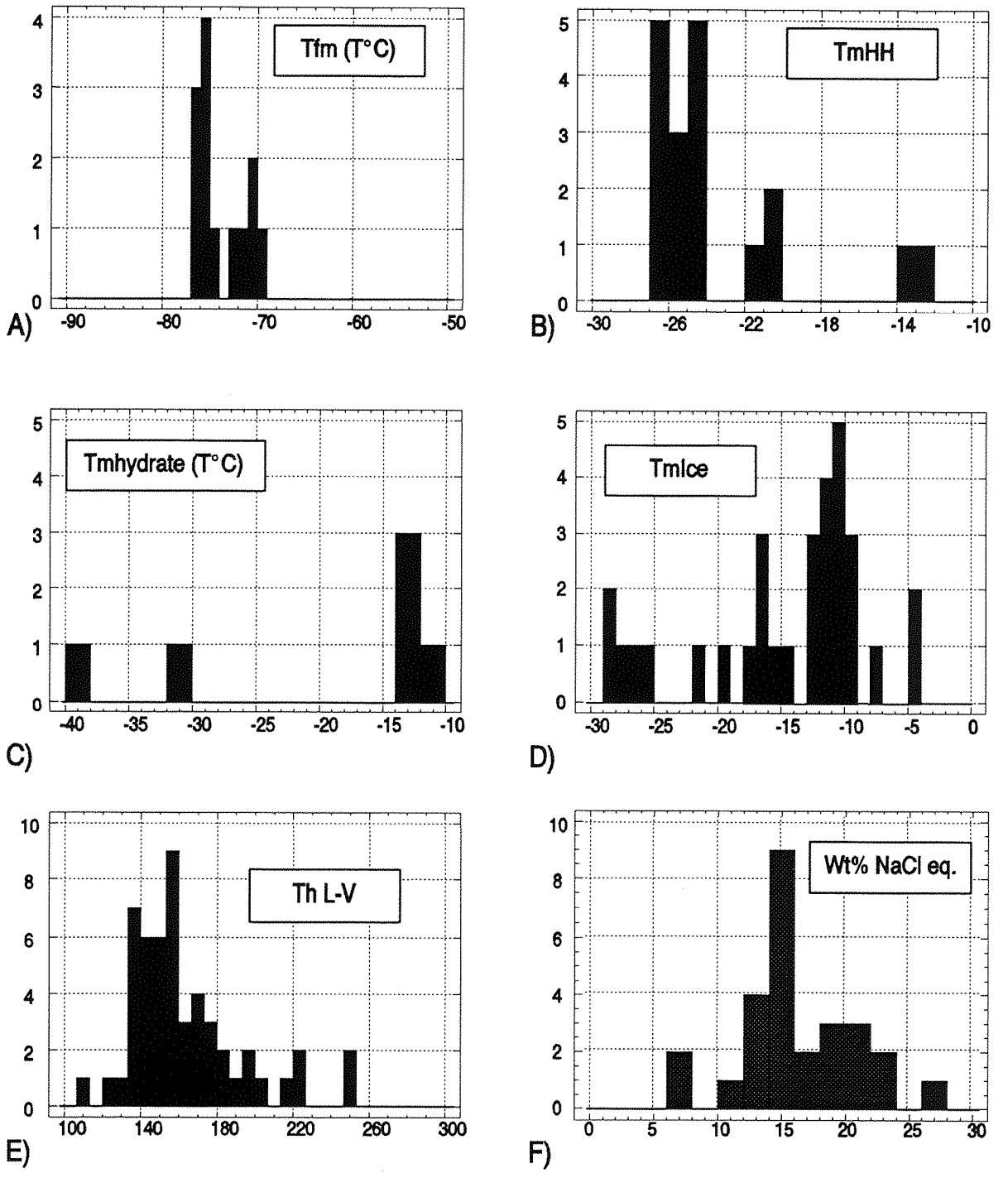

Figure 5.16 **Summary histograms for the Corpo Quatro type T1 fluid inclusions from Q3 calcite-bearing veins.**

Total homogenization temperatures in the range 110 to 250°C, with the modal value of 155°C (*Fig. 5.16*), are much lower than that observed in type T1 inclusions from Q2-A and host-rock quartz (*Fig. 5.15*).

Although the T_{fm} of these inclusions gives no indication of fluid composition, the T_{rm} around -37 to -45 is suggestive of either a NaCl-$FeCl_3$ or a NaCl-$MgCl_2$-rich fluid (Borisenko, 1977). The Na-Mg-H_2O ternary diagram has been used to calculate salinities (*Fig. 5.16*) which lie between 5 and 15% sodium and 4 and 11% magnesium, equating to between 7 and 24 Wt % NaCl eq.

Table 5.3 **Summary statistics for type T1 inclusions from different quartz hosts. (range, and, in brackets, mean (_x_), mode)**

Phase Change (°C)	Host quartz and vein quartz		Q3 Veins
	Type T1a	Type T1b	T1
T_{fm}	-89 to -68 (-77, -79)	-66 to -50 (-58, -61)	-77 to -70 (-74, -76)
T_{rm}	-30 to -62 (-52, -41)	Rare	-44 to -37 (-39, -40)
Tm_{HH}	-46 to -3 (-21, -24)	-54 to -23 (-37, -42)	-27 to -12 (-23, -26)
Tm_h	-43 to 0 (-29, -42)	-22 to -24 (-23, -23)	-40 to -10 (-20, -14)
Tm_{Ice}	-48 to -2 (-22.8, -27 and -12)	-37 to -7 (-20.2, -22)	-29 to -4 (-15, -11)
Th (L-V)	120 to 380 (197, 205)	150 to 245 (202, 203)	110 to 250 (163, 154)
Ts_H	None	None	7 to 24
Salinity (Wt% NaCl eq.)	4 to 34 (19.7, 23)	Only 1 reading (22.1,)	7 to 26 (16, 14)

Type T2 Inclusions: Q2-B veins and host-rock quartz

Type T2 inclusions from the Corpo Quatro Formation have been observed and studied in quartz from the Rochas Bandadas (chips 3, 10, 11 and 19), the Xistos Granadas (chip 9) and biotite-rich Q2-B mineralized veins (chips 17 and 35). The inclusions from the separate hosts (vein- and host rock-quartz)

are plotted in the histograms in *Figure 5.17*. Like the T1 inclusions, the type T2 (L-V-S±SS) inclusions from the different quartz hosts cannot be divided further on their physical properties. Neither, however, can they be divided on microthermometric behaviour.

Instantaneous freezing in most of the type T2 inclusions takes place on supercooling to between -70 and -140°C. Some, particularly those containing multiple daughter phases, do not freeze even after rapid cyclic heating-cooling, or after several hours held at low temperatures (<-100°C). This is believed to be a result of metastability caused by the extreme salinity of the fluids (Roedder, 1971).

Type T2 inclusions begin to show signs of melting between -96 and -61°C (occasionally higher), with a modal value of -79°C, the same as that observed in the T1a inclusions. On slow heating following the initial melt, complete re-freezing has been observed in some type T2 inclusions until a rapid phase of melting occurs between -60 and -54°C. Where this occurs, the final ice melting temperature is between -32 and -16°, and is followed by Tm_{HH} between -20 and +4°C. A similar pattern is observed in inclusions in which no melting burst is observed, but here complete melting occurs at lower temperatures. Tm_{ice} is between -57 and -34°C, followed by Tm_{HH} between -48 and -20°C. A second hydrate, similar to the grey-white hydrate observed in the type T1 inclusions, is present in some of the high salinity Type T2 inclusions. The second hydrate has a very wide range in melting temperature (Tm_h) of between -75 and +16°C (*Fig. 5.17D*), with no real mode. This positive melting temperature is a result of metastability. Again, this hydrate is unidentifiable using microthermometry.

On heating, type T2, like type T1 inclusions, always undergo liquid-vapour homogenization to the liquid phase, suggesting that no boiling or unmixing of the fluids has taken place. $Th_{l\text{-}v}$ generally occurs between 155 and 230°C, prior to halite dissolution (Ts_H from 160 to 260, rarely up to 500°C) and dissolution of the white daughter mineral believed to be sylvite (Ts_S from 100 to 200°C). The third daughter mineral, identified by SEM as iron-chloride, is rarely observed to dissolve before the inclusion decrepitates at 400 to 500°C, which may indicate either disequilibrium or the effects of post-trapping modification.

The salinity of most type T2 fluid inclusions must, by definition, exceed 26.6 Wt% NaCl eq. (saturation level of NaCl; Roedder, 1984), as daughter minerals are present. However, with Tm_{ice} often as low as -50°C, even in two-phase (L-V) inclusions, it is not possible to calculate the salinity using the Potter *et al.* (1978) Tm_{ice} method (equation 5.1). The salinity of these inclusions has been calculated using the ternary diagram in the system $CaCl_2$-NaCl-H_2O (ref), although this too assumes that $Tm_{ice} \geq -52°$ (the eutectic for this system; Borisenko, 1977). Salinity in most cases is therefore calculated as Wt% Ca + Wt% Na, and is listed in Appendix D2.

The approximate salinities for inclusions containing daughter minerals can be calculated using Ts_H, shown graphically in *Figure 5.17F*. These values, however, provide only a conservative estimate of the true salinity, as the second daughter mineral, which in most cases dissolves only partially prior to decrepitation, results in a decrease in the solubility of halite in the fluid (Shepherd *et al.*, 1985).

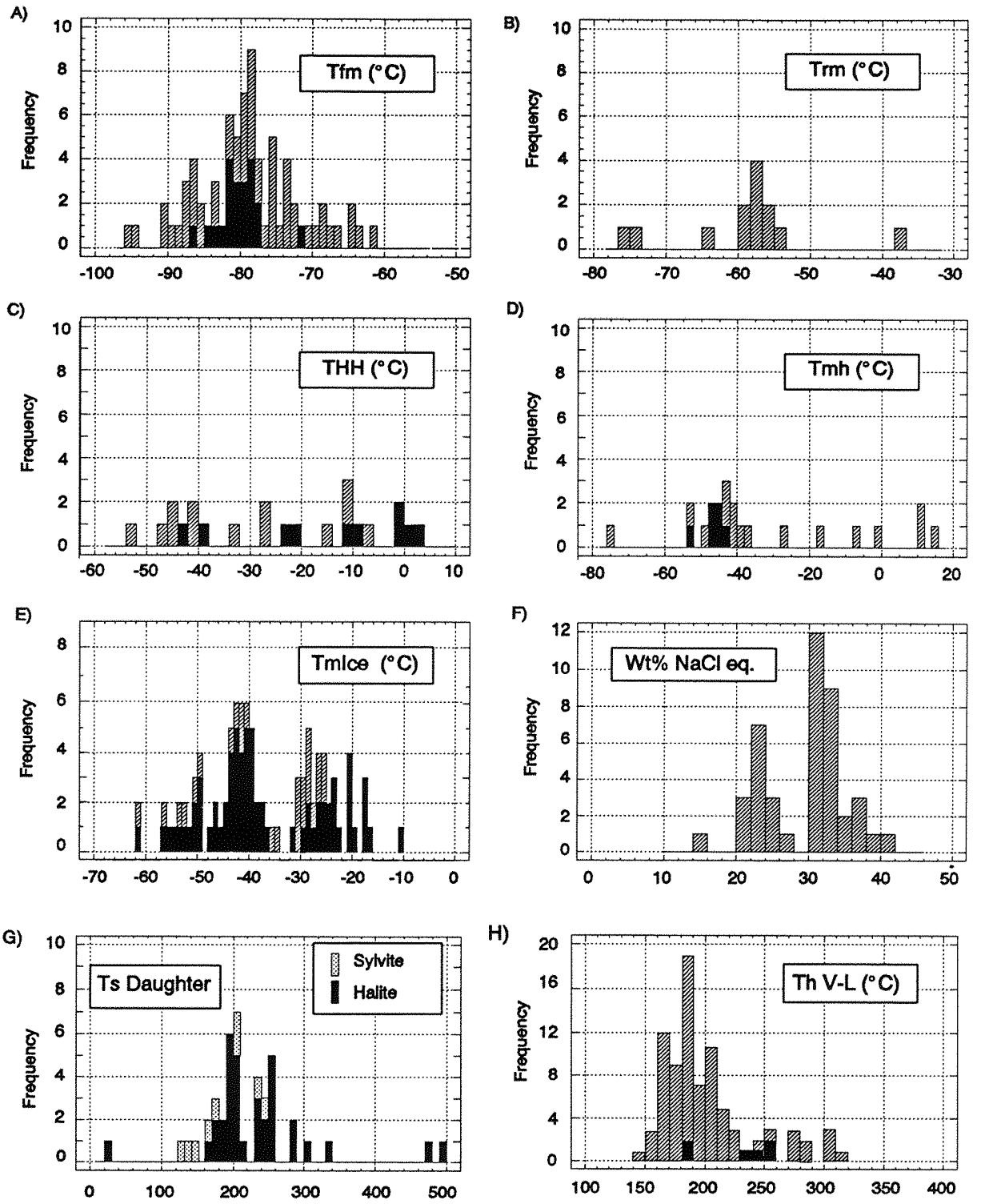

Figure 5.17 **Summary histograms for the Corpo Quatro type T2 multisolid fluid inclusions from Q2-B veins (solid) and Rochas Bandadas (shaded).**

T_{fm} for both type T1 and type T2 inclusions is exceptionally low, between -50 and -95°C. The lowest known equilibrium eutectic of natural fluids occurs in Li-bearing Ca-, K- or Mg-rich solutions, and the mineral assemblage at Pojuca gives no evidence for the presence of a large lithium component. The low eutectic observed in types T1 and T2 inclusions can be explained by a sub-solidus melting caused by the presence of metastable hydrates in the frozen solution, which is known to cause metastable eutectics (Davis *et al.*, 1990), and result in clear solids beginning to darken as low as -80 to -90°C in $MgCl_2$- and $CaCl_2$-bearing NaCl-rich aqueous systems (*Fig. 5.18*).

The stable eutectic in these complex inclusions is best interpreted using T_{rm} (Davis *et al.*, op.cit.) which in type T1a inclusions occurs mainly between -36 and -46°C suggesting the presence of iron or magnesium chloride in a sodium-rich solution, and in type T2 inclusions occurs predominantly between -53 and -65°C, signifying a $CaCl_2$-NaCl-?KCl-H_2O fluid (Borisenko, 1977). The presence of halite, sylvite and iron-chlorides in type T2 inclusions, however, indicates that the fluids are far from simple, and the lack of experimental data on any more than the most basic systems means that it is impossible to determine the exact composition from microthermometric data alone, and an approximation to a theoretical ternary system must be used to estimate salinity and trapping conditions (*Fig. 5.19A*).

A summary of microthermometric data has been plotted using salinity (calculated from Tm_{Ice} and Ts_H) against total homogenization temperature, showing those inclusions which homogenize by dissolution of halite as well as those which undergo vapour to liquid homogenization. This plot (*Fig. 5.19B*) shows how the inclusions fit into three separate groups, with slight overlap. Type T1 (early veins) and T2 aqueous inclusions display similar homogenization temperatures, as shown by the histograms (*Figs. 5.15 and 5.17*), while type T2 have a much higher salinity. The later timing of type T2 is not, as might be expected, represented by a decrease in temperature and it can therefore be concluded that the interval between the two sets of fluids was minimal. Type T1 inclusions from Q3 veins show a significantly lower Th_{tot}, and are inferred to represent a later fluid event.

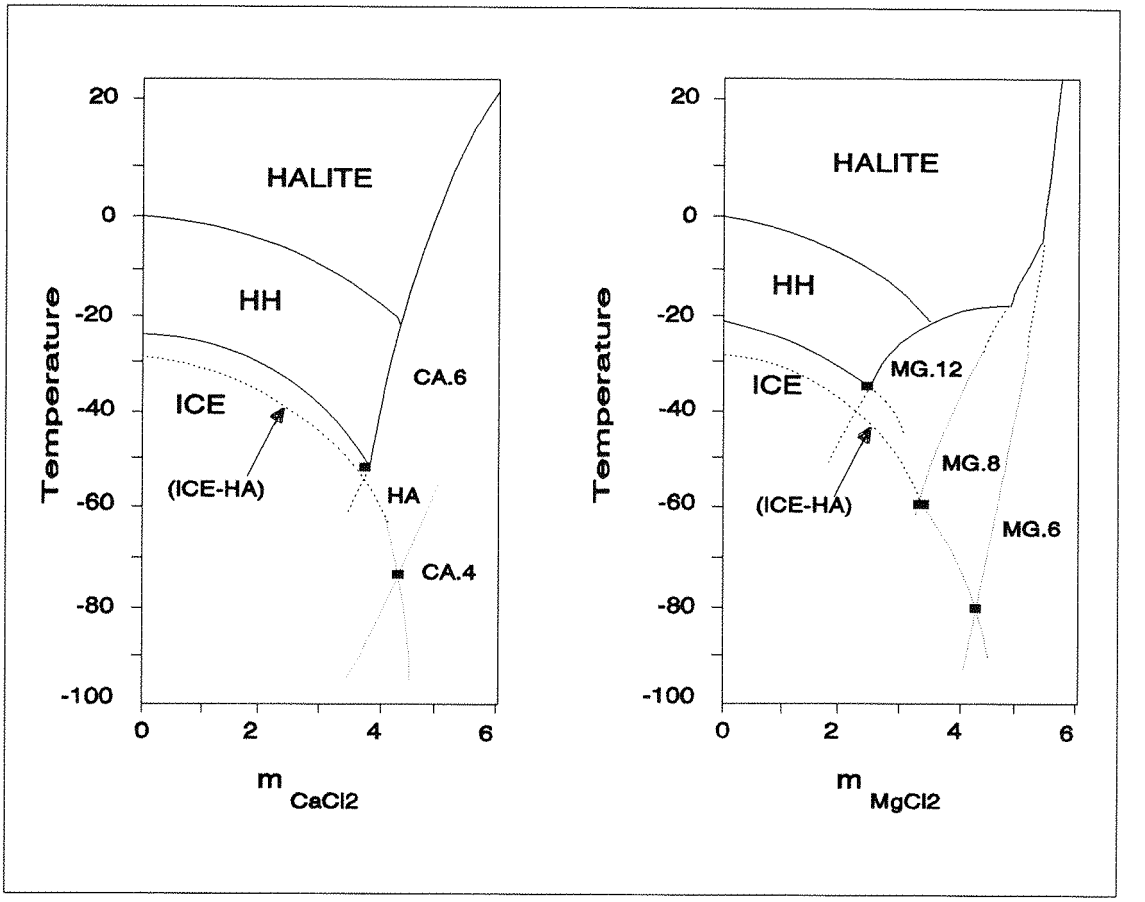

Figure 5.18 **Univariant curves for the systems NaCl-$CaCl_2$-H_2O and NaCl-$MgCl_2$-H_2O, showing the positions of the stable and sub-solidus metastable eutectics at which 'first melting' may occur. Stability fields of calcium- and magnesium hydrates also shown. (After Davis *et al.*, 1990)**

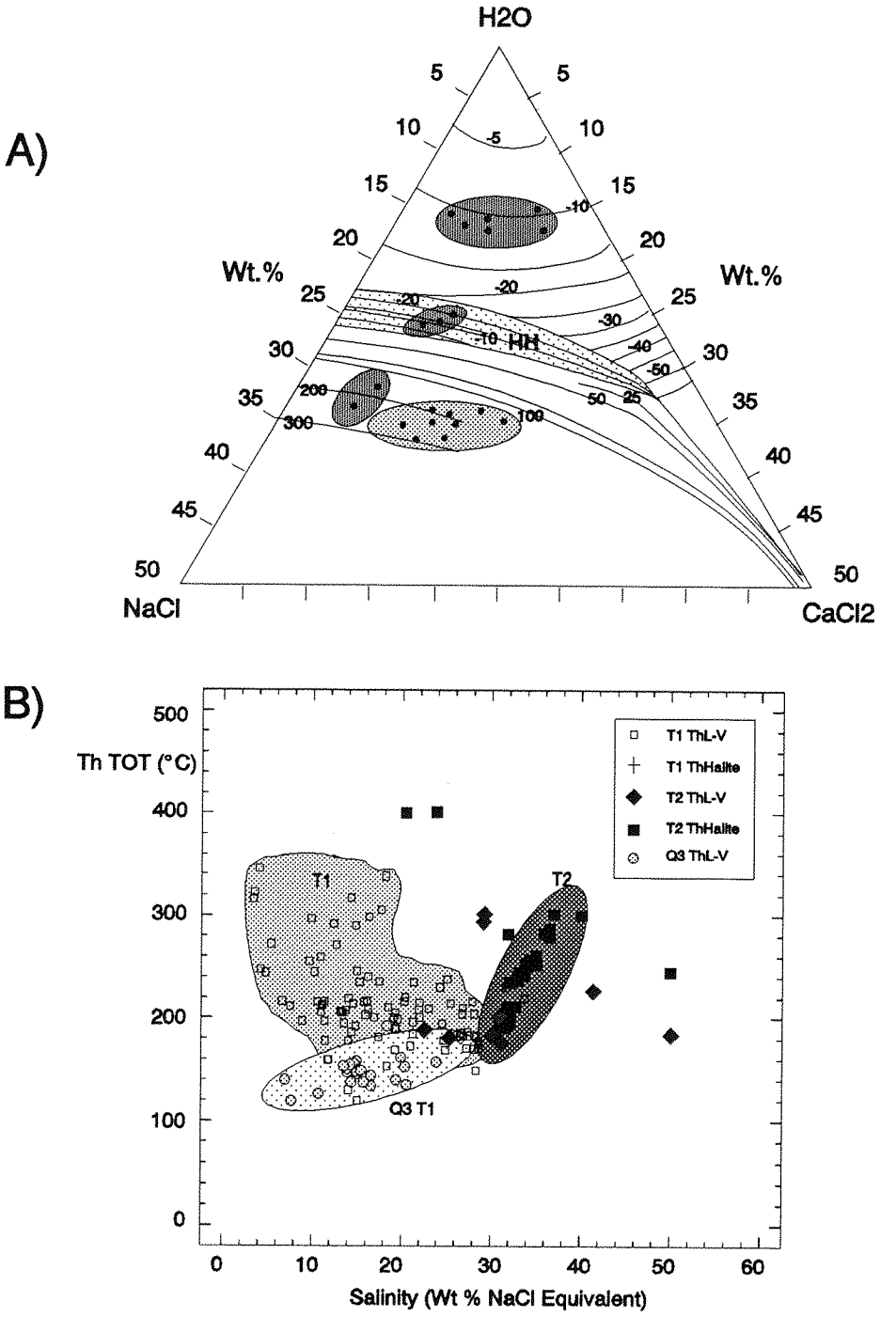

Figure 5.19 **A. Ternary diagram of the system H_2O-NaCl-$CaCl_2$, showing the positions of the T1 and T2 fluid inclusions from the Corpo Quatro Formation, by approximation to this chemical system. Note both high and low salinity of type T1 inclusions; B Summary plot of total homogenization against salinity for the aqueous inclusions in the Corpo Quatro Formation. Salinity calculated using the equation of Potter *et al.* (1978) for L-V and using Ts_H for L-V-S inclusions.**

Table 5.4 **Summary statistics for type T2 fluid inclusions**

Phase Change (°C)	Temperature range	Mean ($\bar{x}$)	Mode
T_{fm} (n=78)	-96 to -61	-77	-80
T_{rm} (n=10)	-76 to -55	-59	-57
Tm_{HH} (n=25)	-53 to +4	-20.2	-11
Tm_h (n=21)	-75 to +15	-32.6	-43
Tm_{ice} (n=96)	-62 to -10	-36.9	-42
Th (L-V) (n=82)	155 to 230	200.7	170
Ts_H (n=34)	160 to 340	234	210
Ts_S (n=9)	120 to 245	181.4	166
Salinity (wt.% NaCl eq)	15 to 41		31

Type T3 Inclusions:

Type T3 inclusions have been studied in both metamorphosed and vein quartz (chips 10 and 35). They contain between 40 and 100% by volume gas, and so require measurements of Tm_{CO2} and Th_{CO2} to be made in order to establish the composition of the gas phase in addition to those made on aqueous inclusions to ascertain the salinity. T_{fm} and T_{rm} were not measured, as the minor H_2O phase is frequently masked by frozen CO_2.

The Tm_{CO2} of pure carbon dioxide is -56.6°C. The measured Tm_{CO2} of type T3 inclusions lies between -57 and -62°C, with modes at -58 and -61.5°C (*Fig. 5.20*), which, being outside the ±0.5°C error margins of Tm_{CO2} measurement, is indicative of two separate populations. The decrease in CO_2 melting temperature suggests that the gas phase contains impurities such as CH_4 or N_2 (Shepherd *et al.*, 1985). This should also result in the decrease in Th_{CO2}, but no direct correlation between melting and homogenization temperature of CO_2 exists, and there is no evidence of separate populations from the spatial distribution or from other microthermometric characteristics of the inclusions.

Tm_{Ice} covers a wide range, from -2 to -23°C, but is mainly concentrated between -7 and -11°C. The small number of Tm_{Ice} measurements is not a statistically valid sample, but the high volume of CO_2 in most of these inclusions prevents ice melting from being observed. Similarly, cyclic freezing at different temperatures failed to produce bubble squeeze (see section 5.4.1), in all but six inclusions, so clathrate melting was rarely observed.

The best estimate of salinity for most of the carbonic fluid inclusions comes from Tm_{Ice}. In the absence of clathrate, Tm_{ice} should be representative of true salinity, but in the case of the T3 inclusions, clathrate melts between 1 and 4°C. It is possible to estimate salinity in the presence of CO_2 clathrate,

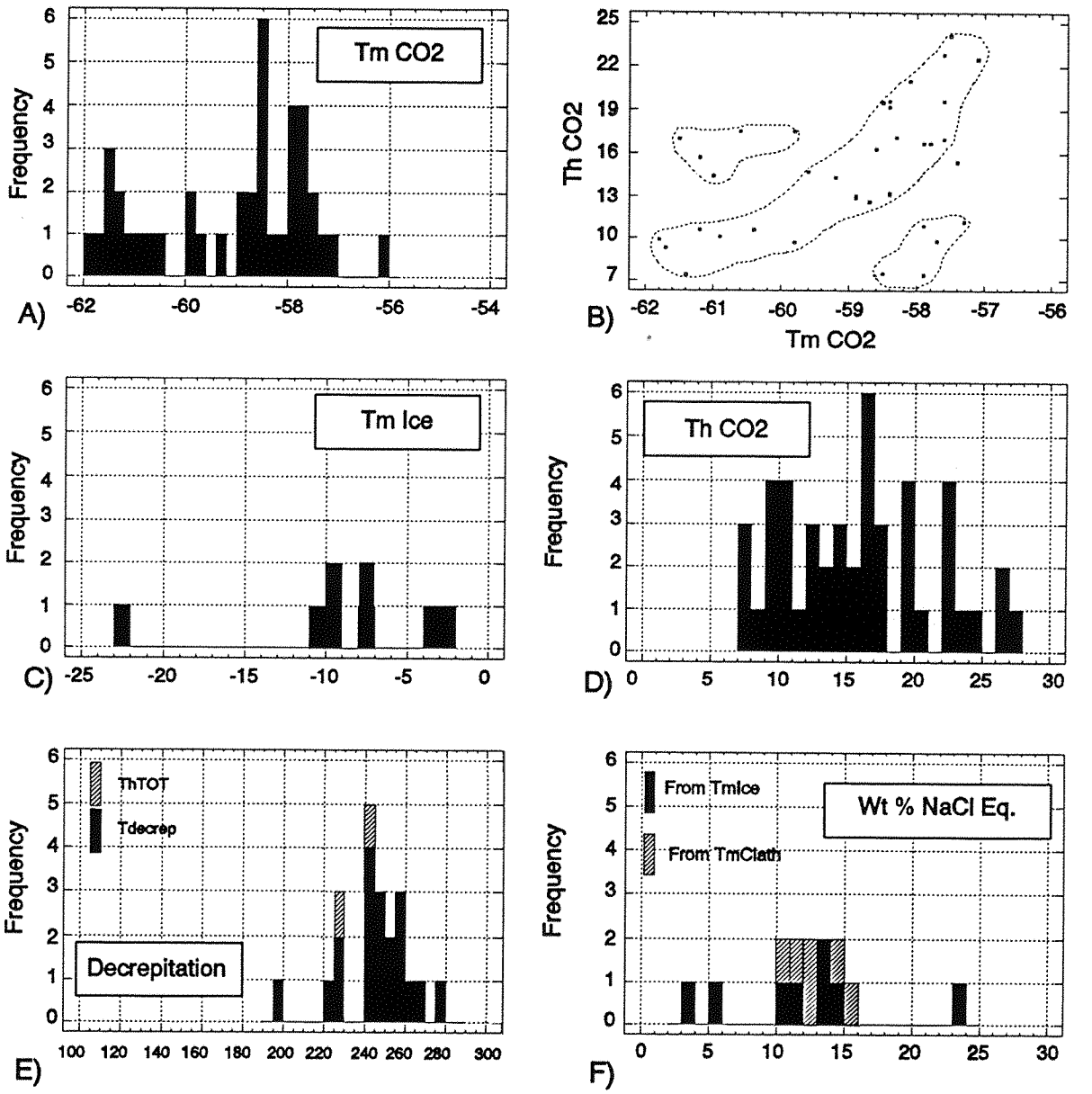

Figure 5.20 **Summary histograms for the Corpo Quatro type T3 aqueo-carbonic fluid inclusions from Q2 veins and Rochas Bandadas.**

according to the salinity curve of Collins (1979). However, the presence of CH_4 in clathrate raises its melting temperature. Salinities calculated from Tm_{ice} are in the region 10 to 15 Wt% NaCl eq., and those from Tm_{Clath}, using the Collins (1979) equation (*Equation 5.2*), also lie between 10 and 16 Wt, indicating that this is a good estimate of salinity of T3 inclusions.

Total homogenization was only observed in two of the carbonic inclusions, once to H_2O_L at 229°C and once to $CO_2(L)$ at 242°C. This indicates that unmixing of the two phases occurred prior to trapping, and that the inclusions therefore lie on a solvus, and are representative of trapping conditions. All other inclusions decrepitated between 195 and 280°C , prior to Th_{TOT}, which is again indicative that trapping occurred around this temperature.

Type T3 inclusions are relatively easy to interpret using microthermometric data alone, although Raman analysis confirmed the presence of CH_4 and the absence of N_2 (see section 5.5). It would be expected with impure gas phases that Th_{CO2} decreases with decreasing Tm_{CO2} and therefore with increasing impurities. However, *Figure 5.20* shows no real correlation between melting and homogenization temperatures of CO_2. Anomalies occur because the type T3 inclusions are of variable fill, and therefore of variable density, and an increase in density (fill) also decreases Th_{CO2} (Roedder, 1984). In order to achieve a straight line on a Th_{CO2} and Tm_{CO2} plot, degree of fill must be equal, and the anomalous values on *Figure 5.20* may be explained by variation in density.

The data for type T3 inclusions with Tm_{CO2} higher than -59°C can be plotted on the mole % CH_4 graph (*Fig. 5.21*), where the CH_4 content is found to lie between 4 and 12.5 mol%, and the molar volume lies between 0.5 and 0.7 cm^3 $mole^{-1}$. Most of the inclusions with Tm_{CO2} lower than -60°C, however, do not plot on *Figure 5.21*, as the measured Th_{CO2} is too high. Raman analysis of type T3 inclusions shows no apparent difference in composition between the two sub-groups. Although not all the inclusions in this sub-group form visible clathrates on freezing, it is probable that clathrates are present. The presence of clathrates during melting of solid carbonic phases have been shown to result in variable Tm_{CO2}, changing the composition of the clathrates and carbonic phase with equilibration time, which will effect the estimation of gas composition from Tm_{CO2} vs Th_{CO2} graphs (Murphy and Roberts, in prep). This may explain why, even though the inclusions contain no nitrogen, they do not plot on the CH_4 graph in their predicted positions.

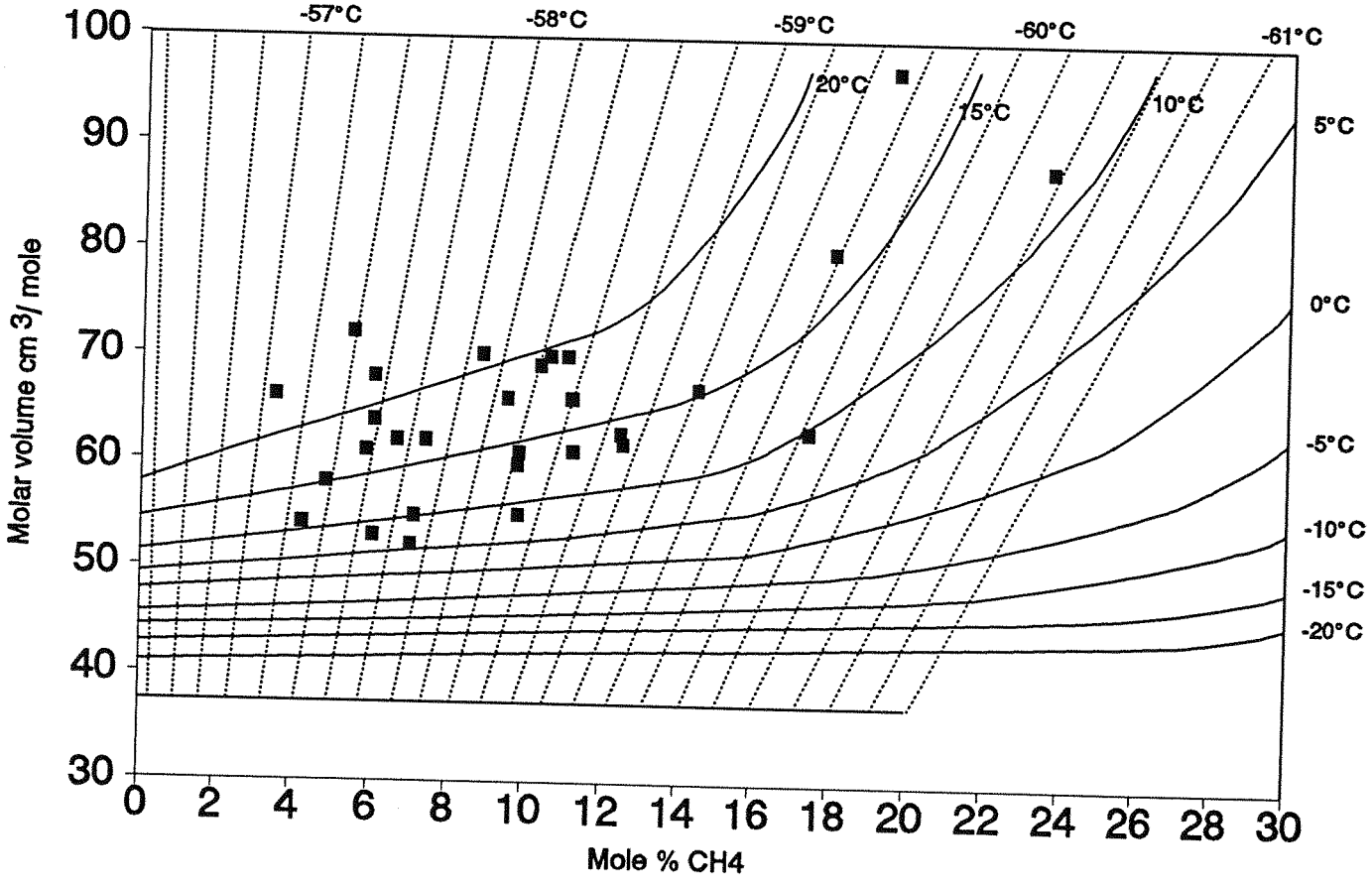

Figure 5.21 **Graph calculating the mole composition of CO_2-DH_4 mixtures in carbonic inclusions which homogenize to the liquid phase. Calculated using Tm_{CO_2} and Th_{CO_2}. Solid lines = Th_{CO_2}, dashed lines = Tm_{CO_2}. (After Heyen *et al.*, 1982)**

5.5 *DETERMINATION OF FLUID COMPOSITION USING LASER RAMAN SPECTROSCOPY (LRS)*

Micro-LRS allows for the non-destructive analysis of fluid inclusions. By focusing a monochromatic laser beam inside an inclusion, covalently bonded molecules become 'excited' and produce scattered radiation. The vibrational frequency of the resulting energy is represented by *stokes* and *anti-stokes* scattering, or **Raman Shift**, and is unique for each known polyatomic species (Raman and Krishnan, 1928). The theory of laser Raman spectroscopy is covered in detail by a number of workers, principally Herzberg (1945), and the application of laser Raman spectroscopy to geological studies is detailed by Dhamelincourt *et al.* (1979), Rosasco *et al.* (1975) and McMillan (1989). Although LRS is widely applied to the analysis of polyatomic gas species such as CO_2, CH_4 and N_2 in fluid inclusions (Seitz *et al.*, 1987; Ramboz *et al.*, 1985), daughter minerals, which are commonly inorganic salts, are monatomic species and as such do not produce a Raman shift. Dubessy *et al.* (1982) has shown that stoichiometric hydrates of components in solution show characteristic spectra based on the number of H_2O molecules trapped in the hydrate lattice, and therefore that by growing low temperature hydrates, it is possible to identify daughter minerals found in saline fluid inclusions.

The identification of gas components in type T3 aqueo-carbonic inclusions was relatively straight forward, requiring Raman analysis to be carried out at room temperature (*Appendix D1*). The study of types T1 and T2 inclusions, however, requires Raman analysis to be carried out at very low temperatures (Dubessy *et al.*, 1982), and the analytical technique used is therefore different to that used at room temperature.

5.5.1 *Experimental technique for the LRS analysis of Types T1 and T2 inclusions:*

Salt-hydrates have a distinct molecular spectra, enabling a Raman spectra to be produced. The most intense, and hence the most useful vibrational lines on the spectra are those created by the internal vibrations of the water molecule. These water molecules will be located in different crystallographic sites depending on the hydrate produced, and result in Raman shifts in the water 'stretching' region 3300 cm^{-1} to 3600 cm^{-1}, and the 'bending' region 1500 cm^{-1} to 1700 cm^{-1}.

In order to study polyatomic hydrates in fluid inclusions using LRS, the Linkam THM600 heating-freezing apparatus used for microthermometric studies was attached to the sample stage of an Olympus BH-2 microscope coupled with a Jobin-Yvonne Raman Microprobe MOLE, model S3000. A long-working-distance Nikon *100 lens is used, and optical examination is possible using a t.v. monitor. The laser Raman is fitted with an Astromed CCD multichannel detector, cooled to 132K using liquid nitrogen. The laser is a 4W Argon beam with a typical source output of 600mw for these analyses.

Calibration of the instrumentation was carried out using the Raman peak of a fluorescent light bulb, which was measured with the detector open, and corrected to the known position of 1122.6 cm^{-1}. This method of calibration is accurate to $\pm 4cm^{-1}$. Calibration of the Linkam apparatus is not undertaken for this type of analysis, as it is peak-position, and not absolute temperature, which is important in the interpretation of Raman spectra.

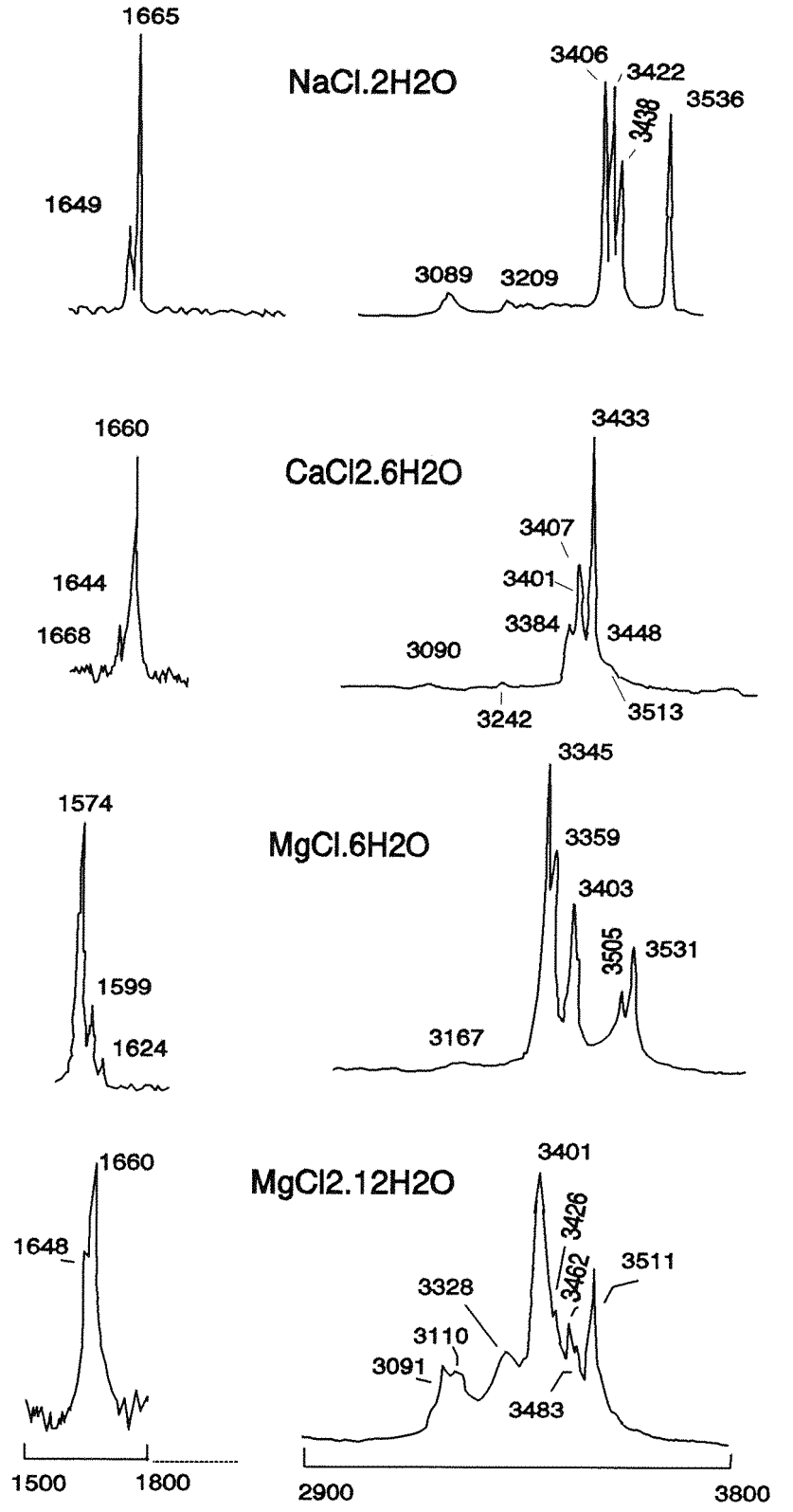

Figure 5.22 **Defined spectra for the hydrates $NaCl.H_2O$, $CaCl_2.6H_2O$, $MgCl_2.6H_2O$ and $MgCl_2.12H_2O$. Peaks labelled in cm^{-1} and show the bending region (1500-1700) and the stretching region (3000-4000 cm^{-1}) normally associated with salt hydrates. (after Dubessy *et al.*, 1982)**

The doubly-polished fluid inclusion (quartz) wafers used for micro-thermometric analyses are placed in the sample holder of a Linkam THM600 heating-freezing stage. The sample chamber of the Linkam stage is made air-tight by sealing the space between the stage and microscope objective with rubber O-rings. No cover-slip is necessary.

A monochrometer slit size of 150mm was found to produce optimum results, and a grating of 600g/mm (intermediate slit 24.9mm) allowed a spectra to be obtained for the whole area of interest (3000 - 3700 cm^{-1}) in one reading.

Hydrates were formed in the fluid inclusions by both supercooling, resulting in the analysis of a fine-grained ice-hydrate mixture, and the sequential freezing method used to establish T_{fm} (see section 5.4.1), whereby nucleation of the inclusions was initiated after supercooling to ~-120°C, with repeated heating and freezing allowing a single large salt-hydrate crystal to grow. Spectra were obtained at temperatures from -70 to -180°C, on both 'supercooled' and 'grown' hydrates. An optimum run-time of 900s was found to avoid fluorescence from the sample, with two consecutive spectra added together. The addition of more than two consecutive runs on a single hydrate provided no significant increase in peak definition. Spectra are generated and manipulated using the PRISM® software package.

5.5.2 *Analytical Results for types T1 and T2 inclusions*

Characteristic spectra have been measured for synthetic hydrates ($NaCl.2H_2O$, Hydrohalite; $CaCl_2.6H_2O$ (Ca.6), antarcticite; $MgCl_2.6H_2O$ (Mg.6); $MgCl_2.12H_2O$ (Mg.12); $FeCl_3.6H_2O$; $KCl.MgCl_2.6H_2O$, carnallite; and $LiCl.5H_2O$) by Dubessy *et al.* (1982; 1992), and the most common of these are given in *Figure 5.22*. Little further work has been documented in this field.

Raman analyses have been carried out on hydrates in both types T1 and T2 inclusions, in order to establish which hydrates are present, and which result in the low eutectic melt observed in the aqueous inclusions in this study. Daughter minerals in these inclusions failed to produce Raman spectra, confirming that they are halides rather than carbonate minerals. In order to try and identify the species present in the fluids, hydrates formed in the fluid inclusions at low temperature were analyzed. The quality and resolution of hydrate spectra was found to vary greatly depending on the chip temperature at the time of the run, the method of freezing (super-cooled or sequential freezing), size of inclusion and volume of liquid present.

The growth of hydrates was most readily observed in the largest (20x30μm) of the L-V-Type inclusions, where the growth of hydrate crystals is more easily observed. It was not possible, however, to find inclusions of this size in all of the samples used. Of these, the best spectra were formed from those inclusions which contain no daughter minerals.

The effect of Temperature on Raman Spectra

The resolution of ice and hydrate spectra increase dramatically below ~-140°C, conforming with the findings of Ford and Falk (1968; 1969) and Dubessy *et al.* (1982). Above this temperature, discernable

Table 5.5 **Theoretical peak positions for some common hydrate spectra (Dubessy *et al.*, 1982) and experimental peak positions for fluid inclusions in this study. Abbreviations: sc = supercooled inclusion, seq.fr = sequentially frozen inclusion, bwn = brown, clr = clear, 1*900s = number and duration of runs.**

cm^{-1}	3100	3113	3211	3232	3239	3327	3345	3367	3398	3410	3423	3437	3475	3508	3538	Operating Conditions.	Type
Ice	✓✓	✓				✓											
$NaCl.2H_2O$			✓							✓✓	✓✓	✓			✓✓		
$CaCl_2.6H_2O$					(✓)				✓	✓		✓✓		✓			
$MgCl_2.6H_2O$							✓✓							✓	✓		
$MgCl_2.12H_2O$		✓				✓			✓✓		✓			✓			
$FeCl_3.6H_2O$						✓					✓				✓✓		
$KCl.MgCl_2.6H_2O$									✓	✓		✓					
30/A - 12 1	✓			✓		✓				✓	✓✓	✓	✓	(✓)	✓	-162°C, 1*600s, s'c brown	Na+Mg or Ca
30/A - 12 2	✓	✓				✓				✓	✓	✓	✓		✓	-162°C, 2*800s, s'c brown	Na+Mg or Ca
30/A - 12 5	✓									✓	✓	✓	✓		✓	-154°C, 2*600s, s'c clear	Na
30/A - 14 7	✓		✓	✓	✓				✓	✓	✓		✓			-180°C, 1*1800s, s'cooled	Na+Ca
30/A - 1 8	✓	✓			✓					✓	✓	✓			✓	-75°C, 1*1800s, s'cooled	Na+ice
30/A - 1 9	✓	✓		✓					✓	✓	✓				✓	-150°C, 2*900s, s'cooled	Ca+Na
30/A - 1 10	✓			✓						✓✓	✓✓	✓			✓	-167°C, 2*900s, 'grown'	Na (+Ca)
30/A - 14 11	✓			✓						✓	✓			✓	✓	-167°C, 2*900s, 'grown'	Na (+Ca)
10/E - 5 B11	✓		✓		✓			✓	✓✓		✓✓			✓		-180°C, 'grown'	Mg+Ca
10/E - 6 B13	✓		(✓)		(✓)			(✓)	(✓)			✓✓		✓✓		-180°C, hydrate on DM	Mg+Ca
3/A B22			✓		✓				✓	✓		✓				-170°C, 3*200s, 'grown' (l-v-ss)	$CaCl_2.6H_2O$

spectra were rarely produced (*Fig. 5.23A*). This phenomena is independent of the measurement of either grown or frozen hydrate-mixtures, and prevents the monitoring of metastable hydrate evolution on heating, believed to be responsible for the metastable and stable eutectics observed during microthermometric phase changes.

The effect of the cooling method on Raman Spectra

The resolution of spectra is higher when focusing the laser beam on a hydrate which has been grown using the sequential freezing method than one which has been formed by supercooling (*Fig. 5.23B*). This is a result of a grown hydrate having a better defined crystal structure on which the beam can be focused, rather than the beam being directed at a mixture of different hydrates, ice and water. However, the spectra produced using supercooled liquids can still be read, and is a quicker and more practical way of determining the hydrates in a small inclusion. This method also allows for the detection of a number of hydrates at once, which is not possible using a grown hydrate.

Results

In most cases, the laser beam was focused on a supercooled mixture of hydrates and gas, and in all cases an ice spectra was produced. None of the inclusions analyzed produced a Raman peak in the bending region (1500-1800 cm^{-1}). A summary of peaks obtained is given (*Table 5.5*). Most of these inclusions are of L-V-type, from chalcopyrite-bearing quartz veins or mineralized Rochas Bandadas. Sample 3/A was the only daughter mineral-bearing inclusion to produce a good spectra.

$NaCl.2H_2O$ is the dominant hydrate spectra in all of the runs. Other than hydrohalite, the single most dominant peak throughout the spectra is the 3232 cm^{-1} Ca.6 peak. In most cases, however, either one or both of the 3475 and 3508 cm^{-1} Ca.6 peaks are missing.

Given that Raman peaks for single hydrate species may vary in relative intensity depending on the orientation of the crystal (Dubessy *et al.*, 1982), only the peak positions, and not the relative intensities, can be used to identify a spectra. In terms of peak position, measured spectra in this study closely resemble a mixture of the tabulated hydrate peaks, including both $FeCl_3.6H_2O$ and $CaCl_2.6H_2O$, as well as hydrohalite. In the absence of the bending-region peaks, the spectra produced by a hydro-halide can therefore rarely be identified unambiguously. Although this combination of peaks implies that mixed hydrates are being formed, the most dominant peaks in those Raman runs which produced well defined spectra (*Fig. 5.24A* compared with *Fig. 5.24C*) correspond with the hydrohalite spectra of Dubessy *et al.* (1982). It can therefore be assumed that the major hydrate being formed in these fluid inclusions is that of hydrohalite.

Accuracy of Peak Position

Peak accuracy when calibrated using the spectra of fluorescent light (1122.6 cm^{-1}) is to ± 4 cm^{-1}. This is accurate enough to compare with the peaks documented by Dubessy *et al.* (1982), as the spectra

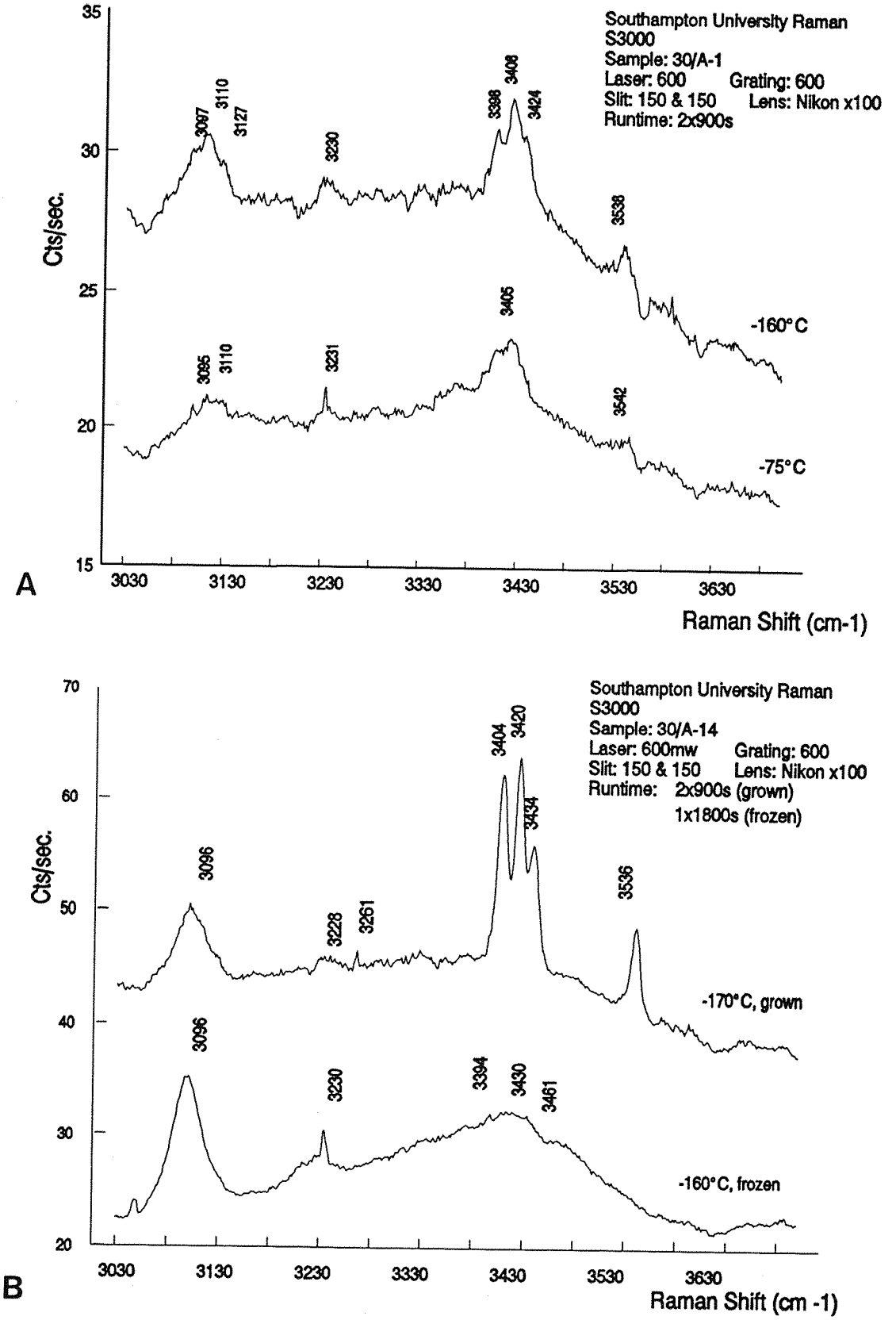

Figure 5.23 **Raman spectra for hydrates formed in type T1 fluid inclusions. A Variation in peak quality with temperature (-160° and -75°C); B Variation in Raman spectra by measuring grown and supercooled hydrates.**

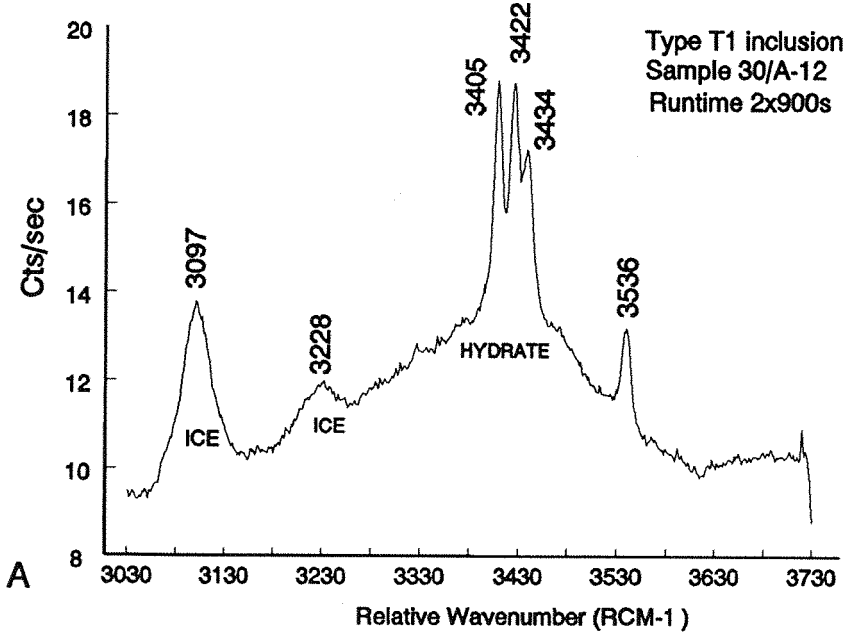

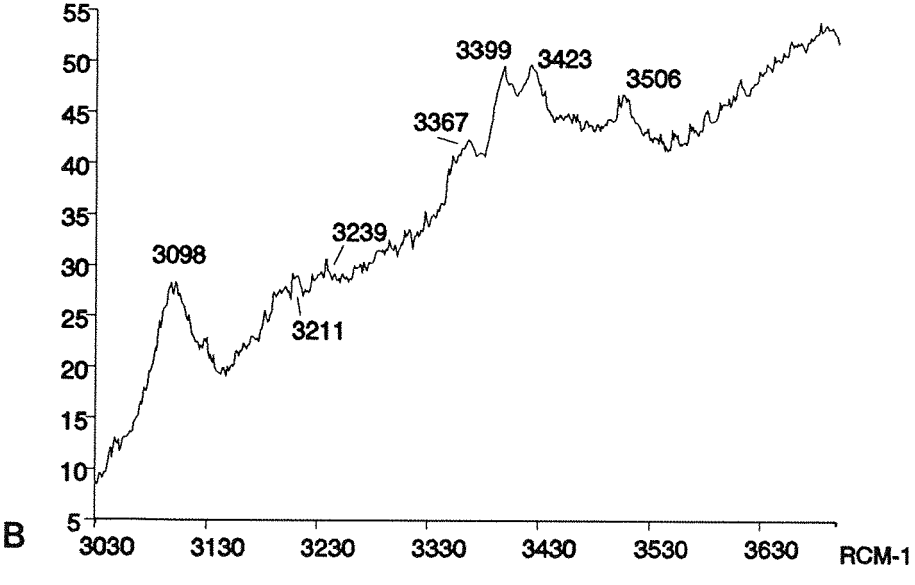

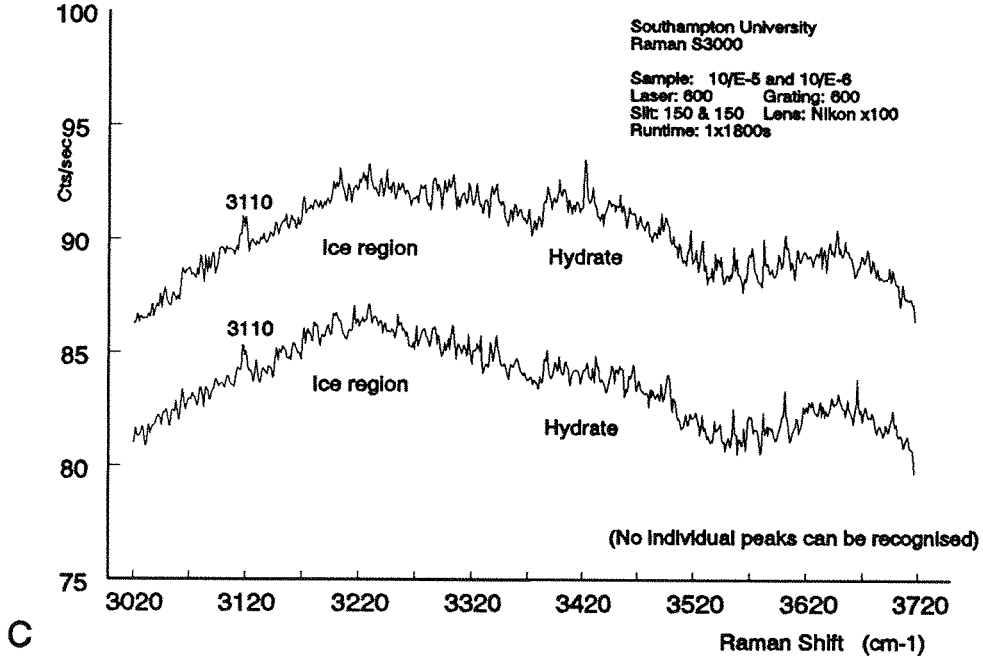

Figure 5.24 Raman spectra produced from frozen hydrates in fluid inclusions from the Pojuca C4 deposit. A. Hydrate grown in L-V T1 inclusion, at -170°C; B. Spectra of hydrates grown in inclusion 30/A-14 at -170°C, showing different peaks to those developed in 'A'; C. Raman spectra from hydrate mixtures grown in type T2 L-V-S inclusion - no defined peaks are produced.

are interpreted from the combination of peaks rather than the presence of one peak in particular. However, it can be seen that without the presence of the 'bending' peaks, the spectra are ambiguous and the accuracy to ± 1 cm^{-1} would not help.

Analysis of Inclusion 30/A-12

This inclusion is a type T1, L-V inclusion, of 15x8μm and 0.85 fill. Although it is small, it was used because it occurs in clear quartz, unobstructed by other inclusions around it, and it contained two different hydrates during microthermometric analysis. The inclusion displays first melting at -77°C, a rapid melting phase around -45°C, and Tm_{ice} at -29. Hydrohalite melts at a metastable +4.8°C, and a second, grey hydrate, is observed to melt at -9.7°C. The stable eutectic, T_{rm}, may be indicative of a calcium-bearing fluid, while the T_{fm} could indicate the presence of either a metastable Ca- or Mg- hydrate (Spencer *et al.*, 1990).

The inclusion has been run several times under slightly varied conditions to analyze for hydrates, and the dominant peaks are the 3101 and 3425 cm^{-1} ice and hydrohalite peaks respectively (*Table 5.5*). Other peaks have also been recognised, including the 3327 cm^{-1} peak, which may either be an ice, $MgCl_2.12H_2O$ or $FeCl_3.6H_2O$ peak, and at 3475 and 3232 cm^{-1}, which are not documented in any of the hydrates generated by Dubessy *et al.* (1982), neither are they 'laser' lines or quartz peaks. The 3327 cm^{-1} peak is present in only the first two of the three 30/A-12 runs. In these two, the inclusion was observed to freeze to a brown, granular solid rather than a clear solid, and it would appear, therefore, that the granular appearance and brown colouration in the first two runs was produced by the presence of either antarcticite $FeCl_3.6H_2O$ or $MgCl_2.12H_2O$. It is also clear, however, that the main spectra for each of these hydrates (3538 and 3398 cm^{-1} respectively) was not produced in either case, suggesting that the dominant hydrate throughout is $NaCl.2H_2O$, with the presence of an additional, possibly co-existing, possibly mixed, unknown hydrate.

Using the 'growth' method of hydrate formation, only the solid with the highest melting point may be grown to a suitable size for analysis. Spectra were not produced for any of the subsequent solids formed in any fluid inclusions. In the case of low salinity fluids, where the 'final' solid is ice, large hydrate crystals can not be formed. In high salinity fluids, the residual solid will be a hydrate, but in a complex fluid several hydrates may be formed at low temperatures, and in most naturally occurring fluid inclusions only one of these, the largest and first formed, can be analyzed successfully. In the case of all fluid inclusions studied from the Pojuca deposit, this hydrate was found to be hydrohalite, although the formation of other peaks not assigned to the hydrohalite spectra means that in the case of complex fluids, until detailed spectra for more hydrates are available, LRS is not a useful tool in the identification of fluid composition.

5.5.3 *Experimental technique for the LRS analysis of Type T3 inclusions:*

Analysis of the gas composition of carbonic inclusions is undertaken using the equipment

described in section 5.5.1, but is carried out at room temperature so the heating-freezing stage is not necessary. The doubly-polished quartz wafer is placed directly on the sample stage and the laser beam focused in the gas phase. Ideal times for the formation of gas peaks depends on the condition of the quartz chip, but in most cases x minute runs on the appropriate areas produced good spectra.

Using a grating of 1800 cm^{-1} (intermediate slit 7mm), the laser Raman was centred at 1320 to detect the 1285 cm^{-1} and 1388 cm^{-1} CO_2 peaks, 2330 cm^{-1} for the N_2 peak and 2917 cm^{-1} for the CH_4 peak.

Gas components can be quantified using the integrated peak ratios of the 2917 cm^{-1} CH_4 peak and the 1388 cm^{-1} CO_2 peak. The Dubessy (1989) and Kerkhof and Kisch (1993) method has been adopted to calculate peak ratios:

$$Z\ CO_2 = Area\ CO_2\ (1388) \ /\ 1.49 \qquad \textit{(Equation 5.3)}$$

and

$$Z\ CH_4 = Area\ CH_4\ (2917) \ /\ 7.57 \qquad \textit{(Equation 5.4)}$$

where: Z = molar fraction in the carbonic phase
1.49 and 7.57 are the relative Raman cross-sections, and have been calculated for the 514.532-nm laser (Dubessy, 1989)

There is some controversy over the relative Raman cross-sections by which to divide the areas of the 2917 cm^{-1} CH_4 and 1388 cm^{-1} CO_2 peaks. The 1.49 and 7.57 values used by Dubessy (1989) have been chosen as they were calculated for a laser of the same wavelength as that used at Southampton, but it has been shown that the choice of values does not significantly alter the geological interpretation of the CH_4:CO_2 ratio.

Density of the aqueous phase (ρ_L) is estimated from the degree of fill and the density of the NaCl solution, by assuming that the density of the solution is ≈1.1 (at 10-15 wt% NaCl eq.; Shepherd *et al.*, 1985) and density of the gaseous phase (ρ_V) calculated using ZCH_4 and Th_{CO2} (van den Kerkhof, 1988). The bulk composition can be calculated using the equations of Ramboz *et al.* (1985):

$$nCO_2 = \frac{F.\rho_v.Z_{CO_2}}{44-16Z_{CH_4}-28Z_{N_2}} \qquad \textit{(Equation 5.5)}$$

$$nCH_4 = \frac{F.\rho_v.Z_{CH_4}}{44-16Z_{CH_4}-28Z_{N_2}} \qquad \textit{(Equation 5.6)}$$

$$nH_2O = \frac{(1-F).\rho_L}{18} \qquad \textit{(Equation 5.7)}$$

The molar fraction of each species (CO_2, CH_4 and H_2O in this case) is calculated using the following

Ramboz *et al.* (1985)equation:

$$X_i = \frac{ni}{nH_2O+nC_2O+nCH_4} \qquad \textit{(Equation 5.8)}$$

ρ_v is determined from Th_{CO2} and Z_{CH4} using CH_4-CO_2 molar volume graphs (Kerkhof, 1988), and ρ_{bulk} from the equation:

$$\rho_{bulk} = \rho_V F + \rho_L(1-F) \qquad \textit{(Equation 5.9)}$$

where: ρ_V = Density of carbonic phase(s)
ρ_L = Density of aqueous phase
F = Degree of fill (Carbonic phase)
n = Bulk composition of fluid inclusion
X = Bulk molar fraction of species

5.5.4 *Analytical Results for type T3 inclusions*

Laser Raman Spectroscopy carried out at room temperature on type T3 fluid inclusions has shown the presence of CO_2 and CH_4 in the carbonic phase, with pronounced peaks at 1288, 1388 and 2917 cm^{-1} (*Fig. 5.25*). Eight inclusions were analyzed, covering a variable fill, Tm_{CO2} and Th_{CO2} range on order to test for a correlation between decreasing Tm_{CO2} and Th_{CO2} and increasing CH_4 content. The molar fractions for the carbonic type T3 inclusions are calculated and presented in *Table 5.6.*

Bulk compositions (X) range from 2.6 to 14.6 mol.% CH_4, 19 to 64 mol.%. CO_2 and 28 to 73 mol.% H_2O, with CO_2-CH_4 ratios (Z) between 93:7 and 74:26. Although a general correlation exists between Th_{CO2}, Tm_{CO2} and ZCH_4 (*Fig. 5.26*), showing that as ZCH_4 increases, Tm_{CO2} and Th_{CO2} both decrease, these do not lie on a perfect straight line. In reality, only inclusions with equal molar volume in the carbonic phase can be compared, and points of equal molar volume have therefore been joined in *Figures 5.26A&B*, which also show the predicted lines of Tm_{CO2} and Th_{CO2} according to Heyen *et al.*, (1982). These show that, in the case of Th_{CO2}, data of equal molecular volume does indeed follow the correlation expected. However, this is not the case for the Tm_{CO2} data, with the data plotting outside the expected field, and no correlation existing.

The Raman ZCH_4 data against Th_{CO2} (in the absence of clathrate) has been plotted on *Figure 5.27*, from which it is clear that the measured Tm_{CO2} is different to that expected, in most cases by more than 0.5°, which is the allowed error margin used for this phase change (see section 5.4.1). The laser Raman at Southampton has been calibrated and is believed to be accurate to $\pm 4\%CO_2$ (totalled to 100%; Roberts and Kerkhof, *pers.com.*), which suggests that although microthermometric data gives an indication of relative CH_4 content, it cannot be used to accurately evaluate the volume of CH_4 in a fluid inclusion at room temperature. This is in agreement with the work of Seitz *et al.* (1987), who have found that methane is depleted in residual fluids at low temperature in the H_2O-CO_2-CH_4 system, due to the

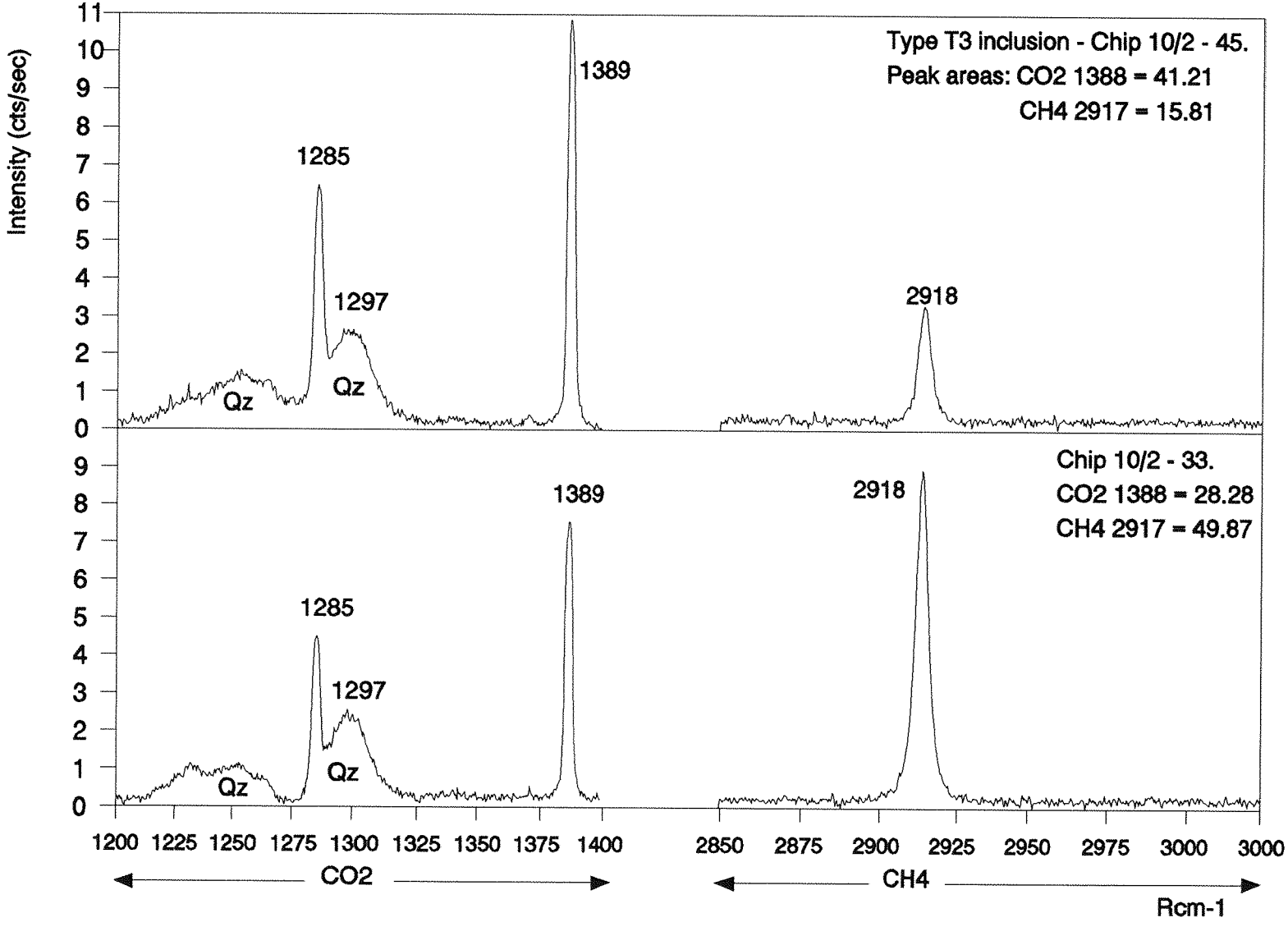

Figure 5.25 Raman spectra from the carbonic phases in type T3 aqueo-carbonic inclusions, with laser beam focused in the liquid CO2. Spectra show variation in CO2:CH4 ratios.

Table 5.6 **Raman Analyses of Type 3 CO_2-CH_4 fluid inclusions. Z = mol. fraction of gas phase, X = mol. fraction of total inclusion. d_V = density of gas phase (calculated using Kerkhof, 1988), d_L = density of aqueous phase, (calculated using ref.---), d_{bulk} = bulk density, Tm and Th $_{CO2}$ from microthermometric analyses, mol.volumes from FLINCOR program.**

Sample	CO2 Peak area	CH4 Peak area	Z_{CO2}	Z_{CH4}	Fill (CO2)	Mol.Vol (Carbonic Phase	d_V g/cm^3	d_L g/cm^3	X_{CO2}	X_{CH4}	X_{H2O}	d_{bulk}	Tm_{CO2}	Th_{CO2}	Mol.Vol cm^3/mol (total)
10-2/32	88.262	42.483	0.913	0.087	0.5	63	0.718	0.550	0.325	0.031	0.645	0.634	-57.4	15.4	41.7
10-2/33	28.285	49.873	0.742	0.258	0.7	100	0.398	0.320	0.421	0.146	0.433	0.375	-58.7	12.6	76.5
10-2/36	24.991	39.357	0.763	0.237	0.6	does not lie on plot		0.440					-60.6	17.5	?
10-2/38	58.300	100.200	0.747	0.253	0.5	92	0.434	0.550	0.196	0.066	0.738	0.492	-61.7	9.3	46.7
10-2/39	17.303	8.401	0.913	0.087	0.5	84	0.538	0.550	0.267	0.026	0.708	0.544	-57.1	22.5	45.8
10-2/42	12.329	10.499	0.856	0.144	0.5	92	0.472	0.550	0.231	0.039	0.730	0.511	-58.4	19.2	46.8
10-2/44	41.218	15.801	0.930	0.070	0.6	66	0.693	0.440	0.463	0.035	0.502	0.592	-59.8	17.5	50.6
10-2/02	62.751	31.302	0.911	0.089	0.7	56	0.806	0.320	0.649	0.064	0.287	0.660	-58.5	7.5	52.6

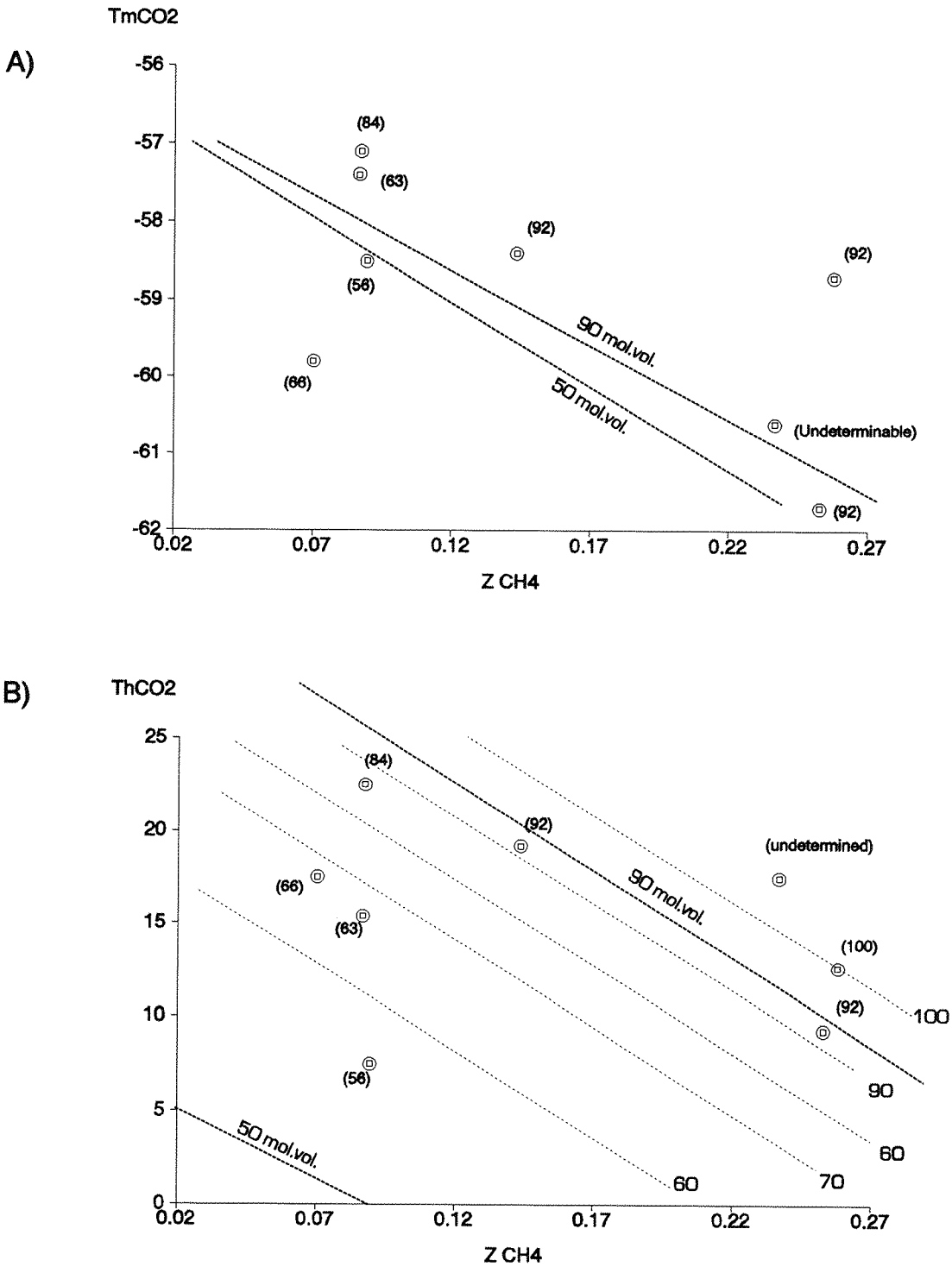

Figure 5.26 **Relationship between: A Tm_{CO2} and ZCH_4; B Th_{CO2} and ZCH_4. Thick dashed lines = predicted positions (after Heyen *et al.*, 1982) and dotted lines = measured molecular volume (Raman). A relationship between molar volume, Th_{CO2} and methane content is apparent. Actual mol.vol. in brackets. 40, 50, 60 etc = g/cm^3.**

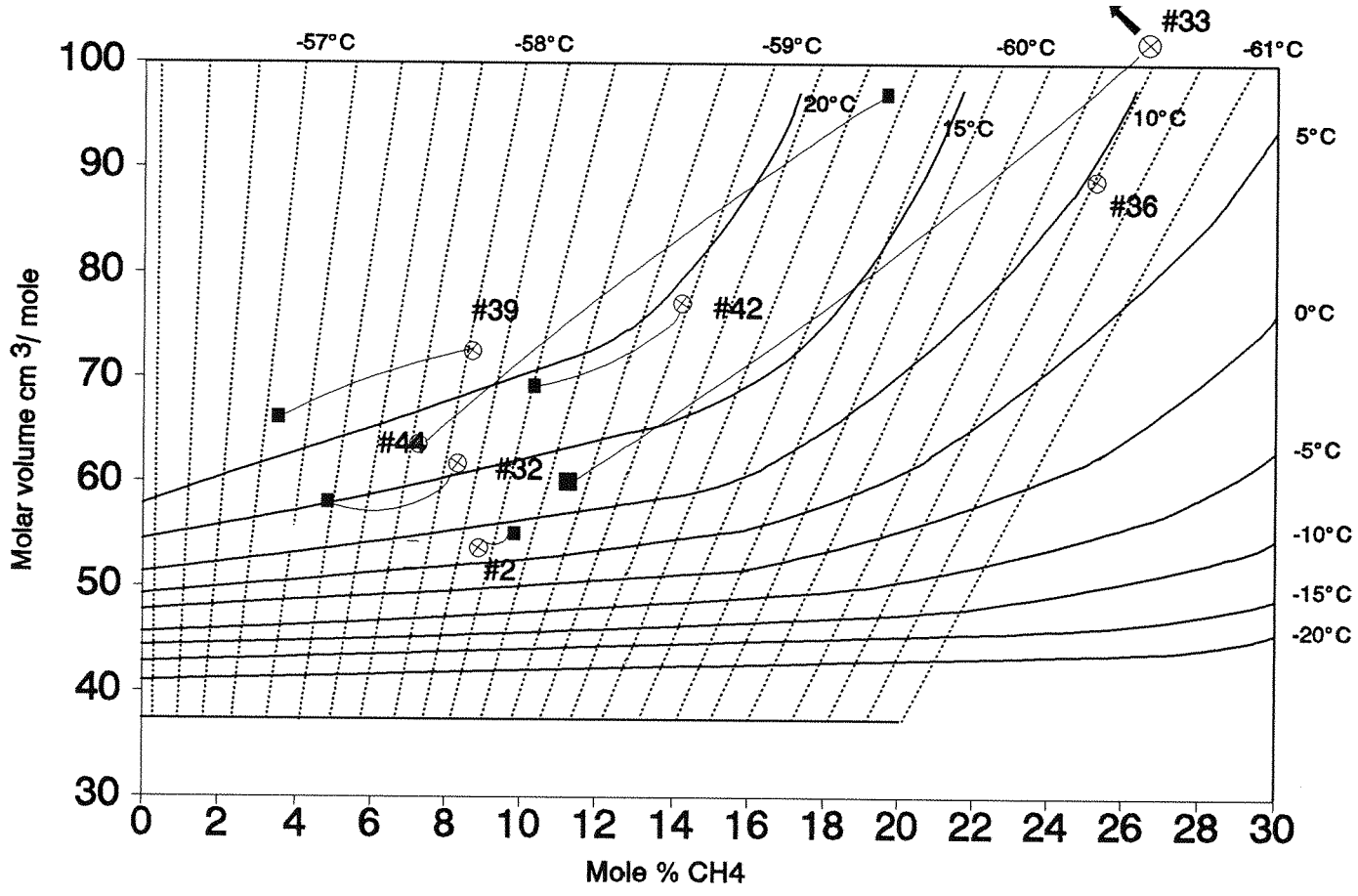

Figure 5.27 **Graph showing the mole composition of CO_2-CH_4 mixtures of type T3 carbonic inclusions analyzed using laser Raman spectroscopy. Raman vs. microthermometric positions plotted. Solid lines = Th_{CO2}, dashed lines = Tm_{CO2}. Sample numbers in brackets. (After Heyen *et al.*, 1982)**

presence of clathrate, which, at the CO_2 triple point, preferentially consumes CH_4 over CO_2, therefore underestimating CH_4 content in the carbonic phase.

5.6 *DICP ANALYSIS OF FLUIDS FROM THE POJUCA C4 DEPOSIT*

The complex fluid compositions made evident by the microthermometric study of types T1 and T2 inclusions demands the use of a method of direct geochemical analysis to determine the dissolved components present in the fluids.

Inductively-coupled plasma (ICP) laser ablation spectroscopy of single inclusions, as described by Rankin *et al.* (1992), was carried out on some of the larger (up to 20μm) highly saline inclusions present in the Pojuca Rochas Bandadas quartz. This, however, proved unsuccessful as the area ablated by the laser beam is between 75 and 100μm across, and invariably contained minute traces of silicate minerals such as biotite and grunerite. Fluid inclusions from vein quartz, although hosted by 'clean' quartz, are small (10 to 15μm) and do not contain sufficient volumes of fluid to exceed the minimum detection limit of the spectrometer. The bulk method of decrepitation was therefore employed to determine fluid chemistry.

5.6.1 *Experimental Technique*

Decrepitation-linked inductively-coupled plasma atomic emission spectroscopy (D-ICP) was applied using the equipment at Imperial College, London, on clean chips of quartz from several vein generations. D-ICP involves the thermal decrepitation of fluid inclusions in quartz contained in a silica tube and heated to 600°C. The resulting volatilised material (fluid ± daughter minerals) is carried in a steady stream of argon gas into the plasma torch of the spectrometer.

The D-ICP method has the advantage that only the components contained in the fluid inclusions, and easily oxidised elements such as sulphur from sulphide minerals, will be volatilised, and gangue minerals such as silicates will not be included. There is also the disadvantage that multiple fluid populations will be analyzed in single samples if quartz chips are not picked with extreme care, and that daughter minerals may not be released and the quantity of elements contained therein may be underestimated.

0.2g of clean quartz chips (preparation technique documented in *Appendix D1.3*) has been proved to be the optimum sample size for reproducible results using D-ICP (Wilkinson,J.J., *pers.com.*, 1993). The careful picking of quartz can, to some extent, limit the inevitable problems caused by the presence of multiple populations and fluid compositions in a sample, and results from this bulk geochemical method must be treated carefully.

Decrepitation ICP was unavoidably carried out using two separate spectrometers. Samples labelled with the suffix *'J'* were run on a machine with a lower detection level than those with no suffix. Two splits of each sample *'J'* were run, and the reproducibility generally good (less than 20% variation)

for each split. To compare data from each spectrometer, three samples were run on both machines. The result, shown clearly in *Figure 5.28*, is the apparent absence of some elements in the same sample.

Data is automatically calculated to a sodium ratio, by obtaining the peak area for each element (in kilopulses) and removing background level (acquired by running a blank between each sample), and calibrated with respect to a standard. Detection limits are much better for the second set of data (the 'J' samples) than the first, and so 'J' samples are used to look at elemental variation through the vein types.

Table 5.7 **D-ICP ratios against sodium for fluid inclusions: bulk analyses. (sufix W = white quartz, suffix C = clear quartz, where two splits of the same sample are taken).**

Na/Element		Ca	K	B	Li	Cu	Zn	Mg	P	Fe	Mn	Ba	Cr	Sr
F73	IF	2.6	5.2			3002	158	730		39	68	80		176
G33	Qz-Bi		8.7			914	1158	1579		111	201	221		223
G90J	(Q1)	2.6	4.9	ERR	341	1374	413	215	81	94	222	217	362	219
F14	Qz-Cpy	2.3	9.4			1127	1030	131		608	794	376		296
F14J	(Q2-A)	2.3	11.0	1106	147	8984	5500	1585	262	1998	1089	471	1644	368
G34	"	2.2	5.4			5994	456	1181		209	221	197		133
G80	"	1.8				0	4154	864		218	159	201		184
G92	"	4.5	5.4			7411	217	1374		77	129	125		250
G93	"	2.0				2293	0	89		0	239	343		17
F74WJ	Qz-Bi	2.5	11.0	1022	210	ERR	2562	864	254	985	794	454	1199	393
F74CJ	±cpy	2.7	14.8	672	216	ERR	4271	671	ERR	1402	613	454	828	415
F94W	(Q2-B)	2.1	9.3			3716	380	271		277	73	146		232
F94WJ	"	2.1	8.0	257	194	ERR	293	3379	837	196	78	164	1945	271
F94CJ	"	1.95	9.3	222	166	5102	265	1578	568	140	74	119	812	228
G100J	"	1.8	6.2	896	592	ERR	60	1622	507	72	173	85		136
G91	BARREN	1.8				5329	196	0		384	68	192		127
G99	(Q3)	2.6				7227	1350	531		1118	172	222		175
G99J	"	3.9	ERR	ERR	166	ERR	232	42	ERR	ERR	210	194		249
G95	Qz-Cc	3.9				1148	2737	120		1202	2157	425		309
G97	"			Below	Detection	Limit								
F96J	"	3.9	17.0	802	237	ERR	1185	545	ERR	703	689	447	1355	385
F97J	"	3.0	9.9	ERR	672	ERR	ERR	131	ERR	ERR	1182	387	160	251

5.6.2 *Analytical Results*

Because the volume of material analyzed is not known, a ratio method must be employed to interpret D-ICP data (Wilkinson, 1990). Computer generated ppm equivalent are traditionally ratioed to sodium, the most abundant cation in most crustal fluids (Alderton *et al.*, 1982), and Na:element ratios provide an immediately interpretable graphical representation of cation content.

Table 5.7 shows the results of D-ICP analysis for all elements which exceeded both the detection limit and the blank sample values. The results are tabulated according to quartz-type, i.e. barren quartz±biotite (Q1), quartz-chalcopyrite and quartz-biotite±chalcopyrite (Q2), quartz-calcite (Q3) and Rochas Bandadas quartz.

It is clear that fluid inclusions in all generations are dominated by sodium and calcium, while potassium, although also present, is far less abundant. The composition of individual fluid populations in a vein set is best estimated by ratioing average vein-fluid data to sodium, as presented in *Table 5.7.*

Table 5.8 **D-ICP. Element ratios to 10,000ppm Na, for fluids from four distinguishable vein sets (data from 'J' samples; shaded values represent the major influx of the particular element)**

Vein type	Qz±Biot	Qz-Cpy±Bi	Qz-Cpy-Biot	Qz-cc
Generation	Q1	Q2-A	Q2-B	Q3
Na	10,000	10,000	10,000	10,000
Ca	3500	**4500**	**5000**	2800
K	**2000**	800	**1100**	900
B	-	10	20	12
Li	30	**70**	50	40
Cu	10	-	-	-
Zn	20	20	**40**	20
Mg	**50**	10	10	**150**
P	**120**	40	20	-
Fe	**110**	70	**100**	10
Mn	50	50	**70**	50
Ba	40	50	**100**	50
Cr	30	10	10	20
Sr	50	50	50	50

Table 5.8 indicates peaks in certain elements which may suggest their affinity to certain vein generations. For example, Mg has its maximum in the quartz-calcite veins (Q3) and is barely present in other vein types, while Zn, Ba and Ca peak in qz-cpy±biot (Q2) veins, suggesting that their presence in earlier vein sets is due to secondary fluid inclusions of Q2 age.

A similar pattern to that observed in *Table 5.8* is indicated by the graphic representation in *Figures 5.28A-C*, which plot each sample separately. although the peaks are not so apparent.

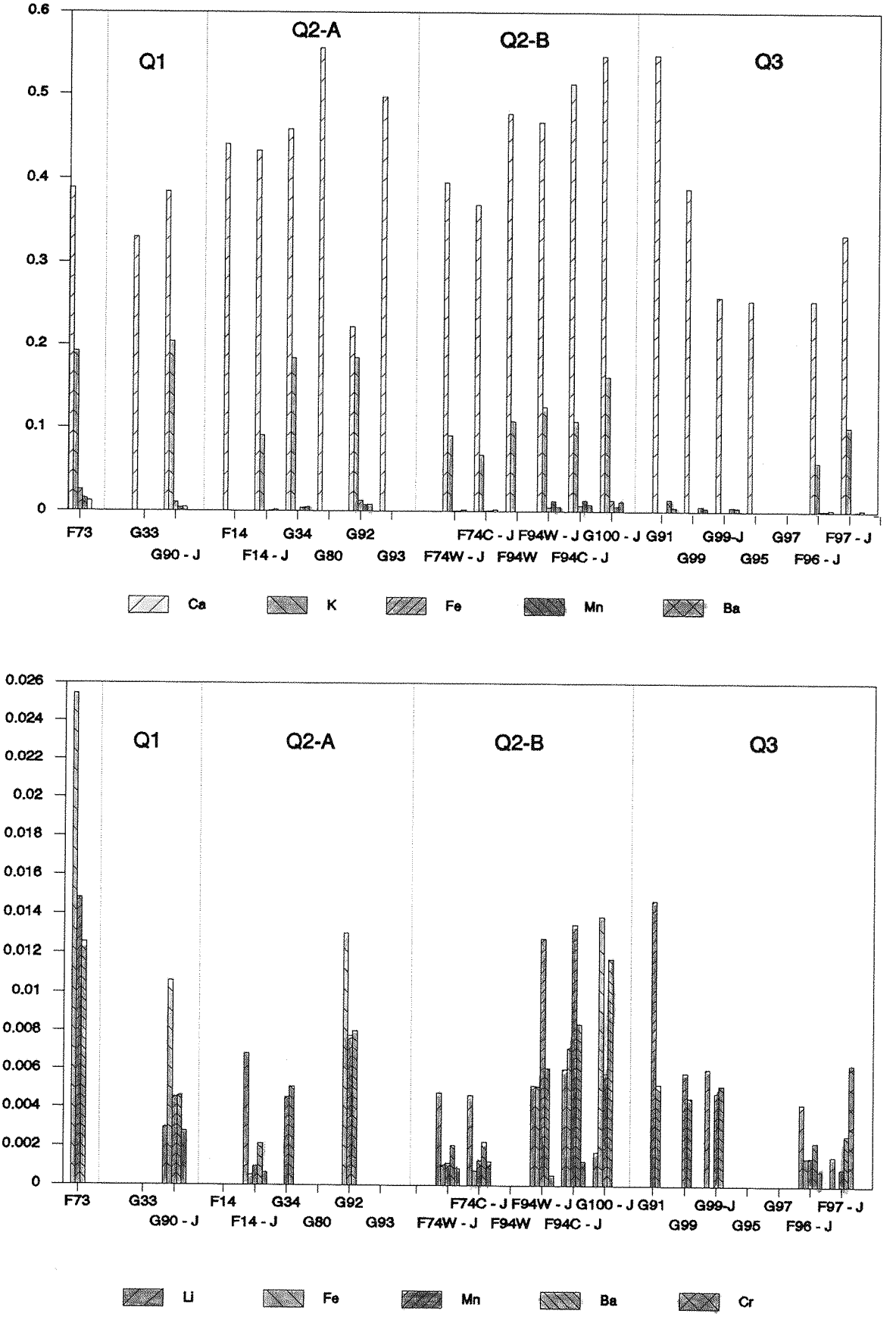

Figure 5.28 **Graphic representation of the DICP results for types Q1, Q2-A, Q2-B and Q3 veins. Each element ratioed to sodium.**

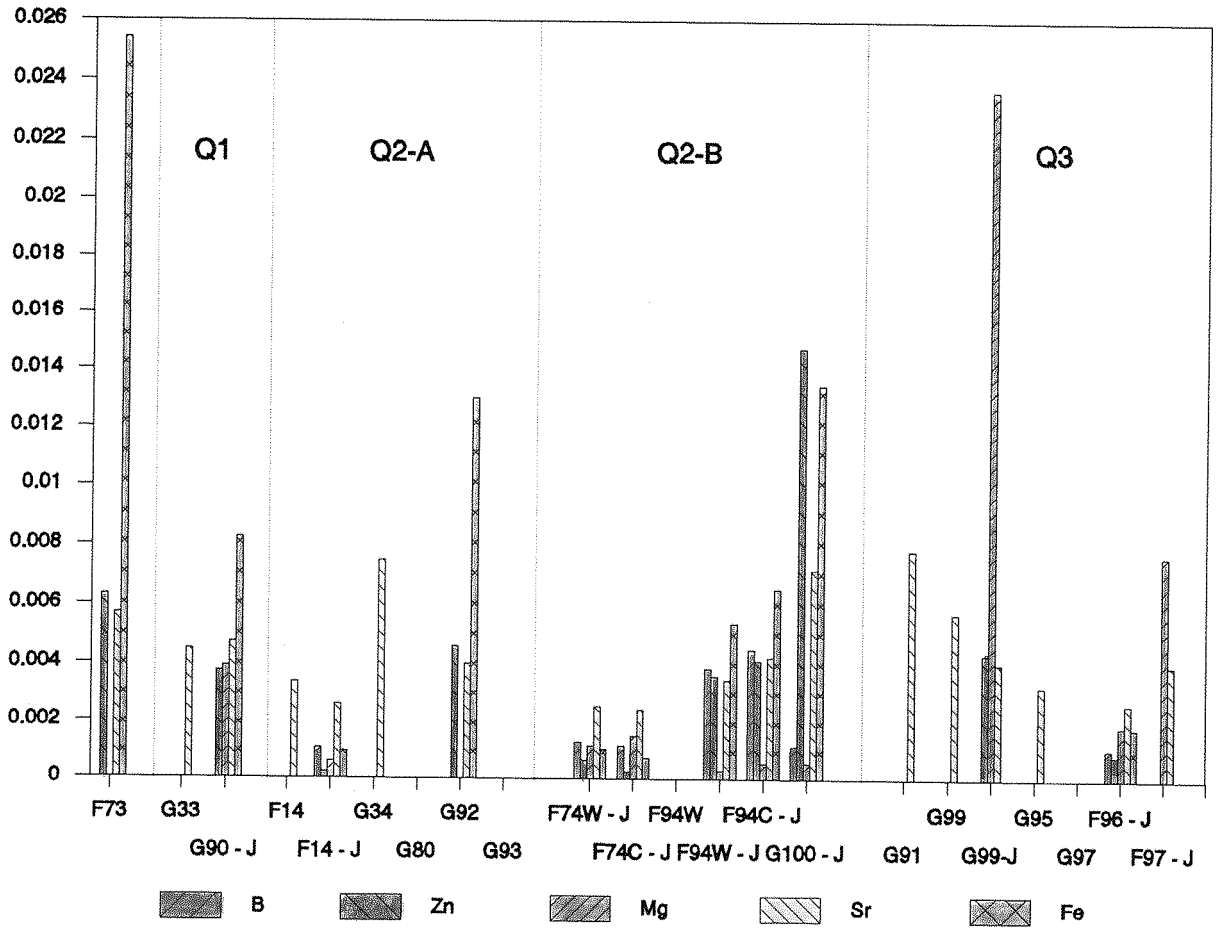

Figure 5.28 (cont..) **Graphic representation of the DICP results for types Q1, Q2-A, Q2-B and Q3 veins. Each element ratioed to sodium.**

Figures 5.28B&C also display the enrichment of Mn and the corresponding depletion in Ba and Fe in the barren quartz and quartz-calcite veins relative to the sulphide- and biotite-bearing quartz. A comparison between different quartz types within a single sample has been made by separating 'clear' quartz, believed to be related to mineralization, from 'white' quartz during sample preparation. This was done using samples F94 and F74. *Figure 5.28A* shows that the white quartz, in each case, apparently contains more potassium relative to sodium, while the patterns of elemental ratios for all the minor elements in F94C and F94W (*Fig. 5.28B&C*) are virtually identical, but with different intensity. The relative concentrations of all elements except Na are therefore the same in the white as in the clear quartz, and the white quartz has a higher Na content. This is suggestive that the white quartz, which was probably precipitated earlier than the clear quartz and rich in primary Na-bearing inclusions, was enriched in the trace elements by secondary the fluids responsible for clear quartz deposition.
A fluid composition can thus be established:

Table 5.9 **Summary table of the vein fluid chemistry in the major quartz-vein types in the Pojuca C4 deposit.**

Vein Type	Fluid Chemistry
Qz-Biot (Q1)	Na, Ca, K ± Fe, P, Mg
Qz-cpy (Q2-A)	Na, Ca
Qz-cpy-biot (Q2-B)	Na, Ca, K, Fe
Qz-cc (Q3)	Na, Mg ± Ca, K

5.6.3 *Alkali Geothermometry*

Alkali geothermometry is a relatively simple method of estimating the last rock-water equilibrium temperature of veins by utilizing D-ICP data. It is based on the principal that the alkaline cations present in a fluid are in equilibrium with the surrounding wall-rock and is independent of pressure (Giggenbach, 1988). Several geothermometers are available, using Ca-bearing mineral assemblages such as feldspar-mica-calcite or plagioclase-epidote-calcite to establish an equilibria with Na-K-Ca fluids (Truesdell, 1976; Giggenbach, 1988; Fournier, 1981 and Fournier and Truesdell, 1973).

Fluid-rock equilibria is rare in most hydrothermal systems (Giggenbach, 1988), and there is no definite evidence for a equilibrium existing in the Pojuca deposit. The application of alkali geothermometers may, therefore give erroneous results, and must be used with a certain amount of caution. The abundance of mica in both the wall-rock and quartz veins, as well as the high alkali-element concentration in the fluids, however, suggests that at least some degree of equilibrium was attained during

vein formation, and the method can be applied to calculate approximate temperatures of formation which can then be combined with microthermometric data to provide a more accurate interpretation than would otherwise be possible.

Table 5.10 **Formation temperatures calculated using alkali geothermometer equations of Fournier (1976), Truesdell (1981) and Giggenbach (1988).**

	Truesdell 1976	Fournier 1981	Giggenbach 1988	Fluid Type
Qz-biot (Q1)				
G33	203.0	229.2	243.7	Mainly
G90-J	279.7	286.9	296.5	Type T1
Qz-cpy (Q2)				
F14-J	177.5	209.0	224.8	Type T1
G34	265.1	276.2	286.8	and
G92	265.1	276.2	286.8	Type T2
Qz-biot-cpy (Q2)				
F74W-J	177.5	208.9	224.8	
F74C-J	148.8	185.6	202.8	Mainly
F94W-J	195.5	223.3	238.2	Type T2
F94C-J	212.8	236.9	250.8	
G100-J	245.5	261.7	273.6	
Qz-cc (Q3)				
F96-J	136.7	175.4	193.2	Type T1
F97-J	188.6	217.9	233.1	Low salinity

Results

The main problem encountered while using alkali geothermometry on D-ICP data is the presence of multiple fluid inclusion populations in a single sample, as discussed in section 5.6.1, so that it is impossible to acquire Na/K ratios for single fluid types. It must, therefore, be assumed that the majority of inclusions in a single sample are primary and represent the overall composition of the vein-generating fluid. i.e. that early quartz-biotite (Q1) veins and quartz-chalcopyrite (Q2-A) veins are rich in type T1 moderate salinity inclusions with some secondary type T2 inclusions and Q2-B veins contain predominantly type T2 highly saline inclusions, while Q3 quartz-calcite veins contain low salinity type T1 l-v inclusions.

Based on the Na/K geothermometers, fluids from the main mineralizing stage (Q2-A) range in temperature from 210 to 276° (Fournier, 1981) or 225 to 286°C (Giggenbach, 1988). This corresponds approximately with the upper range of homogenization temperatures established for type T1 inclusions

using micro-thermometry (*Fig. 5.15*). Fluids from late-stage, biotite-bearing, mineralizing veins (Q2-B) yield temperatures in the range 185 to 236 or 202 to 273°C using the Fournier (1981) and Giggenbach (1988) equations respectively. These are slightly lower than for the Q2-A fluids, as would be expected from later fluids, and again compare well with type T2 homogenization and dissolution temperatures. Interestingly, 'white' quartz yields higher formation temperatures than 'clear' quartz from samples F74 and F94, indicating that the white slightly pre-dates the clear quartz.

Quartz-biotite veins believed to be representative of Q1 hydrothermal activity yield the highest temperatures, at up to 296.5°C using Giggenbach's (1988) equation, while quartz-calcite, believed from structural relationships to be the latest fluid phase, gives the lowest formation temperature, as low as 136.7°C (Truesdell, 1976).

5.7 *INTERPRETATION OF FLUIDS IN THE POJUCA C4 DEPOSIT*

Full interpretation of the fluids, particularly of types T1 and T2 inclusions, from microthermometric data alone is not absolute, and the addition of D-ICP and Raman analyses has allowed the hydrothermal fluid compositions to be constrained further.

5.7.1 *Estimation of Trapping Conditions*

Pressure and temperature of entrapment of fluid inclusions can be determined by constructing lines of equal density with respect to temperature and pressure, or *isochores*. Although it has been shown that P-V-T properties of mixed systems (Ca-Na-K-Mg-Cl-H_2O) can be modelled according to the relatively simple NaCl-H_2O system to within 1% error (Potter and Clynne, 1978), the system Na-Ca-K-Cl-H_2O, developed by Zhang and Frantz (1987), has been used to construct isochores for types T1 and T2 fluid inclusions following D-ICP analysis which showed the dominance of these cations in the Pojuca fluids. Type T3 inclusions in the CO_2-CH_4-H_2O system are modelled using the FLINCOR computer programme, utilizing the Holloway (1981) equation of state.

The computer programme ZANG constructs isochores for aqueous solutions and requires knowledge of wt.% NaCl, $CaCl_2$ and KCl and Th_{L-V}. Isochores are generated for temperatures from homogenization to ~1200°C. For fluid inclusions in most natural hydrothermal systems it is necessary to consider temperatures only up to ~700°C. The salinities used for these constructions were calculated from Tm_{Ice} and Ts_H (L-V and L-V-S inclusions respectively). Ts_H gives an underestimate of salinity in L-V-S-S inclusions, as solubility data is unavailable for these multi-component systems. Salinities of fluid inclusions in which $Tm_{Ice} \leq 28$°C (the metastable eutectic for the NaCl-H_2O system; Davis *et al.*, 1990), cannot be estimated using the Potter *et al.* (1978) method (Equation 5.1), and ternary diagrams for mixed systems must be employed. These give salinity as Wt% Na and Ca individually, and isochores can be plotted more accurately using the Zhang and Frantz equation, although *Figure 5.29* shows that the discrepancy between

isochores generated using the two methods of salinity estimation is minimal.

Isochores have been constructed for vein fluids, for which alkali geo-thermometers are available, and for inclusions from the metasedimentary units of types T1, T2 and T3.

Type T1: Rochas Bandadas.

Using the Zhang and Frantz (1987) equation of state, isochores were calculated for the modal Th and Wt% NaCl eq. values of 192-225°C and 19-27.5% respectively (*Fig. 5.30*). Given that the maximum temperature of halite dissolution in these inclusions is at 283°C, a minimum trapping pressure of ~1Kb is found, corresponding with the trapping temperature of 286°C given by the alkali geothermometer. In the absence of a definitive upper geothermometer, maximum trapping conditions can only be estimated, using the peak metamorphic conditions (U.Greenschist - L.Amphibolite, 480°C, 5.5Kb) and the pressure conditions of the synchronous development of green hornblende in the Rochas Bandadas (see Chapter 3), which has been estimated at between 3 and 5Kbar. These maximum conditions are coincident, giving a maximum trapping temperature of 470°C (*Fig. 5.30*).

Type T1: Q2-A Veins.

Isochores for type T1 inclusions in quartz-rich mineralizing veins have been constructed using microthermometric data from chips 17, 26, 30, 31, 35, 36, 40 and 41 (*Fig. 5.31*). Isochore A uses the minimum modal values, of 180°C and 12 Wt% Nacl eq., while isochore B uses the maximum values, 220°C and 15 Wt% NaCl eq. (homogenization and salinity respectively). No Ts_H is available to use as a lower limit for these inclusions, but the Q2-A-vein alkali geothermometer provides a minimum equilibrium temperature of 286°C, corresponding with a minimum pressure of 1.2Kb. This temperature compares well with that obtained as a lower limit in *Figure 5.31A*. The upper limit of 5Kbar, used for the host rock T1 fluid inclusions, has been applied in the absence of a more suitable ceiling, giving a maximum temperature of ~450°C.

The vein and host rock isochores for type T1 inclusions are of limited use in the absence of an independent geothermometer, but from the information available it can be estimated that the fluids were trapped under PT conditions of between 286 and 470°C, and 1.2 and 5Kbar

Type T2: Rochas Bandadas.

Isochores were plotted for type T2 inclusions from the host-rock quartz using minimum and maximum modal values of Th (160-215°C) and salinity (21-35%). These isochores are plotted in *Figure 5.30B*. A maximum Th_{TOT} is seen by the dissolution of halite at 494°C, although measurements at such high temperatures are uncommon. Most of the daughter minerals show complete dissolution before ~290°C, or do not dissolve prior to decrepitation. This gives approximate minimum trapping conditions of 290° and 1.5 Kbar. The only limit on maximum P-T conditions can be given by the estimated hornblende formation pressure used for type T1 inclusions. However, given the geological history, type

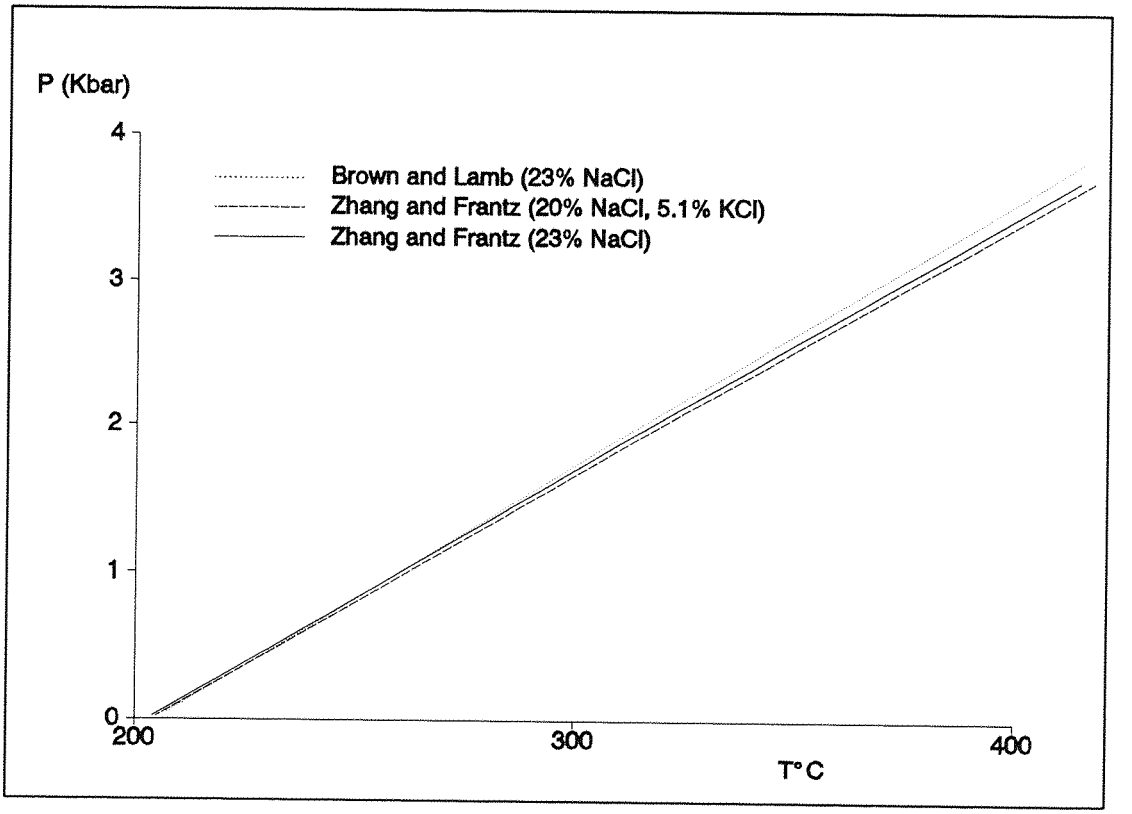

Figure 5.29 **Isochores plotted using two methods of calculation: Zhang and Frantz (1987) and Brown and Lamb (1989), to show that little variation exists between the methods.Isochores calculated for 23 Wt.% NaCl and Th_{L-V} 205°C, and for 20% NaCl, 5.1% KCl and 205°C.**

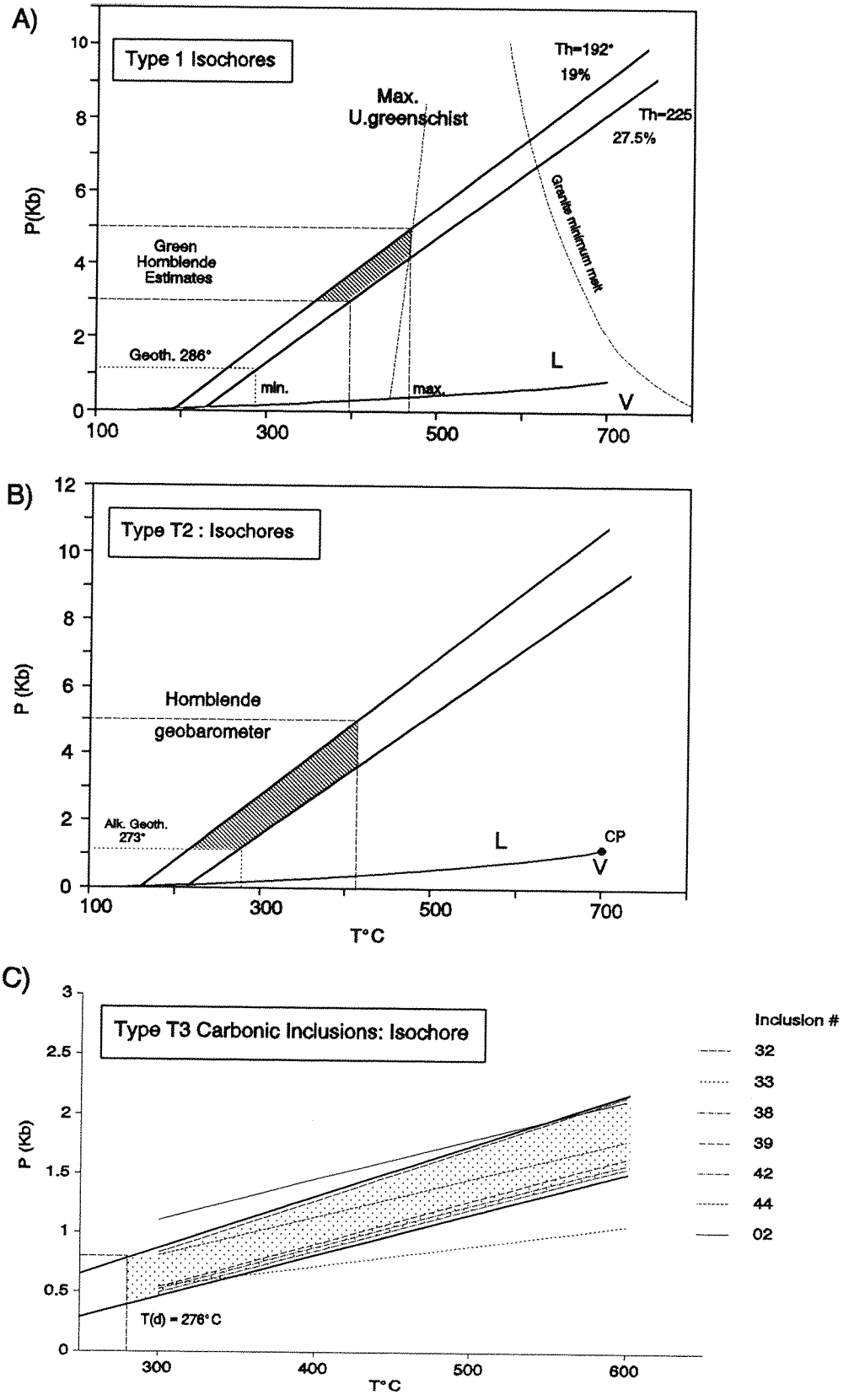

Figure 5.30 **Isochores plotted for fluid inclusions from the Corpo Quatro Formation metasedimentary quartz. A T1 inclusions; B T2 inclusions; C T3 aqueo-carbonic inclusions. A and B plotted using Zhang and Frantz (1987), based on salinity and homogenization. C plotted using Holloway (1981).**

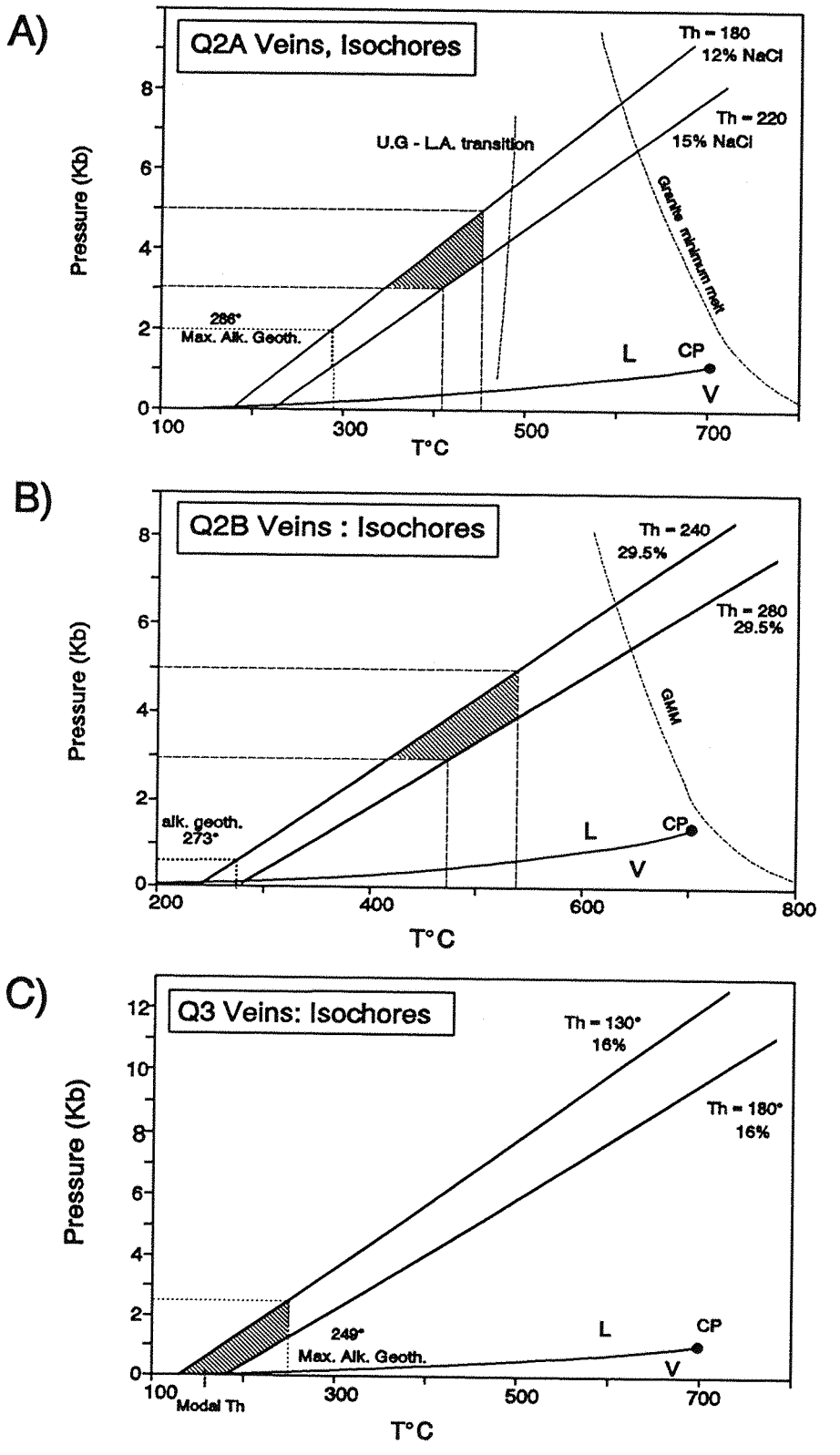

Figure 5.31 **Isochores plotted for fluid inclusions from the Corpo Quatro vein quartz. A Q2-A inclusions; B Q2-B inclusions; C Q3 inclusions. Plotted using Zhang and Frantz (1987), based on salinity and homogenization.**

T2 fluids, which post-date type T1 fluids (see section 5.2.1), would seem more likely to have formed at a lower pressure than type T1, and therefore below 5Kbar. A tentative maximum trapping temperature of 410°C has therefore been estimated from *Figure 5.30B*.

Type T2: Q2-B Veins.

Composed of type T2 inclusions similar to those observed in the host-rock quartz, these give modal Th and salinity values between 240 and 280°C and 29.8 Wt% NaCl eq. respectively. Isochores with these characteristics are plotted in *Figure 5.31B*.

The alkali geothermometer for Q2-B veins gives a minimum equilibria temperature of 273°C, again comparing well with the main Th_{TOT} in *Figure 5.17*. This gives a minimum trapping pressure of 0kb, while a maximum must again be defined using the hornblende geobarometer. The granite minimum-melt curve has been plotted on the isochore, to show the maximum PT conditions for granite-related fluids, at 6.8kb and 660°.

Type T3

Isochores for carbonic inclusions have been calculated using the Holloway (1981) 'soup' equation of state for CO_2-CH_4-H_2O fluids, in the FLINCOR software package. The resulting isochores give much lower P-T conditions than those provided by the Zhang-Frantz isochores for aqueous inclusions (*Fig. 5.30C*), with a decrepitation temperature of ~276°C equivalent to a maximum pressure of trapping at 1Kb.

The presence of CO_2 inclusions in apparent coexistence with T1 fluids should indicate an absolute trapping temperature. However, the CO_2-CH_4 fluids appear to represent a boiling assemblage, and as such their isochore has a low pressure gradient, which only intersects the type T1 isochore at conditions of less than 1Kbar and 300°C. This is lower than the minimum alkali geothermometer, and is therefore interpreted as a result of boiling and differential pressures.

Type Q3 Veins: late fluids.

Late type T1 inclusions in quartz-calcite ± chlorite veins produce the isochores shown in *Figure 5.31C*, with modal Th values between 130 and 180°C, and Wt % NaCl eq.= 16%. The alkali geothermometer for these veins gives minimum P-T conditions of 1.3Kb and 249°C, whereas it is not possible to place an upper limit on conditions from the isochores.

A summary of P-T trapping conditions for fluid inclusion types is presented in *Table 5.11*.

Table 5.11 **Summary of fluid inclusion entrapment conditions.**

	Trapping Temperature (°C)	Trapping Pressure (Kb)
TYPE T1 (Early, Q2-A and Rochas Bandadas)	283 to 470	1.2 to 5
TYPE T2 (Q2-B and Rochas Bandadas	273 to 410	1.5 to 5
TYPE T3 (Aqueo-carbonic, Rochas Bandadas	276 →	1 →
TYPE T1 (Late, Q3 veins)	249 →	1.3 →

5.8 *FLUID CONCLUSIONS*

By combining all the data (microthermometric, LRS and D-ICP), an attempt can be made at suggesting a chemical composition of each of the major fluid events in the Pojuca C4 deposit. Fluid types will be considered as type T1(Q2-A), type T2(Q2-B), type T3 and Type T1(Q3).

Q1 Fluids:

Little data is available on type T1 fluids from early Q1 veins. D-ICP analyses have indicated the dominance of Na, Ca and K, with minor Fe. No daughter minerals are present.

Type T1 (Q2-A) Fluids:

Microthermometric data gives little insight into the composition of these fluids. The metastable eutectic, at around -70°C, may be the result of a number of hydrates, in particular $CaCl_2.6H_2O$ or $MgCl_2.6H_2O$. The melting burst, seen in these inclusions between -62 and -52, and from -46 to -35, could be indicative of either a metastable eutectic for Mg.8 and a stable eutectic for Mg.6, or two stable eutectics for Ca.6. and Mg or Fe hydrates respectively.

Raman analyses of hydrates are also far from conclusive, but indicate that $MgCl_2$ and $CaCl_2$ hydrates may be forming in addition to $NaCl.2H_2O$.

The presence of halite as a daughter mineral in some of the inclusions implies that NaCl is the dominant halide, as confirmed by the D-ICP data, which also shows the presence of calcium and potassium (up to 5% Ca and 0.9% K), with minor iron (up to 0.1% Fe; 0.26% $FeCl_2$). No magnesium was detected in type T1 fluids using the D-ICP method of chemical analysis, and it is therefore inferred that Ca and Na with minor K are the dominant components.

Type T1 (Q3) Fluids:

Microthermometric data on these two-phase aqueous inclusions gives similar results to the type T1 inclusions described in section 5.7.3b, with a metastable eutectic at -70 to -80°C and a melting burst at around -40, seemingly indicating the presence of Mg-hydrates. D-ICP data also suggests that Mg is a component, although far from a major one, in these fluids, where it still only reaches 1.3% (5% $MgCl_2$; assuming a modal value of 14wt.% NaCl eq. and maximum Na:Mg ratio of 42). It is also evident from D-ICP data that Li and Mn are present in these late fluids, making type Q3 fluids Na-Ca-Mg±Li±Mn-rich.

Type T2 (Q2-B)

Like the fluids described in section 5.7.3b, T_{fm} from microthermometric gives little indication of fluid composition. T_{Rm}, however, is between -50 and -60°C and is strongly indicative of the stable NaCl-$CaCl_2$ eutectic (-55°C), ±KCl or $MgCl_2$ (-52.5°C). Hydrohalite has been identified, and one other hydrate is present. The ice melting temperature gives no compositional information but is indicative of high salinities.

LRS of type T2 inclusions, as discussed previously, gives poor hydrate spectra, which, as shown in *Table 5.6*, may represent Ca.6. The dominance of Ca-Na is also shown by D-ICP data, in which K, ±Fe, Ba, Mn and Li are also present. Assuming a modal salinity of 31wt.% NaCl in these inclusions, this can be equated to ~5.75% Ca (16.9% $CaCl_2$), ~1.3% K (2.5% KCl) and ~900ppm Fe. Li, which reaches concentrations of only 730ppm, is unlikely to be responsible for the first-melting in the -80°C temperature region. Type T2 fluids also contain minor boron and zinc (up to 550ppm and 2015ppm respectively).

The presence of the daughter minerals halite, (Na,K)Cl and iron-chloride, identified on the SEM, contradicts the D-ICP data, which shows little iron in the fluids. It is possible, however, that $FeCl_3$ is not being vaporized during the decrepitation process, and the presence of daughter salts only indicates saturation of the liquid with respect to the particular salt at room temperature, not necessarily the most abundant fluid in the solution (Kwak *et al.*, 1986).

Type T3

Microthermometric data signifies the presence of carbon dioxide and either methane or nitrogen in the carbonic phase, as well as salts in the aqueous phase of these inclusions. The sparsity of type T3 inclusions throughout the samples means that no D-ICP data could be obtained, and the absence of T_{fm} or T_{Rm} from microthermometric studies means that no attempt at cation identification can be made. Clathrate and ice melting temperatures, however, give a wide range of salinity, from 3.4 to 24Wt% NaCl eq.

Raman analyses at room temperature show that CH_4 is responsible for Tm_{CO2} depression, forming a molar fraction of up to 15% in these inclusions, while CO_2 constitutes up to 65%. This variation in composition is indicative of un-mixing, possibly associated with a boiling system. Nitrogen is absent in type

T3 inclusions.

5.9 DISCUSSION

The study of veining made in the preceding chapter indicates that although sulphide mineralization is predominantly situated within the C4 Rochas Bandadas, it was introduced into the Corpo Quatro Formation by a series of hydrothermal events, which have resulted in the development of veins, of dominantly quartz-chalcopyrite composition, throughout the sequence. This is strongly supportive of the belief that copper, and therefore zinc, in the Pojuca Corpo Quatro Formation is of an epigenetic origin.

Within veins, the chalcopyrite predominantly occurs in those of extensional, quartz ± biotite nature which are hosted by normal faults, and is concentrated in dilational jogs. Ascertaining the relative timing of the different vein sets is difficult, because very few cross-cutting relationships can be observed in the C4 Formation. However, the order of hydrothermal events (Q1 barren quartz, Q2-A quartz-chalcopyrite ± biotite, Q2-B quartz-biotite ± chalcopyrite, Q3 quartz and/or calcite) is supported both by the nature of the calcite in relation to quartz, forming at the of margins and as a matrix to pre-existing Q2 quartz veins, and by the overprinting of vein-hosted chalcopyrite by acicular biotite. The association of chalcopyrite with albitization and with epidote-feldspar-tourmaline veining, all of which post-date the peak metamorphic fabric and mineral assemblages in the host rocks, provides evidence that the copper mineralization was introduced during a major, late-stage, hydrothermal event.

The relationship of granitic veins to the Pojuca Granite in the western part of the C4 deposit is not completely understood, due mainly to the lack of exposure and the scarcity of both the veins and the granite body in the drillcore. However, the deformation of the granitic veins and their relationship with sulphide mineralization, combined with the age of the Pojuca Granite (1800Ma., Machado *et al.*, 1991) implies that the granitic veins pre-date the Pojuca Granite by some time. The relationship between the granitic veins and quartz-biotite-chalcopyrite stockwork also implies that this initial magmatic event may have been responsible for at least some of the copper mineralization in the Pojuca area. However, other fluid and mineralization sources cannot be disregarded at this stage, and will be discussed further in Chapter 6.

With the exclusion of early, metamorphically altered type T5 fluid inclusions, the inclusions associated with the Corpo Quatro deposit have been divided into four predominant types. These were formed as the result of three main hydrothermal events: early type T1 inclusions are of moderate to high salinity, and found in the metasedimentary quartz and in Q2-A veins; type T2 inclusions, which are highly saline containing halite, sylvite and Fe-chloride daughter minerals, are found within the metasediments and Q2-B veins; and late T1 inclusions, which are of lower salinity than the early T1 inclusions, are found in the late Q3 quartz and calcite veins. Establishing the relative timing of the fluid inclusions is problematic, particularly when the quartz veins display several hydrothermal overprints, and is based on their presence in particular vein generations and association with specific mineral phases; for example,

the T2 inclusions, found mainly in Q2-B veins and associated with late biotite in the metasedimentary quartz, are therefore interpreted as being of later timing than the T1 inclusions found in Q2-A veins and in co-existence with sulphide minerals in the host rocks. The timing of the aqueo-carbonic types T3 and T4 inclusions is unknown, as their presence in the samples studied is limited. T3 inclusions have only been observed within metasedimentary quartz, and due to their CH_4 content, it has been considered that they may represent a metamorphic fluid, where H_2O-CO_2-CH_4 inclusions are relatively common (Roedder, 1984). They do, however, occur in close spatial association with T1 and occasionally T2 inclusions, and are seen to cross-cut intergrain boundaries as secondary inclusions, and have therefore been tentatively placed with the early (post-peak metamorphic) T1 inclusions. Although the timing of T4 inclusions is also uncertain, their occurrence in late fractures across Q2-A chalcopyrite-bearing quartz, and the exhibition of daughter minerals similar to those observed in T2 inclusions, demonstrates their affinity to the T2 type inclusions.

The division of type T1 inclusions into those found in Q2 and those in Q3 veins is obvious, but problems are encountered in quartz from the metasedimentary host rocks, where it is impossible to distinguish between early and late T1 inclusions. Although it is probable that some of the T1 'Rochas Bandadas' fluid inclusions presented in the early T1 histograms are actually from late Q3 veins, a comparison between the T1-Q3 and T1-Rochas Bandadas histograms shows that there is not a great deal of overlap, so it is acceptable to say that at least the majority of Rochas Bandadas T1 inclusions represented in this study are of the early type T1.

Microthermometric studies of naturally occurring fluid inclusions are rarely simple, particularly when the inclusions are of a complex chemical nature, where they cannot realistically be compared with the simple, extensively documented systems such as H_2O-NaCl, H_2O-CO_2, or CO_2-CH_4. Whereas the first melt, or eutectic temperature, is considered a useful tool in the identification of the major species present, the T_{fm} of the aqueous fluid inclusions in this study has proved an obstacle in their chemical interpretation. It has been considered that the phase change observed in these inclusions around -90 to -60°C may not be melting, but the sub-solidus crystallization of an amorphous glass. There is, however, much evidence that the phenomena observed is that of first-melting, as minute quantities of liquid have been observed between the individual grains, which form the typical 'crazy paving' texture described by Shepherd *et al.* (1985), and the process of sequential freezing, carried out on some of the inclusions, results in first melting at the same low temperature. The presence of the rapid melt, seen as low as -76°C in a few of the inclusions, also confirms that the T_{fm} is a true melting phenomena rather than crystallization, as described by Heinrich *et al.* (1989), and the phase change has been interpreted as the result of metastable hydrates present in the mixture.

The division of the early type T1 inclusions into groups a and b is based on distinct populations on a T_{fm} and Tm_{ice} plot (*Fig.5.15*). Whilst the difference in T_{fm} can be interpreted as a contrast in major chemical components in solution, this effect may be due to the presence of metastable hydrates in the inclusions, because no locational or optical distinction can be made between the inclusions, which occur

within the same sample population. Those inclusions with a first melt below -68°C are thought to have undergone a metastable eutectic, which is followed by a stable eutectic, occasionally between -62 and -52°C, but generally between -46 and -30°C. Those inclusions with a eutectic above -68° show no rapid melt phase, and are interpreted as having undergone a low temperature metastable eutectic followed by gradual melting. This is in general agreement with the findings of Davis *et al.* (1990), who researched low eutectic melting in $MgCl_2$- and $CaCl_2$-bearing solutions. It is possible, but unlikely, that there is a chemical variation between the two groups, caused by extensive inhomogeneity at the time of trapping. A similar problem is incurred by the apparent presence of a bimodal population in type T3 aqueo-carbonic inclusions, where the modal values of Tm_{CO2} at -58 and -61 are indicative of a variation in composition of the carbonic phase. The Raman study, however, indicated that although there is a variation in CH_4 content, it does not reflect the Tm_{CO2}, with inclusions which show Tm_{CO2} at -58.7 and -58.5°C containing 25.8 and 8.9 mol.% CH_4 (in the carbonic phase) respectively. Although this problem could be caused by the re-equilibration of clathrates during heating, this idea is rejected as the inclusions all underwent exactly the same thermometric conditions with respect to time during the measurement of phase changes, and should therefore display the same relative increase or decrease in Tm_{CO2} with variable ZCH_4. It is therefore believed that the variable ZCH_4 in these inclusions is a result of inhomogeneous trapping, and the variation in Tm_{CO2} is unexplained.

The observation of homogenisation in fluid inclusions is generally one of the most prominent phase changes to be observed. Complete homogenisation of type T2 inclusions containing multiple daughter minerals, however, was rarely established. On dissolution of halite, sylvite, and the vapour bubble, further heating by up to 300°C failed to homogenize the iron-chloride. This results in difficulties when interpreting isochores, as total homogenization is not known. There are several reasons for the inability to dissolve a daughter mineral prior to decrepitation, the first and most obvious reason being that the phase is not in fact a daughter mineral but a trapped phase. This has been ruled out as the chloride, which has been identified as such by SEM, undergoes dissolution to approximately two-thirds of its original volume on slow heating. Another reason for incomplete homogenization is the post-entrapment modification of a fluid inclusion. The homogenization of the other daughter phases, combined with the relative uniformity of Th_L in the inclusions and the constant phase ratios observed indicate that this is unlikely. Metastability of a daughter phase is thought to be the most reasonable explanation for the inability to homogenize the iron-chloride before decrepitation occurs, and if the inclusion was left at a high temperature for several days, the daughter mineral may eventually reach equilibrium with the solution and dissolve.

D-ICP shows that the fluids are dominated by Na and Ca, with subordinate K and minor Fe. The presence of K- and Fe-chlorides as daughter minerals opposes this, and is a discrepancy which may be caused by the inability of the daughter minerals to be volatilized during decrepitation ICP, and therefore they are not being measured. Although the fluids are evidently saturated in Fe and K, these cations may not necessarily be abundant in the solution (Wilkinson, 1990), therefore resulting in the inability to detect

hydrates of iron using Raman analysis.

D-ICP suggests that the Q3 veins are relatively enriched in magnesium compared with the other fluid events. Whilst T_{fm} and T_{Rm} data suggest that $MgCl_2$ may be important, it plays a small part in the overall composition of the fluid according to D-ICP, and therefore has less effect on the eutectic temperature than the more dominant calcium. It has been considered that the high magnesium value could come from the calcite in the vein samples. Although the samples were carefully washed in acid prior to analysis, and all the carbonate was removed, minute amounts of calcite may feasibly remain in microfractures in the quartz, being liberated only on decrepitation. However, if this was true, the Ca:Na as well as the Mg:Na ratios might be expected to increase, which is not the case in Mg-rich samples.

The hydrates study made using laser Raman spectroscopy was not as successful as was suggested from the study of synthetic hydrates made by Dubessy *et al.* (1982), and it proved impossible to identify the hydrates responsible for the low temperature (metastable) eutectics. The lack of hydrates produced from type T2 inclusions is thought to be due to the low liquid:solid ratio, leaving insufficient space in which measurable hydrates may form. The only recognisable peaks produced in type T1 inclusions were those of hydrohalite, which, as the only compound formed in the $NaCl-H_2O$ system (Klewe and Pederson, 1974), cannot be responsible for the metastable reaction at ~-79°C in the fluid inclusions studied. Some $MgCl_2.6H_2O$ and $CaCl_2.6H_2O$ peaks were developed, but were insufficient to confidently state that these hydrates are present.

It is therefore concluded that the development of an identifiable hydrate spectra is dependent on: the size of the hydrates being formed, which is a function of the size of the inclusion and the liquid:solid ratio; and the formation of multiple hydrates, with no dominant hydrate. In the multi-component systems observed within most naturally occurring (small) fluid inclusions, only the hydrate with the highest melting temperature may be grown to a sufficient size from which to obtain a spectrum. In most cases in the inclusions studied, this was found to be hydrohalite.

Following the above discussion, and the data presented in the preceding chapter, it is proposed that the mineralizing fluids at Pojuca C4 were of moderate salinity, dominantly H_2O-NaCl-$CaCl_2 \pm KCl$, and may have been accompanied by CO_2-CH_4. The lack of evidence for carbonic species in the vapour phase of the aqueous inclusions indicates that if the CO_2-rich inclusions are associated with mineralization and the early T1 fluids, then unmixing occurred which enables a constraint to be made on the geothermometry and geobarometry of this hydrothermal event. Without the CO_2-bearing inclusions there is little restriction on the upper limit of the fluid trapping temperature.

Fluids associated with late-stage mineralization are highly saline, in the system H_2O-NaCl-$CaCl_2 \pm KCl \pm FeCl_3$, and again have associated carbonic fluids, again indicating that some unmixing of the fluids occurred. The hydrothermal activity in the Pojuca C4 deposit was completed by carbonate-associated fluids (late T1-Q3 veins) of low to moderate salinity, belonging in the H_2O-NaCl-$CaCl_2 \pm MgCl_2$ system.

Comparison of the C4 fluids with other copper-deposit related fluids.

Highly saline fluids are typical of many types of base metal deposits, and are particularly common in porphyry copper-type and granite-related vein deposits (Nash, 1976; Roedder, 1984; Eadington, 1983). The fluid inclusions from controversial deposits such as the copper at Mt. Isa are also known to be highly saline (Heinrich *et al.*, 1989), as are fluids associated with retrograde metamorphism (Crawford, 1979). A careful study and comparison of the Pojuca C4 and other known mineralizing fluids must therefore be made in order to develop a model for the style of mineralization seen in the C4 deposit based on the fluid inclusions.

Typically, porphyry copper-type deposits display fluids which can be likened to those at Pojuca. These include early, highly saline inclusions, which are associated with minor mineralization, and display evidence of boiling and co-existing aqueous and carbonic inclusions. They commonly contain halite, sylvite and anhydrite ± haematite daughter minerals, have salinities greater than 35 wt.% NaCl eq., and Th_{tot} between 250 and 700°C. The main phase of porphyry copper mineralization is generally related to later fluids, which are of lower salinity (0-23wt.%), occasionally contain one or two daughter minerals, and have Th_{tot} <350°C (Nash, 1976). This ore-bearing fluid is commonly identified as H_2O-NaCl-KCl± $FeCl_3$. For example, in the Bougainville deposit, PNG, the ore-bearing fluid has ratios of K/Na=0.24-0.35, Fe/Na=0.09-0.18 and Ca/Na=0.03-0.01 (Eastoe, 1978). This is a typical granite-related fluid, which has a predominance of Na, K and Fe over Ca in solution (Bottrell and Yardley, 1988; Eadington, 1983).

The Pojuca C4 fluids, which are dominantly Na-Ca-rich, appear to be most comparable with the pre- and post-ore fluids at Mt.Isa (*Table 5.12*), where the fluids associated with the main phase of copper mineralization are of moderate salinity (3-20wt.%), and are relatively Ca-poor and K-rich in comparison to the pre-and post mineralizing fluids.

Table 5.12 **Fluid compositions of the ore-related fluids in the Mt. Isa and Pojuca C4 copper deposits (Heinrich *et al.*, 1989).**

	Salinity (wt% NaCl eq)	Ca/Na	ThTot
Pre-ore Fluids, Mt.Isa	~25	0.1-0.4	190-240
Ore-bearing Fluids, Mt.Isa	3-20	<0.06	140-180
Post-ore Fluids, Mt.Isa	23-35	0.2-10	90-140
Type T1 Fluids, Pojuca	4-34	0.22-0.55	120-380
Type T2 Fluids, Pojuca	15-41	0.39-0.54	180-340

Typical syngenetic massive sulphide bodies, with which this deposit has been previously likened, show a mixture of fluid types. For example, the fluids associated with base-metal deposits of Stuart Shelf, South Australia, are aqueous and aqueo-carbonic, have salinities of between 0 and 40wt%, and display

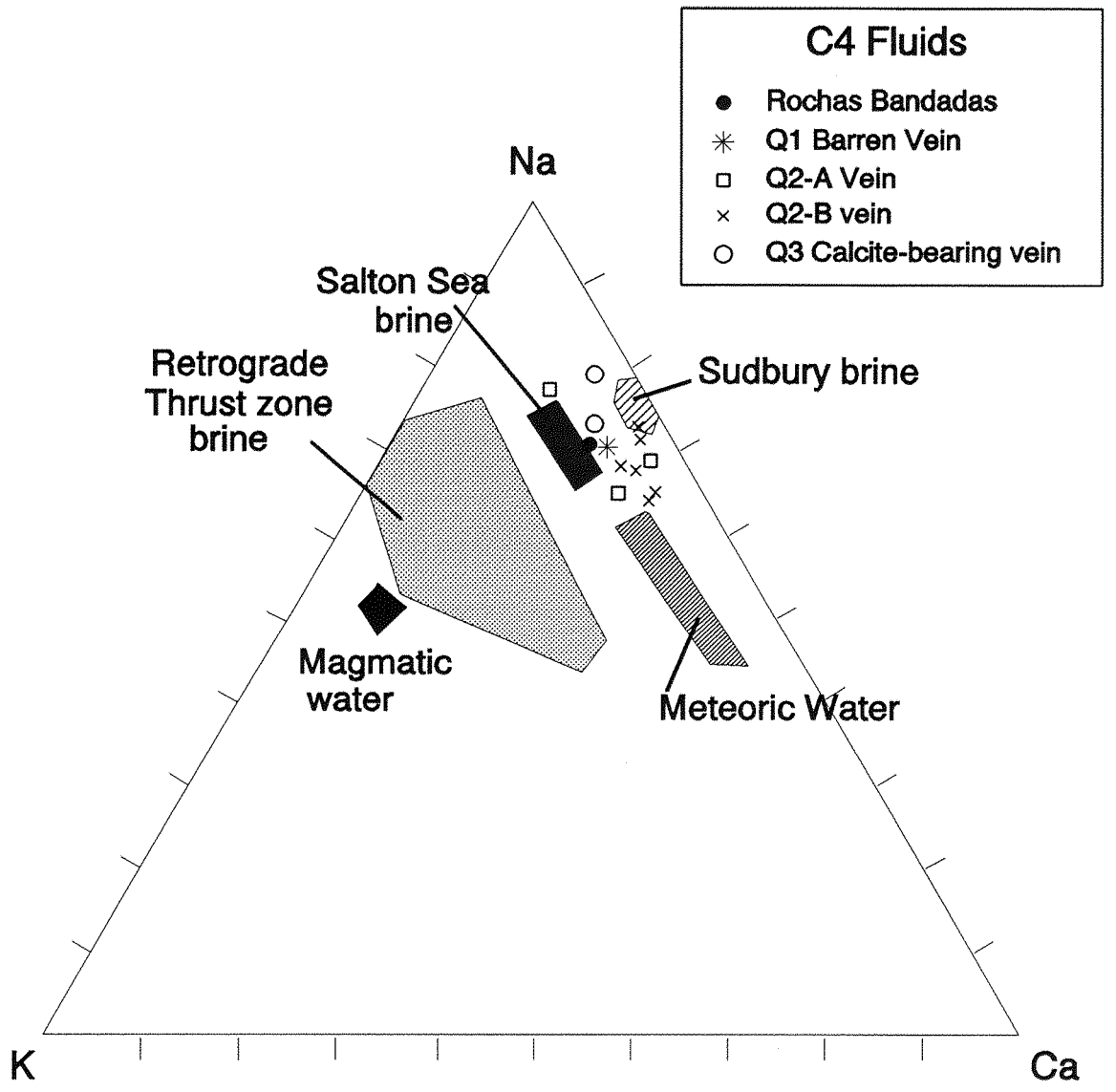

Figure 5.32 **Ternary plot of fluid alkali-metal composition from several terranes, for comparison with the Pojuca C4 fluids. Shaded boxes = fluids from different origins; symbols = C4 fluids. Magmatic field from Gammon *et al.*, 1969 (experimental), Holland, 1972 and Eadington, 1983; Salton Sea data from Ellis, 1979; meteoric field from Rankama and Sahama, 1950; Retrograde metamorphic thrust fluids from Bennett, 1990.**

total homogenization between 130° and 220°C. Although these temperatures are lower than those typically seen at Pojuca, the fluids are similar, with a predominance of Na and Ca.

Figure 5.32 shows the position of the Pojuca fluids in relation to those from other terranes and typical magmatic and meteoric waters. From this it is clear that, providing the DICP results accurately portray the chemistry of each fluid individually, the alkali-metal content of the Pojuca fluids is not representative of true magmatic water. Therefore, for the mineralization in the C4 deposit to be related to granitic activity, the magmatic fluid must have been significantly altered by wallrock interaction.

The high Ca content in the C4 fluids (*Fig. 5.32*) can be compared with both meteoric fluids, and with those found in the Salton Sea. Hypersaline, Ca-rich fluids are also common in metamorphic terranes. These Ca-rich metamorphic fluids, which will be discussed further in Chapter 6, are often been attributed to the metamorphism of evaporite sequences (Knauth and Beunas, 1986). In areas in which evaporites are absent, however, an alternative explanation for the generation of Ca-Na-rich fluids is necessary.

The position of the Pojuca C4 fluids on the alkali-metal plot (*Fig. 5.32*) is based on D-ICP data, which, as has already been shown, is not truly representative of elements which are present within daughter minerals. For example, although Fe does not appear as a significant component of the fluid, Fe-chloride daughter minerals are common. It may therefore be interpreted that the D-ICP potassium value is underestimated, as K is present as sylvite and mixed Na-K chlorides. Taking this into consideration, a higher K-content would place the Pojuca fluids in a similar position on the alkali-metal plot to the highly saline inclusions found in the upper greenschist to upper amphibolite facies Caledonides of Northern Norway. These H_2O-NaCl-$CaCl_2$ fluids have an average salinity of 32 to 34 Wt% NaCl eq., and have interpreted as retrograde metamorphic fluids which achieved their high salinity as a result of low fluid-rock ratio rehydration reactions (Bennett and Barker, 1992). Highly saline brines are commonly produced as the result of the retrograde rehydration of high-grade metamorphic minerals, such as the alteration of garnet and amphibole to chlorite. If this happens in an environment in which infiltration of fluid into the system is slower than the rate at which water is being removed from the solution, an increasingly saline brine is produced (Bennett and Barker, *op.cit.*). The most commonly liberated ion in these rehydration reactions is calcium, generally in the form $CaCl_2$, which results in the fluids becoming enriched in calcium relative to the other ions (Bennett, 1990).

The proximity of the C4 deposit to granitic veins, the vein-related nature of the sulphide minerals, and the post-metamorphic, apparently syn-granitic timing of the sulphide minerals, all indicate that mineralization at Pojuca C4 may be related to the intrusion of a magmatic body in the Pojuca area. However, the variation of the C4 fluid chemistry from that of the typical granitic fluid implies that mineralization may not simply have been the result of reactions between granitic fluids and country rock. Although it is still possible that the Cu-Zn mineralization at Pojuca C4 is related to the intrusion of an older, as yet undiscovered magmatic body similar to that present in the Igarapé Salobo area (Lindenmayer, 1990), the fluid chemistry suggests that a metamorphogenic fluid source is more feasible for mineralization.

Chapter 6 examines the individual models with respect to the mineralogical and structural characteristics of the C4 deposit, and the possible fluid sources which gave rise to mineralization at Pojuca, including a consideration of syngenetic timing and of both the metamorphogenic and magmatic models for the fluid source.

Chapter 6
Discussion

6.1 *THE GEOLOGIC EVOLUTION OF THE CORPO QUATRO FORMATION*

The following discussion attempts to draw on the information presented in this study of the metamorphism, mineralization, fluids and geochemical alteration which have effected the Corpo Quatro Formation, in order to establish a model for the geological history of the Pojuca Corpo Quatro Cu-Zn deposit. The regional geological terminology is the same as that used in Chapter 2.

6.1.1 *The pre-metamorphic petrography of the Corpo Quatro Formation*

It has been established from the petrographic and geochemical nature that, prior to metamorphism, the Corpo Quatro Formation was a conformable volcano-sedimentary sequence comprising two basaltic-andesitic units which sandwich metasedimentary rocks of chemical (iron-formation) and mixed chemical-clastic (metapelitic and intraformational) origin. This study has found the geochemistry of the Corpo Quatro basalts to be comparable with that of the nearby Grão Pará Group basalts, suggesting, in agreement with Gibbs *et al.* (1985) and Olszewski *et al.* (1989), a similar igneous source for the two groups of volcanic rocks. The bimodal nature of the volcanic rocks of the Grão Pará Group (i.e. the presence of both mafic and felsic volcanic suites), and the 'continental' shaped, LREE enriched multi-element plots of basaltic rocks from the Itacaiunas Supergroup (Grão Pará, Igarapé Pojuca and Igarapé Salobo Groups) are both indicative of an intra-continental style eruption for these basalts (Cattell and Taylor, 1990). Trace-element geochemistry, however, indicates the C4 Archaean tholeiitic basalts and basaltic-andesites to be more comparable with present day MORB. The use of multi-element plots in the interpretation of Archaean volcanics must be carried out with some caution, as many of the elements used have the potential for remobilization during the hydrothermal alteration to which the rocks will undoubtedly have been subjected. However, all of the Itacaiunas basalts plotted in this study display similar signatures, indicating that any mobilization of the elements occurred on a regional scale, and there is little regional variation in geochemical attributes. The basalts are therefore considered comparable with one another.

The above conclusion is in contrast to the ideas of Dardenne *et al.* (1988) and Meirelles and Dardenne (1991), who considered the volcanic rocks of the various units in the Itacaiunas Supergroup to represent different depositional environments. These authors interpreted the Igarapé Bahia and Grão Pará volcanics to represent shoshonitic magmas, typically associated with modern crustal rifting related to subduction processes in a back arc basin environment, and similar to the present day Sea of Japan. They also suggested, on the basis of comparison with present day basalts, that the Igarapé Pojuca and Igarapé Salobo basalts were deposited in an ocean arc subduction environment.

The interpretations of Dardenne *et al.* (1988) and Meirelles and Dardenne (1991) were made using comparisons with major and trace element geochemistry of modern basalts. However, data presented by Oliveira *et al.* (1993) has suggested that many Archaean basaltic suites, such as those of the Fortesque Group, Western Australia, which display intra-continental style magmatism and lithological

associations (fault-related clastic deposition, iron-formation and plateau-type lava flows), are geochemically comparable with modern-day volcanic rocks evolved in destructive arc settings. It is therefore proposed that although the Archaean Igarapé Pojuca and Grão Pará Groups appear to show the multi-element signatures of modern within-plate volcanism (Gibbs *et al.*, 1985; Olszewski *et al.*, 1989; this study), the interpretation according to trace and major element geochemistry must, in the absence of REE data, be supported by the relationship of the basalts to other lithological units with the sequence.

Geochemical and petrographic characteristics of the metasediments which are conformably interbedded with the Corpo Quatro metabasalts have indicated these rocks to have a chemical and chemical-clastic affinity. Both the magnetite- and silicate-Rochas Bandadas show mineralogical micro- and meso-banding characteristic of chemical BIF deposits, comparable for example with those found in the Hamersley Basin in the Pilbara Block (Western Australia; Morris, 1993).

Iron-formations are generally classified as either Algoma or Lake Superior types, according to their depositional characteristics as classified by Gross (1965). The basic lithological and geochemical associations of these types were outlined in Chapter 4, where it was shown that the Pojuca iron-formations are most comparable in their geochemistry with the Lake Superior type, but their lithological association with mafic volcanics and clastic sedimentation suggests a closer correlation with the Algoma-type iron-formation. This pattern has been found throughout the Carajás iron-formations, in which the association of late Archaean BIF with volcanic rocks indicates an Algoma-type environment, while the thicknesses and lateral persistence of the Carajás iron-formations are more comparable with those of Lake Superior type (Hoppe *et al.*, 1987). An environment of deposition of the Corpo Quatro iron-formation therefore cannot be determined from the type of iron-formation alone.

Both Algoma- and Lake Superior-type iron-formations are generally subdivided into different facies, in order to establish the expected mineralogy, geochemistry and depositional environment of the unit. Metamorphism of these facies typically results in the development of a characteristic mineral assemblage. Metamorphosed oxide facies iron-formation is composed of quartz and magnetite, and other silicate minerals are rarely developed, even at high (lower amphibolite and above) metamorphic grades. Sulphide facies iron-formation, which is typically fine-grained pyrite-rich black shale composed of quartz-magnetite-carbonate prior to metamorphism, undergoes alteration to pyroxene-fayalite-pyrrhotite-bearing units on high grade metamorphism (Klein, 1973), whereas carbonate facies iron-formation frequently exhibits alteration from carbonate-bearing assemblages to grunerite. Similarly the metamorphism of quartz-silicate assemblages in a metamorphosed silicate facies iron-formation produces amphibole and/or pyroxene-rich schists and gneisses (Klein, 1973). The Pojuca Rochas Bandadas, which is composed of alternating horizons of quartz-amphibole ± magnetite or ilmenite and contains no carbonate or pyroxene minerals, fits none of these classic assemblages, and the dominant silicate mineral, grunerite, may be formed as the result of metamorphism of either carbonate- or silicate facies iron-formation. The Rochas Bandadas only shows similarities with the iron-formation found in the Igarapé Salobo Group, and neither of these are directly analogous to typical, established iron-formation facies. Given the considerable alteration in these rocks, it seems inappropriate to classify them according to a pre-metamorphic facies.

From the Rochas Bandadas at the base to the Xistos Quartzos at the top of the Corpo Quatro

Formation, an increase in clastic sedimentation is demonstrated by an enrichment in K, Al Zr and Ti in barren rock, which is believed to represent an increasing input of detrital material such as clay minerals, zircon and rutile. This chemical change is complemented by an increase in the presence of sub-angular to angular quartz clasts, which are virtually identical to those seen above the chert-jaspilite horizons of the Carajás Iron-formation in the N4E iron mine to the east of Pojuca (Hoppe *et al.*, 1987), and are believed to have formed as the result of sedimentological intraformational brecciation of underlying silica-rich iron-formation. Most of the clastic component in the Rochas Fragmentos can be attributed to volcanic material, which has the same geochemical characteristics as the surrounding C4 metabasalts (see Chapter 4), and has been mixed with continued chemical sedimentation. The increase in clastic sedimentation up the sequence corresponds with that observed in many of the worlds Archaean iron-formation sequences, and strongly suggests that the Igarapé Pojuca Group, in the area of the Corpo Quatro deposit, has not been overturned.

6.1.2 *The depositional and metamorphic history of the Corpo Quatro Formation.*

The depositional environment

A depositional environment for the Corpo Quatro Formation can be established using the geochemical and lithological interpretations of the sequence, combined with a knowledge of the regional geology of the Carajás Belt.

The Corpo Quatro and other sulphide deposits in the region were previously believed to be of syngenetic origin, and former regional depositional and tectonic models for the Carajás belt have included a setting for the deposition of VMS-style deposits. Although the evidence for the Corpo Quatro base-metal deposits being of epigenetic origin are strong, it is not necessary to completely reconsider the depositional and tectonic environment of the Carajás Belt in view of the new interpretation of the C4 ore deposit. Hutchinson (1979) and Lindenmayer (1990) indicated that the volcanics of the Carajás Belt represent products of eruption at a spreading ridge, and that the associated sulphide deposits are the result of volcanogenic, exhalative sulphide mineralization in a Cyprus-style environment. Although trace element geochemistry of the volcanics has suggested an affinity to MORB-type basalts, chemical-clastic metasediments cover a wide area of the Carajás region, not only forming part of the Igarapé Pojuca Group, but throughout the Upper Archaean to Lower Proterozoic Itacaiunas Supergroup (Docegeo 1988). The presence of this clastic material, and its interbedded nature with iron-formation and basalts and basaltic andesites seen in the Carajás Formation, Grão Pará Group, Igarapé Salobo Group and Igarapé Pojuca Group have indicated that the spreading centre environment is an unlikely one for the deposition of these Archaean suites, suggesting instead that these rocks were deposited in a region of intracontinental crustal rifting of older basement (the Xingu Complex, dated at 2851Ma; see Chapter 2).

Deposition probably occurred under shallow sub-aqueous conditions in an intermittently active intracontinental fault bounded extensional basin (*Fig. 6.1A*). This interpretation is supported by the presence of chemical sediments (chert and iron-formation) which became increasing clastic up the sequence. The Upper sediments in the Corpo Quatro Formation are composed of a mixture of chemical sediments (predominantly in the Xistos Granadas) and intraformational siliceous debris. This sedimentary

material has a geochemical composition indicative of mixing between volcanic and iron-formation end-members. The chemical and clastic sediments within a single sequence are frequently intercalated, which may indicate the presence of active syn-sedimentary faulting in the area. It is thought that chemical sedimentation dominated during breaks in clastic deposition, whereas fault movement resulted in uplift, erosion and brecciation of the underlying chemical sediments, and the incorporation of intraformational silica clasts in the subsequent clastic sedimentation.

The widespread development of intercalated chemical and clastic sediments with volcanic, predominantly basaltic, rocks is seen throughout the Carajás Belt. This suggests that these volcano-sedimentary sequences were developed in a rifting environment which also hosted intermittent volcanic activity that diminished over time until the complete cessation of volcanism by the time the clastic sediments of the Rio Fresco Formation were deposited.

This rifting model is in accordance with the suggestions of Olszewski *et al.* (1986), and is comparable with the Archaean mixed chemical-clastic sediments and tholeiitic basalts in the lower Hamersley Basin and Fortesque Group of Western Australia. If this hypothesis is correct, it is believed that the volcanic rocks of the Igarapé Pojuca Group, along with those of the lower Itacaiunas Supergroup, Carajás, and the Fortesque Group, W.A., represent among the oldest intracontinental basalt sequences yet recognised (Oliveira *et al.*, 1993).

The age and metamorphic history of the Corpo Quatro Formation

The tectonic history of the Igarapé Pojuca Group in the area around the C4 deposit can be interpreted in terms of metamorphic and structural aspects of the Corpo Quatro Formation. It has been established that the volcano-sedimentary sequence of the Corpo Quatro Formation was deposited in an intracontinental basin, and together with the other lithological groups of the Itacaiunas Supergroup it has undergone regional metamorphism and tectonic deformation, resulting in the almost vertical orientation of the strata.

It will be considered briefly how the structure of the Pojuca C4 area fits into the previously established regional tectonic models of Sena Costa *et al.* (1990) and Araujo *et al.* (1988), although due principally to lack of exposure, this thesis does not dwell on the structure of the C4 orebody, so previous tectonic models can not be fully evaluated. Whilst it is preferable that the model proposed for the Pojuca area conforms with the regional interpretation, it is also necessary that the regional tectonic history accommodates the deposition of epigenetic sulphide minerals in the C4 and related orebodies.

Radiogenic dating of the Itacaiunas Supergroup has been carried out by Machado *et al.* (1991) using U-Pb and Pb-Pb on zircons from amphibolites and gneisses of the Igarapé Salobo Group and from metabasalts of the Corpo Quatro Formation. The Salobo gneisses were found to give a date of formation of 2851±4Ma, identical to the date obtained from the basement Xingu Complex. However, zircons from the Salobo amphibolites yielded an age of around 2760Ma, with overgrowths dated between 2742 and 2739Ma. Machado *et al.* (*op.cit*) interpreted this to mean that the Igarapé Salobo Group was deposited around 2850Ma, and is coeval with the Xingu Complex, and the later dates (2760Ma and 2742-2732Ma) to represent metamorphic episodes during and after the eruption of the Grão Pará Group volcanics.

However, zircons from the C4 Formation basalts also yield a metamorphic date of 2732±2Ma (Machado *et al.*, 1991), and the 2760Ma date for the Salobo volcanics is similar to that found for the Grão Pará Group volcanics. It is therefore possible that the early date (2851Ma) obtained for the metasedimentary Igarapé Salobo Gneiss was from a detrital zircon, originated from the Xingu Complex. In this case, the amphibolite date represents the true timing of eruption, making the volcanics of the Igarapé Salobo Group roughly coeval with those of the Grão Pará Group. In either case, the 2742-2732Ma metamorphic event affecting both the Igarapé Salobo and Pojuca Groups, and was the dominant regional metamorphism to occur in the Corpo Quatro Formation, reaching lower amphibolite grade.

The tectonic model proposed by Araujo *et al.* (1988) suggests that the basin into which the Itacaiunas Supergroup was originally deposited was a roughly east-west trending pull-apart basin, which subsequently closed by sinistral strike slip compression resulting in basin inversion and regional metamorphism. Most of the strike-slip movement was taken up by ductile oblique thrusting at the northern and southern edges of the belt (Araujo *et al.*, 1988), resulting in a higher degree of metamorphism at the edges than in the centre, and the development of vertical to sub-vertical strata at the belt margins. The regional transpression appears to have resulted in the development of a positive flower structure in the Carajás region, generating the broad ESE-WNW orientated Serra dos Carajás synclinorium in its present form (Araujo *et al.*, 1988). There is evidence for continued strike-slip movement, along the major Carajás fault, which cross-cuts the Carajás Belt. This model was described briefly in Chapter 2.

Although is not possible to confirm the theories of Araujo *et al.* (1988) and Sena Costa *et al.* (1990) from the small amount of exposure in the area of the C4 deposit, the structure in the area around the C4 deposit is dominated by ductile and brittle deformation in the form of shear zones, faults and quartz veins, which post-date peak metamorphism. It would appear from exposure in the G1-C4 adit that most of the strike slip movement was taken up by the Rochas Fragmentos, along ductile shear zones which display retrograde metamorphic assemblages, and that whilst these shear zones provided pathways for late retrograde fluids, the earlier, mineralizing fluids appear to have been channelled through brittle, NW-SE orientated normal and reverse faults in the more competent Rochas Bandadas. The presence of both normal and reverse faults of similar ages in conformable with a strike slip regime, with the normal faults predominantly occurring perpendicular to the direction of regional movement. However, the local structure indicates that in the Pojuca area, brittle failure was succeeded by ductile shear deformation. This does not necessarily agree with the model proposed by Sena Costa *et al.* (1990), who suggested that whilst brittle deformation and flower structures were being formed in the central part of the Carajás Belt, ductile deformation was concurrent with regional metamorphism at the belt margins. The structural model is shown schematically in *Figure 6.1.*

Peak regional metamorphism in the Pojuca Corpo Quatro Formation achieved a maximum of lower amphibolite grade, established from mineral assemblages (garnet-quartz-biotite in the metapelites) and using graphite Raman spectra as a metamorphic indicator. The use of graphite spectra to indicate metamorphic grade is considered valid, as the graphite in the Rochas Bandadas is an integral component of the mineral assemblage, occurring as inclusions within syn-metamorphic garnet and therefore pre-dating

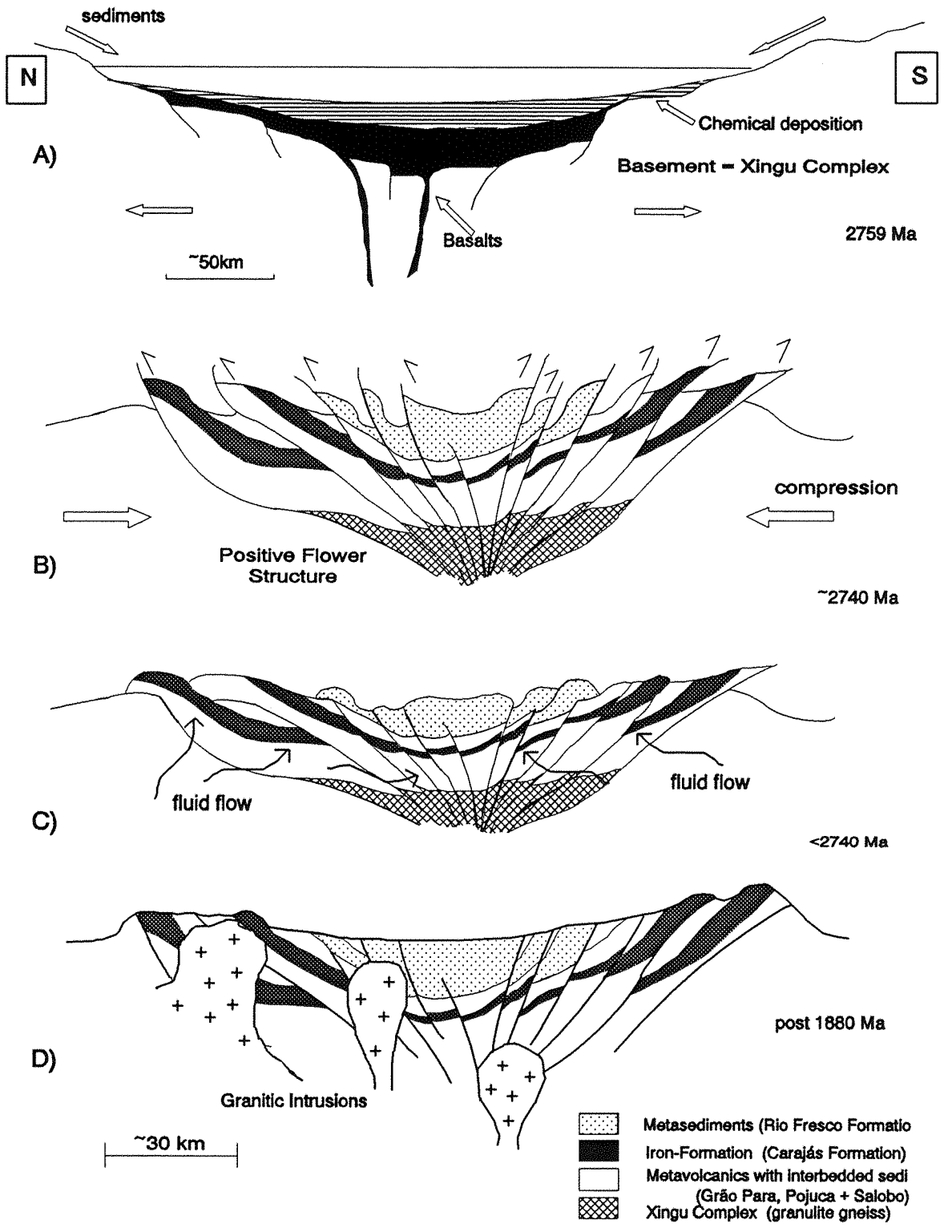

Figure 6.1 **Schematic representation history of the Carajás region; A Deposition of basalts and sediments in an intra-continental rift system; B Compression and metamorphism of the Carajás Belt; C Retrograde metamorphism showing flow of fluids through the strata from below; D Post-metamorphic intrusion of granitic bodies (Carajás and Pojuca Granites).**

the regional metamorphic event. This method gives a metamorphic grade of staurolite-kyanite-andalusite, using the two most reliable features of the Raman spectra (D/O and D-peak intensity). Amphibole formation pressures have determined a maximum pressure of between 5 and 7kb, which corresponds with a maximum temperature of between 450 and 600°C at lower amphibolite grade (Yardley, 1989). A narrower temperature range was established from the metabasite mineral assemblage (hornblende-biotite-oligoclase), with the maximum metamorphic temperature lying between 500 and 580°C (Maruyama *et al.*, 1983).

Peak regional metamorphism at Pojuca was followed by intense hydrothermal alteration, which is manifested by albitization in metabasalts and sulphide enrichment in the metasediments, and by the intrusion of granitic veins which cross-cut the metamorphic fabric. These events were associated with brittle fracturing and the development of epidote-K-feldspar and quartz veins. There is also evidence for late ductile shearing in the Corpo Quatro Formation, which is displayed by the occasional shear deformation of quartz veins and sulphide minerals, and the development of an intensely schistose fabric in narrow (up to 3m) regions within the Rochas Fragmentos and granitic veins. These shear zones display retrograde metamorphic alteration assemblages of chlorite, quartz and biotite, and are overprinted by almandine garnet. As discussed in Chapter 3, this has been interpreted as the result of minor thermal metamorphism.

6.2 *SUMMARY OF THE MAIN FEATURES IN THE CORPO QUATRO DEPOSIT*

In order to make a comprehensive discussion for the style of mineralization and the associated geochemical alteration, and to propose a genetic model for ore genesis at the Pojuca Corpo Quatro deposit, the facts which have already been established in the preceding chapters have been summarized in the following section.

6.2.1 *Sulphide mineralization*

Mineralization in the Corpo Quatro Cu-Zn deposit consists of pyrrhotite, chalcopyrite and sphalerite, with subordinate amounts of pyrite and nickel-arsenides, in addition to very minor quantities of molybdenite and gold, which can be divided into two separate stages of ore deposition. The main ore stage is characterized by Cu- and Zn-sulphides which predominantly occur as banded, apparently stratiform, mineralization and as fracture-fill phases cross-cutting the mineral assemblages of the Rochas Bandadas, where they show intimate relationships with hornblendized Fe-Mg amphiboles. The relationships between sulphide minerals usually shows that pyrrhotite, which occurs predominantly in the banded-style of mineralization, is replaced by chalcopyrite which has in turn been replaced by sphalerite. However, in fracture-style mineralization throughout the metasediments sphalerite and/or chalcopyrite are commonly found without pyrrhotite.

Nickel-arsenides, pentlandite, gold and molybdenite all occur as late-stage replacements of the copper-, iron- and zinc sulphides, and were generated during a second phase of ore deposition.

The majority of the sulphide minerals show no signs of deformation or metamorphism, although in some sections of drillcore, disseminated chalcopyrite and pyrrhotite are elongate parallel to a schistose

fabric, indicating that they have undergone tectonic deformation. Pyrite sometimes displays brittle deformation, and is sometimes intergrown with pyrrhotite lamellae with a myrmekitic texture. Rarely, molybdenite is found contained within the Pojuca Granite in the western part of the Pojuca area and in the Pojuca Leste body.

6.2.2 *Wallrock Alteration*

In close proximity to the sulphide-bearing strata of the Corpo Quatro Formation, the metavolcanics are occasionally observed to have been intensely altered to an albite-chlorite-chalcopyrite ± epidote and tourmaline bearing assemblage. In the G1-C4 adit this product of intense sodic alteration is known as the Albite Zone, and it contains minor gold and underlies the sulphide-rich metasediments. Albitization also occurs in small (~1m-wide) patches apparently related to small faults in both the upper and lower metavolcanic rocks, and overprints all metamorphic assemblages in the host basalt.

Wallrock alteration on a microscopic scale exists in the form of hornblendization of grunerite and anthophyllite within millimetres of sulphide minerals in both Banded and Fracture stye mineralization in the Rochas Bandadas, although this relationship is not observed in the Rochas Fragmentos.

Cordierite-anthophyllite alteration in the upper metabasalts of the Corpo Quatro Formation is apparently unrelated to sulphide mineralization, and shows alteration to a biotite-anthophyllite-rich assemblage.

6.2.3 *Mineralization and veining*

The initial and main stage of ore deposition at Pojuca shows a close spatial relationship with quartz veining, in which moderate to high salinity (10-30 wt.% NaCl eq) fluid inclusions dominate, and gas-bearing fluid inclusions are minor. Sulphide mineralization in the Corpo Quatro metasedimentary rocks is also accompanied by these fluid inclusions, which are two (sometimes three) phase aqueous and Na-Ca-rich. Chalcopyrite and minor pyrite also occur in epidote (±K-feldspar) veins in metabasalt, particularly within close proximity (2-3m) of zones of albite-magnetite-sericite-chlorite-rich bleached rock (albitization).

The main stage of mineralization at Pojuca was post-dated by a second vein generation, in which quartz and biotite are the predominant phases, with lesser amounts of chalcopyrite. These later veins contain hypersaline fluid inclusions, which have a mean salinity of around 31 wt.% NaCl eq., and contain two or three daughter minerals, including halite, sylvite and iron-chloride. Ni- and Mo-bearing minerals are rarely found in veins, but have been interpreted as synchronous with the later stage of ore deposition by their textural relationships with other sulphide minerals.

Quartz veining in the western part of the prospect shows a close association with granitic veins, with sulphide-rich quartz veins observed extending from the granitic veins which intrude the sequence.

6.2.4 *Fluid Composition*

Two main fluid populations dominate in the Corpo Quatro deposit. The fluids responsible for the

main phase of Cu-Zn mineralization in the Corpo Quatro Formation are Na-Ca ± K-rich and of variable salinity (4 to 34 wt% eq.). These fluids homogenize to the liquid phase at temperatures of between 120 and 380°C, with a modal value of 205°C, which has been interpreted using isochores to indicate a trapping temperature of between 283 and 470°C. In the same quartz, and apparently the same population as these aqueous inclusions, are CO_2-CH_4-H_2O-rich fluids inclusions, which undergo homogenization and decrepitation at around 270°C, indicative that they were trapped at this temperature. There is some evidence that these aqueo-carbonic inclusions represent boiling, in that the fill varies from 0-70% water, and they contain up to 50% CO_2 and 15% CH_4. There is, however, little evidence that these inclusions underwent unmixing with the aqueous inclusions during their deposition. The main stage of copper-zinc mineralization was post-dated by later sulphide ± nickel arsenide and molybdenite deposition, accompanied by highly saline Na-Ca-rich fluids. Inclusions representative of this fluid contain a number of daughter minerals, namely halite, sylvite and Fe-chlorides. These, too, display total homogenization to liquid, at between 160 and 340°C, with a modal value of 210°C. A trapping temperature has been estimated using isochores, at between 273 and 410°C, indicating these fluids to have trapped at slightly lower temperatures than those associated with the main stage of mineralization.

High salinity fluids are commonly developed in regions of retrograde metamorphism, particularly if evaporites are present, and in areas of granitic activity. They are abundant in base-metal deposits, as chloride-rich solutions are particularly adept at transporting copper, lead and zinc as chloride complexed species, and are also typical of porphyry copper-style mineralization. Na-Ca-rich fluids are particularly associated with retrograde metamorphic belts, as a result of fluid-rock alteration of garnet and amphiboles to biotite and chlorite, which releases the cations Na^+ and Ca^{2+} (Bennett and Barker, 1992).

6.3 TIMING OF THE MINERALIZATION

One of the main aims of this study has been to determine the genesis of the sulphide mineralization in the Pojuca Corpo Quatro Formation. From the preceding chapters it is clear that the mineralization appears to be of an epigenetic nature. However, the origin of Archaean iron-formation-hosted base-metal (± gold) deposits has been the cause of much controversy over the years, with several genetic models being presented. The possibility that the Pojuca C4 deposit may be syngenetic, as proposed by previous workers (Hutchinson, 1979; Medeiros Neto, 1987) and that the sulphide minerals, particularly chalcopyrite, in quartz veins could have been produced by the local remobilization of sulphides into veins, must therefore be considered.

It has been proposed that sulphide-precious metal mineralization in Archaean rocks, including BIFs and their associated sedimentary and volcanic suites, may be attributed to one of three main mechanisms: i) exhalative deposition of sulphide minerals during volcanogenic processes (VMS deposits); ii) remobilization of exhalative sulphides; and iii) epigenetic deposition and selective replacement of pre-existing mineral phases (particularly iron-oxides). These models have been extensively discussed in the literature in recent years, particularly relating to the BIF-hosted Au deposits of Western Australia (Groves *et al.*, 1987; Large *et al.*, 1988; 1989), the Mount Isa and related copper deposits of the Cloncurry district, Queensland, Australia (Davidson *et al.*, 1989, Williams and Heinnemann, 1992), and some of the North

American stratabound deposits (Sangster and Scott, 1976). Some of these deposits, particularly those of the Noranda region, Quebec, and the VMS deposits of Ducktown, Tennessee (Craig and Vokes, 1992) have been unequivocally interpreted as having been formed by remobilization of pre-existing phases. Many of the world's stratabound sulphide deposits, however, such as the Cu-Zn-Pb-Au deposits of Western Australia (Groves *et al.*, 1987) and Canada, and the Cloncurry-Mount Isa inlier deposits (Williams and Heinnemann, 1992) are constantly being re-evaluated.

6.3.1 *The epigenetic vs. syngenetic controversy*

In order to identify mineralization as syngenetic iron-formation-hosted or VMS-type, a number of diagnostic criteria must be proved. These have been stated by a number of workers, notably Sangster (1972), Sangster and Scott (1976) and Groves *et al.* (1987). These criteria, listed in *Table 6.1*, are based on both iron-formation-hosted stratabound mineralization and VMS bodies in mixed sedimentary-volcanic sequences, such as those of the Manitouwadge District, Ontario, and will be examined in relation to the Pojuca C4 deposit.

Table 6.1 **Diagnostic criteria for the identification of syngenetic exhalative vs. epigenetic base-metal sulphide deposits (Sangster, 1972; Sangster and Scott, 1977; Groves *et al.*, 1987)**

	EXHALATIVE	EPIGENETIC
1	The sulphides and contained precious metals were involved in all phases of deformation and metamorphism undergone by the host rocks.	Sulphide minerals post-date at least the early stages, if not all, of the deformation and metamorphism recorded by the host iron-formation.
2	The contacts between the orebodies and their lateral extensions are transitional, and the mineralization shows no spatial relationship to fracturing or veining.	Mineralization shows a strong structural control, and is especially concentrated near to fractures or veining.
3	The wallrock alteration associated with mineralization is asymmetric, concentrated mainly or completely in the footwall of the orebody.	Wallrock alteration may be present in the hangingwall as well as the footwall.
4	The deposit demonstrates zoning, exhibited by morphological and mineralogical segregation. There is typically a basal, pyrite-chalcopyrite-rich stringer zone, and a pyrite-sphalerite-rich top, in which Zn and Pb are concentrated in the upper part, and Cu in the lower part. Textural zoning is also developed, with sphalerite generally forming banded sulphides whereas chalcopyrite is usually massive.	Although controls on mineralization may be lithological, no mineralogical or textural zoning is apparent in the sulphides.
5	The footwall contact between barren rock and the orebody is gradational, whereas and the contact with the hangingwall is sharp.	The contacts between sulphide-rich and barren metasediments are sharp.
6	Several orebodies are commonly developed at or near the same stratigraphic horizon.	
7	There is a general association with felsic volcanism, although this is most common in VMS deposits hosted only by volcanic rocks. In mafic-associated deposits, cordierite-anthophyllite assemblages represent thermally metamorphosed quartz-chlorite alteration pipes.	

These are, however, general observations, and no one single factor can be taken to indicate, unequivocally, the timing of the mineralization in relation to the host rock. While many Archaean BIF-hosted sulphide deposits display some of the syngenetic-style features, many show definite evidence for an epigenetic origin. The Pojuca C4 deposit, interpreted from this study as being epigenetic in origin, shows some of the features suggestive of syngenetic deposition. The criteria listed in *Table 6.1* will be considered by point.

1) The C4 deposit contains some sulphides which show signs of having undergone deformation; pyrite in the Rochas Fragmentos shows brittle deformation, and is frequently enveloped by pyrrhotite. This pyrrhotite may either have been metamorphically remobilized by ductile flow, and nucleated around the pyrite, or formed as a result of increased temperature and sulphur activity during the metamorphism of pyrite (see Chapter 3). Pyrrhotite is occasionally located in fold hinges, again indicating ductile flow during metamorphism. Pyrrhotite, and occasionally chalcopyrite, also display elongation parallel to the schistose fabric developed in the shear zones within Rochas Fragmentos, indicating that they have been deformed by a shearing event. This shear deformation, however, has also been observed in the granitic veins which cross-cut the regional metamorphic textures in the Corpo Quatro Formation, and does not prove a syngenetic origin for the deposition of the sulphides, but merely introduction prior to shearing.

Other than these minor signs of deformation, chalcopyrite, pyrrhotite and sphalerite display none of the evidence typically associated with metamorphosed sulphides, such as ductile flow and remobilization into dilational zones, recrystallized intergrowths of sulphides, and metamorphically induced twinning. It is therefore interpreted that most of the sulphide minerals (with the exception of pyrite and some pyrrhotite) are post-peak metamorphic.

2) Contacts between sulphide-rich and barren Rochas Bandadas are difficult to assess, due to the lack of exposure in the deposit, but a close spatial relationship between sulphide-rich Rochas Bandadas and quartz-chalcopyrite-rich fractures and veins has been demonstrated.

3) The Pojuca C4 deposit exhibits albitic and cordierite-anthophyllite alteration assemblages, which are regarded as being typical of VMS deposits, representing alteration pipes to exhalative mineralization and commonly found in Abitibi and Noranda massive sulphide deposits (Sangster and Scott, 1976; Morton and Franklin, 1987). These alteration zones, however, do not show the asymmetrical distribution typical of syngenetic deposits, and both assemblages have also been recorded in environments completely unrelated to mineralization. The albitization, especially, is developed in both the upper and lower volcanic units of the Corpo Quatro Formation, where it exhibits sharp contacts with its host, and has overprinted the metavolcanics rather than undergone metamorphism itself. The present study has therefore interpreted albitization at Pojuca C4 as a late stage hydrothermal event, which shows similarities with the albitic alteration seen in a number of the Cloncurry deposits of the Mt. Isa Inlier (Oliver *et al.*, 1993; P.J.Williams, *pers.com.* 1993), and in the magnetite-copper ores of the Kiruna district, north Sweden (Blake and Williams, 1993), which are believed to be wholly related to fluid-wallrock interaction. Cordierite-anthophyllite alteration can also be explained by isochemical thermal metamorphism of basaltic rocks resulting from the nearby intrusion of a granitic body (Sangster and Scott, 1976).

4) Mineralogical zoning, as described by Sangster (1972), is observed to some extent in the Pojuca

C4 deposit. For example, in terms of composition, the sphalerite: chalcopyrite ratio appears to be higher in the Xistos Granadas than the Rochas Bandadas, although zinc values are highest and most uniform in the Rochas Bandadas. This mineralogical variation, however, occurs in the intercalated sequences, and is controlled by lithological variation rather than structural position relative to any feeder zone which might be present, and is therefore not equivalent to the zoning described for exhalative deposits.

The morphological zoning typical of volcanogenic deposits is also absent in the Corpo Quatro deposit. The observation that chalcopyrite is rarely present as 'banded' mineralization in typical syngenetic VMS deposits (Sangster and Scott, 1976) may not be true for iron-formation-hosted sulphide deposits, where much of the mineralization takes on a stratiform appearance. However, the Fe-sulphide which dominates most volcanogenic deposits is pyrite, and in over 70% of the North American VMS deposits Zn is more abundant than Cu (Sangster and Scott, 1976); neither of these factors is true for the Pojuca deposit.

Mineralization in a VMS deposit would be expected to be immediately underlain by a stringer-form of mineralization. Although minor chalcopyrite is present in the metavolcanics underlying the C4 orebody, this is related to quartz-filled fractures and not of sufficient quantity to be regarded as a stringer zone.

A common source for metals in base-metal exhalative massive-sulphide deposits is the leaching from seafloor basalts at or near the basalt-seawater interface. It was noted in Chapter 4 that copper is depleted in the host metabasalts and enriched in the Albite Zone relative to typical Archaean basalts. However, a corresponding zinc depletion is not observed. It has also been observed that hydrothermally altered basaltic rocks may have acted as the source for epigenetic copper concentrations, particularly where the basalts have been shown to display copper depletions of up to 40ppm (Knutson *et al.*, 1992), which is comparable with the depletion in the C4 basalts.

5) Although the Pojuca deposits (C1, 2, 3 and 4, and Pojuca Leste) display several bodies at or near the same lithological horizon on a regional scale, i.e. within the metasediments of the Igarapé Pojuca Group, and they are dominantly confined to the chemical sediments, they do not occur in the same stratigraphic horizon relative to a potential exhalative source, as discussed in point 4) above. It is therefore established that the zoning is controlled by a lithologic rather than structural position.

The C4 and related deposits in the Pojuca area share none of the other similarities with typical syngenetic-interpreted VMS deposits such as the common, although not essential association with felsic pyroclastic rocks, and it is therefore concluded that the mineralization at Pojuca is not of an exhalative nature.

6.3.2 *Sulphide enrichment by remobilization*

Most authors who favour the syngenetic origin of base-metal deposits argue for their subsequent remobilization by hydrothermal activity. Although there is little conclusive proof for or against the concentration of BIF-hosted base-metal sulphides by remobilization, deposits commonly construed as having undergone local remobilization tend to display sulphide deformation and metamorphism in the form of pyrite rotation and durchbewegung textures in pyrrhotite and chalcopyrite. Most of the sulphide

minerals of the Pojuca C4 deposit, as previously established, show no evidence of having undergone deformation, and those which do have been proved to be of post-metamorphic timing.

On a larger scale, the presence of continuous, abnormally high precious metal background values in the country rock is sometimes used as evidence of remobilization. For example, the presence of above average Au-values in distal, sulphide-poor BIF around gold deposits is taken to indicate that sulphide-gold enrichment was produced by local remobilization (Groves *et al.*, 1987). As the C4 deposit is not Au-rich (up to a maximum of 0.5ppm, with a mean of <0.05ppm), this principle cannot be applied at Pojuca.

The small-scale (several metres) spatial relationship between sulphide-rich Rochas Bandadas and quartz veins has been interpreted by Medeiros Neto (1987) as the local remobilization of sulphides into veins. This is possible when it is considered that sulphides are abundant several metres from obvious quartz-fracture systems in the C4 deposit, which suggests that not all the mineralization is structurally (epigenetically) controlled. However, there are abundant small chalcopyrite-filled fractures cross-cutting magnetite bands in the BIF, which display the replacement of magnetite rather than extraction of sulphides from the strata. This would imply large scale remobilization rather than local 'sweating out' of silicates and sulphides from the iron-formation. Davidson *et al.* (1989) considered the confinement of sulphides to iron-formation to imply local remobilization, and observed that discordant veins reflect the mineralogy of the immediate wallrock in the Tank Trough deposit, Mount Isa, where magnetite veins cross-cut quartz-magnetite BIF whereas chalcopyrite is only found in veins which cross-cut sulphide-bearing strata. This was taken as evidence to support the remobilization theory. Neither the confinement of sulphides to iron-formation nor the presence of select minerals in veins are applicable to the C4 deposit, and although Medeiros Neto (1987) suggested that hydrothermal veins related to the granitic bodies in the Carajás area were responsible for the remobilization of pre-existing syngenetic sulphide mineralization, the only evidence for remobilization remains in the pyrrhotite seen in fold hinges and in late-stage shear zones in the Rochas Fragmentos.

Although it is not possible to rule out remobilization on a regional scale, i.e. the redistribution of sulphide minerals by hydrothermal fluids which have been introduced from several kilometres away, this could still be considered as the epigenetic sulphide enrichment of the Corpo Quatro Formation. It is therefore concluded that sulphide mineralization in the Pojuca C4 deposit is of epigenetic nature, and the result of the introduction of late, post-peak metamorphic, mineralizing fluids.

6.4 *SOURCE OF THE MINERALIZING FLUIDS*

In order to establish a genetic model for the Corpo Quatro deposit, the origin of the mineralizing fluids must be determined. The possible fluid sources which must be considered are essentially magmatic, considering the intimate relationship between sulphide-bearing quartz veins and granitic veins, and late metamorphic, considering the post-peak metamorphic style of the mineralization. The mixing of meteoric water with either of these is also a possibility, but without stable isotope data it is not possible to establish this. Connate water is unlikely to have been present in the Corpo Quatro Formation following the amphibolite grade metamorphism and dehydration of the primary sediments, and seawater is also an

improbable fluid source in the post-peak metamorphic environment.

The main features of the Corpo Quatro deposit, described above, can be compared with the two main styles of mineralization which are the result of late-metamorphic and magmatic fluids. Firstly, there are a number of similarities between the Corpo Quatro deposit and porphyry copper/mesothermal base-metal vein deposits, which contain high salinity fluid inclusions generated by magmatic fluids. Secondly, the Corpo Quatro deposit shows very strong similarities with many Archaean stratabound base-metal deposits, such as those of the Cloncurry district in the Mt Isa Inlier, Queensland, Australia, which have recently been reinterpreted as epigenetic, metamorphogenic deposits (Blake and Williams, 1993; Oliver *et al.*, 1993).

Fluid inclusions from the Corpo Quatro Formation are also comparable with fluid populations from a number of different geological environments; the moderate to high salinity aqueous inclusions which dominate the Corpo Quatro fluids being particularly comparable with those found in porphyry copper, retrograde metamorphic, and metamorphogenic base-metal deposit terranes (Nash, 1976; Oliver *et al.*, 1993; Williams, 1993).

6.4.1 *Magmatic (porphyry and vein) deposits*

Porphyry copper deposits and mesothermal vein deposits are commonly generated by fluids with a granitic signature, and are located near to major magmatic intrusive bodies. They are rarely found in terranes older than 450Ma, although low grade deposits with porphyry copper characteristics are known in Proterozoic (Haib, Namibia) and Archaean (Western Australia) rocks (Gustafson, 1979). Porphyry copper deposits form as the result of the emplacement of hydrous magmas into permeable rock, and they tend to display two main phases of hydrothermal alteration. Associated fluids are typically composed of several inclusion populations, which represent boiling systems (vapour-rich as well as liquid-rich inclusions), contain minor amounts of volatiles (up to 3 mole percent CO_2), and have salinities ranging from 0 to >50 wt.% eq. (Nash, 1976).

The main hydrothermal phase in porphyry copper deposits is related to the deposition of Cu-Fe sulphides, and is commonly associated with propylitic, albitic and potassic alteration. The dominant fluids at this stage are highly saline (typically 30-60 wt.% eq) and may contain halite, sylvite and anhydrite daughter minerals (Roedder, 1984; Dilles and Einaudi, 1992). Sulphide minerals occur within fractures and quartz veinlets or disseminated within the potassic alteration zone. This main phase of mineralization commonly consists of pyrite, chalcopyrite and bornite (Edwards and Atkinson, 1986). Later stage, post-ore fluids are generally of lower salinity (~2-13 wt.% NaCl eq), and are associated with sodic (albite), chloritic and sericitic alteration (Dilles and Einaudi, 1992).

The porphyry copper mineral assemblages found in the propylitic and potassic alteration zones are particularly relevant to the Pojuca C4 deposit. Propylitic alteration is characterized by albite and epidote, with the alteration of plagioclase to epidote + albite + sericite, hornblende to actinolite, and biotite to chlorite. This assemblage is commonly found at depth, where it surrounds epidote veins, whereas at higher crustal levels propylitic (albitic) zones may also contain pyrite ± chalcopyrite ± magnetite. Potassic alteration zones are rich in veins of biotite-quartz-K-feldspar and chalcopyrite-molybdenite-bornite, and,

in later veins of epidote, chalcopyrite may also be abundant (Dilles and Einaudi, 1992). The fluids in equilibrium with the potassic ore zones form at temperatures between 500 and 700°C (Evans, 1987), and the main stage of mineralization often accompanies the intrusion of granitic porphyry dykes, as seen in the porphyry copper deposits of the Yerington district, Nevada (Dilles and Einaudi, 1992).

Mesothermal vein and replacement deposits containing both precious and base metals occur in quartz veins and as massive wallrock replacement. The alteration assemblages, with the exception of the absence of a potassic zone, are similar to those found in porphyry copper systems, and include chloritization, carbonitization or sericitization. Albite, sericite and epidote are common products of wallrock alteration in these deposits, which tend to be generated by moderate salinity fluids at temperatures of between 200 and 300°C (Evans, 1987).

The granite-related fluids with which both porphyry copper and mesothermal vein deposits are associated have a characteristic fluid chemistry, which is also present in both tin-bearing and barren granite systems. The magmatic fluids, regardless of salinity, are dominated by NaCl and KCl, with Na:K ratios of around 0.5 (Holland, 1972). The calcium content of the fluids is low (Ca:Na <0.1), and high FeCl values are not uncommon (Fe:Na= 0.09 to 0.18; Eadington, 1983). Typical alkali-metal ratios from granitic fluids are presented below:

Table 6.2 **Typical compositions of magmatic fluids compared with the Pojuca mineralizing fluids (after Eadington, 1983)**

Location	K:Na	Ca:Na
Bougainville, PNG (Cu)	.24	.03
Mole Granite, NSW (Sn)	.43	-
Bolivian Granites (Sn)	.66	.02
Pojuca T1 Fluids	.01-.18	.22-.56
Pojuca T2 Fluids	.11-.17	.37-.55

6.4.2 *Retrograde metamorphogenic deposits*

The retrograde metamorphogenic class of ore deposit was introduced by Pohl (1992) to describe the method of ore accumulation as a direct result of retrograde metamorphic fluids in orogenic belts. It is a term which can be applied to deposits such as those of the Cloncurry district, Mount Isa, which, like the Pojuca C4 deposit, is associated with quartz veins and occurs in iron-formation and related Archaean metasediments. These deposits differ from magmatic vein deposits, in that they are dominantly stratabound, and have been interpreted as being of post-peak metamorphic origin, deposited from mixed metamorphic and meteoric fluids during retrograde metamorphism (Blake and Williams, 1993).

Albitization is the typical alteration assemblage associated with this type of deposit, particularly in the Mount Isa district, where zones of white albitization pre-date the main phase of sulphide

mineralization, and pink, haematite-rich albite ± epidote-chlorite-calcite-magnetite assemblages post-date the mineralization. These alteration assemblages have been interpreted as the result of peak-metamorphic and retrograde fluids interacting with the wallrock (typically magnetite-bearing iron-stones; Oliver *et al.*, 1993; Blake and Williams, 1993).

Fluid inclusions associated with the main phase of mineralization in these deposits (eg. Pegmont, Mary Kathleen) are generally of high salinity (up to 60 wt.% NaCl eq.), and may be formed at temperatures up to 450-500°C (Oliver *et al.*, 1993; Williams, 1993), although fluids of between 200-400°C are common in metamorphic-associated sulphide deposits. The fluids are Na-K-rich, and contain halite, sylvite and iron-chloride daughter minerals like those found in the late-stage Corpo Quatro fluids. These fluids have been interpreted as being late metamorphic fluids, associated with retrograde mineral reactions.

The retrograde metamorphic environment is known to be ideal for sulphide deposition, as the solubility of metals in solution decreases with cooling of the metamorphic belt, leading to precipitation of sulphide minerals (Pohl, 1992). Sodium-calcium-rich brines, common in base-metal deposits, are known to be effective solvents of base metals (White, 1967) and are the common product of retrograde metamorphic re-hydration reactions (Crawford *et al.*, 1979; Bennett, 1990). The generation of high salinity fluids, which are typically associated with evaporitic sequences or late orogenic granites, is especially common in greenschist to upper amphibolite facies metamorphic sequences, where Na-Ca-rich brines are produced during the rehydration of minerals such as garnet and amphibole to chlorite on retrogression, as shown below:

$$\text{Garnet (Ca-rich)} + 6H_2O \rightarrow \text{Chl} + H^+_{(aq)} + X_{(aq)}$$

$$2\text{Garnet} + 2K^+_{(aq)} \rightarrow \text{Biot} + X_{(aq)}$$

$$\text{Hbl} + 2K^+ \rightarrow \text{Biot} + 2X_{(aq)}$$

Providing the introduction of water into the system is minimal, these fluids then become increasingly saline and calcium-rich as retrogressive reactions continue (Bennett and Barker, 1992), therefore providing ideal conditions for the transportation of metals as chloride-complexed species.

6.4.3 *Method of metal-transport in the fluids*

The most likely method of metal transport in the Corpo Quatro deposit, in view of the high salinity Cl-bearing fluids and the temperature at which the fluids would be transported (>250°C), is by chloride complexing in the presence of low amounts of reduced sulphur. These conditions would prevent the metals from being deposited until conditions are favourable, and is applicable for either of the genetic models being considered.

Sulphide precipitation from chloride complexed species is occurs when environmental changes affect the solubility of metals being carried in the fluid. This can occur because of a sudden increase of fluid pH, which is caused by boiling or an abrupt change in wallrock (and subsequent wallrock alteration), or it can be the result of a decrease in either temperature or chloride content of the transporting fluid (Barnes, 1979; Evans, 1987).

The retrograde metamorphic environment provides the ideal setting for the transportation and deposition of metals by chloride complexing, as previously discussed. Cations such as Na^+ and Ca^{2+} are continuously being added to the high salinity fluids, therefore reducing the amount of chloride available for combining with metal species and resulting in the deposition of ore. Combined with a sulphur-rich environment, provided by the pyrrhotite-bearing Rochas Bandadas, this is believed to be the dominant method by which metals were transported and deposited in the Corpo Quatro Formation.

6.4.4 *Possible genesis of base-metal deposition in the Corpo Quatro deposit*

The genesis of the mineralization and associated features in the Pojuca area can be accounted for using both of the genetic models outlined above. The proposed models applied to the Pojuca C4 deposit are summarized in *Figure 6.2*, and described below:

Magmatic-associated ore genesis

The magmatic model postulates that lower amphibolite grade regional metamorphism of the Corpo Quatro Formation was followed by the intrusion of a magmatic body at depth. From the age of mineralization relative to metamorphic fabrics and mineral assemblages, it must be inferred that this intrusion was an orogenic event. Assuming that the retrogression observed in the Corpo Quatro Formation belongs to the same orogenic episode as peak regional metamorphism, the magmatic body would have been emplaced soon (within 50-70Ma) after peak-metamorphism. Although a large granitic body of this age has not yet been identified in the field, its presence is inferred from granitic dykes which cross-cut the metamorphosed sequence and closely relate to chalcopyrite mineralization and quartz veining. The absolute ages of these granitic dykes is unknown. There is supporting evidence for the presence granitic activity earlier than the Pojuca Granite, 25km away from Pojuca in the Salobo 3A area; the Old Salobo Granite has been dated at 2530Ma (Machado *et al.*, 1991), which post-dates metamorphic activity, and it is speculated that this may also have been active in the Pojuca area.

In the magmatic model, which is summarized in *Figure 6.2*, fluids expelled from the granitic mass and from its associate granitic veins subsequent to crystallization were responsible for the deposition of sulphide minerals, and the copper and zinc were probably of magmatic origin. Fluid flow would predominantly have occurred through conduits generated during the intrusion of the deep-seated magmatic body, or during the preceding regional metamorphism. This fluid flow resulted in the deposition of ore minerals in quartz veins associated with the early, moderate salinity type T1 fluids. The T1 fluids have slightly higher K:Na ratios than the later, type T2 fluids, and are roughly comparable with the chemistry of the Bougainville granitic fluids (see Table 6.2).

The copper-rich albitic alteration zone in the C4 deposit is an alteration assemblage typically associated with the main stage of ore deposition in porphyry and magmatic vein deposits. A relationship with the main ore stage at Pojuca is supported by the presence of massive and disseminated chalcopyrite in the albitic zones. However, albitization is commonly observed surrounding epidote veins, which are known to post-date the granitic veins in the C4 deposit, implying that the timing of the albitization was, at the earliest, late-main-stage mineralization.

The magmatic model for ore genesis at Pojuca does not truly account for the second stage of sulphide precipitation in quartz-biotite veins and in the host rock. This is associated with high salinity fluids, whereas the late stage mineralization in magmatic deposits is typically generated by low salinity (2-13 wt.% NaCl eq.) fluids and associated with albitic and chloritic, not potassic, alteration.

Metamorphogenic ore deposition

In this model, summarized in *Figure 6.2*, it is postulated that mineralization was generated by fluids of retrograde metamorphic origin, and not related to magmatic fluids. Relative to the regional metamorphism, this study dates sulphide mineralization as a post-peak and pre/syn-retrograde event, during which fluids were circulated through the Corpo Quatro Formation, stripping metals from the host rocks and redepositing them as sulphides under favourable conditions. This theory is supported by the depletion of copper in the C4 basalts relative to comparable volcanics in the Carajás Belt, although as already discussed a corresponding zinc depletion is not observed, indicating that metals may also have been leached from units distal to the Corpo Quatro Formation.

It is proposed that the fluids responsible for ore deposition were not derived from the dehydration reactions undergone during metamorphism of the Igarapé Pojuca Group, as these fluids would have been released through veins during prograde metamorphic conditions. These fluids may, however, be represented by the very early, barren quartz (Q1) veins in the C4 Formation. Several fluid sources must be considered in view of this model, in which the origin of mineralizing fluids is not as clearly defined as it is for the magmatic model of ore genesis. The source of retrograde fluids favoured by many workers is by the devolatilization of deeper strata during or subsequent to overthrusting of already metamorphosed units (Kerrich and Fyfe, 1981). However, the lack of regional understanding of the Carajás Belt, particularly the lower Itacaiunas Supergroup, means that this hypothesis for mineralizing fluids in the Corpo Quatro Formation is purely speculative. An alternative water source in the mineralizing process is that produced by downward fluid flow. Deep penetration (6-12km) of both meteoric and sea water is known to be effective in hydration and mineralization of metamorphic belts and the formation of gold deposits, by the downward percolation of fluids from the surface through the sequence via faults and shear zones.

Without stable isotope data from the fluids, neither one of these fluid sources can be ruled out. Whichever fluid source is supported, there is a need for fluid pathways through the Corpo Quatro Formation. There is evidence for brittle-ductile structures in the form of vein-bearing fault zones in the Igarapé Pojuca Group, which may have been generated during uplift and shearing in the post-peak metamorphic environment, and micro-fractures throughout the host rocks are evident from the cross-cutting trails of fluid inclusions seen in quartz, and these are thought to be sufficient for the flow of fluids to generate retrograde metamorphism and sulphide mineralization over several tens of millions of years.

The metamorphogenic model therefore suggests that Na-Ca-rich retrograde metamorphic fluids, driven by an external heat source, were circulated along faults and microfractures throughout the Pojuca Corpo Quatro Formation following peak regional metamorphism. There is no direct evidence for the heat engine, and although the fluids may have been driven by the introduction of a magmatic body at depth, the regional heat produced by the metamorphic Carajás Belt is more feasible.

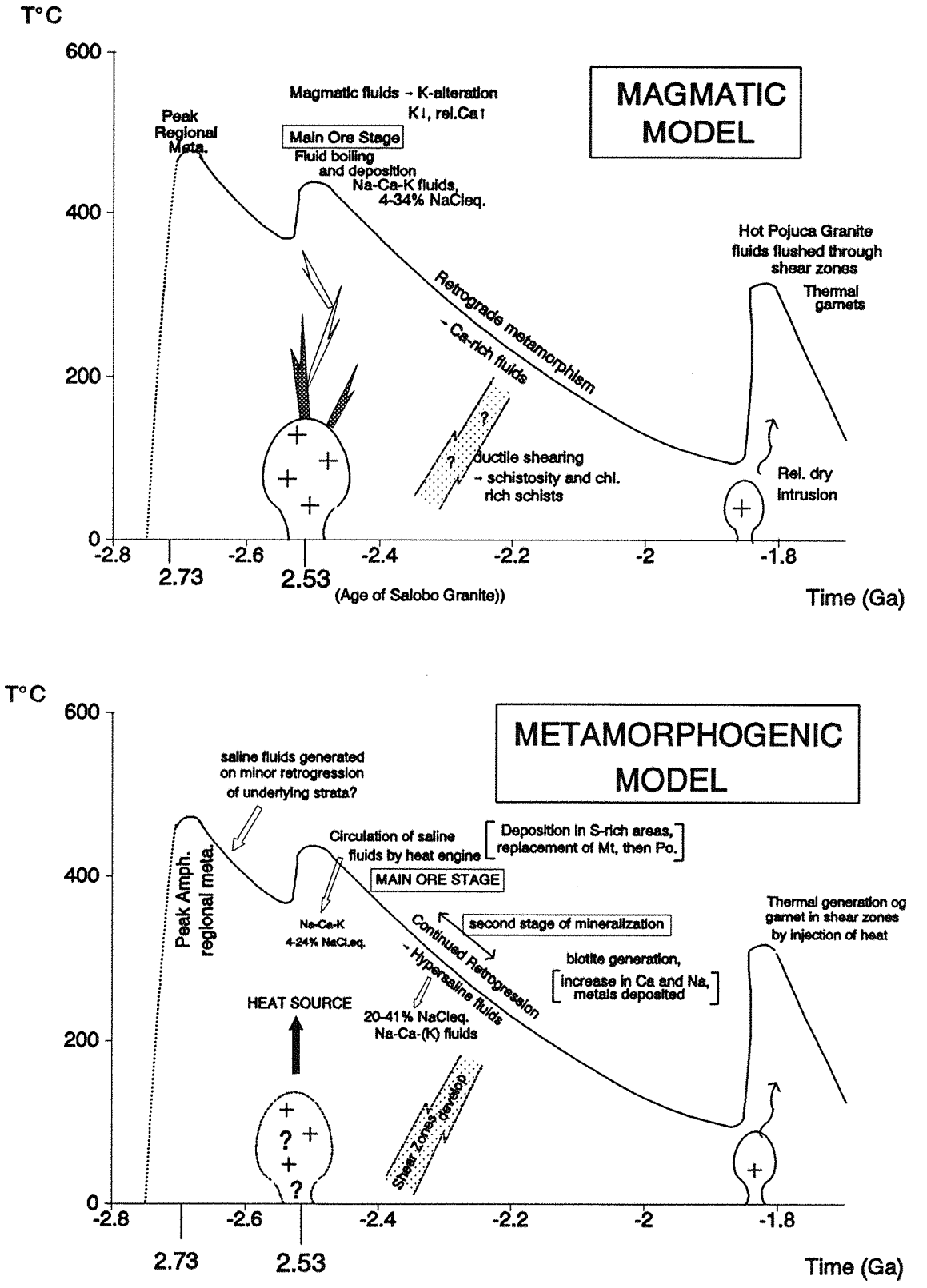

Figure 6.2 **Schematic representation of the possible models of ore genesis in the Corpo Quatro copper-zinc deposit, plotting time against approximate temperature. Scales not absolute. A Magmatic model; B Metamorphogenic genesis of sulphide mineralization.**

Following leaching of metals from the strata, regional cooling of the belt resulted in the sodic (albitic) and sodic-calcic (hornblende) alteration observed in the Corpo Quatro Formation, which accompanied the deposition of sulphide minerals from Na-Ca-rich fluids. These sulphide minerals were deposited in quartz and tourmaline veins, and as disseminated and fracture-hosted sulphides predominantly in the iron-rich sediments of the Corpo Quatro Formation. This initial stage of mineralization began with the precipitation of Cu-Fe-sulphides, progressing to the replacement of both chalcopyrite and pyrrhotite by sphalerite. Albitization in the retrograde model is interpreted as a product of retrograde metamorphic fluids, and as such is similar to albitization observed in the Cloncurry deposits (Williams, 1993; Oliver *et al.*, 1993). It is not, however, believed to be a post-mineralization event (like that at Cloncurry), rather it is thought to have been synchronous with the initial stage of ore deposition.

Continued retrogression in the Corpo Quatro Formation appears to have resulted the second stage of sulphide mineralization, which is associated with hypersaline fluids and quartz-biotite veining. This is interpreted as the result fluid-wallrock interaction under low fluid-rock ratio conditions. The alteration of amphiboles and garnets to biotite and chlorite in retrogressive reactions is accompanied by an increase in Na^+ and Ca^{2+} relative to Cl in the fluids, therefore depleting the Cl available for metal complexing in the solution and resulting in ore deposition. The late stage of mineralization at C4 is also characterized by minor nickel and molybdenite deposition, with the nickel enrichment manifested by increases in Ni in the mineralized relative to the barren Rochas Bandadas and Xistos Granadas, indicating the introduction of Ni and precipitation of Ni-arsenides at this stage.

6.4.5 *A critical evaluation of mineralization at Pojuca C4*

In order to establish which of the models outlined above is applicable to the situation at Pojuca, it is necessary to consider the origin and chemistry of the mineralizing fluids, the nature of the chemical overprint on the pre-existing mineral assemblages in relation to the sulphide enrichment, and the timing of the mineralization and alteration in relation to other geological events in the Carajás region.

Mineralizing Fluids

Many fluid inclusion studies related to epigenetic granite-related and metamorphogenic base-metal deposits have displayed an affinity between hypersaline fluids and the main stages of mineralization, whereas fluids of lower salinity are commonly associated with early- or late-stage alteration and only minor mineralization (Nash, 1976; Heinrich *et al.*, 1989; Banks and Russell, 1992). The converse is evident at Pojuca, although the early ore-related fluids are not unlike those seen in other deposits, and have salinities up to 34 wt.%, which is not particularly 'low'.

The estimated trapping temperatures for the mineralizing fluids at Pojuca, inferred from the isochore diagrams in Chapter 5, has indicated that although the total homogenization temperature is the same for type T2 (Ts_H = 210°) as for type T1 inclusions, the modal trapping temperature of the Corpo Quatro fluid inclusions decreases from between 283° and 470°C in the early, type T1, inclusions to 273-410°C in the later, T2, multisolid inclusions. These temperatures are too low for typical granite-related fluids, and are comparable with retrograde environment fluids described in section 6.4.2. Dissolution of

the iron-chloride daughter in some of the T2 inclusions has rarely been observed, even when the temperature is held at 450 to 500°C for up to one hour. This could imply trapping of the late stage T2 fluids (responsible for the second-stage mineralization, quartz-biotite ± chalcopyrite Q2-B veins) occurred at temperatures in excess of 500°C, i.e. at higher temperatures than the earlier, T1 fluids. There has, however, been little or no wallrock alteration associated with the late biotite-bearing veins, as might be expected from a high temperature fluid injection, and it would therefore appear more likely that the inability to achieve Th_{tot} is a function of metastability of the iron-chloride phase.

Fluid Chemistry

The chemistry of the fluids throughout the post-metamorphic history of the Corpo Quatro Formation is consistently sodium-calcium-rich, with the Ca:Na ratio falling between 0.22 and 0.56 and the K:Na ratio between 0.06 and 0.18. As established in Chapter 5, fluids in which calcium dominates over potassium are comparable with present day Salton Sea brines, with metamorphic fluids similar to the retrograde fluids found in many orogenic belts, such as the Caledonides of Northern Europe (Bennett and Barker, 1992), and with ore-related fluids from base metal deposits in the Canadian Shield. The alkali-metal ratios of these fluids are atypical of most granitic fluids (*Table 6.2*; Holland, 1972), suggesting that unless the fluids have undergone significant modification prior to deposition, the Pojuca C4 deposit is not related to magmatic fluids, as indicated by the field relationships between some quartz-sulphide-bearing and granitic veins. Modification from an initially Na-K-Ca-rich fluid to a Na-Ca-(K) bearing fluid would require a relative enrichment in calcium and a slight depletion in potassium, which could occur as a result of extensive modification by wallrock interaction in one of two ways: i) The significant enrichment of calcium and removal of potassium in the fluid, which would result from the retrograde alteration of amphibole and garnet to biotite; or ii) the depletion of both K and Na in the fluid, resulting in a relative enrichment in calcium. K-depletion of may occur in reactions such as the intense potassic alteration seen in porphyry copper systems, although in the Pojuca deposit potassic alteration is only seen to a minor extent, in the metavolcanics, and in the Rochas Fragmentos, where retrograde metamorphism has resulted in the replacement of garnet and amphibole by biotite. Sodium depletion, too, could be accounted for by alteration, in the form of intense albitic alteration, which is present to a larger extent in the Corpo Quatro Albite Zone.

Although this modification of the fluid chemistry is feasible, it would be more reasonable to explain the Corpo Quatro fluid composition in terms of the similar fluids found in ore deposits in metamorphosed belts, therefore making the metamorphogenic model the most acceptable source of the Corpo Quatro fluids.

Wallrock alteration in the Corpo Quatro Formation

In discussing the mechanism of sulphide enrichment in the Corpo Quatro Formation, the alteration associated with mineralization must also be considered. The dominant alteration assemblage associated with sulphide mineralization in the ore-bearing strata is the hornblendization of the metamorphic Fe-Mg-amphiboles in contact with chalcopyrite and pyrrhotite. The intimate spatial

association clearly indicates that both sulphide mineralization and hornblendization in the Rochas Bandadas were the result of post-metamorphic sodic-calcic alteration around sulphide mineralization, thought to have been caused by the same, ore-bearing, type T1, Na-Ca-rich fluid.

Albitization in the C4 deposit is the other dominant alteration phase in the Corpo Quatro Formation, and with the presence of abundant tourmaline, it is similar to the sulphide-rich propylitic alteration seen in porphyry copper deposits. However, as discussed in section 6.3.1 it is also similar to albitization observed in a number of base-metal sulphide deposits worldwide, including those in Noranda, Quebec, and in the metamorphogenic deposits of the Cloncurry district of Australia.

Having established that the ore-bearing fluids and associated wallrock alteration post-date peak-metamorphism in the Pojuca C4 deposit, the exhalative alteration pipe was ruled out in section 6.3.1. However, albitization in porphyry copper deposits is attributed to syn-mineralization fluids, and in the Pegmont (Pb-Zn) and the Mary Kathleen (U-REE and Cu) deposits of the Cloncurry district it has been interpreted as being the result of late, retrograde metamorphic reactions, associated with Na-rich, high salinity fluids (Oliver *et al.*, 1993), and comparable with that seen at Pojuca.

The relative timing of the albitic alteration is harder to interpret than the hornblendization. In the Cloncurry deposits, the albitization is late-stage, and contains only minor amounts of sulphide minerals, whereas the Pojuca C4 Albite Zone contains significant amounts of both massive and disseminated chalcopyrite as well as minor gold. As such it would appear that the Na-rich fluids responsible for albitization of the C4 basalts were copper-bearing, and therefore that this alteration was synchronous with one of the ore stages. This is comparable with magmatic-related albitization in porphyry-style deposits, which is sulphide-rich and synchronous with both the early and the late stages of ore mineralization.

There is no direct fluid inclusion evidence for the relationship between albitization and mineralization, and as such may be related to either the main stage or the later stage of mineralization. However, in addition to stringer-type chalcopyrite and chalcopyrite-tourmaline veinlets in the C4 Albite Zone, the albitization is also cross-cut by epidote-chalcopyrite veins, indicating that copper mineralization continued after the introduction of the initial Na-rich mineralizing fluids. This is also in evidence in the biotite-rich quartz (Q2-B) veins throughout the Corpo Quatro Formation, which host small amounts of sulphides and post-date the main Q2-A phase of mineralization. As such, this suggests continued chalcopyrite precipitation rather than the local remobilization of pre-existing phases by later fluids.

Timing of the mineralization

It has been established with some certainty that there were two stages of sulphide mineralization in the Pojuca C4 deposit. Both stages of mineralization post-dated peak metamorphism, and occurred prior to the retrograde reactions in the silicates of the Corpo Quatro Formation. Evidence for this is found in the metabasalts, where sulphide minerals pseudomorph cleavage of amphiboles which have subsequently been replaced by retrograde silicates, and in the metasediments where sulphide minerals also formed along the cleavage of amphiboles, which were then replaced by or cross-cut by biotite. In order to establish the chronological position of granitic veins and the Pojuca Granite in relation to the

mineralization and the history of the deposit, field relationships must be considered.

The Pojuca Granite, which is found at the base of most of the western C4 boreholes, has been dated at 1880Ma. (Machado *et al.*, 1991). This age, young in relation to the age of metamorphism in the region, complies with intrusive relationships between the granitic body and the host Corpo Quatro Formation. Apart from the presence of garnet overprinting chlorite assemblages in zones of intense schistosity in the Corpo Quatro Rochas Fragmentos, this intrusion shows no evidence of thermal metamorphism on the country rocks into which it intruded. The Pojuca Granite has therefore been interpreted as being a relatively dry intrusion. There is little direct evidence for the age relationship between the Pojuca Granite and any of the veining events in C4, however it is possible to infer that mineralization occurred prior to retrograde metamorphism, and the Pojuca Granite was intruded as an anorogenic, late-stage body in the history of the Carajás region (Docegeo, 1988), and it is not possible that this body was responsible for Cu and Zn sulphide mineralization at Pojuca.

The small number of **granitic veins** present in the C4 deposit (as well as those found in abundance in the C2 deposit) and the related granitization and branching quartz-chalcopyrite veins all overprint the metamorphic mineral assemblage and therefore post-date peak regional metamorphism. There is, however, no evidence for the age relationship between these granitic veins and retrograde metamorphism, and hence it cannot be confirmed that the granitic veins are related to the same intrusive event as the Pojuca Granite. However, the granitic veins have themselves been overprinted by a shearing event similar to that observed in the Corpo Quatro Formation host rocks, and by a phase of calcite veining. Epidote-chalcopyrite veins are also observed to post-date the granitic veins. There is no direct evidence in the granite veins for the age relationship between the epidote veining and the shear event, although epidote veins carry chalcopyrite mineralization, and chalcopyrite and pyrrhotite show some deformation by the shearing event, implying that the shearing post-dates the epidote veining.

6.5 SUMMARY OF SUPPORTING EVIDENCE

Both the magmatic and metamorphogenic models, summarized in *Figure 6.2*, account for the post-peak metamorphic, pre-retrograde timing of the ore deposition, varying primarily in the source of the ore-bearing fluids.

The main supporting evidence for the magmatic model lies in the close association between the granitic dykes and chalcopyrite-bearing quartz veins in the Pojuca area. The alteration assemblages, such as chalcopyrite-rich epidote, and albite-sericite-chlorite-ilmenite, also closely resemble the propylitic alteration observed in some porphyry copper deposits (e.g. Iron Mask, British Columbia; Thompson *et al.*, 1992) and magmatic vein deposits. The association of moderate salinity aqueous and aqueo-carbonic fluid inclusions with the main stage of ore mineralization may be interpreted as showing some evidence of boiling, and this too is comparable with magmatic-associated vein deposits.

There are, however, a number of drawbacks with this model. One major problem is the lack of substantial evidence for a granitic body at depth. The intrusion of the 2530Ma Old Salobo Granite in the Salobo 3A area was a relatively minor event, and the ~200Ma gap between the identified peak metamorphism in the Pojuca area, at 2732Ma, and the intrusion of the Old Salobo Granite, means that

if the peak- and retrograde metamorphic assemblages belong to the same orogenic event, the possibility that granitic activity of this age was responsible for pre-retrograde mineralization is remote.

The contrast between the chemistry of the C4 fluids and typical granitic fluids also presents a problem, and substantial pre-depositional modification of the fluids is necessary in order to explain their composition using the magmatic model. Although sulphide minerals in the Pojuca C4 deposit are commonly found in quartz veins and associated with tourmaline in albitic alteration, the disseminated and stratabound nature of the ore minerals is contrary to typical magmatic-related mineralization, which is generally concentrated in a particular zone of alteration rather than in a lithological horizon. The location of the sulphide minerals in the C4 Rochas Bandadas is therefore suggestive that deposition was by chemical reduction of the fluid on contact with iron-rich strata, an effect not commonly associated with vein deposits.

The main evidence for the retrograde model lies in the stratabound nature of the mineralization, the affinity of the ore-bearing fluids to those found in typical retrograde metamorphic terranes, and the presence of the albitic alteration zone, which is comparable to those which have been interpreted as retrograde features in other metallogenic regions.

Both models explain the timing of the main stage of copper-zinc mineralization in terms of post-peak, pre-retrograde metamorphism, followed by the deposition of late-stage hydrothermal ores including minor chalcopyrite, subordinate sphalerite, gold, nickel-arsenides and molybdenite. The source of the Au, Ni and As is unknown, but may be similar to the Cu and Zn, which were hydrothermally stripped from the rock by mineralizing fluids.

Following extensive discussion as to the style of the Corpo Quatro deposit and the fluids responsible for its deposition, a conclusion must be reached on the nature of this orebody. Evidence has suggested that although the fluids in the Corpo Quatro Formation show several similarities to those found in typical porphyry systems, they are most similar to those fluids associated with retrograde orogenic belts. They can also be compared with known mineral deposits, particularly those in the Mount Isa and Cloncurry district of Australia, with which the Corpo Quatro deposit is almost identical. The fluids have therefore provided the best indication as to the genesis of the orebody at Pojuca, which, it would seem most likely, is the result of retrograde fluid flow through an iron-formation host-rock, during which sulphide minerals were deposited in a stratabound nature. The granitic source, however, can not be conclusively ruled out.

6.5.2 *Mechanisms of sulphide deposition*

It needs to be considered why the sulphide mineralization is dominantly found within the iron-rich Rochas Bandadas, and is less abundant in the Rochas Fragmentos, and how it was deposited in these strata. The predominance of sulphide minerals in the Rochas Bandadas can probably be explained in terms of base-metal 'dumping' at a lithological boundary, and by the abundance of iron-oxide horizons in the Rochas Bandadas. It has been observed that the majority of the sulphide minerals are located in horizons parallel to the mineralogical banding, and, in many cases, they appear to be replacing magnetite

and/or ilmenite laminae. It is proposed, therefore, that Banded Sulphide precipitation in the Rochas Bandadas is a selective replacement of iron-bearing species, resulting from the sulphidation of magnetite to pyrrhotite by aqueous sulphur species in weakly reducing fluids (Phillips *et al.*, 1984). The subsequent alteration of pyrrhotite to chalcopyrite was most likely induced by the contact of copper-zinc-bearing chloride-rich fluids with sulphur-bearing strata, and the consequent replacement of iron-sulphide by chalcopyrite and sphalerite.

It is proposed that the main method of disseminated and vein sulphide precipitation in the Rochas Bandadas was caused by a change in the physio-chemical state of the fluid; ie. that the movement of the fluid into the iron-rich strata caused precipitation of metals, while ore deposition in the Rochas Fragmentos was the result of retrogression, and increased alkali-metal content in the fluids thereby decreasing the availability of chloride in solution and resulting in the deposition of sulphide minerals. These assertions are supported by the observation that, in the Banded Rochas Bandadas mineralization, Cu- and Zn sulphides appear to form as replacement phases, whereas in the Fracture, disseminated and vein styles these minerals form primary phases, and display no intimate relation with pyrrhotite.

Retrograde fluids had only minor effects on the Rochas Bandadas, where they resulted in some replacement of amphibole by biotite. It is probable, therefore, that these late fluids were channelled by microfractures in the Rochas Bandadas, which appear to have suffered brittle deformation throughout their post-peak metamorphic history, whereas in the Rochas Fragmentos, where the effects of retrograde metamorphism is severe, the late mineralizing fluids were channelled in shear zones. These main shear zones, in which a schistose fabric has been developed, post-date both the granitic veins and the sulphide mineralization in the Rochas Fragmentos. They are therefore thought to have developed during retrograde metamorphism, where a ductile regime existed prior to complete cooling of the belt.

It is believed, in both models, that there was little activity in the Pojuca region between the end of retrograde metamorphism, which probably occurred between 50 and 70Ma after peak metamorphic conditions (estimated by comparison with Phanerozoic time scales), and the intrusion of the Pojuca Granite at 1880Ma. Although the Pojuca Granite is believed to have been a relatively dry intrusion, it is thought to have resulted in the thermal metamorphism of phyllosilicates, particularly in the relatively permeable zones of intense schistosity in the Rochas Fragmentos, during which chlorite was replaced by late-stage garnet. In these areas of intense schistosity, the zinc-rich spinel gahnite is sometimes observed to display identical textures to this late, overprinting garnet, and therefore these two minerals are interpreted as being the only thermal effect of the Pojuca Granite on the surrounding rocks.

Chapter 7
Conclusions and Future Research

CONCLUSIONS

1 The Corpo Quatro Formation

The Corpo Quatro Formation, which forms the lower half of the Igarapé Pojuca Group and outcrops in the area around the Pojuca Corpo Quatro copper-zinc orebody, dips towards the south-west at an angle of between 50 and 90°. The Corpo Quatro Formation is composed of a metamorphosed, conformable sequence of volcanic and sedimentary units.

2 The country rocks

The metavolcanics of the Corpo Quatro Formation are of basaltic and basaltic andesite composition according to the alkali-silica classification, and are comparable in terms of immobile trace element geochemistry (Ni, Ce, Cr and Zr) with the basalts of the Grão Pará Group and the Igarapé Salobo Group, which also form part of the Carajás Belt. Trace element ratios indicate the C4 volcanics to be typical of Archaean basalts, and although discrimination diagrams are ambiguous, they predominantly plot as within-plate tholeiites, complementing the LREE enrichment which is indicative of eruption in a continental, extensional basin.

Relative to other basalts of the Carajás Belt, the Corpo Quatro basalts display enrichment in the relatively mobile elements Fe, K and Rb, and depletion in Ca and Sr, as well as in Ti. The local variation of these elements is representative of post-depositional modification.

3 The host sequence

The sedimentary sequence of the Corpo Quatro Formation lies between two basaltic units. It often forms a repeated sequence. The basal unit of this sedimentary sequence is termed the Rochas Bandadas, and is an iron-formation comprising between 30 and 45% Fe_2O_3. This unit is composed of alternating laminae of quartz, grunerite and magnetite (the magnetite-Rochas Bandadas) or quartz, grunerite, hornblende and sulphide minerals (the silicate-Rochas Bandadas).

The basal Corpo Quatro iron-formation grades upwards into a series of metasedimentary rocks termed the Rochas Fragmentos, characterized by the presence of sub-angular to sub-rounded quartz clasts. These have been interpreted as intraformational clasts formed by the syn-sedimentary erosion of the underlying iron-formation.

At the base of the Rochas Fragmentos is a quartz-grunerite-graphite-almandine garnet-biotite-rich schist, termed the Xistos Granadas. This is a mixed facies comprising between 12 and 37% Fe_2O_3, and is also strictly an iron-formation. From the Rochas Bandadas to the Xistos Granadas, the enrichment displayed in the 'heavy' detrital elements (Ti, Zr, V, Y and Cr) and aluminium, and the decrease in silica and iron, are indicative of an increased sedimentary input into the unit.

The Xistos Granadas is overlain by quartz-chlorite and quartz-hornblende-rich schists known as the Xistos Quartzos. This unit contains only 18 to 20% Fe_2O_3, and as such cannot be classed as an iron-formation, but its high aluminium content (12%) identifies it as a ferruginous pelite, a typical clastic Archaean sediment in terms of geochemistry. The only major geochemical variation between the two Rochas Fragmentos units is an enrichment in K and Na, interpreted as representing an increase in clay component of the clastic sediments.

The clastic material, which was admixed with the products of continued chemical sedimentation to form the Rochas Fragmentos, is volcanic in origin, and is thought to have been eroded from the lower Corpo Quatro volcanics or from similar, older basalts.

4 **Metamorphism**

In the area of the Pojuca Corpo Quatro deposit, the sedimentary and volcanic rocks of the Corpo Quatro Formation have undergone one major regional metamorphic event, which reached upper greenschist to lower amphibolite grade. This resulted in the development of the metamorphic mineral assemblage of almandine garnet-quartz-biotite in the Rochas Fragmentos, although none of the characteristic metapelite minerals (plagioclase feldspar or Al-silicates) are present. Using graphite as a metamorphic indicator, it has been established that the metamorphic zone reached by the sequence is between the garnet and the staurolite-andalusite zone. This is supported by the mineral assemblages throughout the sequence. A tentative upper limit on pressure has been placed between 5 and 7kb using aluminium in amphibole as a geobarometer, which corresponds to a temperature of between 450 and 600°C according to the upper greenschist - lower amphibolite boundary. No empirical data have been obtained for temperatures.

5 Following peak metamorphism, the lithological units of the Corpo Quatro Formation experienced retrograde metamorphism. During this phase, amphibole and garnet in the Rochas Fragmentos and metavolcanic units underwent at least partial replacement by biotite, whereas the Rochas Bandadas display only minor alteration to phyllosilicates.

Although these retrogressive reactions are believed to be the result of fluid flow during regional cooling of the metamorphic belt from the peak metamorphic conditions, there is no definitive evidence that retrogressive metamorphism is not the product of an entirely separate metamorphic phase.

6 **Granitic activity**

The Corpo Quatro Formation has been intruded, in the area of the Corpo Quatro deposit, by at least two phases of granitic magmatism. The first phase is represented by granitic veins, which are up to 2m wide and composed of plagioclase, orthoclase feldspar and quartz. This magmatic event post-dates peak metamorphism in the Corpo Quatro Formation. The second phase of granitic intrusion is represented by the Pojuca Granite, an adamellite stock dated at

1800Ma in the western part of the Pojuca Corpo Quatro area. This body cross-cuts the strata, but has had little obvious effect on the immediate wallrock.

7 **Post-metamorphic deformation**

The units comprising the Corpo Quatro Formation have been overprinted by shear zones, which are up to 3m wide, and resulted in the development of an intensely schistose fabric in the rock. This shear deformation took place after the development of retrograde biotite, and provided local fluid pathways for the migration of fluids in the chlorite metamorphic zone. This resulted in the extensive alteration of peak-metamorphic amphibole and retrograde biotite to chlorite (ripidolite). Shear zones have been observed in all strata of the Corpo Quatro Formation except the Rochas Bandadas, which have responded by brittle faulting rather than ductile deformation.

8 There is some evidence for minor thermal metamorphism in the area, which resulted in the formation of almandine garnet overprinting chlorite zone assemblages in the shear zones. This is a local effect, with garnet as the only product, therefore excluding the possibility of a second regional metamorphic episode. The event is therefore interpreted as a local result of thermal by the late intrusion of the Pojuca Granite.

9 **Quartz Veining**

There is evidence for at least four generations of post-peak-metamorphic veins in the Pojuca Corpo Quatro Formation. The earliest veins are composed of barren quartz, and may represent fluid channels developed during peak metamorphism. These are post-dated by quartz-chalcopyrite veins, which have been classified as Q2-A-type veins. The fluid which generated these Q2-A veins has been identified in type T1 fluid inclusions as an aqueous Na-Ca ± K-rich solution of moderate (3-34 wt.%) salinity, homogenizing to the liquid phase at a mean temperature of 200°C. Seemingly in the same population as type T1 fluid inclusions in quartz from the metasediments are aqueo-carbonic inclusions which contain up to 15%CH_4 and 50%CO_2. These homogenize at their trapping temperature of around 280°C. The source of the CO_2 and methane in these fluids is believed to be the devolatilization of underlying graphite-bearing sediments during metamorphism.

Q2-A veins are slightly post-dated by quartz-biotite veins which contain subordinate chalcopyrite. These are classified as Q2-B veins and contain fluids which have a similar chemical composition to those found in the Q2-A veins, with salinities between 15 and 41 Wt.%NaCl eq. The primary fluid inclusions in Q2-B veins, which are also abundant as secondary trails in host rock quartz, contain multiple daughter minerals which have been identified as halite, sylvite, iron-chloride and mixed sodium-potassium-iron chlorides. The fluids are Na-Ca-rich and have a lower K:Na ratio than the Q2-A fluids. This is interpreted to mean that the calcium is highly soluble

and resides in the fluid phase, whereas iron and potassium are less soluble, forming solid daughter phases. Total homogenization is rarely achieved in iron-chloride-bearing fluid inclusions, probably due either to metastability or low solubility of this phase. Halite dissolution is between 160 and 340°C, and homogenization to liquid occurs at a mean temperature of 210°C. Trapping temperature is estimated from isochores at between 273 and 410°C. The presence of type T4, multisolid aqueo-carbonic fluid inclusions provides evidence of CO_2 at the time of trapping of these fluids.

Q2-B veins are the final ore-bearing veins evident at Pojuca, and are post-dated by barren quartz-calcite or calcite-only veins, which were generated by low to moderate salinity (7-26 wt.% NaCl eq.) fluids of similar chemical composition to those in type Q2-A and Q2-B veins, i.e. Na-Ca-rich, with minor K. Small amounts of Mg have been detected in type Q3 veins using D-ICP analysis.

The similarity of the fluids throughout the post-peak metamorphic vein history is strongly indicative that the fluids were all generated in a similar manner and from the same source.

10 Sulphide mineralization

Sulphide mineralization in the Corpo Quatro Formation is concentrated in the Pojuca iron-formation, more precisely in the silicate-Rochas Bandadas, where it predominantly occurs as Banded and Fracture-Hosted pyrrhotite, chalcopyrite and sphalerite. Sulphide mineralization (particularly chalcopyrite) shows an intimate relationship with quartz veins throughout the sequence.

Two phases of pyrrhotite formation are evident, the first as a result of the metamorphism of pre-metamorphic pyrite, and the second forming on sulphidation of magnetite horizons. Copper and zinc mineralization post-date peak-metamorphism, overprinting metamorphic amphiboles and replacing pyrrhotite in the Rochas Bandadas stratiform sulphides. This main phase of mineralization is accompanied by the sodic-calcic alteration of pre-existing grunerite to ferro-actinolitic and ferro-tschermakitic hornblende.

Two phases of chalcopyrite deposition are evident from its presence in two generations of quartz veins, as well as in zones of albitization and in cross-cutting veins of tourmaline and epidote. The textural relationship between sphalerite and stratiform chalcopyrite indicate replacement by sphalerite, but the relative age relationships between late chalcopyrite, sphalerite and the subsidiary minerals (molybdenum, gold and nickel-bearing phases) is unclear. The following paragenetic sequence for sulphide and ore mineralization in the Corpo Quatro Formation is proposed:

Pyrite (probably diagenetic)

Pyrrhotite (a product of metamorphism of pyrite)

Pyrrhotite (sulphidation of magnetite) and chalcopyrite

Minor chalcopyrite and sphalerite

+ pentlandite, molybdenum, gold and nickel-arsenides.

11 **Albitization**

The principal alteration assemblage in the Corpo Quatro metabasalts is the Albite Zone, which is a bleached, albite-rich product of hydrothermal alteration, characterized by the mineral assemblage albite-chlorite ± hornblende, and containing appreciable amounts of both chalcopyrite and gold (up to 1% copper and 0.1ppm Au). Albitization forms as alteration haloes around epidote and K-feldspar, is cross-cut by epidote-chalcopyrite veins and numerous chalcopyrite-tourmaline veinlets, and frequently hosts massive ilmenite. The albitization is interpreted as the result of intense sodic alteration by retrograde metamorphic fluids interacting with the host metabasalts and believed to be of the same fluid generation as the main stage of ore mineralization at Pojuca.

12 **Ore deposition**

Fluid transport of the metals prior to their deposition in the Corpo Quatro Formation was by chloride complexing in the moderate to high salinity fluids responsible for generating both the Q2-A and Q2-B quartz veins. Sulphide deposition was dominantly controlled by lithological variation, believed to be the result of wallrock Na-Ca alteration of Fe-rich amphiboles and the reaction of the ore-bearing fluids with sulphur (pyrrhotite) in the Rochas Bandadas. In the Rochas Fragmentos, where wallrock alteration associated with sulphide deposition is not obvious, deposition is believed to have been dominantly from the later, Q2-B fluids, and controlled by the increased salinity caused by fluid retrogression as garnet and hornblende underwent retrograde reactions to biotite and chlorite, thus releasing Na^+ and Ca^{2+} cations into the fluid and reducing the chloride available for metal-ion complexing, enhancing sulphide deposition in close proximity to these retrograde sites. Mineralization ceased prior to the formation of the late, Q3 calcite veins

The intimate association between chalcopyrite and granitic veins, however, means that the mineralization at Pojuca could also, arguably, be interpreted as being related to the intrusion of an as yet undiscovered magmatic body at depth, which provided a heat and fluid source in a porphyry copper-style setting. From the evidence presented, this theory seems unlikely, but without stable isotope data to validate either one of the hypotheses, the magmatic association cannot be ruled out.

FUTURE RESEARCH

This is the first detailed study carried out on mineralization in the Pojuca area of Carajás, and as such it has concentrated on one part of the area - that around the Pojuca Corpo Quatro orebody. Due to time constraints, some aspects of the study have not been carried out in as complete a way as they might, and further work would allow a more definitive model to be established.

It is proposed, therefore, that future study should involve a closer look at the fluids, in particular to determine more conclusively the chemistry of the mineralizing fluids, to provide suitable models for the method of metal transport and ore deposition. The stable isotope characteristics of the mineralizing fluids need also be studied in order to place constraints on the fluid source and thus gain a better understanding of ore genesis.

The parcel of radiogenic (Pb-Pb) isotope studies of the sulphide minerals in the Corpo Quatro deposit would not only establish beyond any doubt the epigenetic nature of the mineralization, but combined with dating of the granitic veins would allow for a better time constraint on both of these events relative to retrograde metamorphism in the region. However, the errors on this type of radiogenic dating are significant, and a more preferable course might be to use absolute dating on the peak and retrograde metamorphic events, to give an approximate date to the sulphide mineralization.

Whilst detailed structural mapping of the orebody would allow a better interpretation of the tectonic controls on mineralization to be made, it has already been pointed out in this study that exposure in the area is severely limited. Detailed structural analysis might therefore only be possible should the deposit be brought into production, thus creating more surface exposure.

It is also necessary to carry out regional scale studies on the controls on sulphide mineralization, initially in the other Pojuca orebodies (C1, C2, C3 and Pojuca Leste) to establish the relationship of these to the C4 body, and subsequently to compare the C4 deposit with similar deposits in the region, namely the Igarapé Bahia and Salobo Três Alpha orebodies. Detailed comparisons of the mineralizing fluids and associated geochemical alteration in these deposits would allow for a comparison to be made between these and the C4 orebody.

Tectonic studies, as already indicated, are difficult in Serra dos Carajás, and the only constraints which can feasibly be placed on the tectonic history of the region are those established by studying the metamorphic conditions which prevailed. Although this study has estimated the maximum pressure and subsequently the temperature of peak metamorphism, the need to accurately evaluate these components is recognised in order to significantly advance the regional understanding of the Carajás Belt.

APPENDICES

A: Abbreviations and Sample Locations

B: Wholerock Geochemical Analysis

C: Microanalysis of Minerals

D: Microanalysis of Fluid Inclusions

E: Geological Map of the Pojuca G1-C4 Adit (inside back cover)

ABBREVIATIONS USED:

Mineralogical terms:

Ab	-	Albite
Amph	-	Amphibole
Anth	-	Anthophyllite
Biot	-	Biotite
Cc	-	Calcite
Chl	-	Chlorite
Cord	-	Cordierite
Cpy	-	Chalcopyrite
Ep	-	Epidote
Fib.amph	-	Fibrous amphibole
Fspar	-	Feldspar
Gar	-	Garnet
Grph	-	Graphite
Hbl	-	Hornblende
Ilm	-	Ilmenite
Kspar	-	Potassium feldspar
Mt	-	Magnetite
MVI	-	Upper Metavolcanics
MVII	-	Lower Metavolcanics
Plag	-	Plagioclase feldspar
Po	-	Pyrrhotite
Py	-	Pyrite
Qz	-	Quartz
Sph	-	Sphalerite
Sulphs	-	Sulphide minerals
Torm	-	Tourmaline

Sample Type:

M	-	Mineralized Sample
B	-	Rochas Bandadas
V	-	Vein Sample
Mag	-	Magnetite-rich sample
F	-	Rochas Fragmentos sample
A	-	Sample displaying alteration

Fluid Inclusion terms:

Decrep.	-	Temperature of decrepitation
T_{fm}	-	Eutectic (first melt) temperature
Th_{CO2}	-	Homogenization of CO_2 gas to CO_2 liquid
Th_{TOT}	-	Total homogenization of CO_2 and water
Th_{V-L}	-	Temperature of water vapour to liquid homogenization
Tm_{Clath}	-	Melting temperature of gas hydrate (clathrate)
Tm_{CO2}	-	Melting temperature of solid CO_2
Tm_h	-	Melting temperature of hydrate other than Hydrohalite
Tm_{hh}	-	Melting temperature of hydrohalite
Tm_{ice}	-	Final melting of ice
T_{rm}	-	Burst of melting (Rapid Melt) temperature
Ts_H	-	Temperature of dissolution of halite crystal
Ts_S	-	Temperature of dissolution of other daughter mineral
Wt% NaCl. eq.	-	Salinity of fluid inclusion, equivalent to weight % NaCl
l	-	liquid
v	-	vapour
s	-	solid
fr.	-	freeze
lt	-	light
dk	-	dark
yel	-	yellow - colours
gr	-	green on
br	-	brown freezing
clr	-	clear
CP	-	crazy paving texture
gran.	-	granular texture

Sample Number	Bore-hole	m	Sample Type	Description
F1	Furo 48	126	VM	Mineralization in composite vein, MVII
F2	" 48	204	M	Mineralization associated with grunerite-anthophyllite, in MVII
F3	" 62	233	V	Barren vein in MVII - Qz-Cc-Chl-Biot
F4	" 48	117	IIA	Metasomatized MVII with tourmaline
F5	" 62	206.2	II	Volcanics at 'smooth' contact with Rochas Bandadas, i.e. no intense fracturing or schistosity
F6	" 48	201.3	VM	Biotite schist with mineralization
F7	" 48	120.5	IIA	Metasomatized MVII
F8	" 65	175		
F9	" 62	198.45	MB	Banded- and fracture-type cpy and po in laminated Qz-Hbl-Mt
F10	" 62	122	V	Mineralized veins cross-cutting barren veins (Qz+Cc)
F11	" 52	119.5	F	Typical Garnet-Fibrous amphibole-rich Xistos Granadas. No banding.
F12	" 52	120.5	BM	Qz-Hbl-rich banded ore (po and cpy)
F13	" 52	125.25	BF	Garnet-rich Rochas Bandadas
F14	" 52	133.6	V	Qz vein with minor cpy in chloritized garnet-hbl-qz rock, with fracture mineralization
F15	" 52	135.6	VM	Qz vein in hbl-rich Rochas Bandadas. Cpy in vein and host
F16	" 52	141.8-141.8	BM	Magnetite-rich Rochas Bandadas, with po and cpy. Gold enriched in assay result.
F17	" 52		BM	Fractured sulphide-rich Rochas Bandadas
F18	" 52		B	Fibrous-amphibole-rich rock in Rochas Bandadas
F19	" 52		BM	Zn-rich Rochas Bandadas. No gahnite present. Schistose fabric in fib. amphs.
F20	" 52		BM	Cpy, minor po and magnetite, not banded, in Rochas Bandadas
F21	" 52		B	Schistose amphiboles and banded magnetite
F22	" 50	214.85	Mag	Magnetite in fractures, + cpy + po - Rochas Bandadas
F23	" 50	214.45	Mag	Magnetlte in hornblende - Rochas Bandadas
F24	" 50	201.25		Calcite + biotite vein, with sulphide (cpy)
F25	" 43	178.15		Qz-vein in gold-rich rock (Rochas Bandadas). up to 9.4ppm Au -not visible
F26	" 43	178.6	VM	Qz-vein in Au-rich qz-hbl-Rochas Bandadas. No gold present.
F27	" 43	178.4	M	Typical sulphide mineralization
F28	" 40	151.9	M	Sulphide-magnetite-rich hbl-qz-Rochas Bandadas. 151.2m = 0.74 ppm Au
F29	" 59	148.0	M	Qz-hbl rock (Rochas Bandadas) with cpy in massive fractures
F30	" 59	148.9	V	Minor sulphide in calcite vein
F31	" 51	83.2	I	Coarse massive actinolite/grunerite? layer in MVI. Cross-cuts plagioclase, chlorite and minor cpy

Sample Number	Bore-hole	m	Sample Type	Description
F32	" 51	88.5	IA	Feldspar horizon in MVI, similar to Albite Zone in G1C4
F33	" 51	92.4	IA	Cordierite-anthophyllite alteration to MVI
F34	" 51	98.1	FM	
F35	" 51	100.0	B	Banded garnets in black matrix (Qz-grph-biot), + qz + fib. amphibole
F36	" 51	109.4	M	Fracture and disseminated sulphides in 'hornblendite'
F37	" 51	111.1	M	" " " " in hbl-garnet-rich Rochas Bandadas
F38	" 51	114.8	MB	Massive euhedral cpy-po mineralization in banded qz-hbl Rochas Bandadas
F39	" 51	118.5	Mag	Disseminated euhedral, and banded magnetite and fibrous amphiboles
F40	" 51	119.05	M	Disseminated sulphides in fibrous amphibole
F41	" 55	115.8	BM	Relationship between amphiboles (hbl) and po mineralization in banded qz-hbl
F42	" 51	122.3	BM	Banded qz-hbl mineralization
F43	" 51		B	Banded qz-hbl-mt
F44	" 51	135.7		Relationship between fracture and disseminated mineralization and garnet in Rochas Bandadas
F45	" 51			
F46	" 51	143.0	F	Chloritization of garnets and sulphides
F47	" 51	146.3		Banded quartz - fib.amphibole ± garnet and minor fracture-hosted cpy. Some disseminated Mt.
F48 - F53	" 51	156-181	II	Sampled every 5m for typical lower metavolcanic unit
F54	" 53	351.6	V	Molybdenum in quartz vein in MVII. (The only moly sample found)
F55	" 53	347.7	VM	Mineralized quartz vein in metasomatized volcanic
F56	" 53	315.8	VB	Intensely fractured MVII-Rochas Bandadas boundary
F57	" 58	141	IIV	Chloritized mineralized quartz veins in MVII
F58	" 63	85	F	Grunerite-garnet-rich Rochas Fragmentos
F59	" 55	55.85	IIM	Pre-silicate mineralization in MVII
F60	" 55	218.7	IIVM	Quartz vein and mineralization in MVII
F61	" 55	220	IIVM	" " " " " "
F62	" 49	222.15	BMag	BIF - Oxide facies Rochas Bandadas
F63	" 49	151.2	BMag	" " " " "
F64	" 63	150.4		Banded gar-hbl rock with cpy matrix
F65	" 42	47.1	IIA	Cpy-rich qz patches in cord-anth rock
F66	" 42	254.5	IIV	Ep vein and py-cpy mineralization
F67	" 42	328.9	IIV	2-phase vein, Fspar then cc+chl, +cpy mineralization + ilmenite
F68	" 63	151-152	G	Granite at contact with Rochas Bandadas
F69	" 63	149.8	MB	Fracture and parallel mineralization in qz-hbl Rochas Bandadas
F70	" 63	83.7	MB	Banded hbl+qz - sulphs along hbl cleavage

Sample Number	Bore-hole	m	Sample Type	Description
F71	" 63	48.2	MF	'stretched' sulphs (cpy and po) in sheared Xistos Granadas
F72	" 52	162.5	BM	Sheared Rochas Bandadas - undeformed qz + sulphs schistose amphs + deformed sulphs
F73	" 52	152.7	B	Rochas Bandadas qz to compare with vein qz in F74
F74	" 52	135	V	Recent vein qz + cpy in Rochas Bandadas - growth faces visible in qz.
F75	" 52	91	V	Sulph-cc-chl (-qz) vein
F76	" 52	77.4	F	Xistos Quartzos
F77	" 52	62.7	IA	Metasomatised Upper metavolcanic
F78	" 52		I	'Normal' metavolcanic
F79	" 52	68.7	F	Schistose sulphide-rich Xistos Quartzos
F80	" 42	287	V	Qz-cpy vein 1m above Albite Zone contact
F81	" 42	290.5		Albite Zone - massive ilm + qz, at Albite Zone-MVII contact
F82	" 42	290		Ep + discrete ilm patches in chl-ab rock
F83	" 42	291	V	Barren qz cross-cutting Albite Zone
F84	" 51	129.3	MB	Schistose fabric in Rochas Bandadas
F85	" 50	59		Qz-sph vein in MVII
F86	" 50	85		Sph veinlet in qz from Xistos Quartzos
F87	" 50	84.5		Sheared qz-cpy vein in Xistos Quartzos
F88	" 50	95.0		Xistos Quartzos
F89	" 50	111.3		Xistos Quartzos
F90	" 50	113		Xistos Granadas
F91	" 50	124.5		Flowed and faulted mt. cpy and po along fault, not folded
F92	" 50	126		Qz-sulph-Biot vein
F93	" 50	150		Qz-po, folded
F94	" 50	152		Qz-cpy-Biot vein, with qz from Rochas Bandadas
F95	" 50	169.5		Barren Rochas Bandadas - qz-hbl, 95% qz
F96	" 50	205.5		Qz-cc vein in MVII
F97	" 50	212.0		" " " "
F98	" 50	250		Cpy-torm mineralization associated with albitized MVII
C2-1	" 12			Granite vein and related cpy in biot-schist

ADIT SAMPLES : G1C4

Sample Number	Wall (L/R)	m	Description
G1	L	63.0	Albitization in Lower metavolcanics, + minor disseminated cpy
G2	L	63.2	Albite Zone + cpy mineralization
G3	L	91.6	Garnet-poor schist in footwall of a shear zone
G4	L	92.3	Garnet schist from hanging wall of shear zone
G5	L	92.8	Banded garnet-rich rock

Sample Number	Wall (L/R)	m	Description
G6	R	98.5	Sulphide-rich Rochas Bandadas
G7	L	87.5	Sulphide-rich Rochas Bandadas - qz-amph-mt. banding 120/60S
G8	R	104.0	Qz vein in shear zone on Rochas Fragmentos
G9	R	134.9	Xistos Quartzos
G10	R	134.2	Chloritized Xistos Granadas in shear zone
G11	R	128.0	Xistos Granadas
G12	R	121.9	Xistos Granadas in shear zone - rotation garnets?
G13	L	120.8	Barren qz veining in shear zone, in Xistos Granadas
G14	R	115.3	Non-banded mineralized garnet schists
G15	L	113.9	Qz veining in fault:
G16	L	113.9	
G17	R	113.8	
G18	R	113.8	
G19	R	113.8	
G20	R	113.8	
G21	R	113.5	
G22	R	113.0	
G23	R	114.3	
G24	R	106.8	Massive grunerite
G25	L	110.9	Material thickly bedded with #G24 grunerite
G26	L	108.8	Barren quartz vein in fault
G27	R	103.7	Massive quartz-plagioclase vein in fault
G28	L	103.7	Plagioclase veins in metasediments
G29	L	102.7	
G30	L	102.7	
G31	R	101.7	
G32	Roof	102.3	
G33	L	101.3	Quartz veins in fault - old, 'grey' quartz in contact with more recent white quartz
G34	L	101.4	Cpy mineralization in fault-hosted quartz vein
G35	R	97.5	Sulphide-rich Rochas Bandadas
G36	L	94.5	Sulphide-rich Rochas Bandadas
G37	R	100.5	Sulphide-rich Rochas Bandadas
G38	L	92.0	Fault hosted quartz vein
G39	R	88.5	
G40	R	91.2	Old, dark grey quartz vein - Q1.
G41	R	91.0	Old, grey mineralized quartz vein
G42	R	91.0	Schistose wall-rock round #G41
G43	R	87.3	Schistose Xistos Granadas - at schistose contact
G44	R	86.5	Schistose Rochas Bandadas (Transition zone)

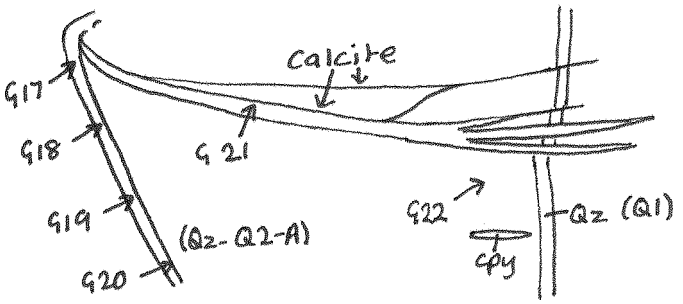

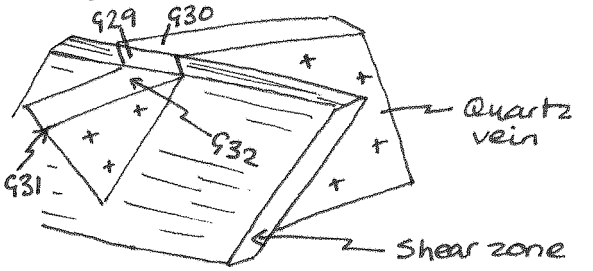

Sample Number	Wall (L/R)	m	Description
G45	R	84.7	Mt-fib.amph-rich Rochas Bandadas
G46	R	84.7	Rochas Bandadas
G47	R	84.7	Rochas Bandadas
G48	L	84.7	Quartz banding with cpy enrichment in Rochas Bandadas. Cpy vein-related?
G49	L	84.7	Late mineralized quartz vein
G50	R	80.7	Vein quartz in fault, minor mineralization (cpy)
G51	L	78.0	Host-rock with cc-vein
G52	R	78.2	Host-rock
G53	R	75.9	Ilmenite-rich rock
G54	L	73.5	Albite Zone
G55	R	74.0	Calcite vein in MVII between Albite Zone and Rochas Bandadas. One of many, very narrow (1-2mm) cc-veins
G56	R	72.8	Pure ilmenite
G57	R	71.7	'Old' quartz, with cpy mineralization in vertical vein
G58	L	62.9	Albite Zone with cpy mineralization
G59	R	69.2	MVII
G60	L	66.5	Minor cpy in Albite Zone, MVII
G61	R	61.9	Tourmaline 'vein' in Albite Zone, with cpy mineralization
G62	R	60.1	Pure plagioclase band from Albite Zone, with minor cpy mineralization
G63	R	57.5	Albite Zone - from gold-rich area but sample lacks mineralization
G64	R	58.3	Cpy-rich Albite rock from Au-rich Albite-Zone
G65	L	58.1	Calcite vein in fault
G66	L	58.2	Ophitic black volcanic rock
G67	L	54.0	MVII
G68	R	51.9	Fracture in Albite rock filled with cpy
G69	R	44.5	Quartz vein and mineralization in fault
G70	L	44.4	Plagioclase vein in MVII
G71	R	37.9	Chlorite vein in MVII
G72	R	35.8	Part of a multiphase plag-Kspar vein system
G73	L	35.4	Extensional? quartz vein
G74	R	35.0	Qz-chl+cpy vein
G75	L	27.2	MVII
G76	R	25.2	Plagioclase vein + alteration in MVII
G77	R	21.4	Ep-cpy vein
G78	L	17	Host-rock at fault zone
G79	L	17.05	Quartz vein from fault zone (#G78)
G80	R	16.05	Quartz vein from extensional? fault
G81	R	12.2	MVII
G82	R	10.3	MVII from fault zone
G83	L	5.2	Massive amphibole alteration around fault-related albitization
G84	R	4.1	Stockwork of tourmaline veinlets in albitization
G85	L	1.8	MVII
G86	R	2.9	Biotite alteration close to albitization (#G84)

Sample Number	Wall (L/R)	m	Description
G87	R	67.5	Plagioclase at albitized - un-albitized MVII boundary
G88	R	130	Qz-gar-rich Xistos Granadas
G89	R	123	Q3? Qz-cc-cpy vein
G90	R	103	Quartz from massive Q2 qz-biot-cpy vein with cc at margin, in sulphide-rich Rochas Bandadas
G91	R	100	Quartz from massive barren qz-biot vein, cuts #G92
G92	L	100	Quartz from massive cpy-bearing quartz vein
G93	L	100	Barren ?Q1? vein. Appears older than #G92
G94	R	102	Quartz from massive cpy-bearing quartz vein
G95	L&R	92	Quartz from qz-cc-cpy vein (cc at margin and in vein). In sulphide-rich schistose Xistos Granadas
G96	R	84	As #G95, different vein
G97	L	84	Quartz from qz-cc vein with minor py at contact with wallrock
G98	R	112.8	Vertical Q2 qz-biot-cpy vein in Rochas Bandadas
G99	R	119	Qz-cc from barren Q3 vein in Xistos Granadas
G100	L	127	As #G98
G101	L	114.5	Cpy-po-rich Rochas Bandadas
G102	R	113.8	Qz-cpy vein in fault, and surrounding wallrock
G103	R	111	Massively banded amphibole (grunerite) and quartz, forming decimeter banding

CHIP #	SAMPLE #	worked	LITHOLOGY	INCLUSIONS	Type (if not host)
1	G25		Thick interbeds with grunerite	Lots, small	
2	G51		MVII above albite	" "	
3	F12	✓	Folded Qz-Hbl, Bdd with Po & Cp	Good, q.big	
4	F47		Bdd Qz-Aff	Lots + daughter minerals	
5	F38		Bdd Qz-Hbl (frac/bdd qz?)	small, trails	
6	F24		Cc-biot vein + mineral^{zn} (.21ppm Au)	Rubbish	Q2-3?
7	bob2	✓	Mt-rich Rochas Bandadas, Qz-grun-Mt	q.good	
8	F42		Bdd Qz-hbl + sulphides	mess, tiny inclns	
9	bob4	✓	Bdd gar-gahn-qz	OK	
10	G7	✓	Sulphide rich Bdd rock	Huge, good trails	
11	G46	✓	Bdd rocks	" " "	
12	F41		Bdd qz-hbl	" " "	
13	G9		Xistos Quartzos	Too thin	
14	G3		Xistos Quartzos (no garnet)	T2+1 trails, small	
16	G12		Xistos Granadas (schistose)	Small	
17	G19	✓	Qz vein + cpy	loads, huge T1,3?	Q2A
18	bob4		bdd qz-garn-gahnite	Rubbish	
19	G7	✓	Sulphide rich Rochas Bandadas	Good, T1,2,3. big	
20	G3		Xistos Quartzos	Loads, too small	
21	G8		Qz vein in SZ (Rochas Fragmentos)	Old qz T1,2, new T3.	?
22	G57		Qz-cpy vein (old)	Clr qz nr sulph OK	Q2A
23	G100	✓	Qz-Cpy-Biot vein	Excellent, T1,2.	Q2B
24	F96		Qz-carb vein, good growth planes.	Small	Q3
25	G99	✓	Minor mineralized calcite vein	Excellent, T1	Q3
26	G98	✓	Vertical Qz-Cc-Cpy vein (as 24)	Loads, small.	Q2A
27	G95	✓	" " " "	" "	Q3
28	F97		MVII Qz-Carb vein (no cc)	Gd. Small, clear	Q3
29	G89		Main Qz-Cpy-Cc vein	T1, small	Q2A
30	G92	✓	Massive Qz vein	T1, small	Q2A
31	G92	✓	Massive Qz vein	small areas OK, T1	Q2A
32	G91	✓	Massive barren Qz vein	loads, big, 2nd 1+2	Q3
33	G96		Qz-Cc-Cpy vein in Xistos Granadas	OK, few lvs, most lv	Q2A?
34	G99		Barren Qz	few, q.small, T1	Q3
35(A-D)	G100	✓	Qz-Cpy-Biot vein	Excellent, T1,2.	Q2B
36	F74	✓	Qz-cpy-Biot vein	Good, l-v.	Q2A
37	G90		Massive mineralized vein		Q2A
38	F73		Quartz (barren)		Q3
40	G94	✓	Massive cpy-bearing Qz vein		Q2A
41	G98	✓	Qz-biot-cpy vein in Rochas Bandadas		Q2B

X-Ray Fluorescence: Sample Preparation and Analytical Techniques

The X-Ray fluorescence (XRF) bulk geochemical analysis has been carried out on both the metasedimentary and metavolcanic rocks in the Corpo Quatro Formation, in order to determine the primary geochemistry and changes undergone on mineralization. Analyses are carried out on glass beads (major elements; wt.%) and pressed powder pellets (trace elements; ppm).

Sample size is limited primarily by core-diameter, but where possible samples of ~1-2 kg were used. Samples were crushed in a jaw-crusher into chips less than 2cm across. These chips were then ground using a Tema mill with tungsten carbide components, and the resulting powder was split for bead and pellet production.

Pellets are made with ~10g of sample, uniformly mixed with ~1ml of aqueous binder (7% w/v solution of polyvinyl alcohol in water), compressed in a pellet die to a pressure of ~12 tonnes. The resulting pellets are dried in an oven at 80°C for at least 12 hours before analysis takes place.

Glass beads are made with pre-ignited powder, mixed with flux (Spectroflux 100B: Lithium metaborate and di-lithium tetraborate). Ignition, which removes all volatiles in the powder, is usually carried out at 1000°C for 1-2 hours. This, however, occasionally resulted in the powders fusing, so an ignition time of 1 hour at 900°C was used. Loss on ignition (LOI) is noted. A flux to sample ratio of 5:1 was used for the metavolcanic samples, while 10:1 ratio was used and ammonium bromide added to the metasedimentary samples, as this was found to reduce their tendency to crack on cooling, caused by the high iron content. The powder mixture was heated for approx. 10 minutes in a platinum-gold crucible at 1150°C, stirring twice, then turned into a platinum casting-dish and cooled with a jet of air. The addition of ammonium bromide to the sample resulted in the majority of beads coming away from the dish without cracking. Some beads, however, had to be remade several times.

Samples with high Cu contents were found to have low major-element totals, and were re-analyzed for copper, calibrating the copper analyses with beads made from sample F11 (0% Cu), with added 1, 2, 5 and 10% CuO.

The beads and pellets were analyzed at the University of Southampton using a Philips PW1400 fully automatic sequential XRF spectrometer, for which the theoretical detection limits are given in *Table B1.1*. International reference materials were run during each set of analyses (metavolcanics and metasediments), to determine analytical error. These data are also presented in *Table B1.1*.

Table B1.1 **Measured and predicted values for international reference materials used during the analysis of C4 metavolcanics and metasediments by XRF Spectrometry.**

	NIM-G			BE-N			BCR			BHVO			3*LLD
	Measured		Known	Measured		Known	Measured		Known	Measured		Known	(determination
%	Basalts	Sediments		Basalts	Sediments		Basalts	Sediments		Basalts	Sediments		level)
SiO2	-	75.82	75.7	39.21	39.50	38.20	-	-	-	49.35	-	49.94	
TiO2	-	0.10	0.09	2.70	2.68	2.61	-	-	-	2.73	-	2.71	
Al2O3	-	11.92	12.08	10.01	10.24	10.07	-	-	-	13.43	-	13.80	
Fe2O3	-	1.73	2.02	12.94	13.10	12.84	-	-	-	12.14	-	12.23	
MnO	-	0.01	0.02	0.20	0.20	0.20	-	-	-	0.17	-	0.17	
MgO	-	0.07	0.06	13.28	13.41	13.15	-	-	-	7.08	-	7.63	
CaO	-	0.80	0.78	14.18	14.42	13.87	-	-	-	11.32	-	11.40	
Na2O	-	3.34	3.36	3.20	3.19	3.18	-	-	-	2.16	-	2.26	
K2O	-	5.08	4.99	1.42	1.48	1.39	-	-	-	0.52	-	0.52	
P2O5	-	0.00	0.01	1.09	1.10	1.05	-	-	-	0.27	-	0.27	
SO3	-	0.00	-	0.00	0.00	0.00	-	-	-	0.00	-	0.00	
Rb	328	-	320	46	46	47	47	47	47	-	-	-	4.5
Sr	11	-	10	1379	1372	1370	330	334	330	-	-	-	4.5
Y	146	-	143	28	26	30	37	37	38	-	-	-	4.5
Zr	288	-	300	254	246	265	190	191	190	-	-	-	4.5
Nb	53	-	53	103	106	100	14	15	14	-	-	-	4.5
Th	52	-	51	11	11	11	6	6	6	-	-	-	6.0
U	20	-	15	3	4	2	4	3	2	-	-	-	10.5
Pb	39	-	40	5	7	4	15	17	14	-	-	-	6.0
Zn	53	-	50	120	123	120	126	134	130	-	-	-	3.0
Ni	4	-	8	263	262	267	12	13	13	-	-	-	4.5
Cr	9	-	12	331	330	360	19	16	16	-	-	-	9.0
V	0	-	2	243	243	235	420	407	407	-	-	-	10.5
Ba	134	-	120	1065	1076	1025	720	718	681	-	-	-	21.0
La	121	-	109	87	83	82	29	26	25	-	-	-	12.0
Ce	203	-	195	151	151	152	60	50	54	-	-	-	21.0
As	4	-		0	0	2	0	0	0	-	-	-	15.0
Mo	1	-		4	6	3	4	3	1	-	-	-	4.5
Sn	5	-	2	0	1		1	0	3	-	-	-	12.6
Bi	0	-		0	0		0	0	0	-	-	-	6.0
Sb	0	-		0	0	0	0	0	1	-	-	-	6.0
Cu	20	-	10	73	86	72	29	44	19	-	-	-	4.5

Table B2.1 **Geochemistry of the C4 Metavolcanics (G60, 61 = Albite Zone; F33 = Cordierite-Anthophyllite)**

Major Elements														
	F48	F49	F50	G52	F53	G59	G67	G75	G81	G85	G60	G61	F33	Mean
SiO2	52.17	52.11	51.62	48.96	54.45	52.98	43.2	53.66	48.09	51.48	57.99	57.83	59.97	52.4
TiO2	0.53	0.70	0.70	0.43	0.75	0.67	1.61	0.65	0.71	0.6	3.3	0.11	0.39	0.7
Al2O3	14.75	15.22	15.29	3.75	14.11	14.73	17.09	14.89	15.29	15.37	19.36	20.12	9.22	14.9
Fe2O3	18.95	16.56	15.94	25.75	15.09	14.45	20.03	14.74	19.9	16.49	6.62	3.82	21.22	16.2
MnO	0.12	0.19	0.14	0.14	0.15	0.13	0.13	0.27	0.21	0.2	0.07	0.04	0.2	0.16
MgO	5.14	5.34	5.18	9.17	5.39	5.23	6.35	5.17	4.83	4.79	1.31	1.17	4.26	5.2
CaO	3.57	5.63	5.04	10.9	5.21	5.21	4.2	5.8	5.1	6.19	1.1	6.09	2.22	5.1
Na2O	2.45	3.3	3.09	0.44	2.99	2.79	1.87	4.4	3.21	3.41	8.44	8.35	2.26	3.01
K2O	1.49	1.56	2.42	0.33	1.85	2.77	4.52	0.81	1.89	1.1	1.34	1.27	0.84	1.87
P2O5	0.6	0.08	0.09	<0.1	0.09	0.08	0.02	0.07	0.07	0.08	0.01	<0.1	0.07	0.17
Sum	99.77	100.7	99.51	99.92	100.1	99.04	99.02	100.4	99.3	99.71	99.54	98.80	100.65	
LOI(%)	4.8	1.3	1.2	0.3	1.3	1.2	1.3	1.2	0.8	1.0	1.3	1.2	0.5	
Trace Element														
MnO	1125	1805	1356	1348	1453	1310	1144	2558	2061	1963	630	423	1875	1502
TiO2	4485	6837	7246	4146	7561	7231	15430	6070	7581	6154	32599	918	3849	6585
Rb	69	70	127	4	107	166	296	38	89	45	79	68	48	97.4
Sr	40	84	76	3	63	103	71	80	55	80	40	36	41	74.3
Y	28	24	25	44	28	21	46	19	22	15	2	7	13	23.5
Zr	91	92	90	40	103	90	123	86	93	76	183	112	67	90.3
Nb	7	7	7	7	8	6	9	7	8	7	15	3	6	6.8
Th	0	0	0	0	0	0	0	0	0	0	0	0	0	0
U	0	0	0	0	0	0	0	0	0	0	0	0	0	0
Pb	0	0	0	0	0	0	0	0	0	0	0	0	0	0
Zn	65	63	58	39	54	52	73	54	66	65	26	13	183	59.4
Ni	46	63	53	105	51	50	83	53	66	51	28	19	42	52.2
Cr	15	17	16	14	14	16	21	17	18	15	11	13	9	15.4
Cr	110	178	194	187	138	161	192	181	208	198	10	2	123	163
V	188	239	223	322	226	203	399	196	204	205	19	24	126	214
Ba	388	344	532	0	356	534	926	172	504	288	173	79	94	406
La	49	7	16	7	11	12	214	10	13	7	8	0	9	17.1
Ce	90	25	23	42	26	22	265	13	36	17	11	1	22	33.8
As	0	0	0	0	0	0	0	0	0	0	0	0	31	0
Mo	1	1	3	3	2	2	0	1	3	2	1	6	2	1.9
Sn	0	1	6	11	9	3	14	5	5	4	2	5	0	3.7
Bi	0	0	0	0	0	0	0	0	0	0	0	0	0	0
Sb	0	0	0	0	0	0	0	0	0	0	0	0	0	0
Cu	30	22	31	13	20	29	17	60	14	21	1150	846	295	25.6

Table B2.2 **XRF geochemical data for the C4 Rochas Bandadas**

	Barren Rochas Bandadas				Mineralized Rochas Bandadas					
Major Elements (Wt%)										
	F47	B2	F43	F95	G101	F16	F17	F40	F9	G7
SiO2	55.59	53.79	61.94	95.09	40.70	59.87	48.05	40.30	56.52	59.40
TiO2	0.12	0.03	0.09	0.21	0.32	0.13	0.09	0.24	0.08	0.15
Al2O3	1.61	0.29	0.95	0.97	8.49	3.10	2.33	5.36	2.50	4.93
Fe2O3	38.07	45.52	30.49	2.70	33.17	29.60	43.16	42.42	31.50	22.57
MnO	0.24	0.49	0.18	0.04	0.26	0.36	0.30	0.56	0.31	0.25
MgO	3.96	1.54	1.68	0.60	3.90	1.41	1.20	3.13	1.74	3.90
CaO	0.91	0.43	4.61	0.69	6.92	4.51	3.14	4.56	5.08	7.68
Na2O	0.00	0.00	0.00	0.00	0.48	0.19	0.00	0.14	0.03	0.24
K2O	0.30	0.06	0.11	0.09	1.10	0.45	0.25	0.51	0.35	0.19
P2O5	0.01	0.06	0.16	0.00	0.03	0.04	0.05	0.07	0.32	0.20
SO3	0.02	0.00	0.01	0.00	1.74	0.09	0.80	0.79	0.47	0.06
CuO	0.30	0.10	0.06	0.07	2.48	0.90	1.45	1.77	1.68	0.01
SUM	101.13	102.31	100.28	100.47	99.60	100.66	100.83	99.87	100.59	99.58
LOI	+0.525	+1.88	+0.57	0.635	1.745	0.41	0.755	0.775	1.04	0.145
Trace Elements (ppm)										
Rb	30	0	8	25	150	8	13	9	11	83
Sr	1	0	3	1	18	5	1	8	4	3
Y	5	5	16	7	14	11	11	15	21	17
Zr	27	7	18	133	79	51	25	60	39	78
Nb	4	4	8	6	6	6	4	6	8	7
Th	3	0	1	5	0	3	1	3	4	2
U	0	1	2	4	0	0	0	3	2	1
Pb	4	2	3	2	3	3	3	5	2	3
Zn	229	606	539	2226	237	2967	936	700	1576	161
Ni	66	8	27	38	62	50	83	59	52	51
Ga	5	3	5	11	16	5	10	6	2	12
Cu	3626	1107	623	727	22900	9027	13953	15812	15867	120
Cr	0	0	0	10	25	3	0	6	0	0
V	24	5	15	3	263	20	16	45	8	11
Ba	51	13	17	33	102	57	32	44	37	24
La	4	4	28	2	7	25	11	19	37	26
Ce	0	0	42	4	32	33	30	30	48	24
MnO	2308	4680	1845	504	2623	3544	2977	5397	3153	2462
TiO2	1066	112	815	2155	3348	1202	815	2465	727	1441
As	0	0	0	0	0	0	0	0	0	0
Mo	4	6	7	9	2	9	3	11	42	2
Sn	6	4	3	0	4	7	17	20	14	0
Bi	0	0	0	0	0	0	0	0	0	0
Sb	0	0	0	0	0	0	0	0	0	0
W	508	401	1185	252	332	540	408	52	704	441

Table B2.3 **XRF geochemistry of the C4 Xistos Granadas.**

	Barren Xistos Granadas						Mineralized Xistos Granadas					
Major Elements (Wt%)												
	F90	F13	G88	F11	F58	G23	B1	F35	G11	G42	F46	F34
SiO2	52.64	77.50	52.76	38.36	59.36	58.59	75.39	66.30	61.25	70.61	40.26	53.24
TiO2	0.56	0.16	0.54	0.23	0.26	0.20	0.08	0.23	0.59	0.25	0.42	0.25
Al2O3	12.71	6.69	12.56	15.83	9.52	8.30	1.01	7.13	13.61	8.98	7.40	6.64
Fe2O3	24.58	12.52	28.72	37.84	27.10	22.47	21.82	21.42	26.71	16.10	37.11	29.5
MnO	0.34	0.21	0.32	1.81	0.46	0.26	0.23	0.40	0.19	0.09	0.28	0.44
MgO	5.13	1.54	4.61	2.49	3.94	2.31	0.70	2.04	4.86	4.35	6.16	4.44
CaO	1.49	0.94	1.56	3.17	0.79	6.39	0.46	0.86	2.04	0.21	2.30	1.57
Na2O	0.25	0.25	0.00	0.00	0.00	0.47	0.01	0.00	0.05	0.00	0.00	0.00
K2O	3.44	0.79	1.76	0.11	1.09	0.51	0.23	0.60	3.07	1.55	1.42	1.01
P2O5	0.07	0.05	0.06	0.04	0.06	0.07	0.02	0.09	0.08	0.04	0.10	0.10
SO3	0.00	0.00	0.06	0.03	0.00	0.11	0.00	0.11	0.02	0.00	0.34	0.24
CuO	0.10	0.00	0.05	0.20	0.10	0.05	0.13	1.15	0.02	0.01	5.94	2.22
SUM	101.33	100.65	103.00	100.11	102.68	99.72	100.09	100.34	102.5	102.18	101.74	99.67
LOI	1.11	0.47	1.01	+2.61	0.675	0.335	0.195	1.734	0.145	2.52	3.52	1.47
Trace Elements (ppm)												
Rb	98	70	3	3	55	194	24	50	37	149	129	100
Sr	1	10	4	1	1	28	1	2	6	21	2	4
Y	10	15	21	101	21	13	4	22	26	14	10	23
Zr	196	81	110	88	187	76	17	88	99	80	110	82
Nb	10	8	8	5	8	7	4	8	5	7	7	8
Th	11	8	7	5	12	1	0	5	3	2	11	6
U	3	5	1	0	6	1	1	4	1	1	0	1
Pb	2	5	3	3	5	3	2	7	4	2	4	4
Zn	676	121	575	271	762	197	2151	218	413	314	2508	914
Ni	25	11	28	2	13	55	16	67	117	56	136	105
Ga	12	8	9	3	14	12	4	7	11	15	12	8
Cu	1501	94	525	2054	1245	586	1385	10692	201	108	44534	18799
Cr	219	59	202	79	0	1	0	14	187	0	17	66
V	197	17	190	76	27	19	12	34	194	11	102	37
Ba	459	165	274	29	138	51	59	77	367	171	223	186
La	9	158	19	27	23	146	24	120	7	7	7	53
Ce	13	243	13	39	41	214	37	177	8	19	0	74
MnO	2764	1931	2593	17072	4052	2517	2265	3539	1384	850	2685	3970
TiO2	6261	1658	5843	2678	2760	1957	819	2524	5744	2655	4723	2945
As	34	14	0	0	2	0	4	0	0	0	0	130
Mo	266	20	4	5	7	2	3	20	40	3	8	7
Sn	0	0	5	0	4	1	1	6	27	1	12	9
Bi	0	0	0	0	0	0	0	0	0	0	0	0
Sb	0	0	0	0	0	0	0	0	0	0	0	0
W	258	1664	511	999	677	437	1054	758	65	256	0	336

Table B2.4 **XRF geochemistry of the C4 Xistos Quartzos.**

	Barren Xistos Quartzos		Mineralized Xistos Quartzos		
Major Elements (Wt%)					
	F88	F89	G43	G12	F76
SiO2	55.87	56.74	69.34	56.59	43.88
TiO2	0.60	0.54	0.19	0.53	0.54
Al2O3	12.32	12.06	9.10	12.05	12.50
Fe2O3	18.01	20.17	19.19	26.53	28.72
MnO	0.15	0.12	0.10	0.09	0.22
MgO	3.17	4.38	4.64	6.27	2.35
CaO	7.89	1.98	0.23	1.48	8.02
Na2O	1.52	0.64	0.00	0.03	0.79
K2O	1.56	4.05	0.28	0.53	1.98
P2O5	0.08	0.06	0.07	0.06	0.07
SO3	0.00	0.06	0.04	0.00	0.19
CuO	0.01	0.23	0.00	0.00	0.40
SUM	101.19	101.04	103.17	104.17	99.67
LOI	0.79	1.25	3.284	3.548	0.845
Trace Elements (ppm)					
Rb	35	18	4	51	100
Sr	2	5	1	35	5
Y	10	50	10	24	25
Zr	71	104	94	104	95
Nb	6	7	8	8	7
Th	3	8	5	3	3
U	0	9	3	2	1
Pb	2	5	3	4	4
Zn	290	119	96	141	162
Ni	49	20	2	32	39
Ga	12	14	3	14	14
Cu	125	2254	65	35	4589
Cr	218	180	0	232	176
V	152	169	27	170	174
Ba	138	647	35	49	244
La	40	6	0	4	15
Ce	73	0	4	7	25
MnO	1449	1204	927	797	2169
TiO2	5646	5569	1696	4667	5802
As	0	0	4	0	0
Mo	5	27	5	2	3
Sn	0	27	0	19	30
Bi	0	0	0	0	0
Sb	0	0	0	0	0
W	147	582	1806	778	298

C1 Semi-quantitative analysis of minerals: Analytical techniques

Semi-quantitative analyses of silicate, sulphide and oxide minerals and fluid inclusion daughter-minerals from the Corpo Quatro deposit have been carried out on carbon coated polished thin sections and fluid inclusion chips respectively, using electron micro-analysis.

Sulphide and oxide minerals, as well as daughter minerals, were analyzed using a scanning electron microscope (SEM, model Jeol JSM 6400) at the University of Southampton, while silicate and some oxide analysis were undertaken by electron probe micro-analysis (Cambridge Instruments Microscan 9) at the Open University, under the guidance of Dr.A.Tindle. EPMA was used after the SEM analyses of olivine standards were found to contain spurious SiO_2 and Fe_2O_3 values, and up to 1.7 wt.%. Na_2O + CaO (*Table C1.1*). Daughter mineral analyses were undertaken by SEM after full re-calibration of the equipment.

The SEM is equipped with an energy dispersive X-ray analysis system (EDS), and a tungsten hairpin filament. An accelerating voltage of 20 kV, a probe current of $0.5x10^{-10}$A, and a working distance of 39mm were used as optimum working conditions. Secondary electron imaging allows topographical and compositional variation to be observed, making it ideal for the study of the inside of fluid inclusions, and back-scatter electron images detect large variation in composition, at a higher resolution than the SEI (3.5nm compared with 10nm). Individual silicate crystals were not discernable on the SEM images. The magnification range is 10 to 300,000X, the optimum spatial resolution for analysis of most minerals is 5μm. When running properly the SEM is accurate to about 10% relative, and has a minimum detection limit of 0.2wt%.

The EPMA is equipped with a wavelength spectrometer, making detection limits a magnitude better than the SEM. An acceleration voltage of 20kV, a probe current of 30nA, and a defocused beam of diameter 10-15μm were used. Detection limit varies depending on the element, but averages 0.01 to 0.02 wt%, and accuracy depends on the count rate and concentration of the element, but is generally 2-3 times the detection limit.

Apart from having lower detection limits and better accuracy, advantages of EPMA over SEM are: The optics are that of a standard reflected-transmitted light microscope, with 10X and 1000X magnification, so minerals can be distinguished prior to analysis; EPMA is calibrated by running standard sample blocks (containing real and synthetic minerals, and metals) at the beginning of each session, and drift monitored throughout the day by the analysis of the standard **ABG**. All data, calculated on the basis of the number of oxygens in the relevant mineral, is corrected using the ABG values from the start and end of a sample batch. Unlike SEM, where point selection is manual, EPMA analyses points are pre-set by computer, and can be left to run overnight.

The software **Amph FU's** (Fe^{2+}/Fe^{3+}) and **Chlorite FU's** (Fe^{2+}/Fe^{3+}), for use with the **Excel** package and available from A.Tindle at the O.U., has been employed to interpret the silicate data. These spreadsheets calculate Fe^{2+} and Fe^{3+}, and H_2O content, and re-calculate chlorite, which always gives totals of 89-90%, to 100%. The minerals are also named according to chemical composition (according to the classification of the International Mineral Association), and, in the case of

amphiboles, estimates of pressure of formation can be made using the equations of Holiister *et al.*, 1987 and others.

Table C1.1 **Measured against known values of major elements in clinopyroxene and olivine standard sample 'Alabaster 1833.4m' (S.Roberts), using the Jeol JSM 6400, Southampton University.**

	CLINOPYROXENE				OLIVINE			
	SEM		Known value		SEM		Known Value	
	Wt. %	Formula Value	Wt. %	Formula Value	Wt. %	Formula value	Wt. %	Formula value
SiO2	53.67	1.96	53.93	1.97	57.05	1.32	40.43	1.00
TiO2	-	-	0.04	0.00	-	-	0.02	0.00
Al2O3	0.59	0.03	1.41	0.06	0.53	0.01	-	-
FeO	3.31	0.10	3.76	0.11	7.73	0.15	11.74	0.24
MnO	-	-	0.13	0.00	-	-	0.19	0.00
MgO	18.73	1.02	18.39	1.00	32.81	1.14	47.42	1.75
CaO	22.41	0.88	21.27	0.83	1.40	0.03	0.07	0.00
K2O	-	-	-	-	-	-	-	-
Na2O	1.29	0.09	0.60	0.04	0.35	0.02	-	-
SiO2	56.47	2.04	54.01	1.97	57.00	1.32	40.65	1.00
TiO2	-	-	0.06	0.00	-	-	0.02	0.00
Al2O3	0.00	0.00	1.29	0.06	0.00	0.00	-	-
FeO	3.76	0.11	4.09	0.12	7.15	0.14	11.63	0.24
MnO	-	-	0.14	0.00	-	-	0.17	0.00
MgO	17.18	0.93	19.84	1.08	34.10	1.18	47.63	1.75
CaO	22.58	0.88	19.84	0.77	0.99	0.02	0.06	0.00
K2O	-	-	-	-	-	-	-	-
Na2O	0.00	0.00	0.06	0.00	0.76	0.03	-	-
SiO2	54.71	1.99	53.27	1.97	59.16	1.36	40.58	6.01
TiO2	-	-	0.04	0.00	-	-	0.02	0.00
Al2O3	0.00	0.00	1.59	0.07	0.00	0.00	-	-
FeO	1.84	0.06	3.46	0.11	7.10	0.14	11.48	1.42
MnO	-	-	0.13	0.00	-	-	0.31	0.04
MgO	18.41	1.00	17.81	0.98	32.93	1.13	47.56	10.50
CaO	25.04	0.97	21.96	0.87	0.68	0.02	0.06	0.01
K2O	-	-	-	-	-	-	-	-
Na2O	0.00	0.00	0.09	0.00	0.00	0.00	-	-

Abbreviations:

Each point analyzed using the electron microprobe has been identified using a three letter code. The letters used in these names the following rules: The first letter represents the optical identification of the mineral. The second letter indicates the form or the colour which the mineral takes. The third letter identifies each point individually.

Mineral Names:

N or H	Hornblende or other amphibole
R	Grunerite
T	Biotite, or brown chlorite
L	Chlorite
GN	Garnet
GH	Gahnite

Mineral forms:

G	Green (note, some green hornblende sample points are simply labelled 'N')
W	White
T	Tabular
A	Amorphous
F	Euhedral, fibrous
P	Platy (chlorite and biotite)

It will be noted that many of the points originally identified as amphibole and as biotite proved, on analysis, to be chlorite. This is a result of the chemical alteration of the mineral, which has retained its primary appearance.

Sample numbers and mineral identifications are listed below:

Sample #G43:

LAA	Gahnite altered to chlorite	GNA	Garnet (overprinting chlorite)	RFC	Fibrous grunerite
LFC	Schistose chlorite	GNB	Garnet "		
LPA	"	vGNC	Garnet altered to chlorite		
LPB	"	GHA	Gahnite	RFD	"
TFE	Fibrous grunerite, altered to chlorite	GHB	Gahnite	TPB	green-brown chlorite

Sample #G3:

HGH	Pale green hornblende	HGW	White amphibole	TFK	White needle
HGI	Fibrous green hornblende	HGG	Green amphibole (Same crystal as HGW)	TFL	Brown biotite in sulphide
HGJ	Dark green alteration product of HWF	TFH	Brown phase around sulphide	TFM	As TFL, green
HWF	White amphibole	TFI	White phase around sulphide		
HGK	Pale green hornblende	TFJ	Brown phase around sulphide		

Sample B2:

RAA	Non-twinned, colourless	RFB	Same crystal as
RAB	amphibole	RAC	RFA
RTC	Euhedral, colourless amph.	RAD	Clear amphibole, next to
RFA	Twinned, colourless amph.	RAE	sulphide.

Sample F18:

LPC	Platy, schistose chlorite TPB	Green biotite, altered to chlorite	
NWF	White amph. altered to NGH	TPC	K-poor brown biotite around sulphide
NGH	Green alteration product of NWF	TPD	"
		TPE	"
TPF	Green-brown biotite	TPI	Green biotite
TPG	"	NGI	Green amphibole
TPH	"	TPJ	Biotite
HWG	White amphibole		

Sample #G37

NGB	Green amphibole in sulphides	HWA	White amph (altered to NGB)
NGC	"	HWB	" " NGF
NGD	Green-brown cleaved amph.	HWC	" " NGE
NGE	Green-brown amphibole	HWD	Clear amphibole with brown staining
NGF	Blue-green amphibole	HWE	White amph, altered to NGG
NAB	"		
TFA	Fibrous brown biotite	TFB	Same grain as TFA

Appendix C2 *Amphibole Data (EPMA)*

	RAA	RAB	RTC	RFC	RFA	RFB	RAC
Raw Data							
SiO2	49.41	49.53	49.47	47.35	49.41	49.45	49.52
TiO2	0.03	0.02	0.02	0.02	0.03	0.02	0.02
Al2O3	0.27	0.27	0.27	0.38	0.27	0.16	0.25
FeO	46.13	46.11	46.46	44.48	46.32	45.69	45.58
MnO	0.85	0.82	0.00	0.82	0.82	0.80	0.86
MgO	1.95	2.05	2.03	1.97	2.08	2.07	2.05
CaO	0.35	0.37	0.41	0.86	0.37	0.33	0.37
Na2O	0.07	0.07	0.07	0.09	0.05	0.02	0.05
K2O	0.00	0.00	0.00	0.01	0.00	0.00	0.00
Cl	0.28	0.26	0.28	0.20	0.26	0.11	0.18
Cr2O3							
No. of oxygens	23	23	23	23	23	23	23
Reformatted oxide percentages							
SiO2	49.41	49.53	49.47	47.35	49.41	49.45	49.52
TiO2	0.03	0.02	0.02	0.02	0.03	0.02	0.02
Al2O3	0.27	0.27	0.27	0.38	0.27	0.16	0.25
Cr2O3	0.00	0.00	0.00	0.00	0.00	0.00	0.00
Fe2O3	0.00	0.00	0.00	0.00	0.00	0.00	0.00
FeO	46.13	46.11	46.46	44.48	46.32	45.69	45.58
MnO	0.85	0.82	0.00	0.82	0.82	0.80	0.86
MgO	1.95	2.05	2.03	1.97	2.08	2.07	2.05
CaO	0.35	0.37	0.41	0.86	0.37	0.33	0.37
Na2O	0.07	0.07	0.07	0.09	0.05	0.02	0.05
K2O	0.00	0.00	0.00	0.01	0.00	0.00	0.00
Cl	0.28	0.26	0.28	0.20	0.26	0.11	0.18
H2O*	1.78	1.79	1.78	1.74	1.79	1.82	1.80
sub-total	101.12	101.29	100.79	97.92	101.40	100.47	100.68
O=F,Cl	0.06	0.06	0.06	0.05	0.06	0.02	0.04
TOTAL	101.05	101.23	100.72	97.87	101.34	100.44	100.64
Si	8.272	8.272	8.290	8.200	8.258	8.312	8.298
Al iv	0.000	0.000	0.000	0.000	0.000	0.000	0.000
Al vi	0.053	0.053	0.053	0.078	0.053	0.032	0.049
Ti	0.004	0.003	0.003	0.003	0.004	0.003	0.003
Cr	0.000	0.000	0.000	0.000	0.000	0.000	0.000
Fe3+	0.000	0.000	0.000	0.000	0.000	0.000	0.000
Fe2+	5.647	5.630	5.703	5.645	5.652	5.612	5.590
Mn	0.121	0.116	0.000	0.120	0.116	0.114	0.122
Mg	0.487	0.510	0.507	0.509	0.518	0.519	0.512
Ca	0.063	0.066	0.074	0.160	0.066	0.059	0.066
Na	0.023	0.023	0.023	0.030	0.016	0.007	0.016
K	0.000	0.000	0.000	0.002	0.000	0.000	0.000
Cl	0.079	0.074	0.080	0.059	0.074	0.031	0.051
OH	1.921	1.926	1.920	1.941	1.926	1.969	1.949
TOTAL	16.669	16.673	16.652	16.746	16.683	16.657	16.657
Na+K	0.023	0.023	0.023	0.032	0.016	0.007	0.016
Mg/(Mg+Fe2)	0.079	0.083	0.082	0.083	0.084	0.085	0.084
Fe3/(Fe3+Alvi)	0.000	0.000	0.000	0.000	0.000	0.000	0.000
Amphibole name	FALSE	FALSE	FALSE	FALSE	FALSE	FALSE	FALSE
(monoclinic alternative)	grunerite	grunerite	grunerite	grunerite	grunerite	grunerite	grunerite
Pressure Estimates							
P for Ca-amphiboles	P not valid	P not valid	P not valid	P not valid	P not valid	P not valid	P not valid
Hollister et al. 87	-4.5	-4.5	-4.5	-4.3	-4.5	-4.6	-4.5
Johnson & Rutherford 89	-3.2	-3.2	-3.2	-3.1	-3.2	-3.3	-3.3
Schmidt 92	-2.8	-2.8	-2.8	-2.6	-2.8	-2.9	-2.8

Barometers are only valid for calcic amphiboles

Appendix C2 *Amphibole Data (EPMA)*

	RAD	RAE	NGB	NGC	NGD	NGE	NGF
Raw Data							
SiO2	48.87	48.94	39.14	40.77	47.34	43.48	40.69
TiO2	0.03	0.03	0.18	0.26	0.15	0.18	0.18
Al2O3	0.25	0.40	14.60	10.97	3.53	8.67	11.83
FeO	45.81	45.42	28.14	30.70	37.26	32.34	30.59
MnO	0.01	0.80	0.26	0.00	0.69	0.47	0.35
MgO	2.05	2.11	1.93	2.63	4.33	3.24	2.43
CaO	0.37	0.39	10.75	9.69	3.42	7.37	8.85
Na2O	0.05	0.07	1.25	1.10	0.40	0.81	1.04
K2O	0.00	0.00	0.92	0.50	0.26	0.57	0.88
Cl	0.22	0.15	2.14	1.32	0.68	1.27	1.77
Cr2O3							
No. of oxygens	23	23	23	23	23	23	23
Reformatted oxide percen							
SiO2	48.87	48.94	39.14	40.77	47.34	43.48	40.69
TiO2	0.03	0.03	0.18	0.26	0.15	0.18	0.18
Al2O3	0.25	0.40	14.60	10.97	3.53	8.67	11.83
Cr2O3	0.00	0.00	0.00	0.00	0.00	0.00	0.00
Fe2O3	14.97	15.84	4.49	13.36	40.76	22.50	15.88
FeO	32.34	31.17	24.10	18.68	0.58	12.09	16.30
MnO	0.01	0.80	0.26	0.00	0.69	0.47	0.35
MgO	2.05	2.11	1.93	2.63	4.33	3.24	2.43
CaO	0.37	0.39	10.75	9.69	3.42	7.37	8.85
Na2O	0.05	0.07	1.25	1.10	0.40	0.81	1.04
K2O	0.00	0.00	0.92	0.50	0.26	0.57	0.88
Cl	0.22	0.15	2.14	1.32	0.68	1.27	1.77
H2O*	1.77	1.80	1.35	1.54	1.71	1.57	1.44
sub-total	100.93	101.70	101.11	100.81	103.85	102.22	101.64
O=F,Cl	0.05	0.03	0.48	0.30	0.15	0.29	0.40
TOTAL	100.88	101.66	100.63	100.52	103.70	101.94	101.24
Si	8.007	7.957	6.097	6.335	7.017	6.592	6.254
Al iv	0.000	0.043	1.903	1.665	0.617	1.408	1.746
Al vi	0.048	0.033	0.777	0.344	0.000	0.142	0.397
Ti	0.004	0.004	0.021	0.030	0.017	0.021	0.021
Cr	0.000	0.000	0.000	0.000	0.000	0.000	0.000
Fe3+	1.616	1.693	0.523	1.520	4.124	2.443	1.781
Fe2+	3.878	3.703	3.120	2.364	0.066	1.459	2.033
Mn	0.001	0.110	0.034	0.000	0.087	0.060	0.046
Mg	0.501	0.511	0.448	0.609	0.957	0.732	0.557
Ca	0.065	0.068	1.794	1.613	0.543	1.197	1.457
Na	0.016	0.022	0.378	0.331	0.115	0.238	0.310
K	0.000	0.000	0.183	0.099	0.049	0.110	0.173
Cl	0.061	0.041	0.565	0.348	0.171	0.326	0.461
OH	1.939	1.959	1.435	1.652	1.829	1.674	1.539
TOTAL	16.135	16.145	17.278	16.911	15.592	16.402	16.774
Na+K	0.016	0.022	0.560	0.431	0.164	0.348	0.482
Mg/(Mg+Fe2)	0.114	0.121	0.126	0.205	0.936	0.334	0.215
Fe3/(Fe3+Alvi)	0.971	0.981	0.402	0.815	1.000	0.945	0.818

Amphibole name	FALSE	anthoph.	ferro-pargasite	ferro-tscherm.	magnesio-anthoph.	magnesio-hornblende	ferro-tscherm.
(monoclinic alternative)	grunerite	grunerite		hornblende	magnesio-c	hornblende	hornblende
Pressure Estimates							
P for Ca-amphiboles	P not valid	P not valid			P not valid		
Hollister et al. 87	-4.5	-4.3	10.4	6.6	-1.3	4.0	7.3
Johnson & Rutherford 89	-3.3	-3.1	7.9	5.0	-0.9	3.1	5.6
Schmidt 92	-2.8	-2.6	9.7	6.6	-0.1	4.4	7.2
Barometers are only valid fc							

Appendix C2 *Amphibole Data (EPMA)*

	NGG	NGI	NAA	NAB	NWF	NGH	NGG
Raw Data							
SiO2	50.29	47.53	39.72	44.18	52.83	45.37	50.29
TiO2	0.08	0.07	0.31	0.32	0.07	0.09	0.08
Al2O3	1.07	8.13	10.65	8.71	0.49	8.85	1.07
FeO	41.09	21.37	32.97	30.07	31.53	25.66	41.09
MnO	0.79	0.17	0.32	0.36	0.39	0.28	0.79
MgO	4.97	8.85	3.62	3.34	11.73	8.71	4.97
CaO	0.52	11.22	7.66	9.47	1.29	7.42	0.52
Na2O	0.15	0.86	0.84	0.92	0.06	0.82	0.15
K2O	0.02	0.27	0.33	0.32	0.02	0.40	0.02
Cl	0.04	0.59	0.82	0.87	0.31	0.59	0.40
Cr2O3							
No. of oxygens	23	23	23	23	23	23	23
Reformatted oxide percen							
SiO2	50.29	47.53	39.72	44.18	52.83	45.37	50.29
TiO2	0.08	0.07	0.31	0.32	0.07	0.09	0.08
Al2O3	1.07	8.13	10.65	8.71	0.49	8.85	1.07
Cr2O3	0.00	0.00	0.00	0.00	0.00	0.00	0.00
Fe2O3	0.00	2.89	16.70	5.17	15.77	11.94	15.58
FeO	41.09	18.77	17.94	25.42	17.34	14.92	27.07
MnO	0.79	0.17	0.32	0.36	0.39	0.28	0.79
MgO	4.97	8.85	3.62	3.34	11.73	8.71	4.97
CaO	0.52	11.22	7.66	9.47	1.29	7.42	0.52
Na2O	0.15	0.86	0.84	0.92	0.06	0.82	0.15
K2O	0.02	0.27	0.33	0.32	0.02	0.40	0.02
Cl	0.04	0.59	0.82	0.87	0.31	0.59	0.40
H2O*	1.89	1.86	1.64	1.68	1.91	1.81	1.80
sub-total	100.91	101.21	100.55	100.76	102.21	101.20	102.74
O=F,Cl	0.01	0.13	0.18	0.20	0.07	0.13	0.09
TOTAL	100.90	101.07	100.37	100.57	102.14	101.06	102.65
Si	8.173	7.048	6.257	6.871	7.855	6.791	7.866
Al iv	0.000	0.952	1.743	1.129	0.086	1.209	0.134
Al vi	0.205	0.469	0.235	0.468	0.000	0.353	0.064
Ti	0.010	0.008	0.037	0.037	0.008	0.010	0.009
Cr	0.000	0.000	0.000	0.000	0.000	0.000	0.000
Fe3+	0.000	0.318	1.852	0.589	1.558	1.265	1.610
Fe2+	4.893	2.297	2.211	3.220	1.904	1.757	3.109
Mn	0.109	0.021	0.043	0.047	0.049	0.036	0.105
Mg	1.204	1.956	0.850	0.774	2.600	1.943	1.159
Ca	0.091	1.783	1.293	1.578	0.206	1.190	0.087
Na	0.047	0.247	0.257	0.277	0.017	0.238	0.045
K	0.004	0.051	0.066	0.063	0.004	0.076	0.004
Cl	0.011	0.148	0.219	0.229	0.078	0.150	0.106
OH	1.989	1.852	1.781	1.771	1.922	1.850	1.894
TOTAL	16.735	17.150	16.843	17.055	16.286	16.868	16.192
Na+K	0.051	0.298	0.323	0.341	0.021	0.314	0.049
Mg/(Mg+Fe2)	0.197	0.460	0.278	0.194	0.577	0.525	0.272
Fe3/(Fe3+Alvi)	0.000	0.404	0.887	0.557	1.000	0.782	0.962

Amphibole name	FALSE	magnesio-hornblende	ferro-tscherm.	magnesio-hornblende	anthoph.	magnesio-hornblende	anthophyllit
(monoclinic alternative)	grunerite		hornblende	hornblende	cummingtor	hornblende	grunerite
Pressure Estimates							
P for Ca-amphiboles	P not valid				P not valid		P not valid
Hollister et al. 87	-3.6	3.3	6.4	4.2	-4.3	4.0	-3.6
Johnson & Rutherford 89	-2.6	2.6	4.9	3.3	-3.1	3.1	-2.6
Schmidt 92	-2.0	3.8	6.4	4.6	-2.6	4.4	-2.1
Barometers are only valid fc							

Appendix C2 *Amphibole Data (EPMA)*

	HWA	HWB	HWC	HWD	HWE	HWG
Raw Data						
SiO2	41.42	48.82	49.22	41.75	49.70	52.68
TiO2	0.14	0.10	0.10	0.37	0.09	0.09
Al2O3	11.36	2.54	1.88	11.13	1.42	0.69
FeO	31.22	39.19	39.14	29.74	40.29	31.13
MnO	0.41	0.77	0.80	0.00	0.85	0.49
MgO	2.50	4.70	4.86	2.56	4.87	11.73
CaO	8.33	2.07	1.88	9.88	1.29	1.64
Na2O	0.98	0.28	0.26	1.05	0.15	0.12
K2O	0.87	0.10	0.07	0.51	0.07	0.06
Cl	1.97	0.36	0.33	1.26	0.18	0.41
Cr2O3						
No. of oxygens	23	23	23	23	23	23
Reformatted oxide percen						
SiO2	41.42	48.82	49.22	41.75	49.70	52.68
TiO2	0.14	0.10	0.10	0.37	0.09	0.09
Al2O3	11.36	2.54	1.88	11.13	1.42	0.69
Cr2O3	0.00	0.00	0.00	0.00	0.00	0.00
Fe2O3	18.10	0.00	14.53	5.12	0.00	15.61
FeO	14.93	39.19	26.06	25.13	40.29	17.08
MnO	0.41	0.77	0.80	0.00	0.85	0.49
MgO	2.50	4.70	4.86	2.56	4.87	11.73
CaO	8.33	2.07	1.88	9.88	1.29	1.64
Na2O	0.98	0.28	0.26	1.05	0.15	0.12
K2O	0.87	0.10	0.07	0.51	0.07	0.06
Cl	1.97	0.36	0.33	1.26	0.18	0.41
H2O*	1.40	1.80	1.81	1.57	1.85	1.89
sub-total	102.41	100.73	101.80	100.33	100.76	102.49
O=F,Cl	0.44	0.08	0.07	0.28	0.04	0.09
TOTAL	101.97	100.65	101.73	100.05	100.72	102.40
Si	6.305	7.907	7.731	6.540	8.079	7.809
Al iv	1.695	0.093	0.269	1.460	0.000	0.121
Al vi	0.343	0.392	0.079	0.595	0.272	0.000
Ti	0.016	0.012	0.012	0.044	0.011	0.010
Cr	0.000	0.000	0.000	0.000	0.000	0.000
Fe3+	2.002	0.000	1.529	0.592	0.000	1.544
Fe2+	1.836	4.731	3.048	3.228	4.835	1.877
Mn	0.053	0.106	0.106	0.000	0.117	0.062
Mg	0.567	1.135	1.138	0.598	1.180	2.592
Ca	1.359	0.359	0.316	1.658	0.225	0.260
Na	0.289	0.088	0.079	0.319	0.047	0.034
K	0.169	0.021	0.014	0.102	0.015	0.011
Cl	0.508	0.099	0.088	0.335	0.050	0.103
OH	1.492	1.901	1.912	1.665	1.950	1.897
TOTAL	16.634	16.843	16.321	17.136	16.781	16.320
Na+K	0.458	0.109	0.093	0.421	0.062	0.046
Mg/(Mg+Fe2)	0.236	0.193	0.272	0.156	0.196	0.580
Fe3/(Fe3+Alvi)	0.854	0.000	0.951	0.499	0.000	1.000
Amphibole name	ferro-tscherm.	anthophyllit	anthophyllit	magnesio-h	FALSE	anthophyllit
(monoclinic alternative)	hornblende	grunerite	grunerite	hornblende	grunerite	cummingtor
Pressure Estimates						
P for Ca-amphiboles		P not valid	P not valid		P not valid	P not valid
Hollister et al. 87	6.7	-2.0	-2.8	6.8	-3.2	-4.1
Johnson & Rutherford 89	5.2	-1.4	-2.0	5.2	-2.3	-3.0
Schmidt 92	6.7	-0.7	-1.4	6.8	-1.7	-2.4
Barometers are only valid fc						

Appendix C2 *Amphibole Data (EPMA)*

	HGH	HGI	HGJ	HGK	HGG	HWF	HGW
SiO2	47.07	47.19	44.12	46.02	44.46	48.91	48.72
TiO2	0.14	0.16	0.16	0.16	0.16	0.03	0.02
Al2O3	3.55	3.40	5.83	4.17	5.93	0.72	0.35
FeO	32.42	32.82	33.28	33.16	32.86	42.89	43.88
MnO	0.49	0.47	0.48	0.47	0.42	1.18	1.18
MgO	2.65	2.67	2.22	2.26	2.26	2.80	2.73
CaO	10.76	10.76	9.96	10.38	10.68	1.66	0.88
Na2O	0.49	0.45	0.79	0.64	0.76	0.11	0.07
K2O	0.24	0.24	0.38	0.30	0.39	0.02	0.01
F	0.04	0.00	0.00	0.00	0.04	0.00	0.00
Cl	0.37	0.39	0.54	0.41	0.63	0.09	0.10
Total	98.22	98.55	97.76	97.97	98.59	98.41	97.94
No. of O	23	23	23	23	23	23	23
Reformatted oxide percentages							
SiO2	47.07	47.19	44.12	46.02	44.46	48.91	48.72
Al2O3	3.55	3.40	5.83	4.17	5.93	0.72	0.35
Cr2O3	0.00	0.00	0.00	0.00	0.00	0.00	0.00
Fe2O3	6.11	6.71	11.24	7.90	8.57	0.00	0.00
FeO	26.93	26.78	23.17	26.05	25.15	42.89	43.88
MnO	0.49	0.47	0.48	0.47	0.42	1.18	1.18
MgO	2.65	2.67	2.22	2.26	2.31	2.80	2.73
CaO	10.76	10.76	9.96	10.38	10.68	1.66	0.88
Na2O	0.49	0.45	0.79	0.64	0.76	0.11	0.07
K2O	0.24	0.24	0.38	0.30	0.39	0.02	0.01
F	0.04	0.00	0.00	0.00	0.04	0.00	0.00
Cl	0.37	0.39	0.54	0.41	0.63	0.09	0.10
H2O*	1.77	1.79	1.72	1.76	1.69	1.83	1.81
	100.60	101.01	100.60	100.52	101.19	100.23	99.75
O=F,Cl	0.10	0.09	0.12	0.09	0.16	0.02	0.02
Total	100.50	100.93	100.48	100.43	101.03	100.21	99.73
Si	7.387	7.384	6.957	7.257	6.974	8.151	8.214
Al iv	0.613	0.616	1.043	0.743	1.026	0.000	0.000
Al vi	0.044	0.012	0.040	0.032	0.070	0.141	0.070
Ti	0.017	0.019	0.019	0.019	0.019	0.004	0.003
Cr	0.000	0.000	0.000	0.000	0.000	0.000	0.000
Fe3+	0.712	0.779	1.299	0.920	0.994	0.000	0.000
Fe2+	3.488	3.452	2.976	3.374	3.240	5.288	5.422
Mn	0.065	0.062	0.064	0.063	0.056	0.167	0.169
Mg	0.620	0.623	0.522	0.531	0.540	0.696	0.686
Ca	1.809	1.804	1.683	1.754	1.795	0.296	0.159
Na	0.149	0.137	0.242	0.196	0.231	0.036	0.023
K	0.048	0.048	0.076	0.060	0.078	0.004	0.002
F	0.020	0.000	0.000	0.000	0.020	0.000	0.000
Cl	0.098	0.103	0.144	0.110	0.168	0.025	0.029
OH	1.882	1.897	1.856	1.890	1.813	1.975	1.971
TOTAL	16.952	16.935	16.920	16.950	17.023	16.782	16.747

Amphibole name	ferro actinolite	ferrian-ferro actinolite	ferri-ferro hornblende	ferrian-ferro actinolite	ferrian-ferro hornblende	anth-ophyllite	anthophy

Appendix C2 *Biotite Data (EPMA)*

	TFA	TPD	TPE	TPF	TPG	TPH	TPI	TPJ
SiO2	44.68	35.61	35.38	35.86	36.34	35.66	34.59	34.92
TiO2	0.05	1.27	2.29	0.82	0.77	0.78	0.67	0.80
Al2O3	5.59	15.49	14.15	16.12	15.93	15.39	15.73	14.95
FeO	35.85	24.92	25.48	23.44	23.05	24.30	25.81	26.23
MnO	0.00	0.06	0.06	0.08	0.03	0.06	0.08	0.09
MgO	2.57	8.48	8.54	9.30	9.67	9.37	9.26	9.12
CaO	0.11	0.03	0.03	0.16	0.03	0.01	0.07	0.03
Na2O	0.04	0.06	0.02	0.07	0.07	0.07	0.02	0.02
K2O	1.65	3.76	8.94	8.74	8.47	8.91	7.86	8.40
F	0.00	0.08	0.04	0.12	0.12	0.08	0.12	0.04
Cl	0.06	0.20	0.83	1.00	0.69	1.01	0.77	0.93
No. of oxygens	28.00	28.00	28.00	28.00	28.00	28.00	28.00	28.00
SiO2	44.68	35.61	35.38	35.86	36.34	35.66	34.59	34.92
TiO2	0.05	1.27	2.29	0.82	0.77	0.78	0.67	0.80
Al2O3	5.59	15.49	14.15	16.12	15.93	15.39	15.73	14.95
Cr2O3	0.00	0.00	0.00	0.00	0.00	0.00	0.00	0.00
Fe2O3	11.39	5.90	0.71	1.13	1.38	0.43	0.46	0.00
FeO	25.60	19.61	24.84	22.43	21.80	23.91	25.40	26.23
MnO	0.00	0.06	0.06	0.08	0.03	0.06	0.08	0.09
MgO	2.57	8.48	8.54	9.30	9.67	9.37	9.26	9.12
CaO	0.11	0.03	0.03	0.16	0.03	0.01	0.07	0.03
Na2O	0.04	0.06	0.02	0.07	0.07	0.07	0.02	0.02
K2O	1.65	3.76	8.94	8.74	8.47	8.91	7.86	8.40
F	0.00	0.08	0.04	0.12	0.12	0.08	0.12	0.04
Cl	0.06	0.20	0.83	1.00	0.69	1.01	0.77	0.93
H2O*	11.48	11.53	11.48	11.47	11.66	11.42	11.39	11.38
Total	103.22	102.08	107.31	107.30	106.97	107.10	106.41	106.91
O=F,Cl	0.01	0.08	0.20	0.28	0.21	0.26	0.22	0.23
TOTAL	103.21	102.00	107.10	107.02	106.76	106.84	106.19	106.68
Si	8.95	7.03	6.76	6.74	6.84	6.76	6.66	6.72
Al iv	0.00	0.97	1.24	1.26	1.16	1.24	1.34	1.28
Al vi	1.37	2.77	2.10	2.49	2.54	2.37	2.38	2.26
Ti	0.01	0.19	0.33	0.12	0.11	0.11	0.10	0.12
Cr	0.00	0.00	0.00	0.00	0.00	0.00	0.00	0.00
Fe3+	1.72	0.88	0.10	0.16	0.20	0.06	0.07	0.00
Fe2+	4.29	3.24	3.97	3.53	3.43	3.79	4.09	4.22
Mn	0.00	0.01	0.01	0.01	0.00	0.01	0.01	0.01
Mg	0.77	2.50	2.43	2.61	2.71	2.65	2.66	2.61
Ca	0.02	0.01	0.01	0.03	0.01	0.00	0.01	0.01
Na	0.03	0.05	0.01	0.05	0.05	0.05	0.01	0.01
K	0.84	1.89	4.36	4.19	4.07	4.31	3.86	4.12
F	0.00	0.10	0.05	0.14	0.14	0.10	0.15	0.05
Cl	0.04	0.13	0.54	0.64	0.44	0.65	0.50	0.61
OH*	15.96	15.77	15.41	15.22	15.42	15.25	15.35	15.34
Total	34.00	35.52	37.32	37.19	37.12	37.35	37.19	37.37
Oxidized	no	no	yes	yes	yes	yes	yes	yes
Fe/Fe+Mg	0.89	0.62	0.63	0.59	0.57	0.59	0.61	0.62

Appendix C2 *Chlorite Data (EPMA)*

Raw Data	LAA	LFC	LPA	LPB	GNC	HGC	HGB
SiO2	29.90	23.57	23.32	29.10	29.94	42.15	40.74
TiO2	0.66	0.09	0.10	0.48	0.15	0.05	0.05
Al2O3	16.70	22.50	22.23	17.85	14.01	2.53	1.81
FeO	32.08	32.56	31.99	33.63	34.30	42.70	45.38
MnO	0.12	0.11	0.09	0.15	0.18	0.75	0.82
MgO	8.18	10.03	9.96	6.84	9.76	1.51	1.45
CaO	0.04	0.03	0.01	0.12	0.12	0.15	0.34
Na2O	0.02	0.02	0.02	0.02	0.02	0.09	0.02
K2O	4.29	0.00	0.05	2.63	0.99	1.37	0.94
F	0.11	0.00	0.00	0.04	0.04	0.07	0.00
Cl	0.19	0.05	0.05	0.12	0.04	0.15	0.22
Total	92.29	88.96	87.82	90.98	89.55	91.52	91.77
No. of oxygen:	28	28	28	28	28	28	28
	Reformatted oxide percentages based on 28 oxygens						
	(with Fe2+/Fe3+ and OH calculated assuming full site occupancy)						
SiO2	29.90	23.57	23.32	29.10	29.94	42.15	40.74
TiO2	0.66	0.09	0.10	0.48	0.15	0.05	0.05
Al2O3	16.70	22.50	22.23	17.85	14.01	2.53	1.81
Cr2O3	0.00	0.00	0.00	0.00	0.00	0.00	0.00
Fe2O3	0.00	0.00	0.00	1.39	1.14	8.18	6.91
FeO	32.08	32.56	31.99	32.38	33.27	35.34	39.16
MnO	0.12	0.11	0.09	0.15	0.18	0.75	0.82
MgO	8.18	10.03	9.96	6.84	9.76	1.51	1.45
CaO	0.04	0.03	0.01	0.12	0.12	0.15	0.34
Na2O	0.02	0.02	0.02	0.02	0.02	0.09	0.02
K2O	4.29	0.00	0.05	2.63	0.99	1.37	0.94
F	0.11	0.00	0.00	0.04	0.04	0.07	0.00
Cl	0.19	0.05	0.05	0.12	0.04	0.15	0.22
H2O*	11.13	11.06	10.93	11.10	11.00	10.88	10.73
Total	103.42	100.01	98.75	102.22	100.66	103.22	103.19
O=F,Cl	0.09	0.01	0.01	0.04	0.03	0.06	0.05
TOTAL	103.33	100.00	98.73	102.17	100.63	103.15	103.14
Si	6.168	5.095	5.100	6.113	6.433	8.868	8.766
Al iv	1.832	2.905	2.900	1.887	1.567	0.000	0.000
Al vi	2.325	2.831	2.838	2.612	2.013	0.649	0.470
Ti	0.102	0.015	0.016	0.076	0.024	0.008	0.008
Cr	0.000	0.000	0.000	0.000	0.000	0.000	0.000
Fe3+	0.000	0.000	0.000	0.219	0.185	1.295	1.119
Fe2+	5.548	5.899	5.862	5.689	5.979	6.219	7.047
Mn	0.021	0.020	0.017	0.027	0.033	0.134	0.149
Mg	2.516	3.232	3.247	2.142	3.126	0.474	0.465
Ca	0.009	0.007	0.002	0.027	0.028	0.034	0.078
Na	0.016	0.017	0.017	0.016	0.017	0.073	0.017
K	2.258	0.000	0.028	1.409	0.543	0.735	0.516
F	0.144	0.000	0.000	0.053	0.054	0.093	0.000
Cl	0.133	0.037	0.037	0.085	0.029	0.107	0.160
OH*	15.724	15.963	15.963	15.861	15.917	15.800	15.840
Total	36.794	36.020	36.028	36.217	35.947	34.488	34.636
Oxidized	yes	yes	yes	yes	yes	no	no
Fe/Fe+Mg	0.6880124	0.6460356	0.64352	0.7339291	0.6634869	0.9407052	0.9461158
Variety	brunsvigite	ripidolite	ripidolite	brunsvigite	no name	no name	no name

Appendix C2 *Chlorite Data (EPMA)*

Raw Data	TFH	TFI	TFJ	TFK	TFL	TFM
SiO2	44.28	43.96	38.51	40.43	45.27	46.92
TiO2	0.05	0.03	0.03	0.05	0.03	0.03
Al2O3	2.26	2.02	0.91	1.64	3.36	1.77
FeO	40.95	41.79	48.90	46.88	38.60	41.38
MnO	0.75	0.73	0.84	0.79	0.62	0.72
MgO	1.86	1.32	1.36	1.32	1.49	1.43
CaO	0.37	0.04	0.13	0.07	0.16	0.01
Na2O	0.07	0.02	0.00	0.02	0.04	0.02
K2O	0.97	1.39	0.29	0.72	1.73	1.57
F	0.00	0.00	0.04	0.00	0.00	0.00
Cl	0.10	0.17	0.16	0.21	0.11	0.23
Total	91.66	91.47	91.17	92.13	91.41	94.08
No. of oxygen:	28	28	28	28	28	28
	Reformatted oxide percentages based on 28 oxygens					
	(with Fe2+/Fe3+ and OH calculated assuming full site occupancy)					
SiO2	44.28	43.96	38.51	40.43	45.27	46.92
TiO2	0.05	0.03	0.03	0.05	0.03	0.03
Al2O3	2.26	2.02	0.91	1.64	3.36	1.77
Cr2O3	0.00	0.00	0.00	0.00	0.00	0.00
Fe2O3	9.95	9.60	5.30	6.67	10.94	11.19
FeO	32.00	33.16	44.13	40.88	28.75	31.31
MnO	0.75	0.73	0.84	0.79	0.62	0.72
MgO	1.86	1.32	1.36	1.32	1.49	1.43
CaO	0.37	0.04	0.13	0.07	0.16	0.01
Na2O	0.07	0.02	0.00	0.02	0.04	0.02
K2O	0.97	1.39	0.29	0.72	1.73	1.57
F	0.00	0.00	0.04	0.00	0.00	0.00
Cl	0.10	0.17	0.16	0.21	0.11	0.23
H2O*	11.20	11.05	10.39	10.71	11.33	11.49
Total	103.86	103.49	102.09	103.50	103.83	106.68
O=F,Cl	0.02	0.04	0.05	0.05	0.02	0.05
TOTAL	103.83	103.45	102.04	103.46	103.80	106.63
Si	9.119	9.129	8.611	8.737	9.165	9.317
Al iv	0.000	0.000	0.000	0.000	0.000	0.000
Al vi	0.567	0.512	0.245	0.428	0.833	0.430
Ti	0.008	0.005	0.005	0.008	0.005	0.004
Cr	0.000	0.000	0.000	0.000	0.000	0.000
Fe3+	1.542	1.500	0.892	1.084	1.667	1.672
Fe2+	5.511	5.759	8.253	7.388	4.868	5.200
Mn	0.131	0.128	0.159	0.145	0.106	0.121
Mg	0.571	0.409	0.453	0.425	0.450	0.423
Ca	0.082	0.009	0.031	0.016	0.035	0.002
Na	0.056	0.016	0.000	0.017	0.031	0.015
K	0.510	0.736	0.165	0.397	0.893	0.795
F	0.000	0.000	0.057	0.000	0.000	0.000
Cl	0.070	0.120	0.121	0.154	0.075	0.155
OH*	15.930	15.880	15.822	15.846	15.925	15.845
Total	34.095	34.203	34.816	34.645	34.054	33.980
Oxidized	no	no	no	no	no	no
Fe/Fe+Mg	0.9251032	0.9466999	0.9527685	0.9522104	0.9356253	0.941977
Variety	no name	no name	no name	no name	no name	no name

Appendix C2 — *Chlorite Data (EPMA)*

Raw Data	TFC	TPB	TFE	TPC	LPC	TFF	LPD
SiO2	35.69	26.29	33.73	32.37	24.16	40.44	25.83
TiO2	0.07	0.89	0.03	1.19	0.09	0.09	0.09
Al2O3	17.16	16.01	11.21	15.94	20.69	15.13	19.53
FeO	35.21	34.59	34.57	29.85	33.74	27.30	33.44
MnO	1.29	0.14	0.24	0.09	0.12	0.11	0.12
MgO	4.86	8.78	9.45	7.68	9.71	7.91	9.43
CaO	1.50	0.03	0.19	0.03	0.03	0.43	0.03
Na2O	0.00	0.00	0.10	0.00	0.02	0.00	0.02
K2O	0.05	2.09	0.26	7.26	0.01	0.03	0.21
F	0.00	0.15	0.00	0.00	0.00	0.00	0.04
Cl	0.01	0.11	0.01	0.22	0.06	0.05	0.06
Total	95.84	89.08	89.79	94.63	88.63	91.49	88.80
No. of oxygen:	28	28	28	28	28	28	28
	Reformatted oxide percentages based on 28 oxygens						
	(with Fe2+/Fe3+ and OH calculated assuming full site occupancy)						
SiO2	35.69	26.29	33.73	32.37	24.16	40.44	25.83
TiO2	0.07	0.89	0.03	1.19	0.09	0.09	0.09
Al2O3	17.16	16.01	11.21	15.94	20.69	15.13	19.53
Cr2O3	0.00	0.00	0.00	0.00	0.00	0.00	0.00
Fe2O3	7.27	0.00	3.56	0.00	0.00	11.41	0.77
FeO	28.67	34.59	31.37	29.85	33.74	17.03	32.74
MnO	1.29	0.14	0.24	0.09	0.12	0.11	0.12
MgO	4.86	8.78	9.45	7.68	9.71	7.91	9.43
CaO	1.50	0.03	0.19	0.03	0.03	0.43	0.03
Na2O	0.00	0.00	0.10	0.00	0.02	0.00	0.02
K2O	0.05	2.09	0.26	7.26	0.01	0.03	0.21
F	0.00	0.15	0.00	0.00	0.00	0.00	0.04
Cl	0.01	0.11	0.01	0.22	0.06	0.05	0.06
H2O*	12.09	10.58	11.22	11.53	10.92	12.22	10.95
Total	108.66	99.66	101.37	106.16	99.56	104.85	99.83
O=F,Cl	0.00	0.09	0.00	0.05	0.01	0.01	0.03
TOTAL	108.66	99.57	101.36	106.11	99.54	104.84	99.80
Si	6.938	5.736	7.122	6.404	5.280	7.684	5.593
Al iv	1.062	2.264	0.878	1.596	2.720	0.316	2.407
Al vi	2.947	1.927	1.946	2.271	2.617	3.176	2.600
Ti	0.010	0.146	0.005	0.177	0.015	0.013	0.015
Cr	0.000	0.000	0.000	0.000	0.000	0.000	0.000
Fe3+	1.064	0.000	0.565	0.000	0.000	1.632	0.126
Fe2+	4.661	6.447	5.539	5.069	6.190	2.706	5.929
Mn	0.212	0.026	0.043	0.015	0.022	0.018	0.022
Mg	1.408	2.855	2.974	2.265	3.163	2.241	3.044
Ca	0.312	0.007	0.043	0.006	0.007	0.088	0.007
Na	0.000	0.000	0.082	0.000	0.017	0.000	0.017
K	0.025	1.163	0.140	3.664	0.006	0.015	0.116
F	0.000	0.207	0.000	0.000	0.000	0.000	0.055
Cl	0.007	0.081	0.007	0.148	0.044	0.032	0.044
OH*	15.993	15.712	15.993	15.852	15.956	15.968	15.901
Total	34.640	36.572	35.338	37.468	36.037	33.887	35.875
Oxidized	no	yes	yes	yes	yes	no	yes
Fe/Fe+Mg	0.8025503	0.6930539	0.6723847	0.6911538	0.6618058	0.6594351	0.6654942
Variety	no name	brunsvigite	no name	no name	ripidolite	no name	ripidolite

Appendix C2 *Garnet/Gahnite Data (EPMA)*

	GNA	GNB	GHA	GHB
	Garnet		Gahnite	
	GNA	GNB	GHA	GHB
SiO2	37.52	37.57	0.06	0.06
TiO2	0.05	0.07	0.02	0.03
Al2O3	21.08	20.85	54.33	55.02
FeO	36.77	36.82	12.84	12.55
MnO	2.26	2.25	0.06	0.06
MgO	1.43	1.45	1.12	1.03
CaO	2.64	2.51	0.01	0.01
Na2O	0.00	0.00	0.00	0.00
K2O	0.00	0.00	0.00	0.00
F	0.00	0.00	0.00	0.00
Cl	0.00	0.00	0.00	0.00
Total	101.75	101.52	99.64	100.53
No. of O	12	12		

Reformatted oxide percentages based on 12 oxygens and with Fe2+/Fe3+ calculated assuming full occupancy

SiO2	37.52	37.57
Al2O3	21.0826732	20.847222
Cr2O3	0	0
Fe2O3	0.13198209	0.2137139
FeO	36.6512363	36.62769
MnO	2.26	2.25
MgO	1.43	1.45
Total	101.765892	101.53863
Al vi	1.988	1.970
Ti	0.003	0.004
Cr	0.000	0.000
Fe3+	0.008	0.013
Fe2+	2.451	2.455
Mn	0.153	0.153
Ni	0.000	0.000
Zn	0.000	0.000
Total	8.000	7.995
Almandine	81.630	81.787
Andradite	0.398	0.650
Grossular	7.161	6.599
Pyrope	5.696	5.826

Sphalerite **(Sample G43)**

	At.%	Wt%	At.%	Wt%	At.%	Wt%		
Zn	39.09	54.77	41.05	56.64	39.2	55.03	40.05	55.62
S	54.12	37.19	52.36	35.44	54.71	37.67	52.94	36.06
Cu	0	0	0.88	1.18	0	0		
Fe	6.22	7.44	5.72	6.74	6.09	7.31	8.31	7.01
Ti	0.58	0.59	0	0	0	0		
								(With Gahnite)
Zn	41.77	56	41.94	55.93	41.43	55.65	42.59	58.76
S	52.18	34.31	52.17	34.12	52.47	34.57	52.67	35.64
Fe	5.15	5.9	4.85	5.52	5.2	5.96	4.74	5.59
Pb	0.89	3.79	1.05	4.43	0.9	3.82		
Zn	45.69	59.32	44.12	57.52	44.32	57.23	43.03	59.2
S	47.83	30.46	48.52	31.03	47.05	29.81	52.25	35.26
Fe	5.48	6.08	6.29	7.01	7.48	8.26	4.72	5.54
Pb	1.01	4.14	1.07	4.44	1.15	4.71		

Pyrite **(Sample G43)**

	At.%	Wt.%	At %	Wt %
Fe	30.23	40.48	31.88	44.39
S	66.66	51.25	66.75	53.38
Zn	2.12	3.33	1.37	2.23
Pb	0.99	4.94		

Chalcopyrite **(Sample G43)** **(Sample F16B)**

	At %	Wt %	At %	Wt%	At %	Wt%
Fe	23.7	28.36	24.21	29.97	24.23	29.79
S	51.04	35.06	52.59	37.39	51.56	36.39
Cu	24.55	33.42	22.61	31.85	23.72	33.18
Zn	0	0	0	0	0.49	0.63
Pb	0.71	3.15	0.6	0.78	0	0

			with Au		**Gold**	**(Sample F16B)**	
	At %	Wt%	At %	Wt%		At %	Wt %
Fe	24.5	30.22	21.86	26.67	Au	64.01	77.04
S	52.03	36.85	54.3	38.04	Ag	33.16	21.86
Cu	23.47	32.93	22.14	30.73	Cu	2.83	1.1
Co	0	0	0.76	0.98			
Au	0	0	0.7	3.01			
Ag	0	0	0.24	0.57			

Ilmenite (Sample F18) **(Compounds)**

FeO	47.31	47.8	47.53
TiO2	52.69	52.2	52.47

	At %	Wt %	At %	Wt %	At %	Wt %	At %	Wt %
Fe	34.29	47.5	33.84	46.7	33.78	46.65	34.01	46.84
Ti	33.39	39.67	34.42	40.74	34.43	40.77	34.47	40.72
O	32.31	12.82	31.75	12.55	31.79	12.58	31.52	12.44

Unknowns

White sulphide in BOB6 (has blue anisotropy)

	At %	Wt %	At %	Wt %
Co	26.84	29.38	26.19	28.95
As	32.66	45.44	31.85	44.76
S	38.08	22.68	39.61	23.88
Fe	2.41	2.5	2.35	2.46

Ni-Co-Arsenides in sphalerite

	At %	Wt %	At %	Wt %	At %	Wt %
Zn	0	0	0	0	0	0
Fe	18.02	15.97	7.56	8.04	17.1	14.82
S	2.4	1.22	33.99	20.77	0	0
Cu	0	0	0	0	0	0
Co	33.57	31.38	30.97	34.78	33.52	30.64
As	33.34	39.63	18.36	26.22	38.09	44.26
Ni	12.67	11.8	9.12	10.2	11.29	10.28

Sphalerite containing unknown **Pyrrhotite (Sample F16B)** **Inclusion in Pyrrhotite**

	At %	Wt %	At %	Wt %	At %	Wt %	At %	Wt %
Zn	36.84	49.56	33.26	44.98	0	0	0.52	0.74
Fe	7.05	8.1	7.09	8.19	45.38	59.14	9.06	11.19
S	50.08	33.05	50.53	33.52	54.62	40.86	50.04	35.47
Cu	0	0	2.3	3.02	0	0	0	0
Co	0	0	0.8	0.97	0	0	34.6	45.08
As	6.03	9.29	6.01	9.32	0	0	0	0
Ni	0	0	0	0	0	0	5.79	7.51

D1: Sample preparation and analytical techniques

D1.1 Microthermometry

Microthermometric analyses have been carried out using doubly polished quartz chips prepared as described by Shepherd *et al.* (1985, section 2.5). The chips are 100 to 150μm thick, and 15 to 20mm diameter.

Analyses took place using a Linkam THM600 heating-freezing stage mounted on a Leitz Dialux microscope, with long working distance objectives. The THM600 is similar to the TH600 described by Shepherd (*op.cit*), where the doubly polished quartz chip being studied (split into separate pieces each less than 12mm diameter) is placed on a sapphire window, and sealed from the outside atmosphere. Liquid nitrogen (temperature -192°C) is then pumped into the stage and circulated around the sample by rubber hoses. The maximum rate of cooling for the Linkam stage is 99°s^{-1}, and the sample is frozen at this rate to between -120° and -180°C. The THM600 model is also equipped so that cycles of set temperature limits and rates may be pre-programmed.

Calibration of the heating-freezing stage is necessary in order to monitor and correct for any drift which occurs during the day, and the daily variation caused by atmospheric as well as internal apparatus conditions. A standard, of known composition, must be used. For measuring low temperature phase changes a pure CO_2-H_2O inclusion is usually used. Two measurements must be made, i.e. Tm_{CO2} and Tm_{Ice}, and the δT°C from the theoretical value is recorded. The Southampton Linkam stage is calibrated for values less than 0°C, and from a graph plotted using the two δT values (*Fig. D1.1*) all measurements recorded during the day can be corrected. Values greater than 0°C are corrected in the same way, using deviation from the known values for Tm_{Clath}, Th_{CO2}, etc.

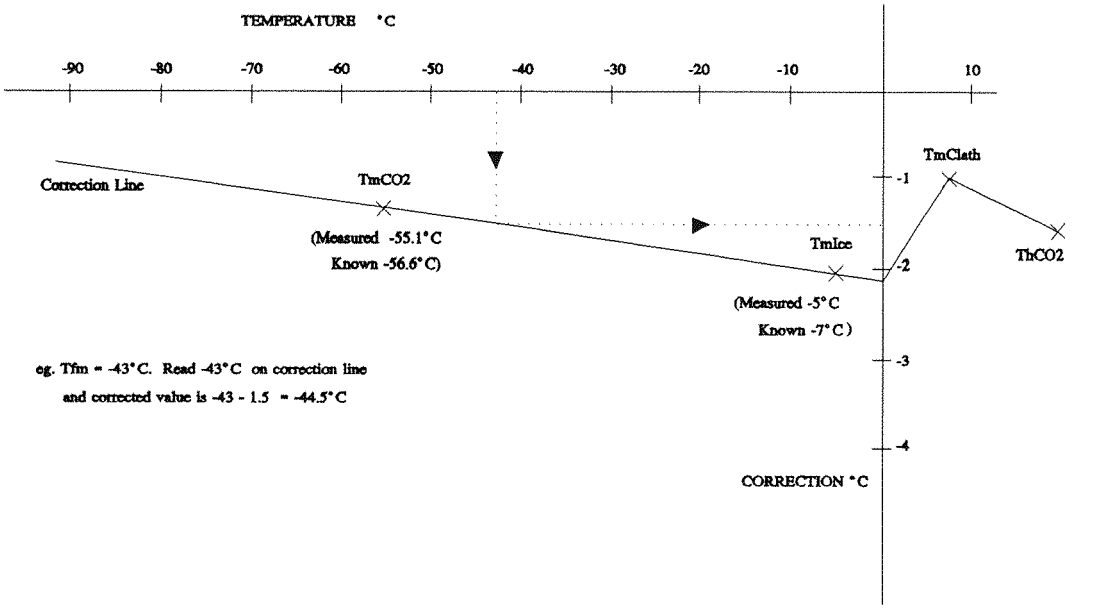

Figure D1.1 **Typical calibration graph for microthermometric analysis, plotted using Tm_{CO2} and Tm_{Ice}.**

D1.2 Laser Raman Spectroscopy

Laser Raman (LRS) analysis was carried out on the same doubly polished chips used for microthermometric purposes, using a Jobin-Yvonne Raman Microprobe MOLE, model S3000, fitted with an Astromed CCD multichannel detector (cooled with liquid N_2 to 132K) was used, with a Coherent 4W Argon laser of 600mW source output (514.5nm, green-line laser). An Olympus BHVO microscope coupled with the Raman allows optical examination.

Analysis of carbonic phases (CO_2, CH_4, N_2) are carried out at room temperature, by placing the quartz chip directly onto the microscope stage. The laser beam is focused on the gas phase of the fluid inclusion, using a magnification of between 50X and 80X. Run times of between 10 and 15 minutes for each gas were found most suitable. Detection limits for the common gases are: N_2 = 0.001 - 0.002 mole%, CH_4 = 0.002 - 0.004 mole%. The vibrational frequency spectra produced are used to identify the gases present, while peak area ratios can be used to calculate semi-quantitative relative concentrations, using the equations defined by Dubessy (1989) and Kerkhof and Kisch (1993). There is much controversy at present over the values by which to divide the CO_2 and CH_4 peaks, but for the given working conditions the following equations were used:

$$Z\ CO_2 = Area\ CO_2\ (1388) / 1.49$$

and

$$Z\ CH_4 = Area\ CH_4\ (2917) / 7.57$$

where: Z = molar fraction in the carbonic phase
1.49 and 7.57 are the relative Raman cross-sections, calculated for the 514.532-nm laser

Analysis of hydrates must be carried out at temperature of around -170°C, using the Linkam heating-freezing stage described in *Appendix D1.1.* The analytical technique used for this is described in detail in Chapter 5, section 5.5.1.

Doubly-polished fluid inclusion (quartz) wafers were placed in the sample holder of a Linkam TMS600 heating-freezing apparatus, which sat on the working stage of the microscope. The sample chamber of the Linkam stage was made air-tight using rubber O-rings to make a seal between the stage and a long-working-distance Nikon *100 lens. No cover-slip is necessary.

Optimum working conditions for the laser were found to be with a slit size of 150mm. A grating of 600g/mm (intermediate slit 24.9mm) allowed a spectra to be obtained for the whole area of interest (3000 - 3700 counts/sec) in one reading.

D1.3 D-ICP

Decrepitation-linked ICP-MS is a method of bulk fluid analysis, which was carried out on clean quartz separates from the Pojuca Corpo Quatro Formation. The quartz is in the form of 'chips', 0.5 to 2mm across, which are prepared by crushing and cleaning. Vein and host rock quartz is crushed in a fly press, and the resulting fragments are sieved to retrieve the 500μm to 2mm fraction. These chips are then hand picked to remove any obvious contaminants such as biotite, calcite and sulphide minerals, and re-picked carefully under a binocular microscope to remove any quartz chips which contain trace contaminant phases.

3-4g of 'clean' quartz chips are then boiled for 24 hours in 2M HNO_3, changing the acid every 8 hours, to removes any residual surface material from the quartz. To remove any remaining trace of acid or cations on the chip surface, the samples are then boiled in a bath of triple distilled water for 2-4 hours, changing the water once, and air dried at 80°C.

The clean quartz separates are stored in nitric-acid-soaked, washed, glass vials, to avoid pollution prior to analysis.

D-ICP was carried out at Imperial College, London, under the guidance of Barry Coles. The ICP instrumentation is standard, and described by Rankin *et al.* (1990). Clean quartz chips were heated in a test tube to 650°C, to decrepitate the fluid inclusions, and the resulting fluid carried in Ar gas, via a 10 port valve, to the ICP. After a 10-20s preflush, the sample was run for an integration time of 45s, for the optimum response (*Fig. D1.2*).

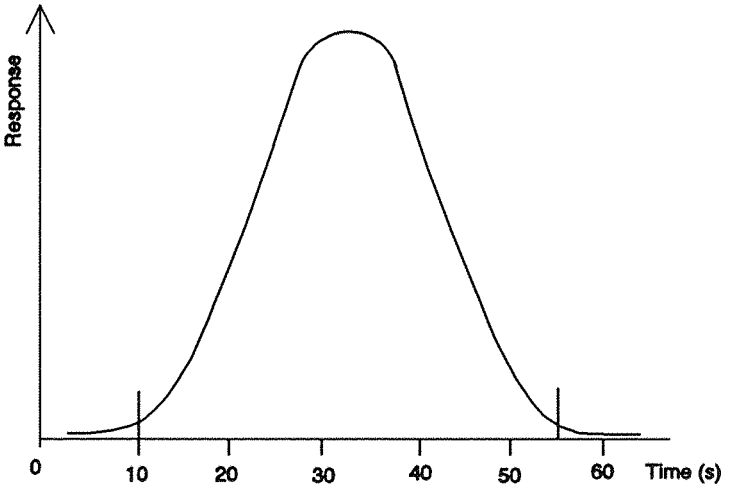

Figure D1.2 **Response time vs. time from start of heating quartz chips for D-ICP analysis.**

Two different ICPs were used for analysis: The first set of analyses was carried out on an ARL34000C simultaneous ICP-AES, as described by Rankin *et al.* (1990). These data were calibrated by recording 'blanks' between each sample, and a standard at the end of the session to correct all the data. The second set was carried out on an ARL3500B simultaneous ICP-AES, using the calibration method described by Rankin *et al.* (1993). The analytical error is imposed by the variation of the 'blank' value of an element known not to be present in the sample, in this case Lu. The detection limit used is equal to twice the standard deviation of the variation from the mean ratio of x:Lu, where x is the element in question, and is equal to δx. The error of the Na/Ca ratio, therefore, is δNa/δCa. Detection limits are given in Table D1.1.

The precision and accuracy are not easily measured, as this is a destructive method of

analysis and a sample cannot be re-run for precision. Reproducibility can be established by running two samples from the same quartz split, but variation in the data sets is a result of both sample variation and instrument error, and the two are indistinguishable.

Table D1.1 Detection limits (ppm) of D-ICP anaiytical measurements, calculated for samples prefixed by 'J' in this study, for the ARL3500B simultaneous ICP-AES.

Na	Ca	K	Fe	Mg	Mn	Ba
30.83	13.52	2.49	25.51	13.27	18.82	2.05
Zn	Cu	Li	P	B	Sr	Cr
11.99	5.11	6.88	5.91	3.58	7.09	1.93

Aqueous Fluid Inclusions: Microthermometric Data

Chip	Incln #	TYPE	Tfm	TRm	TmHH (green)	Tmh (grey)	Tml	TsH (Green□)	TsS (rect)	ThL	Decrep	Salinity (Tml)	Salinity (TsS)	Ternary Na	Diagram Ca	Wt% NaCl eq	Comments	Size	Fill
3-B	3	l-v	-71	-41.1	-24.6		-12.4			299	400	6.4		7.5	7	16.4	fr. -64	980	0.9
	4	l-v								209.5	"						"	72	0.85
	5	l-v	-81				-12.2			207.9	"	16.2				16.2		240	0.85
	6	l-v	-72		-30.4		-10.5			214.5	"	14.5		5	10	14.5	"	280	
	7	l-v	-77.4							leaked	"								
	8	l-v	-73.2		-25.8		-18.5			"	"	21.6		11	12	21.6			
	9	l-v	-79.7				-17.8			"	"	21				21			
	10	l-v								200.2	"								
	11	l-v-s								217.2	"								
	12	l-v-s-s						283	430+	210.2									
3-C	1	l-v	-76.5	-41.2			-19.4			201.5		22				22	fr-76 to cl	80	0.9
	2	l-v	-72.4	-38.7			-16.9			221.1		20.3				20.3		70	0.85
	3	l-v	-74.8	-43			-17.8			173		21				21		64	0.85
	4	l-v	-71.5				-19.3			208.2		22				22	fr-82 -cl	196	0.8
	5	l-v	-74.7	-37.7			-25.4			162.7				2	17			54	0.9
	6	l-v	-73.6				-26			209									0.8
10-2	8	l-v-s	-33.4				-10.8	-		245.4	-	14.8				14.8		216	0.9
	22	l-v	won't freeze					-	-										0.7
	23	l-v	-83.8				-48.2	-	-	195.3			13.7(l)			13.7		72	0.9
	25	l-v				-22.5	-9.7	-	-	230.45			31.7			31.7		240	0.85
	28	l-v	-88.8				-20	-	-	219.7			33.7			33.7		180	0.8
	29	l-v-s	won't melt or freeze on cyclic freezing					235.1	-	205.2								84	0.75
	30	l-v					-28.3	11.7	(green, round)			26				26		90	
	31	l-v				-40.9	-18.1			212.0	235	21.3				21.3		63	
	31a	l-v-s						211.7											
	47	l-v	<-61.5		-25		-15.9					19.5				19.5			
	54	l-v					-13.5	-		236.3	-	17.5				17.5		96	0.75
	56	l-v					-11.9	-			-	15.9				15.9		80	0.8
	57	l-v					-10.8	-		289.5	-	14.8				14.8		270	0.75
	58	l-v					-11.3	-		235.1	-	15.3				15.3		80	0.8
	59	l-v					-12.3	-		205	-	13.3				13.3		64	0.85
	61	l-v					-15.4	-			-	19				19			
	70	l-v	-71.8		-39.8	-41.5	-34.2	-		216.8	-	27.8				27.8			0.9
	71	l-v	-73.8		-41.1 ((y)		-34.8	-		204.5	-	28				28			0.95

Chip	Incln #	TYPE	Tfm	TRm	TmHH (green)	Tmh (grey)	Tml	TsH (Green□)	TsS (rect)	ThL	Decrep	Salinity (Tml)	Salinity (TsS)	Ternary Na	Diagram Ca	Wt% NaCl eq	Comments	Size	Fill
10-2	75	I-v(s)	-72.7		g	-0.1 gr)	-30.1	11.5		208.2	(green, round)	26.8				26.8			
	98	I-v	-63.2				-24	-		208.8	-	23				23		154	0.85
	99	I-v	-70.1				-38.7	-		197	-							96	0.9
	102	I-v					-24.5	-		215.1	-	25.5				25.5		32	0.8
10-4	2	I-v	-		-	-	-22.6	-			-	24.4				24.4			
	3	I-v	-70.7		-	-	-11.2	-			-	15.2				15.2			
	4	I-v	-65.1		-54.2	-	-36.5	-			-								
	5	I-v	-		-	-		-			-						won't freeze		
	6	I-v	-		-	-	-8.8	-			-	12.6				12.6			
	7	I-v	-		-	-	-5.2	-			-	8.1				8.1			
	8	I	-		-	-	-18.1	-			-	21.2				21.2			
	17	I-v	?-34.9		-8.6		-22.5	-		-	230	24.3				24.3			
	18	I-v					-26.2	-		183.1	-	26.8				26.8			
	25	I-v			c.-7.8			-		-	-								
	26	I-I	too cloudy to measure					-		-	216.3								
10	1	I-v	-		-	-	-33.4	-			-	27.2				27.2			
-B	2	I-v	-		-	-	-33	-			-	27				27			
	5	I-v	-		-	-	-35.1	-			-	28				28			
	6	I-v	-		-	-	-30.6	-			-	26.8				26.8			
10	1	I-v	No change on cooling or heating																
-E	2	I-v-s	-76.5			-41.5	-36.8										FeCl-K?		
	3	I-v-s	-76			-41.8	-38.2										"		
	4	I-v-s	-80.1		-5.6G		-39.6										"		
	5	I-v-s	-72.5		1.8 (Fe)	-41.7 G	-32.9												
	6	I-v-s	-70.5				-36.3												
	7	I-v				-41.9	-34.6										solid at low T		
	8	I-v	No change on heating-freezing																
	9	I-v	-74.8				-42.8												
	10	I-v	-81.3				-36.6					34							
	13	I-v	?-42				-33.1						32.5						0.5
	14	I-v																	0.2
	19	I-v	-33.3			-22.5	-6					9.2				9.2	Hydrate br.		0.9
11-1	1	I-v-s	-58.2	-40	-24.8		-19.4					22	-	12	11	22			
	2	I-v					-19.6					22.4	-			22.4			
	3	I	-61.7				-15.6					19.3	-			19.3			

Chip	Incln #	TYPE	Tfm	TRm	TmHH (green)	Tmh (grey)	Tml	TsH (Green□)	TsS (rect)	ThL	Decrep	Salinity (Tml)	Salinity (TsS)	Ternary Na	Ternary Ca	Diagram Wt% NaCl eq	Comments	Size	Fill
11-1	4	I-v					-20.3					22.9	-			22.9			
	5	I-v	-58.8		-41.1		-20.4					22.9	-	3	20	22.9			
	6	I-v	-60.3		-42.7		-19.6					22.3	-	1.5	20	22.3			
	7	I-v	-61.5		-42.5		-19.8					22.5	-	3	20	22.5			
	8	I-v	-58.3		-42.7		-21					23.4	-			23.4			
	9	I-v	-58.7		-41.5		-20.6					23.1	-	1.5	21	23.1			
	10	I-v	can't	see			-21.8					23.9	-			23.9			
	11	I-v	-60.2		-42.6		-21.4					23.6	-	3	18	23.6			
	12	I-v	-58.1				-22.6					24.4	-			24.4			
	13	I-v	-63.3		-34.8		-17.3					20.7	-	2.5	19	20.7			
	14	I-v	-62.7										-	1.5	21.5				
	15	I-v	-63.3		-38.5		-22.2					24.2	-			24.2			
	16	I-v	-62.2		-45.7		-22.8					24.6	-			24.6			
11-1	17	I-v	-61.5	?			-22.6					24.4	-			24.4			
11-2	1	I-v	-53.7				-16.5					20	-			20			
	2	I-v-s	-70.6				-38						-						
	3	I-v	too small				-18.3					21.4	-			21.4			
	4	I-v	-56		-26.6		-20.3					22.9	-	11	12	22.9			
	5	I-v					-17.3					20.7	-			20.7			
	6	I-v											-						
	7	I-v	-59.4		-30.1		-22.9					24.6	-	6	18	24.6			
	8	I-v	-61.5				-23.6					25.1	-			25.1			
	9	I-v	-61.3				-20.5					23	-			23			
	10	I-v	-54.5		-32.5		-17.6					20.9	-	2.5	18	20.9			
	11	I-v	-62		-32.5		-22.6					24.4	-	3	19	24.4			
	13	I-v	-59.5				-22.1					24.1	-			24.1			
	14	I-v	-50.1				-21.5					23.7	-			23.7			
	15	I-v	too small				-21.1					23.4	-			23.4			
	16	I-v	-59.5				-20.7					23.1	-			23.1			
	17	I-v	-55.1				-20.7					23.1	-			23.1			
	18	I-v	-54.4				-22.2					24.2	-			24.2			
	19	I-v	-56.8		-24.5		-18.7					21.7	-	11	12	21.7			
	20	I-v	-50.3		-39.6		-20.8					23.2	-	3	18	23.2			
	21	I-v	-59	-31.77			-21.6					23.8	-			23.8			
	22	I-v	-55.9				-24.6					25.7	-			25.7			
	23	I-v	-55.8																

Chip	Incln #	TYPE	Tfm	TRm	TmHH (green)	Tmh (grey)	Tml	TsH (Green□)	TsS (rect)	ThL	Decrep	Salinity (Tml)	Salinity (TsS)	Ternary Na	Diagram Ca	Wt% NaCl eq	Comments	Size	Fill
17-1	1	l-v	-79.7				-25.7	-	-			i	-				in Calcite	108	0.85
	2	l-v						-	-	188.1		r	-				in Calcite	50	0.8
	3	l-v						-	-	189		r	-				in Calcite	80	0.8
	4	l-v						-	-	187.5		e	-				in Calcite	30	0.8
	15	l-v	-81	-56.7	2.4		-31.7				300	g.	-	11	18		freeze -62	98	
	16	l-v	-78.1	-58			-32.3			193.6			-					96	0.8
	17	l-v	-79.4	-60			-27.3			183.9		S	-					84	0.75
	25	l-v-s	-81.1	-54.5	-24.1	-42.5	-27.2	Decrep. 350.	no dissoln	187.7		e						170	0.85
												c							
	26	l-v						-	-			o	-				meta-stable	80	
	27	l-v	-79	-52.5			-29.6	-	-			n	-				no bubble	80	
	28	l-v	-78.8	-56			-23.4	-	-	169.3		d.	-					160	0.9
	30	l	-79				-30.3	-	-	-19.7			-					126	1
	31	l-v	-	-	-	-	-	-	-	255.7		P	-					81	0.8
	32	l-v	-	-	-	-	-	-	-	277.5		R	-					63	0.8
	33	l-v	-	-	-	-	-	-	-	219.7		I	-					35	0.8
	34	l-v	-	-	-	-	-	-	-	284.1		M	-					64	0.5
	35	l-v	-	-	-	-	-	-	-	295.7		A	-						
	36	l-v	-	-	-	-	-	-	-	297.8		R	-						
	37	l-v	-	-	-	-	-	-	-	231.7		Y	-						
	38	l-v	-	-	-	-	-	-	-	241			-						
	39	l-v	-	-	-	-	-	-	-	167.9		Irreg.	-						
	40	l-v	-	-	-	-	-	-	-	294.6			-						
17-4	1	l-v	-76.8	-33.4	-23.5		-10.1			131	408	14		7	5	14			0.85
	2	l-v-s	-72.6	-35	-24		-15.5			190	383	19.2				19.2	freeze-69		0.8
	3	l-v	-71.3		-19.2		-15.6			169.7		19.3				19.3			0.8
	4	l-v					-15.5			189.5	390	19.2				19.2			0.8
	5	l-v-s	-79	-38	-15.2	-13	-23.1				200	24.7		14	9	24.7			0.85
	6	l-v	-60	-36	-23.2		-14.5			153.4		18.36		8	7	18.36			0.9
	7	l-v	-73	-36.7			-13.4			182	330	17.37				17.37			0.9
	8	l-v-s	-83.3	-37.8	-14.1		-10.1			179.3	200	14				14	neck down		0.85
	9	l-v-s		-36.2			-13.1			200.8		17				17			0.8
	10	l-v	c.-30							301.2	350								0.6
	11	l-v	-74.1	-37.4	-22.5		-10.7			193.1	380	14.7		7	5	14.7	freeze -65		0.9
	12	l-v	-69.1	-36.9			-10.3			186.2		14.3				14.3			0.9
	13	l-v	-82	-38.8	-22.9		-12			216.4		16		10	5	16			0.8

Chip	Incln #	TYPE	Tfm	TRm	TmHH (green)	Tmh (grey)	Tml	TsH (Green□)	TsS (rect)	ThL	Decrep	Salinity (Tml)	Salinity (TsS)	Ternary Na	Diagram Ca	Wt% NaCl eq	Comments	Size	Fill
17-4	14	l-v		-44.5	-19.8		-11.1					15.1				15.1			
	15	l-v-s								206.5									
17-5	1	l-v	-78.5	-43.2			-14.3			339.2		18.2				18.2	freeze -70	30	0.7
	2	l	-73.4				-12.3					16.3				16.3		14	1
	3	l					-11.8					15.8				15.8		8	1
	4	l-v	-76.2				-11.8			215.9		15.8				15.8		8	0.9
	5	l-v					-11			119		15				15		9	0.9
	6	l					-17.7					21				21		6	1
	7	l-v					-13.6			305.6		17.6				17.6		10	0.7
	8	l	-77	-42			-12.8					16.8				16.8		10	1
	9	l-v	-77.8				-10.2			317		14.2				14.2		20	0.85
	10	l-v	doesn't freeze							378.3								10	0.7
	11	l-v	doesn't freeze							316.5								14	0.75
	12	v																20	0.2
	13	v-l	doesn't freeze							400+								16	0.7
	14	l-v								208.7								10	0.85
CALCITE																			
25-A	1	l-v	-70		-24.3	-	-9.8	-		147		13.8		7	6		fr -50 br	<15* 25	0.8
	2	l-v	-70		-24	-	-12.3	-		136.1		16		8	7		"	"	0.85
	3	l-v	-69.9		-26	-	-16.6	-		>200	200	20.1		10	8			"	0.7
	4	l-v	-72.9			-	-15.7	-		140.8		19.4						"	0.8
	5	v-l				-	-19.9	-			-	22.6						"	0.6
	6	l-v	-74.8		-20.6	-	-17	-		134.8	-	20.4		15	6			"	
	7	l-v			-26	-	-11.4	-		158	-	15		9	7			"	
	8	l-v	-75		-25.6	-	-10.7	-		156.5	-	14.7		8	7			"	
	9	l-v				-		-		136.5	-							"	
	10	l-v	-76.3		-25.7	-	-12.4	-		144	-	16.4		8	7			"	
	11	l-v	-76.7		-26.5	-	-16.9	-		153.7	-	20.3		10	8		fr -71	<20* 15	0.95
	12	l-v				-	-4.4	-		140.5	-	7					fr -53	"	1
	13	l-v			-20.4	-	-11.7	-		137.6	-	15.7		10	5			"	0.9
	14	l-v			-25.2	-	-14.6	-		192.6	-	18.4		10	7.5			"	0.9
	15	l-v				-	-16.4	-		161.8	-	20						"	0.9
	16	l-v				-	-12.7	-		133.7	-	16.7						"	0.95
	17	l-v	-75.6		-24.9	-13.5	-11.5	-		150	-	15.5		8	6		fr -61 br	300	0.85

Chip	Incln #	TYPE	Tfm	TRm	TmHH (green)	Tmh (grey)	Tml	TsH (Green□)	TsS (rect)	ThL	Decrep	Salinity (Tml)	Salinity (TsS)	Ternary Na	Diagram Ca	Wt% NaCl eq	Comments	Size	Fill
25-A	18	l-v			-24.7	-10.4	-9.5	-		153	-	13.4		7	6		fr -55 to gr	180	0.8
	19	l-v			-	-	-9.8	-		151.9	-	13.8					"	144	0.8
	20	l-v			-	-	-10.2	-		154	-	14.2						144	0.8
	21	l-v			-24.5	-13.8	-11.1	-		148.5	-	15		8	6			150	0.8
	22	v-l	can't see any liquid					-			-							225	0.2
	23	v-l	can't see any liquid					-			-							169	0.2
	24	v-l	can't see any liquid					-			-							500	0.2
	25	l-v	-76.2		-26.4	-12.8	-10.4	-		137.8	-	14.4		8	7			600	0.85
	26	l-v			-	-	-7.1	-		127.8	-	10.6					lt. outline	120	0.8
	27	l-v			-	-	-4.9	-		120.1	-	7.7					"	25	0.8
	28	l-v	-71		-	-	-10.1	-		154	-	14					fr -60 to gr	120	0.85
	29	l-v	-75.4	-43.4	-26.1		-21.8	-		157.6	-	23.9		12	11		fr -81 to clr	252	0.95
	30	l-v			-21.3		-10.9	-		145.3	-	14.9		10	4				
	OTHER INCLUSIONS FROM # 25A							-		146	-							144	0.8
			-		-	-	-	-		173.9	-							100	
			-		-	-	-	-		148.1	-							180	0.85
			-		-	-	-	-		109	-								0.8
			-		-	-	-	-		140	-							16	0.8
			-		-	-	-	-		155	-							1050	0.8
			-		-	-	-	-		156.2	-								0.85
			-		-	-	-	-		142.1	-							36	0.8
26-A	1	l-v	-78.5		-27		-27.5							9	14		Cc. Freeze		
	2	l-v	-77.3		-20.7		-27.7							10	14		to clear		
	3	l-v	-76.1				-33										"		
	4	l-v	-78				-28.1					18.4				18.4	"		
	5	l-v	-73.8				-14.6				< 321	16.9				16.9	"		
	6	l-v	-75.2				-12.9				< 321	9.2				9.2	Calcite. Fr		
	7	l-v	-76.1				-6				< 321						to gran.		
	10	l-v					-3.9				321	6.2				6.2	"		
	12	l-v			-31.9		-6.4	-	-			9.7		4	5	9.7	"		
	13	l-v					-6.3	-	-	255		9.6				9.6	"		
	14	l-v			-22.4	-31.8	-8.9	-	-	271.4		12.8		7	7	12.8	"		0.7
	15	l-v			-30.1		-8.5	-	-	292		12.3		6	7.5	12.3	"		0.75
	16	l-v					-10	-	-	220.4		14				14	"		0.7
	17	l-v					-5.8	-	-			8.9				8.9			0.75
	18	l-v					-23.4	-	-	237.6							Lt. outline		0.8

Chip	Incln #	TYPE	Tfm	TRm	TmHH (green)	Tmh (grey)	Tml	TsH (Green□)	TsS (rect)	ThL	Decrep	Salinity (Tml)	Salinity (TsS)	Ternary Na	Diagram Ca	Wt% NaCl eq	Comments	Size	Fill
26-A	19	I-v					-12.1	-	-	241		16.14				16.14			0.85
	20	I-v					-7.4	-	-	259.5		10.9		7	7	10.9			0.75
	21	I-v			-23.8		-6.5	-	-	296.7		9.9				9.9			
	22	I-v						-	-										0.85
	23	I-v					-11.4	-	-			15.4				15.4			
	24	I-v	-76.2	-40.5	-24		-11.4					15.4		8	7	15.4	Quartz		
	25	I-v			-27.6		-7.5					11.1		4	6				
	26	I																	
	27	I-v			-4.7														
	28	I-v	-78.4	-41	-24.5	-31.9	-14.3					18.2		9	8				
30-A	1	I-v	-75.3	-38.9	-12.1		-26.9	-				24.8	-	12.5	12	24.8	fr. -92° clr	2000	0.85
	2	I-v-s?	-81.2		-25.6		-14.9					18.4	-			18.4	irreg.		
	3	I-v		-41.7	-9.6	-6.6	-26.8	-				25.2	-	14	12	25.2	shapes		0.9
	4	I-v	-76.2		-13.5		-26.6	-				24.2	-	14	12.5	24.2		"	0.9
	5	I-v	-81	-44.3	-9.9		-25.7	-				25.2	-	14	12	25.2		" 300	0.95
	6	I-v	-85.8	-44.6	1.8		-28.9	-					-				"	1800	0.95
	7	I-v			-23.2		-25.8	-				22	-	13	10	22	"	800	
	8	I-v	-75.7	-38.8			-25.5	-					-				freeze to	600	0.9
	9	I-v	-74	-40.9	-23.6		-26	-					-	13	10		clear	360	0.8
	10	I-v	-80.9		-25.8		-20.6	-				23.1	-	11	11	23.1	gr-br freeze	810	0.9
	11	I-v	-80.9	-39.2	-19		-25.7	-				22	-	12	11	22	freeze -73	480	0.9
	12	I-v	-77.1	-45.3	4.8	-9.7	-28.9	-					-				gr freeze	1250	0.85
	13	I-v	-78		4.9		-27.8	-					-				br freeze	440	0.8
	14	I-v	-78.1	-39.3	-23		-23.5	-				23	-	13	8	23		4500	0.9
	15	I-v	-81.7	-43.4	-25.6		-25	-					-	13	10		IN CALCITE	450	0.8
	16	I-v	-79.4		-25.6		-21.7	-				23.8	-	11	11	23.8	IN CALCITE	280	0.8
	17	I-v	-78.5		-25.8		-21.6	-				23.7	-	11	11	23.7	IN CALCITE	225	0.8
	18	I-v			-3.1		-26.8	-				26	-	15	10	26	IN CALCITE	300	0.8
	19	I-v	-78.9	-			-21.5	-				23.6	-			23.6	IN CALCITE	176	0.8
31-C	1	I-v	-68.1	-42	-24		-22.8	-	-	194.8		24.6		11	10	24.6	Lt. outline		0.95
	2	I-v					-9.7	-	-	207.6		13.7				13.7			0.9
	3	I-v					-9.6	-	-	205.2		13.5				13.5	Lt. outline		0.9
	4	I-v	-60.3				-11.9	-	-	203.2		15.9				15.9	Lt. outline		0.95
	5	I-v					-5.7	-	-	196.5		8.8				8.8	Lt. outline	128	0.9
	6	I-v					-2.6	-	-	246.2		4.3				4.3	Dk. outline	156	0.7
	7	I-v					-2.9	-	-	244.5		4.8				4.8	Lt. outline	144	0.9
31-C	8	I-v					-6.8	-	-	244.4		10.2				10.2	Dk. outline	100	0.8
32-D	1	I-v	-75.1	-37		-31.1	-25.5	-	-	183.1		26.3				26.3	Primary?	180	0.9
	2	I-v						-	-	223.9							"	112	0.9

Chip	Incln #	TYPE	Tfm	TRm	TmHH (green)	Tmh (grey)	Tml	TsH (Green□)	TsS (rect)	ThL	Decrep	Salinity (Tml)	Salinity (TsS)	Ternary Na	Diagram Ca	Wt% NaCl eq	Comments	Size	Fill
	3	l-v						-	-	172							"	54	0.9
	4	l-v					-26.2	-	-	184.7							"	54	0.9
	5	l-v						-	-	174.5							Secondary	105	0.85
	6	l-v			-12.4	-39	-28	-	-	170				5	10		irreg.	120	0.85
	7	l-v	c. -70		-13.8		-27.1	-	-	172.3				5	10		"	105	0.8
	8	l-v						-	-	163.7							"	80	0.9
	9	l-v					-28.9	-	-	171.7							"	36	0.8
	10	l-v						-	-	164.9							"	216	0.9
	11	l-v	-	-	-	-	-	-	-	215.4							Reg.	152	0.8
	12	l	-	-	-	-	-	-	-								shaped	40	1
	13	l-v	REGULAR							198.3							Primary?	36	0.8
	14	l-v	INCLUSIONS							249.8							(As 1-4)	60	0.8
	15	l-v	AS Ch.#32 1-4							156.4							"	108	0.95
	16	l-v	"							246.7							"	96	0.75
	17	l-v	"							195.2							"	36	0.8
	18	l-v	"							173.5							"	24	0.8
	19	l-v	-	-	-	-	-	-	-	204							"	48	0.85
	20	l-v	-	-	-	-	-	-	-	223.1							"	40	0.9
35-D	1	l-v	<-55				-16.7	-		215.9	-	20.2		11.5	10			72	0.9
	2	l-v			-23.5		-15.6	-		205.7	-	19.3						80	0.9
	3	l-v					-14.6	-		210.7	-	18.4						60	0.9
	4	l-v-s	<-70	-31.6	-31.6		3?	340			-						freeze c.39	240	0.9
	5	l-v					-3.3	-		272.1	-	5.4						70	0.7
	6	l-v					-2.4	-		345.5	-	4						140	0.7
	7	l-v					-2.1	-		317.5	-	3.5							
	8	l-v					-2.1	-		323	-	3.5							
36-A	1	l-v	-81		-31		-23			178.4		24.7		8	14		slight bubble	120	0.8
	2	l-v								189.5							round, Tfm	70	0.85
	3	l-v	-81.3	-40	-30.7		-18			195		21.2		7	12.5		bubble	70	0.8
	4	l-v	-80.3				-18.2			184.5		21.3					rounding, hh	"	0.9
	5	l-v	-80.2				-15.9			198.8		19.5					rims and	"	0.8
	6	l-v								203.5							granulation	"	0.8
	7	l-v	-80.8				-18.9			216.2		21.9					(CP)occurs	"	0.85
	8	l-v					-7.8			177.2		11.5					at Tfm.	"	

Chip	Incln #	TYPE	Tfm	TRm	TmHH (green)	Tmh (grey)	Tml	TsH (Green□)	TsS (rect)	ThL	Decrep	Salinity (Tml)	Salinity (TsS)	Ternary Na	Diagram Ca	Wt% NaCl eq	Comments	Size	Fill
36-A	9	I-v					-8			159.6		11.7					Primary,	35	0.9
	10	I-v					-7.4			206.8		11					negative	"	0.85
	11	I-v			-23.2		-7.8			197	350	11.5		6	5		xtal.	"	0.9
	12	I-v					-7.5			212.6		11.1						"	0.85
	13	I-v			-21.7		-7.4			211.1		11		7	5			"	0.85
	14	I-v					-7.8			216.5	347	11.5						"	0.8
	15	I-v			-24.5		-7.1			215.9		10.6		6	5			"	0.9
	17	I-v	-75				-28.6			182.1								117	0.95
	18	I-v	-78.5				-26.2			202.9							freeze -60	70	0.9
	19	I-v								194							to -70	70	0.8
	20	I-v-?s					-28.4			184	200							"	0.9
	21	I-v	-79.6		-25.2					184.9								"	0.95
	22	I-v					-15.4			200.7		19.1						"	0.85
	23	I-v								203.5								"	0.8
	24	I-v								209.2								"	0.8
	25	I-v								182.9	328							"	0.75
	26	I-v								217.8	360							"	0.8
	27	I-v								201								"	0.85
	28	I-v								207								"	0.85
40-A	1	I-v	-69.4		-22.2		-4.1	-	-	216		6.6		4	3.5	6.6	Dk. outline	162	0.8
	2	I-v	-78.1	-37	-25.8		-9.3	-	-	206		13.2		7	6	13.2	Dk. outline	140	0.9
	3	I-v					-4.8	-	-	212.2		7.6				7.6	Dk. outline	120	0.8
	4	I-v						-	-	227							Dk. outline	600	0.8
	5	I-v						-	-	224.8							Dk. outline	63	0.85
	6	I-v						-	-	215							Dk. outline	108	0.8
	7	I-v						-	-	223.6							Dk. outline	30	0.8
	8	I-v					-29.2	-	-	175.4							Lt. outline	108	0.85
	9	I-v						-	-	255.3							Dk. outline	18	0.8
	10	I-v	-78.7	-40	-41.1	-34.8	-29	-	-	179.1				2	18		Lt. outline	96	0.9
	11	I-v	-75.3				-28.4	-	-	148.7							Lt. outline	40	0.85
41-A	1	I-v	-	-	-	-	-	-	-	215.5								352	0.8
	2	I-v	-	-	-	-	-	-	-	-								140	0.75
	3	I-v	-	-	-	-	-	-	-	181.2								80	0.9
	4	I-v	-	-	SAME	AS	CHIP	-	-	182.7								100	0.85
	5	I-v	-	-	-	-	-	-	-	185								144	0.85
	6	I-v	-	-	-	# 26	(QUARTZ)	-	-	166.4								112	0.8
	7	I-v	-	-	-	-	-	-	-	216.2								80	0.8
	8	I-v	-	-	-	-	-	-	-	216.4								36	0.75
	9	I-v	-	-	-	-	-	-	-	229								240	0.8

Chip	Incln #	TYPE	Tfm	TRm	TmHH (green)	Tmh (grey)	Tml	TsH (Green□)	TsS (rect)	ThL	Decrep	Salinity (Tml)	Salinity (TsS)	Ternary Na	Ternary Ca	Diagram Wt% NaCl eq	Comments	Size	Fill
TYPE 2																			
10-2	7	I-v-s			?-46.7		-51	-	143	275.7								270	0.8
	8	I-v-s	-33.4				-10.8	-	-	245.4		14.8		1.5	10	14.8		216	0.9
	10	I-v-s-s	-74.7		-46.3		-43.3	192.7	-	186.5			31.7			31.7		108	0.85
	12	I-v-s-s				-61.6		183.7	-	186.3			31.2			31.2		54	0.85
	13	I-v-s-s	-75.0				-52.1	209.2	207.1	185.8			32.1	14	26	32.1		130	0.8
	14	I-v-s	-86.7				-56.7	-	208	173.4								21	0.85
	15	I-v-s					-43.6	163.6	-	182.7			30.2	12	25	30.2		108	0.85
	16	I-v-s	won't melt or freeze					198.4	-	206.2			31.9			31.9		170	0.9
	17	I-v-s	won't melt or freeze					189.6	134	206			31.5			31.5		180	0.85
	18	I-v-s-s	-95.4		-45.8	-43.4	-50.5	197	-	280.6			31.9			31.9		315	0.85
	19	I-v	-89.3					-	-	185.6								208	0.8
	20	I-v-s	?		-40.8		-41.4	-	174	183.3								180	0.8
	21	I-v-ss	-94.7				-46.3	202.7	-	180.1			32	14	26	32		330	0.9
	26	I-v-s-s	won't melt or freeze on cyclic cooling					192.9	no diss	-								270	
	27	I-v			-38.5		-37.7	-	-		295		22.6(l)			22.6	leaked	375	0.75
	48	I-v-s					-55.7		no diss	196.5								200	0.8
	50	I-v-s					-46.4		no diss	253.8								200	0.8
	51	I-v-s					-44.3			-	< 306							176	0.8
	52	I-v-ss					-43.1	hidden	- can't see	-								180	0.85
	53	I-v-ss						301.7	no diss.	187.6			37			37		336	0.85
	55	I-v-ss					-53.9	210	-	199.3							no diss.	120	0.8
	72	I-v-s	-78.9				-49.6												0.9
	73	I-s	-78.8		-52.9 (clear)		-49.8												1
	74	I-v	-79.9				-40.7												
	76	I-v-s	won't freeze																0.9
	77	I-v-2s	-75.6																0.9
	78	I-v-s	-78.2				-41.4												0.95
	79	I-v	-78		-		-40.8	-	-	289.4								252	0.8
	80	I-v	-73.4		-		-40.7	-	-	275.6								54	0.75
	81	I-v	?		-			Can't see		-									
	82	I-v	-73.4		-		-31.3	Covered in Dirt		-									
	83	I-v			-		-29.9			-									
	84	I-v			-		-27.5	-	-	202.3								84	0.85
	85	I-v-s	-77.4		-		-42	179.2		198.1			31			31		54	0.9
	86	I-v	-69.9		-		-26.9	-	-	202.1								36	0.85
	87	I-v	won't freeze					-	-	216.1								120	0.9
	88	I-v-s	won't freeze					195.1	-	189.9			32			32		66	0.85

Chip	Incln #	TYPE	Tfm	TRm	TmHH (green)	Tmh (grey)	Tml	TsH (Green□)	TsS (rect)	ThL	Decrep	Salinity (Tml)	Salinity (TsS)	Ternary Na	Diagram Ca	Wt% NaCl eq	Comments	Size	Fill
	89	l-v-s	-79.5		-		-61.5	?	-	206.4								360	0.9
10-2	90	l-v-s	-79.1		-		-42.7	Can't	See										
	91	l-v			-		-37.9	-	-	205.3								18	0.9
	92	l-v	-80.9			-7.7	-28.2	-	-	210.2								72	0.85
	93	l-v			-		-28.2	-	-	203.4								24	0.9
	94	l-v-s	-90.4		-		-54.8				< 306								
	95	l-v-s	-76.7		-		-41.3		-	226.4	352		41.5			41.5		180	0.85
	96	l-v	-75.7		-		-38.8	-	-	199.8								120	0.9
	97	l-v	-75.7		-		-44.2	-	-	195.6								80	0.9
	100	l-v	won't freeze					-	-	208.5								210	0.95
	101	l-v-s	-80.1				-42.6	198.8	no diss.	223.4								120	0.8
10-B	3	l-v-s				-	-49.2												
	4	l-v-s				-	-47.5												
	7	l-v-s	-64.8				-45.5												
11-2	24	l-v-s	-71.1			-45.9	-40.5												
17-1	11	l-v	-78.8	-57.8	-0.2	-43.8	-28.4	-	-	298		i	-	12	17		freeze -83	600	0.5
	12	l-v	-81.6	-57	1.7	-44.9	-28.6	-	-	300.9		r	-	11	18		freeze yel-gr	1120	0.8
	13	l-v	-79		2.6		-28.7	-	-	301.5		r	-	11	18			240	0.7
	14	l-v-s-s					-29.6				350	e							
	18	l-v-s-s?	-78.6	-59			-30.7			277.7	360	g.					freeze on cooling	170	0.8
	19	l-v	-80.7	-59	-10.6		-30.3				< 350		-	10	18				
	20	l-v	-77.3	-57	-23.3		-25.9				< 350		-	13	14				
17-1	21	l-v-s	-81.5	-53.8	-14.5		-26.7		no dis.	185.2	355	sec-	>42	>24	>15			170	0.8
	22	l-v-s-s	-78.5		-8.9		-26.8		no dis.		355	ond-	>42	>24	>17			160	
	23	l-v	-77.8				-27.2				< 350	ary	-					121	0.7
	24	l-v-s-s	-78.4	-64			-29		no dis.	186.1	355							204	0.9
19-1	1	l-v-3s							166.2	180.6							Cracks	23	0.85
	2	l-v-3s	-85.8	-37.6	-26.8	14.5	-25.2	207		184.9		26.1	31.9	19	14	31.9		20	0.9
	3	l-v-s					-19.8			189.1		22.5				22.5	appear in	20	0.8
	4	l-v-s	-83.6			10.2	-20.3	250.9		165.3		22.9	33.8			33.8		18	0.85
	5	l-v-2s				11	-23.9	236		164	345	25.3	33			33	Quartz	23	0.85
	6	l-v-s			-11.7					206.2									0.85
	7	l-v-s	-53							182.6	372								
	8	l-v-s								170.1	"						at 350 C		
	9	l-v-s	-48.8				-24			181.3	"	25.3				25.3			
	10	l-v								182.6	"								
	11									165.2	"								
	12									304.4	"								

Chip	Incln #	TYPE	Tfm	TRm	TmHH (green)	Tmh (grey)	Tml	TsH (Green□)	TsS (rect)	ThL	Decrep	Salinity (Tml)	Salinity (TsS)	Ternary Na	Diagram Ca	Wt% NaCl eq	Comments	Size	Fill
19-1	13									310.2	"								
19-2	1	l-v-sss	-72.5		-6.5		-39.7	211.3		174.6		32.45	32.5	15	25	32.5			
	2	l-v-s	-75.1				-39.1	202.1		172.1		31.9	31.8	12	26	31.8			
	3	l-v-s	-79.3				-36.8	174.9		177.6		30.94	31	12	23	31			
	4	l-v-ss	-75.9		-27.1	-41.2	-43.4	242.6	120.5	169.8			33.5	15	23	33.5			
	5	l-v-ss	-78.3			-49.5	-50	251.2		163.6			33.8	18	25	33.8			
	6	l-v-?s	-68.5			-36	-39.2			174.9									
	7	l-v	-66.6			-43.2	-26.4			192.5									0.8
	8	l-v-s	won't freeze					250.7		160.5			33.8						
35-A	1	l-v-s	-81.3	-	-	-	-52										s=0.15	286	0.95
	2	l-v-s	-80	-	-	-	-43.2										s=0.1	120	0.95
	3	l-v-2s	-84.4	-	-39.2	-40.3	-41							5	26		s=0.2 ▌,□	405	0.9
	4	l-v-2s	-83.7	-	-	-52.6	-56.8										s=0.15 ▌,□	300	0.95
	5	l-v-s	-	-	-	-	-										s=0.1 □	200	0.9
	6	l-v-s	-79.1	-	12.6		-30.5										s=0.03 □	375	0.9
	7	l-v-s	-82.4	-	-	-	-50.4										s= faint	96	0.9
	8	l-v-s	-81.7	-	-	-	-41.7										s=0.2	225	0.9
	9	l-v-s	-79.9	-	-	-	-42.2										s=0.7	70	0.9
	10	l-v		-	-	-	-49.7	-											
	11	l-v	-86.8	-	-	-	-53.8	-						4	27			364	0.8
35-A	12	l-v	-80.1	-55	-42.5	-47	-34.3	-									re-freeze @ -71	288	0.8
	13	l-v-s		-73.8	-1.6	-	-61							5	25		s=0.15 □	140	0.85
	14	l-v	-86	-	-	-46.2	-35.5	-						13	13			196	0.8
	15	l-v		-75.8	-20	-	-25	-				26							
3-A	1	l-v-s-s	-90.3		-32.2		-40.5	-	234.4	171.1				15	24		□	144	0.95
	2	l-v-s-s	-87	-56.5	25		-42.2	256.7	-	145.7			34.5	15	25	34.5	▌	225	0.95
	3	l-v-s	-87.5				-39.2	cl.circle	241.3	169.0			33.5	17	21	33.5	□	60	0.95
	4	l-v-s-s	-85				-41.8	some dis.by	300	169.8			>37	>19	>21		□+ ▌	80	0.95
	5	l-v-s-?s	-87.5	-56.9	-10.7	-1.4	-42.4	-	245	168.1				32	25		cl.□+o	300	0.95
	6	l-v-s	-86.3				-40.2	237		172			33			33	"	168	0.95
	7	l-v-s-s?s	-83.5		-41.2	-53.3	-39.7	some dis.by	300	167.8			>37	>19	>21		"	360	0.95
	8	l-v-s-s	will					285.5		154.1			36.5			36.5		120	0.9
	9	l-v-s	not					-	207.6	155.7	250							80	0.95
	10	l-v-s-s	freeze					260		155.6			35			35		81	0.95
	11	l-v-s-s			-45.9			280.5		161.8			36.3			36.3		42	0.95
	12	l-v-s	-	-	-	-	-	238.2	-	167.7			33			33			0.9
	13	l-v	-	-	-	-	-	-	-	209.6									0.85

Chip	Incln #	TYPE	Tfm	TRm	TmHH (green)	Tmh (grey)	Tml	TsH (Green□)	TsS (rect)	ThL	Decrep	Salinity (Tml)	Salinity (TsS)	Ternary Diagram Na	Ternary Diagram Ca	Wt% NaCl eq	Comments	Size	Fill
3-B	1	l-v-s-s							Decrep.										
	2	l-v-3s	-81.9				-38.5		Decrep								freeze @ -85		
9-2	1	l-v-?s	-70.5			-27	-17	>397		193.4	-	20.4				20.4	Fill dm=.3 wh□		.8
	2	l-v	-64.8				-20.1	-			-	22.7				22.7			.75
	3	l-v	-74.7				-24.3	-		204.4	-	25.5				25.5			
	5	l-v	-67.2				-20.2	-			-	22.8				22.8			
	6	l-v	-61.9				-20.6	-			-	23.1				23.1			.8
	7	l-v-?s	-73.3					>397			-								.8
	9	l-v	-72.2			-17.3	-23.4	-		210.8	-								.8
	10	l-v-s	-73.8				-16.7	-		216.2	-	20.2				20.2			.75
	11	l-v	-68				-17.6	-		215.7	-	20.9				20.9			.6
	12	l-v	-77.6				-23.2	-			-	24.8				24.8			.75
	13	l-v-?s	-63.4				-25.8	23.2		179.4	(green)	26.5				26.5			.8
	14	l-v-s	-40							180.3	180.3								
	17	l-v-s-s						338.5		180.1	>550								
	20	l-v-s-s						494			>550								
	21	l-v-s-s						479.4			>550								

Type T1 fluid inclusions are found in Chips #3, 10 and 11 (Rochas Bandadas)
Chips #26, 30, 31, 35, 36, 40 and 41 (Q2-A veins)

Type T2 fluid inclusions are found in Chips #3, 10, 11 and 19 (Rochas Bandadas)
Chips #17 and 35 (Q2-B veins)
Chip #9 (Xistos Granadas)

Q3 type T1 fluid inclusions are found in Chips #25 and 32

Aqueo-carbonic Fluid Inclusions: Microthermometric Data. TYPE T3.

Chip & Incln.	Phases (at room T°C)	TmCO2	Tmice	Tm Clath	ThCO2	ThTOT	Dcp	Salinity (TmI)	Salinity (TmCl)	Wt% NaCl	δbulk (mic.)	δ(bulk) (Raman) g/cm^3	Mol.Vol. (Raman)	Fill (%CO2)
10-2 1	I	-57.8	-	-	16.7						0.81			90
2	I-I	-58.5	-	-	7.5		265.6				0.88	.66	52.6	70
3	I-I-s	-57.6	-	-	17	242 - V	242.3				0.8			80
4	I-I-s	-57.9	-7.7	-	10.9	229 - L	242.2	11.3			0.85			40
5	I-I	-59.2	-	-	14.3	-	-				0.83			40
6	I	-61.4	-	- -		-	-							80
9	I	-61.2	-	-	15.7	-	-							100
24	I-I	-57.6	-9.4	-	19.6	-	196.1	13.4	13.4					
32	I-I	-57.4	-	-	15.4	-	258.8					.63	41.7	50
33	I-I	-58.7	-	-	12.6	-	259.7					.38	76.5	70
34	I-I	-61.4	-2.3	-	7.4	-	259.8	3.4						40
35	I-I	-57.9	-	-	16.7	-						-	-	60
36	I-I	-60.6	-	-	17.5	-	245							60
37	I-I	-58.3	-	?2.8	17.1	-	276		12					50
38	I-I	-61.7	-22.1	-	9.3	-		24				.49	46.7	50
39	I-I	-57.1	-	c.3.8	22.5	-			10.8			.54	45.8	50
40	I-I	-58.4	-	-	13.1	-								40
41	I-I	-57.7	-	-	9.8	-	247.5							55
42	I-I	-58.4	-	-	19.2	-						.51	46.8	50
43	I-I	-57.6	-	-	22.8	-								60
44	I-I	-59.8	-	-	17.5	-	263					.59	50.6	50
45	I-I	-57.5	-	-	24.1	-	250.6							60
46	I-I	-61.8	-	-	9.9	-	251.1							30

Chip & Incln.		Phases (at room T°C)	TmCO2	Tmice	Tm Clath	ThCO2	ThTOT	Dcp	Salinity (Tml)	Salinity (TmCl)	Wt% NaCl	δbulk (mic.)	δ(bulk) (Raman) g/cm^3	Mol.Vol. (Raman)	Fill (%CO2)
10-4	1	l-l	-61.5	-	2.3	17				12.4					20
	9	l-l	-65.2	-	-	8.6									
	10	l	-58.4	-	-	13.2									100
	11	l-l	-60.4	-	-	10.6		247.5							50
	12	l-l	-61.2	-10.8	?1.0	10.6			14.8	15					50
	13	l-l	-59.8	-9.3	-	9.7			13.2						50
	14	l-l	-58.9	-	-	12.9		222.7							100
	15	l-l	-58.1	-	-	21		247							100
	16	l-l	-58.9	-3.2	-	13		228.3	5.2			.83			50
	19	l-l	-60.9	?-7.3	-	10.1			10.8						70
	20	l-l	too small	-	-	22.6						.76			60
	21	l-l	-58.5	-	-	19.5						?21mol			
	22	l-l	-59.6	-	<3.4	14.7									60
	23	l-l	-58.4	-	-	19.6									100
	24	l-l	-58.6	-	-	16.3									100
10-E	15	l-l	-61	-	-	14.4									80
	16	l	-57.3	-	0.2	11.2				14.5					90
	17	l	-57.9	-	-	7.4						0.88			100
	18	l	can't see		-	16.4						0.81			100
	20	l	-56	-	- -										100
T4	21	l-l-v	too small to freeze			22.9									
35/A-	22	l-l-v	"			26.3									
	23	l-l-v-sss	"			27.7									
	24	"	"			26.8									
	25	"	"			24.0									

LIST OF REFERENCES

References

Alderton D.H.M, Thompson M., Rankin A.H. and Chryssoulis S.L, **1982.** Developments of the ICP-linked decrepitation technique for the analysis of fluid inclusions in quartz. *Chem.Geol.* 37 203-213

Andrade F.G., Nakashima J. and Podestá P.R., **1986.** Deposito de manganes da Serra dos Buritirama, Pará. **In:** Departamento Nacional da Produção Mineral., *Principais Depositos Minerais do Brasil: Ferro e metais da industria do aco.* Brasilia: DNPM/CVRD. 153-66

Araujo O.J.B., Maia R.G.N., João X.S.J. and Costa J.B.S., **1988.** A megaestruturação Arqueana da folha Serra dos Carajás. 7° *Cong.Latino-Americano Geol.*, Belém, Pará. 324-338

Arndt N.T. and Jenner G.A., **1986.** Crustally contaminated komatiites and basalts from Kambalda, Western Australia *Chem.Geol.* **56.** 229-255

Baker J., van Reenen D.D., van Schalkwyk J.F. and Newton R.C. **1992.** Constraints on the compposition of fluids involved in retrograde anthophyllite formation in the Limpopo Belt, South Africa. *Precambrian Research* 55 327-336

Banks D.A. and Russell M.J., **1992.** Fluid mixing during ore deposition at the Tynagh base-metal deposit, Ireland. *Eur.Jour.Min.* 4 921-931

Barnes H.L., **1979.** (ed.). *Geochemistry of hydrothermal ore deposits.* Wiley and Sons, 798p

Beisiegel V. de Rui and Farias N.F., **1978.** Ocorrências de cobre na Serra dos Carajás. *Anais 30° Cong.Bras.Geol.* 4. Recife. 1419-1430

Bennett D.G. **1990.** *The role of fluids during retrograde metamorphism, associated with thrust zones in the Caledonides of North Norway.* University of Southampton, U.K. Unpublished PhD Thesis.

Bennett D.G. and Barker A.J., **1992.** High salinity fluids - the result of retrograde metamorphism in thrust zones. *Geochim. Cosmochim. Acta* **56.** 81-95

Blake K. and Williams P.J., **1993.** Magnetite-bearing ironstones in the Cloncurry District, West Queensland, Australia and comparisons to the Kiruna iron ores. *MDSG Geol.Soc.London Annual Meeting; December 1993, London: Abstracts volume*

Blake T.S. and Groves D.I., **1987.** Continental rifting and the Archaean-Proterozoic transition. *Geol.* **15.** 229-232

Borisenko A.S., **1977.** Study of the Salt Composition of Solutions of gas-liquid inclusions in minerals by the cryometric method. *Geologiya i Geofizika* 8 16-27

Bottrell S.H. and Yardley B.W.D., **1988.** The composition of a primary granite-derived ore fluid from S.W. England determined by fluid inclusion analysis. *Geochim. Cosmochim. Acta* **52.** 585-588

Brown P.E. and Lamb W.M., **1989.** P-V-T properties of fluids in the system H_2O-CO_2-NaCl: New graphical presentations and implications for fluid inclusion studies. *Geochim. Cosmochim. Acta* **53.** 1209-1221

Cattell A.C. and Taylor R.N., **1990.** Archaean basic magmas. **In:** Hall R.P. and Hughes D.J, *Early Precambrian Basic Magmatism.* New York: Chapman and Hall. 11-39

Collins P.L.F. **1979.** Gas hydrates in CO_2-bearing fluid inclusions and the use of freezing data for estimation of salinity. *Econ.Geol.* 74 1435-1444

Companhia Vale do Rio Doce, **1972.** Distrito ferrifero da Serra dos Carajás. *26° Cong.Bras.Geol.*, Belém, Pará. 78-80

Condie K.C., **1985.** Secular variation in the composition of basalts: an index to mantle evolution. *J.Pet.* 26. 545-563

Condie K.C., **1990.** Geochemical characteristics of Precambrian basaltic greenstones. **In:** Hall R.P. and Hughes D.J, *Early Precambrian Basic Magmatism.* New York: Chapman and Hall. 40-55

Cook N.J. and Halls C., **1991.** Deformation and metamorphism of sulphide ores at Sulitjelma, Norway. *Min.Soc.Gt.Britain and Ireland Winter Conference, Cardiff: Abstracts volume*

Corset J. Dhamelincourt P. and Barbillat J., **1989.** Raman Microscopy. *Chemistry in Britain.* June 1989 612-616

Cox K.G., Bell J.D. and Pankhurst R.J., **1979.** *The Interpretation of Igneous Rocks.* London: Allen and Unwin 450pp

Craig J.R., **1991.** The Metamorphism of Pyrite and Pyritic Ores. *Min.Soc.Gt.Britain and Ireland Winter Conference, Cardiff: Abstracts volume*

Craig J.R. and Vaughan, D.J., **1981.** *Ore Microscopy and Ore Petrography.* Wiley.

Craig J.R. and Vokes F.M., **1993.** The metamorphism of pyrite and pyritic ores: An overview. *Min. Mag.* 57 3-19

Craig J.R. and Vokes F.M., **1992.** Ore mineralogy of the Appalachian-Caledonian stratabound deposits. *Ore Geol.Rev.* 7 77-123

Crawford M.L., **1981.** Phase equilibria in aqueous fluid inclusions. **In:** Hollister L.S. and Crawford M.L. (Eds) *MAC Short Course in Fluid Inclusions: Applications to petrology* Min.Assoc.Canada Short Course Handbook 6 75-100

Crawford M.L., Filer J. and Wood C., **1979.** Saline fluid inclusions associated with retrograde metamorphism. *Bull.Mineral.* 102 562-568

Dardenne M.A., Ferreira Filho C.F. and Meirelles M.R., **1988.** The role of shoshonitic and calc-alkaline suites in the tectonic evolution of the Carajás District, Brazil. *J.South American Earth Sciences.* 1 363-372

Davidson G.J., Large R.R., Kary G.L and Osborne R., **1989.** The deformed iron-formation-hosted Starra and Trough Tank Au-Cu mineralization: A new association from the Proterozoic Eastern Succession of Mount Isa, Austrailia. *Econ.Geol.* 84 135-150

Davis D.W., Lowenstein T.K. and Spencer R.J., **1990.** Melting behaviour of fluid inclusions in laboratory-grown halite crystals in the systems NaCl-H_2O, NaCl-KCl-H_2O, NaCl-$MgCl_2$-H_2O and NaCl-$CaCl_2$-H_2O. *Geochim. et Cosmochim. Acta* 54 591-601

Dhamelincourt P., Beny J.M., Dubessy J. and Poty B. **1979.** Analyse d'inclusions fluides à la microsonde MOLE à effet Raman. *Bull.Mineral.* 102. 600-610

Dilles J.H. and Einaudi M.T., **1992.** Wallrock alteration and hydrothermal flow paths about the Ann-Mason porphyry copper deposit, Nevada - A 6km vertical reconstruction. *Econ.Geol.* 87 1963-2001

Docegeo (Rio Doce Geologia e Mineração), **1982.** *Salobo 3A Copper Deposit.* Docegeo/Companhia Vale do Rio Doce. **Internal Rpt.**

Docegeo (Rio Doce Geologia e Mineração), **1987.** *Lithostratigraphic review of the Carajás District and Southern Pará, Brazil.* **Docegeo Technical Report.**

Docegeo (Rio Doce Geologia e Mineração), **1988.** Revisão Litoestratigrafica da Provincia Mineral de Carajás. **In:** *Provincia Mineral de Carajás - Litostratigrafia e principais depositos minerais: Anais 35° Cong.Bras.Geol.*, Belém, Pará. 11-56

Dorr, J.N.V.II, **1964.** Supergene Iron Ores of Minas Gerais, Brazil. *Econ.Geol.* 59 1203-1240

Dorr, J.N.V.II, **1973.** Iron Formation in South America. *Econ.Geol.* 68 1005-1022.

Dubessy J., **1989.** Advances in COHNS fluid geochemistry based on micro-Raman spectrometric analysis of fluid inclusions. *Eur. Jour. Min.* 1. 517-534

Dubessy J., Audeoud D., Wilkins R. and Kosztolany C., **1982.** The use of the Raman Microprobe Mole in the determination of the electrolytes dissolved in the aqueous phase of fluid inclusions. *Chem. Geol.* 37 137-150

Dubessy J. Boiron M-C., Moisette A., Monnin C. and Sretenskaya N., **1992.** Determinations of water, hydrates and pH in fluid inclusions by micro-Raman spectrometry. *Eur. J. Min.* 4 885-894

Eadington P.J., **1983.** A fluid inclusion investigation of ore formation in a tin-mineralized granite, New England, New South Wales. *Econ.Geol.* 78 1204-1221

Edwards, A.B., **1965.** *Textures of the Ore Minerals and Their Significance.* Aus. Inst. Min. Met. 242pp.

Edwards R. and Atkinson K., **1986.** *Ore deposit geology and its influence on mineral exploration.* London: Chapman and Hall. 466p

Ellis A.J., **1979.** Explored geothermal systems. **In:** Barnes H.L. (Ed.) *Geochemistry of hydrothermal ore deposits.* Wiley and Sons. 632-683

Evans A.M., **1987.** *An introduction to ore geology.* 2nd Edition. Geoscience Texts; Blackwell Scientific Publications.

Ferreira Filho J.C.M. and Danni J.C.M., **1986.** *Geology and Geochemistry of the Bahia Prospect, Copper*

Sulphide Deposit, Carajás District, Brazil. Univ. de Brasilia. **Unpubl.Rpt.**

Ford T.A. and Falk M., **1969.** IR study of hydrogen bonding in sodium chloride dihydrate. *J.Mol.Struct.* 3 445-452

Fournier R.O., **1981.** Application of water chemistry to geothermal to geothermal exploration and reservoir engineering. **In:** Rybach L. and Muffler L.J.P. (Eds) *Geothermal systems: principals and case histories.* Chichester: Wylie and Sons 109-143

Fournier R.O. and Truesdell A.H., **1973.** An empirical Na-K-Ca geothermometer for natural waters. *Geochim. Cosmochim. Acta* 37 1255-1275

Franklin, J.M, Lydon, J.W. and Sangster, D.F., **1981.** Volcanic Associated Massive Sulphide Deposits. *Econ.Geol.* 75th Anniversary Volume. 485-627

Frost, B.R., **1973.** Ferroan gahnite from Quartz-Biotite-Almandine Schist, Wind River Mountains, Wyoming. *Am.Min.* 58 831-834

Gammon J.B., Borcik M., and Holland H.D., **1969.** Potassium-sodium ratios in aqueous solutions and coexisting silica melts. *Science* 63. 179-181

Gibbs A.K. Wirth K.R., Hirata W.K. and Olszewski W.J. **1985.** *Age and composition of the Graõ Pará Group Volcanics, Serra dos Carajás.* 2° Simp.Geol.Amaz., Belém, Pará. 16pp

Giere R., **1989.** Hydrothermal mobility of Ti, Zr and REE: Examples from the Bergell and Adamello contact aureoles (Italy). *Terra Nova* 2. 60-67

Giggenbach W.F., **1988.** Geothermal solute equilibria. Derivation of Na-K-Mg-Ca geoindicators. *Geochim. Cosmochim. Acta* 52 2749-2765

Gill R.O.C., **1979.** Comparative petrogenesis of Archaean and modern low-K tholeiites. A critical review of some geochemical aspects. **In:** Ahrens, L.H. (Ed) *Origin and Distribution of the Elements 2.* Oxford: Pergamon Press. 431-447

Gilligan, J.M., **1990.** *The Geology, Geochemistry and Genesis of Gold Mineralization Associated with Archaean Iron-Formation, Lennox Mine, Zimbabwe.* University of Southampton, U.K. Unpublished PhD Thesis.

Gole M.J., **1981.** Archaean Banded Iron Formations, Yilgarn Block, Western Australia *Econ.Geol.* 76. 1954-1974.

Goodwin A.M., **1973.** Archaean Iron-formations and tectonic basins of the Canadian Shield. *Econ.Geol.* 68. 915-933

Govindaraju, K., 1989. 1989 Comilation of Working Values and Sample Description for 272 Geostandards. *Geostandards Newsletter* 13 1-113

Grant J.A., **1986.** The Isocon Diagram: A simple solution to Gresens' equation for metasomatic alteration.

Econ.Geol. 81. 1976-1982

Gresens R., **1967.** Composition-volume relationships of metasomatism. *Chem.Geol.* 2. 47-55

Gross G.A., **1965.** Geology of iron deposits in Canada. I. General geology and eveluation of iron deposits. *Geol.Surv.Can. Econ.Geol.Rpt.* 22.

Gross G.A., **1980.** A classification of iron-formations based on depositional environments *Can.Min.* 18. 215-222

Gross G.A., **1988.** *Gold Content and Geochemistry of iron formation in Canada.* Geol.Surv.Canada. Special Paper 86-19

Gross G.A. and McLeod C.R., **1980.** A preliminary assessment of the chemical composition of iron-formations in Canada. *Can.Min.* 18. 223-229

Groves D.I., Phillips G.N., Falconer L.J., Houstoun S.M., Ho S.E., Browning P., Dahl N. and McNaughton N.J., **1987.** Evidence for an epigenetic origin for BIF-hosted gold deposits in Greenstone Belts of the Yilgarn Block, Western Australia. **In:** Ho S.E. and Groves D.I. (eds.) Recent advances in understanding Precambrian gold deposits. Univ. Western Australia. Spec.Publ. No.11 167-179

Gustafson L.B., **1979.** Porphyry copper deposits and calc-alkaline volcanism. **In:** McElhinny M.W. (ed). *The earth, its origin, structure and evolution.* London: Academic Press. 427-468

Hall D.L., Sterner S.M. and Bodnar R.J., **1988.** Freezing point depression of some NaCl-KCl-H_2O solutions. *Econ.Geol.* 83 197-202

Hall R.P. and Hughes D.J., **1990.** Basic magmatism and crustal evolution. **In:** Hall R.P. and Hughes D.J., (Eds) *Early Precambrian Basic Magmatism.* New York: Chapman and Hall. 1-7

Hatch F.H., Wells A.K. and Wells M.K., **1972.** *Petrology of Igneous Rocks.* London: George Allen and Unwin.

Haynes F.M., **1985.** Determination of fluid inclusion compositions by sequential freezing. *Econ.Geol.* 80 1436-1439

Heinrich C.A., Andrew A.S. and Wilkins R.W.T., **1989.** A fluid inclusion and stable isotope study of synmetamorphic copper ore formation at Mount Isa, Australia. *Econ.Geol.* 84 529-550

Herzberg G., **1945.** *Molecular spectra and molecular structure, Vol.2. Infrared and Raman spectra of polyatomic molecules.* New York: Van Nostrand Reinhold. 632p

Heyen G., Ramboz C. and Dubessy J., **1982.** Simulation des equilibre de phases dans le system CO_2-CH_4 en dessous se 50°C et de 100 bar. Application aux inclusions fluides. *C.R.Acad.Sc.Paris.* t.294 serie II 203-206.

Hirata W.K., Beisiegel V.R., Bernardelli A.L., Ferias N.F., Saueressig R., Meireles E.M. and Tiexeira J.T., **1982.** *Serra dos Carajás-Pará state: iron, manganese, copper and gold deposits:* Int.Symp.Archaean and Early Proterozoic Geologic Evolution and Metallogeny. 1st, Salvador, Bahia, Brazil. Excursion

Guide. 40-76

Hoffman A.W., **1988.** Chemical differentiation of the earth: The relationship between mantle, continental crust, and oceanic crust *Earth Planet.Sci.Letts.* **90.** 297-314

Holland H.D., **1972.** Granites, solutions and base metal deposits. *Econ.Geol.* 67 281-301

Holloway J.R. **1981.** Compositions and volumes of supercritical fluids in the earth's crust. **In:** Hollister L.S. and Crawford M.L. (Eds) *MAC Short Course in Fluid Inclusions: Applications to petrology* Min. Assoc.Canada Short Course Handbook 6 13-38

Hoppe A., Schobbenhaus C. and Walde D.H.G., **1987.** Precambrian iron-formation in Brazil. **In:** Appel P.W.U. and LaBerge G.L. (Eds.), *Precambrian Iron-formations.* Athens: Theophrustus Publications S.A. 347-390

Hsu L.C., **1968** Selected phase relationships in the system Al-Mn-Fe-Si-O-H: A model for garnet equilibrium. *Jour.Pet.* 9 40-83

Huston D.L. and Large R.R., **1989.** A chemical model for the concentration of gold in volcanogenic massive sulphide deposits. *Ore Geol.Rev.* 4 171-200

Hutchinson R.W., **1979.** *Report on Docegeo copper projects, MM-1, Salobo, and regional geological relationships, Pará, Brazil.* **Internal Technical Rpt.** 17pp

James, H.L., **1955.** Zones of Regional Metamorphism in the Precambrian of Northern Michigan. *Geol. Soc. America Bull.* 66 1455-1488

Jensen L.S., **1976.** *A new cation plot for classifying sub-alkalic volcanic rocks.* Ontario Division of Mines Misc. Paper 66

Kerkhof A.M. van den, **1988** *The system CO_2-CH_4-N_2 in fluid inclusions: theoretical modelling and geological applications.* PhD Thesis. Free University of Amsterdam Press. pp206

Kerkhof A.M. van den and Kisch H.J., **1993.** CH_4-rich inclusions from quartz veins in the Valley-and-Ridge province and the anthracite fields of the Pennsylvania Appalachians-Reply. *Am.Min.* 78 220-224

Kerrich R. and Fyfe W.S., **1981.** The gold carbonate association: source of CO_2 and CO_2 fixation reactions in Archaean lode gold deposits. *Chem.Geol.* 33. 265-294

Kimberley M., **1989.** Nomenclature for Iron Formations *Ore Geol.Rev.* 5. 1-12

Klein, C., **1973.** Changes in Mineral Assemblages with Metamorphism of some Banded Precambrian Iron-Formations. *Econ.Geol.* 68 1075-1088

Klein, C., **1978.** Regional Metamorphism of Proterozoic Iron-Formation, Labrador Trough, Canada. *American Mineralogist* 63 898-912

Klein, C., **1983.** Diagenesis and Metamorphism of Precambrian Banded Iron-Formations. **In:** Trendall,

A.F. and Morris, R.C. (eds), 1983. *Developments in Precambrian Geology 6: Iron-Formation Facts and Problems*. 558pp. Elsevier.

Klewe B. and Pederson B., **1974.** The crystal structure of sodium chloride dihydrate. *Acta Cryst.* 30. 2363-2371

Knauth L.P. and Beunas M.A., **1986.** Isotope geochemistry of fluid inclusions in permian halite, with implications for the isotopic history of ocean water and the origin of saline formation waters. *Geochim. Cosmochim. Acta* 50. 2481-2497

Knutson J., Donnelly T.H., Eadington P.J. and Tonkin D.G., **1992.** Hydrothermal alteration of Middle Proterozoic basalts, Stuart Shelf, South Australia - A possible source for Cu mineralization. *Econ. Geol.* 87 1054-1077

Kwak T.A.P., Brown W.M., Abeysinghe P.B. and Tan T.H., **1986.** Fe solubilities in very highly saline hydrothermal fluids; their relation to zoning in some ore deposits. *Econ.Geol.* 81 447-465

Large R.R., Huston D.L., McGoldrick P.J., Ruxton P.A. and McArthur G., **1989.** Gold distribution and genesis in Australian volcanogenic massive sulphide deposits and their significance for gold transport models. *Econ.Geol.* 84 520-536

Large R.R., McGoldrick P.J., Berry R.F. and Young C.H., **1988.** A tightly folded, gold-rich, massive sulphide deposit: Que River Mine, Tasmania. *Econ.Geol.* 83 681-693

Leake, B.E., **1978.** Nomenclature of amphiboles. *Min.Mag.* 42 533-563.

Lindenmayer Z.G., **1990.** *Salobo Sequence, Carajás, Brazil: Geology, geochemistry and metamorphism.* University of Western Ontario, London, Ontario. Unpubl. PhD Thesis.

Lindenmayer Z.G., Fyfe W. and Machado N., **1988.** Deposito do Salobo; efeitos do metamorphismo e metassomatismo sobre a mineralização. *Anais 35° Cong.Bras.Geol.* Belém. 3. 1243-1250

Machado N, Lindenmayer Z., Krogh T.E. and Lindenmayer D., **1991.** U-Pb geochronology of Archaean magmatism and basement reactivation in the Carajás Area, Amazon Shield, Brazil. *Precambrian Research.* 49. 329-354

Machamer J.F., Tolbert G.E. and L'Esperance R.L., **1991.** The discovery of Serra dos Carajás. *Econ.Geol.* **Monograph 8** 275-285

Maruyama S., Suzuki K. and Liou J.G., **1983.** Greenschist-amphibolite transition equilibria at low pressures. *J.Pet.* 24 583-604

McMillan P.F., **1989.** Raman Spectroscopy in Mineralogy and Geochemistry. *Ann.Rev.Earth Planet.Sci.* 17 255-283

Medeiros Neto F.A. **1987.** Mineralizacoes Characteristiçoes auriferas da area Pojuca: Extração, transporte e deposição a partir de fluidos hidrotermais salinos. *34° Cong.Bras.Geol.*

Medeiros Neto F.A. and Villas J.M.B., **1985.** Geologia da jazida de Cu-Zn do Corpo Quatro 4E-Pojuca,

Serra dos Carajás. *2° Simp.Geol.Amaz.* Belém, Pará. 3 97-112

Meirelles M.R. and Dardenne M.A, **1991.** Vulcanismo basaltico de afinidade shoshinitica em ambiente de arco Arqueano, Groupo Graõ Pará, Serra dos Carajás - Pará. *Rev.Bras.Geosciencias.* 21. 41-50

Meschede M., **1986.** A Method of Discriminating Between Different Types of Mid-ocean Ridge Basalts and Continental Tholeiites with the Nb-Zr-Y Diagram. *Chem. Geol.* 56 207-218

Miyashiro A., **1978.** *Metamorphism and Metamorphic Belts.* London: George Allen and Unwin.

Morris R.C., **1993.** Genetic modelling for Banded Iron-Formation in the Hamersley Group, Pilbara Craton, Western Australia. *Precamb.Res.* 60 243-286

Morton R.L. and Franklin J.M., **1987.** 2-fold classification of Archaean volcanic-associated massive sulphide deposits. *Econ.Geol.* 82. 1057-1063

Murphy P.J. and Roberts S., **in prep.** Laser Raman Spectroscopy of differential partitioning in mixed-gas clathrates in H_2O-CO_2-N_2-CH_4 fluid inclusions: Implications for microthermometry. Submitted to *Geochim. Cosmochim. Acta.*

Nash J.T., **1976.** Fluid inclusion petrology. Data from porphyry copper deposits and applications to exploration. *Geol.Surv.America Prof.Paper* 907-D d1-d15

Nebel M.L., Hutchinson R.W. and Zartman R.E., **1991.** Metamorphism and polygenesis of the Madem Lakkos polymetallic sulphide deposit, Chilkidiki, Greece. *Econ.Geol.* 86 81-105

Nold J.L., **1983.** The Holden Mine, a metamorphosed volcanogenic deposit in the Cascade Range of Washington. *Econ.Geol.* 78 944-953

Oliveira E.P., Winter C.J., Sachs L., Batista J.J, Figueiredo B. and Foster R.P., **1993.** Limiting factors in applying geochemistry to tectonic setting identification in continental areas: implications to the Carajás basic metavolcanics, Brazil. *4° Cong.Bras.Geoquimica.* Brasilia. 20-22

Oliver N.H.S., Cartwright I., Wall V.J. and Golding S.D., **1993.** The stable isotope signature of kilometre-scale fracture-dominated metamorphic fluid pathways, Mary Kathleen, Australia. *J.Met.Geol.* 11 705-720

Olszewski W.J., Gibbs A.K. and Wirth K.R., **1986.** Geochemical and isotopic constraints on the tectonic setting of the Serra dos Carajás Belt, Eastern Pará, Brazil. **In:** De Wit, M.J. and Ashwal L.D. *Workshop on the Tectonic Evolution of Greenstone Belts.* Houston, Texas: Lunar and Planet. Inst. 162-164

Olszewski W.J., Wirth K.R., Gibbs A.K. and Gaudette H.E., **1989.** The age, origin and tectonics of the Graõ Pará Group and associated rocks, Serra dos Carajás, Brazil: Archaean continental volcanism and rifting. *Precambrian Research.* 42. 229-254

Pasteris J.D. and Wopenka B., **1991.** Raman spectra of graphite as indicators of degree of metamorphism. *Can.Min.* 29 1-9

Pearce J.A. and Cann J.R., **1973.** Tectonic setting of basic volcanic rocks determined using trace element analysis. *Earth Planet Sci.Letts.* **19.** 290-300

Phillips G.N., Groves D.I. and Martyn J.E., **1984.** An epigenetic origin for Archaean banded iron-formation-hosted gold deposits. *Econ.Geol.* **79.** 162-171

Pohl W., **1992.** Defining metamorphogenic mineral deposits - an introduction. *Min.Pet.* **45.** 145-152

Potter I.I. and Clynne M.A., **1978.** Solubility of highly soluble salts in aqueous media - Part 1, NaCl, KCl, $CaCl_2$, Na_2SO_4 and K_2SO_4 solubilities to 100°C. *J.Research USGS.* **6** (6) 701-703

Potter I.I, Clynne M.A. and Brown D.L., **1978.** Freezing point depression of aqueous sodium chloride solutions. *Econ.Geol.* **73** 284-285

Raman C.V. and Krishnan K.S., **1928.** A new type of secondary radiation. Nature **121** 501.

Ramboz C., Schnapper D. and Dubessy J., **1985.** The *P-V-T-X-*fO_2 evolution of H_2O-CO_2-CH_4-bearing fluid in a wolframite vein: Reconstruction from fluid inclusion studies. *Geochim. Cosmochim. Acta* **49** 205-219

Ramos J.F., Moura C.A., Melo C.F., Pereira J.L., Serique J.S. and Rodrigues R.M., **1984.** Uma discusão sobre as sequencias sedimentares tidas Formação Rio Fresco, Sudeste do Pará. *33° Cong.Bras.Geol.* Rio de Janeiro. 50-51

Rankama K. and Sahama T.G., **1950.** *Geochemistry.* University of Chicago Press; Chicago.

Rankin A.H., Herrington R.J., Ramsey M.R., Coles B, Christoula M. and Jones E., **1993.** Current developments and applications of ICP-AES techniques for the geochemical analysis of fluid inclusions in minerals. **In:** Maurice Y. (ed.) *Proc. 8th Quadrennial IAGOD symp. E.* Schweitzerbartische Verlagsbuchhandlung (Nagele u Obermiller), D-7000 Stutgart. 183-198.

Rankin A.H., Ramsey M.R., Coles B, Van Langevelde F. and Thomas C.R., **1992.** The composition of hypersaline, iron-rich granitic fluids based on laser-ICP and synchrotron-XRF microprobe analysis of individual inclusion in topaz, Mole Granite, eastern Australia. *Geochim. Cosmochim. Acta* **56** 67-79

Roedder E., **1971.** Metastability in fluid inclusions. *Soc.Mining Geol. Japan* **Spec.Issue 3** (proc.IMA-IAGOD meetings 1970) 327-334

Roedder E., **1984.** *Fluid Inclusions: Reviews in Mineralogy* **12** Min. Soc. America. 646p

Roedder E. and Bodnar R.J., **1980.** Geologic pressure determinations from fluid inclusion studies. *Ann.Rev.Earth Planet.Sci.* **8** 263-301

Rosasco G.J., Roedder E. and Simmons J.H., **1975.** Laser-excited Raman spectroscopy for non-destructive partial analysis of individual phases in fluid inclusions in minerals. *Science* **190.** 557-560

Rollinson H.R., **1992.** Another look at the constant sum problem in geochemistry *Min.Mag.* **56.** 469-476

Rumble D. III, **1976.** *Oxide Minerals: Reviews in Mineralogy* 3 Min. Soc. America. 502p

Sangster D.F., **1972.** Precambrian volcanogenic massive sulphide deposits in Canada: A review. *Geol.Surv.Can.* **Paper 72-22** 40p

Sangster D.F. and Scott S.D., **1976.** Precambrian, stratabound, massive sulphide Cu-Zn-Pb sulphide ores of North America. **In:** Wolf K.H. (ed.) *Handbook of stratabound and stratiform ore deposits* **Vol.6.** Amsterdam: Elsevier Scientific Publishing. 129-222

Saueressig R., **1988.** Deposito de cobre e zinco do Corpo Quatro, Pojuca. *Anais 35° Cong.Bras.Geol.*, Belém, Para. 115-119

Seitz J.C., Pasteris J.D. and Wopenka B., **1987.** Characterization of CO_2-$CHb4_{.H}2_O$ fluid inclusions by microthermometry and laser Raman microprobe spectroscopy: Inferences for clathrate and fluid equilibria. *Geochim. Cosmochim. Acta* **51** 1651-1664

Sena Costa J.B., Teixeira N.P., Lima Pinheiro R.V. and Bemerguy R.L., **1990.** Os sistemas estruturais transcorrentes do Cinturão Itacaiunas na região de Curionópolis, Leste do estado do Pará. *Anais do 36° Cong.Bras.Geol.* **5** Natal. 2345-2357

Shepherd T.J., Rankin A.H and Alderton D.H., **1985.** *A practical guide to fluid inclusion studies.* Blackie and Son Ltd. 239pp

Silva G.G. da, Lima M.J.C., Andrade A.R.F., Issler R.S. and Guimares P., **1974.** Geologia. **In:** *Projeto Radam. Folha SB-22 Tocantins: Geologia, geomorfologia, solos, vegetação e uso potencial da terra.* Rio de Janeiro: Departamento nacional da produção mineral.

Snyder G.L., Hall R.P., Hughes D.J and Ludwig K.R, **1990.** Early Precambrian rocks of the USA. **In:** Hall R.P. and Hughes D.J., (Eds) *Early Precambrian Basaltic Magmatism.* New York: Chapman and Hall. 191-220

Spencer R.J., Møller N. and Weare J.H., **1990.** The prediction of mineral solubilities in natural waters: A chemical equilibrium model for the Na-K-Ca-Mg-Cl-SO_4-H_2O system. *Geochim. Cosmochim. Acta* **54** 575-590

Spry A., **1969.** *Metamorphic textures.* Oxford: Pergamon Press. 350pp

Taylor S.R. and McLennan S.M., **1985.** *The continental crust: its composition and Evolution.* Oxford: Blackwell 312pp

Thompson J.B.Jr., **1972.** Oxides and Sulfides in Regional Metamorphism of Pelitic Schists. *24th Int.Geol.Cong.* Montreal **sec.10 Pt.10** 27-35

Thompson J.F.H., Lang J.R. and Stanley C.R., **1992.** Porphyry deposits in the cordillera of British Columbia. *MDSG Geol.Soc.London Annual Meeting; December 1992, Leicester: Abstracts volume*

Truesdell A.H., **1976.** GEOTHERM, a geothermometric computer programme for hot spring systems. *Proc. 2nd UN Symposium on the development and use of geothermal resources, San Francisco.* 1 LIII-LXXIX

Turner, F.J., **1968.** *Metamorphic Petrology - Mineralogical and Field Aspects.* McGraw-Hill Book Company. 403pp

Turnock A.C. and Trueman D.L., **1990.** Ironstones of mixed sedimentary and hydrothermal origin in the Archaean greenstone belt at Bird Lake, Manitoba. **In:** Spencer R.J. and Ming Chou, I. *Fluid-mineral interactions: A tribute to H.P.Eugster.* The Geochemical Society. 143-155

White D.E., **1974.** Ore forming fluids of diverse origins. *Econ.Geol.* 69. 954-973

Wilkinson J.J., **1990.** The role of metamorphic fluids in the development of the Cornubian orefield - Fluid inclusion evidence from south Cornwall. *Min.Mag.* 54 219-230

Williams P.J., Adshead N.D. and Pendergast W.J., **1993.** Late-orogenic fracturing and metallogeny in metamorphic belts: Examples from the Cloncurry Area, NW Queensland, Australia. *MDSG Geol.Soc.London Annual Meeting; December 1993, London: Abstracts volume*

Williams P.J. and Heinnemann, **1992.** Maramungee: A Proterozoic skarn deposit in the Cloncurry District, Mount Isa Inlier. *Econ.Geol.* 88 1114-1134

Wirth K.R., Gibbs A.K. and Olszewski W.J., **1986.** U-Pb zircon ages of the Graõ Pará Group and Serra dos Carajás granite. *Rev.Bras.Geoscienc.* 16. 195-200.

Wirth K.R., Oliveira E.P, Silva SA J.H., and Tarney J, **1990.** Early Precambrian basic rocks of South America. **In:** Hall R.P. and Hughes D.J., *Early Precambrian Basic Magmatism.* New York: Chapman and Hall. 379-405

Wopenka B. and Pasteris J.D., **1993.** Structural characterization of kerogens to granulite-facies graphite: Applicability of Raman microprobe spectroscopy. *Am.Min.* 78 533-557

Yardley B.W.D., **1989.** *An introduction to metamorphic petrology.* Longman. 248p

Zhang Y-G. and Frantz J.D. **1987.** Determination of the homogenization temperatures and densities of supercritical fluids in the system NaCl-KCl-$CaCl_2$-H_2O using synthetic fluid inclusions. *Chem. Geol.* 64 335-350

Geological Map of the G1C4 Adit, Pojuca Corpo Quatro Cu-Zn Deposit, Carajás, Brazil.

Mapped by C.J.Winter

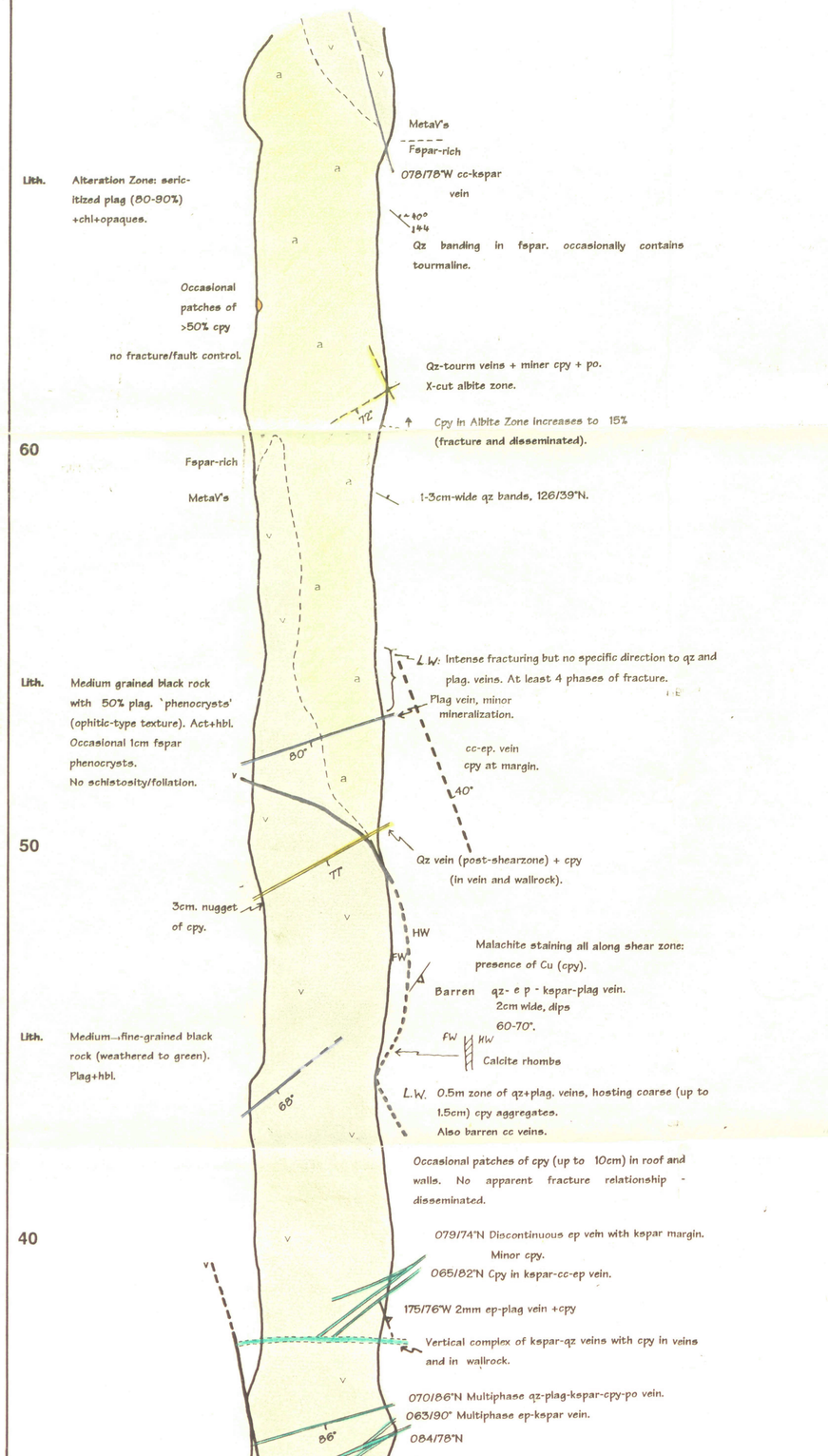

Structure

- Fault: defined, inferred
- Vein: defined, inferred
- Fault with veining
- Bedding
- Lithological Boundary: defined, inferred

Vein mineralogy:

- Quartz
- Calcite
- Plagioclase
- Epidote-Kspar
- Ilmenite
- Chalcopyrite

Abbreviations

amph	-	amphibole
act	-	actinolite
biot	-	biotite
cc	-	calcite
chl	-	chlorite
cpy	-	chalcopyrite
ep	-	epidote
fspar	-	feldspar (undefined)
garn	-	garnet (almandine)
grn	-	grunerite
hbl	-	hornblende
kspar	-	potassium feldspar
mt	-	magnetite
plag	-	plagioclase feldspar
po	-	pyrrhotite
py	-	pyrite
qz	-	quartz
tourm	-	tourmaline

Lithological Divisions

- v — Metavolcanic - fine grained amphibolite
- a — Albite Zone - sericitized plagioclase

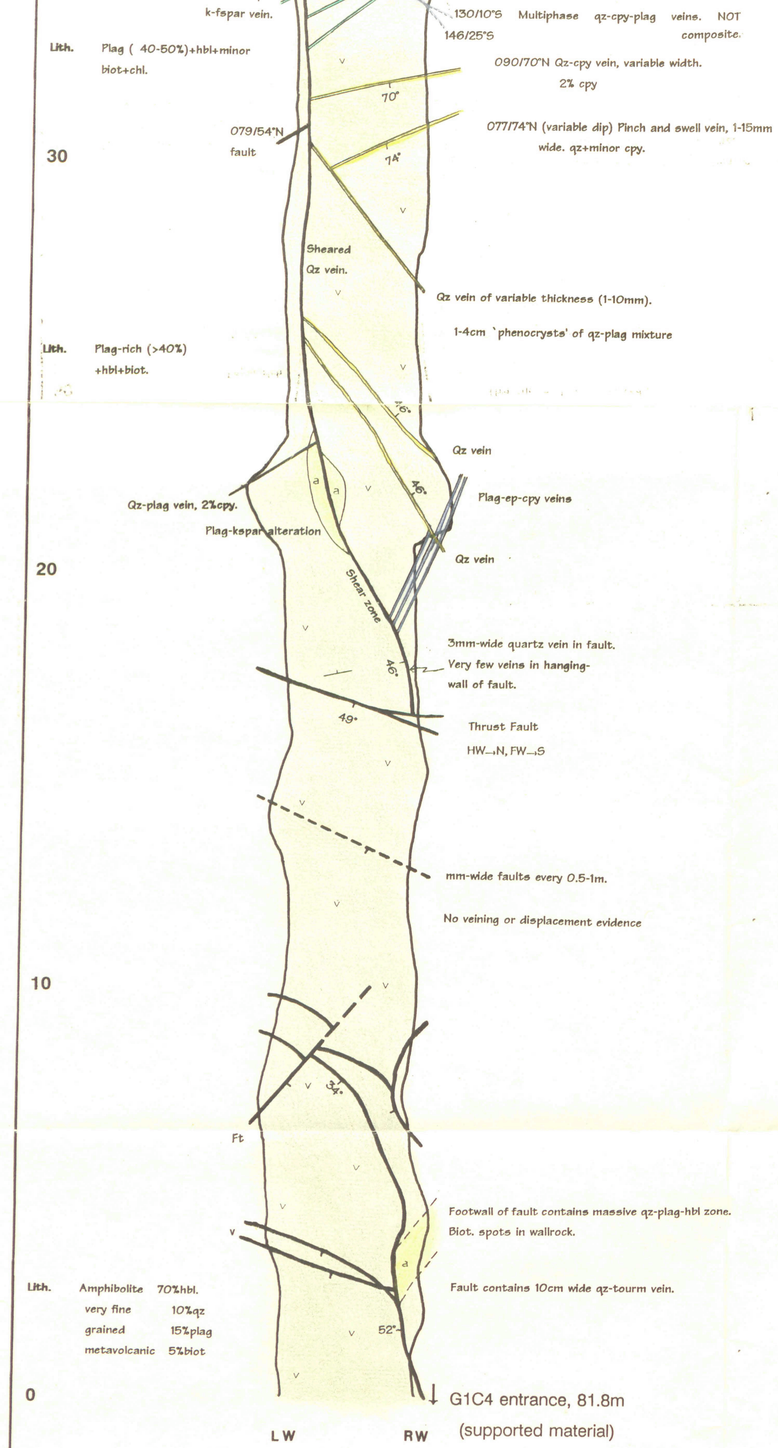

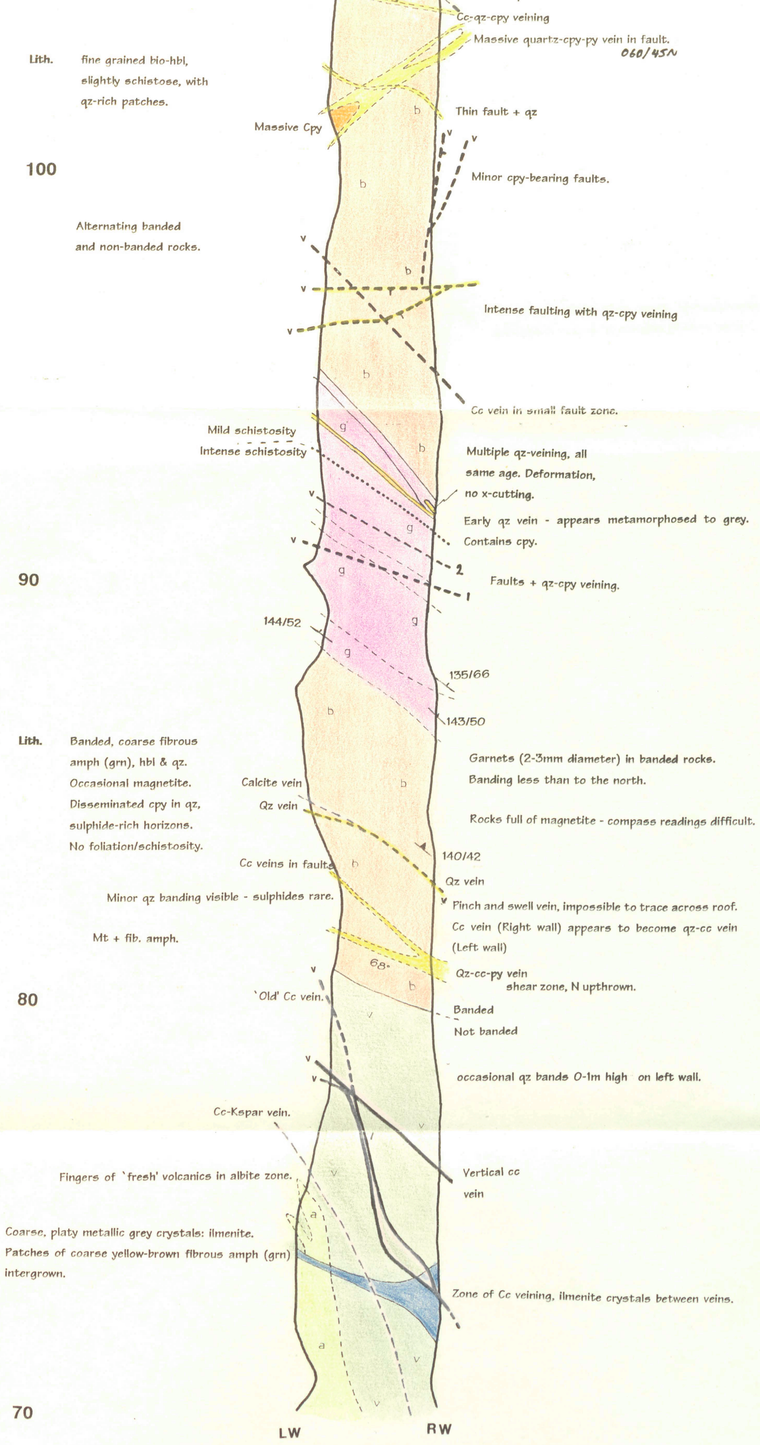

b Rochas Bandadas - Quartz - grunerite - hornblende ± magnetite ± sulphides

g Xistos Granadas - garnet-rich quartz - biotite - garnet schists

q Xistos Quartzos - quartz - biotite - hornblende schists

Fibrous Amphibolite

10 - Distance (m) from start of unsupported section in G1C4. (0m = 81.8m from adit entrance)

LW - Left wall

RW - Right Wall

Scale 1:100

0 m 5